

**Interpretation of vertical and lateral seismic
profiles: some case histories**

by

Ronald Clifford Hinds

Submitted in partial fulfilment of the
requirements for the degree of

Doctorate in Science
(Exploration Geophysics)

in the

**DEPARTMENT OF GEOLOGY,
FACULTY OF SCIENCE,
UNIVERSITY OF PRETORIA**

PRETORIA, SOUTH AFRICA

DECEMBER 1994

ABSTRACT

Interpretation of vertical and lateral seismic profiles: some case histories

By: Ronald C. Hinds
Leader: Prof. C. P. Snyman
Co-leaders: Dr. N. L. Anderson
Dr. R. J. Kleywegt

The integrated processing and interpretation of VSP data are developed to work together in order to enhance the final VSP interpretation. Furthermore, the interpretive processing of the VSP data within the case histories are reviewed along with the incorporation of the final VSP results (both near and far offset data) into the integrated geological/geophysical interpretations presented in the case studies. This thesis has attempted to personify the term "interpreter/processor" as first highlighted in Hardage (1985).

The case histories pertain to oil and gas exploration in carbonate reef and sandstones in the Western Canadian Sedimentary Basin (WCSB). The Lanaway case history (Hinds et al., 1994a) pertains to the exploration of the Lanaway/Garrington oil field located in central Alberta, Canada. The surface seismic interpretation over the reef crest differed dramatically from the isopach of the reef-encasing shales derived from the geological logs of a borehole drilled into the reef crest. To understand the discrepancy, a VSP survey was performed and the data were interpretatively processed. The results were integrated with the known geology of the field area to uncover possible reasons for the surface seismic anomaly.

The Ricinus case history (Hinds et al., 1993c) is a study in reef hunting within the Ricinus

field in central Alberta, Canada, using the far offset VSP survey. Existing surface seismic was used to infer that a well drilled into the interpreted North-east corner of the Ricinus reef would be successful in penetrating oil bearing carbonate reef. The well was drilled; however, the well missed the reef and a near and far offset VSP survey was used to seismically image possible reef buildups in an area around the well.

The Fort St. John Graben case history (Hinds et al., 1991a; Hinds et al., 1993a) highlights exploration of a gas-filled channel sandstone using near and far offset (lateral) VSP surveys. An exploration well was drilled within the study area which intersected the target zone sandstone (the basal Kiskatinaw of the Upper Carboniferous). The target sandstone had a high shale content and was not reservoir quality. A near offset and two far offset VSP surveys were run in the exploration well to image out to a distance of 350 m to the North-west and to the East of the well. The VSP, surface seismic and geology results (from the geological logs of the exploration and surrounding wells) are integrated to infer a clearer picture of the sand/shale relationships of the basal Kiskatinaw and detailed faulting of the Carboniferous strata around the well and within the surface seismic line area.

The Simonette field case history (Hinds et al., 1991b; Hinds et al., 1993b) involves using VSP results to image the slope of a low-relief carbonate reef. The low-relief reef examined using the VSP data is located at the extreme end of a North-east reef spur of the Simonette Reef located in North-west Alberta, Canada. An exploration well drilled in the low-relief reef penetrated the edge of the reef. The VSP surveys were run in order to infer details of the reef slope. The interpretation of the VSP data was integrated with all other exploration data to infer the location of the crest of the low-relief reef and to assist in determining whether to whipstock the exploration well or not.

Samevatting

Interpretasie van vertikale en laterale seismiese profiele: enkele gevallestudies

Deur: Ronald C. Hinds

Leier: Prof. C. P. Snyman

Mede-leiers: Dr. N. L. Anderson

Dr. R. J. Kleywegt

Die geïntegreerde verwerking en interpretasie van vertikale seismiese profileringsdata (VSP) word ontwikkel om saam te werk ten einde die finale VSP - interpretasie te verbeter. Verder word 'n oorsig gegee van die interpretatiewe prosessering van VSP - gegewens aan die hand van gevalle - studies waarin die finale VSP - resultate (naby - en verafstande) as 'n geïntegreerde geologiese\ geofisiese interpretasie gegee word. Die proefskrif poog ook om die term "interpreteerder\ prosesseerder" soos deur Hardage (1985) uitgelig, te verpersoonlik.

Die gevallestudies het betrekking op olie- en gaseksplorاسie in karbonaatrief en sandsteen in die Wes - Kanadese Sedimentere Kom (WCSB). Die Lanaway - geval (Hinds et al., 1994a) verwys na die eksplorاسie van die Lanaway\Garrington olieveld in Sentraal - Alberta , Kanada. Die oppervlak - seismiese interpretasie oor die rifkruin het dramatiese verskil van die isopag van die skalies wat die rif omsluit, soos verkry van die geologiese staat van 'n boorgat in die rifkruin. Om die verskil te verstaan is 'n VSP - opname gemaak en die gegewens is interpretatief verwerk. Die resultate is geïntegreer met die bekende geologie van die gebied

om moontlike verklarings te vind vir die oppervlak - seismiese anomalie.

Die Ricinus - geval (Hinds et al., 1993c) is 'n studie in rifopsoring in die Ricinus - veld in Sentraal - Alberta, Kanada, waarin 'n verafstand VSP - opname gebruik is. Bestaande oppervlak - seismiese gegewens is gebruik om af te lei dat 'n boorgat in die noordoostelike hoek van die Ricinus - rif oliedraende karbonaatrief sou tref. Die boorgat het egter die rif gemis en naby - en verafstand VSP - opnames is gebruik om moontlike rif - opbou naby die boorgat seismies af te beeld.

Die Fort St. John Graben - gevallestudie (Hinds et al., 1991a; Hinds et al., 1993a) belig die eksplorاسie van 'n gasge vulde kanaalsandsteen deur middel van naby - en verafstand VSP opnames. 'n Eksplorاسieboorgat in die studiegebied het die teiken sandsteensone (die onderste Kiskatinaw van die Bo - Karboon) getref, maar die sandsteensone het 'n hoë skalie - inhoud en was nie van reservoir gehalte nie. 'n Naby - en twee verafstand VSP - opnames is in die eksplorاسie - boorgat gemaak om die geologie tot op 'n afstand van 350m noordwes en oos van die boorgat vas te stel. Die resultate van VSP -, oppervlak - seismiese en geologiese gegewens (van geologiese state van die eksplorاسie - en omliggende boorgate) is geïntegreer om 'n duidelike beeld af te lei van die sandsteen\skalie - verhouding van die onderste Kiskatinaw en van detail verskuiwings van die Karboon - strata rondom die boorgat en naby die oppervlak - seismiese lyn.

Die Simonetteveld - gevallestudie (Hinds et al., 1991b; Hinds et al., 1993b) behels die gebruik van VSP - resultate om die helling van 'n lae - reliëf karbonaat vas te stel. Die lae - reliëf rif wat deur middel van VSP - opnames ondersoek is, is geleë aan die einde van 'n noordoostelike rif - uitloper van die Simonette - rif in Noorwes - Alberta, Kanada 'n

Eksplorasiëboorgat in die lae - reliëf rif het die rand van die rif getref. Die VSP - opname is gedoen om die besonderhede van die rihelling af te lei. Die interpretasie van die VSP - data is geintegreer met al die ander eksplorasiëgegewens om die kruin van die lae - reliëf rif vas te stel en om te help in die besluit of die eksplorasiëboorgat gedeflekteer moet word of nie.

TABLE OF CONTENTS

CHAPTER 1

INTRODUCTION

| | | |
|-------|--|----|
| 1.1 | Vertical seismic profiling (VSP) | 1 |
| 1.2 | Aims and objectives of this study | 3 |
| 1.3 | Acknowledgements | 5 |
| 1.4 | VSP fundamentals | 7 |
| 1.4.1 | Near and far offset (lateral) VSP surveys | 7 |
| 1.4.2 | Primary and multiple up- and downgoing waves | 9 |
| 1.4.3 | Far offset geometries | 21 |

CHAPTER 2

INTERPRETIVE PROCESSING

| | | |
|---------|--|----|
| 2.1 | Processing runstreams | 38 |
| 2.2 | Near offset data processing IPP's | 41 |
| 2.2.1 | Separation of up- and downgoing waves | 41 |
| 2.2.2 | Median filtering | 43 |
| 2.2.2.1 | Review of the median filter | 45 |
| 2.2.2.2 | Median filtering and multiple contaminated VSP | 46 |

| | | |
|-----------|--|-----|
| | data | |
| 2.2.2.3 | Median filtering and tubewave contaminated data | 51 |
| 2.2.2.4 | Difference panels to aid in filter length | 53 |
| | determination | |
| 2.2.3 | Karhunen-Loeve (K-L) filtering | 55 |
| 2.2.3.1 | Review of the K-L transform | 57 |
| 2.2.3.2 | K-L filtering and multiple contaminated data | 59 |
| 2.2.4 | 2-D Fourier transform filtering | 61 |
| 2.2.4.1 | Review of F-K filtering | 62 |
| 2.2.4.2 | F-K filtering and multiple contaminated VSP data | 67 |
| 2.2.4.3 | F-K filtering and tubewave contaminated VSP data | 79 |
| 2.2.4.4 | F-K filtering in other wavefield separation | 84 |
| | methods | |
| 2.2.4.5 | F-K filtering using interactive screen processing | 84 |
| 2.2.4.5.1 | Using interactive F-K filtering to wavefield | 86 |
| | separate | |
| 2.2.4.5.2 | The effect of changes in the F-K mute zones | 91 |
| 2.2.5 | τ -P filtering | 99 |
| 2.2.5.1 | Review of τ -P filtering | 101 |
| 2.2.5.2 | Route A: τ -P transformation on only the upgoing | 104 |
| | events | |
| 2.2.5.3 | Route B: Subtraction of $Z_{\text{down}}(\text{FRT})$ from the | 108 |
| | $Z(\text{FRT})$ data | |
| 2.2.5.4 | Route C: τ -P spatial interpolation during | 108 |

| | | |
|---------|---|-----|
| | wavefield separation | |
| 2.2.5.5 | Route D: τ -P spatial interpolation of Z(FRT) before wavefield separation | 114 |
| 2.2.5.6 | Future directions for τ -P filtering in wavefield separation | 118 |
| 2.2.6 | VSP deconvolution and corridor stacks | 120 |
| 2.2.6.1 | Deconvolution IPP | 121 |
| 2.2.6.2 | Corridor stack IPP's | 123 |
| 2.2.6.3 | $Z_{up}(+TT)$ Corridor stack IPP | 125 |
| 2.2.6.4 | $Z_{up(decon)}(+TT)$ Corridor stack IPP | 128 |
| 2.3 | Far offset data processing IPP's | 131 |
| 2.3.1 | Time invariant polarization: isolation of the downgoing P-wave | 133 |
| 2.3.2 | Time variant polarization: isolation of the upgoing P-wave | 138 |
| 2.3.3 | VSP-CDP transformation and migration | 142 |
| 2.3.4 | Far offset deconvolution | 144 |
| 2.3.5 | Problematic far offset interpretive processing | 150 |
| 2.3.5.1 | Time variant polarization of the Ricinus case study data | 152 |
| 2.3.5.2 | Far offset deconvolution of the Ricinus case study data | 158 |
| 2.4 | Integrated displays | 162 |

| | | |
|-------|---------------------------------------|-----|
| 2.4.1 | Integrated Log Display (ILD) | 162 |
| 2.4.2 | Integrated Seismic Display (ISD) | 165 |
| 2.4.3 | Integrated Interpretive Display (IID) | 165 |

CHAPTER 3

THE LANAWAY FIELD CASE STUDY

| | | |
|-------|---|-----|
| 3.1 | Carbonate reef development in the Western Canadian Sedimentary Basin | 175 |
| 3.1.1 | Lanaway Field | 178 |
| 3.2 | Well Nomenclature | 180 |
| 3.3 | Lanaway Field (at the VSP well) | 181 |
| 3.4 | VSP data acquisition | 186 |
| 3.5 | VSP interpretive processing | 190 |
| 3.5.1 | P-wave separation to output $Z_{up}(+TT)$ data | 191 |
| 3.5.2 | VSP deconvolution | 193 |
| 3.5.3 | Inside and outside corridor stacks | 196 |
| 3.6 | Integrated interpretation | 199 |
| 3.7 | Discussion on integrated interpretation | 211 |

CHAPTER 4

THE RICINUS FIELD CASE STUDY

| | | |
|-------|--|-----|
| 4.1 | The Ricinus Field | 215 |
| 4.2 | Ricinus Leduc reef | 218 |
| 4.3 | VSP data acquisition | 222 |
| 4.4 | Interpretive processing of near offset (199 m) VSP data | 225 |
| 4.4.1 | Upgoing P-wave event separation | 225 |
| 4.4.2 | VSP deconvolution | 229 |
| 4.4.3 | Inside and outside corridor stacks | 233 |
| 4.5 | Interpretive processing of the far offset (1100 m) VSP data | 236 |
| 4.5.1 | Hodogram-based rotation | 238 |
| 4.5.2 | Time-variant model-based rotation | 241 |
| 4.5.3 | Deconvolution of the far offset data | 245 |
| 4.5.4 | VSP-CDP mapping | 247 |
| 4.6 | Integrated interpretation | 252 |
| 4.7 | Interpretation discussion | 254 |

CHAPTER 5

CASE STUDY OF THE FORT ST. JOHN GRABEN AREA

| | | |
|-------|---|-----|
| 5.1 | Introduction | 258 |
| 5.2 | Geological overview | 262 |
| 5.2.1 | Tectonic and depositional history of the Peace River Embayment | 262 |
| 5.2.2 | Lower Carboniferous: Fort St. John Graben Area | 266 |
| 5.3 | Original interpretation and well results | 271 |
| 5.4 | VSP interpretation | 275 |
| 5.5 | Near offset (149 m) VSP interpretive processing | 276 |
| 5.5.1 | P-wave event separation | 277 |
| 5.5.2 | Near offset VSP deconvolution | 279 |
| 5.5.3 | Inside and outside corridor stacks | 281 |
| 5.6 | Far offset VSP interpretive processing | 284 |
| 5.6.1 | Far offset data from offset FSJG1 | 284 |
| 5.6.2 | Hodogram-based rotation: offset FSJG1 | 285 |
| 5.6.3 | Time-variant model-based rotation: offset FSJG1 | 288 |
| 5.6.4 | VSP-CDP mapping: offset FSJG1 | 290 |
| 5.6.5 | Far offset data from offset FSJG2 | 292 |
| 5.7 | Integrated interpretation | 297 |
| 5.8 | Conclusion | 302 |

CHAPTER 6

SIMONETTE REEF CASE HISTORY

| | | |
|-------|---|-----|
| 6.1 | Simonette Field | 306 |
| 6.2 | Simonette low-relief reef | 312 |
| 6.3 | VSP interpretation | 316 |
| 6.4 | Near offset (252 m) VSP interpretive processing | 318 |
| 6.4.1 | P-wave separation | 318 |
| 6.4.2 | Near offset VSP deconvolution | 320 |
| 6.4.3 | Inside and outside corridor stacks | 323 |
| 6.5 | Interpretive processing of the far offset | 326 |
| | VSP data | |
| 6.5.1 | Hodogram based rotation | 327 |
| 6.5.2 | Time-variant model-based rotation | 329 |
| 6.5.3 | VSP-CDP mapping of the far offset VSP data | 331 |
| 6.6 | Integrated interpretive display | 336 |
| 6.7 | Conclusions | 340 |

CHAPTER 7

| | | |
|--|-----------------------------|-----|
| | Conclusions and discussions | 341 |
|--|-----------------------------|-----|

APPENDIX

| | | |
|-----|---|------------|
| A.1 | Median filtering | 347 |
| A.2 | Karhunen-Loeve (K-L) filtering | 349 |
| A.3 | F-K filtering | 352 |
| A.4 | τ -P filtering | 354 |
| A.5 | VSP deconvolution | 356 |
| A.6 | Hodogram-based single angle polarizations | 359 |
| A.7 | Time-variant polarization | |
| | REFERENCES | 361 |

LIST OF FIGURES

| | | |
|------------|---|----|
| Figure 1.1 | The field layout of the (zero) near and far offset VSP surveys (from Hinds et al., 1989a). | 8 |
| Figure 1.2 | The up- and downgoing waves propagating to the wellbore geophone sonde can be compressional P-waves that vibrate in the direction of travel or Shear SV- or SH-waves that vibrate normal to the direction of travel, either in the plane of the source and receiver or out of the plane (from Hinds et al., 1989a). | 10 |
| Figure 1.3 | Examples of the up- and downgoing raypaths (A) and depth-traveltime diagrams (B) for both primary and multiple reflections (from Hinds et al., 1989a). | 11 |
| Figure 1.4 | The near offset data correction used to place the data into pseudo-two-way traveltime (+TT). | 13 |
| Figure 1.5 | Upgoing wave events in (+TT) time (left) and downgoing waves in (-TT) time (right) are displaced to align the upgoing primary event generated at the depth Z_2 (labelled U-P on the left) with the horizontally aligned event first break curve (labelled D-P on the right; from Hinds et al., 1989a). | 15 |
| Figure 1.6 | The constant time shift between the up- and downgoing primaries and multiples for the surface-generated (A) and interbed multiples (Hardage, 1985). | 17 |
| Figure 1.7 | Synthetic VSP seismograms illustrating surface generated (panel 1) and interbed (panel 2) up- and downgoing multiple events (from Hinds et al., 1994c). | 19 |
| Figure 1.8 | The splitting of the downgoing shear wave into a fast and slow (polarized) shear waves due to linear cracks. | 22 |

| | | |
|-------------|---|----|
| Figure 1.9 | The location of a fault that could cause near offset VSP downgoing waves to be recorded on all three channels, X , Y and Z . | 23 |
| Figure 1.10 | The orthogonal coordinate system of the local X , Y , and Z geophones along with the coordinate axis (HMIN , HMAX , Z' and HMAX') that will be used as the principal axis in the hodogram (non-time variant) analysis (from Hinds et al., 1989a) | 25 |
| Figure 1.11 | For the case of a deviated borehole, the triaxial geophone package receives contributions of P-, SV-, and SH- waves on all geophones. | 27 |
| Figure 1.12 | The geometry for time-variant rotations. | 28 |
| Figure 1.13 | Synthetic VSP seismograms for the up- and downgoing primary and surface-generated multiple events for offsets of 0, 200, 400, 600 and 800 m (panel 1-5, respectively). | 31 |
| Figure 1.14 | Synthetic VSP seismograms for the up- and downgoing primary and interbed generated multiple events for offsets of 0, 200, 400, 600 and 800 m (panel 1-5, respectively). | 32 |
| Figure 2.1 | Wavefield separation IPP of the Fort St. John Graben case study (Hinds et al., 1993a) data using the median filter and subtraction method (Hinds et al., 1989a). | 47 |
| Figure 2.2 | Wavefield separation IPP of the tubewave contaminated data using the median filter and subtraction method (Hinds et al., 1989a). | 52 |
| Figure 2.3 | Downgoing event panels separated from Z(-TT) data using a 3, 5, 7, 9 and 11 point median filter (panels 1-5, respectively). | 54 |

| | | |
|-------------|--|----|
| Figure 2.4 | Wavefield separation IPP of the Fort St. John Graben case study (Hinds et al., 1993a) data using the K-L filter and subtraction method (Hinds et al., 1986). | 60 |
| Figure 2.5 | Depth-FRT time and F-K domain plots for the Fort St. John Graben case study (Hinds et al., 1993a) near offset data. | 64 |
| Figure 2.6 | Categorization of the types of F-K mutes. | 66 |
| Figure 2.7 | $Z(\mathbf{FRT})$ and $Z_{up}(\mathbf{FRT})$ data wavefield separated using the median filter and various F-K operations for the Fort St. John Graben data (Hinds et al., 1993a) near offset multiple contaminated data. | 68 |
| Figure 2.8 | F-K plot of the $Z(\mathbf{FRT})$ Fort St. John Graben case study data (Hinds et al., 1993a) shown in panel 1 of Figure 2.7. | 69 |
| Figure 2.9 | F-K plot of the median filter and subtraction method derived $Z_{up}(\mathbf{FRT})$ data (shown in panel 2 of Figure 2.7). | 71 |
| Figure 2.10 | F-K plot of the $Z_{up}(\mathbf{FRT})$ data shown in panel 3 of Figure 2.7. | 73 |
| Figure 2.11 | F-K plot of the $Z_{up}(\mathbf{FRT})$ data shown in panel 4 of Figure 2.7. | 74 |
| Figure 2.12 | F-K plot of the $Z_{up}(\mathbf{FRT})$ data shown in panel 5 of Figure 2.7. | 76 |
| Figure 2.13 | F-K plot of the $Z_{up}(\mathbf{FRT})$ data shown in panel 6 of Figure 2.7. | 77 |
| Figure 2.14 | F-K based wavefield separation IPP of the tubewave contaminated data using surgical muting of both the downgoing P-wave and tubewave F-K events. | 80 |
| Figure 2.15 | F-K based wavefield separation IPP of the tubewave contaminated data using F-K quadrant attenuation. | 81 |

| | | |
|-------------|---|----|
| Figure 2.16 | Z(FRT) (panel 1) and Z_{up}(FRT) wavefield separated data using the median filter plus subtraction method (panel 2) and the various F-K muting methods (panels 3-6) on the Z(FRT) tube wave contaminated data. | 83 |
| Figure 2.17 | F-K plot of data resulting from the application of F-K surgical muting to the median filter-based wavefield separation results (prefiltered data is shown in panel 6 of Figure 2.2). | 85 |
| Figure 2.18 | Single operation interpretive processing initial screen display showing the input Z(FRT) data of the Fort St. John Graben case study (Hinds et al., 1993a). | 88 |
| Figure 2.19 | F-K plot of the data shown in Figure 2.18. | 89 |
| Figure 2.20 | The "results" interactive processing display following the muting (reject filtering) of the F-K data inside the mute polygon shown in Figure 2.19. | 90 |
| Figure 2.21 | The Fort St. John Graben Z_{up}(FRT) data (Hinds et al., 1993a) resulting from median filter-based wavefield separation (plus subtraction). | 93 |
| Figure 2.22 | F-K plot of the data shown in Figure 2.19 illustrating the surgical mute reject polygons enveloping both the up- and downgoing F-K events (aliased and non-aliased portions included). | 94 |
| Figure 2.23 | The filtered output of the data in Figure 2.21 following the application of the F-K polygon surgical mutes shown in Figure 2.22. | 96 |
| Figure 2.24 | F-K plot of the data shown in Figure 2.21 illustrating the surgical mute reject polygons enveloping both the up- and downgoing tubewave F-K events (aliased and non-aliased portions included), however, excluding the muting of any upgoing P-wave F-K events. | 97 |

| | | |
|-------------|--|-----|
| Figure 2.25 | The filtered output of the data in Figure 2.21 after the application of the polygon surgical mutes shown in the F-K plot of Figure 2.24. | 98 |
| Figure 2.26 | The concept of the forward and inverse τ - P transform (after Hardage, 1985). | 102 |
| Figure 2.27 | τ - P (route A) based wavefield separation IPP of the Fort St. John Graben (Hinds et al., 1993a) multiple contaminated data. | 105 |
| Figure 2.28 | The equivalent F-K surgical mute pass zone to the τ - P filter used to create the resultant data in panel 3 of Figure 2.27. | 107 |
| Figure 2.29 | τ - P (route B) based wavefield separation IPP of the tubewave contaminated data using τ - P downgoing event separation and then subtraction of the $Z_{\text{down}}(\mathbf{FRT})$ from the $Z(\mathbf{FRT})$ to output the $Z_{\text{up}}(\mathbf{FRT})$ data. | 109 |
| Figure 2.30 | F-K plot of the tubewave contaminated data showing the aliased tubewave F-K event intersecting (at the crossing of the red lines) the upgoing P-wave F-K event at 0.00833 m^{-1} spatial frequency (K) and 37 hz. | 111 |
| Figure 2.31 | τ - P (route C) wavefield separation IPP using τ - P upgoing event separation on $Z(\mathbf{FRT})$ with 30 m trace separation and inverse τ - P transformation using trace interpolation to create 15 m trace spacing. | 112 |
| Figure 2.32 | F-K plot of the interpolated tubewave contaminated $Z_{\text{up}(\text{interp})}(\mathbf{FRT})$ data where the aliased tubewave F-K event intersects the upgoing P-wave F-K event at 0.00833 m^{-1} spatial frequency (K) and 37 hz. | 113 |
| Figure 2.33 | τ - P based wavefield separation IPP of the tubewave contaminated data using τ - P upgoing wave isolation (filtering out P values outside the range of the upgoing P-wave events). | 115 |

| | | |
|--------------|--|-----|
| Figure 2.34A | Panels 1 to 4 of the τ - P based wavefield separation IPP using the interpolated $Z(\text{FRT})$ tubewave contaminated data. | 116 |
| Figure 2.34B | Panels 5 to 7 of the τ - P based wavefield separation IPP using the interpolated $Z(\text{FRT})$ tubewave contaminated data. | 117 |
| Figure 2.35 | F-K plot of the interpolated $Z(\text{FRT})$ data shown in panel 1 of Figure 2.34. | 119 |
| Figure 2.36 | Deconvolution IPP for the Fort St. John Graben data (Hinds et al., 1993a). | 122 |
| Figure 2.37 | The schematic definition of the outside and inside corridor stack. | 124 |
| Figure 2.38 | Ray and depth/time plots, $Z_{\text{down}}(-\text{TT})$ and $Z_{\text{up}}(+\text{TT})$, showing the top and bottom generating interfaces for interbed multiples (modified from Hinds et al., 1989a). | 126 |
| Figure 2.39 | Corridor stack IPP of the Fort. ST John Graben $Z_{\text{up}}(+\text{TT})$ data (Hinds et al., 1993a). | 127 |
| Figure 2.40 | Corridor stack IPP of the Fort. ST John Graben $Z_{\text{up}(\text{decon})}(+\text{TT})$ data (Hinds et al., 1993a). | 129 |
| Figure 2.41 | Hodogram-based polarization IPP for the Fort St. John Graben (FSJG1) far offset data (Hinds et al., 1993a). | 135 |
| Figure 2.42 | The reflection angle for upgoing raypaths emerging at the geophone at A from deeper interfaces decreases. | 139 |
| Figure 2.43 | Time-variant polarization IPP for the Fort St. John Graben (FSJG1) far offset data (Hinds et al., 1993a). | 140 |
| Figure 2.44 | VSP-CDP and Kirchhoff migration IPP for the Fort St. John Graben (FSJG1) far offset data (Hinds et al., 1993a). | 143 |

| | | |
|-------------|--|-----|
| Figure 2.45 | Hodogram-based polarization IPP for the Fort St. John Graben (FSJG2) far offset data (Hinds et al., 1993a). | 145 |
| Figure 2.46 | Time-variant polarization IPP for the Fort St. John Graben (FSJG2) far offset data (Hinds et al., 1993a). | 146 |
| Figure 2.47 | VSP-CDP and Kirchhoff migration IPP for the Fort St. John Graben FSJG2 far offset data (Hinds et al., 1993a). | 147 |
| Figure 2.48 | VSP-CDP and migration IPP for the Simonette far-offset non-deconvolved data (Hinds et al., 1993b). | 149 |
| Figure 2.49 | VSP-CDP and Kirchhoff migration IPP for the Simonette far-offset deconvolved data (Hinds et al., 1993b). | 151 |
| Figure 2.50 | Time-variant polarization IPP for the Ricinus data (Hinds et al., 1989a; Hinds et al., 1994b) using the example far-offset processing initially presented in the "processing runstreams" section of chapter 2. | 153 |
| Figure 2.51 | VSP-CDP IPP for the Ricinus data (Hinds et al., 1989a; Hinds et al., 1993c) using the Z''_{up} data shown in Figure 2.50. | 154 |
| Figure 2.52 | Modified time-variant polarization and wavefield separation IPP for the Ricinus data (Hinds et al., 1993c) following processing decisions made using interpretive processing. | 156 |
| Figure 2.53 | VSP-CDP IPP for the Ricinus data (Hinds et al., 1989a; Hinds et al., 1994b) using the Z''_{up} data shown in Figure 2.52. | 157 |
| Figure 2.54 | VSP-CDP IPP for the Ricinus data (Hinds et al., 1994b) with the Z''_{up} data shown in Figure 2.51 as input and data enhancement using a 9-point median filter. | 159 |

| | | |
|-------------|---|-----|
| Figure 2.55 | VSP-CDP IPP for the Ricinus data (Hinds et al., 1994b) with the Z''_{up} data shown in Figure 2.51 as input and data enhancement using a 11-point median filter. | 160 |
| Figure 2.56 | Far offset deconvolution IPP for the Ricinus data (Hinds et al., 1994b).a Note the deconvolution induced noise by comparing panels 4 and 5. | 161 |
| Figure 2.57 | VSP-CDP IPP for the Ricinus $Z''_{up(decon)}(+TT)$ data (Hinds et al., 1994b). | 163 |
| Figure 2.58 | Integrated log display (ILD) for the Ricinus data (Hinds et al., 1989a; Hinds et al., 1994b). | 164 |
| Figure 2.59 | Integrated seismic display (ISD) for the Ricinus case study data (Hinds et al., 1989a; Hinds et al., 1994b). | 166 |
| Figure 2.60 | Integrated Interpretive Display (IID) of the Lanaway case study data (Hinds et al., 1989a; Hinds et al., 1994a). | 167 |
| Figure 3.1A | Stratigraphy from the Quaternary (Cenozoic) to the Upper Jurassic (Mesozoic) periods of the Central Plains area of the Western Canada Sedimentary Basin (after AGAT Laboratories, 1988; Anderson et al., 1989d; Hinds et al., 1994a and c). | 171 |
| Figure 3.1B | Stratigraphy from the Upper Jurassic (Mesozoic) to the Upper Devonian (Paleozoic) periods of the Central Plains area of the Western Canada Sedimentary Basin (after AGAT Laboratories, 1988; Anderson et al., 1989d; Hinds et al., 1994a and c) | 172 |
| Figure 3.1C | Stratigraphy from the Upper Carboniferous (Paleozoic) period to the Precambrian of the Central Plains area of Western Canada Sedimentary Basin (after AGAT Laboratories, 1988; Anderson et al., 1989d; and Hinds et al., 1994a and c) | 173 |

| | | |
|-------------|---|-----|
| Figure 3.2 | Regional location map of the Lanaway study area (with permission of Talisman Resources Inc.; from Hinds et al., 1994a and 1994c). | 174 |
| Figure 3.3 | Detailed map of the Lanaway study area displaying the seismic section traverse for the seismic data shown in Figures 3.7, 3.8, 3.14 and 3.15 and the locations of the wells used in the geological cross-sections shown in Figures 3.4, 3.5 and 3.6 (from Hinds et al., 1994a and 1994c). | 179 |
| Figure 3.4 | West-east geologic cross-section A-A' (refer to Figure 3.3 for well locations). | 182 |
| Figure 3.5 | West-east geologic cross-section B-A' (refer to Figure 3.3 for location). | 183 |
| Figure 3.6 | North-south geologic cross-section C-C' (refer to Figure 3.3 for location). | 185 |
| Figure 3.7 | North-south oriented example seismic line showing the geophysical interpretation at the VSP well site prior to drilling (refer to Fig. 3.3 for location). | 187 |
| Figure 3.8 | Enlarged version of the apparent time-structural anomaly at the Leduc level (shown in Fig. 3.7). | 188 |
| Figure 3.9 | Interpretive processing panel depicting the wavefield separation of the near offset VSP data (from Hinds et al., 1989a; Hinds et al., 1994a and c) | 192 |
| Figure 3.10 | Interpretive processing panel depicting the deconvolution of the near offset VSP data (from Hinds et al., 1989a; Hinds et al., 1994a and c). | 195 |
| Figure 3.11 | Interpretive processing panel illustrating the utility of the nondeconvolved inside and outside corridor stacks for the near offset VSP data (from Hinds et al., 1989a; Hinds et al., 1994a and c). | 197 |

| | | |
|-------------|---|-----|
| Figure 3.12 | Interpretive processing panel illustrating the utility of the deconvolved inside and outside corridor stacks for the near offset VSP data (from Hinds et al., 1989a; Hinds et al., 1994a and c). | 198 |
| Figure 3.13 | Integrated interpretive display (IID) showing the interpretation of the available exploration data for the Lanaway Field case study (from Hinds et al., 1994a and c). | 200 |
| Figure 3.14 | Post-VSP interpretation of the north-south oriented seismic line (location shown in Figure 3.3). | 203 |
| Figure 3.15 | Enlarged version of the post-VSP interpretation of the north-south oriented seismic line (shown in Fig. 3.14). | 204 |
| Figure 3.16 | Shunda isopach map showing the absence of Shunda at the VSP well (from Hinds et al., 1994a and c). | 207 |
| Figure 3.17 | Ireton isopach map showing the drape of the Ireton shales along the example seismic line (shown in Figs. 3.14 and 3.15; from Hinds et al., 1994a and c). | 208 |
| Figure 4.1 | Detailed map of Ricinus study area showing the location of the wells used in the geological schematic section shown in Figures 4.2 and 4.4, the seismic data shown in Figures 4.3, 4.5 and 4.17, and locations for Leduc Formation level wells in the Ricinus Field area (from Hinds et al., 1993c; Hinds et al., 1994c). | 214 |
| Figure 4.2 | Schematic section depicting the envisioned subsurface geology at the VSP well site prior to the drilling of the VSP well (from Hinds et al., 1993c; Hinds et al., 1994c). | 216 |
| Figure 4.3 | Interpretation of the example seismic data prior to the drilling of the VSP well (at CDP 258; from Hinds et al., 1993c; Hinds et al., 1994c). | 220 |

| | | |
|-------------|--|-----|
| Figure 4.4 | Schematic section depicting the subsurface geology at the VSP well site, and the relationships between wells 6-9 and 7-15 (locations shown in Figure 4.1) and the VSP well (from Hinds et al., 1993c; Hinds et al., 1994c). | 221 |
| Figure 4.5 | Current, preferred interpretation of the example seismic data shown within the integrated log display (ILD; see chapter 2; from Hinds et al., 1993c; Hinds et al., 1994c). | 223 |
| Figure 4.6 | Interpretive processing panel depicting the wavefield separation of the near offset VSP data (from Hinds et al., 1989a; Hinds et al., 1993c; Hinds et al., 1994c). | 226 |
| Figure 4.7 | Interpretive processing panel depicting the deconvolution of the near offset VSP data (from Hinds et al., 1989a; Hinds et al., 1993c; Hinds et al., 1994c). | 230 |
| Figure 4.8 | Interpretive processing panel illustrating the utility of the nondeconvolved inside and outside corridor stacks for the Ricinus near offset $Z_{up}(+TT)$ data (from Hinds et al., 1989a; Hinds et al., 1993c; Hinds et al., 1994c). | 234 |
| Figure 4.9 | Interpretive processing panel illustrating the utility of the deconvolved inside and outside corridor stacks for the Ricinus near offset $Z_{up(decon)}(+TT)$ data (from Hinds et al., 1989a; Hinds et al., 1993c; Hinds et al., 1994c). | 235 |
| Figure 4.10 | Interpretive processing panel depicting the hodogram-based rotation of the far offset Ricinus VSP data (from Hinds et al., 1989a; Hinds et al., 1993c; Hinds et al., 1994c) | 239 |

| | | |
|-------------|---|-----|
| Figure 4.11 | Interpretive processing panel depicting the time-variant model-based rotation of the far offset Ricinus VSP data resulting from the suggested processing runstream in chapter 2 (from Hinds et al., 1989a; Hinds et al., 1993c; Hinds et al., 1994c). | 242 |
| Figure 4.12 | Interpretive processing panel depicting the time-variant model-based rotation of the far offset Ricinus VSP data resulting from interpretive processing (from Hinds et al., 1989a; Hinds et al., 1993c; Hinds et al., 1994c). | 244 |
| Figure 4.13 | Interpretive processing panel depicting the far offset deconvolution of the Ricinus VSP data (from Hinds et al., 1993c; Hinds et al., 1994c). | 246 |
| Figure 4.14 | Interpretive processing panel showing VSP-CDP transformation of the non-deconvolved far offset Ricinus VSP data (from Hinds et al., 1993c; Hinds et al., 1994c). | 248 |
| Figure 4.15 | Interpretive processing panel showing the VSP-CDP transformed results for the far offset Ricinus VSP data resulting from the suggested "normal" runstream in chapter 2 (from Hinds et al., 1989a; Hinds et al., 1993c; Hinds et al., 1994c). | 250 |
| Figure 4.16 | Interpretive processing panel showing the VSP-CDP transformed results for the deconvolved far offset Ricinus VSP data (from Hinds et al., 1993c; Hinds et al., 1994c). | 251 |
| Figure 4.17 | Integrated seismic display showing the VSP-CDP transformed far offset $Z''_{up}(+TT)$ data merged with the surface seismic data (from Hinds et al., 1989a; Hinds et al., 1993c; Hinds et al., 1994c). | 253 |
| Figure 5.1 | Stratigraphy of the Fort St. John Graben study area (modified from Richards, 1989). | 259 |

| | | |
|-------------|--|-----|
| Figure 5.2 | Map of Western Canadian Sedimentary Basin tectonic elements showing the Peace River Embayment, Prophet Trough, Sukunka Uplift, cratonic platform and Fort St. John Graben (Barclay et al., 1990) | 260 |
| Figure 5.3 | Detailed area map of the Fort St. John Graben showing the Bear Canyon, Josephine, Bonanza and George faults (from Richards et al., 1994). | 261 |
| Figure 5.4 | Diagrammatic summary of the depositional and tectonic history of the Peace River Embayment area (from Cant, 1988) from the Cambrian to the Cretaceous periods. | 264 |
| Figure 5.5A | Block diagram showing the Fort St. John Graben by the end of the Golata Formation time (from Barclay et al., 1990). | 269 |
| Figure 5.5B | Block diagram showing the Fort St. John Graben by the end of the Kiskatinaw Formation time (from Barclay et al., 1990). | 269 |
| Figure 5.5C | Block diagram showing the Fort St. John Graben by the end of the Taylor Flat Formation time (from Barclay et al., 1990). | 270 |
| Figure 5.5D | Block diagram showing the Fort St. John Graben by the end of the Belloy Formation time (from Barclay et al., 1990). | 270 |
| Figure 5.6 | Location of the Fort St. John Graben as outlined by the Belloy Formation isopach map (from Barclay et al., 1990). | 272 |
| Figure 5.7 | Peace River Embayment stratotectonic elements including the Fort St. John Graben (from Barclay et al., 1990). | 272 |
| Figure 5.8 | Example surface seismic data displaying the original interpretation of the owners of the 9-24 well (preceding the drilling of the well; from Hinds et al., 1993a). | 273 |

| | | |
|-------------|--|-----|
| Figure 5.9 | Interpretive processing panel depicting the wavefield separation of the near offset Fort St. John Graben VSP data (from Hinds et al., 1993a). | 278 |
| Figure 5.10 | Interpretive processing panel depicting the deconvolution of the near offset Fort St. John Graben VSP data (from Hinds et al., 1993a). | 280 |
| Figure 5.11 | Interpretive processing panel illustrating the inside and outside corridor stacks of the $Z_{up}(+TT)$ data (from Hinds et al., 1993a). | 282 |
| Figure 5.12 | Interpretive processing panel illustrating the inside and outside corridor stacks of the $Z_{up(decon)}(+TT)$ data (from Hinds et al., 1993a). | 283 |
| Figure 5.13 | Interpretive processing panel depicting the hodogram-based rotation of the Fort St. John Graben FSJG1 far offset VSP data (from Hinds et al., 1993a). | 286 |
| Figure 5.14 | Interpretive processing panel depicting the time-variant model-based rotation of the Fort St. John Graben FSJG1 far offset VSP data (from Hinds et al., 1993a). | 289 |
| Figure 5.15 | Interpretive processing panel depicting the VSP-CDP transformed and Kirchhoff migrated results of the Fort St. John Graben FSJG1 far offset VSP data (from Hinds et al., 1993a). | 291 |
| Figure 5.16 | Interpretive processing panel depicting the hodogram-based rotation of the Fort St. John Graben FSJG2 far offset VSP data (from Hinds et al., 1993a). | 294 |
| Figure 5.17 | Interpretive processing panel depicting the time-variant model-based rotation of the Fort St. John Graben FSJG2 far offset VSP data (from Hinds et al., 1993a). | 295 |

| | | |
|-------------|--|-----|
| Figure 5.18 | Interpretive processing panel depicting the VSP-CDP transformed and Kirchhoff migrated results of the Fort St. John Graben FSJG2 far offset VSP data (from Hinds et al., 1993a). | 296 |
| Figure 5.19 | Integrated interpretive display of the Fort St. John Graben exploration data (from Hinds et al., 1993a). | 298 |
| Figure 5.20 | Current, preferred surface seismic interpretation (from Hinds et al., 1993a). | 299 |
| Figure 5.21 | Geologic cross-section incorporating information from the surface seismic, VSP and geologic well log results (from Hinds et al., 1994c). | 301 |
| Figure 5.22 | Plan map of the FSJG1 offset source area showing the fault locations as interpreted from the VSP and surface seismic data (from Hinds et al. 1994c). | 303 |
| Figure 6.1 | Ireton isopach map of the main and low-relief Simonette reef within the eastern Woodbend depositional realm (from Hinds et al., 1993b and 1994c). | 308 |
| Figure 6.2 | Geologic cross-section A-A' traversing the wells shown in Figure 6.1 (from Hinds et al., 1993b and 1994c). | 309 |
| Figure 6.3 | Example surface seismic data over the low-relief reef displaying the original interpretation of the owner of the data (from Hinds et al., 1993b and 1994c). | 311 |
| Figure 6.4 | Ireton to Leduc isochron map resulting from the original interpretation of the seismic lines within the area of the low-relief reef (from Hinds et al., 1993b and 1994c). | 313 |
| Figure 6.5 | The preferred Ireton to Leduc isochron resulting from the updated interpretation (using the VSP results) of the seismic lines in the area of the low-relief reef, the VSP results and geologic borehole data (from Hinds et al., 1993b and 1994c). | 314 |

| | | |
|-------------|---|-----|
| Figure 6.6 | Interpretive processing panel depicting the wavefield separation of the near offset (252 m) offset Simonette VSP data (from Hinds et al., 1993b and 1994c). | 319 |
| Figure 6.7 | Interpretive processing panel depicting the deconvolution of the near offset (252 m) Simonette VSP data (from Hinds et al., 1993b and 1994c). | 321 |
| Figure 6.8 | Interpretive processing panel illustrating the utility of the inside and outside corridor stacks of the near offset (252 m) Simonette $Z_{up}(+TT)$ data (from Hinds et al., 1993b and 1994c). | 324 |
| Figure 6.9 | Interpretive processing panel illustrating the utility of the inside and outside corridor stacks of the near offset (252 m) Simonette $Z_{up(decon)}(+TT)$ data (from Hinds et al., 1993b and 1994c). | 325 |
| Figure 6.10 | Interpretive processing panel depicting the hodogram-based rotation of the far offset (524 m) Simonette VSP data (from Hinds et al., 1993b and 1994c). | 328 |
| Figure 6.11 | Interpretive processing panel depicting the time-variant model-based rotation of the far offset (524 m) Simonette VSP data (from Hinds et al., 1993b and 1994c). | 330 |
| Figure 6.12 | Interpretive processing panel showing the VSP-CDP transformed and Kirchhoff migrated far offset (524 m) $Z''_{up}(+TT)$ data (from Hinds et al., 1993b and 1994c). | 332 |
| Figure 6.13 | Interpretive processing panel showing the VSP-CDP transformed and Kirchhoff migrated far offset (524 m) $Z''_{up(decon)}(+TT)$ data (from Hinds et al., 1993b and 1994c). | 335 |

- Figure 6.14 Integrated interpretive display showing the interpretation of the available exploration data for the Simonette reef case study (from Hinds et al., 1993b and 1994c). 337
- Figure 6.15 Current, preferred interpretation of the example seismic section. The Z-marker is laterally continuous at the 13-15 well location and the reef slope has been reinterpreted to be at least 150 m to the East of well 13-15 (from Hinds et al., 1993b and 1994c). 339

LIST OF FLOWCHARTS

| | | |
|-------------|---|-----|
| Flowchart 1 | An example of the interpretive processing decision-making flowchart for the median filter plus subtraction wavefield separation processing (Hinds et al., 1994c). | 34 |
| Flowchart 2 | An example of the interpretive processing flowchart for the median filter plus subtraction wavefield separation processing (Hinds et al., 1989a). | 44 |
| Flowchart 3 | An example of the interpretive processing flowchart for the K-L wavefield separation processing (Hinds et al., 1994c). | 56 |
| Flowchart 4 | An example of the interpretive processing flowchart for the interactive F-K wavefield separation processing used for event identification (Hinds et al., 1994c). | 87 |
| Flowchart 5 | An example of the interpretive processing flowchart for the interactive F-K wavefield separation processing used for the attenuation of tubewave events on $Z_{up}(\mathbf{FRT})$ data (Hinds et al., 1994c). | 92 |
| Flowchart 6 | An example of the interpretive processing flowchart for the τ -P wavefield separation processing (Hinds et al., 1994c). | 100 |

CHAPTER 1

INTRODUCTION

1.1 Vertical seismic profiling (VSP)

The geometry of the VSP survey separates the method from other types of borehole and surface related surveys. The surface seismic survey is conducted with the geophones (or hydrophones in the case of marine seismics) and the sources being on or near the surface. In crosswell seismology or CWS (Hardage, 1992), both the sources and receivers are in boreholes. For the reverse VSP (RVSP; Hardage, 1992), the source is in the borehole and the receivers are on the surface. The VSP technology, data and interpretation presented in this thesis relate to a survey with sources on the surface and receivers in the borehole.

How has the VSP survey been doing in comparison to the other seismic surveys? Recently, Zimmerman and Chen (1993) ranked the VSP to yield superior interpretable data from deeper depths in comparison to the RVSP results. The viability of RVSP and CWS data will closely follow the development of the downhole seismic sources (Hardage, 1992). The downhole geophone tool (sonde) used in the VSP survey is operated in a seismic environment which involves less background noise in comparison to the surface geophone (RVSP and surface seismics). The locking arm on the sonde has changed from spring loaded (a derivative of the caliper tool) to being hydraulically operated (enough force to almost bend steel borehole casing). The increased level of geophone coupling to the formations

surrounding the borehole increases the seismic signal reception (Hardage, 1985). Multi-level geophone sondes with independent locking arm units have resulted in a reduction of VSP survey cost and less coupling resonances.

What has happened in the past with respect to interpretation? In theory, as explorationists, we would like to integrate the interpretation of the VSP data with the processing of the same data. In this way, both activities would complement and guide each other. In practice, however, they seem to be done separately. This may be due to time constraints placed on the seismic interpreter as a result of heavy work load or to the specialization of the interpreter and the processor to one or the other task. First, the VSP data are usually processed using whatever methods are available to the processor. The processing typically proceeds to output a product which is the separated upgoing wavefield events in pseudo-two-way traveltime. Thereafter, the interpreter takes the final result data panel and, in conjunction with available geological data, interprets the different VSP events. Unfortunately, the interpretation is usually done in the absence of input from the processor. The insight of at least the first pass of the processing has been lost to the interpreter.

1.2 Aims and objectives of this study

The aim of this thesis will be to:

- (1) develop the methodology of Interpretive Processing (Hinds et al., 1989a) for VSP data using the interpretive processing panels (IPP), interactive data processing, integrated log display (ILD), integrated seismic display (ISD) and the integrated interpretation display (IID);
- (2) review the usage of the processing steps in the individual IPP to illustrate the incorporation of VSP interpretation to minimize processing artifacts (Hinds et al., 1994c);
- (3) present the usage of VSP interpretive processing in four case studies (Hinds et al., 1989a; Hinds et al., 1993b, 1994a and 1994c; Hinds et al., 1993a and 1994b; Hinds et al., 1993c); and
- (4) further the method of integrated geophysical/geological interpretation (Anderson, 1986) using the case studies (Hinds et al., 1989a; Hinds et al., 1991a, 1991b and 1993c; Hinds et al., 1993a and 1994b; Hinds et al., 1993b, 1994a and 1994c).

The integrated processing and interpretation of VSP data will be developed to work together in order to enhance the final VSP interpretation. Furthermore, the interpretive processing of the VSP data within the case histories will be reviewed along with the usage of the final

VSP results (both near and far offset data) into the integrated geological/geophysical interpretations presented in the case studies. This thesis will attempt to personify the term "interpreter/processor" as first highlighted in Hardage (1985).

The case histories pertain to oil and gas exploration in carbonate reef and sandstones in the Western Canadian Sedimentary Basin (WCSB). The Lanaway case history (Hinds et al., 1994a) described in chapter 3 pertains to the exploration of the Lanaway/Garrington oil field located in central Alberta, Canada. The surface seismic interpretation over the reef crest differed dramatically from the isopach of the reef-encasing shales derived from the geological logs of a borehole drilled into the reef crest. To understand the discrepancy, a VSP survey was performed and the data were interpretatively processed. The results were integrated with the known geology of the field area to uncover possible reasons for the surface seismic anomaly.

The Ricinus case history (Hinds et al., 1993c) described in chapter 4 is a study in reef hunting within the Ricinus field in central Alberta, Canada, using the far offset VSP survey. Existing surface seismic was used to infer that a well drilled into the interpreted North-east corner of the Ricinus reef would be successful in penetrating oil bearing carbonate reef. The well was drilled; however, the well missed the reef and a near and far offset VSP survey was used to seismically image possible reef buildups in an area around the well.

The Fort St. John Graben case history (Hinds et al., 1991a; Hinds et al., 1993a) described in chapter 5 highlights exploration of a gas-filled channel sandstone using near and far offset (lateral) VSP surveys. An exploration well was drilled within the study area which

intersected the target zone sandstone (the basal Kiskatinaw of the Upper Carboniferous). The target sandstone had a high shale content and was not reservoir quality. A near offset and two far offset VSP surveys were run in the exploration well to image out to a distance of 350 m to the North-west and to the East of the well. The VSP, surface seismic and geology results (from the geological logs of the exploration and surrounding wells) are integrated to infer a clearer picture of the sand/shale relationships of the basal Kiskatinaw and detailed faulting of the Carboniferous strata around the well and within the surface seismic line area.

The Simonette field case history (Hinds et al., 1991b; Hinds et al., 1993b) described in chapter 6 involves using VSP results to image the slope of a low-relief carbonate reef. The low-relief reef examined using the VSP data is located at the extreme end of a North-east reef spur of the Simonette Reef located in North-west Alberta, Canada. An exploration well drilled in the low-relief reef penetrated the edge of the reef. The VSP surveys were run in order to infer details of the reef slope. The interpretation of the VSP data was integrated with all other exploration data to infer the location of the crest of the low-relief reef and to assist in determining whether to whipstock the exploration well or not.

1.3 Acknowledgements

The thesis contains a variety of datasets and the processing has been performed at a number of facilities using different processing software. The surface seismic and VSP data examined in chapters 3 and 4 were donated by Gulf Canada Ltd. (Hinds et al., 1989a). The surface seismic and VSP data for chapters 5 and 6 were donated by Talisman Resources Inc.

The surface seismic data used in the thesis case histories consisted of post-stack seismic time sections. The VSP data were the raw data; re-processing was then performed on the data. The subsequent processing for the VSP data shown in this thesis was different to that of the industry standard processing at the time of data acquisition.

The VSP processing was performed on the computers of Computalog Ltd. (Calgary) using Halliburton Geophysical Inc. software, on the VAX systems at the University of Pretoria, Talisman Resources Inc. (Calgary) and Anglo-American Prospecting Services (Klerksdorp), using IT&A Insight/1 software and on the Schlumberger computers using Schlumberger propriety software in Paris, France. Rick Kuzmiski taught me the Halliburton software in Calgary and Didier Belaud performed the Kirchhoff migrations shown in the thesis during my research stay in Paris as I was not allowed physical access to the Schlumberger machines. Much of the VSP processing for the work described in chapters 2 and 4 were done using Photon Systems Ltd (Calgary) Quickpro software resident on my 486 DX/2 PC in Pretoria.

The well logs used during the construction of the isopach map and geologic cross-section shown in Figures 6.1 and 6.2 were supplied by Karen Chang of Calgary. The initial interpretations of the surface seismic sections were supplied by the data owners; however, all subsequent interpretations were done during this research. The design of the VSP surveys and supervision of the execution of the field surveys were done by myself as an employee of Gulf Canada Ltd. and as a consultant for Hinds Geophysical Inc. (Calgary).

I would like to acknowledge and thank my supervisors, Prof. C.P Snyman, Dr. N.L. Anderson and Dr. R. Kleywegt for their help and interest in this thesis work.

1.4 VSP fundamentals

1.4.1 Near and far offset (lateral) VSP surveys

The components of the interpretive processing panels are different for the near and the far offset VSP surveys. The near offset VSP survey usually involves the processing the vertical (Z) axis geophone data; whereas the two horizontal (X and Y) and vertical (Z) geophone data are processed for the far offset VSP survey.

A review of the geometries involved in the VSP survey which necessitate the different panel components will be discussed below. A few of the numerous configurations of the VSP survey are shown in Figure 1.1 (Hinds et al., 1989a). A near offset VSP geometry can be described as the source being vertically or near-vertically above the sonde. The near offset VSP has also been termed a "zero offset" VSP survey (Cassell, 1984). In Figure 1.1, the configurations in part (A) using the source S_1 and in (B) using the source S_4 and sonde at location C plus the source S_3 and receiver at location A would be termed near offset VSP source-receiver geometries. The configurations in (A) using the source S_2 and in (B) using the source S_3 and receiver at B or C would be termed far offset VSP (or simply "offset" VSP; Cassell, 1984) geometries.

The far offset VSP geometry for a deviated hole could arise in an offshore well where the airgun is placed near to the drilling platform but the wellbore is deviated to intersect reservoirs quite a distance away from the subsurface location directly below the well.

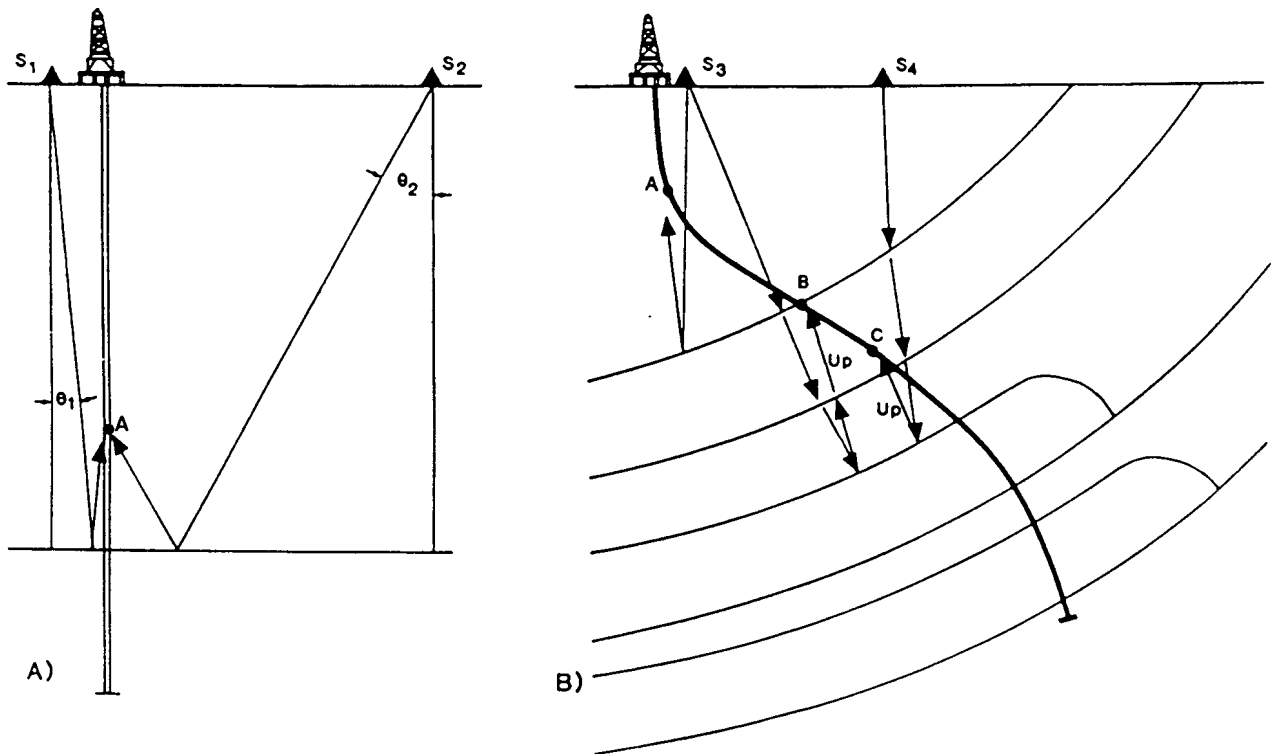


Figure 1.1 The field layout of the (zero) near and far offset VSP surveys.

In part (A), the surface source at S_1 is at a zero-incidence location with respect to the geophone borehole sonde in the vertical non-deviated borehole. The up- and downgoing waves travel vertically down to the reflector and back to the receiver geophone sonde in the borehole. The source at S_2 is a non-zero offset location as the source does not lie directly over the borehole geophone. In part (B) for the deviated borehole, source S_3 is in a zero-offset configuration for the upper vertical (shallow depths) part of the borehole and (non-zero) far offset for the deviated remainder of the borehole. Part (B) is usually represented in the literature as a deviated borehole intersecting horizontal layers which would result in incorrect reflection angles for the migration algorithms (from Hinds et al., 1989a).

In the case where the borehole is deviated but a near offset geometry is desired, the source is moved along the surface and is directly overhead of the sonde within the borehole. This is obviously an expensive procedure as the three-dimensional picture of the location of the sonde must be monitored. The source would move once the "verticality" of the source-receiver geometry needed to be corrected (remember that the Fresnel zone concept relates both to the receiver and source; Hardage, 1985). In land-based VSP surveys, retaining the zero offset geometry can be difficult because bush corridors must be cut and large Vibroseis vehicles may need to be "sledged" over to source locations.

The interpretational definition that I like to use is that a far offset geometry exists whenever partitioning a wavefield (downgoing or upgoing P- or SV-waves) necessitates the polarization of the VSP data in order to isolate that wavefield component onto a single data channel (following an angle-based rotation). In a far offset VSP, reflected and transmitted P, SH, and SV-waves (Fig. 1.2) will be recorded by the sonde with the amplitudes of the various waves being related to the incidence angle onto the geophones.

1.4.2 Primary and multiple up- and downgoing waves

The VSP data contains upgoing and downgoing waves (Fig. 1.3) which can have a variety of origins. Figure 1.3A shows example raypaths of the primary and multiple up- and downgoing waves. Using two interfaces (A and B), Figure 1.3B depicts the location of the VSP events on a depth versus travelttime diagram.

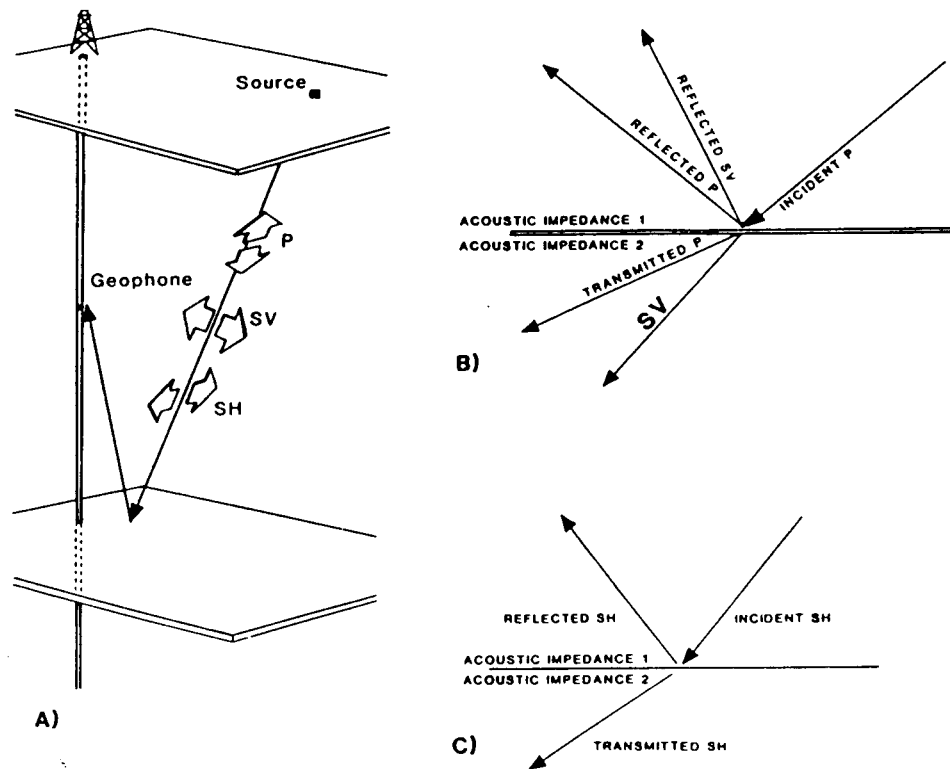


Figure 1.2 The up- and downgoing waves propagating to the wellbore geophone sonde can be compressional P-waves that vibrate in the direction of travel or Shear SV- or SH-waves that vibrate normal to the direction of travel, either in the plane of the source and receiver or out of the plane. Reflections from dipping and contorted geological strata can enable all three of these type wavefields to be recorded on the X, Y, and Z geophones. As shown in part (B), the P- and SV-waves can reflect and transmit as P- or SV-waves at impedance interfaces. The SH incident wave reflects and transmits as an SH wave (C). (from Hinds et al., 1989a).

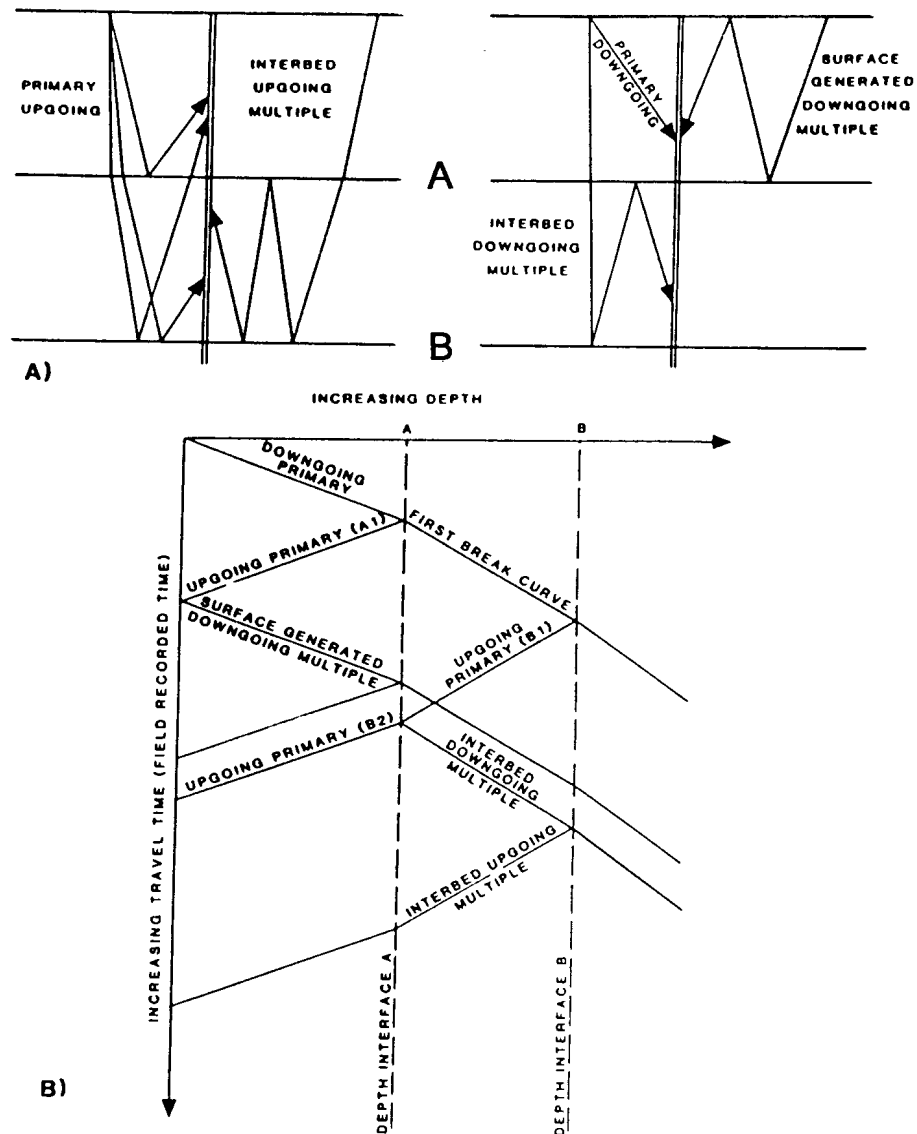


Figure 1.3 Examples of the up- and downgoing raypaths (A) and depth-traveltime diagrams (B) for both primary and multiple reflections. The upgoing rays are illustrated on the left side of (A) whereas the downgoing rays are illustrated on the right side. The geometry for the near offset sources are displayed with exaggerated source offset for clarity. The surface-generated downgoing multiples will be recorded at all subsurface geophone locations whereas the interbed downgoing multiple generated between layers A and B will only be recorded when the geophone is below layer A. Upgoing reflections from layer A will be recorded only at geophone locations above layer A. The up- and downgoing primaries will merge when the geophones are located at the generating interface. A traveltime curve plot for the up- and downgoing rays is shown in part B. The downgoing primary is the first break curve increasing in traveltime from left to right in the diagram and with the exception of head waves is the first recorded signal on each VSP trace. The downgoing wave multiple for the near-offset case parallel the downgoing primary. An upgoing primary (B1) generates a reflected downgoing multiple at interface A, which in turn can generate an interbed upgoing multiple at reflector B (from Hinds et al., 1989a).

Throughout the thesis, the abbreviations FRT, -TT, and +TT (Hinds et al., 1989a) are used repeatedly. FRT is the abbreviation for field recorded time, the term used to describe the time-depth display of the raw field records. FRT include time recording shifts input by airgun delays or Vibroseis recordings. The terms -TT and +TT refer to specific data configurations following trace time shifts. -TT is used in reference to the display on which the first breaks and downgoing P-waves are horizontally aligned and bulk shifted. On these displays, the first break times have been subtracted from each trace, and the modified traces have been bulk-shifted to an arbitrary time-datum (usually to 100 to 200 ms) so that the onset of the first break wavelet is retained. +TT is used in reference to the display on which the first break time of each trace has been added to that trace (plus possible normal moveout or "NMO" corrections), as depicted in Figure 1.4. On the +TT displays, the upgoing events on near offset VSP data are horizontally aligned and should be in pseudo-two-way traveltime.

For the near offset VSP data, one of the important types of events to interpret are the surface-generated and interbed multiples. The ease with which primaries and multiples can be identified was reviewed in early papers by Wuenschel (1976) and Kennett et al. (1980). Some fundamental guidelines for VSP interpretation were set down in the literature in Hardage (1985). The significance of multiples for Western Canadian Sedimentary Basin (WCSB) VSP data was shown in Hampson and Mewhort (1983) and Hinds et al. (1989a).

For the surface-generated multiple, the downgoing wave reflects at an interface and then reflects from the surface back down towards the borehole geophone. The key to the interpretation of the surface-generated multiple is that it must reside on all the VSP traces. Later, in Chapter 2, when the VSP data are placed in the -TT configuration the surface-

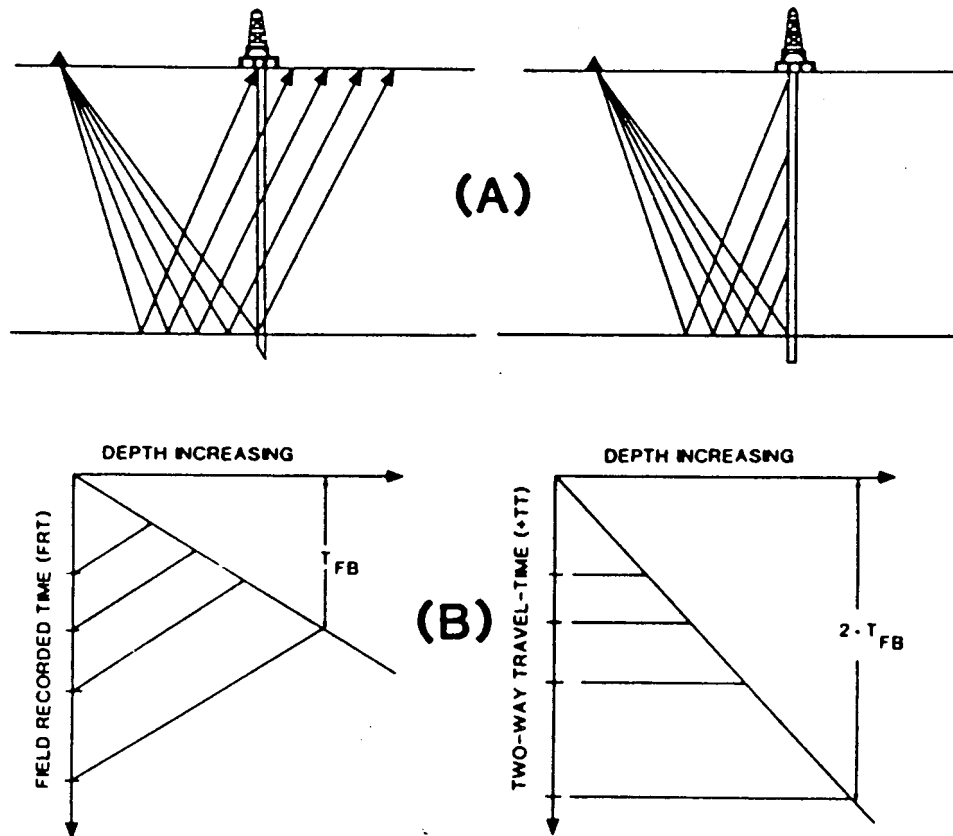


Figure 1.4 The near offset data correction used to place the data into pseudo-two-way traveltime (+TT). Part (A) shows the geometry of the surface seismic with the well superimposed on the raypaths. To the right, the rays that are terminated at the well are different from the surface seismic rays by a traveltime equivalent to the zero-offset first break times of the downgoing rays. In part (B), when the first break traveltimes are added back onto the traces, the time axis changes from field recorded time (FRT) to pseudo-two-way traveltime (+TT) that should be equivalent to the surface seismic two-way traveltime (from Hinds et al., 1989a).

generated multiple will become easily interpretable. The simple corollary to this is that the first break curve shown in Figure 1.3 is the only primary downgoing P-wave on the VSP. It should be noted that if the mode converted P-SV downgoing wave is created at interface A in Figure 1.3, then that mode-converted downgoing wave will also be a primary downgoing wave. Since the only primary downgoing P event is the P-wave event associated with the first break, then later arriving downgoing P events recorded at the sonde are multiples.

Why is this simple information not seen on surface seismics? The answer is that no downgoing waves are recorded by the surface seismic geophones. By placing the VSP data into the +TT data configuration, however, the interpretation of multiples on surface seismics can be facilitated. Figure 1.5 depicts the VSP interbed multiple. As seen in Figure 1.3, the interbed multiple exists as a downgoing wave only below the top generating interface that is responsible for the multiple's existence. The upgoing interbed multiple exists only on the shallowest VSP trace down to the trace recorded at the bottom generating interface. Can these two observations be combined to find a simple way to interpret the interbed multiple? In Figure 1.5, the upgoing wave (+TT) VSP data show that the upgoing interbed multiple mimics the upgoing primary (U-P) from the interface from Z_2 but is delayed by the two-way traveltime between the interface at Z_1 and Z_2 . The other observation which is also used in designing corridor stacks in chapter 2 is that the interbed (or any other) multiple does not intersect the first break curve. Figure 1.3 shows that the upgoing interbed multiple can be mistaken as a surface-generated multiple if a downgoing surface-generated multiple was created with the same time delay as the time difference between the upgoing primary associated with Z_2 and the multiple seen below the Z_2 primary (U-M in Fig. 1.5A). The

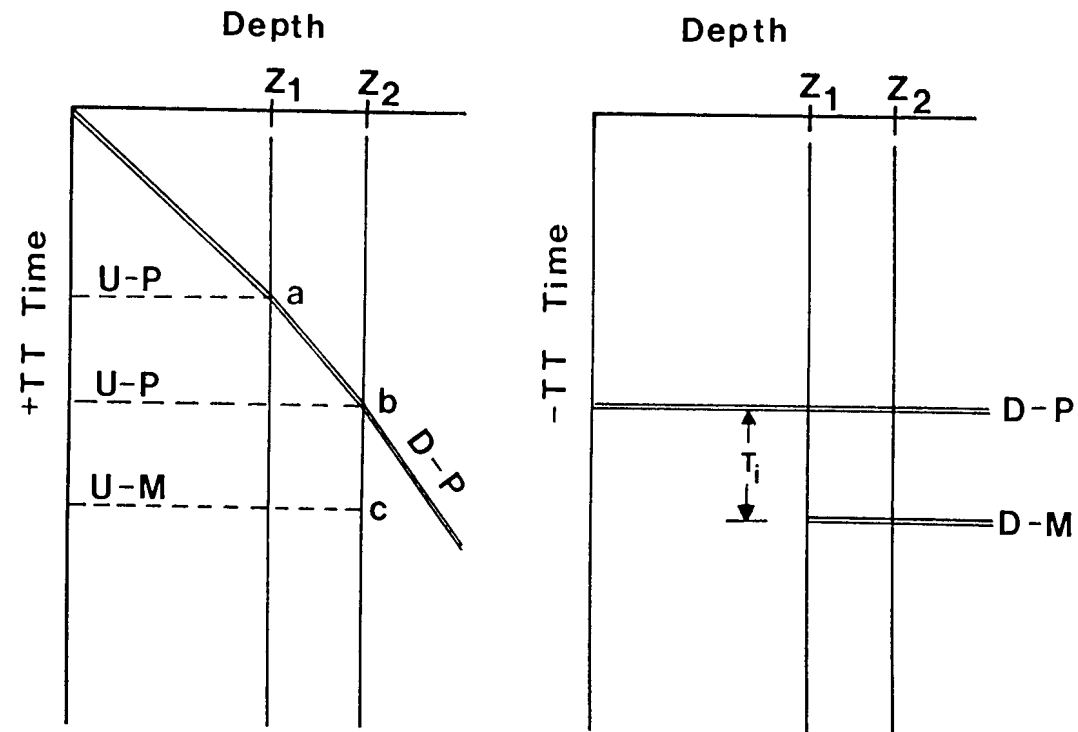


Figure 1.5 Upgoing wave events in (+TT) time (left) and downgoing waves in (-TT) time (right) are displaced to align the upgoing primary event generated at the depth Z_2 (labelled U-P on the left) with the horizontally aligned event first break curve (labelled D-P on the right). This illustrates the equal time separation (T_i) between the U-P and U-M events from interface Z_2 and the D-P and D-M downgoing events.

interpretation is clarified by viewing the (-TT) downgoing events as shown in Figure 1.5B. A downgoing multiple (D-M) is recorded after the primary downgoing wave (D-P) and exists only below the Z_1 interface.

Can the downgoing waves be used to attenuate the upgoing wave multiples? Hubbard (1979) and Gaiser et al. (1984) showed that a deconvolution operator which could collapse the downgoing event wavetrain into a single pulse could be used to attenuate the upgoing multiples. In Figure 1.6 (Hardage, 1985), there is a constant time shift, T_m , between the upgoing primary and multiple and downgoing primary and multiple. The up- and downgoing multiples are linked to their respective primary events by this constant time shift. Since the upgoing wave is the same as the downgoing wave at an interface, an operator designed from the downgoing waves will be able to attenuate the corresponding upgoing wave multiples. In practice, this procedure of using a single deconvolution operator works well with surface-generated multiples.

In Figure 1.5, it can be seen the interbed multiples do not appear on all VSP traces. This implies that independent deconvolution operators would have to be calculated for each VSP trace in order to attempt to combat the interbed upgoing multiple. The multiples that occur after the first break time of the deepest geophone are also difficult to attenuate (one reason being that these events cannot even be confirmed to be multiple or primary events).

For the interpretive processing of near offset VSP data, such an importance is placed on identifying multiples that 75% of the interpretive processing panels have been designed to evaluate the performance of the "up over down" VSP deconvolution procedure. As will be

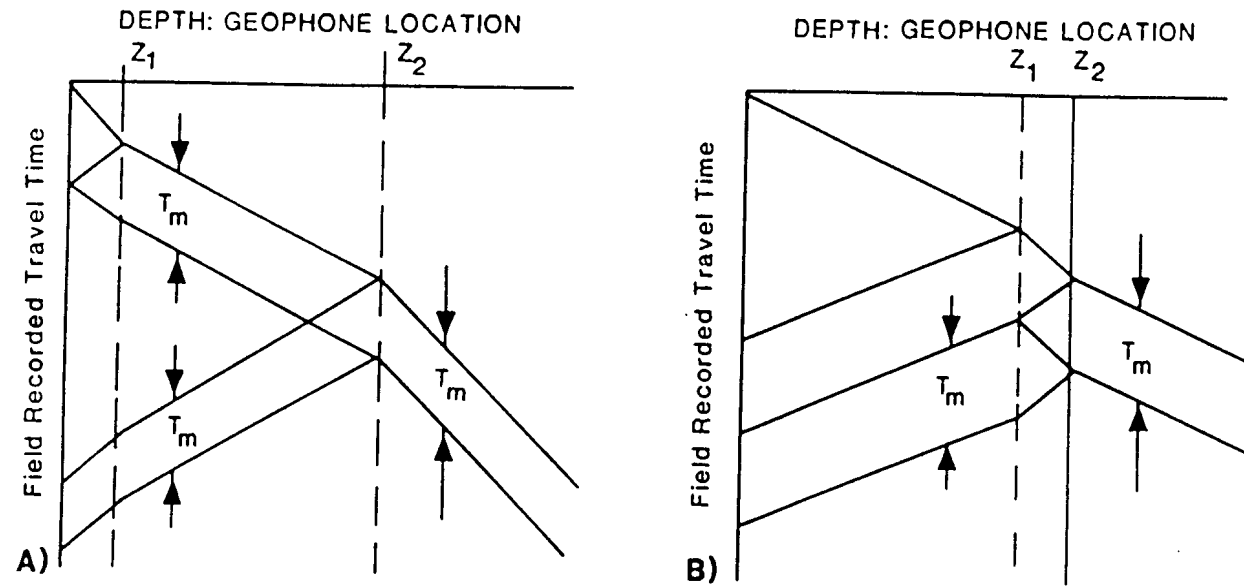


Figure 1.6 The constant time shift between the up- and downgoing primaries and multiples for the surface-generated (A) and interbed multiples (Hardage, 1985). Part (A) is the depth versus FRT configuration for the surface generated multiple. The numerical operator (inverse filter) that attenuates the downgoing multiple (the downgoing event that is time shifted from the primary downgoing event by time T_m) will attenuate the upgoing surface generated multiple. In part (B), the operator that will attenuate the upgoing interbed multiple can be designed from any trace beneath depth location Z_1 (from Hinds et al., 1989a).

seen on the modelled VSP data later in this chapter, the crucial key to multiple attenuation is that the constant time delay between the up- and downgoing multiple events and their associated primary events is preserved on the entire VSP dataset. When the offset of the source begins to approach far offset, the key time lag assumption becomes violated and deconvolution of far offset VSP data may not always work.

Figure 1.7 depicts near offset VSP results of a four layer model illustrating surface-generated multiple contaminated data (panel 1) and interbed multiple contaminated data (panel 2). Compare the modelled results to the schematic VSP events shown in Figure 1.3B. Here a short review is included to show how an interpreter/processor pulls apart the different events that one would see on the modelled (simulating a real) VSP data.

Consider panel 1 of Figure 1.7. The horizontal axis reflects the depth of the recording sonde (in m) and the vertical axis is in the **FRT** time configuration (in s). The first downgoing wave is recognized as the first break on every trace and as the depth increases, the travelttime of the downgoing event also increases (the basic rule for a downgoing VSP event). The downgoing primary wave encounters an acoustic impedance interface at 120 m depth and an upgoing primary event is generated due to the reflection. The upgoing primary intersects the primary downgoing event on the 120 m trace at approximately 0.5 s. The upgoing wave travelttime increases with decreasing depth. This shows the familiar relationship that for the near offset VSP the up- and downgoing events have equal but opposite apparent velocities (Hardage, 1985). At 0.9 s on the surface trace, the upgoing event is turned into a downgoing surface-generated multiple due to the reflection of the upgoing wave at the

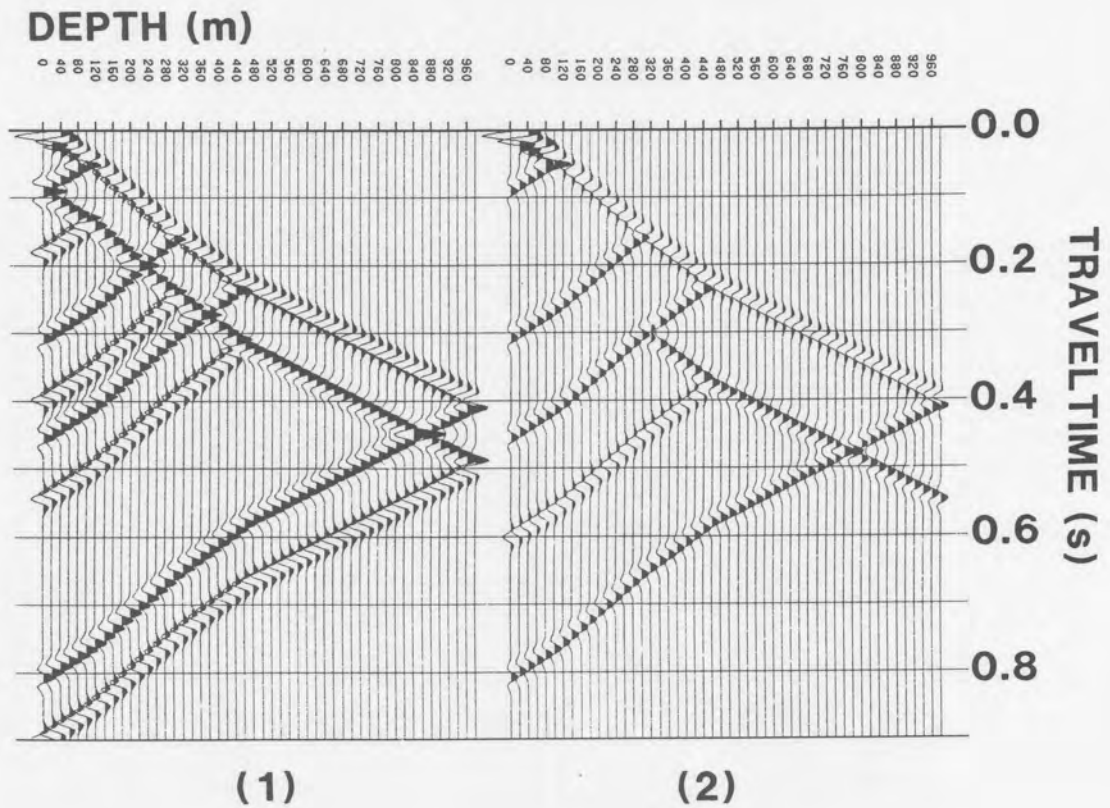


Figure 1.7 Synthetic VSP seismograms illustrating surface generated (panel 1) and interbedded (panel 2) up- and downgoing multiple events. The model used in the ray tracing consisted of four layers with the half space being at the bottom of the borehole. The trace spacing is 20 m. The geometry consists of a near-offset source and a vertical non-deviated borehole. The amplitudes have been equalized and the first arrival on the 0 m trace has been muted for clarity. Note the differences in the location of the up- and downgoing multiple events and the polarity reversals between the various up- and downgoing wave events (from Hinds et al., 1994c).

surface. The downgoing multiple travels back down to the interface at 120 m, transmits downwards as a downgoing multiple and reflects back up to the surface as the first upgoing surface-generated multiple. The other upgoing multiples can thereafter be similarly traced.

The interpreter/processor must get a good understanding of the events on the raw VSP (possibly by gaining the VSP or by separating the up- and downgoing events, amplitude gaining the events independently, and thereafter recombining the two datasets for interpretational reference - REMIX display; Hinds et al., 1989a) as this will lead his interpretive processing right through to the final displays.

The surface-generated downgoing multiple in Figure 1.7 (panel 1) is time delayed from the primary (first break) downgoing event by the time that the downgoing wave took to reach the first interface at 120 m depth and travel back (as an upgoing wave) to the surface. As noted above, the multiple exists on all of the VSP traces. It is clear, visually, that the constant time shift between the downgoing primary and multiple corresponds to the same time delay between all of the upgoing multiples and their respective upgoing primaries.

In panel 2, the interbed up- and downgoing multiples are generated at interfaces 2 and 3 (320 and 480 m depth, respectively). As noted above, the downgoing interbed multiple exists on traces recorded deeper than the top generating interface (at 320 m depth) and the upgoing interbed multiple exists on traces above the 480 m interface (the bottom generating interface). This key to interpretation may be difficult to recognize when using downgoing wavefield separation techniques that smear the downgoing multiple events across adjacent traces.

For interpretative processing, the objective is to first identify the multiples and then to attenuate them the best possible. If attenuation is not completely possible then the knowledge of the multiple contamination must be included in the evaluation of the data.

1.4.3 Far offset geometries

The triaxial geophone sonde is usually employed in a far offset survey; however, there are cases where the near offset VSP survey requires the recording of the **X**, **Y** and **Z** channel data. Shear waves can be generated using shear wave Vibroseis units or through mode conversion at near surface interfaces. When the shear wave passes through vertical fractures (Fig. 1.8; Ahmed, 1989 and 1990), the shear wave can be polarized and split into two resultant shear waves; one which is oriented normal to the fractures and the other parallel. These fast and slow shear waves that exist below the fracture zone would be recorded using a triaxial geophone sonde even though the source could have been located at the well (a near offset source). Another example of a case where a triaxial sonde is required is within the near offset VSP geometry shown in Figure 1.9. The object in this survey is to image the steeply dipping target horizon and to locate the fault. The reflected waves from the target horizon would require a triaxial recording to properly image the horizon. In these cases, the geometry of the target or rock properties themselves are causing orientation changes within the transmitted or reflected wavefields. At any given sonde location, three channels of data are recorded; namely the **Z**, **X**, and **Y** axis data. The **X** and **Y** channels are from the two

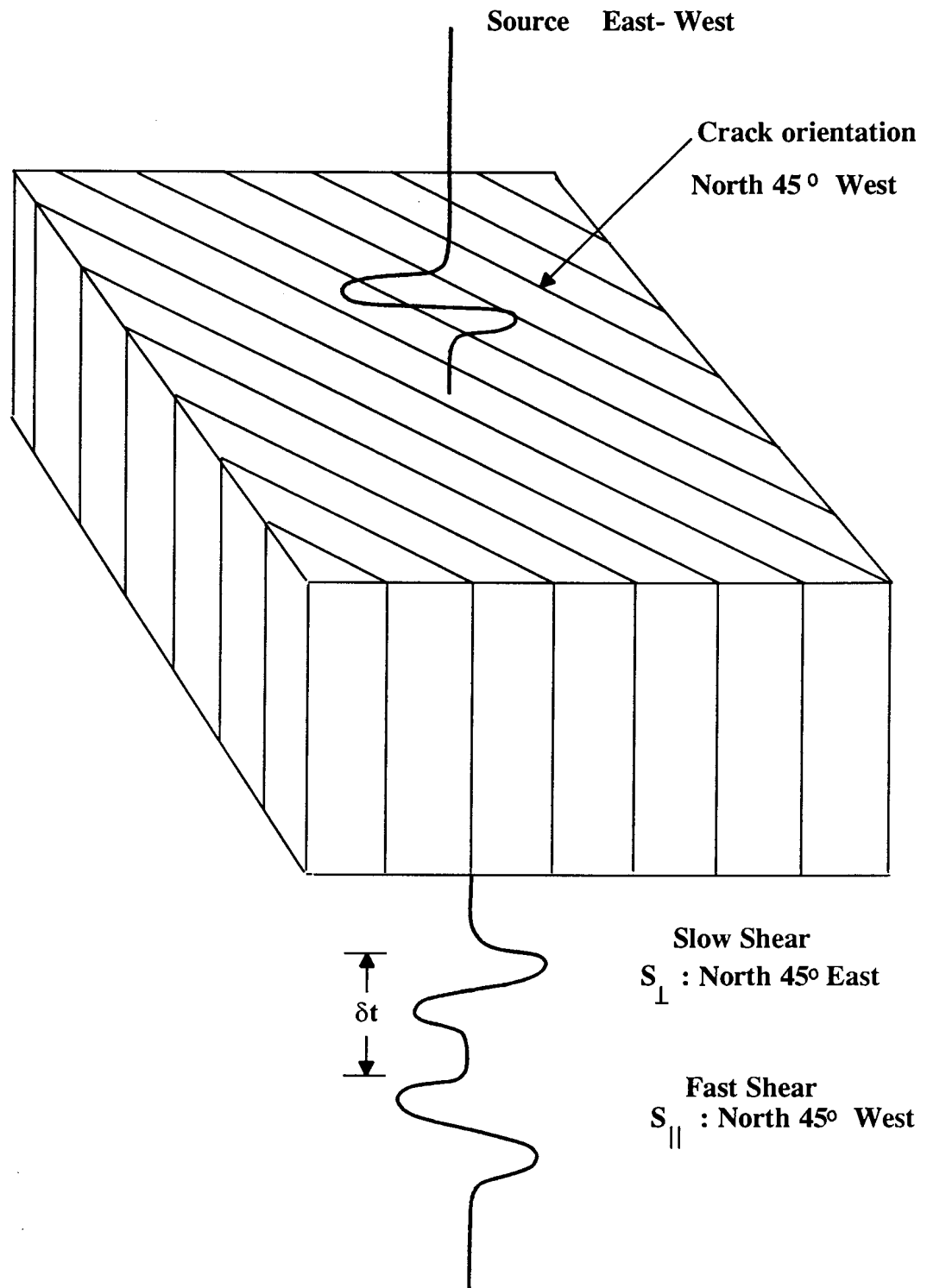


Figure 1.8 Schematic diagram of shear wave splitting caused by the propagation of a SV wave through fractured rock. This type of wave propagation would complicate the waveforms recorded at the triaxial geophone sonde (from Ahmed, 1990).

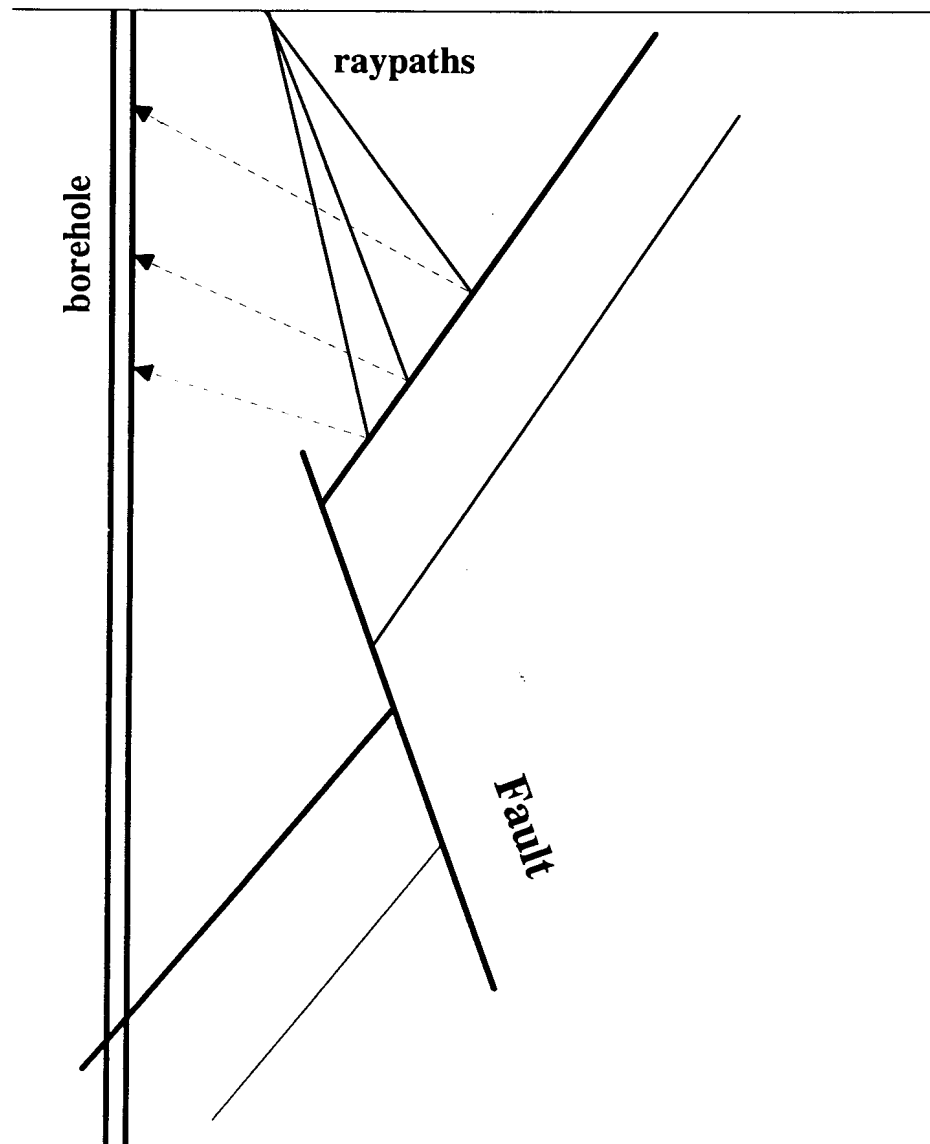


Figure 1.9 From a near offset source, reflected rays propagate to the borehole along complicated paths due to the steeply dipping geology. This would result in the triaxial data requiring special polarization analysis in order to interpret the VSP reflections.

orthogonal horizontal geophones.

As the sonde is raised up the borehole, the horizontal geophones rotate in the borehole. The vertically and horizontally polarized shear wavefields, SV and SH (Bullen and Bolt, 1985), and the compressional P-wavefield energy are contained in varying amounts on the **X** and **Y** data channels.

The first objective when processing triaxial data is to isolate the downgoing P-wave events from the **X** and **Y** channels onto a single data panel. The procedure to do this involves data polarizations which are explained below.

For the far offset VSP surveys, the hodogram analysis (Hardage, 1985; DiSiena et al., 1984) performed on the first break wavelets of the two horizontal datasets (from the same sonde location) can be used to polarize the **X** and **Y** data onto two principal axes normal, **HMIN**, and tangential, **HMAX**, to the plane defined by the source and the well (Fig. 1.10). The resultant **HMIN** and **HMAX** data should contain polarized SH and combined P and SV energy, respectively. The assumption for SH- and SV-wavefield separation is that the two waves are propagated along a similar raypath to the downgoing P-wave (Hardage, 1985).

The hodogram method polarizes the horizontal axis data using the downgoing P-wave energy in the first break wavelet. A time window around the first break is chosen and the data from the two horizontal channels are plotted on an orthogonal axis. For any given time sample in the window, the corresponding **X** and **Y** values are plotted on the graph called a hodogram (Hardage, 1985; Fig. 12.24 of Hinds et al., 1989a). The hodogram usually resembles an

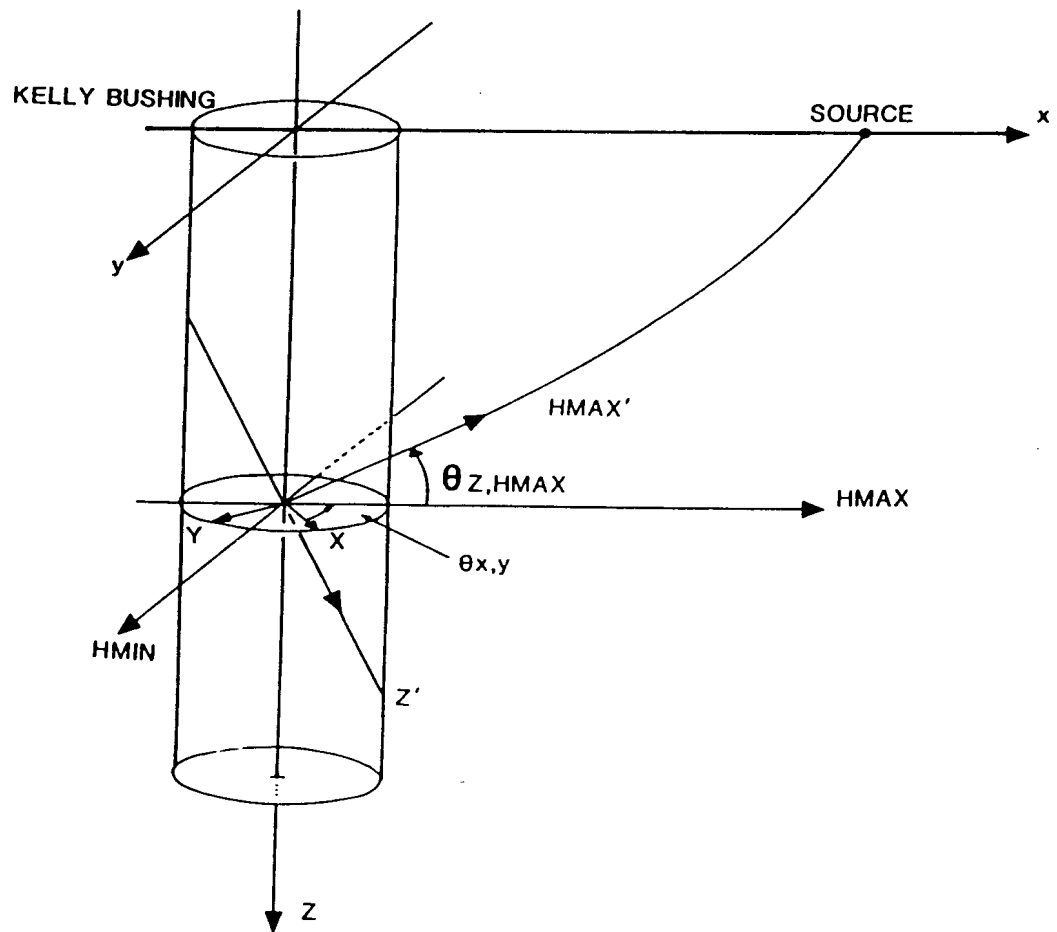


Figure 1.10 The orthogonal coordinate system of the local X , Y , and Z geophones along with the coordinate axis ($HMIN$, $HMAX$, Z' and $HMAX'$) that will be used as the principal axis in the hodogram (non-time variant) analysis (from Hinds et al., 1989a)

ellipse pointing in the direction of the azimuth of the incoming downgoing wave. The angle found in the hodogram analysis is used in a non-time variant rotation matrix equation where the input traces plus the rotation matrix are used to calculate the **HMIN** and **HMAX** traces (see Appendix). The output data will be the **HMAX** panel which contains SV and P-wave energy. For normal purposes, the **HMIN** data are discarded.

The **HMAX** and **Z** data are assumed to be orientated in the plane defined by the well and the source. The second objective is to use hodogram based polarization on the **Z** and the **HMAX** data. The **Z** and **HMAX** data are processed to output the **Z'** and **HMAX'** data using the rotation angle found during a hodogram analysis of the input data. The **HMAX'** data are assumed to predominately contain downgoing P-wave events and upgoing SV-wave events. In chapter 2, the inputs and outputs of the various polarizations are shown and an IPP is developed to ensure data processing quality for the procedures.

Does the geometry play a role in the polarizations? In Figure 1.11, the sonde axes in a deviated borehole and three different source locations are shown. The amount of partitioning onto the various axes can vary significantly depending on the source-receiver geometry within the deviated borehole. The objective with the two rotations, however, is achieved using normal hodogram analysis. The **HMAX'** data panel contains predominately downgoing P and upgoing SV-wave energy and the **Z'** axis data contains downgoing SV and upgoing P energy (Fig. 1.12).

If the up- and downgoing wave particle motion were exactly orthogonal then no further event partitioning processing is necessary. The **Z'** axis data panel would be interpreted following

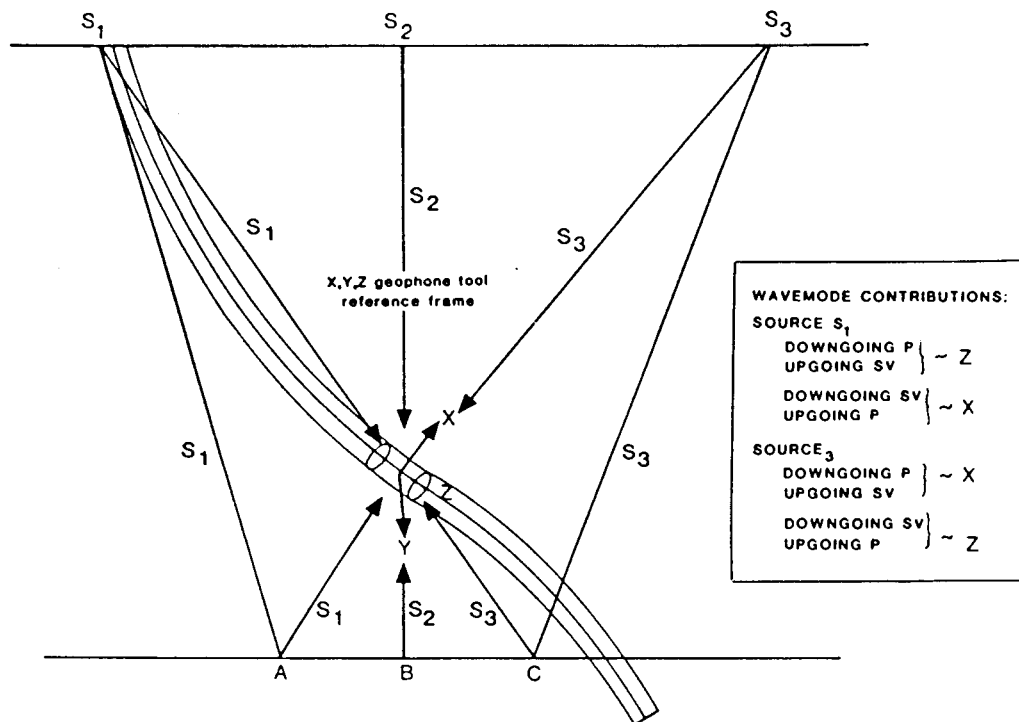


Figure 1.11 For the case of a deviated borehole, the triaxial geophone package receives contributions of P-, SV-, and SH- waves on all geophones. Even for the "near-offset" source location at S_2 , the Z channel data will not contain P waves only. To separate the various wavefield contributions, the data on the three geophones are numerically rotated using hodogram polarization analysis. This is the "theoretical" geometry used in the analysis of the upgoing rays for the deviated borehole. Note that the upgoing rays travel very different directions when the subsurface layers are not horizontal as in Figure 1.1 (from Hinds et al. 1989a).

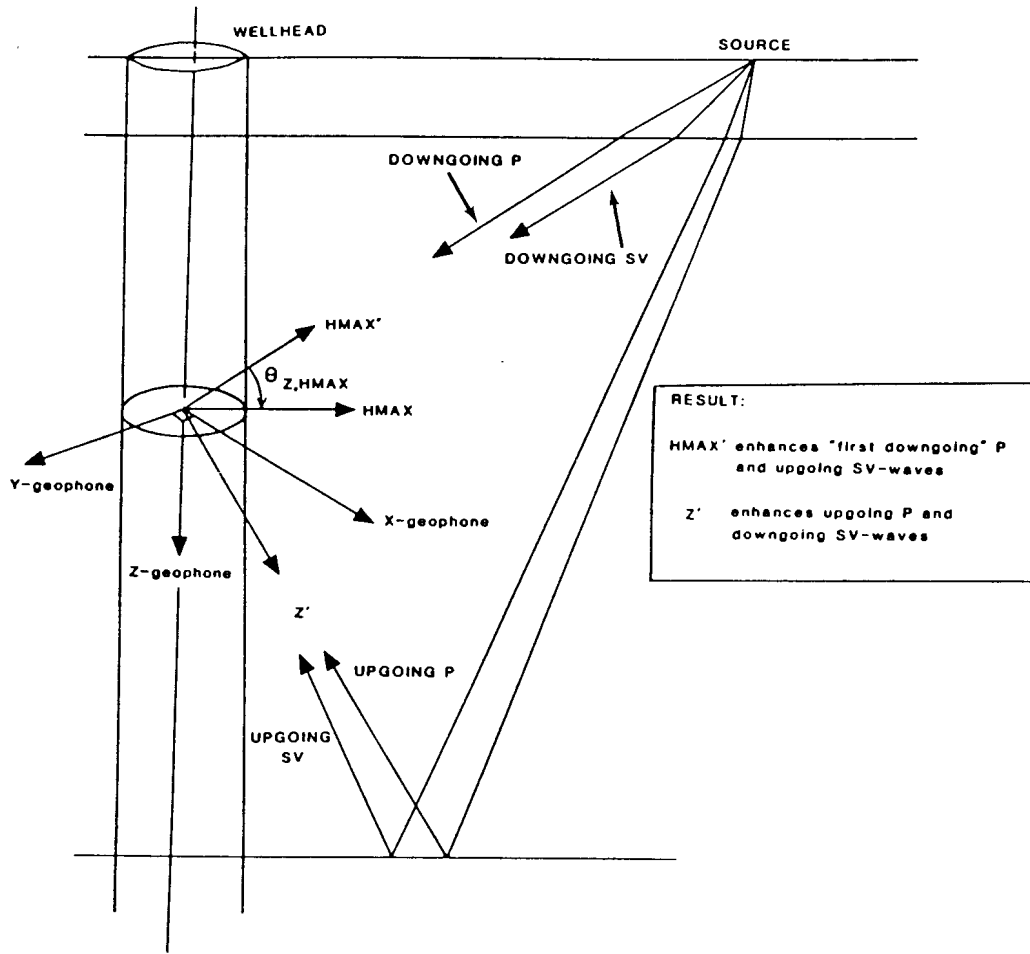


Figure 1.12 The geometry for time-variant rotations. To use the "classical" non-time variant rotations, it is assumed that the **HMAX'** data contain downgoing P- and upgoing SV-wave events only and that the **Z'** data contain upgoing P- and downgoing SV-wave events only. For the **Z'**, **HMAX'** rotation, the polarization analysis is performed on the downgoing primary wavelet (a single angle is chosen per VSP depth trace). The time-variant analysis consists of calculating the changing incidence angles of the upcoming P-wave (or SV) with increasing traveltimes at a single geophone location. The angle for a single layer is shown in the diagram whereas an entire model is input into the calculations which necessitates the time-variant calculation as the upgoing reflection angles change with each new layer used. For a single VSP trace, the angles are interpolated between the calculated model-based (time, angle) pairs to give a (time, angle) pair for each time sample following the first break for that trace (from Hinds et al., 1989a).

the application of normal move-out (NMO) corrections, VSP-CDP (Dillon and Thomson, 1984) mapping and migration techniques. However, as is shown in chapter 2, the **HMAX'** data contain residual upgoing P-wave energy. The angle of the upcoming P-wave recorded on a far offset VSP from the reflection off an interface just below the sonde will be different to the angle from an upgoing P-wave that resulted from a reflection from a much deeper interface. The angle of reflection from the deeper reflector (the angle between the vertical and the downgoing P-wave) will be smaller than the reflection from the shallower interface (both interfaces being below the sonde location).

A time-variant polarization of the upgoing events on given set of **Z** and **HMAX** traces can be performed by windowing the upgoing events and performing hodogram analysis of each event. However, due to the low amplitudes involved in the upgoing events, a model-based system is used to evaluate the time-variant polarization angles (time and angle pairs).

A model of the interfaces is constructed using the near offset first break times and ray-tracing is performed to given sonde model locations. The reflections from the various interfaces recorded at a given geophone location will result in (time, incidence angle) pairs from the modelled upgoing raypaths. These pairs are interpolated to provide a time-variant rotation angle for every time sample for the recorded trace at the same depth as the modelled geophone location. A time-variant polarization of the upgoing wave data from the **Z** and **HMAX** panels yields the **Z''** and **HMAX''** data panels as shown in chapter 2. The **Z''** data are then interpreted and correlated with the surface seismic.

The interpretive processing described in the next chapter drives the quality control decisions

that will allow interpretation to evaluate every step of the processing.

For far offset data, the downgoing waves separated from the HMAX' panel are used to deconvolve the final Z'' data. The constant time delay between the up- and downgoing multiples are assumed to exist; however, are these important time delay relationships valid for far offset data ? Figures 1.13 and 1.14 show the VSP modelled results (Z data) from a 980 m deep modelled borehole for the source offsets of 0, 200 400, 800, and 1000 m for surface-generated and interbed multiples, respectively. At far offsets, both the surface-generated and interbed multiple and primary up- and downgoing waves begin losing the simple time delay relationships found between the primaries and multiples found in the near offset VSP data. In chapter 2 and 6, a data example is given where a 524 m offset VSP was deconvolved with satisfactory results.

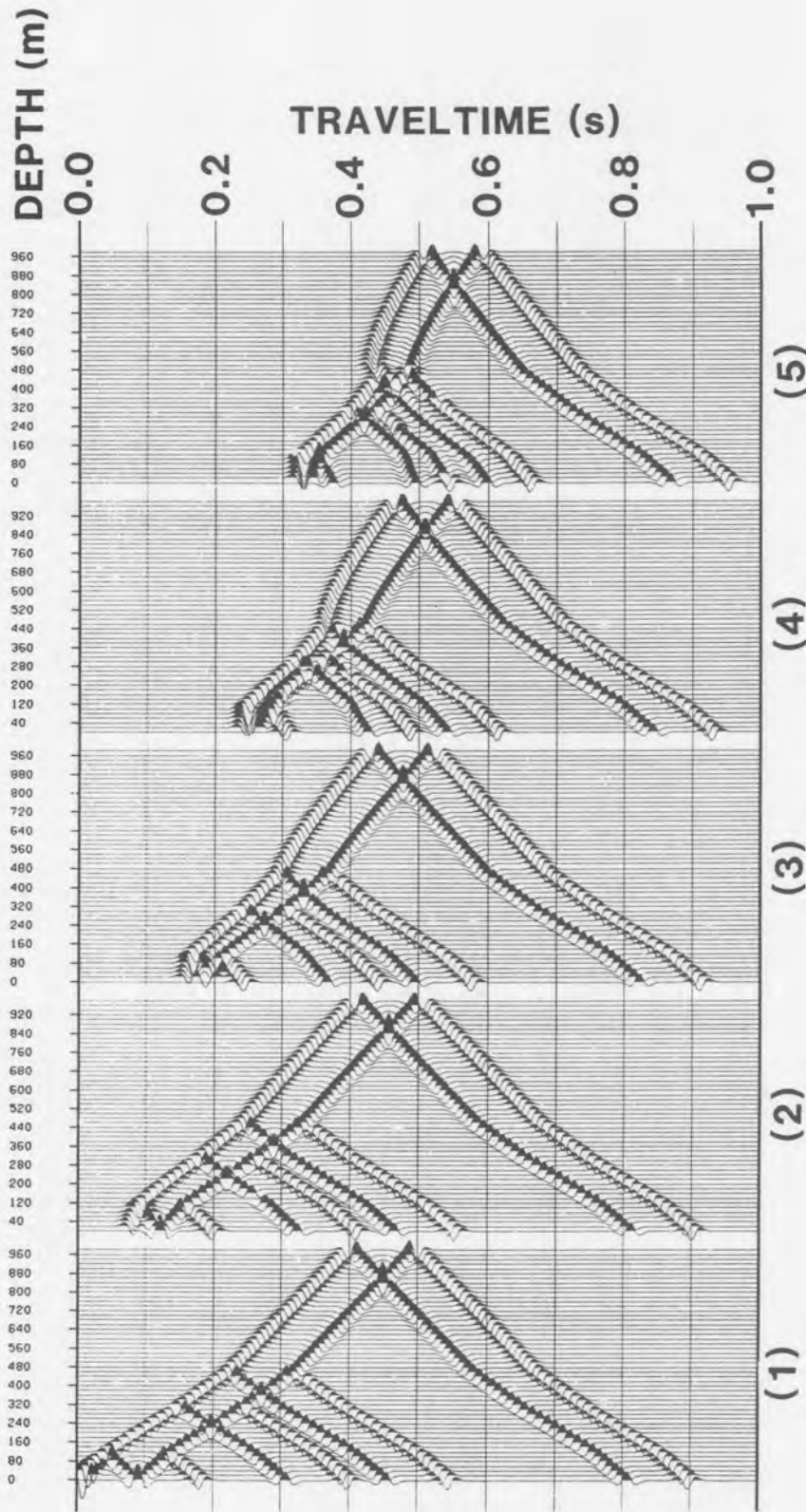


Figure 1.13 Synthetic VSP seismograms for the up- and downgoing primary and surface-generated multiple events for offsets of 0, 200, 400, 600 and 800 m (panel 1-5, respectively). The panels illustrate that the simplistic near offset primary-multiples time delays become complicated and invalid with increasing offset. The simple time delays between primary and multiple events (for near offset geometries) assume that the up- and downgoing wave propagation paths are vertically up and down, respectively. This relationship breaks down for far offset geometries.

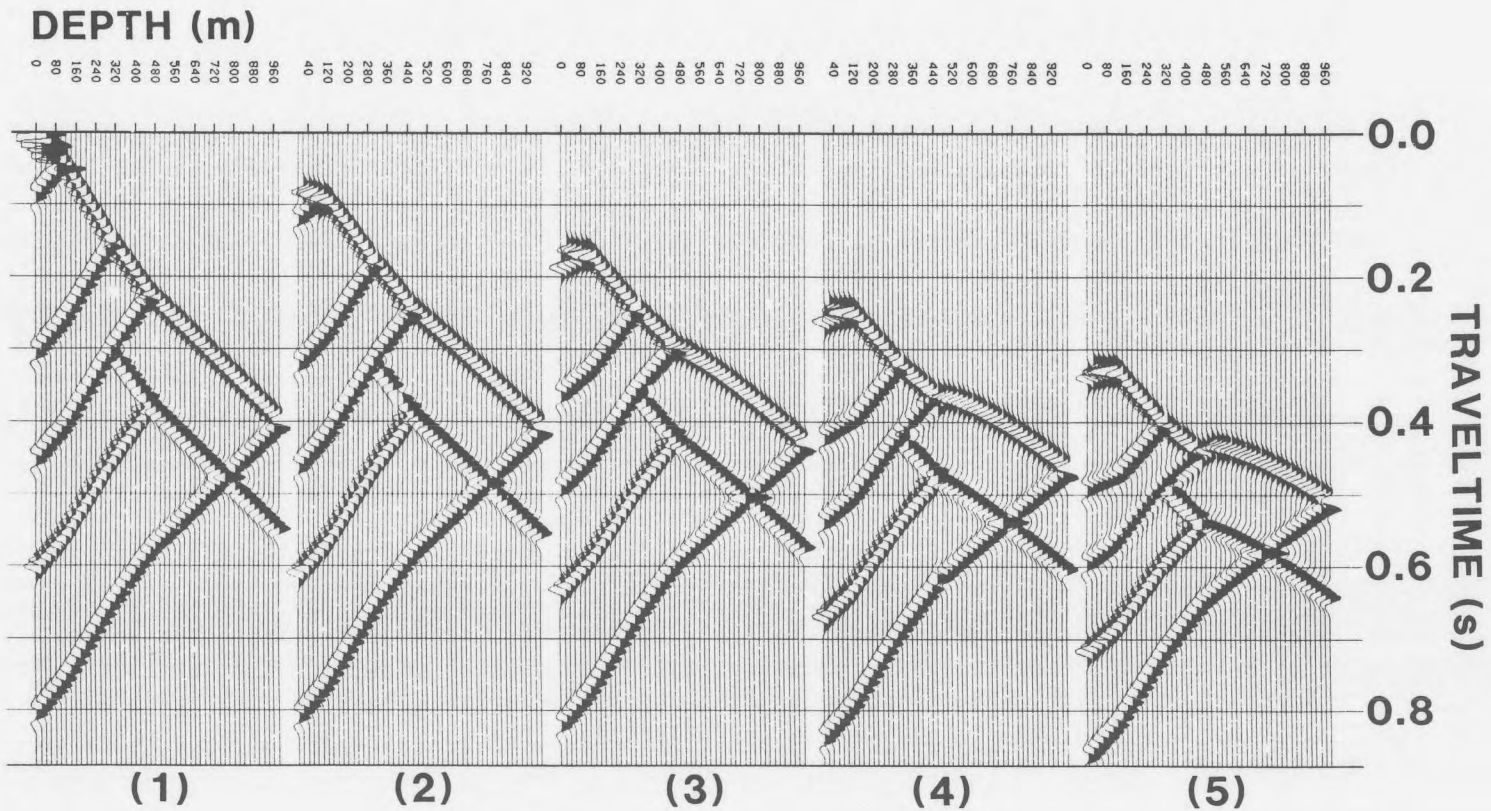


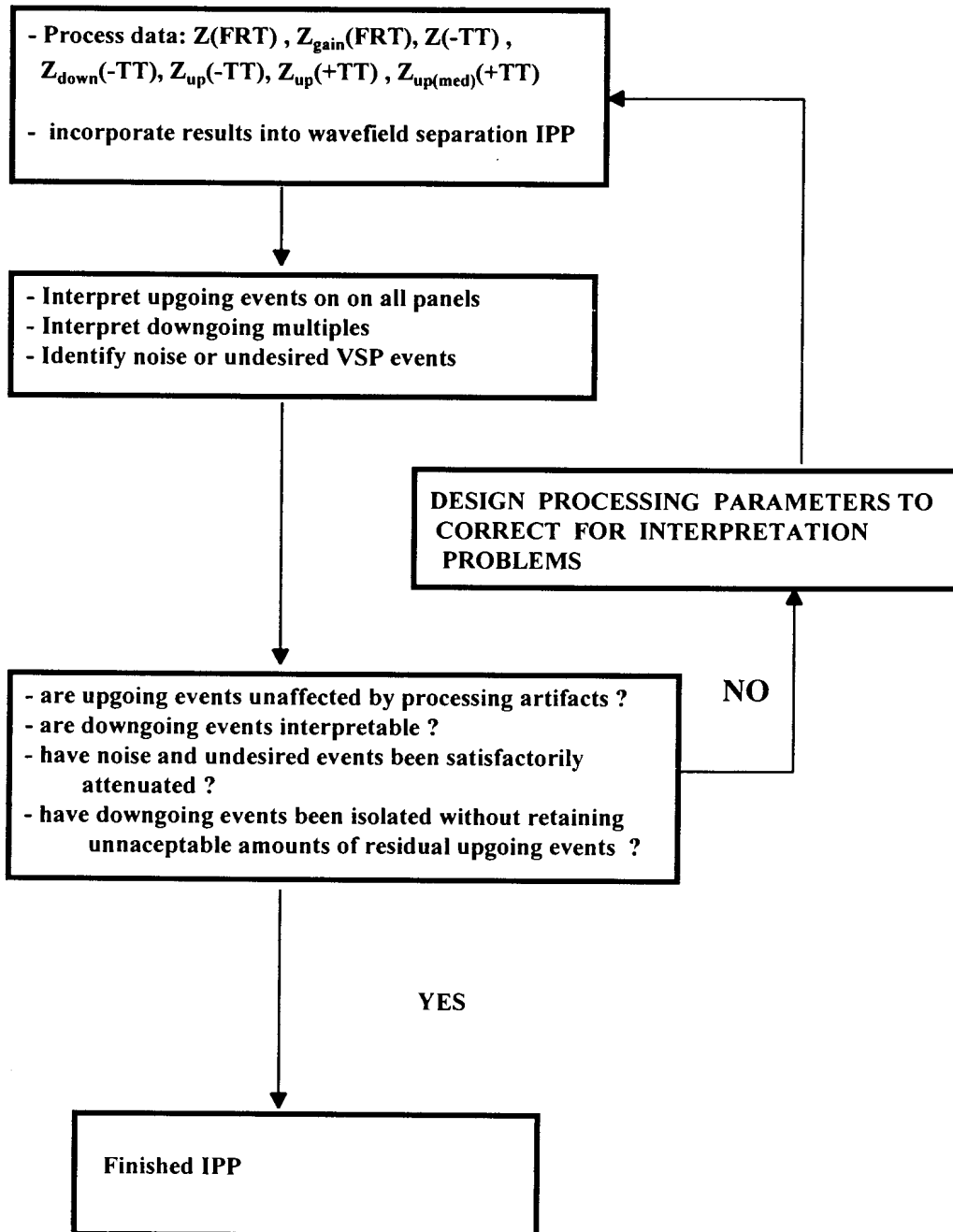
Figure 1.14 Synthetic VSP seismograms for the up- and downgoing primary and interbed generated multiple events for offsets of 0, 200, 400, 600 and 800 m (panel 1-5, respectively).

CHAPTER 2

INTERPRETIVE PROCESSING

The term interpretive processing has been used to describe the use of VSP results in guiding surface seismic processing (Hardage, 1985; Stone, 1981) and for VSP data processed repeatedly whilst modifying a single parameter to estimate reflector dip (Noponen, 1988). Merging of the VSP and intermediate seismic outputs are now emerging that enables the interpreter to continuously gauge the success of multiple attenuation. One such case occurs during model-based transform (MBT) processing (Næss, 1989). Hinds and Durrheim (1993, 1994) used a Karhunen-Loeve (K-L) based multiple attenuation scheme (Jones, 1985; Jones and Levy, 1987) to create an output seismic section that was used as input to MBT processing. Around the well on the seismic line used in that study, the VSP results from the well could be used to further constrain the MBT processing by supplying a model of the primary events in the immediate vicinity of the well.

Interpretive processing of VSP data involves the use of the interpretation of the VSP data to constrain the various processing stages of the VSP data. Flowchart 1 illustrates the procedures of interpretive processing for median filter based wavefield separation. The median filter wavefield separation processing involves amplitude balancing of raw data, static shifting, median filtering to isolate the downgoing events, amplitude balancing of the separated downgoing event data, the subtraction of the data containing up- and downgoing events from the panel containing only downgoing events, static shifting into pseudo-two-way traveltimes and upgoing event enhancement.



Flowchart 1: An example of the interpretive processing decision-making flowchart for the median filter plus subtraction wavefield separation processing (Hinds et al. 1989a).

An interpretive processing panel (IPP) is constructed (described in section 2.2.2) to examine the input and output of the various processing steps used to isolate the upgoing events into the final display, $Z_{up(med)}(+TT)$. Here, the subscript describes the type of events within the data and the term in the bracket refers to the data time configuration (see section 1.4.2). The upgoing events in $Z_{up(med)}(+TT)$ are interpreted; however the interpretation is also placed on the previous outputs along the processing route, such as the $Z_{up}(+TT)$, $Z_{up}(-TT)$, $Z_{down}(-TT)$, $Z(-TT)$, $Z_{gain}(FRT)$ and $Z(FRT)$ data. If any of the processing steps, starting from the raw data, $Z(FRT)$, to the median filtered upgoing event data in pseudo-two-way traveltimes, $Z_{up(med)}(+TT)$, have introduced artifacts that adversely affect the interpretation, then the processing step is modified to eliminate the artifacts. This procedure of generating the IPP and then determining the effect of the processing on the data is repeated until the interpretation is clear of processing artifacts. Using the example of wavefield separation, interpretive processing continues by utilizing the $Z_{up(med)}(+TT)$, $Z_{up}(+TT)$, $Z_{down}(-TT)$ data in the deconvolution processing and within the deconvolution IPP (described in section 2.2.6.1).

An example of processing artifacts is Rieber mixing (Sheriff, 1991) which can occur within Frequency-wavenumber (F-K) wavefield separation processing. As is illustrated further in section 2.2.4, separated upgoing events can be laterally smeared onto depth traces where the event was not recorded if only the narrow range of F-K domain data containing these upgoing events are used during the inverse Fourier transformation. An upgoing multiple event in $Z_{up}(+TT)$ data could then extend laterally beyond its corresponding primary (Hardage, 1985). The multiple event could be misinterpreted to be a primary event and not a multiple event.

This chapter displays the processing of near and far offset VSP data. The interpretive processing is developed through the use of the IPP and interactive screen processing. Where there are alternative processing routes that can be used, as in the case of wavefield separation, the various wavefield separation techniques are reviewed. The various techniques are formulated into the framework of interpretive processing panels. Where a single method can be used in more than one way to perform a single task, such as τ -P wavefield separation processing, a number of different routes are explored. The advantages and disadvantages of using the various routes are then evaluated in terms of the effect on interpretation.

In the far offset VSP processing, a case study presented in this chapter illustrates a normal processing route for the Ricinus data (see chapter 4; Hinds et al., 1989a; Hinds et al., 1993c and Hinds et al., 1994c) which produced results which were contaminated by mode converted downgoing and upgoing SV events. Following the interpretation of these events, it was decided to go back to the **Z(FRT)** and **HMAX(FRT)** data and to perform filtering in order to attenuate the mode converted events at that point in the processing procedure. The data was then successfully reprocessed using wavefield separation and time-variant polarization to output more interpretable results.

The success of far offset VSP deconvolution process is shown to be data dependent. In this chapter, the far offset VSP data of the Ricinus (chapter 4; Hinds et al., 1989a; Hinds et al., 1993c and Hinds et al., 1994c) and Simonette (chapter 6; Hinds et al., 1991b; Hinds et al., 1993b and 1994c) carbonate reef case studies are deconvolved to show the positive and negative effects of far offset VSP deconvolution.

For wavefield separation processing, the use of the median (Hardage, 1985), F-K, K-L (Hinds et al., 1986; Freire and Ulrych, 1988) and τ -P (Hu and McMechan, 1987; Moon et al., 1986; Devaney and Oristaglio, 1986) are demonstrated. In this chapter, it will be shown how the various methods can also be combined to perform individual tasks within another method's wavefield separation IPP. An example of this is the case of using surgical F-K muting to attenuate the aliased tubewave events contaminating the $Z_{up}(+TT)$ data that were originally wavefield separated from the $Z(-TT)$ data using the median filter wavefield separation technique (section 2.2.4.4). Here the surgical F-K muting technique is used for upgoing P-wave event enhancement.

Interactive screen processing is shown to assist interpretive processing in the evaluation of (1) event identification and (2) the effect of processing parameter selection on event isolation. This type of processing is deemed in this thesis to be a part of interpretive processing (Hinds et al., 1994c).

The final VSP products are used in conjunction with other exploration data in the integrated log display (ILD), integrated seismic display (ISD) and the integrated interpretive display (IID). This allows an additional interpretive check on the processing since the geological log and surface seismic data can be compared to the VSP results. These displays are used within integrated geological/geophysical interpretation (Hinds et al., 1989a, Hinds et al., 1991a, 1991b and 1993c; Hinds et al., 1993a and 1994b; Hinds et al., 1993b, 1994a and 1994c).

2.1 Processing runstreams

The main components of VSP processing to be discussed will be:

- (1) up- and downgoing wavefield separation;
- (2) VSP deconvolution (Hubbard, 1979);
- (3) time-invariant polarization;
- (4) time-variant polarization;
- (5) VSP-CDP transformation (Dillon and Thomson, 1984); and
- (6) VSP migration processing.

Wavefield separation runstreams in the literature highlight a single filter or method to perform the wavefield separation (Lee and Balch, 1983; Lee, 1984; Taniel and Michon, 1984; Beydoun et al., 1990; Shuck, 1988a and b). The runstreams highlight the processing steps; however, Hinds et al., (1989a) produced both near and far offset runstreams through the IPP displays that brought full interpretation into the processing picture.

The runstreams however should be considered to be data dependent since every VSP dataset will contain inherent interpretation problems. The suggested processing presented below and elsewhere in VSP literature should be considered as guidelines. An example near offset processing flow using the median filter wavefield separation (used in Hinds et al., 1989a) could include:

1. geometry design and completion of trace headers;
2. editing of the unstacked **Z(FRT)** data;

3. compensation for source timing errors (as an example, the picking of near-source airgun first breaks and subsequent static shifting of the corresponding VSP data);
4. common sonde location gathering and summation;
5. first break picking of first break compensated $Z(\text{FRT})$ data;
6. editing of VSP stacked data;
7. application of a spherical divergence correction for downgoing waves using a velocity model defined by the VSP first break times;
8. static shifting of $Z(\text{FRT})$ data to $-\text{TT}$ alignment, $Z(-\text{TT})$;
9. application of a median filter to $Z(-\text{TT})$ data to isolate downgoing waves and produce the output data, $Z_{\text{down}}(\text{TT})$;
10. scaling of $Z_{\text{down}}(-\text{TT})$ to match the $Z(-\text{TT})$ data;
11. subtraction of scaled $Z_{\text{down}}(-\text{TT})$ from $Z(-\text{TT})$ to output $Z_{\text{up}}(-\text{TT})$;
12. perform multi-window frequency analysis to design and perform time-variant filtering on $Z_{\text{up}}(-\text{TT})$;
13. design deconvolution operator from $Z_{\text{down}}(-\text{TT})$ and apply to $Z_{\text{up}}(-\text{TT})$ to output $Z_{\text{up}(\text{decon})}(-\text{TT})$;
14. statically shift $Z_{\text{up}}(-\text{TT})$ and $Z_{\text{up}(\text{decon})}(-\text{TT})$ data to output $Z_{\text{up}}(\text{FRT})$ and $Z_{\text{up}(\text{decon})}(\text{FRT})$ data, respectively;
15. apply spherical divergence correction for upgoing waves (model-based) to $Z_{\text{up}}(\text{FRT})$ and $Z_{\text{up}(\text{decon})}(\text{FRT})$;
16. apply normal moveout correction (and simultaneously static shift) to output $Z_{\text{up}}(+\text{TT})$ and $Z_{\text{up}(\text{decon})}(+\text{TT})$;
17. application of median and bandpass filter to enhance upgoing events on $Z_{\text{up}}(+\text{TT})$ and $Z_{\text{up}(\text{decon})}(+\text{TT})$;
18. mute the upgoing wavefield data for use in the outside and inside corridor stack IPP's (Hinds et al., 1989a) of $Z_{\text{up}}(+\text{TT})$ and $Z_{\text{up}(\text{decon})}(+\text{TT})$ data;

The wavefield separation route and analysis of multiple contamination will be data dependent.

A reference far offset processing runstream includes two hodogram based trace data rotations, time-variant angle rotation, NMO, VSP-CDP or migration (Hinds et al., 1989a).

Assuming that the **X**, **Y**, **Z** channel data have been edited, common receiver location gathered, stacked and first break picked, an example runstream is presented below:

1. hodogram analysis about a window centred around the first break of the **X(FRT)** and **Y(FRT)** data;
2. rotation of the **X** and **Y** data to output the **HMIN(FRT)** and **HMAX(FRT)** data;
3. hodogram analysis about a window centred around the first breaks of the **HMAX(FRT)** and **Z(FRT)** data;
4. rotation of the **HMAX(FRT)** and **Z(FRT)** data to output the **Z'(FRT)** and **HMAX'(FRT)** data;
5. application of the spherical divergence correction for downgoing waves to the **Z'(FRT)** and **HMAX'(FRT)** data;
6. statically shift the **HMAX'(FRT)** to output **HMAX'(-TT)** data;
7. wavefield separation using the median filter to output **HMAX'_{down}(-TT)** data;
8. scaling of the **HMAX'_{down}(-TT)** data using a scale factor calculated from an analysis of data from a window around the aligned first break wavelets in the **HMAX'(-TT)** data;
9. subtraction of scaled **HMAX'_{down}(-TT)** from **HMAX'(-TT)** to output the **HMAX'_{up}(-TT)** data;
10. wavefield separation of the **Z'(FRT)** data using F-K masking to output the **Z'_{up}(FRT)** data;
11. application of inverse operation of step (4) on **Z'_{up}(FRT)** and **HMAX'_{up}(FRT)** to output **Z_{up(derot)}(FRT)** and **HMAX_{up(derot)}(FRT)**;
12. calculate the time-variant polarization (time, angle pairs) for every depth trace using ray-tracing of upgoing waves reflecting from a model of interfaces created from the first break times and interval velocities of the near offset VSP data;
13. application of the time-variant model-based rotations to the **Z_{up(derot)}(FRT)** and **HMAX_{up(derot)}(FRT)** to output the **Z''_{up}(FRT)** and **HMAX''_{up}(FRT)** data;
14. application of a spherical divergence correction to the **Z''_{up}(FRT)** data using modelled upgoing traveltimes;
15. application of model-based NMO correction to **Z''_{up}(FRT)** data;
16. time-variant bandpass filtering of **Z''_{up}(FRT)** data;
17. statically shift **Z''_{up}(FRT)** data to output **Z''_{up}(+TT)**;
18. application of a median and bandpass filter to **Z''_{up}(+TT)** data;

19. application of VSP-CDP transform to output the $Z''_{up}(+TT)$ data or application of VSP migration to the $Z''_{up}(FRT)$ data to output the Z''_{up} data in the (+TT) versus offset distance away from the well domain;
20. application of a deconvolution operator calculated from the $HMAX'_{down}(-TT)$ data to the $Z''_{up}(FRT)$ to output to $Z''_{up(decon)}(FRT)$ data;
21. replication of steps (14) to (19) to the $Z''_{up(decon)}(FRT)$ data to output the VSP-CDP or migrated $Z''_{up(decon)}$ data in the (+TT) versus offset distance away from the well domain.

2.2 Near offset data processing IPP's

2.2.1 Separation and up- and downgoing waves

The wavefield separation methods described in this section are:

- (1) median filtering;
- (2) Karhunen-Loeve (K-L) filtering;
- (3) Frequency-spatial wavenumber (F-K) filtering; and
- (4) time intercept-slowness (τ -P) filtering.

For each method, an IPP is designed to reflect the processing steps of the wavefield separation process. A description of the filter is reviewed with the mathematics for the filter being reserved for the Appendix. The methods and the associated IPP's are described with interpretation in mind. The example data for each method were chosen to highlight interpretational problems that may occur in using the process.

For the median filtering method, the filtering is used to isolate the downgoing events from $Z(-TT)$ data into $Z_{\text{down}}(-TT)$ data. The $Z_{\text{down}}(-TT)$ data are amplitude balanced to match the $Z(-TT)$ data and then subtracted from the $Z(-TT)$ data to output the $Z_{\text{up}}(-TT)$ data.

Similar to the median filtering wavefield separation method, the K-L filtering isolates the $Z_{\text{down}}(-TT)$ data from the $Z(-TT)$ data. The filtering transforms the $Z(-TT)$ into its principal components with the first (and largest) principal components representing the horizontally aligned downgoing events. The data are inverse transformed using only the first few principal components. Subtraction of the $Z_{\text{down}}(-TT)$ data from the $Z(-TT)$ data yields the separated upgoing events.

The F-K method transforms the $Z(\text{FRT})$ data into the F-K domain. In this domain, the upgoing events reside in the negative wavenumber quadrant and the downgoing events in the positive quadrant. Using quadrant or surgical F-K muting, the downgoing events are muted from the F-K domain. The F-K data are then inverse transformed to output the isolated upgoing events, $Z_{\text{up}}(\text{FRT})$.

In the F-K filtering section, F-K wavefield separation IPP and interactive F-K screen processing are reviewed. The problems encountered in F-K filtering with Rieber mixing (Hardage, 1985), spatial aliasing and events crossing within the F-K domain are addressed.

The τ -P filtering based wavefield separation method relies on the different slownesses of the up- and downgoing events to perform the separation (Hardage, 1992; Hu and McMechan, 1987). In this section, the τ -P filter is used to perform velocity filtering and spatial

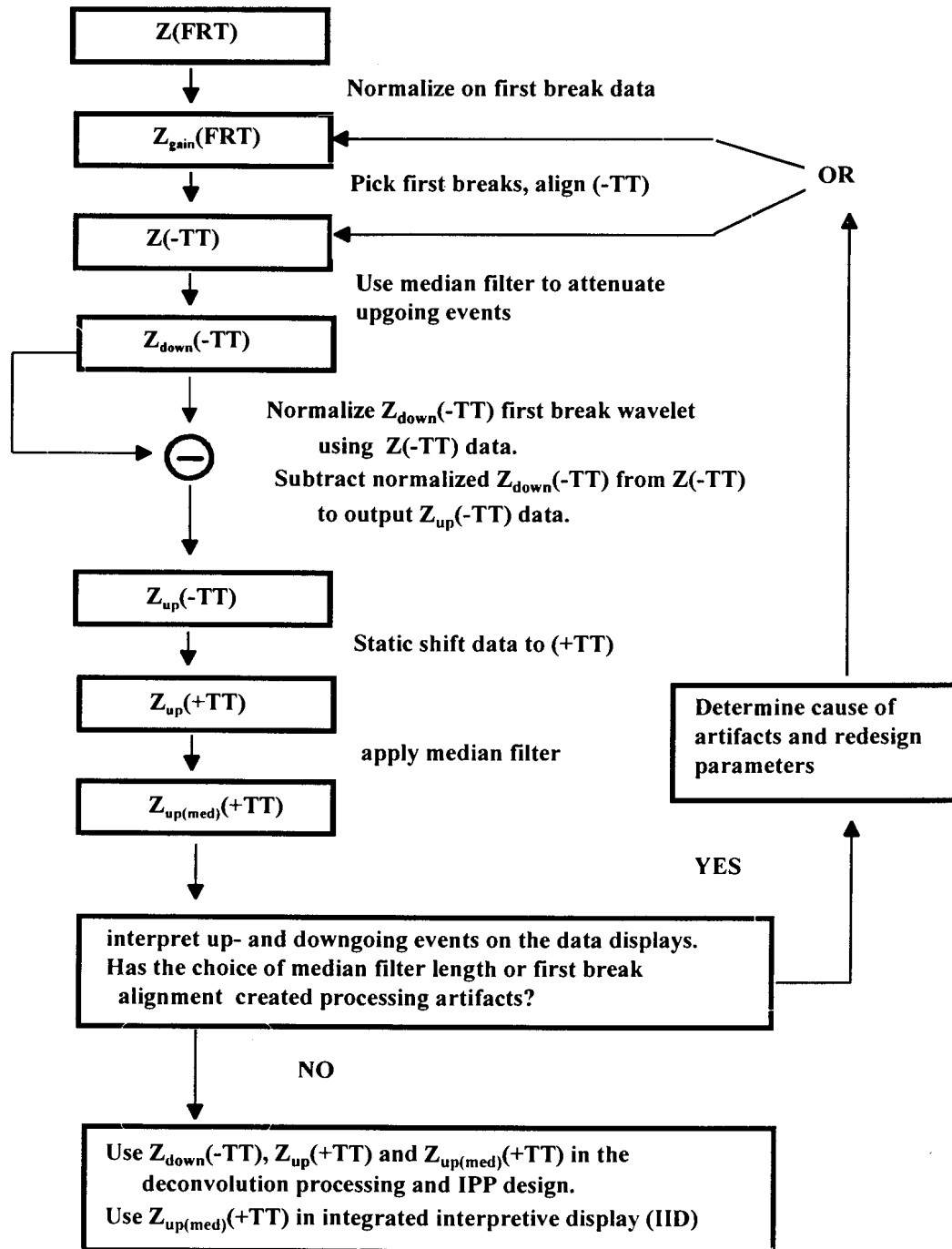
interpolation (Hu and McMechan, 1987). The spatial interpolation is used in the separation step and as a pre-processing step for other wavefield separation methods (Hinds et al., 1994c).

One way to view the examples is to recognise the types of problems (such as random noise, tubewave and SV event contamination) present within each example dataset and then to look for similarities between industry data and the example VSP data. The second way is to compare the chapter 2 data once the data have been interpreted in the case histories. The way in which the various filtering methods shown in chapter 2 have aided or distorted the final interpretations is shown in chapters 3 to 6. The interpretations are not presented in depth in this chapter; however, the development of interpretive processing (IPP and interactive processing) and associated displays is stressed.

2.2.2 Median filtering

In this section, the wavefield separation method will use the median filter. The flowchart of the wavefield separation procedure using the median filter is shown in Flowchart 2. The median filter is used to isolate the downgoing events from the $Z(-TT)$ data into the downgoing event data shown in the $Z_{\text{down}}(-TT)$ panel. The isolated downgoing events are scaled and then subtracted from the up- and downgoing events of the $Z(-TT)$ data resulting in the upgoing event data displayed in the $Z_{\text{up}}(-TT)$ data panel. Following static shifting and further median filtering, the $Z_{\text{up}(\text{med})}(+TT)$ data are interpreted. The interpretation is then placed on all of the data panels starting from the $Z(\text{FRT})$ data to the $Z_{\text{up}(\text{med})}(+TT)$ data.

FLOWCHART - Wavefield separation using the median filter method



Flowchart 2: An example of the interpretive processing flowchart for the median filter plus subtraction wavefield separation processing (Hinds et al., 1989a).

An analysis of the effect of each processing step on the interpretation of the upgoing events is done. When using the median filter for wavefield separation, the two areas that are of concern are (1) the first break picking and (2) the length of the median filters used to perform upgoing event isolation and upgoing event enhancement. The first breaks times are repicked or lengths of the median filters applied are modified and the processing is repeated if improper first break picking or the wrong choice of median filter lengths have resulted in processing artifacts that adversely affect the interpretation. The use of the median filter within a wavefield separation IPP on multiple and tubewave contaminated data are shown in the sections below.

2.2.2.1 Review of the median filter

The theoretical basis of the one- and two-dimensional median filter has been reviewed in Arce et al. (1986), Fitch et al. (1984), Arce and McLoughlin (1984), Gallagher and Wise (1981) and Nodes and Gallagher (1982). Kommedal and Tjostheim (1989) and Hardage (1985) published studies that compared the median filter based wavefield separation methods to other wavefield separation methods.

The input data to the 1-D median filter is a window of data points from a series of depth traces for a single time value. The number of windowed data points can be an even or odd value, ($2N$ or $2N+1$). Since the median filter requires N points before and after the centre data point within the data window, data padding is done at the edge of the dataset (the shallowest and deepest data traces are repeated to perform the padding).

For an example, consider a 7 point median filter. During the filtering, the sliding constant time window would contain data values from 7 depth traces. These seven values are sorted according to magnitude with the centre value of the sort being termed the median value. That median value becomes the value for the fourth depth trace within the same window for the resultant output data. The median filter window keeps sliding across the data until all of the depth traces of the input data have been processed. All of the traces at the next time value are then processed.

For the odd numbered point filter, the median value at the centre of the sorted windowed time series becomes the new value of the output series. When N is even, the mean of the two middle median values is the output of the filter. The equations for the median filtering are discussed in the Appendix.

2.2.2.2 Median filtering and multiple contaminated VSP data

Figure 2.1 is the median filter based wavefield separation IPP for the multiple contaminated near offset data of the Fort St. John Graben case history (Hinds et al., 1991a; Hinds et al., 1993a and 1994b; Hinds et al., 1994c) discussed in detail in chapter 5. The raw $Z(\text{FRT})$ data are equalized using a window centred on the first break wavelets and the resultant data are shown in panel 1 of Figure 2.1. By inspection, it is clear that the downgoing waves are orders of magnitudes larger in amplitude than the upgoing waves (Hardage, 1985). The depth variable increases along the horizontal axis from left to right in panels 1-7 and traveltimes increase downwards. Strong repetitive downgoing multiple wavetrains in panel

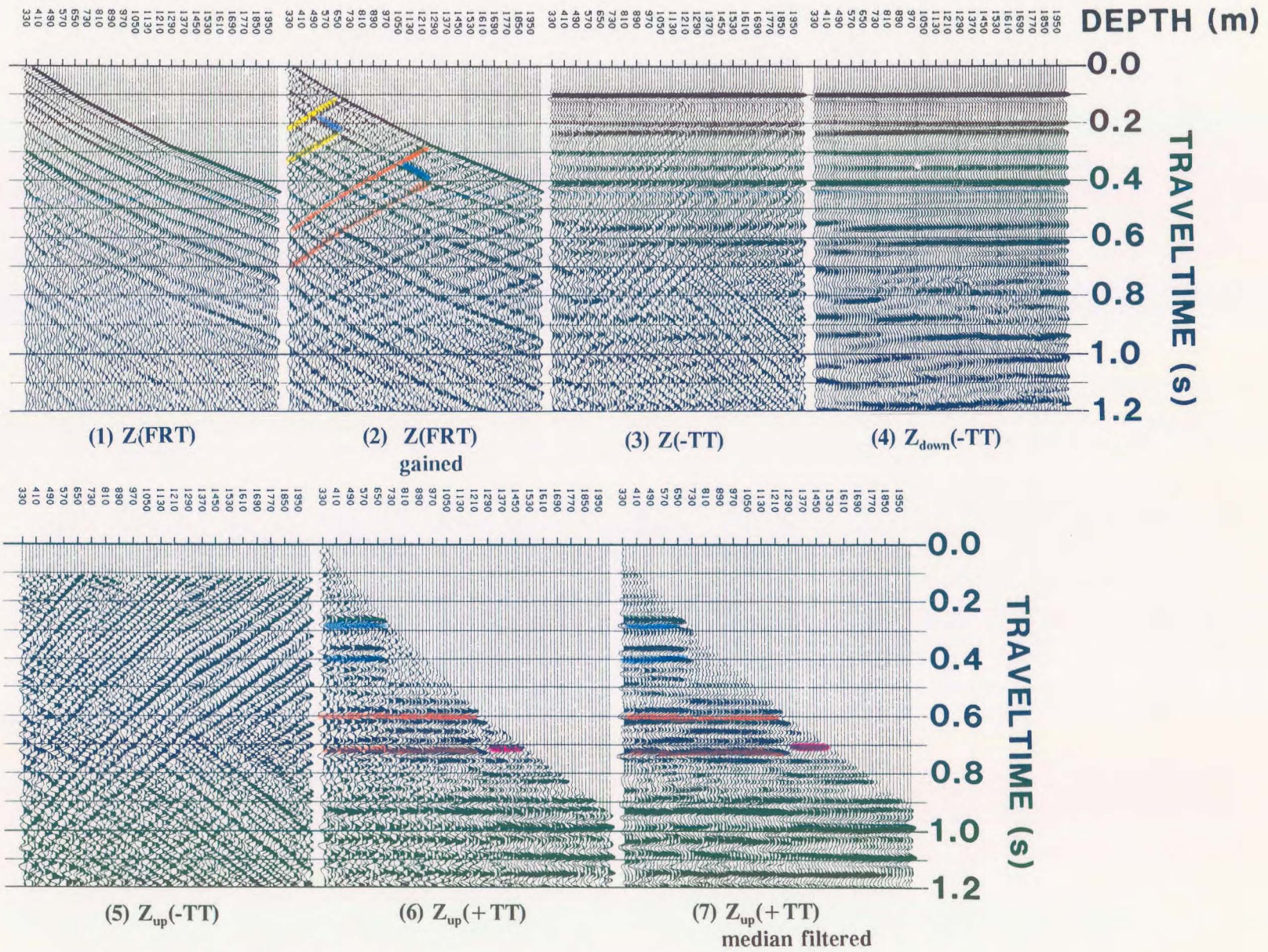


Figure 2.1 Wavefield separation IPP of the Fort St. John Graben case study (Hinds et al., 1993a) data using the median filter and subtraction method (Hinds et al., 1989a).

1 follow the first breaks.

In panel 2, the **FRT** data have been gained (a form of programmed gain control) to show the inter-relationship between the up- and downgoing multiples. One particular multiple represented by the series of reflections beginning with the reflected upgoing event (trough) generated at an interface at about 690 to 710 m (Spirit River Formation; see Chapter 5) can be tracked. The upgoing primary event is highlighted on panel 2. The upgoing event intersects the primary downgoing "curve" at about 0.115 s **FRT** travelttime between the 690 and 710 m traces. The upgoing event can be traced (increasing in travelttime with decreasing depth) back to the shallowest trace (at approximately 0.24-0.25 s). The intersection of the same event with the surface generated downgoing multiple occurs at 0.19 s on the trace for 470 m. The downgoing surface generated multiple (coloured blue) is opposite in polarity (a trough) to the primary downgoing wave (the same polarity as the upgoing primary). The intersection of the two waves is only noted to guide the reader; there is no physical significance to the intersection. If the highlighted portion of the downgoing multiple (coloured yellow) is followed deeper in time to 0.22 s on the 690-710 m trace, it is clear that the downgoing multiple reflects at the 690 m interface and creates an upgoing multiple (a peak). The highlighted upgoing multiple only exists on traces shallower than the 690 m trace (this can be seen more clearly in the absence of downgoing events on panels 5, 6 and 7). We have thus reached our first interpretive processing objective; namely, that this multiple described above must be preserved during the wavefield separation method such that the extent of the upgoing multiple event does not extend to traces deeper than 690 m.

What are the timing relationships? The time delay between the downgoing primary (peak)

and the first strong surface generated downgoing multiple (trough) is the same time delay as between an upgoing primary event (the Spirit River event of Chapter 5; Hinds et al., 1991a; Hinds et al., 1993a and Hinds et al., 1994c) which is a dominant trough at 0.28 s on panel 7 (coloured blue) and the corresponding upgoing multiple (a peak at 0.4 s on panel 7 coloured blue).

A clear upgoing event generated at about 1250 m depth (Nordegg Formation event described in Chapter 5) is highlighted (in orange) on panels 2, 7 and 8 and a set of associated upgoing multiples are generated in the same way as were the multiples described above for the Spirit River Formation interface (at 690 m). The first upgoing multiple of the Nordegg Formation interface resulting from the surface generated downgoing multiple is also highlighted in orange and occurs at approximately 0.725 s on panels 6 and 7. On panel 3, the $Z(\text{FRT})$ data are statically shifted to $Z(-\text{TT})$. The first break is aligned at 100 ms so as not to lose any part of the first break wavelet. If the first break would have been picked as the dominant trough of the first break (following the strong peak) and was shifted to the time origin, then the data appearing before the trough would have effectively been muted.

In panel 4 of Figure 2.1, an 11 point median filter has been used to isolate the horizontally aligned downgoing wavefield events. The median filtering wavefield separation technique is really a three-part exercise. In $(-\text{TT})$ time, the method consists of:

- 1) separating the downgoing waves, $Z_{\text{down}}(-\text{TT})$, from the combined wavefield data, $Z(-\text{TT})$;
- 2) amplitude balancing the separated downgoing waves, $Z_{\text{down}}(-\text{TT})$, with the combined

wavefield data, $Z(-TT)$; and

- 3) subtracting the amplitude balanced downgoing waves, $Z_{\text{down}}(-TT)$ from the combined wavefield data, $Z(-TT)$, to obtain the upgoing events, $Z_{\text{up}}(-TT)$.

The combined wavefield data, downgoing events, and separated upgoing events ($-TT$) are shown in panels 3, 4, and 5, respectively. The data are placed into $(+TT)$ by first break time shifting (as shown in Fig. 1.4). At this stage, a second multiple problem that can be detected using interpretive processing can be seen on Figure 2.1 ! Amidst the upgoing multiples starting from 0.6 - 0.8 s on panels 6 and 7, there is an upgoing primary (since it intersects the first break curve in panel 2, 5, and 6 on the 1470-1490 m traces) at 0.7 s. This primary event which is highlighted in red on panel 7 of Figure 2.1 must be preserved during the deconvolution processing.

Through the use of interpretive processing, it can be determined that the median filter wavefield separation method has preserved the edge (lateral extent) of the upgoing multiples and has preserved the discontinuity between the primary from 1470 m and the multiples in which the primary is superimposed. The $Z_{\text{up}}(\text{FRT})$ data in panel 6 are enhanced using a short length median filter and the enhanced version is presented in panel 7 of Figure 2.1. This has turned out to be a classic multiple data example which can be used for the other wavefield separation methods.

2.2.2.3 Median filtering and tubewave contaminated VSP data

Another example of the median filter based wavefield separation IPP is shown in Figure 2.2 for tubewave contaminated data. Hardage (1981, 1985) gives a thorough description of the tubewave and its appearance on VSP data. The shallowest trace was recorded at 410 m depth so that the origin of the tubewave event could be traced to the surface. The tubewave is most likely due to the first arrival of the Rayleigh ground roll wave and the action of the wave at the wellhead causing vertical motion in the borehole fluid column (Hardage, 1985). This would be categorized as Hardage's Tubewave Mode 2 (Hardage, 1981). The questions are whether one needs to or can attenuate the tubewave in order to better interpret upgoing events that the noise event may be superimposed upon. On panel 2, the gained data reveal that the tubewave event is spatially aliased. Spatial aliasing is discussed in Yilmaz (1987) and Hardage (1985). The depth increment of 30 m was not adequate to sample the low velocity tubewave. The up- and downgoing tubewave events are highlighted on panels 1, 2 and 3.

In the $Z_{\text{down}}(-\text{TT})$ data shown in panel 4, much of the downgoing tubewave event has been eliminated from the combined wavefield data, $Z(-\text{TT})$, shown in panel 3. This implies that the entire downgoing tubewave will not be subtracted out of the $Z(-\text{TT})$ data during the wavefield separation and the aliased part of the tubewave that appears to be upgoing events will remain in the $Z_{\text{up}}(-\text{TT})$ data. In panel 5, the gained separated upgoing data, $Z_{\text{up}}(-\text{TT})$, still contains the high amplitude tubewave event. The aliased tubewave event that has not been eliminated is highlighted in yellow on panels 5-8. The $Z_{\text{up}}(+\text{TT})$ and $Z_{\text{up}(\text{med})}(+\text{TT})$ data in panels 6 and 7, respectively, show the interference of the tubewave with the upgoing

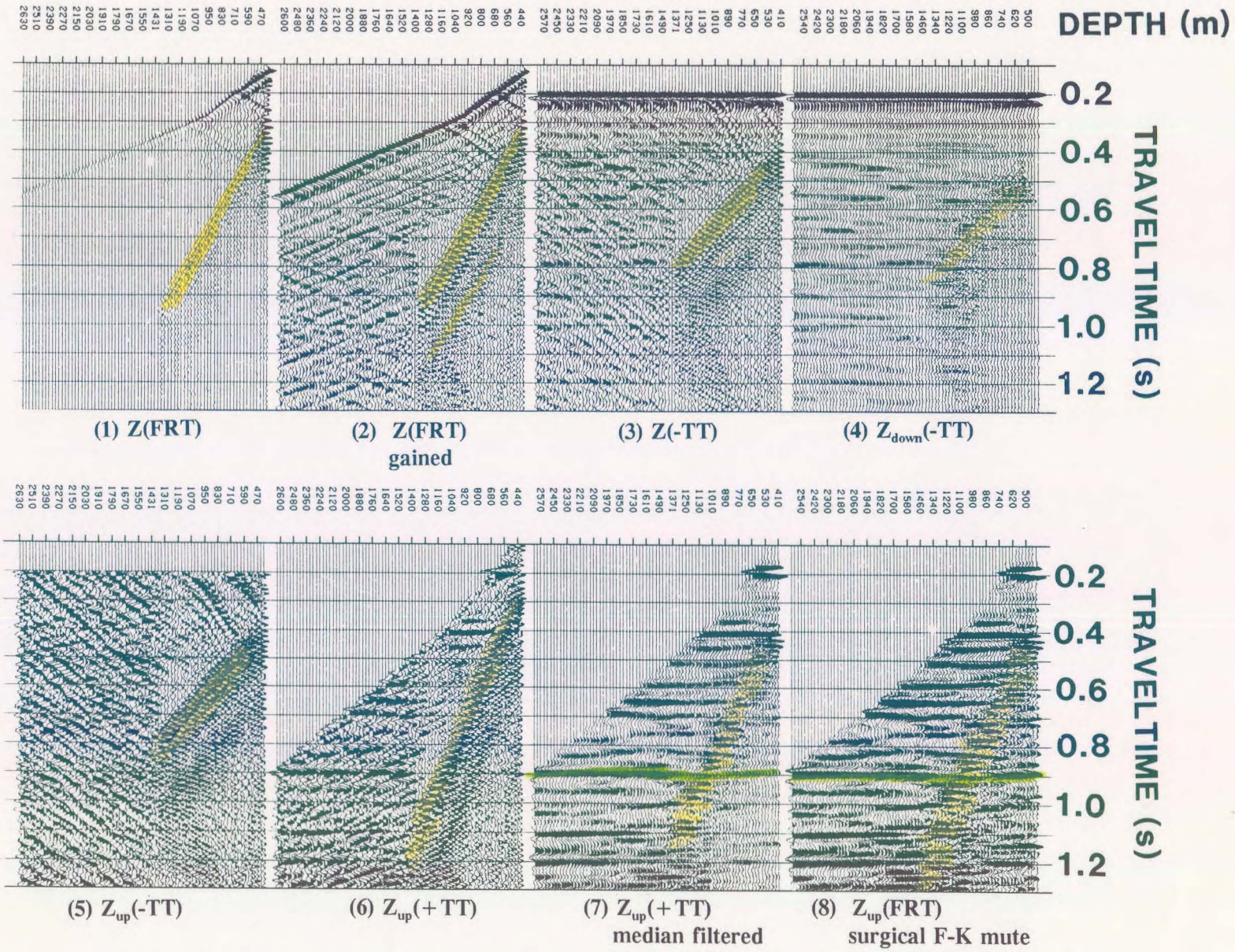


Figure 2.2 Wavefield separation IPP of the tubewave contaminated data using the median filter and subtraction method (Hinds et al., 1989a). The F-K domain plot of the surgical muting (panel 8) is displayed in Figure 2.17.

primary events. A striking example is the interference of the upgoing primary located at 0.9 s and highlighted (in green) on panels 7 and 8.

Panel 8 shows the upgoing events after surgical F-K muting of some of the aliased tubewave F-K response. The F-K plot of the data following the surgical muting is shown later in Figure 2.17. The events surrounding the tubewave event have been raised in amplitude; however, the tubewave event still inhibits the interpretation of the upgoing events along its path where the aliased (appearing as upgoing events "within" the tubewave event) portion of the tubewave event constructively and destructively interferes with the flat lying upgoing P-wave primary events. Using a longer length median filter in producing the $Z_{up(med)}(+TT)$ data of panel 7 would eliminate more of the downgoing tubewave from the data; however, amplitude variations within the upgoing events would not be preserved.

2.2.2.4 Difference panels to aid in filter length determination

Do we have intermediate steps that can be used to choose the length of the median filter to be used? In panels 1-5 of Figure 2.3, a series of $Z_{down}(-TT)$ data panels for a marine near offset VSP have been produced using a 3, 5, 7, 9, and 11 point median filter on the original $Z(-TT)$ data, respectively. The separated downgoing waves appear similar with minor amounts of residual upgoing waves left in panels 1 and 2. In panels 6, 7, 8, and 9, the 11 point median $Z_{down}(-TT)$ data have been subtracted from the 3, 5, 7, and 9 point median filter panels, respectively to form a difference panel. The amount of residual upgoing events left in the downgoing wavefield panels can be shown relatively simply through the use of the difference panels. The 3, 5, and 7 point median filters are not suitable for the wavefield

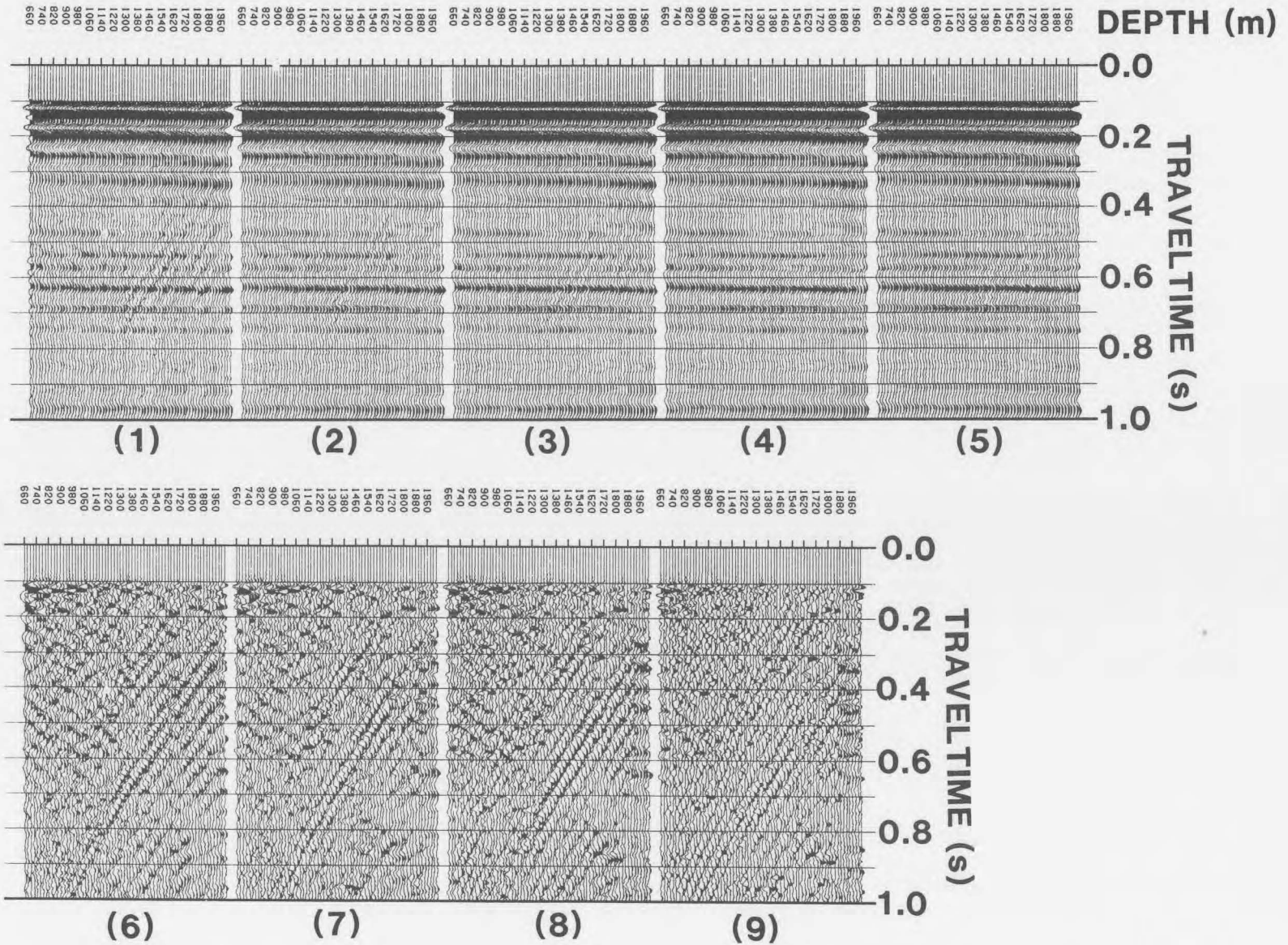


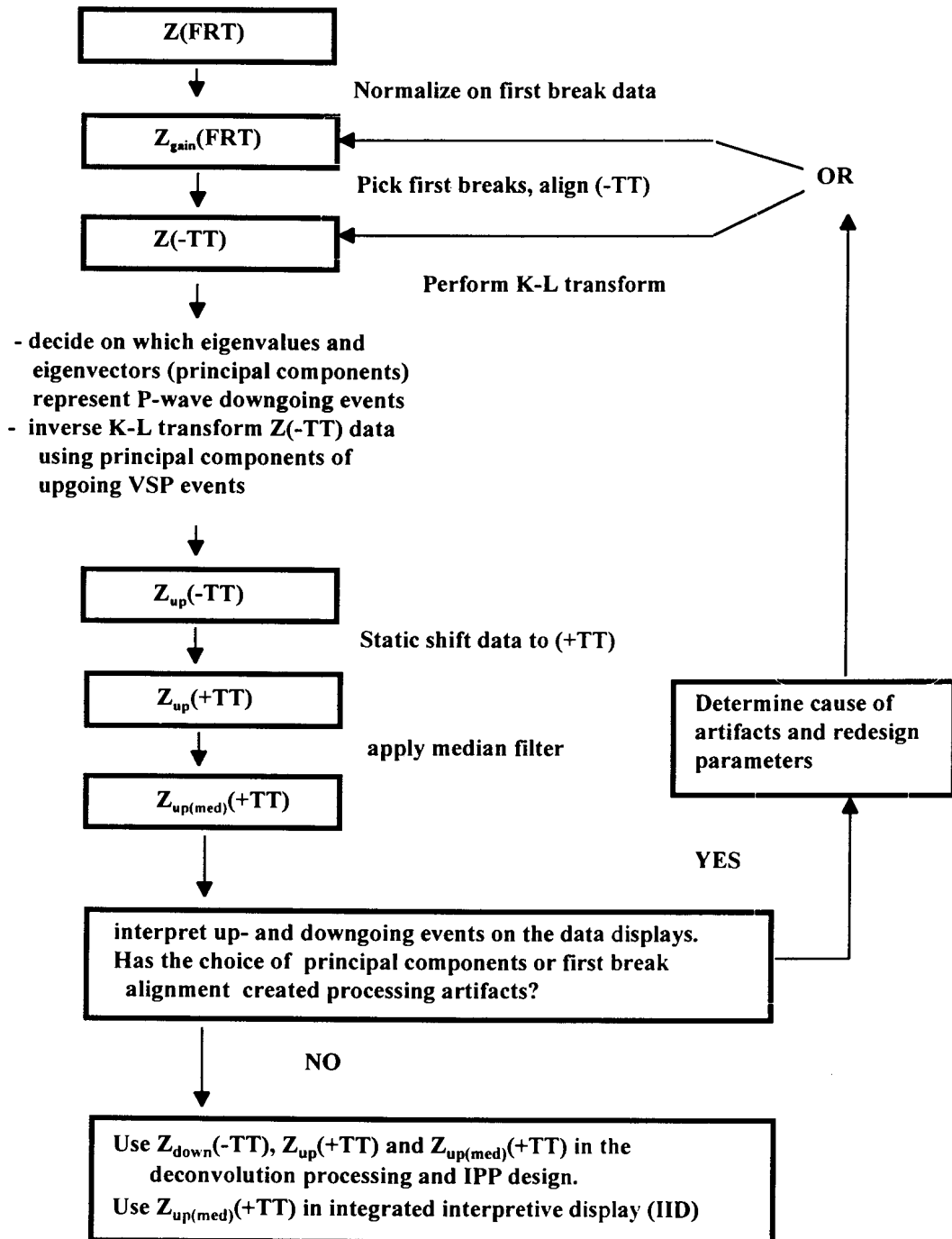
Figure 2.3 Downgoing event panels separated from $Z(-TT)$ data using a 3, 5, 7, 9 and 11 point median filter (panels 1-5, respectively). Panels 6-9 display the subtraction of the data in panel 5 from the data and 1, 2, 3 and 4, respectively.

separation technique with this particular VSP dataset. This exercise is important because any residual upgoing wave events left in the $Z_{\text{down}}(-TT)$ data will be subtracted out of the $Z(-TT)$ during wavefield separation and can never be recovered.

2.2.3 Karhunen-Loeve (K-L) filtering

In this section, the wavefield separation method will use the K-L transform. Flowchart 3 shows the wavefield separation procedure using the K-L transform. The gained $Z(-TT)$ data are K-L transformed; the K-L domain consists of principal components which are related to the eigenvectors of the data autocovariance matrix (see Appendix for details). The eigenvalues associated with the eigenvectors are indicative of horizontal coherency within the data. As shown in the flowchart, the data are reconstructed (inverse K-L transformed) excluding the principal components that represent the horizontally aligned downgoing events. The data within the K-L IPP are interpreted and if processing artifacts have been introduced into the data, those processing steps that introduced the artifacts are modified and repeated until the interpretation of the data is unaffected.

FLOWCHART - Wavefield separation using the K-L transform method



Flowchart 3: An example of the interpretive processing flowchart for the K-L transform wavefield separation processing (Hinds et al., 1994c).

2.2.3.1 Review of the K-L transform

The simplest of assumptions involving the $\mathbf{Z}(-\mathbf{TT})$ data is that the downgoing P-wave event is horizontally aligned and that the downgoing multiples are time-delayed from the primary downgoing event but are similarly "strictly" horizontally aligned during the $(-\mathbf{TT})$ time alignment. This assumption has enabled processors to use the Karhunen-Loeve transform (Hotelling, 1933; Karhunen, 1947; Loeve, 1948, 1955; Watanabe, 1965; Kramer and Mathews, 1956) to selectively evaluate which eigenvectors and eigenvalues are to be used during the data reconstruction (inverse K-L transform) to isolate the upgoing wavefield events (Freire and Ulrych, 1988; Hinds et al., 1986) .

Both the singular value decomposition method (SVD, see Freire and Ulrych, 1988) and the K-L transform use the magnitude of eigenvalues computed through an SVD operation to choose a data reconstruction based on the lateral coherency of the data. Following an eigenanalysis of the autocovariance matrix of the input VSP data (Jackson et al., 1991; Jones and Levy, 1987; Jones, 1985), the largest eigenvalues (Hardage, 1992) will represent the principal components having the greatest amount of coherent energy (Jones and Levy, 1987). The output data are reconstructed using selected principal components (see Appendix). Some of the principal components associated with the largest eigenvalues are not used in the $\mathbf{Z}(-\mathbf{TT})$ data reconstruction. These principal components are interpreted by the processor to represent the downgoing wave events. Leaving out these principal components during the inverse K-L transform results in the $\mathbf{Z}_{\text{up}}(-\mathbf{TT})$ data.

This method has been used whenever it is possible to isolate data into linearly coherent

versus linearly non-coherent data. In surface seismic processing, multiple attenuation of CDP gathers can be effected by applying NMO using the multiple velocity and then using the K-L transform to reconstruct pre-stack events that are not linearly coherent (Jones, 1985; Jones and Levy, 1987; Hinds and Durrheim, 1993 and 1994). Conversely, the interpreted primary events can be aligned using NMO corrections with the "best" primary velocity function. Following the K-L transform, the principal component data are transformed back into CDP gathers using the principal components reflecting the largest eigenvalues. In VSP processing, the -TT downgoing waves are aligned to make the downgoing wavefield data the events that possess the greatest amount of linearly coherent energy (Freire and Ulrych, 1988; Hinds et al., 1986). Following the eigenanalysis, data reconstructed using only the principal components associated with the largest eigenvalues would yield the separated downgoing events. An excellent review of the use of the K-L transform on VSP (and crosswell tomography) data is given in Hardage (1992).

In Jones (1985), it was shown that the application of the K-L transform can preserve the original lateral extent of events as well as separate events based on their linear coherency. This is important whenever one deals with up- and downgoing multiple events. The interpretation of the interbed downgoing multiple depends on showing that the downgoing multiple does not exist on all of the depth traces. The top generating interface (the interface that reflects an upgoing event to create a downgoing multiple event) of the multiple is interpreted as the shallowest trace that the downgoing interbed multiple exists on.

2.2.3.2 K-L filtering and multiple contaminated data

The K-L wavefield separation IPP is displayed in Figure 2.4. Panel 1 displays the data that have been normalized using a calculation window around the primary downgoing event. This normalization of the input data to the SVD step is crucial to the success of the method (Freire and Ulrych, 1988; Hardage, 1992). Another normalization step imbedded in the method can be the normalization of the eigenvalues themselves following the SVD step.

The $Z(-TT)$ data are displayed in panel 2. The trace-to-trace amplitude variation of the separated downgoing events, $Z_{down}(-TT)$, in panel 3 is not seen in the separated downgoing events using the median filter wavefield separation (panel 3 of Fig. 2.1). Panel 3 was constructed using only the first two eigenvalues (related to the first two principal components) created during the K-L transformation. The use of the median filter to separate the downgoing events from the combined wavefield data (section 2.2.2.2) tended to smear and distort downgoing event amplitudes. The K-L separated downgoing events do not require the balancing of the separated downgoing events with the combined wavefield data prior to the subtraction process, $Z_{down}(-TT)$ from $Z(-TT)$, as much as the median filter based wavefield separation.

By subtracting the data in panel 3 from the $Z(-TT)$ data in panel 2, the separated upgoing events, $Z_{up}(-TT)$ data, are output (panel 4). In panel 5, the $Z_{up}(FRT)$ data are shown and an enhanced version of panel 5 using a second K-L filter is presented in panel 6. As a comparison, a 5-point median was also used to enhance the upgoing events contained in $Z_{up}(+TT)$ data and are shown in panel 7. The enhanced upgoing events in panels 6 and 7

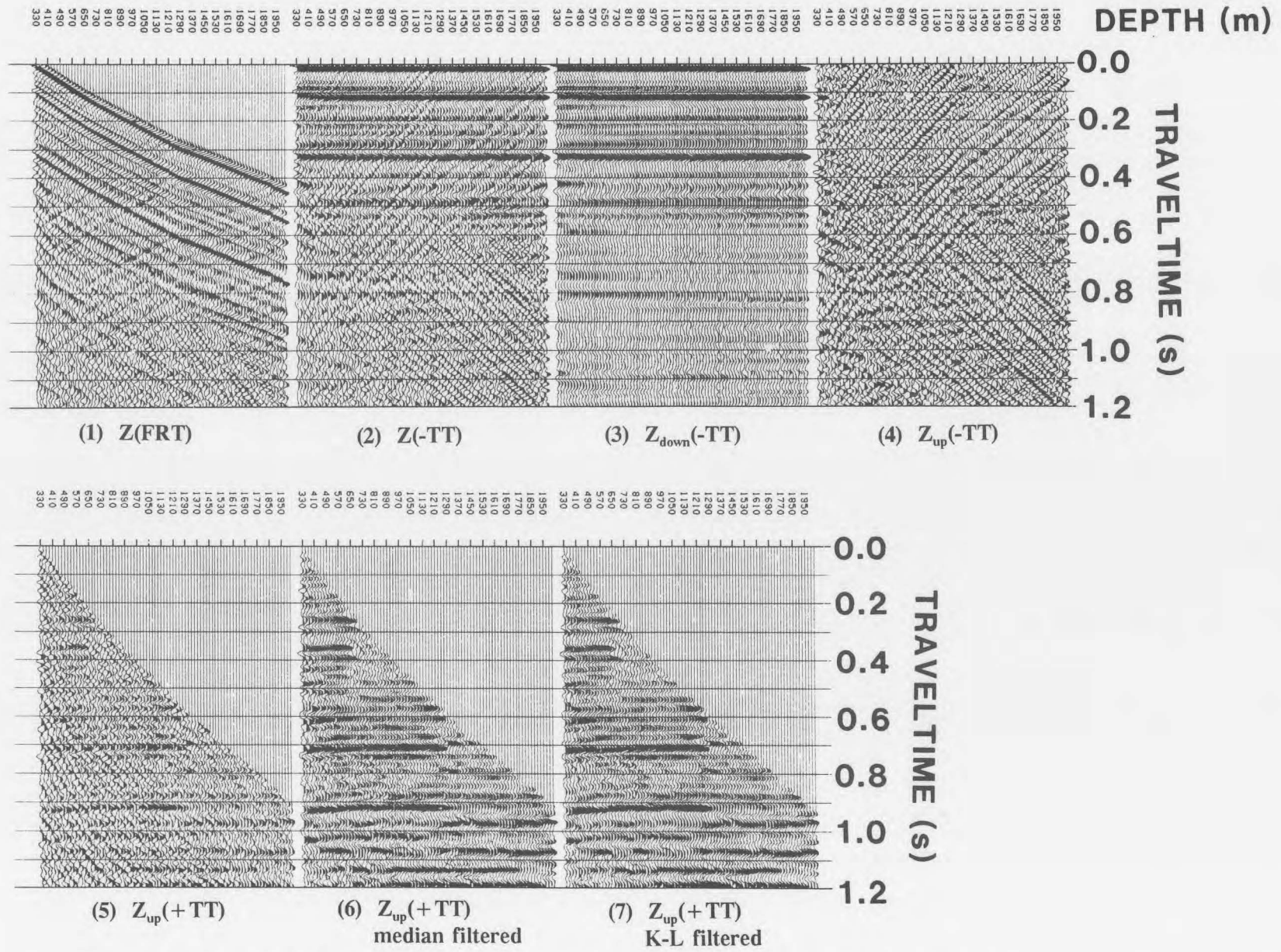


Figure 2.4 Wavefield separation IPP of the Fort St. John Graben case study (Hinds et al., 1993a) data using the K-L filter and subtraction method (Hinds et al., 1986).

are similar (using a 5-point median filter is not a severe application). The primary upgoing event that is embedded in the contaminating multiples appearing beyond the 1210 m depth trace is adequately preserved for interpretation purposes.

The K-L transform method should be used when amplitude preservation is critical and when interbed multiples are being investigated within the separated downgoing events.

2.2.4 2-D Fourier Transform filtering

In this section, the use of F-K domain filtering within the wavefield separation processing will be discussed. In the depth-time domain, the up- and downgoing events cross and interfere with each other; however, the upgoing events in the F-K domain separate from the downgoing events (Hardage, 1985). By attenuating the values of specific portions of the F-K domain representation of the $Z(\mathbf{FRT})$ data, the downgoing events can be eliminated from the inverse F-K transformation. The resultant depth-time data, $Z_{up}(\mathbf{FRT})$, will contain the separated upgoing events. Two types of F-K domain processing are currently available within interpretive processing (Hinds et al., 1994c):

- (1) designing the F-K mute parameters, implementing the parameters within a processing runstream and evaluating the F-K domain wavefield separation IPP; and

(2) using interactive screen processing to compare the input and outputs of the F-K filtering step, evaluating the success of the single step of processing and modifying the F-K filtering parameters until any processing artifacts are minimized.

The term "F-K muting" is used to describe the lowering of F-K domain values within a specific mute window (piece of the F-K domain) in order to attenuate the depth-time events that are represented within that F-K mute window. The boundary between the "window" of data designed to be muted and the remainder of the F-K domain data is usually not a sharp cutoff. The difference in values along the F-K boundary of the muted and non-muted F-K data is gradually "sloped" in order to minimize the 2-D version of Gibb's phenomena. Before the introduction of software packages which accepted polygonal definitions of the F-K zones to be muted, two "input" velocity values would specify the familiar pie-slice (velocity filter) mute (Kanasewich, 1981).

2.2.4.1 Review of F-K filtering

The $Z(\text{FRT})$ data contain up- and downgoing events that respectively map into the negative and positive quadrants of the F-K domain after 2-D Fourier transformation. A linear event in the depth-traveltime (FRT) domain maps as a linear event in the F-K domain. As shown in Hardage(1985), the up- and downgoing P and SV events become separate linear events in the F-K domain.

The relationship between frequency (ω), spatial wavenumber (k_z) and apparent velocity (v) is $\omega = k_z \cdot v$. This means that linear events in the **Z(FRT)** data map into linear events in the F-K domain passing through the F-K domain origin. The slope of the transformed linear events within the F-K domain is equal to the event's apparent velocity in the depth-time domain. Excellent reviews of the F-K domain processing are presented in Hardage (1985, 1992), Hatton et al. (1986), and Yilmaz (1987).

To show the different VSP events in both the depth-time (**FRT**) and F-K domains, the Fort St. John Graben case study near offset **Z(FRT)** data (Hinds et al., 1991a; Hinds et al., 1993a; and Hinds et al., 1994c) are shown in Figure 2.5A and B in the depth-time and F-K domains, respectively. Some of the VSP events within the **Z(FRT)** data are labelled for clarity. The labelled events on Figure 2.5A and B are:

- (1) downgoing P-wave events (positive K quadrant);
- (2) upgoing P-wave events (negative K quadrants);
- (3) downgoing tubewave events; and
- (4) upgoing tubewave events.

For the downgoing tubewave events, the non-aliased data are between 0-35 Hz in the positive K quadrant and the aliased energy "wraps around" between 35-60 Hz in the negative K quadrant (Fig. 2.5B). The part of the downgoing tubewave events that contain frequencies above 35 Hz will visually appear to be upgoing events in the depth-time domain due to spatial aliasing. The cause of the aliasing is the choice of depth increments between the VSP

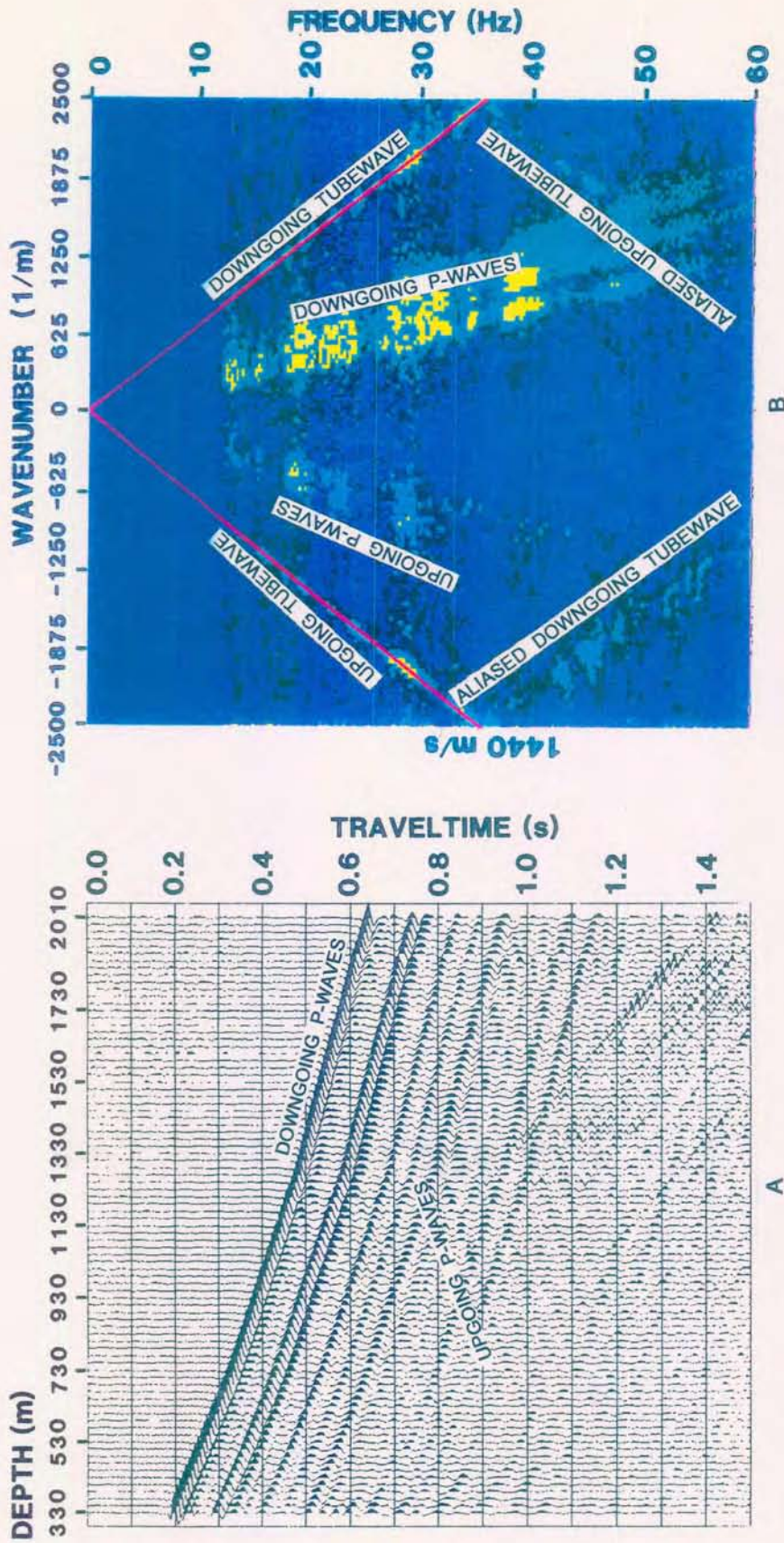



Figure 2.5 Depth-FRT time and F-K domain plots for the Fort St. John Graben case study (Hinds et al., 1993a) near offset data. The up- and downgoing P-wave events separate in the F-K domain. The up- and downgoing tubewave events alias at 35 Hz back into the opposite F-K quadrants.

sonde recording levels. Although  P-wave events do not appear to "wrap around" in F-K space, the depth recording interval was too coarse to properly record all of the tubewave events for the F-K processing. Similarly, for the upgoing tubewave events, the non-aliased energy is between 0-35 Hz in the negative K quadrant and the aliased energy "wraps around" between 35-60 Hz in the positive K quadrant. An excellent review on tubewave aliasing is given in Hardage (1981).

It can be noted that the aliased downgoing tubewave event intersects the upgoing P-wave events at approximately 55 Hz in the negative K quadrant.

In Figure 2.6, the different types of F-K mutes which will be reviewed in more detail later are shown. The muting procedures used in this thesis are:

- (1) F-K quadrant attenuation (the data in one of the K quadrants are muted; Fig. 2.6A);
- (2) Polygon or narrow "reject" zone (similar to pie-slice filtering discussed in March and Bailey, 1983) muting (Fig. 2.6B);
- (3) Polygon or narrow "accept" zone muting (Fig. 2.6C); and
- (4) the interactive polygonal muting (more than one polygon within the F-K domain is specified) shown in Figures 2.6D and E.

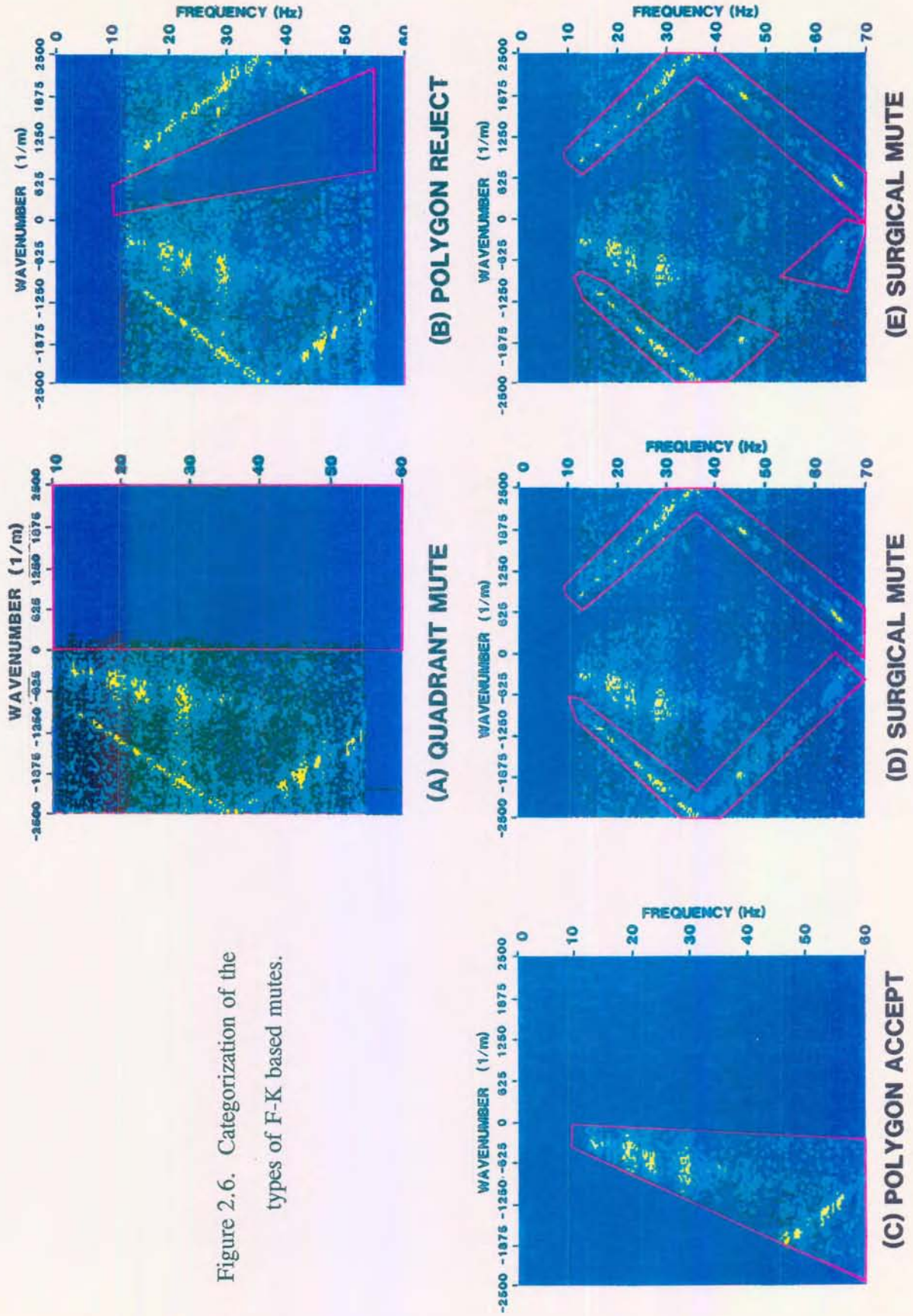


Figure 2.6. Categorization of the types of F-K based mutes.

The interpretation of the separated upgoing events resulting from the use of the different types of F-K filters will be shown below for multiple and tubewave contaminated $Z(\mathbf{FRT})$ VSP data. The F-K mute applications will have an effect on the isolation of primary, multiple and tubewave (aliased and non-aliased) events which will be seen using the F-K domain IPP (Hinds et al., 1994c).

2.2.4.2 F-K filtering and multiple contaminated VSP data

The wavefield separation results obtained following the application of various types of F-K filtering on the near offset Fort St. John Graben case study (Hinds et al., 1991a; Hinds et al., 1993a and 1994b; Hinds et al., 1994c) multiple contaminated $Z(\mathbf{FRT})$ VSP data are shown in Figures 2.7 through 2.13. By examining the suite of resultant $Z_{up}(\mathbf{FRT})$ data in the depth-time domain, interpretation problems caused by the F-K filtering methods can be investigated. The input $Z(\mathbf{FRT})$ data and corresponding F-K plot are presented in panel 1 of Figure 2.7 and Figure 2.8, respectively. The horizontal axis on Figure 2.8 is the wavenumber axis labelled with negative and positive spatial frequencies. The spatial frequencies are in units of 1/m and the labelled values have been multiplied by 10^5 for diagram clarity. The vertical axis is the frequency axis with values in hertz (Hz).

The dominant VSP events represented in the F-K plot of Figure 2.8 are the downgoing P waves shown in the positive K (wavenumber) quadrant. The downgoing tubewave within the depth-time domain appears in panel 1 of Figure 2.7 as the highlighted dispersive wavetrain emerging on the 1310 to 1650 m traces at 1.2 s (\mathbf{FRT}). On the F-K plot of Figure 2.8, the

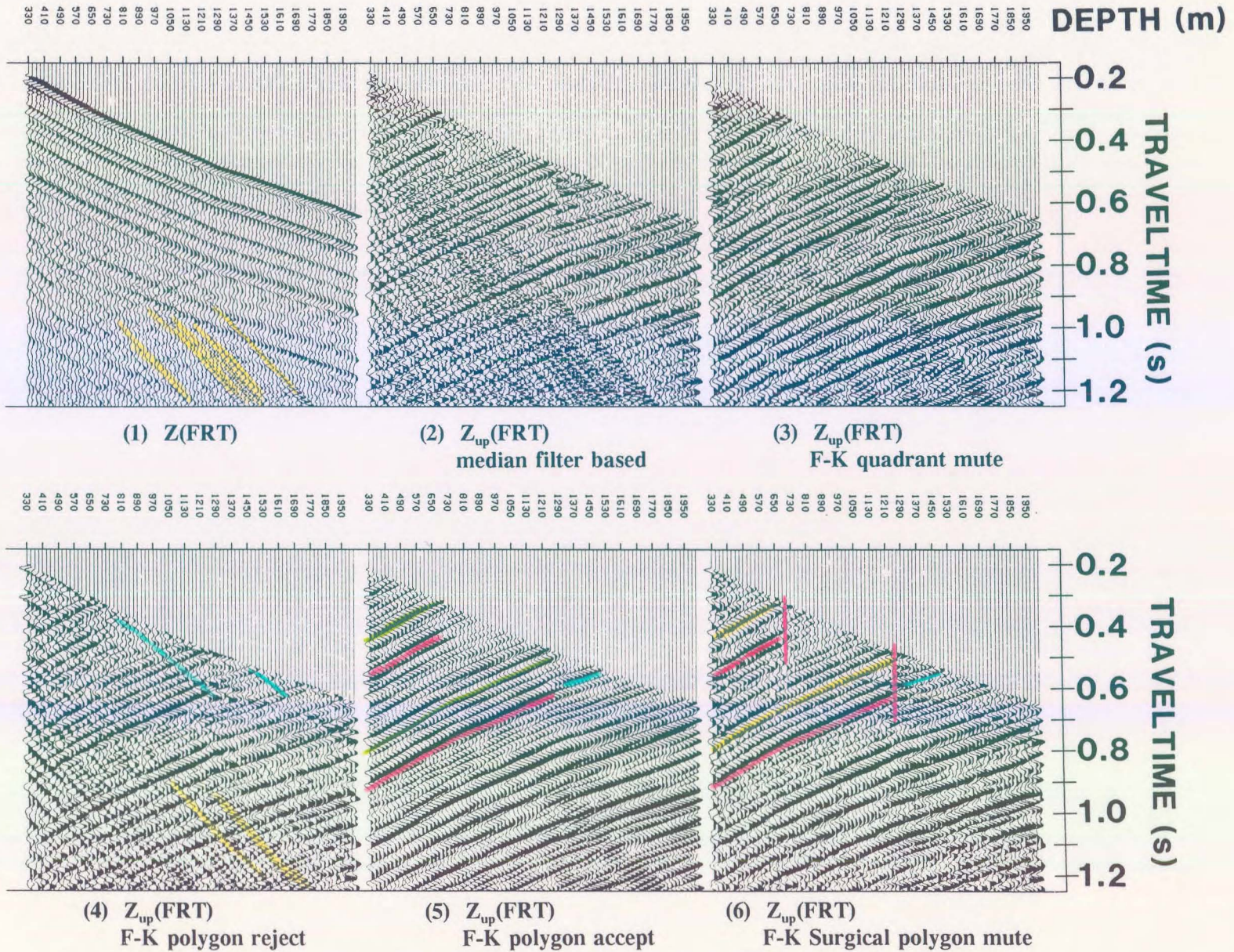


Figure 2.7 $Z(FRT)$ and $Z_{up}(FRT)$ data wavefield separated using the median filter and various F-K operations for the Fort St. John Graben data (Hinds et al., 1993a) near offset multiple contaminated data. The mute designs are shown in Figure 2.6.

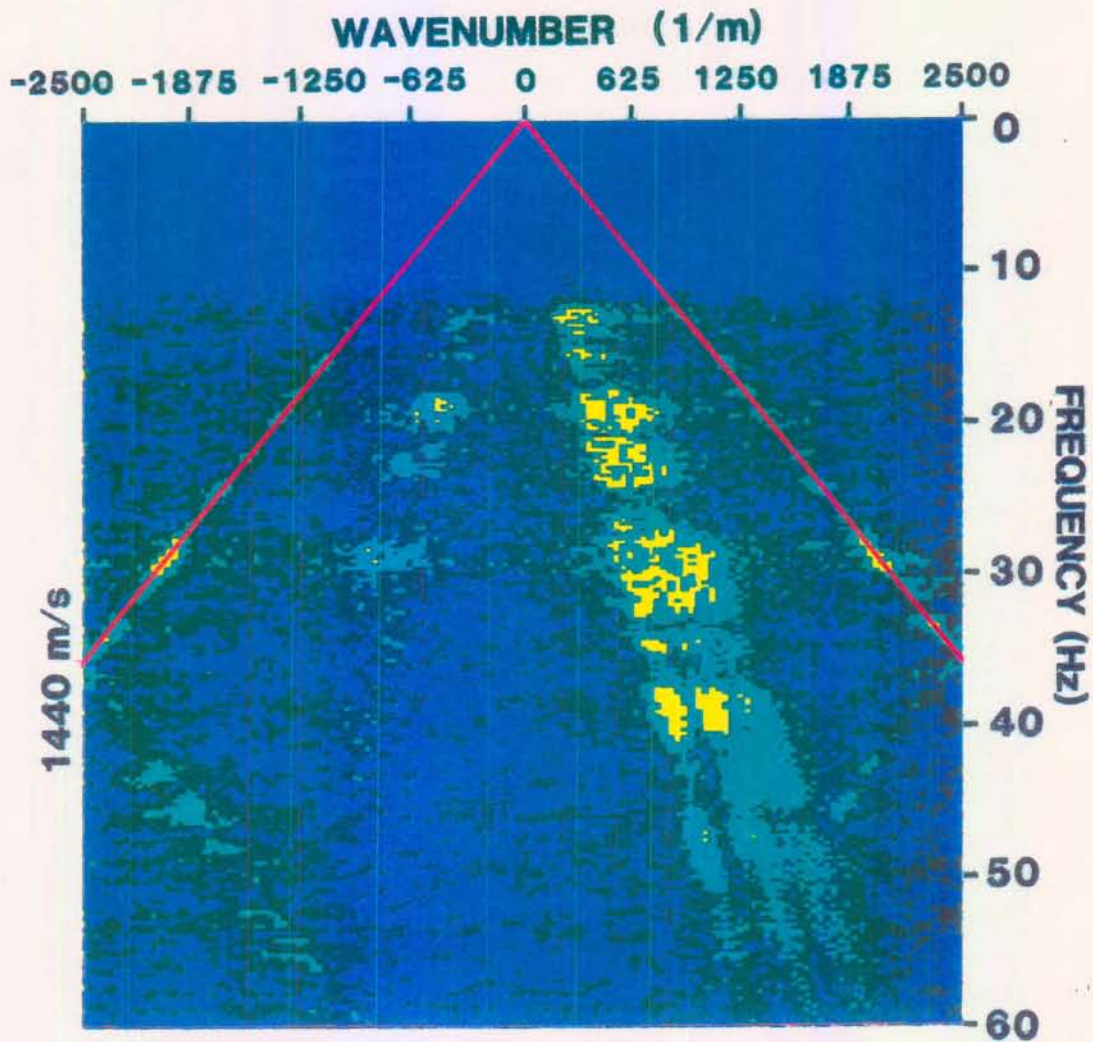


Figure 2.8 F-K plot of the Z(FRT) Fort St. John Graben case study data (Hinds et al., 1993a) shown in panel 1 of Figure 2.7. The annotated red lines define the slope (velocity) of the up- and downgoing tubewave F-K events. Note that the tubewave events alias back into the oppositely-signed F-K quadrants after the linear events exceed the Nyquist K (spatial) frequencies.

downgoing tubewave F-K trend in the positive K quadrant has a slope of approximately 1440 m/s. The unaliased portion is comprised of the F-K amplitudes along a linear trend which starts at the F-K origin and ends at a frequency of 35 Hz and a wavenumber value of 2500 ($\times 10^{-5}$) m^{-1} . The unaliased portions of both the up- and downgoing tubewave events are highlighted in red in Figure 2.8. The "wrap around" occurs at the positive (for downgoing) and negative (for upgoing) Nyquist spatial frequency of $1 / 2 \Delta z (= -1/40 m = 0.025 m^{-1})$. The "wrapped around" parts of the aliased tubewave have been described above.

There is an upgoing tubewave event resulting from the reflection of the downgoing tubewave at the bottom of the borehole (not shown in panel 1 of Fig. 2.7 since only 1.3 s of the original 3 s of data have been plotted). This upgoing tubewave event is seen unaliased in the negative F-K quadrant from 0 to 35 Hz and the aliased portion "wraps back" into the positive F-K domain at higher frequencies. The aliased downgoing tubewave F-K events intersect the upgoing P-wave F-K events at 55-60 Hz in the negative F-K quadrant; however, the bulk of the upgoing P-wave energy resides at lower frequencies.

The median filter wavefield separation result is shown in panel 2 of Figure 2.7 and is used for comparison with the F-K filtering based wavefield separation results of panels 3 to 6. The downgoing tubewave event in the $Z_{up}(FRT)$ data of panel 2 are not appreciably attenuated. An F-K plot (Fig. 2.9) of the $Z_{up}(FRT)$ data in panel 2 shows that only a narrow zone immediately around the downgoing P-wave display has been attenuated. Any attenuated downgoing tubewave data in panel 2 of Figure 2.7 would be a result of the application of a post-median filter bandpass filter applied to eliminate the median filter "whiskers" (Hardage, 1985).

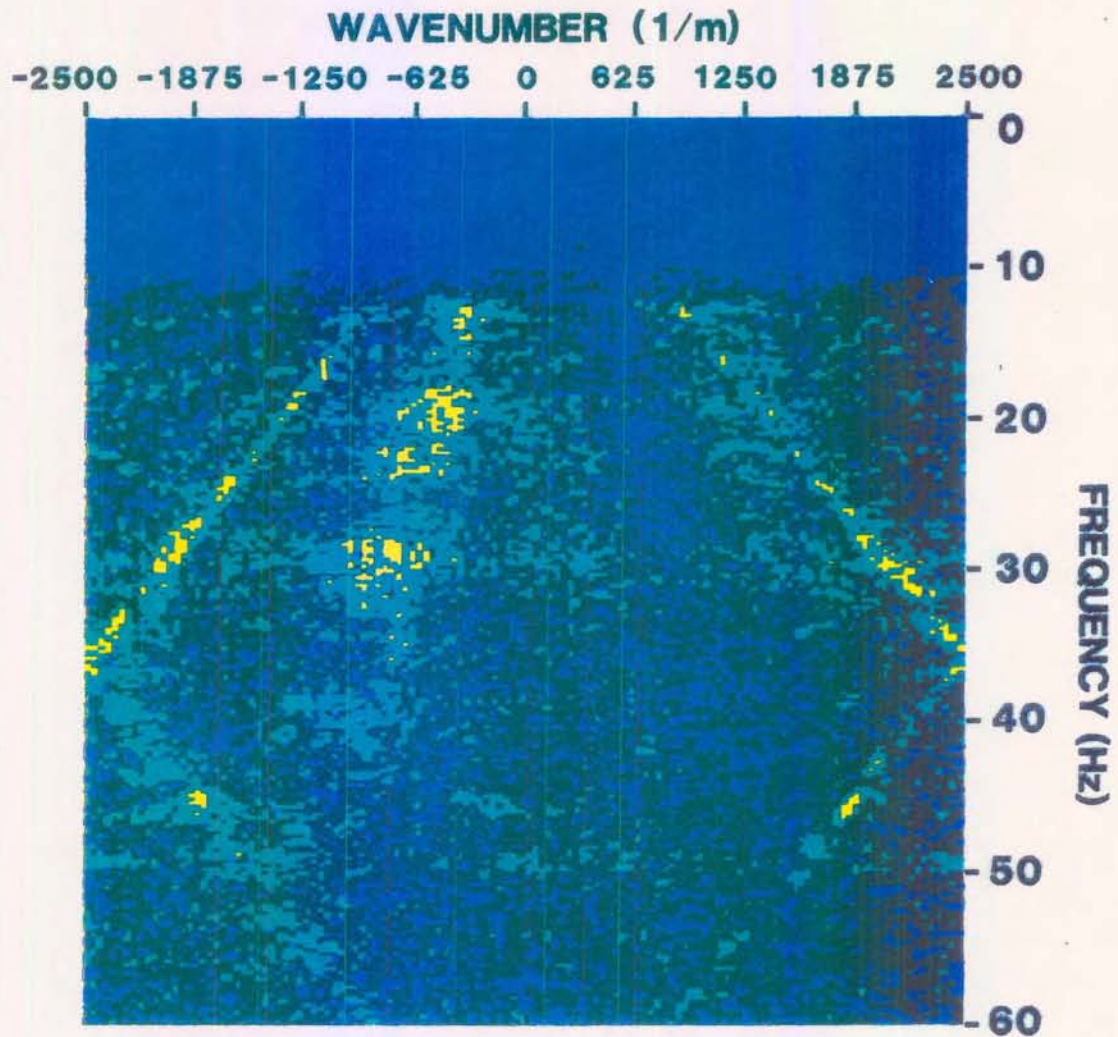


Figure 2.9 F-K plot of the median filter and subtraction method derived $Z_{up}(FRT)$ data (shown in panel 2 of Figure 2.7). The method has rejected the downgoing P-wave events; however, the up- and downgoing tubewave F-K events are relatively unaffected.

Panel 3 of Figure 2.7 displays the result of the simplest and most commonly used type of F-K filtering; namely the masking of the entire positive K quadrant. To evaluate the effect of the F-K quadrant elimination processing on the $\mathbf{Z}(\mathbf{FRT})$ data (panel 1 of Fig. 2.7), the F-K plot of the $\mathbf{Z}(\mathbf{FRT})$ data (Fig. 2.8) can be compared to the F-K plot of the $\mathbf{Z}_{up}(\mathbf{FRT})$ data in panel 3 of Figure 2.7 (F-K plot shown in Fig. 2.10). The downgoing tubewave frequency content below 35 Hz has been attenuated in Figure 2.10; however, the aliased downgoing tubewave (appearing between 36-60 Hz) and the unaliased parts of the upgoing tubewave (between 0-35 Hz) will remain in the $\mathbf{Z}_{up}(\mathbf{FRT})$ data. There is a band of energy associated with a broad k_z range centred at 30 Hz in Figure 2.7 which may be sonde resonance.

In panel 4 of Figure 2.7, the result of attenuating the content of a surgical F-K mute polygon zone around the downgoing P-wave F-K events is shown. The F-K mute zone is highlighted in the F-K domain plot (shown in Fig. 2.11) of the $\mathbf{Z}_{up}(\mathbf{FRT})$ data of panel 4 (Fig. 2.7). Downgoing mode-converted shear waves are retained in the $\mathbf{Z}_{up}(\mathbf{FRT})$ data and are highlighted (in blue) on panel 4. The downgoing mode-converted shear wave events (shown in blue on panel 4) display a similar dip or apparent velocity to that of the downgoing tubewave events (displayed in yellow on panel 4). The upgoing mode-converted shear wave events would plot between the region of the upgoing P-wave and tubewave events in the F-K domain. From an inspection of panel 4 of Figure 2.7, the bulk of the mode-conversions occur at the 690-730 m interface. The surgical mute zone seen in the F-K plot of Figure 2.11 does not encompass the tubewave and mode-converted SV-wave events within the F-K domain resulting in the appearance of these events in the $\mathbf{Z}_{up}(\mathbf{FRT})$ data after the surgical mute wavefield separation procedure.

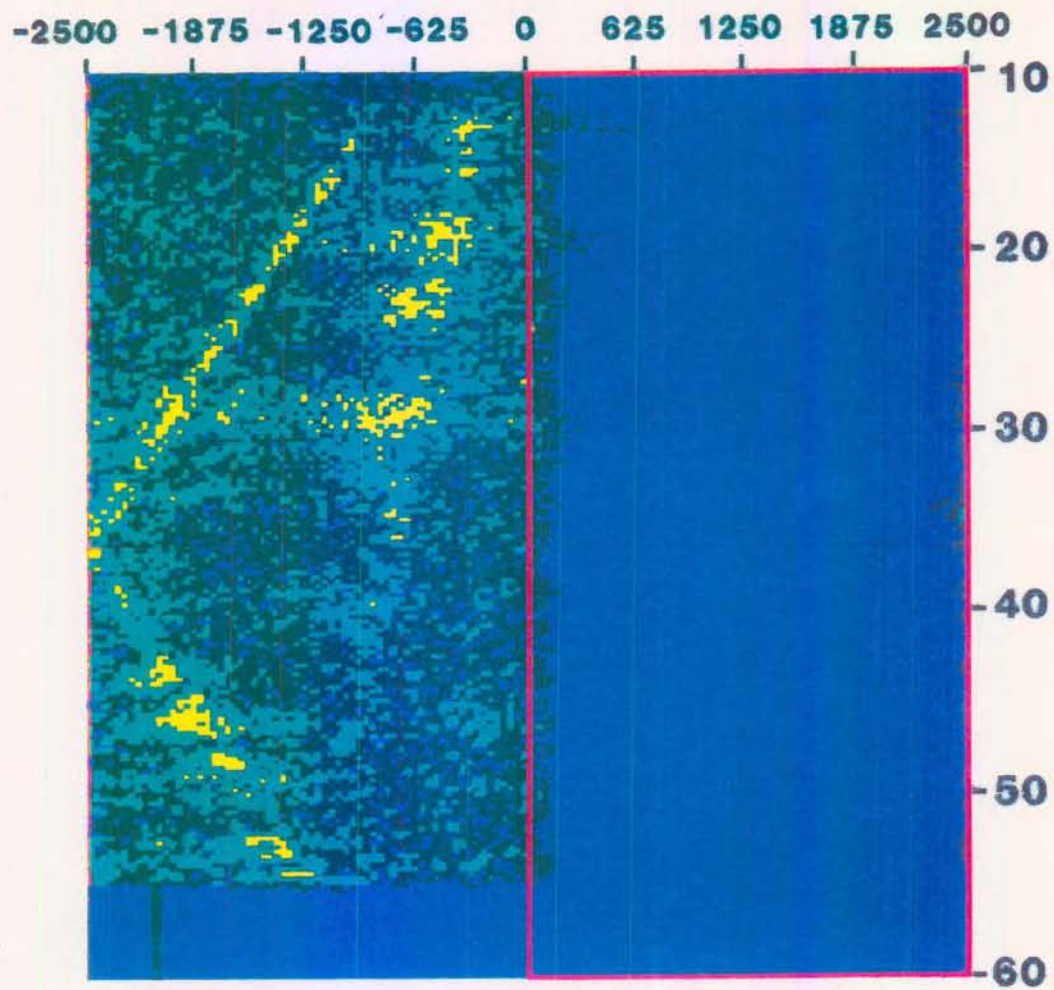


Figure 2.10 F-K plot of the $Z_{up}(FRT)$ data shown in panel 3 of Figure 2.7. The positive spatial wavenumber (K) quadrant has been attenuated. The upgoing and aliased downgoing F-K tubewave events have not been attenuated since these events exist in the retained negative K quadrant.

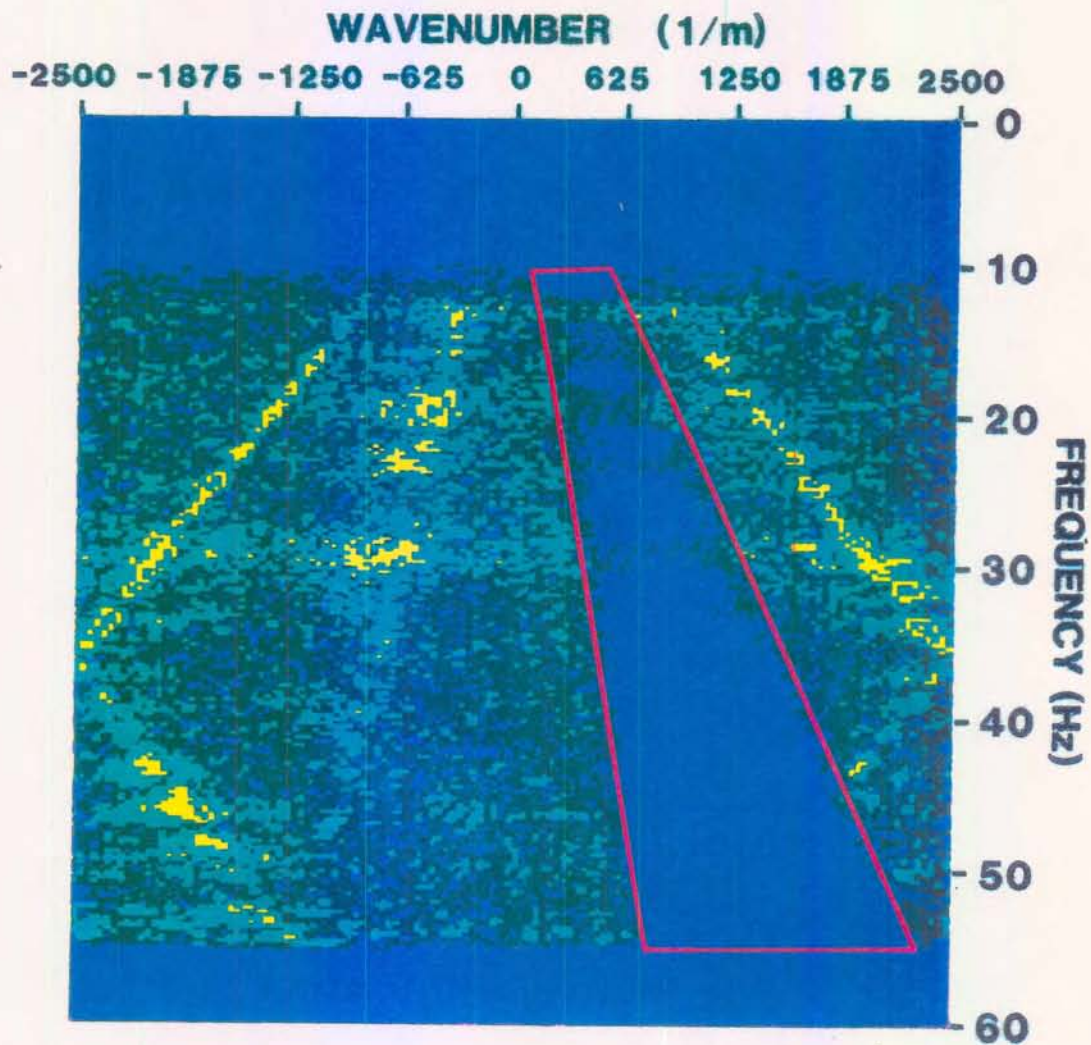


Figure 2.11 F-K plot of the $Z_{up}(FRT)$ data shown in panel 4 of Figure 2.7. A spatially limited reject polygon has been used to attenuate the downgoing P wave F-K events. The applied mute does not appreciably affect the up- and downgoing tubewave F-K events.

The results of applying a "narrow accept" F-K mute filter to the $Z(\mathbf{FRT})$ data are shown in the $Z_{up}(\mathbf{FRT})$ data in panel 5 of Figure 2.7. The F-K response showing the highlighted boundaries of the zone within the F-K domain which was retained is displayed in Figure 2.12. The $Z_{up}(\mathbf{FRT})$ data in panel 5 resulting from the use of the narrow accept F-K muting within the wavefield separation processing is a visual example of Rieber mixing as explained in Hardage (1985). The narrow range of spatial frequencies in the F-K pass zone results in a broad expression of the events in the depth-time domain (also termed F-K smearing).

This can be seen by examining the Spirit River and Nordegg Formation primary and multiple events. The events of the $Z_{up}(\mathbf{FRT})$ resultant data shown in panel 5 (Fig. 2.7) are smeared and the Spirit River multiple (coloured red) event does not truncate sharply at the 690-710 m traces. The Spirit River primary event has been coloured green in panel 5. Amplitude preservation from trace to trace has not been accomplished due to the Rieber mixing. Another example is the primary event (shown in blue) imbedded in the zone of multiples (colored orange) originating from the 1250 m interface (Nordegg Formation) is barely distinguishable as a separate event. The multiple and primary event have been highlighted in panel 5. The cursor in Figure 2.12 is placed at the intersection of the aliased downgoing tubewave and the upgoing P-wave events.

The application of the surgical F-K mute polygon "reject zones" to the $Z(\mathbf{FRT})$ data results in the $Z_{up}(\mathbf{FRT})$ data shown in panel 6 of Figure 2.8. The surgical F-K mutes are highlighted in red within the F-K plot shown in Figure 2.13. The surgical mutes were designed to attenuate the downgoing P-wave and the up- and downgoing tubewave events. Two examples of the lateral truncation of the multiples below their respective primaries are

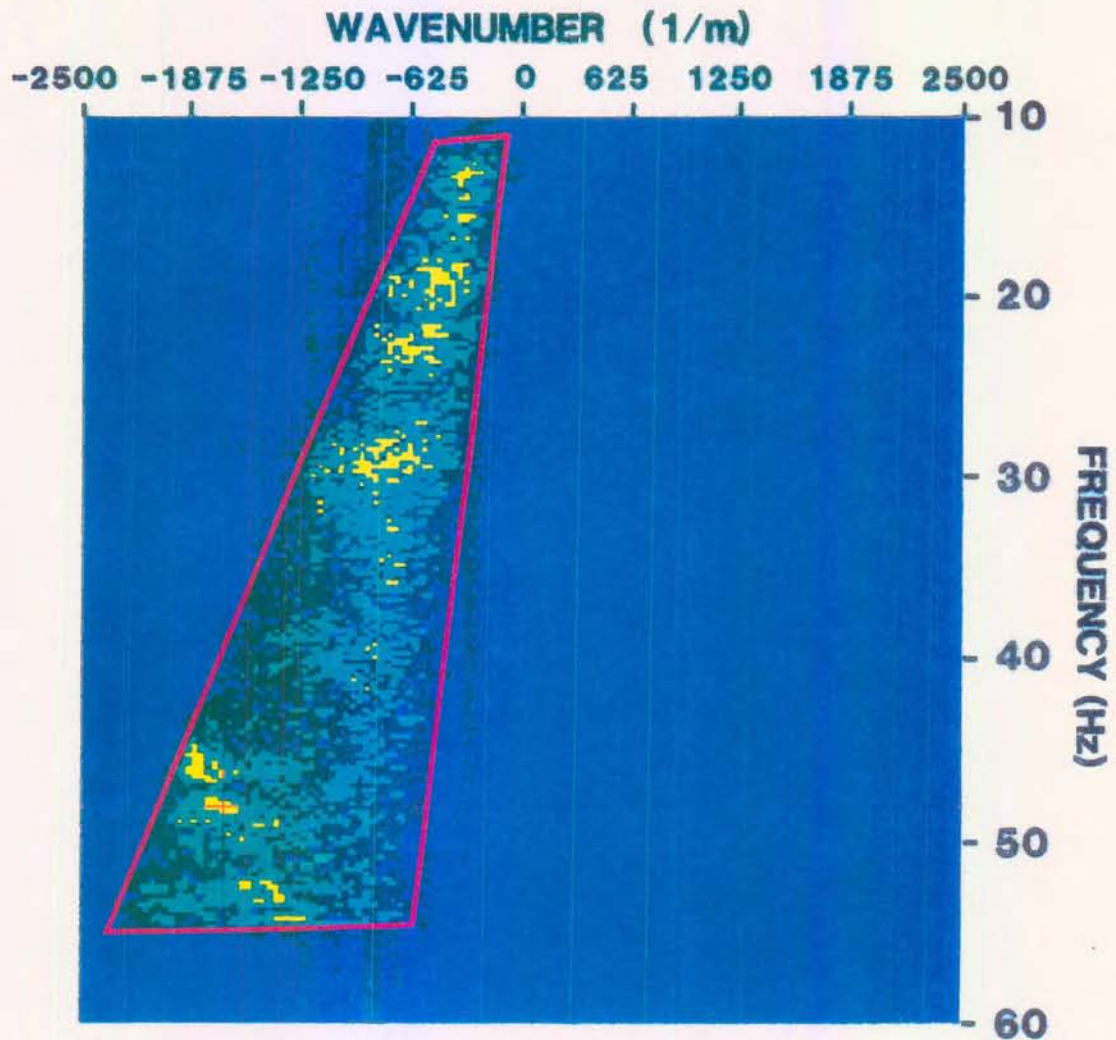


Figure 2.12 F-K plot of the $Z_{up}(FRT)$ data shown in panel 5 of Figure 2.7. A spatially limited F-K accept polygon has been used to isolate and retain the upcoming P wave F-K events. Due to the spatially narrow accept zone, the filtering results in Reiber mixing in the depth-time domain.

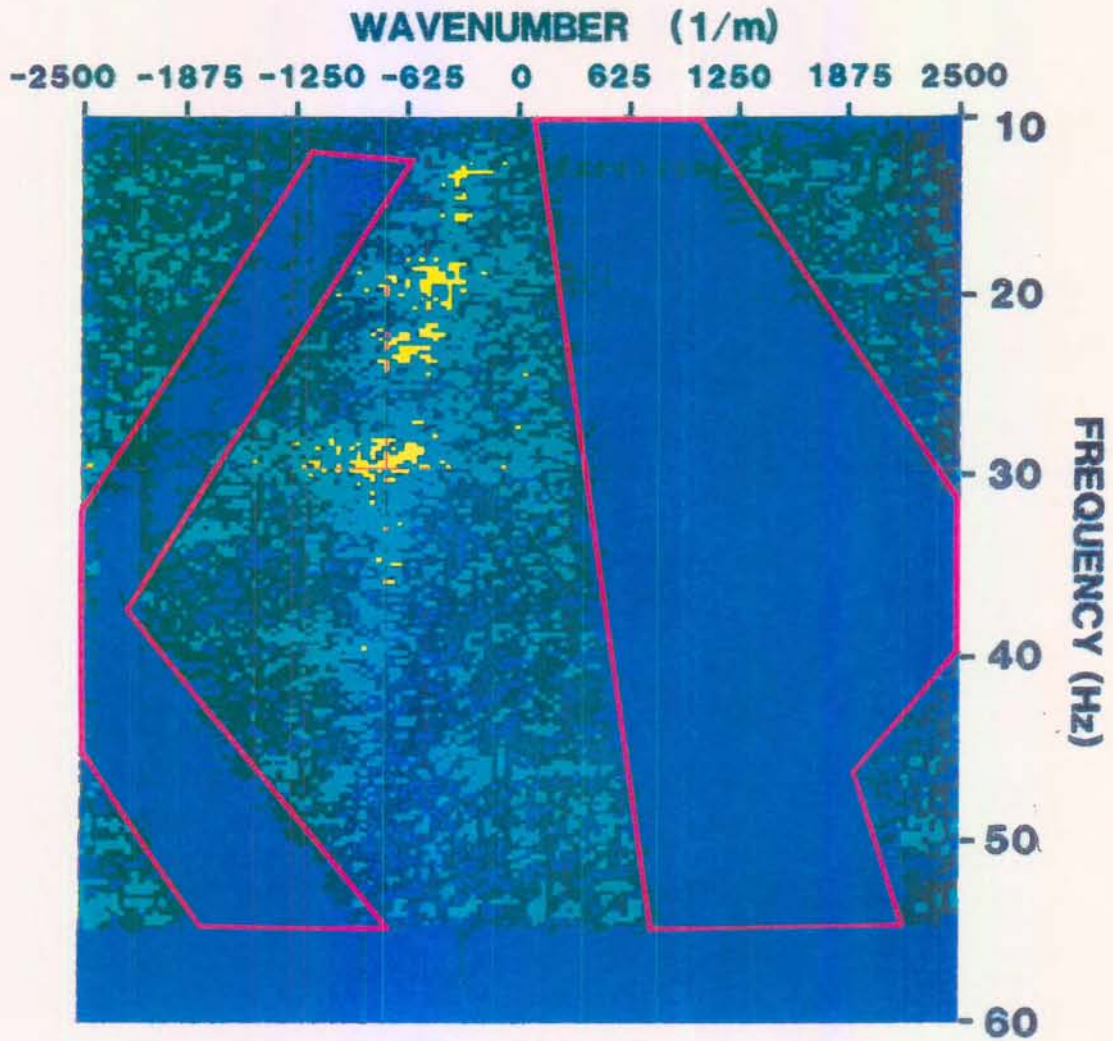


Figure 2.13 F-K plot of the $Z_{up}(FRT)$ data shown in panel 6 of Figure 2.7. F-K polygons outlined in red show the surgically muted reject zones in the F-K domain designed to attenuate the downgoing P wave F-K events and the aliased and non-aliased tubewave F-K events.

shown in panel 6 of Figure 2.7. The primaries are highlighted in yellow and the multiple events are shown in red. The multiple events are not smeared onto traces beyond the depths where the primary events associated with the multiples were generated. To illustrate this, a vertical line in pink has been drawn for both sets of primaries and multiples showing the lateral extent of the events. The surgical F-K muting has attenuated both the downgoing P and up- and downgoing tubewaves and has succeeded in preserving the trace-to-trace amplitude variations (as was done for the median filtered $Z_{up}(\text{FRT})$ data shown in panel 2).

The acceptable types of F-K filtering for the multiple contaminated data shown in panel 1 of Figure 2.7 (the near-offset data from the Fort St. John Graben case study; Hinds et al., 1991a; Hinds et al., 1993a and 1994b; Hinds et al., 1994c) would appear to be the F-K quadrant attenuation (Fig. 2.10) and the surgical F-K muting (Fig. 2.13). What is of concern in the interpretive processing of multiple contaminated data is the lateral truncation of the multiple events and the trace-to-trace amplitude preservation.

2.2.4.3 F-K filtering and tubewave contaminated VSP data

In this section, the interpretive processing panel (IPP) for the F-K based wavefield separation procedure will be introduced using tubewave contaminated $Z(\text{FRT})$ data. The two IPP's shown below will result from the use of:

- (1) surgical F-K domain mutes (Fig. 2.14);
- (2) the attenuation of the positive F-K quadrant (Fig. 2.15).

The tubewave contaminated $Z(\text{FRT})$ data are shown in panel 1 of the IPP in Figure 2.14. The normalized $Z(\text{FRT})$ data contains a dominant aliased downgoing tubewave. The tubewave is highlighted in yellow in panel 1. Panel 2 contains the $Z_{\text{up}}(\text{FRT})$ data resulting from the use of the median filter based separation method (Fig. 2.2). The upgoing wave data highlighted in red in panel 2 are low in amplitude in comparison to the tubewave amplitude shown in yellow. Panel 3 contains the $Z_{\text{up}}(\text{FRT})$ data resulting from the application of surgical muting in the F-K domain which was designed to suppress the downgoing and tubewave events. The aliased downgoing tubewave F-K events which intersected the upgoing P-wave events in the F-K domain were not included in the surgical mute design. The $Z_{\text{up}}(+\text{TT})$ and median filter (3 point) enhanced $Z_{\text{up}}(+\text{TT})$ data are shown in panels 4 and 5, respectively. The upgoing events in the data are easily recognizable after the use of F-K surgical muting wavefield separation.

The IPP for the F-K based wavefield separation method which mutes the positive F-K

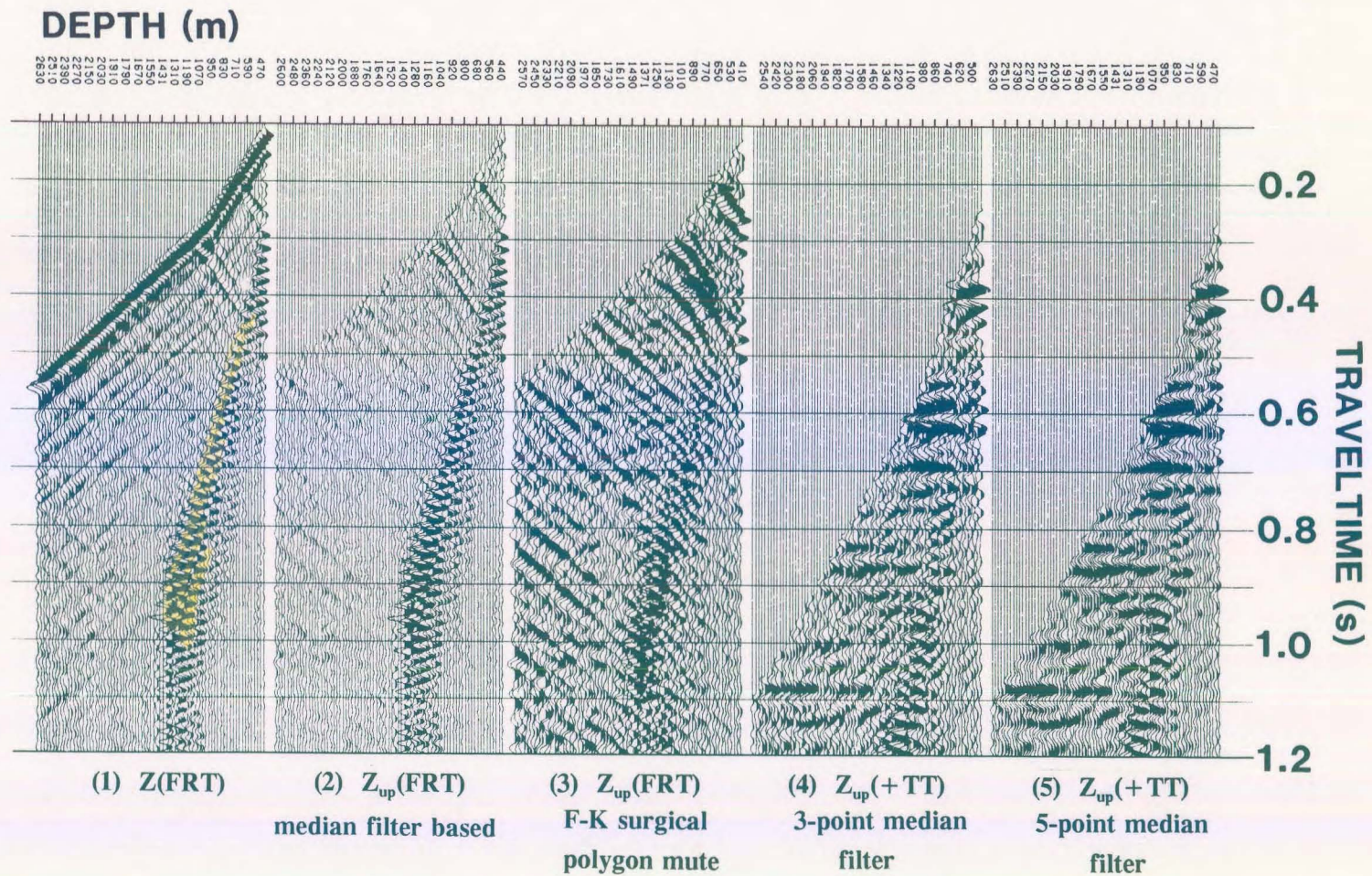


Figure 2.14 F-K based wavefield separation IPP of the tubewave contaminated data using surgical muting of both the downgoing P-wave and tubewave F-K events. Panel 2 is Z_{up}(FRT) data resulting from the median filter and subtraction wavefield separation (included for comparison purposes).

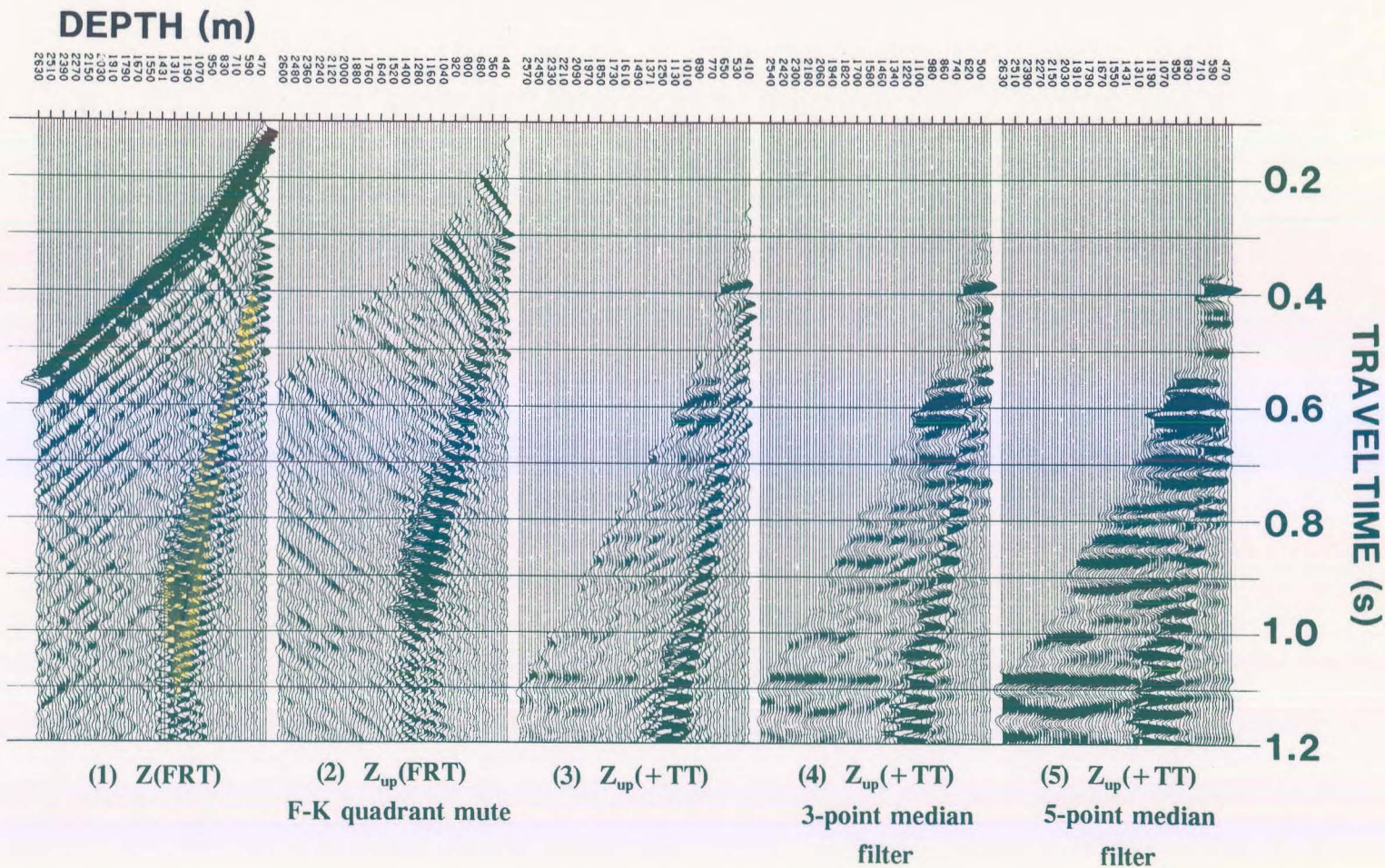


Figure 2.15 F-K based wavefield separation IPP of the tubewave contaminated data using F-K quadrant attenuation.

quadrant (containing the downgoing wave events) is shown in Figure 2.15. The $Z_{up}(FRT)$ data shown in panel 2 contains the aliased downgoing tubewave events (that appear as upgoing events). The $Z_{up}(+TT)$ data are shown in panel 3. The $Z_{up}(+TT)$ data were median filtered using 5- and 11-point median filters and respectively displayed in panels 4 and 5. The quadrant attenuation F-K filtering of the tubewave contaminated data (panel 1) does not solve the problem of the elimination of the aliased tubewave.

This can be seen by comparing the $Z_{up(med)}(+TT)$ data in panel 5 of Figure 2.14 to the $Z_{up(med)}(+TT)$ data of panel 5 of Figure 2.15. The tubewave event has been better attenuated using the F-K surgical muting processing shown in the IPP of Figure 2.14.

The results of wavefield separation of the tubewave contaminated $Z(FRT)$ using the various F-K filtering methods are shown in Figure 2.16. The tubewave contaminated $Z(FRT)$ data are shown in panel 1 (Fig. 2.16). The $Z_{up}(FRT)$ data shown in the remainder of the panels of Figure 2.16 result from the median filter based wavefield separation method (panel 2), F-K quadrant attenuation (panel 3), narrow F-K reject zone muting (panel 4), narrow F-K accept filter muting (panel 5) and surgical F-K muting (panel 6). The IPP in Figure 2.16 has been designed to enable the evaluation of the different types of F-K filtering wavefield separation methods and the median filter method. The surgical muting method resulting in the $Z_{up}(+TT)$ data in panel 6 is the optimum method to be used to enhance the interpretation of the upgoing events. The upgoing events must still be interpreted bearing in mind the tubewave event interference in the upgoing P-wave events. The surgical muting has preserved the upgoing events and has successfully attenuated both the up- and downgoing tubewave (aliased and non-aliased parts) during the wavefield separation procedure.

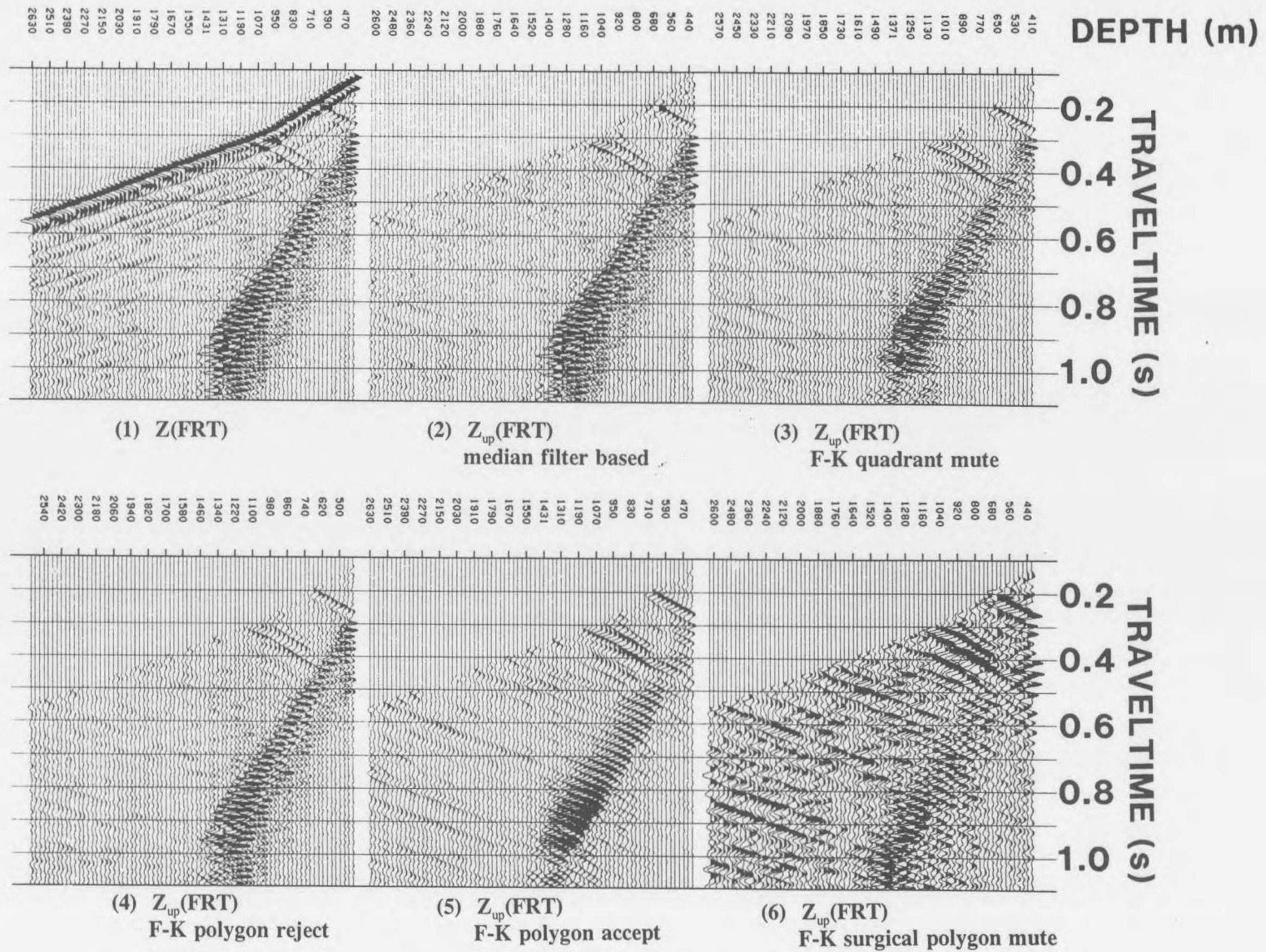


Figure 2.16 $Z(\text{FRT})$ (panel 1) and $Z_{\text{up}}(\text{FRT})$ wavefield separated data using the median filter plus subtraction method (panel 2) and the various F-K muting methods (panels 3-6) on the $Z(\text{FRT})$ tube wave contaminated data.

2.2.4.4 F-K filtering in other wavefield separation methods

In section 2.2.2.3, the median filter based wavefield separation of the tubewave contaminated $Z(\text{FRT})$ data was reviewed. In panels 6 and 7 of Figure 2.2, the $Z_{\text{up}}(+\text{TT})$ data resulting from the use of the median filter are shown. Surgical F-K muting was applied to the $Z_{\text{up}}(\text{FRT})$ following the median filter wavefield separation and these F-K filtered data are shown in panel 8 of Figure 2.2. Figure 2.17 is the F-K plot of the resultant data. The surgical mute used during the filtering was designed to attenuate the tubewave; however, the muted zone of the F-K domain did not include the portion of the aliased tubewave which intersected the upgoing P-wave F-K events.

This is an example of how the F-K filter surgical muting can be combined with other wavefield separation methods.

2.2.4.5 F-K filtering using interactive screen processing

In this section, interactive screen processing will be shown for surgical mute processing in the F-K domain. These examples will illustrate the single step interpretive processing. The input data are shown on one of the bit planes of the interactive monitor display. A bit plane is one of the screen displays within modern graphics systems that can be chosen for display using mouse or keyboard commands. On another bit plane, the F-K domain plot of the input data is displayed and mute zones are interactively chosen within the F-K plot. The result of applying the F-K mutes to the input data is then displayed on yet another bit plane. By

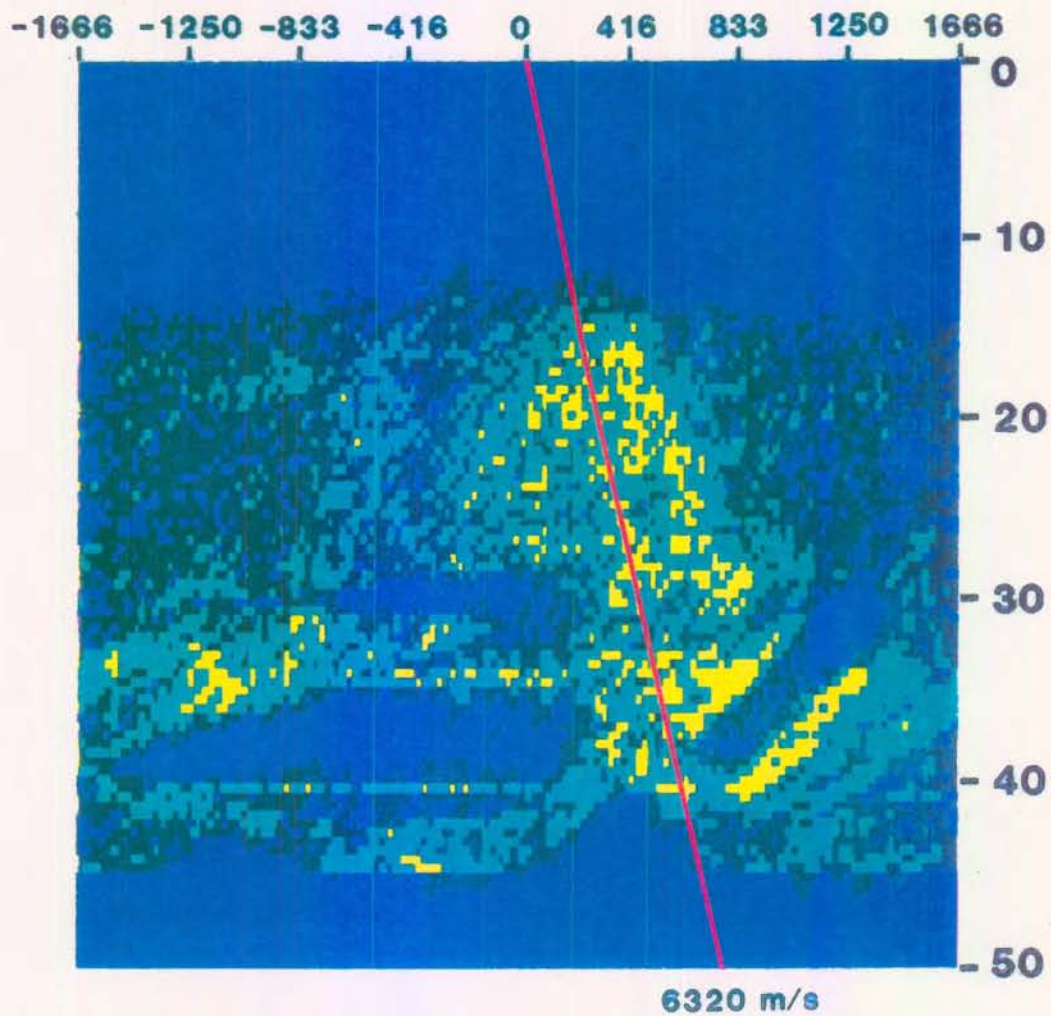


Figure 2.17 F-K plot of data resulting from the application of F-K surgical muting to the median filter-based wavefield separation results (prefiltered data is shown in panel 6 of Figure 2.2). The depth-time equivalent of the displayed F-K data is shown in panel 8 of Figure 2.2.

comparing the input and F-K filtered data, the effect of the application of the surgical muting on interpretation can be evaluated. Once any F-K filtering induced artifacts are minimized, the current F-K mute parameters are then output for use in the wavefield separation runstream.

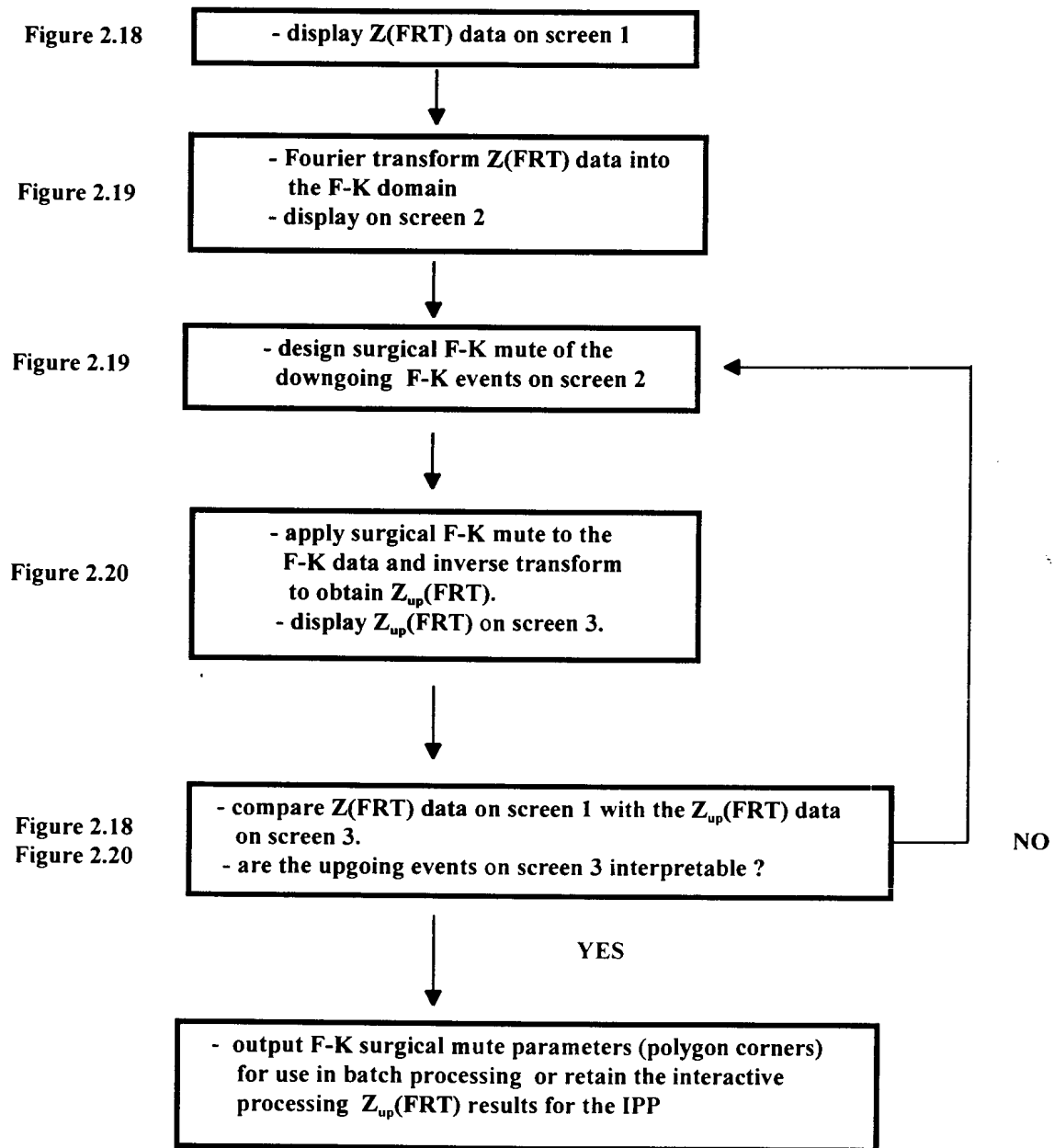
The two examples will use interactive F-K filtering to:

- (1) interpret up- and downgoing event content on $Z(\text{FRT})$ data; and
- (2) enhance $Z_{\text{up}}(\text{FRT})$ data.

2.2.4.5.1 Using interactive F-K filtering to wavefield separate

The processing decisions used in the wavefield separation by interactive F-K processing are shown in Flowchart 4. The $Z(\text{FRT})$ data of the near offset VSP survey of the Fort St. John Graben case study (Hinds et al., 1991a; Hinds et al., 1993a and 1994b; Hinds et al., 1994c) are shown in Figure 2.18. The F-K transformed plot of the same data is shown in Figure 2.19. A surgical F-K polygonal mute zone is designed using on-screen menu commands. The designed mute zone is highlighted in red in Figure 2.19. The F-K data within the mute zone can either be "rejected" (left out of the inverse F-K transformation) or "accepted" (the F-K data outside of the polygonal mute zone is not used in the inverse transform). The resultant $Z_{\text{up}}(\text{FRT})$ data that results from choosing the "rejection" mode is shown in Figure 2.20. The resultant data are plotted onto another bit-plane within the graphics system.

FLOWCHART - Interactive F-K processing (for up- and downgoing event identification)



Flowchart 4: An example of the interpretive processing flowchart of the interactive F-K processing used for event identification (Hinds et al., 1994c).

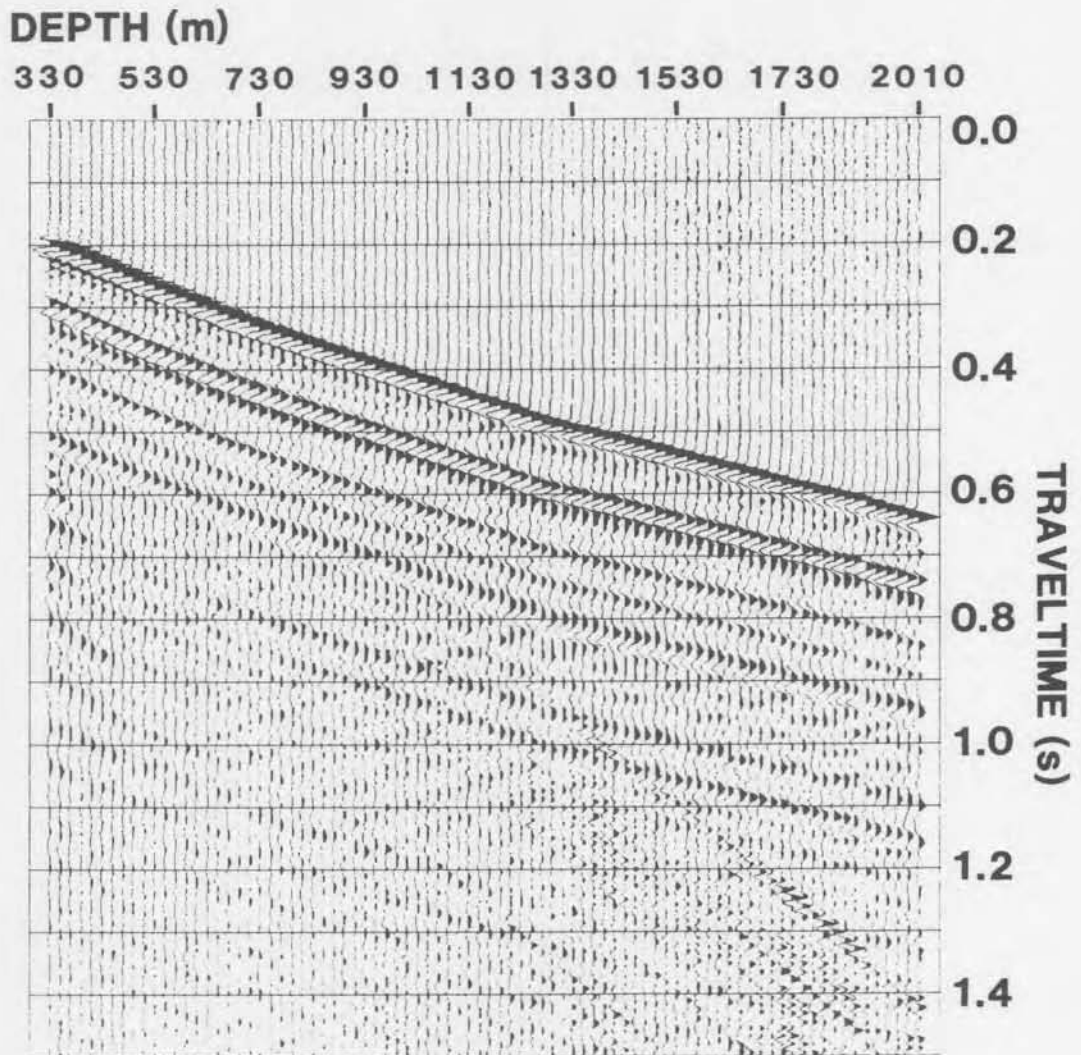


Figure 2.18 Single operation interpretive processing initial screen display showing the input $Z(FRT)$ data of the Fort St. John Graben case study (Hinds et al., 1993a). The objective of the interactive processing (seen in Figs. 2.18 to 2.20) is to understand the different types of up- and downgoing wave events within the data.

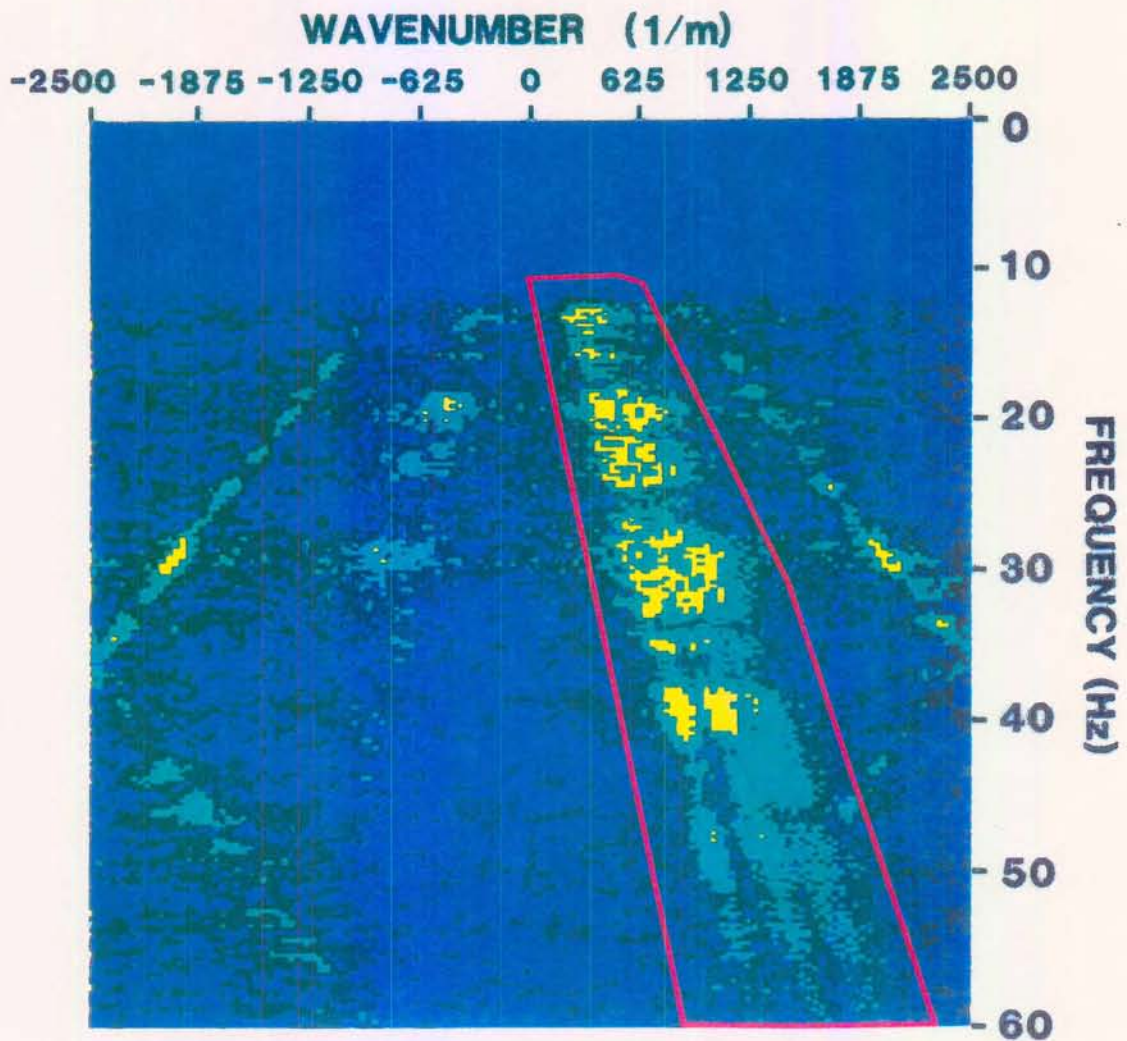


Figure 2.19 F-K plot of the data shown in Figure 2.18. This is the next interactive processing display following the screen presentation of Figure 2.18. A surgical mute polygon is interactively designed and the F-K events within the polygon can either be attenuated or preserved.

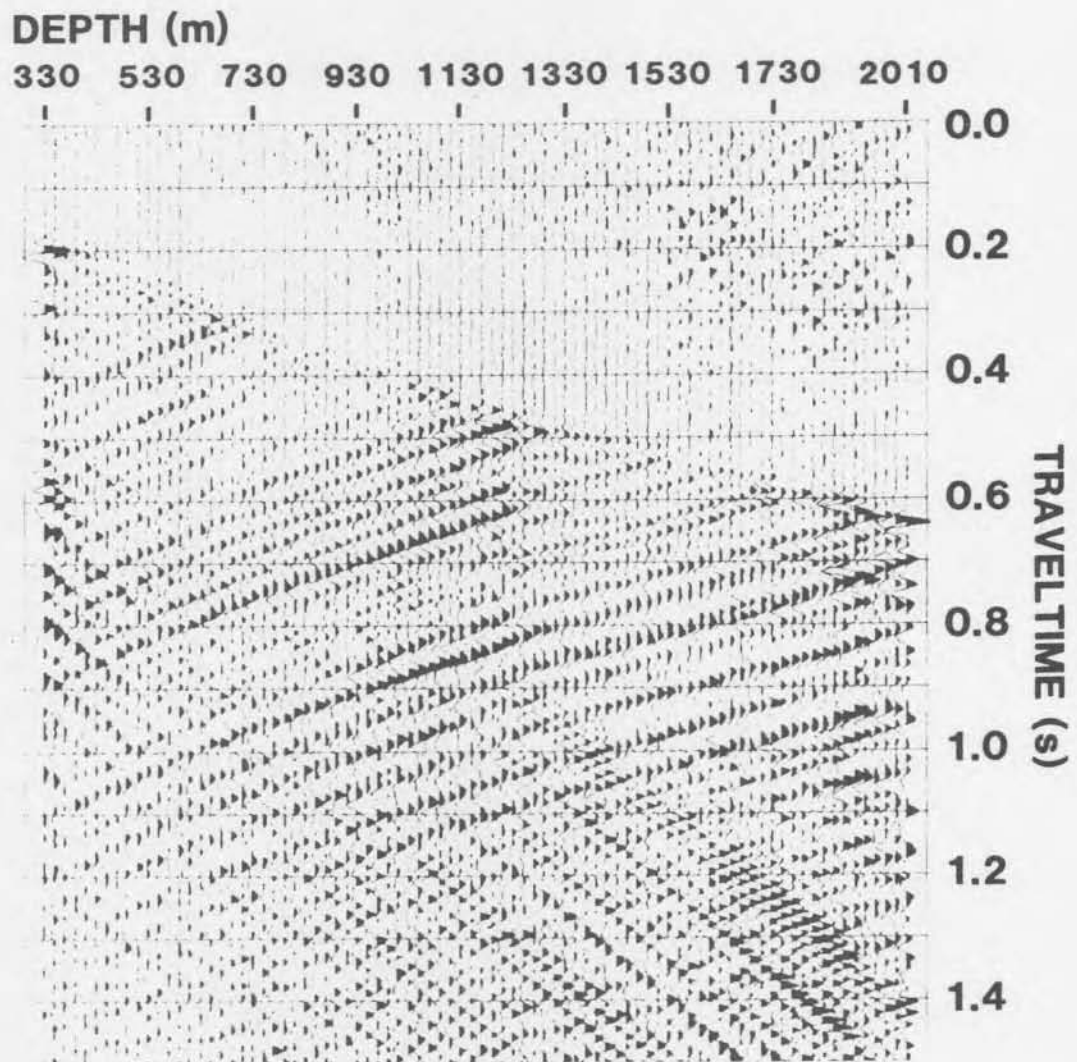


Figure 2.20 The "results" interactive processing display following the muting (reject filtering) of the F-K data inside the mute polygon shown in Figure 2.19. One can flip between the screen images using a mouse-controlled menu to evaluate the application of the polygon surgical mute. The upgoing P-wave and tubewave content of the $Z(\text{FRT})$ data seen in the initial screen display (Fig. 2.18) can now be interpreted.

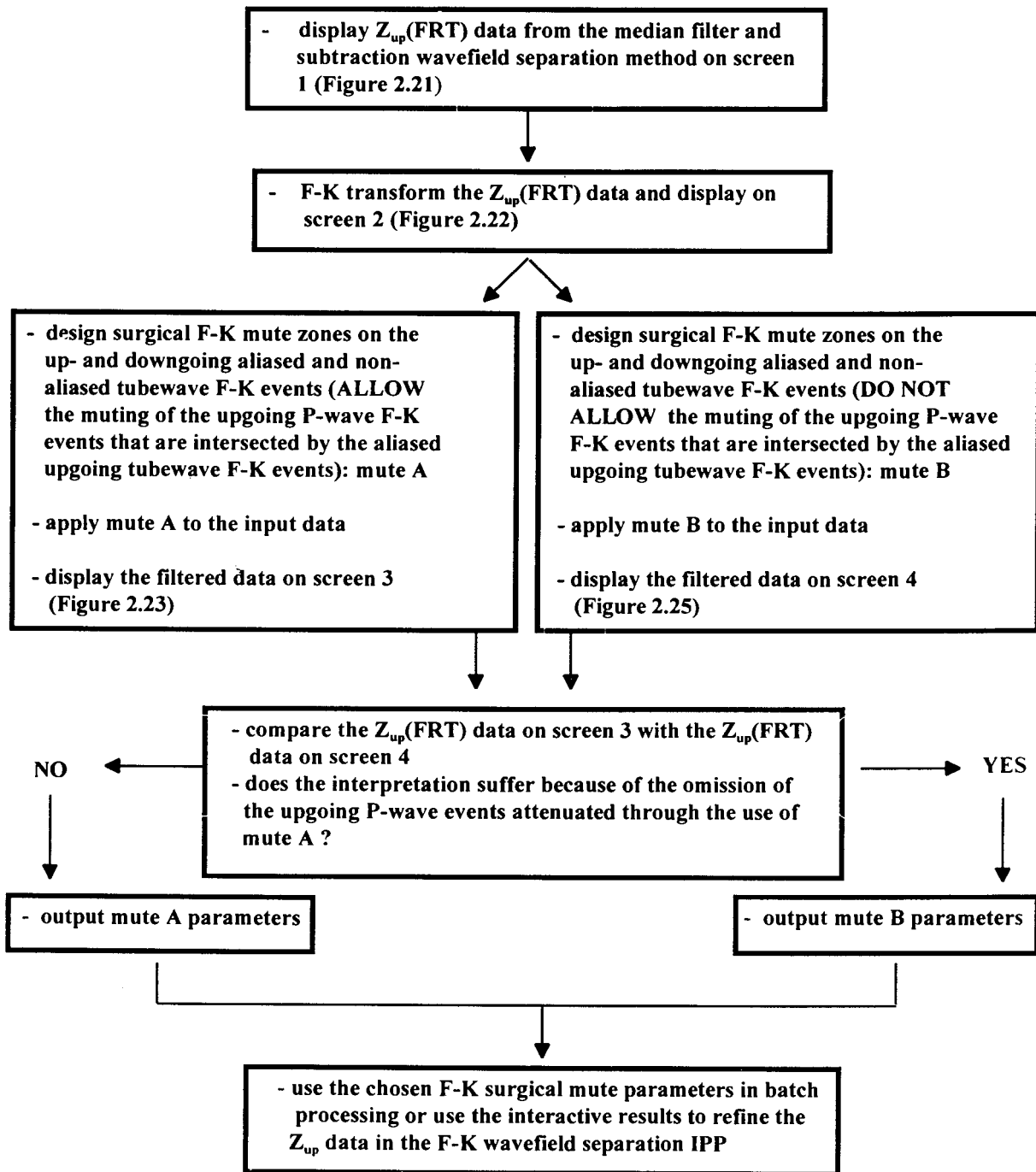
Through the use of on-screen menu commands, the screen can alternatively display the $Z(\text{FRT})$ shown in Figure 2.18 or the filtered data, $Z_{\text{up}}(\text{FRT})$, shown in Figure 2.20. The interpretation of the upgoing events can be started using the $Z_{\text{up}}(\text{FRT})$ data. Moreover, by changing the vertices of the polygon F-K mute within the F-K plot bit-plane display, the effect of the mute design on the interpretation of the upgoing events can be determined. This interactive processing begins to get the processor/interpreter familiar with the wavefield content of the input $Z(\text{FRT})$ data.

2.2.4.5.2 The effect of changes in the F-K mute zones

In this section, the effect of the mute design on a particular segment of the VSP data is examined through the use of F-K interactive processing. The processing decisions made during this interactive F-K processing are shown in Flowchart 5. The example described below encompasses the series of plots in Figures 2.21 to 2.25. The segment of the F-K domain of concern is the aliased portion of the downgoing tubewave in the Fort St. John Graben near offset $Z_{\text{up}}(\text{FRT})$ VSP data (Hinds et al., 1991a; Hinds et al., 1993a and 1994b; Hinds et al., 1994c) which crosses the upgoing P-wave events within the F-K domain (as can be seen in Fig. 2.9).

The input data to the interactive processing are the $Z_{\text{up}}(\text{FRT})$ data resulting from the median filter wavefield separation method (Fig. 2.21). The downgoing tubewave is still evident within the data. The F-K representation of this data is shown in Figure 2.22. The up- and downgoing tubewaves are within the first mute zone polygons outlined in red. The aliased

FLOWCHART - Interactive F-K processing (for F-K mute zone design)



Flowchart 5. An example of the interpretive processing flowchart of the interactive F-K processing used for the attenuation of tubewave events on $Z_{up}(FRT)$ data (Hinds et al., 1994c).

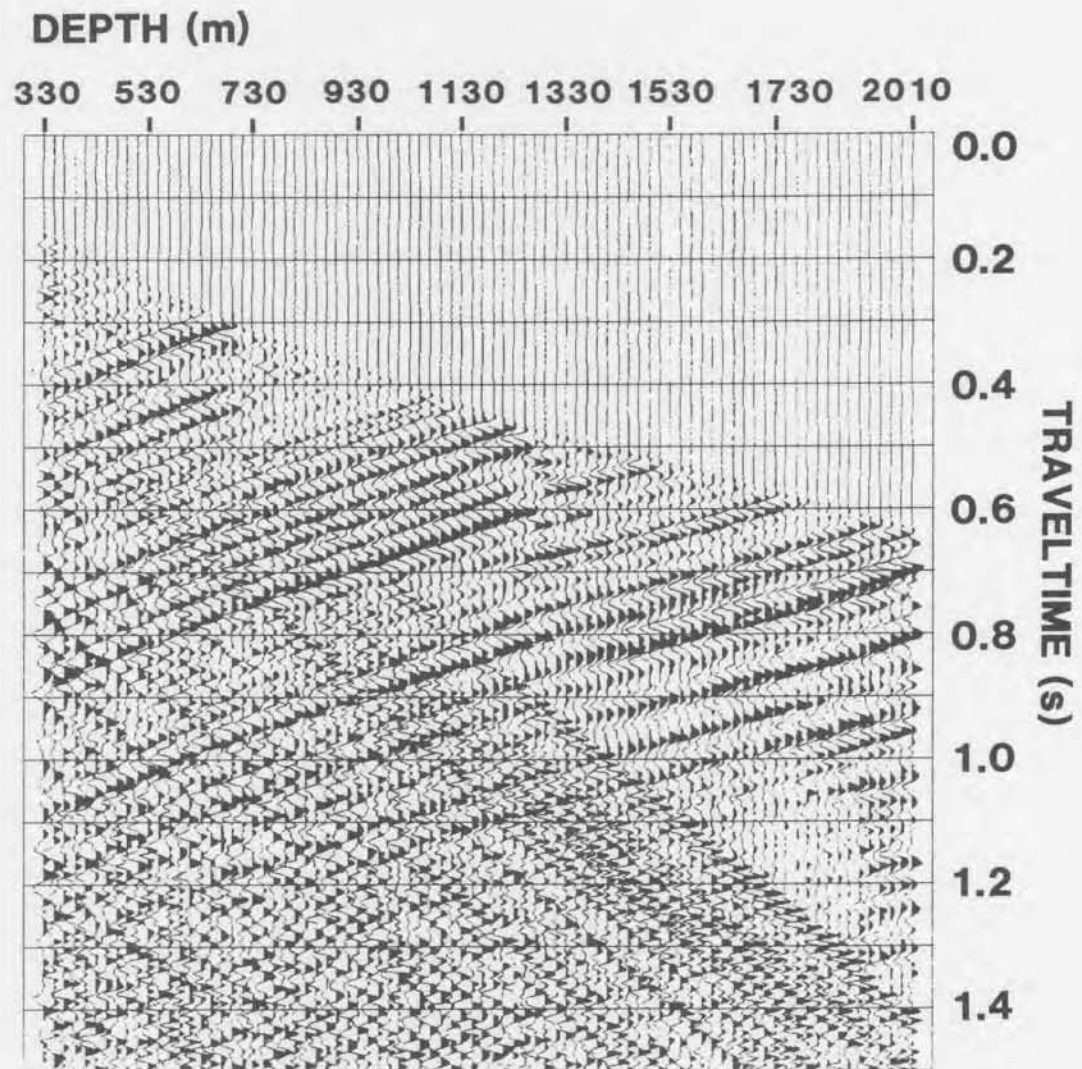


Figure 2.21 The Fort St. John Graben Z_{up} (FRT) data (Hinds et al., 1993a) resulting from median filter-based wavefield separation (plus subtraction). The downgoing tubewave aliased back into the data as an upgoing event. A question that the single operation interactive processing can answer is "how does one design the surgical F-K mute for the attenuation of the tubewave events and what effects, if any, does the design have on the upgoing P-wave events?".

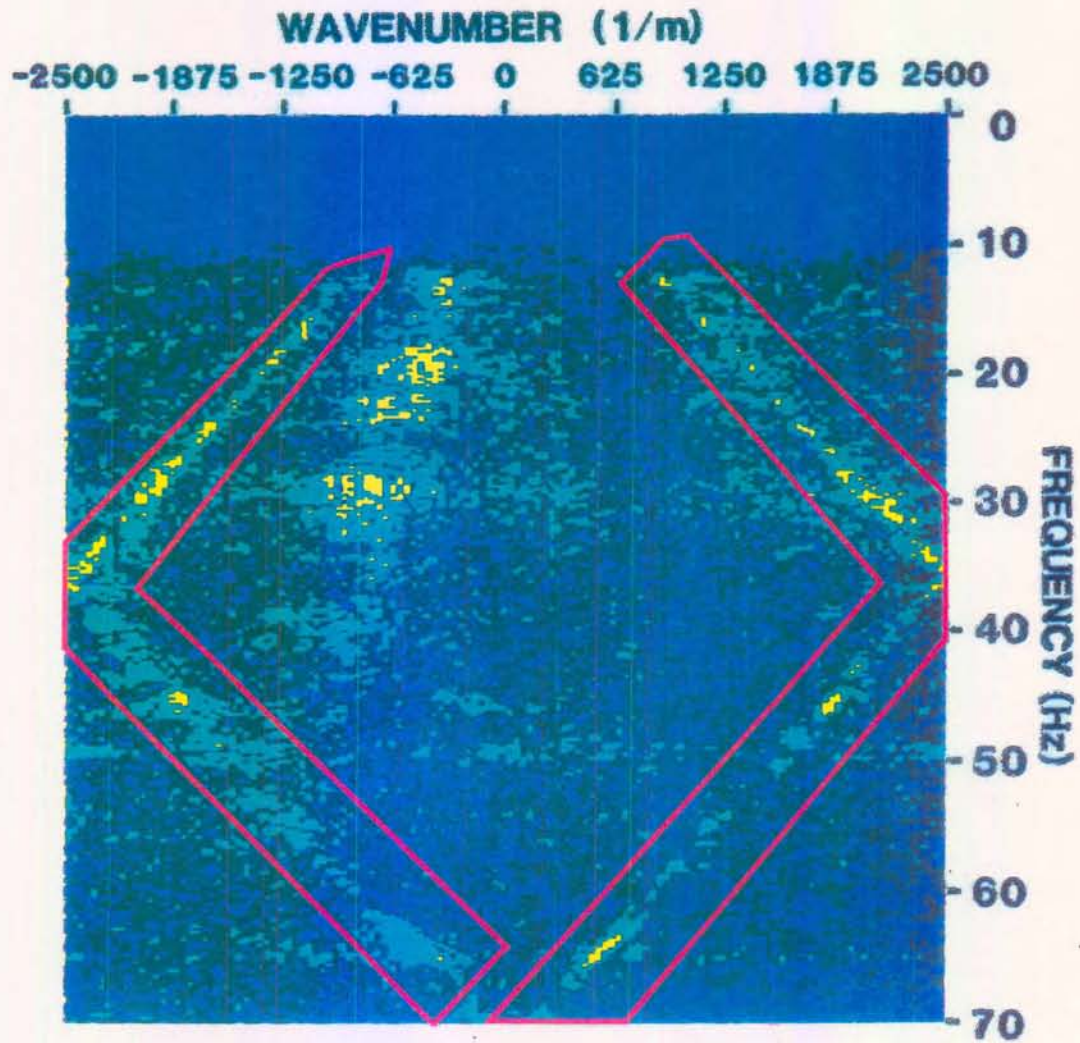


Figure 2.22 F-K plot of the data shown in Figure 2.19 illustrating the surgical mute reject polygons enveloping both the up- and downgoing F-K events (aliased and non-aliased portions included). The polygon in the negative K quadrant intersects the upgoing P-wave F-K events.

part of the downgoing tubewave events in the F-K domain crosses the upgoing P-wave events at approximately -1250 (10^{-5} m^{-1}) on the wavenumber axis and 55 Hz on the frequency axis.

How can the surgical mute F-K polygon be best designed to attenuate this tubewave? The designed F-K surgical mute polygons shown in Figure 2.22 also intersect some of the upgoing P-wave F-K events. Muting the F-K data within these reject zones would eliminate any upgoing P-wave events within the same zones. Would the application of the F-K polygon mutes adversely affect the interpretation of the upgoing P-waves in the depth-time domain? The application of the F-K reject mode of the polygons results in the $Z_{\text{up}}(\text{FRT})$ data shown in Figure 2.23. The downgoing and aliased tubewave events have been attenuated.

By returning to the F-K plot of the original data (Fig. 2.22) and redefining the F-K mute zone to not intersect the upgoing P-wave data, the effect on the interpretation on the upgoing P-wave data by the previous F-K filtering (Figs. 2.22 and 2.23) can be ascertained. The surgical mute polygons are updated to be the same as the design shown in Figure 2.22 except that the portion of the tubewave F-K event intersecting the upgoing F-K P-wave events are not attenuated (Fig. 2.24). This new set of surgical mutes yields the results shown in Figure 2.25. The results in Figures 2.23 and 2.25 can be compared to evaluate the effect of muting the upgoing event F-K data that lie in the $50\text{-}60 \text{ Hz}$ range of the F-K domain during the effort to attenuate all of the tubewave events. The upgoing events in Figures 2.23 and 2.25 are similar and the interpretation of the upgoing events will not be degraded by using the F-K mute shown in Figure 2.22. The F-K procedures shown using Figures 2.18 through to 2.25 is another type of interpretive processing that the "interpreter/processor" can use.

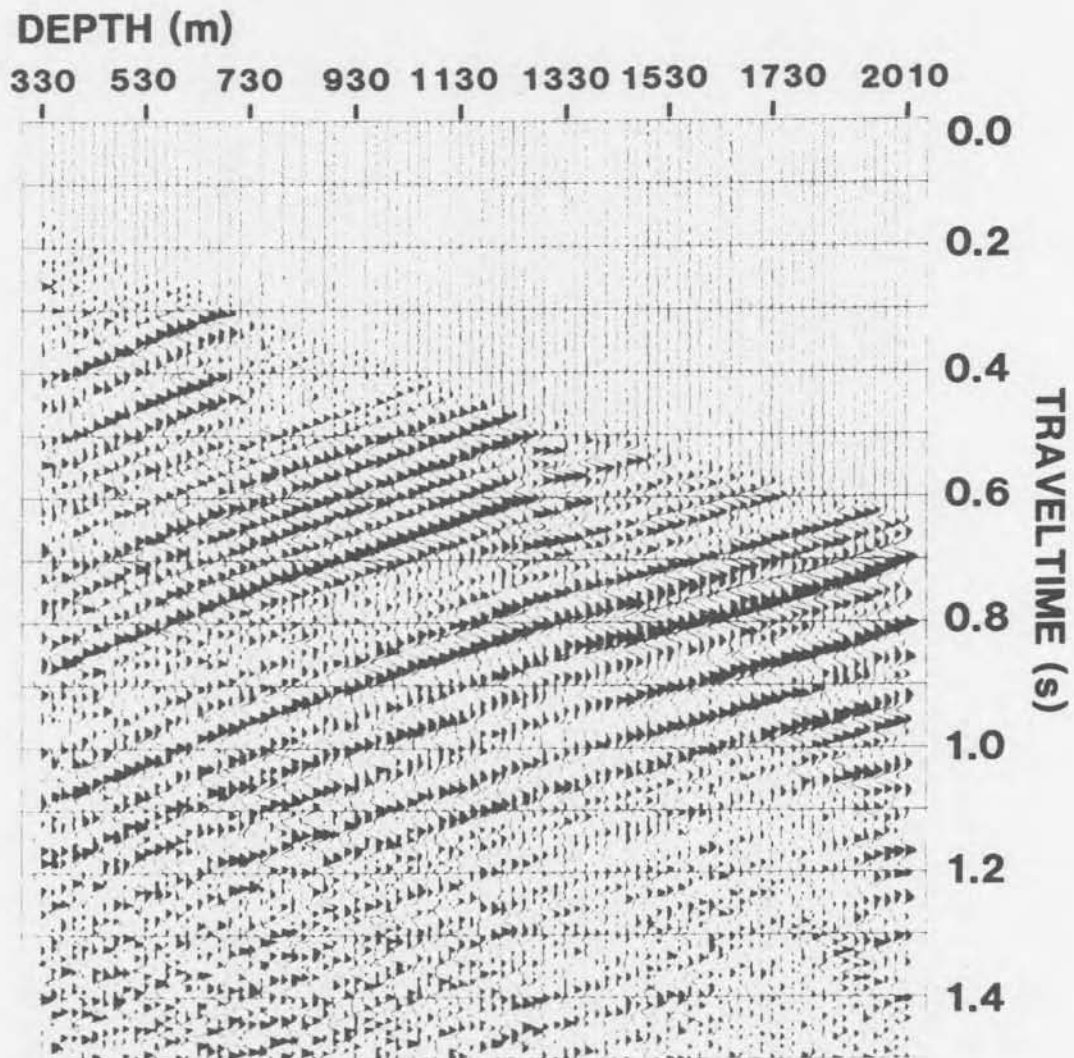


Figure 2.23 The filtered output of the data in Figure 2.21 following the application of the F-K polygon surgical mutes shown in Figure 2.22. The aliased and non-aliased portions of the tubewave events have been attenuated. The next question is "what effect would the application of F-K mute polygons which do not intersect the upgoing F-K events have on the filtered output?".

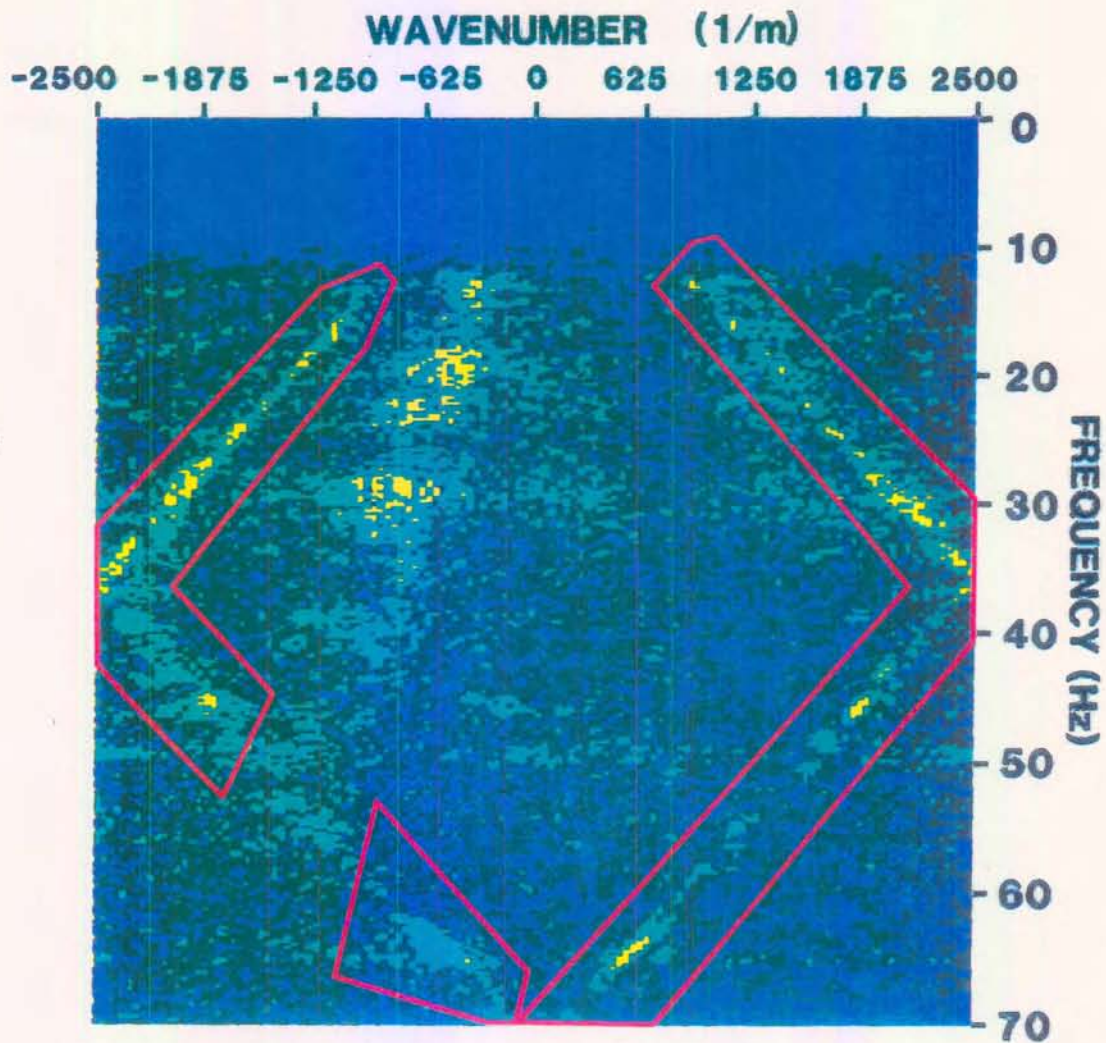


Figure 2.24 F-K plot of the data shown in Figure 2.21 illustrating the surgical mute reject polygons enveloping both the up- and downgoing tubewave F-K events (aliased and non-aliased portions included), however, excluding the muting of any upgoing P-wave F-K events.

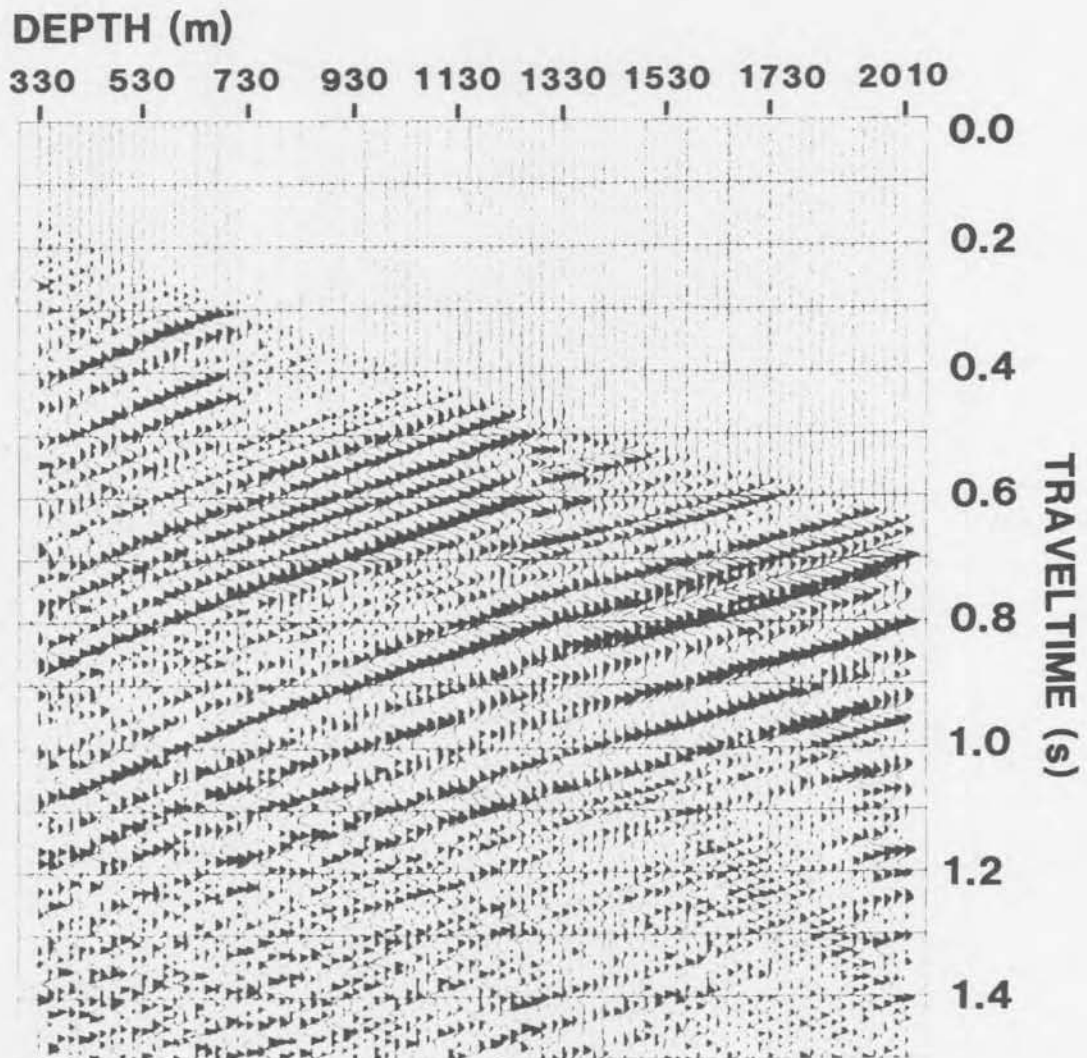


Figure 2.25 The filtered output of the data in Figure 2.21 after the application of the polygon surgical mutes shown in the F-K plot of Figure 2.24. A minor amount of the aliased downgoing tubewave event has been retained in the filtered output.

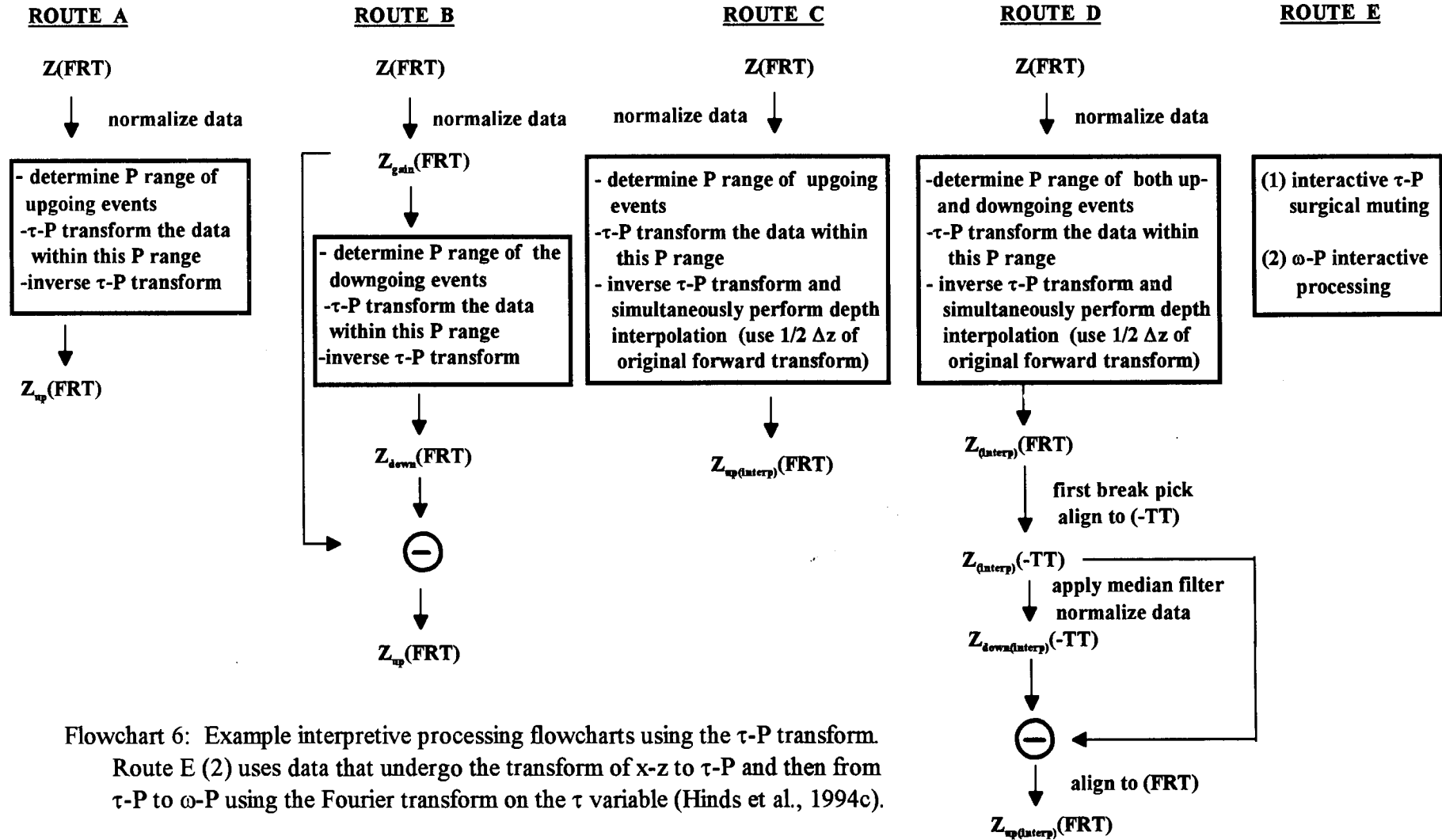
2.2.5 τ -P filtering

In this section, the use of the τ -P or Radon transform (Robinson, 1983; Deans, 1983; Durrani and Bisset, 1984; Turner, 1990, Hu and McMechan, 1987, Moon et al., 1986) within wavefield separation processing will be discussed.

Four routes will be examined in which the τ -P transform is used in wavefield separation. The routes are summarized in Flowchart 6 and consist of (Hinds et al., 1994c)

- (1) Route A: τ -P transform the $Z(\mathbf{FRT})$ data with upgoing event slownesses (P is the inverse of velocity), inverse τ -P transform to output $Z_{\text{up}}(\mathbf{FRT})$ data;
- (2) Route B: τ -P transform the $Z(\mathbf{FRT})$ data with downgoing event slownesses, inverse τ -P transform to output $Z_{\text{down}}(\mathbf{FRT})$ data, subtract the $Z_{\text{down}}(\mathbf{FRT})$ from the $Z(\mathbf{FRT})$ data to output the $Z_{\text{up}}(\mathbf{FRT})$ data;
- (3) Route C: τ -P transform the $Z(\mathbf{FRT})$ data with upgoing event slownesses, inverse τ -P transform using a depth interval parameter of half the original depth spacing to spatially interpolate the $Z_{\text{up}}(\mathbf{FRT})$ data; and
- (4) Route D: τ -P transform the $Z(\mathbf{FRT})$ over both up- and downgoing event slownesses, inverse τ -P transform using half the original depth increment, wavefield separate the

Time intercept - slowness (τ -P) VSP wavefield separation flowcharts



Flowchart 6: Example interpretive processing flowcharts using the τ -P transform. Route E (2) uses data that undergo the transform of x - z to τ -P and then from τ -P to ω -P using the Fourier transform on the τ variable (Hinds et al., 1994c).

$Z_{(\text{interp})}(\text{FRT})$ data using median filter based wavefield separation to output

$Z_{\text{up}(\text{interp})}(\text{FRT})$ data.

The τ -P transform based wavefield separation routes will be applied to both the multiple contaminated and tubewave contaminated $Z(\text{FRT})$ data used in the previous sections. The multiple contaminated data will be used to illustrate the route A processing since Rieber mixing may occur using this processing flow. The preservation of the lateral extent of the multiple events in the $Z_{\text{up}}(\text{FRT})$ data will be examined. The three other routes of τ -P processing will use the tubewave contaminated $Z(\text{FRT})$ data. The tubewave events in these data are spatially aliased and the effect of the processing schemes on the spatially aliased tubewave will be examined.

2.2.5.1 Review of τ -P filtering

A conceptual explanation of the τ -P transform is illustrated in Figure 2.26 (Hardage, 1992; Fig. 136). The τ variable refers to the time intercept of the lines of integration in the time-depth (or time-offset for CDP gathers) domain. The P variable refers to the slowness (inverse of velocity) values associated with the lines of integration. In Figure 2.26A, two lines with different slopes are shown intersecting the example time-depth data point. Integration of the time-depth data along each line, $t=p_1x+\tau_1$ and $t=p_2x+\tau_2$, would yield two values in the τ -P domain as seen in the lower half of Figure 2.26A. The different slopes of the lines refer to different P or slowness values.

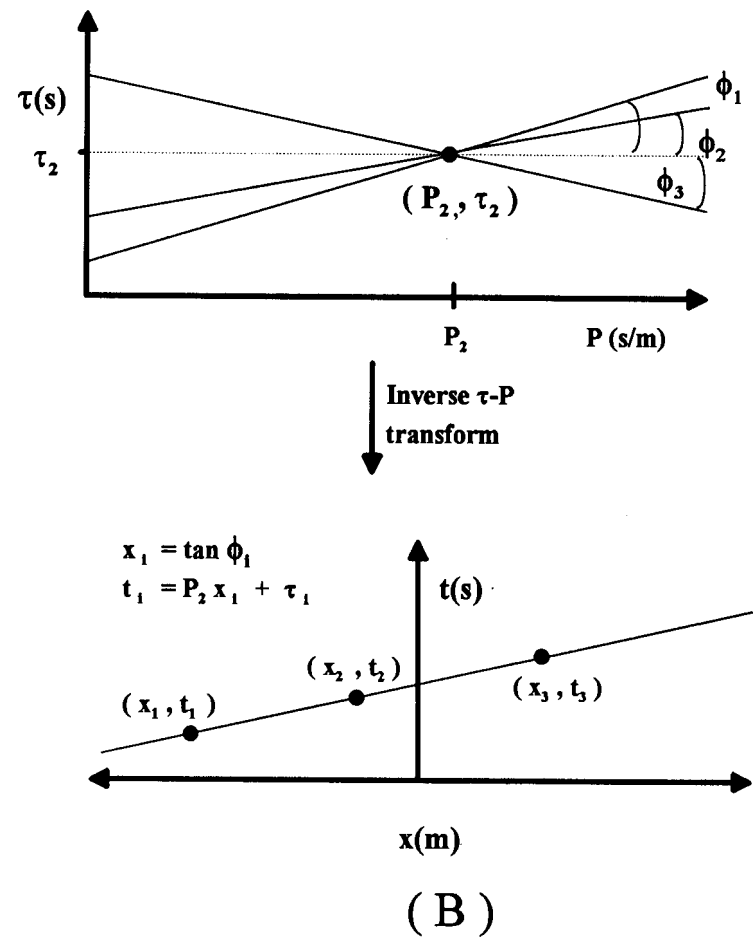
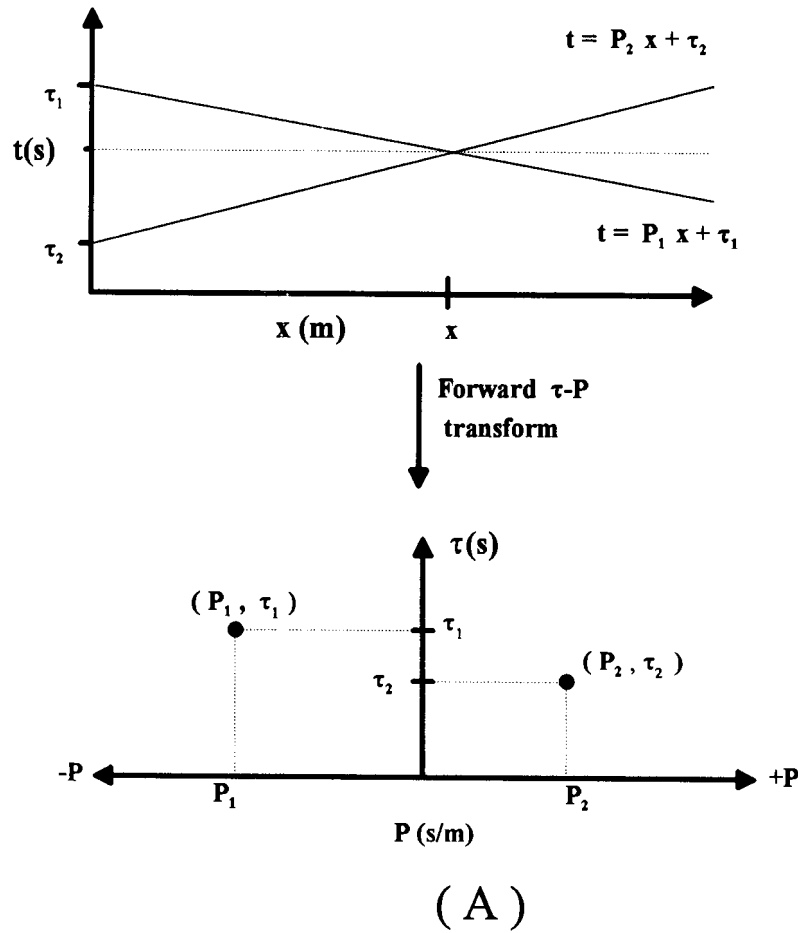


Figure 2.26 The concept of the forward and reverse τ - P transform. The forward transform (Part A) maps a line into a point and the reverse transform (Part B) maps a line in τ - P domain back to a point in the time-offset (depth) domain (from Hardage, 1985).

To perform the inverse τ -P transform (Kappus et al., 1990), the same procedure is done within the τ -P domain. As shown in the top part of Figure 2.26B, three lines of integration through a single point in the τ -P domain results in the values for three points along a straight line in the time-depth domain.

Whereas the F-K transform mapped a line in the time-depth domain into a line intersecting the origin of the F-K domain, the τ -P transform maps a line in the time-depth domain into a point in the τ -P domain. The two transforms are linked through the P or inverse velocity parameter. The Rieber mixing present in the F-K filtering exists in τ -P filtering since the τ -P filtering is based on velocity.

For surface seismic data, the hyperbolic-shaped reflection events on a common depth point (CDP) gather map into ellipses in the τ -P domain (Stoffa et al., 1981). The CDP gather can be transferred into the X^2 - T^2 domain and τ -P transformed to enable multiple attenuation in the surface seismic data. Following interpolation in the X^2 - T^2 domain, the hyperbolic reflection events of the X-T data become linear events in the X^2 - T^2 domain and subsequently "points" in the τ -P domain. The points are smeared due to truncation effects resulting from the transform of finite events (the offset range is not infinite) and the representation of the events with near-zero spatial frequencies (near-offset events at the apex of the reflection hyperbolas). Muting in the τ -P domain results in multiple attenuation (Hinds and Durrheim, 1993 and 1994).

Instead of the hyperbolic events seen in the CDP gather of surface seismic data, the depth-time events of the **Z(FRT)** data are linear. The purpose of the X^2 - T^2 processing of the CDP

gathers in Hinds and Durrheim (1993, 1994) was to transform the hyperbolic events into linear events. Similarly to that work, the VSP linear events will be transformed into "points" following the τ -P transformation. The up- and the downgoing VSP events will map into different quadrants of the τ -P domain because the events have oppositely signed apparent velocities. Wavefield separation can then be realized through the attenuation of the amplitude data in the τ -P domain containing the downgoing events (Hardage, 1992; Hu and McMechan, 1987).

2.2.5.2 Route A: τ -P transformation of only the upgoing events

Rieber mixing may become a factor in τ -P wavefield separation due to the equivalence of the slowness range and F-K narrow pie-slices. To illustrate this, the multiple contaminated **Z(FRT)** data from the Fort St. John Graben case study (Hinds et al., 1991a; Hinds et al., 1993a; Hinds et al., 1994c) will be used in the Route A processing. The effect of the τ -P filtering will be shown in the F-K domain to illustrate the equivalence of the two methods, τ -P and F-K.

The τ -P wavefield separation IPP for Route A is shown in Figure 2.27. The processing runstream for the Route A τ -P processing is shown in Flowchart 6A. The input data to the forward τ -P transform is limited to be the VSP data with velocities similar to the upgoing events.

The normalized and gained **Z(FRT)** data are shown in panels 1 and 2, respectively, of Figure 2.27. The **Z_{up}(FRT)** data shown in panel 3 was a result of the inverse τ -P transformation

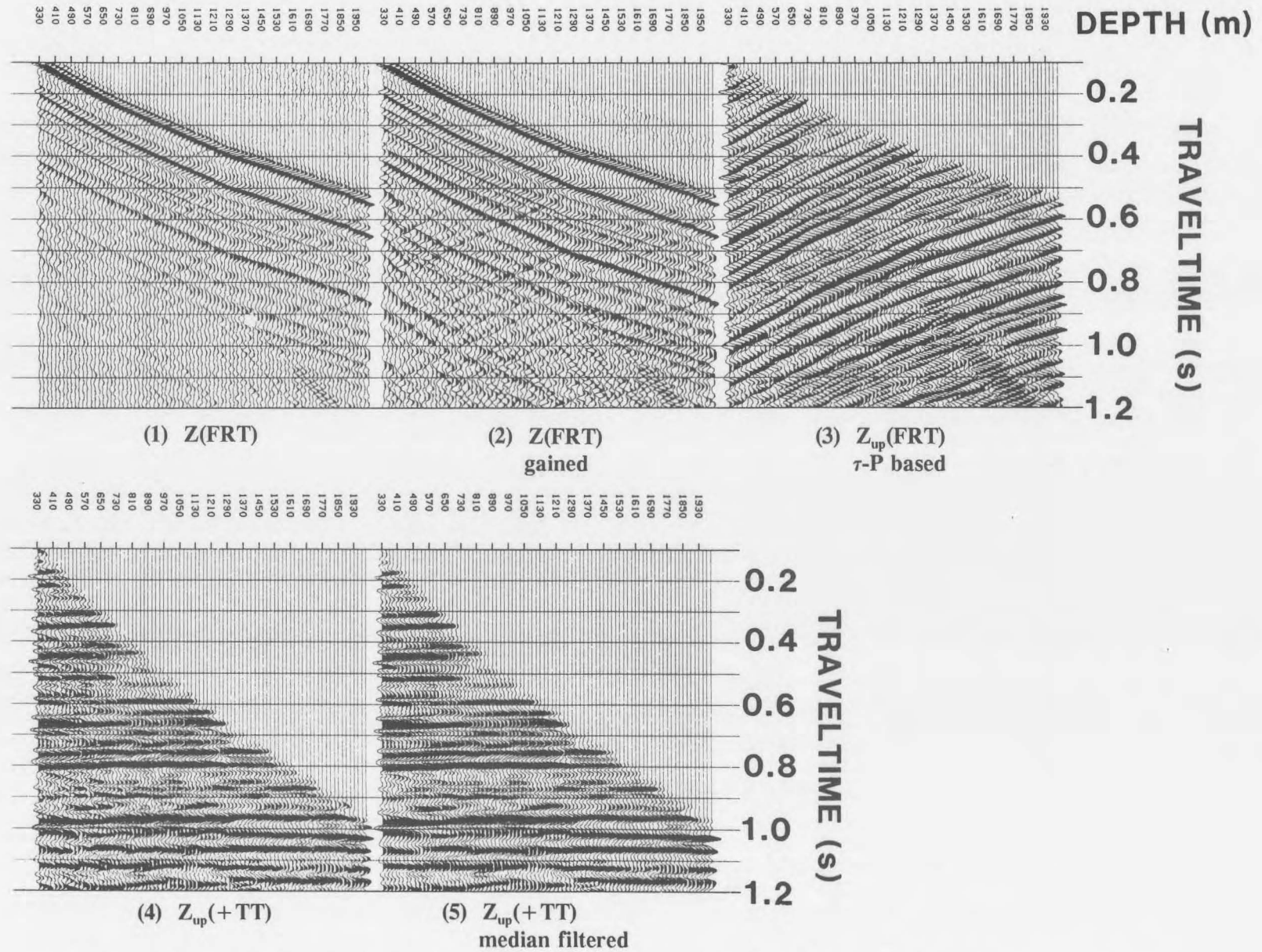


Figure 2.27 τ -P (route A) based wavefield separation IPP of the Fort St. John Graben (Hinds et al., 1993a) multiple contaminated data.

of the isolated upgoing events from the forward τ -P transform of the $\mathbf{Z}(\text{FRT})$ data. The forward τ -P transform of the $\mathbf{Z}(\text{FRT})$ data did not include the slowness values of the downgoing VSP events.

The slowness range in the forward τ -P transformation of the $\mathbf{Z}(\text{FRT})$ data were from near-zero (about -24,000 m/s) to -0.0000035 s/m (-2400 m/s). The F-K plot of the $\mathbf{Z}_{\text{up}}(\text{FRT})$ data from panel 3 of Figure 2.27 is shown in Figure 2.28. The two slowness values define linear cut-offs in F-K space filtering.

The $\mathbf{Z}_{\text{up}}(\text{FRT})$ in panel 3 can be compared to the F-K filtered $\mathbf{Z}_{\text{up}}(\text{FRT})$ data in panel 5 of Figure 2.7. The upgoing event data in panel 5 of Figure 2.7 was isolated from the $\mathbf{Z}(\text{FRT})$ data using the narrow "accept" zone seen in Figure 2.12. The equivalent "accept" zone used in the τ -P processing is larger than the zone used for the F-K wavefield separation. As a result, the $\mathbf{Z}_{\text{up}}(\text{FRT})$ data shown in panels 3,4, and 5 of Figure 2.27 exhibit a lesser degree of Rieber mixing than similar data seen in Figure 2.7.

The two IPP panels (Figs. 2.7 and 2.27) are opposite in polarity. In panels 4 and 5 of Figure 2.27, the highlighted (in orange) isolated trough at 0.755 s appearing on the depth traces between 1270 m and the first break curve is the primary event that is embedded within the series of multiples. The same primary upgoing event appears as a peak (highlighted in blue) in panel 5 of Figure 2.7; however, the trace to trace amplitude contrasts in Figure 2.7 have been smeared by Rieber mixing.

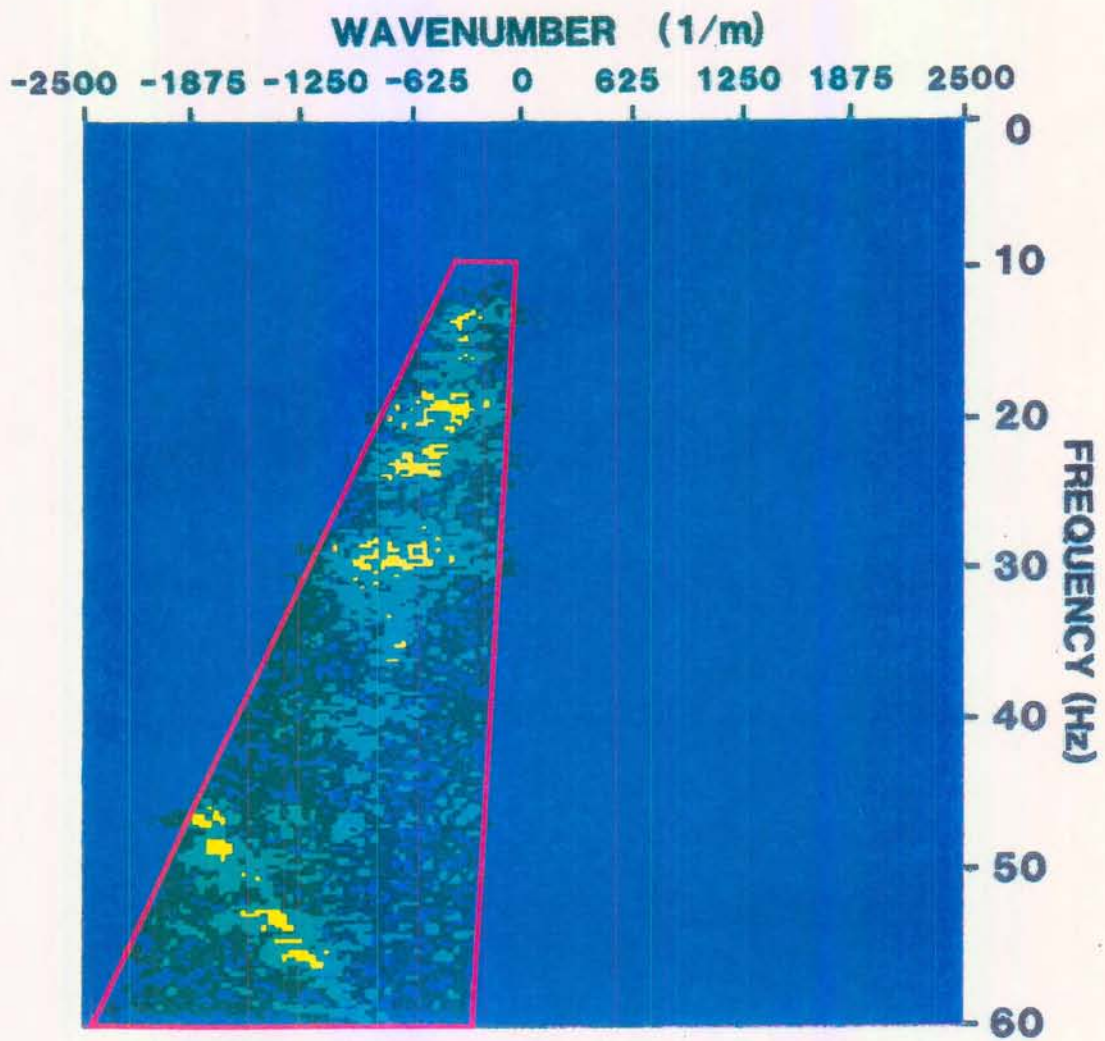


Figure 2.28 The equivalent F-K surgical mute pass zone to the τ -P filter used to create the resultant data in panel 3 of Figure 2.27. This can be compared to the F-K narrow pass zone shown in Figure 2.12.

2.2.5.3 Route B: Subtraction of $Z_{\text{down}}(\text{FRT})$ from the $Z(\text{FRT})$ data

In this section, the downgoing events are isolated from the $Z(\text{FRT})$ data using the τ -P transform. The $Z_{\text{down}}(\text{FRT})$ data are then subtracted from the $Z(\text{FRT})$ data to yield the $Z_{\text{up}}(\text{FRT})$ results.

The wavefield separation IPP for this approach using the tubewave contaminated $Z(\text{FRT})$ data example is shown in Figure 2.29. The $Z_{\text{down}}(\text{FRT})$ data, shown in panel 3, are isolated using τ -P filtering and following scaling, the data are subtracted from the $Z(\text{FRT})$ data (shown in panel 2 of Fig. 2.29) to output the separated upgoing event data, $Z_{\text{up}}(\text{FRT})$, shown in panel 4. This is similar to the results obtained using the median filter based wavefield separation method shown in Figure 2.2. The aliased downgoing tubewave (appearing as upgoing events and highlighted in panel 4) have not been attenuated. This processing route avoids possible Rieber mixing because the action of the τ -P filter is now similar to the use of a narrow "reject" F-K filter to attenuate the upgoing events.

2.2.5.4 Route C: τ -P spatial interpolation during wavefield separation

In this section, the upgoing events are separated from the $Z(\text{FRT})$ data during the transformation to the τ -P domain by using selected slownesses. Trace depth interpolation to a finer depth sampling is performed during the inverse transform. The effect that the spatial interpolation has on the inverse τ -P transformed aliased tubewave will be examined.

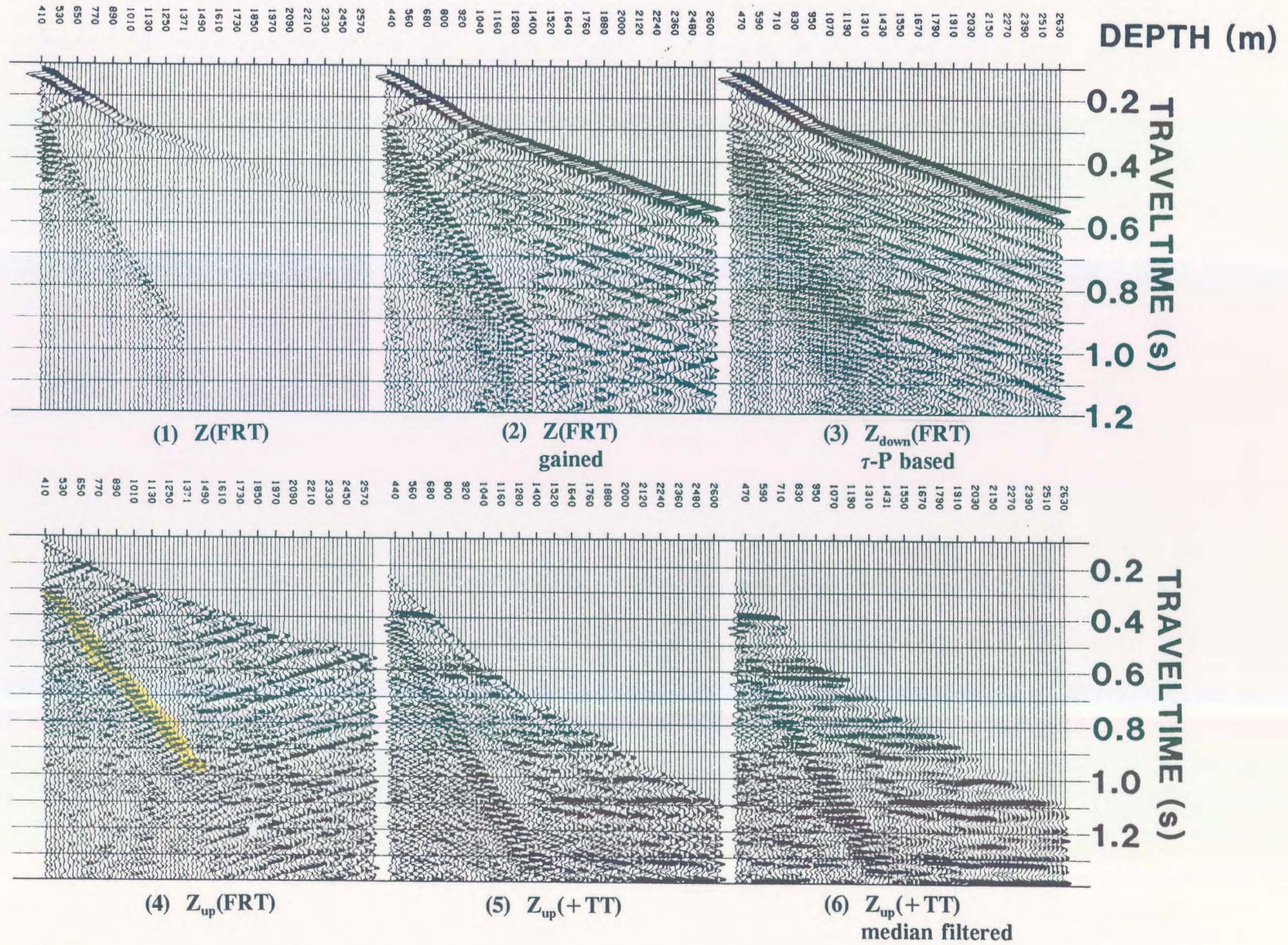


Figure 2.29 τ -P (route B) based wavefield separation IPP of the tubewave contaminated data using τ -P downgoing event separation and then subtraction of the $Z_{down}(FRT)$ from the $Z(FRT)$ to output the $Z_{up}(FRT)$ data.

Figure 2.30 shows the F-K plot of the tubewave contaminated $Z(\mathbf{FRT})$. The downgoing P-wave events are shown in the negative k_z quadrant because the $Z(\mathbf{FRT})$ data came from an early stage of preprocessing. The depth interval for the traces is 30 m and the downgoing tubewave aliases back into the upgoing events. The centre of the intersection is about at 37 Hz and $833 (*10^{-5}) \text{ m}^{-1}$ on the k_z axis. The intersection of the aliased downgoing tubewave with the upgoing P-wave F-K events is highlighted in Figure 2.30 at the cursor location.

The $Z(\mathbf{FRT})$ data are forward τ -P transformed using the slowness range of the upgoing events only. The aliased downgoing tubewave F-K events will also be "retained" during the forward transformation since these events appear in the same slowness range as the upgoing P-wave events due to aliasing. During the inverse transform, the trace spacing sampling interval is redefined to be 15 m. The $Z_{\text{up(interp)}}(\mathbf{FRT})$ data at the interpolated trace spacing of 15 m are displayed in panel 2 of Figure 2.31. The aliased downgoing tubewave events preserved during the inverse τ -P transformation are highlighted in panel 2.

The interpolation performed during the inverse τ -P transform has faithfully interpolated even the aliased tubewave (as is shown in the $Z_{\text{up(interp)}}(\mathbf{FRT})$ F-K plot in Fig. 2.32). The upgoing F-K events are shown in the negative F-K quadrant of Figure 2.32. The intersection of the interpolated aliased tubewave with the interpolated upgoing F-K events is still at 37 Hz and at $833 (*10^{-5}) \text{ m}^{-1}$. This is the same location as the tubewave event intersection with the upgoing events in the F-K domain before interpolation. The major change in the F-K plot is that the K_z Nyquist values have doubled in size from 1666 to $3333 *10^{-5} \text{ m}^{-1}$.

Do the $Z_{\text{up}}(\mathbf{FRT})$ data look markedly different without the interpolation? To answer this, the

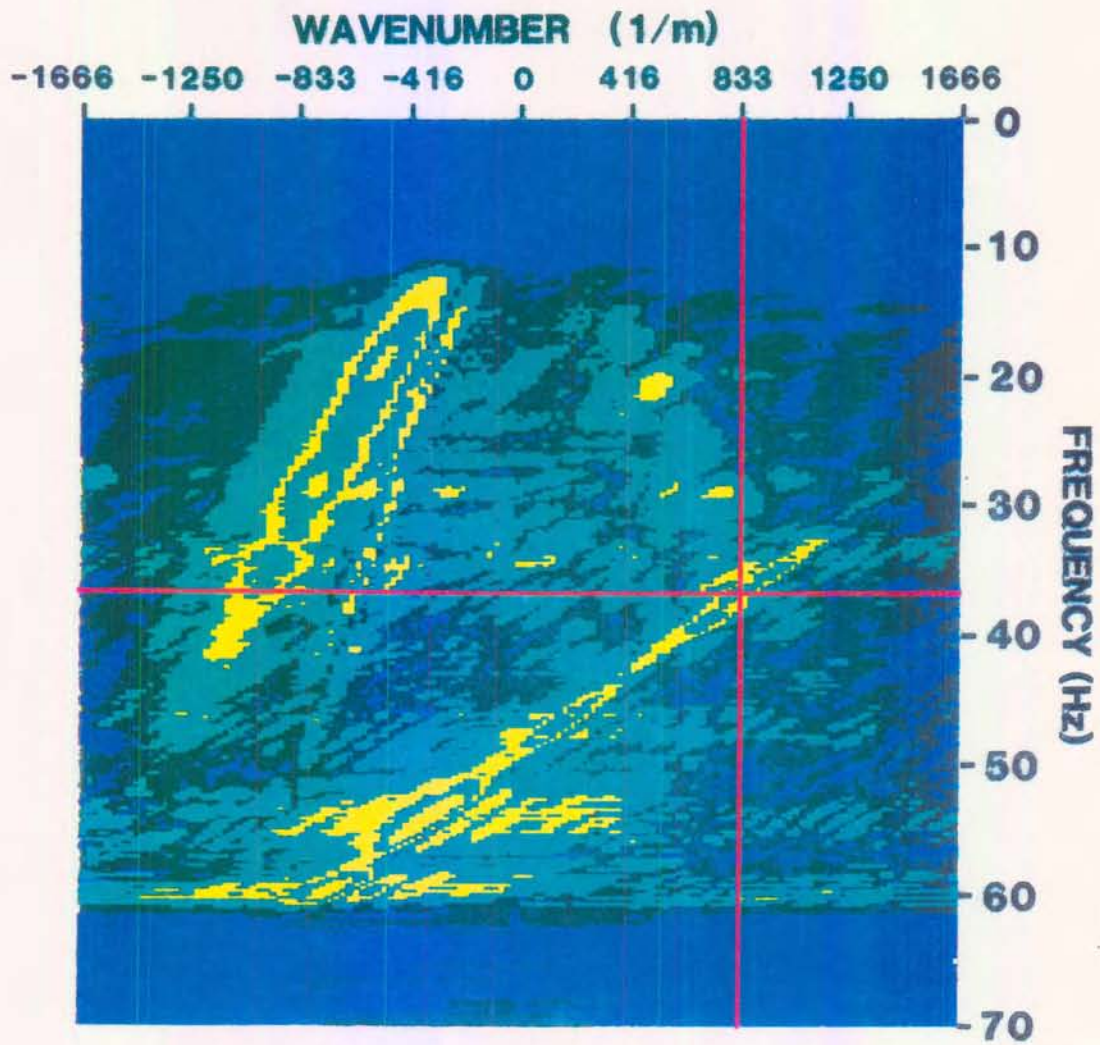


Figure 2.30 F-K plot of the tubewave contaminated data showing the aliased tubewave F-K event intersecting (at the crossing of the red lines) the upgoing P-wave F-K event at 0.00833 m^{-1} spatial frequency (K) and 37 hz.

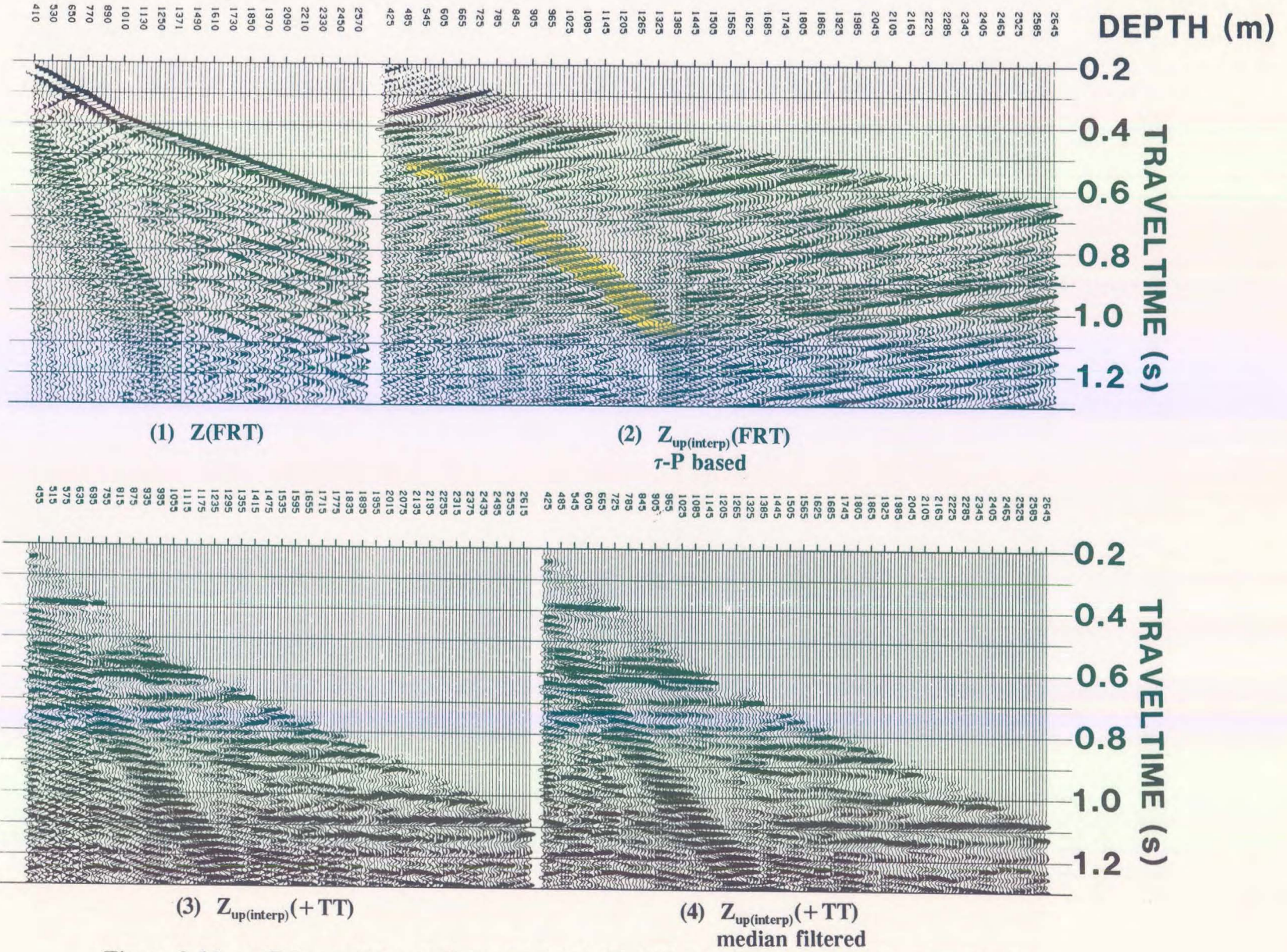


Figure 2.31 $\tau\text{-P}$ (route C) wavefield separation IPP using $\tau\text{-P}$ upgoing event separation on $Z(\text{FRT})$ with 30 m trace separation and inverse $\tau\text{-P}$ transformation using trace interpolation to create 15 m trace spacing.

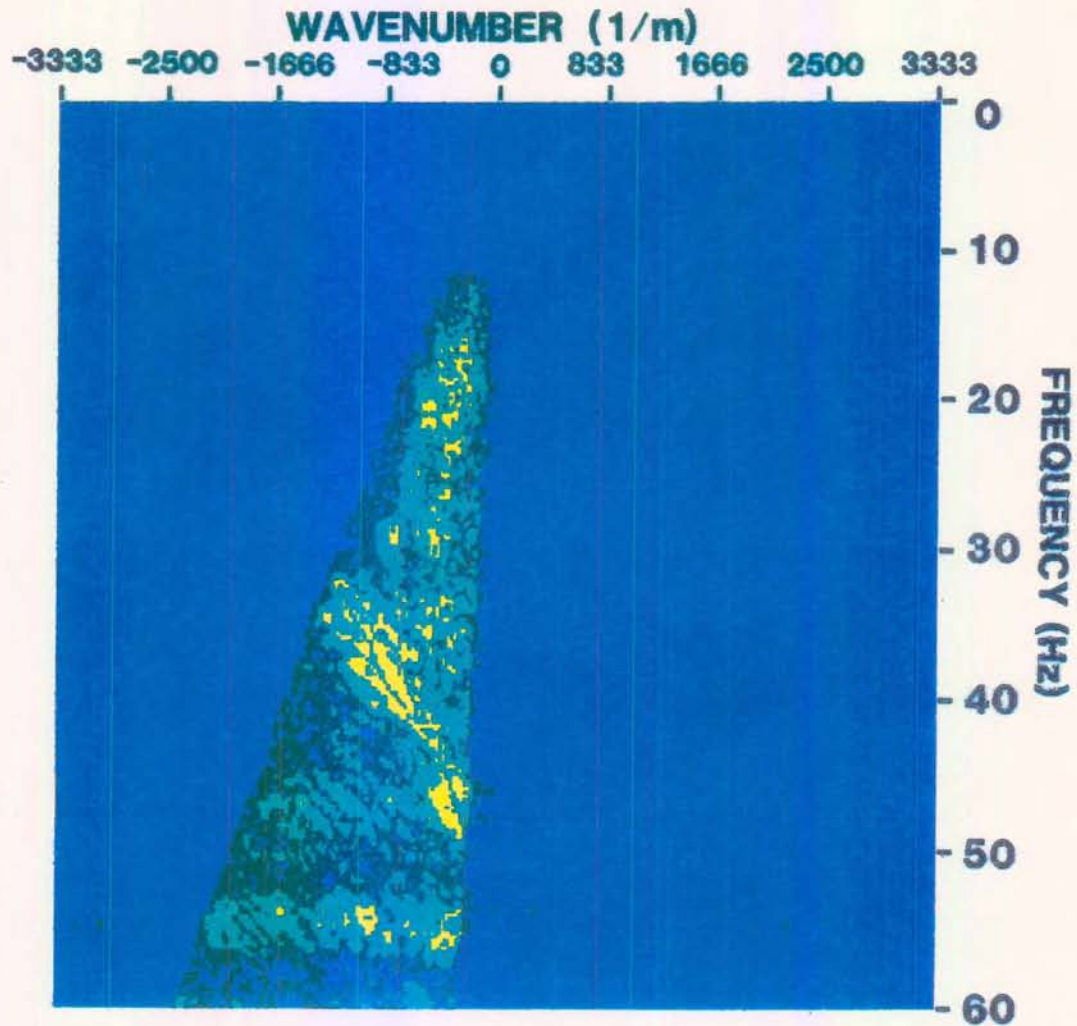


Figure 2.32 F-K plot of the interpolated tubewave contaminated $Z_{\text{up(interp)}}(\text{FRT})$ data where the aliased tubewave F-K event intersects the upgoing P-wave F-K event at 0.00833 m^{-1} spatial frequency (K) and 37 Hz. The range of the wavenumber (K) axis has doubled in value (due to the 15 m trace spacing), however, the intersection of the aliased tubewave and upgoing P-wave F-K events remains the same as in Figure 2.30.

tube wave contaminated $Z(\text{FRT})$ was wavefield separated using the τ -P filtering but without trace interpolation. The resultant $Z_{\text{up}}(+\text{TT})$ data are shown in the IPP of Figure 2.33. By inspection, it is evident that the $Z_{\text{up}(\text{interp})}(+\text{TT})$ interpolated data in panel 4 of Figure 2.31 is similar to the non-interpolated $Z_{\text{up}}(+\text{TT})$ data in panel 4 of Figure 2.33.

2.2.5.5 Route D: τ -P spatial interpolation of $Z(\text{FRT})$ before wavefield separation

In this section, both the up- and downgoing events of the $Z(\text{FRT})$ data are preserved during the forward τ -P transform. Spatial interpolation is performed during the inverse transform and wavefield separation is then performed using median filtering on the $Z_{(\text{interp})}(\text{FRT})$ data. This procedure would be useful when processing a dataset which had irregular depth spacing and required interpolation. Although the tubewave contaminated $Z(\text{FRT})$ data do have regular spacing, the IPP is presented showing median filter wavefield separation using τ -P trace interpolated data.

The spatially interpolated data are shown in panel 1 of Figure 2.34. The results of using the $Z_{(\text{interp})}(\text{FRT})$ data in a median filter based wavefield separation procedure method are shown in panels 2, 3, 4 and 5. In panel 5, the $Z_{\text{up}(\text{interp})}(-\text{TT})$ data with 15 m depth spacing are shown. The $Z_{\text{up}(\text{interp})}(+\text{TT})$ and $Z_{\text{up}(\text{interp};\text{med})}(+\text{TT})$ data are shown in panels 6 and 7, respectively.

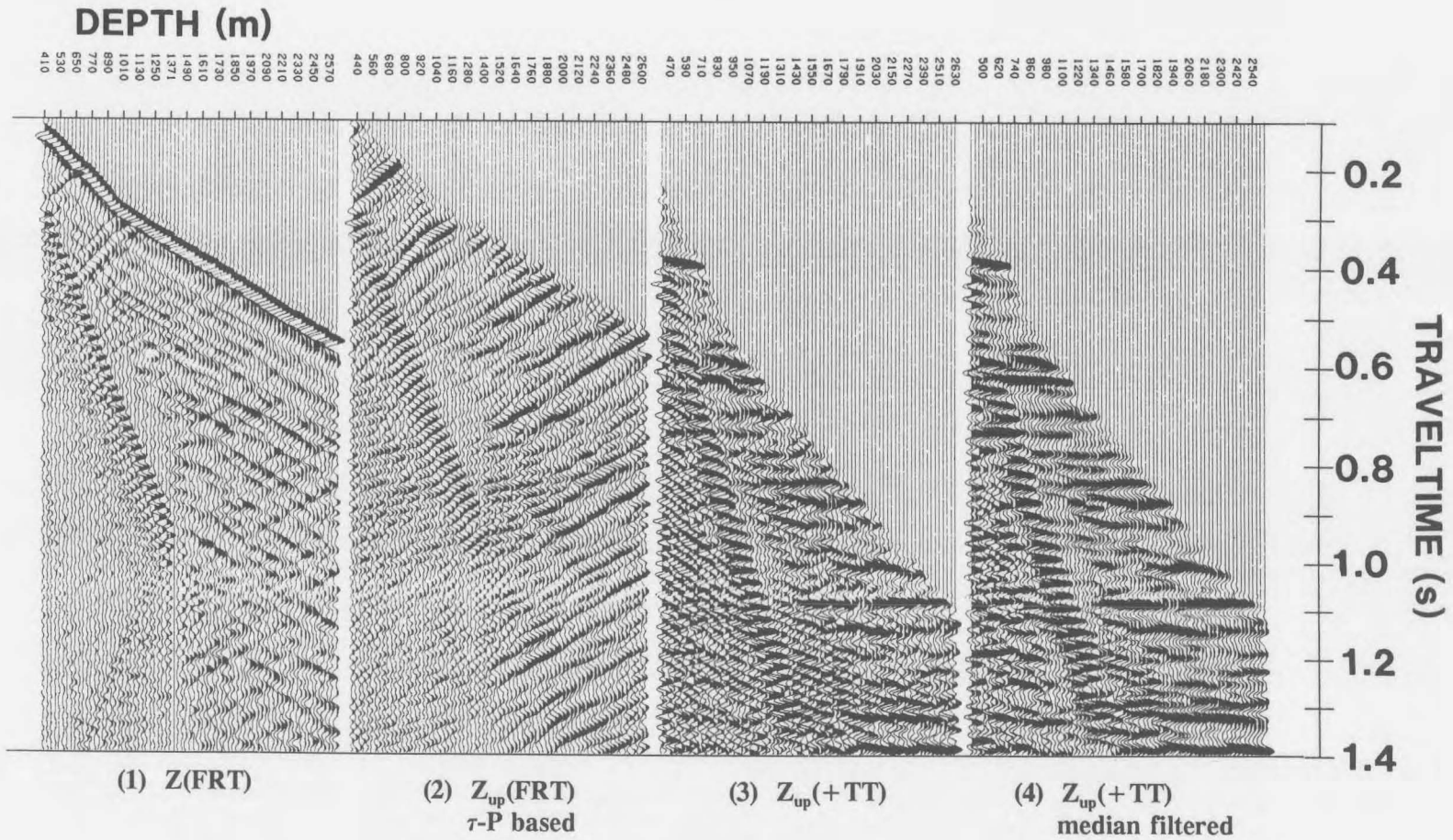


Figure 2.33 τ -P based wavefield separation IPP of the tubewave contaminated data using τ -P upgoing wave isolation (filtering out P values outside the range of the upgoing P-wave events).

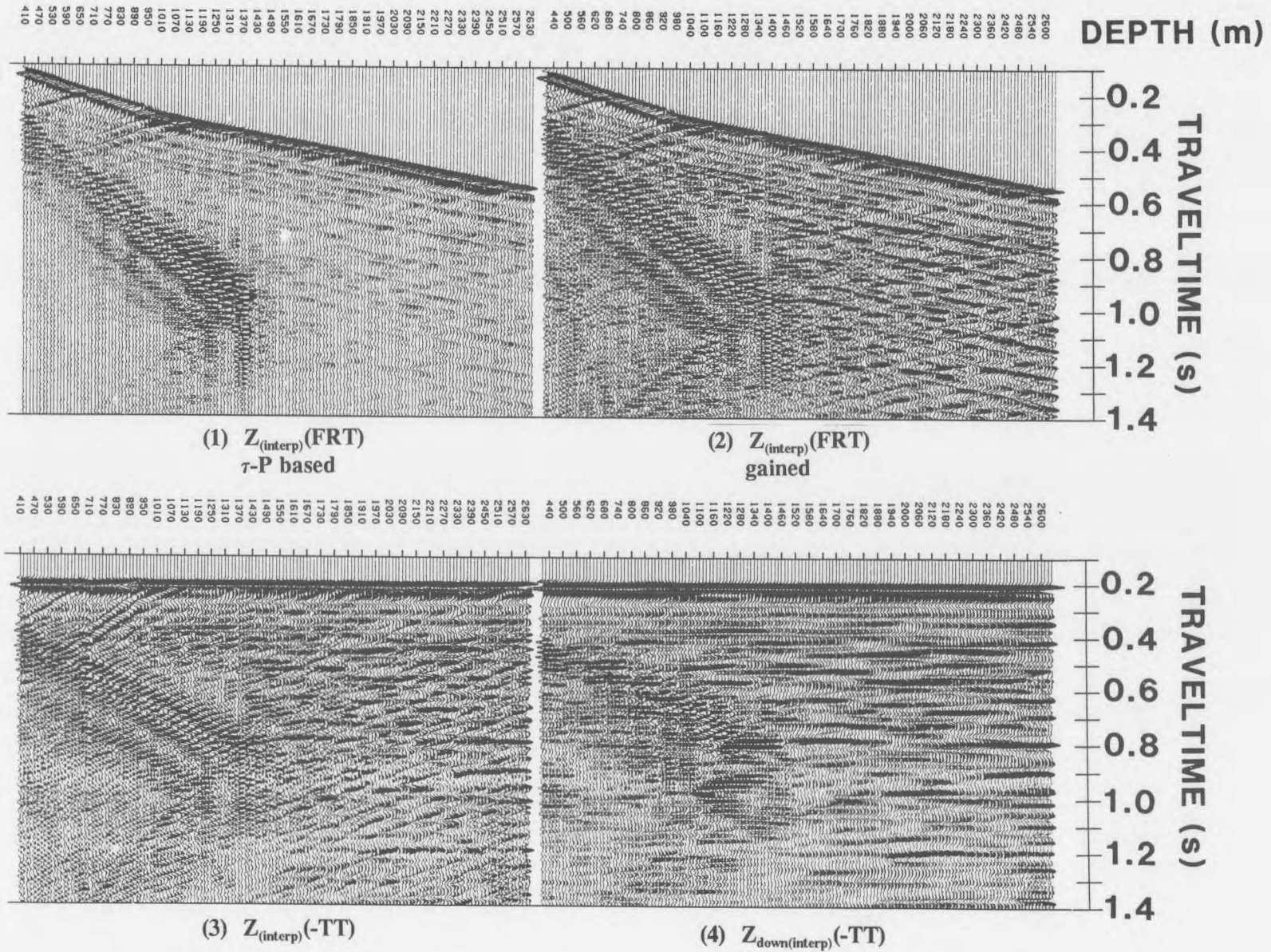
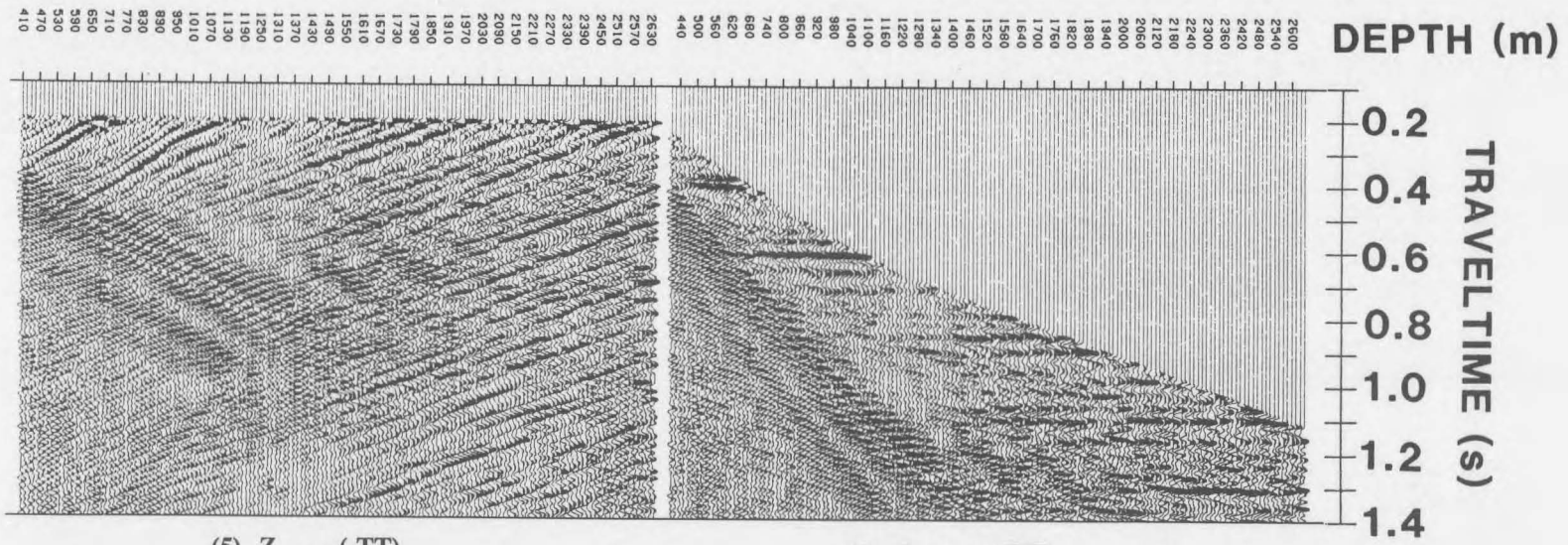
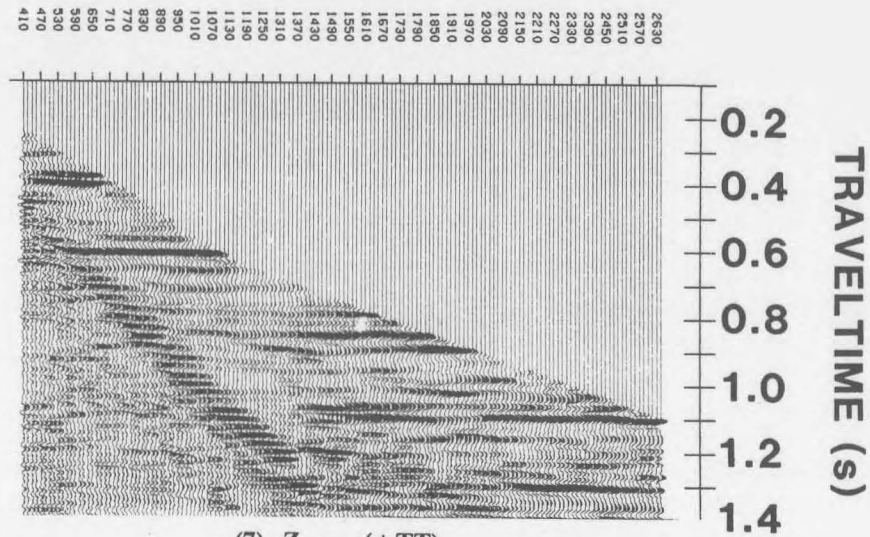


Figure 2.34A Panels 1 to 4 of the τ -P based wavefield separation IPP using the interpolated $Z(FRT)$ tubewave contaminated data.



(5) $Z_{up(interp)}(-TT)$
median filter based

(6) $Z_{up(interp)}(+TT)$



(7) $Z_{up(interp)}(+TT)$
median filtered

Figure 2.34B Panels 5 to 7 of the τ -P based wavefield separation IPP using the interpolated $Z(FRT)$ tubewave contaminated data.

The F-K plot of the interpolated $Z_{(\text{interp})}(\text{FRT})$ data is shown in Figure 2.35. The interpolation method used on the $Z(\text{FRT})$ data was a two-part operation where the up- and the downgoing waves were separated, interpolated and merged to create the $Z_{(\text{interp})}(\text{FRT})$ data. This procedure is equivalent to imposing cutoff slownesses for both the up- and downgoing wavefields during the forward τ -P transformations. This translates into the two "accept" F-K zones as is shown in Figure 2.35.

2.2.5.6 Future directions for τ -P filtering in wavefield separation

The τ -P filtering and IPP's shown in sections 2.2.5.2 to 2.2.5.5 have attempted to familiarize the reader with the many roles that the τ -P filtering can play within wavefield separation. When interactive τ -P muting has become a common processing tool, then interactive interpretive processing can be routinely performed to assist in the examination and elimination of multiple reflections (Hu and McMechan, 1987). If we are limited to slowness filtering (specifying slowness cutoffs during the forward τ -P transformation), then the method will suffer the same limitations as in pie-slice F-K filtering.

The τ -P data can be transformed into the frequency-P domain. In this domain, the tubewave events can easily be muted using interactive processing (Hu and McMechan, 1987). The mute parameters are then used in the processing runstream and used in a combined τ -P and frequency-P IPP.

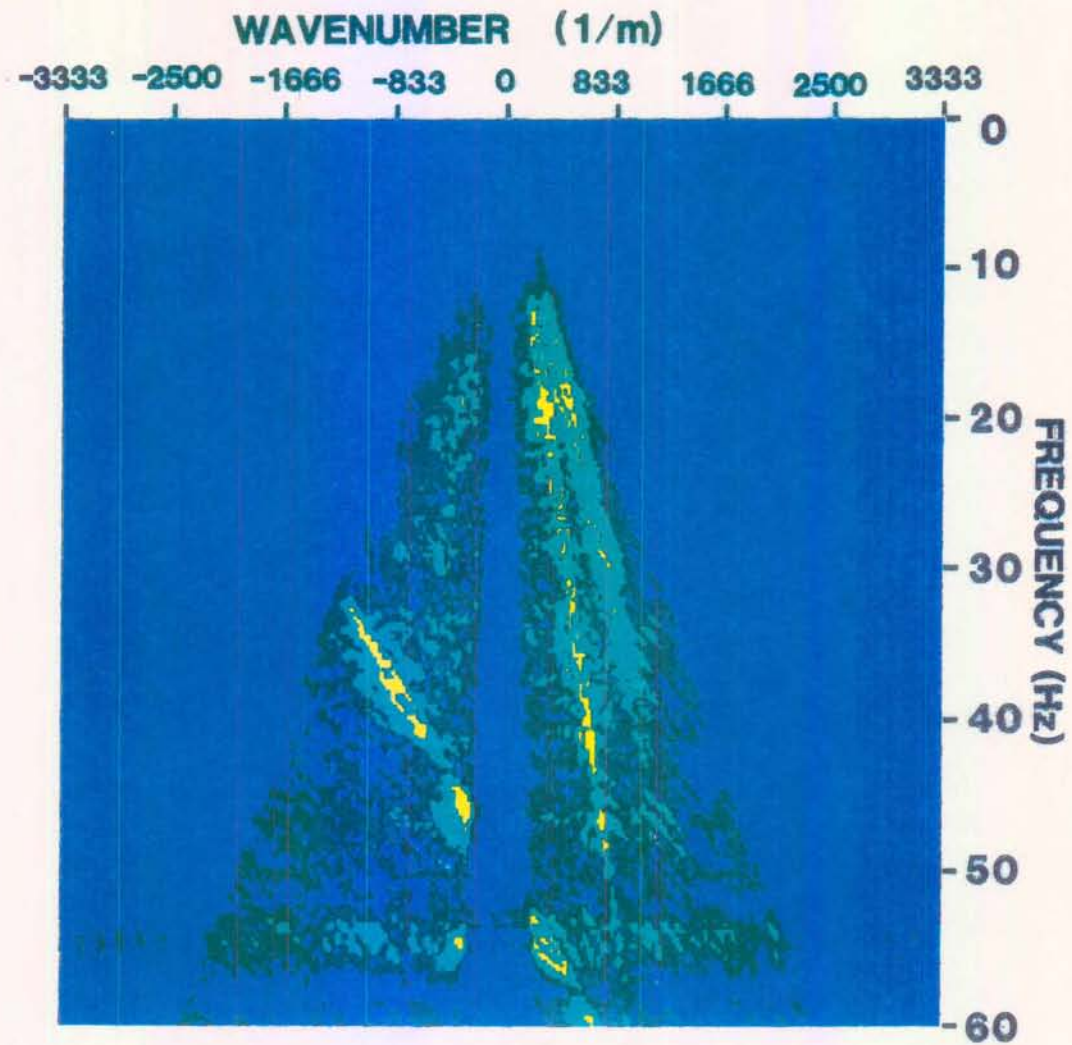


Figure 2.35 F-K plot of the interpolated $Z(\text{FRT})$ data shown in panel 1 of Figure 2.34.

2.2.6 VSP deconvolution and corridor stacks

The procedure of VSP or "up over down" deconvolution (Hubbard, 1979; Gaiser et al., 1984) was introduced in chapter 1. The term "up over down" refers to the computational procedure of the temporal frequency spectrum of $Z_{up}(-TT)$ data being divided by the temporal frequency spectrum of $Z_{down}(-TT)$ data to perform the deconvolution in the Fourier domain. If the spectrum of $Z_{down}(-TT)$ is divided by itself (in the band limited sense), this would result in a zero phase band-limited "multiple free" delta function (Gaiser et al., 1984).

For interpretive processing, the following questions are posed:

- (1) are the multiples attenuated ?
- (2) are the underlying primary events preserved ?
- (3) has the deconvolution processing added unwanted noise ? and
- (4) what are the origins of the multiple events ?

In this section, the following IPP's are developed

- (1) deconvolution IPP: the $Z_{up}(+TT)$ and $Z_{up(decon)}(+TT)$ can be compared directly to evaluate the effect of the deconvolution process on the upgoing events;
- (2) $Z_{up}(+TT)$ data inside and outside corridor stacks: the $Z_{up}(+TT)$, inside and outside corridor stacks and the muted data that go into the stacks can be compared to facilitate multiple identification; and

(3) $Z_{\text{up(decon)}}(+\text{TT})$ data inside and outside corridor stacks: the deconvolved data and the corridor stacks can be used to evaluate the effect of the deconvolution on multiple suppression.

2.2.6.1 Deconvolution IPP

A VSP deconvolution IPP is presented in Figure 2.36 using the Fort St. John Graben case study near offset data (Hinds et al., 1991a; Hinds et al., 1993a and 1994b; Hinds et al., 1994c). Panels 1 and 2 are the $Z_{\text{up}}(+\text{TT})$ and $Z_{\text{up(med)}}(+\text{TT})$ data, respectively. These nondeconvolved data clearly show the multiples (highlighted in yellow on panels 1 and 2) and will be compared to the deconvolved +TT data. The $Z_{\text{down}}(-\text{TT})$ data in panel 3 shows the downgoing event multiple pattern (all of the downgoing events recorded after the arrival of the first break wavelet). To evaluate any increases in the background noise level due to the deconvolution process, the $Z_{\text{up}}(-\text{TT})$ and $Z_{\text{up(decon)}}(-\text{TT})$ data are shown in panels 4 and 5 (Fig. 2.36) can be compared. The $Z_{\text{up(decon)}}(+\text{TT})$ and $Z_{\text{up(decon;med)}}(+\text{TT})$ data are shown in panels 6 and 7.

The first step in the interpretive processing procedure is the detailed interpretation of similar events in panels 2 and 7. A highlighted (in orange) primary event (peak) at 0.595 s (+TT) in panel 2 is severely interfered with by the series of multiple events associated with Spirit River event. The primary event is preserved and continuous across the entire suite of traces in panels 6 and 7.

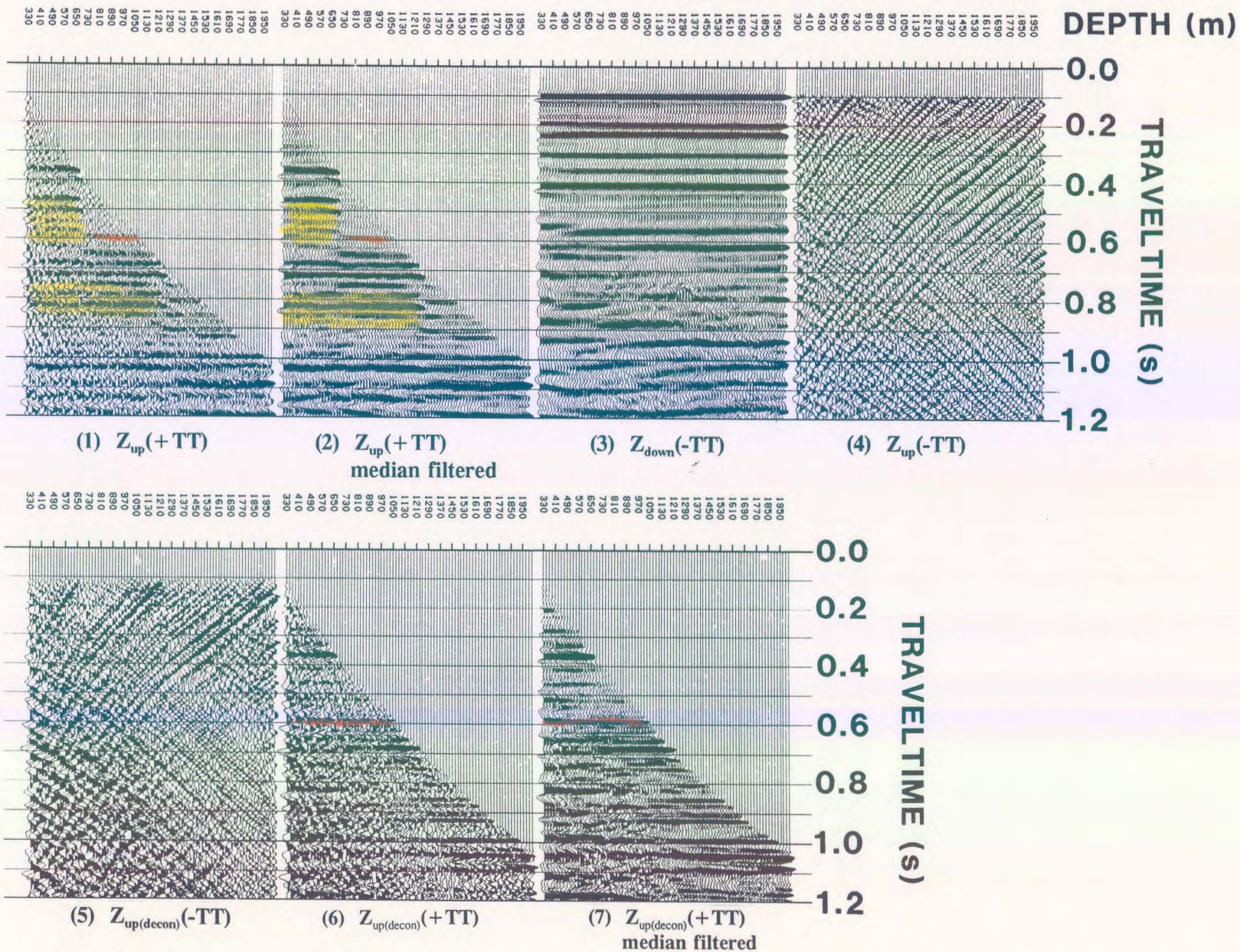


Figure 2.36 Deconvolution IPP for the Fort St. John Graben data (Hinds et al., 1993a). Compare panels 2, $Z_{up}(-TT)$, and 7, $Z_{up(decon)}(-TT)$, to evaluate the attenuation of the multiples seen on panel 2.

2.2.6.2 Corridor stack IPP's

A more detailed investigation into the success of the VSP deconvolution process can be achieved using the corridor stack IPP. The basic premise behind the use of the inside and outside corridor stacks is shown in Figure 2.37 (Hinds et al., 1989a). The time delays between a primary event and associated upgoing multiples are key factors in the interpretation panels designed to facilitate the identification of multiples in the $Z_{up}(+TT)$ data.

Interpreted primary upgoing events intersect the first break curve. Upgoing multiples are recorded later in time at sonde locations above the bottom generating interface due to the added traveltime delay present in the surface generated or interbed multiples. In the $Z_{up}(+TT)$ data (Fig. 2.37), the multiple of a primary reflection is interpreted later in time than the primary event. The upgoing multiple is recorded on the data traces of the shallowest depth down to the depth of the bottom generating interface.

A data corridor of multiple-free upgoing event data will exist immediately in the area of the first break curve of the $Z_{up}(+TT)$ data since the upgoing multiples do not intersect the first break curve. Primary events will dominate a horizontal sum of the "outside corridor" of $Z_{up}(+TT)$ data (Fig. 2.37). If a horizontal sum is performed between the corridor line in the opposite direction from the first break curve ("inside corridor"), both multiples and primary events (if not destructively interfered with by multiples generated at shallower interfaces) will be part of the inside corridor sum (Fig. 2.37).

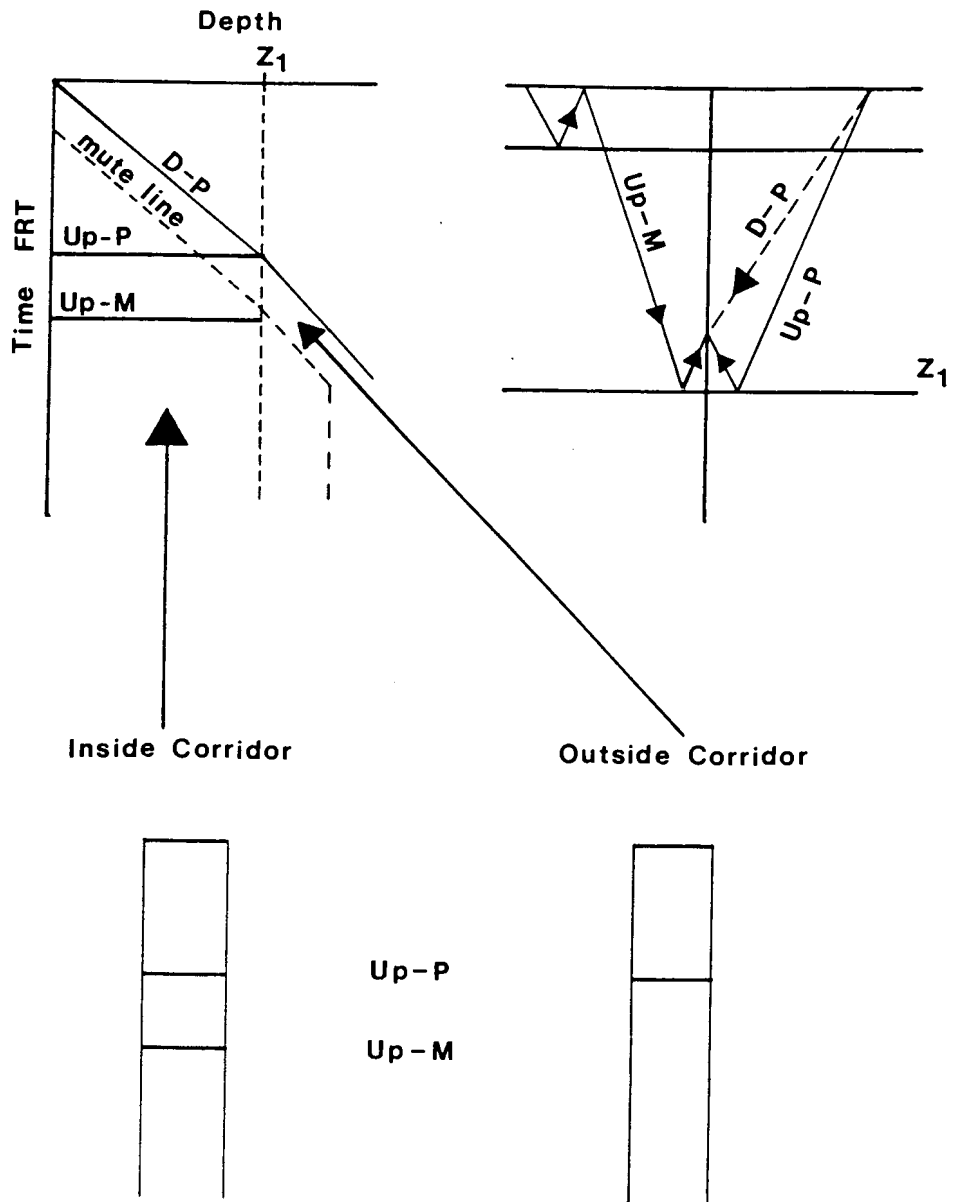


Figure 2.37 The schematic definition of the outside and inside corridor stack. The depth/(+TT) traveltime plot shows the downgoing primary (D-P), upgoing primary (Up-P), and upgoing multiple (Up-M) events with corresponding raypaths shown to the right of the traveltime plot. In the inside corridor, both the primary and multiple upgoing events are retained. For the outside corridor stack, only the primary event (Up-P) is seen after horizontally summing the events in the outside corridor. (after Hinds et al., 1989a).

To locate the interbed multiple generating interfaces, the up- and downgoing multiple pattern will reveal the top and bottom generating interfaces, respectively. The downgoing waves in (-**TT**) time will show the top generating interface and the upgoing waves in (+**TT**) time reveal the bottom generating interface. This is illustrated in Figure 2.38. The simplistic $Z_{\text{down}}(-\mathbf{TT})$ and $Z_{\text{up}}(+\mathbf{TT})$ diagrams in Figure 2.38B and C illustrate the location of the up- and downgoing primary and multiple events. The two data panels can be used to determine the origin of the multiple events.

The corridor stack IPP consists of (Hinds et al., 1989a; Hinds et al., 1994c):

- (1) input $Z_{\text{up}}(+\mathbf{TT})$ data;
- (2) muted $Z_{\text{up}}(+\mathbf{TT})$ before the horizontal summations are performed;
- (3) inside and outside corridor stacks.

2.2.6.3 $Z_{\text{up}}(+\mathbf{TT})$ Corridor stack IPP

The corridor stack IPP for the $Z_{\text{up}}(+\mathbf{TT})$ data is shown in Figure 2.39. Near offset $Z_{\text{up}}(+\mathbf{TT})$ data for the Fort St. John Graben case study (Hinds et al., 1991a; Hinds et al., 1993a; Hinds et al., 1994c) are displayed in panel 1. Two sets of multiple events are highlighted in red. This interpretation is carried over to the muted $Z_{\text{up}}(+\mathbf{TT})$ data in panel 2. This panel contains the data that will go into the inside corridor sum (panel 3).

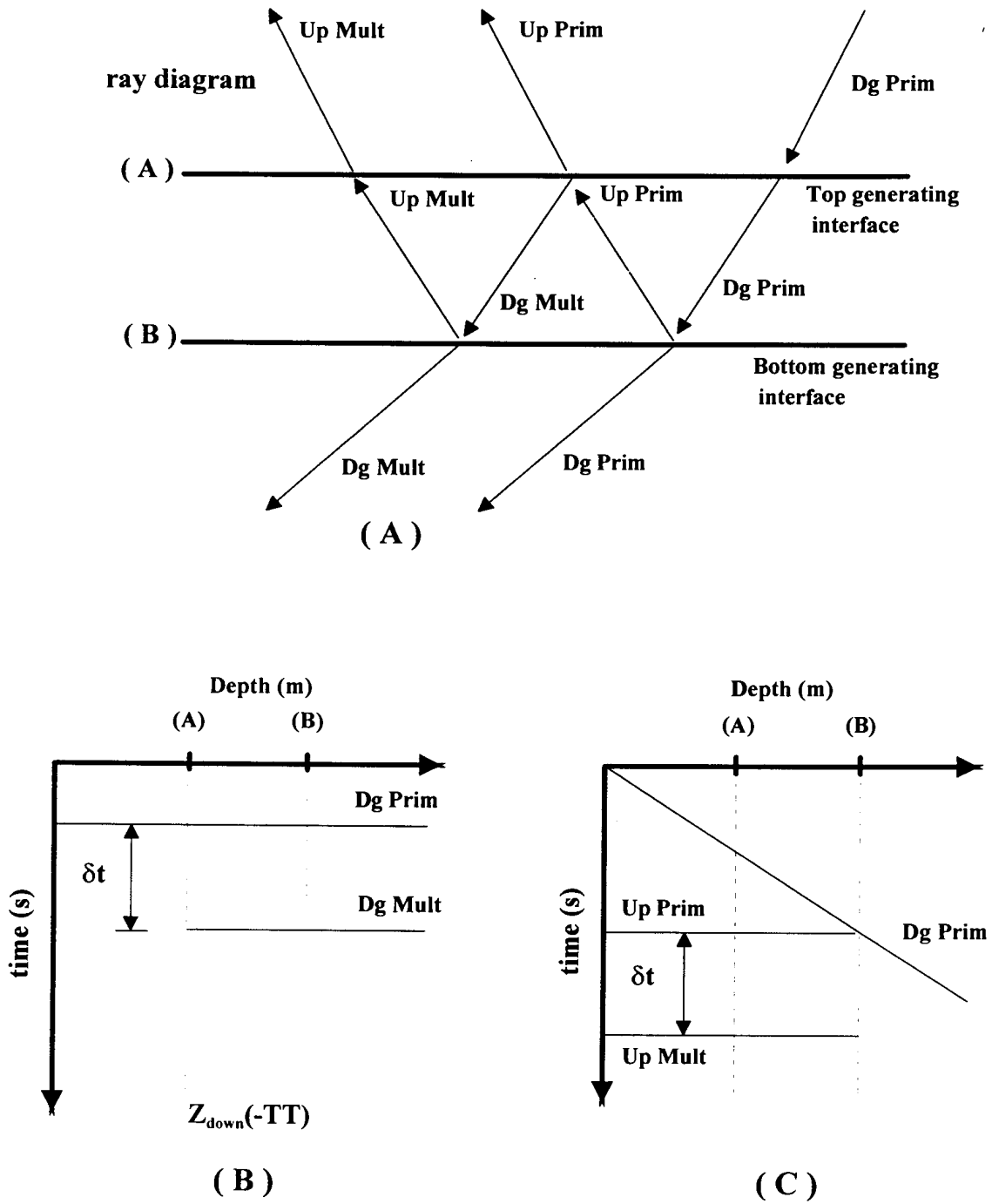


Figure 2.38 Ray and depth/time plots, $Z_{\text{down}}(-TT)$ and $Z_{\text{up}}(+TT)$, showing the top and bottom generating interfaces for interbed multiples (modified from Hinds et al., 1989a).

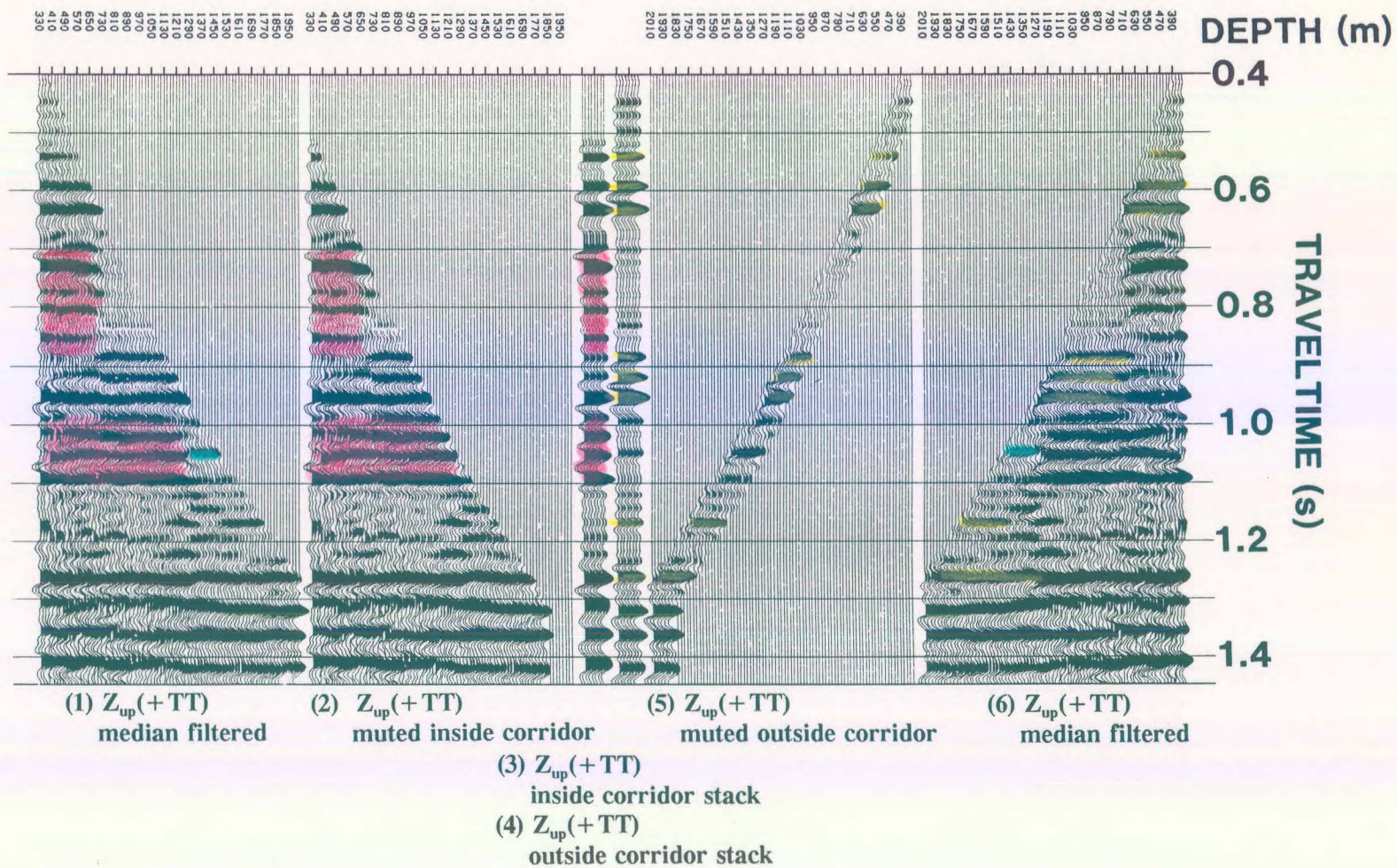


Figure 2.39 Corridor stack IPP of the Fort. St. John Graben $Z_{up}(+TT)$ data (Hinds et al., 1993a). Note the high amplitude multiple events at 0.7-0.8 s and 1.0-1.1 s on the inside corridor stack.

It was stated above that the inside corridor sum will contain multiples and primaries. To see this, the outside corridor sum data in panel 4 are placed next to the inside corridor sum data in panel 3. The multiple events highlighted in red in panel 3 do not appear in the outside corridor stack of panel 4; however, the primary events (shown in yellow) are common to both corridor stack data in panels 3 and 4.

The outside corridor mute data shown in panel 5 contains only primary events (highlighted in yellow at 0.6 s, 0.9-1.0 s, 1.1-1.2 s and at 1.25 s). The events below 1.3 s cannot be interpreted to be either multiple or primaries as there is no longer a first break curve at those recording times. The data in panels 3 and 4 in Figure 2.39 can be used to reliably interpret the multiple and primary event content of the $Z_{up}(+TT)$ data.

2.2.6.4 $Z_{up(decon)}(+TT)$ Corridor stack IPP

The effect of VSP deconvolution processing on $Z_{up}(+TT)$ data can be determined by interpreting a corridor stack IPP that uses the $Z_{up(decon)}(+TT)$ as input. Ideally, the data in both the inside and outside corridor stacks of the $Z_{up(decon)}(+TT)$ data should be multiple free if the deconvolution was successful. These stacks can be compared with the $Z_{up}(+TT)$ outside corridor stacks of Figure 2.39 to interpret the introduction of any deconvolution-generated noise to the data.

In Figure 2.40, the corridor stack IPP for $Z_{up(decon)}(+TT)$ data is presented. The corridor stacks (panels 3 and 4) differ where the deconvolution could not totally attenuate the

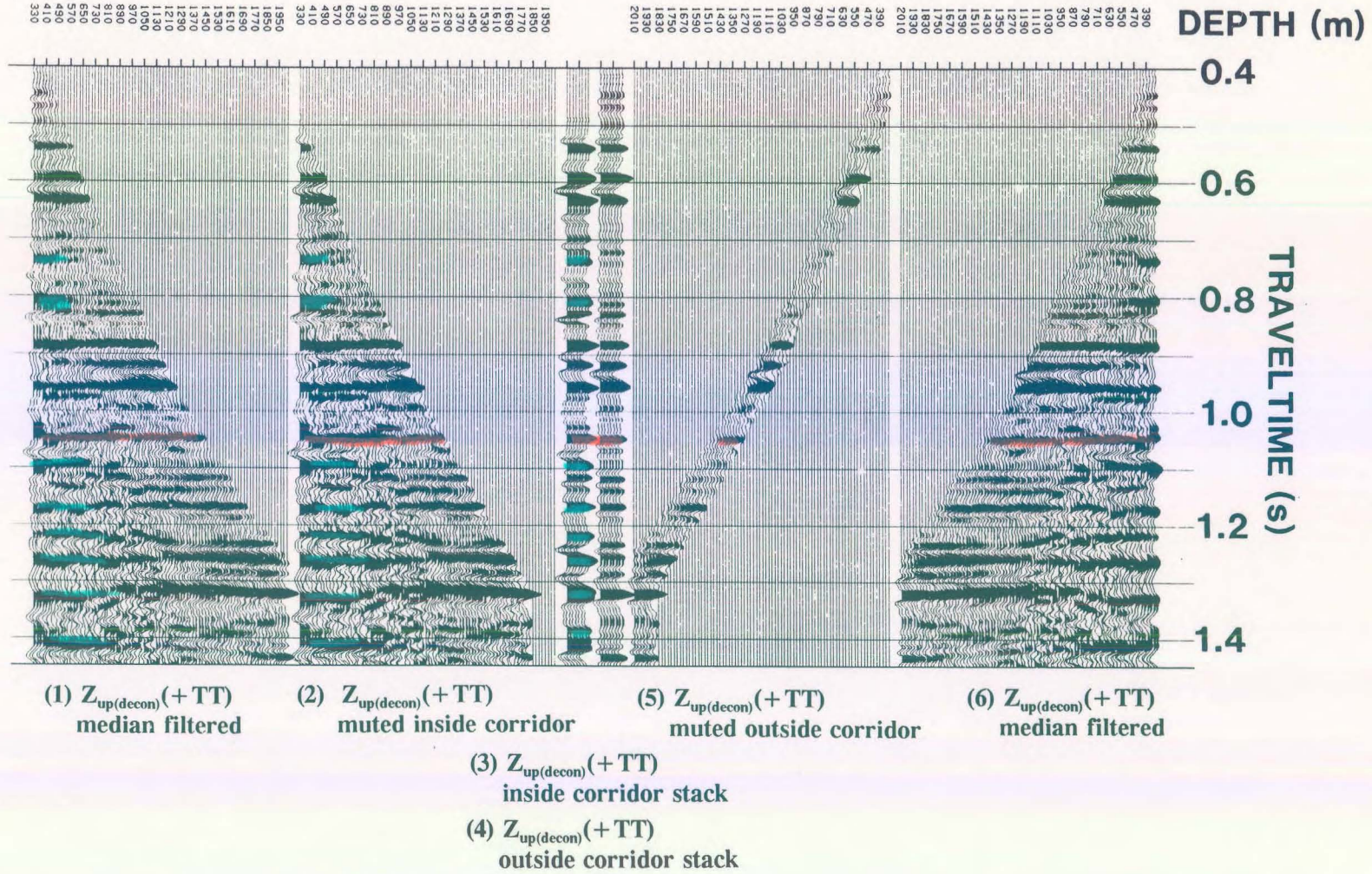


Figure 2.40 Corridor stack IPP of the Fort. St. John Graben $Z_{up(decon)}(+TT)$ data (Hinds et al., 1993a). Residual multiple events are present on the corridor stacks; such as the peak at 0.74 s on panel 3.

multiples on the shallow traces. These remnant multiple events have been highlighted (in blue) on all of the panels of Figure 2.40. A prominent primary highlighted on Figure 2.40 has been enhanced by the deconvolution at 1.05 s. On Figure 2.39, the same highlighted primary event (highlighted in blue) can only be detected at 1.05 s on the 1270 m trace and out to the first break curve. The remainder of the primary event at 1.05 s in Figure 2.39 is destructively interfered with by an upgoing multiple event (coloured red) occurring at the same time.

The outside corridor stack for the $Z_{up}(+TT)$ and $Z_{up(decon)}(+TT)$ data are similar indicating that the deconvolution process did not add appreciable amounts of deconvolution noise within the outside data corridors. The $Z_{up(decon)}(+TT)$ inside corridor stack is different from the outside corridor stack of the same data between 1.2 to 1.3 s. This appears to be caused by a failure of the deconvolution on the shallow traces between those times; however, the interpretation of the near offset data proceeded using the remainder of the deconvolved traces between 1.2 to 1.3 s (traces deeper than 1210 m).

The use of the corridor stack IPP does not end there. In a production processing run, one would take the two IPP paper displays and fold them both in between panels 3 and 4. These are overlain onto the surface seismic section with the same time scale. A comparison between the VSP corridor stacks and surface seismic events can assist in interpreting where the CDP stacking method has not attenuated the multiples. Later in the chapter, the inside and outside corridor stacks will be used as part of the integrated interpretation display (IID) which will bring together a variety of exploration data.

2.3 Far offset data processing IPP's

In this section, the far offset processing will be reviewed and case studies showing the use of interpretive processing within far offset processing will be illustrated. The "normal" far offset processing will consist of

(1) polarization of the $X(\text{FRT})$ and $Y(\text{FRT})$ data into $H\text{MAX}(\text{FRT})$ and $H\text{MIN}(\text{FRT})$ data:

the $H\text{MAX}(\text{FRT})$ data is the projection of the $X(\text{FRT})$ and $Y(\text{FRT})$ data into a plane defined by the well and the source location;

(2) polarization of the $H\text{MAX}(\text{FRT})$ and $Z(\text{FRT})$ data into $H\text{MAX}'(\text{FRT})$ and $Z'(\text{FRT})$

data: the $H\text{MAX}'(\text{FRT})$ data will be polarized in the direction of source and the $Z'(\text{FRT})$ data will be orthogonally polarized to $H\text{MAX}'(\text{FRT})$;

(3) wavefield separation of the $Z'(\text{FRT})$ and $H\text{MAX}'(\text{FRT})$ data into $Z'_{\text{up}}(\text{FRT})$ and

$H\text{MAX}'_{\text{up}}(\text{FRT})$ data;

(4) wavefield separation of the $H\text{MAX}'(\text{FRT})$ data into $H\text{MAX}'_{\text{down}}(\text{FRT})$ data: this will be

used to deconvolve the final output, $Z''_{\text{up}}(\text{FRT})$ into $Z''_{\text{up}(\text{decon})}(\text{FRT})$;

(5) derotation (Hinds et al., 1989a) of the $Z'_{\text{up}}(\text{FRT})$ and $H\text{MAX}'(\text{FRT})$ data into

$Z_{\text{up}(\text{derot})}(\text{FRT})$ and $H\text{MAX}_{\text{up}(\text{derot})}(\text{FRT})$ data;

(6) time-variant polarization of the $Z_{\text{up}(\text{derot})}(\text{FRT})$ and $H\text{MAX}_{\text{up}(\text{derot})}(\text{FRT})$ data into

$Z''_{up}(\text{FRT})$ and $\text{HMAX}''_{up}(\text{FRT})$ data;

(7) VSP-CDP or migration of the $Z''_{up}(+TT)$ data into the $+TT$ versus offset from the well domain.

In the interpretation of the far offset IPP's, a number of crucial observations are being made.

Some of the questions are:

- (1) do the X , Y , and Z data obey the assumptions behind the time invariant polarizations reviewed in chapter 1 (section 1.4.3) ?
- (2) what are the origins of noise seen on the data ?
- (3) how is the noise being propagated onto the output data panels following each processing stage ?
- (4) what is the multiple event content in the VSP-CDP or migrated data ?
- (5) do the multiples in the VSP-CDP or migrated data interfere with the interpretation of primary events ?
- (6) Can the primary and multiple events be differentiated since reflectors imaged away from the well may not intersect the first break curve ?

These questions will be posed again and again during the interpretive processing of the far offset IPP's. The partitioning of the energy of the various wavefields onto the polarization axis and time-variant "axis" will be illustrated using the far offset data contained in Chapter 4 (Ricinus carbonate reef case study; Hinds et al., 1989a; Hinds et al., 1993c; Hinds et al.,

1994c), Chapter 5 (Fort St. John Graben case study; Hinds et al., 1991a; Hinds et al., 1993a and 1994b; Hinds et al. 1994b) and Chapter 6 (Simonette carbonate reef case study; Hinds et al., 1991b; Hinds et al., 1993b and 1994c). The success and failures of far offset deconvolutions will be illustrated using Chapter 4 and 6 data.

A review of the Ricinus carbonate reef case study polarization IPP's will show:

- (1) the results after using "normal" processing runstreams (see section 2.1);
- (2) an analysis of the noise on the polarized results; and
- (3) the modification of the processing runstream to enhance the interpretation of the $Z''_{up}(+TT)$ data.

2.3.1 Time invariant polarization: isolation of the downgoing P-wave

In this section, the $Z(FRT)$, $X(FRT)$ and $Y(FRT)$ data are polarized to isolate the downgoing P-wave events onto a single data panel, $HMAX'(FRT)$. The orthogonal data projection, $Z'(FRT)$, was considered in the past to contain predominantly upgoing P-wave events. Interpretation would be performed on the wavefield separated $Z'_{up}(+TT)$ data and on the VSP-CDP transformed upgoing events. In the next section, time variant polarization will be used to isolate the upgoing P-wave events onto a single output panel, $Z''_{up}(+TT)$.

The polarization analysis presented in this section use hodogram derived rotation angles derived in a time invariant sense. The hodogram analysis is performed on a single window of data around the first breaks of the two input VSP data to yield a single polarization angle.

In the next section, the polarization angle for a pair of input traces is allowed to vary in time along the traces.

In Figure 2.41, the time invariant polarization IPP for the far offset data (700 m offset source location; source location in a direction of 307° from the well) of the Fort St. John Graben case study (Chapter 5) is shown. For reference within this chapter and chapter 5, the dataset will be referred to as the FSJG1 data.

The **X(FRT)**, **Y(FRT)**, and **Z(FRT)** data are shown in panels 1, 2, and 3, respectively. The downgoing P-wave events in the **Z(FRT)** data of panel 3 are highlighted in yellow. In comparison to the panels 1 and 2, the **Z(FRT)** data contain the majority of the downgoing P-wave events.

Primary downgoing P-wave energy is divided in varying amounts on the **X(FRT)** and **Y(FRT)** data shown in panels 1 and 2 (highlighted in yellow) indicating that the geophone sonde was rotating within the borehole during the acquisition of the data. However, the first break wavelet on the two panels show the most consistency for the bottom two-thirds of the borehole indicating that the sonde was rotating slowly during the acquisition at those depths.

The **Z(FRT)** data shown in panel 3 contains a diffraction event (highlighted in purple) in the lower left hand corner of the panel. This diffraction will be unfortunately partitioned onto all of the output data panels (see highlighted purple events in panels 5-7) as a result of further processing. Since these diffraction events are not polarizable in the same way that the up-

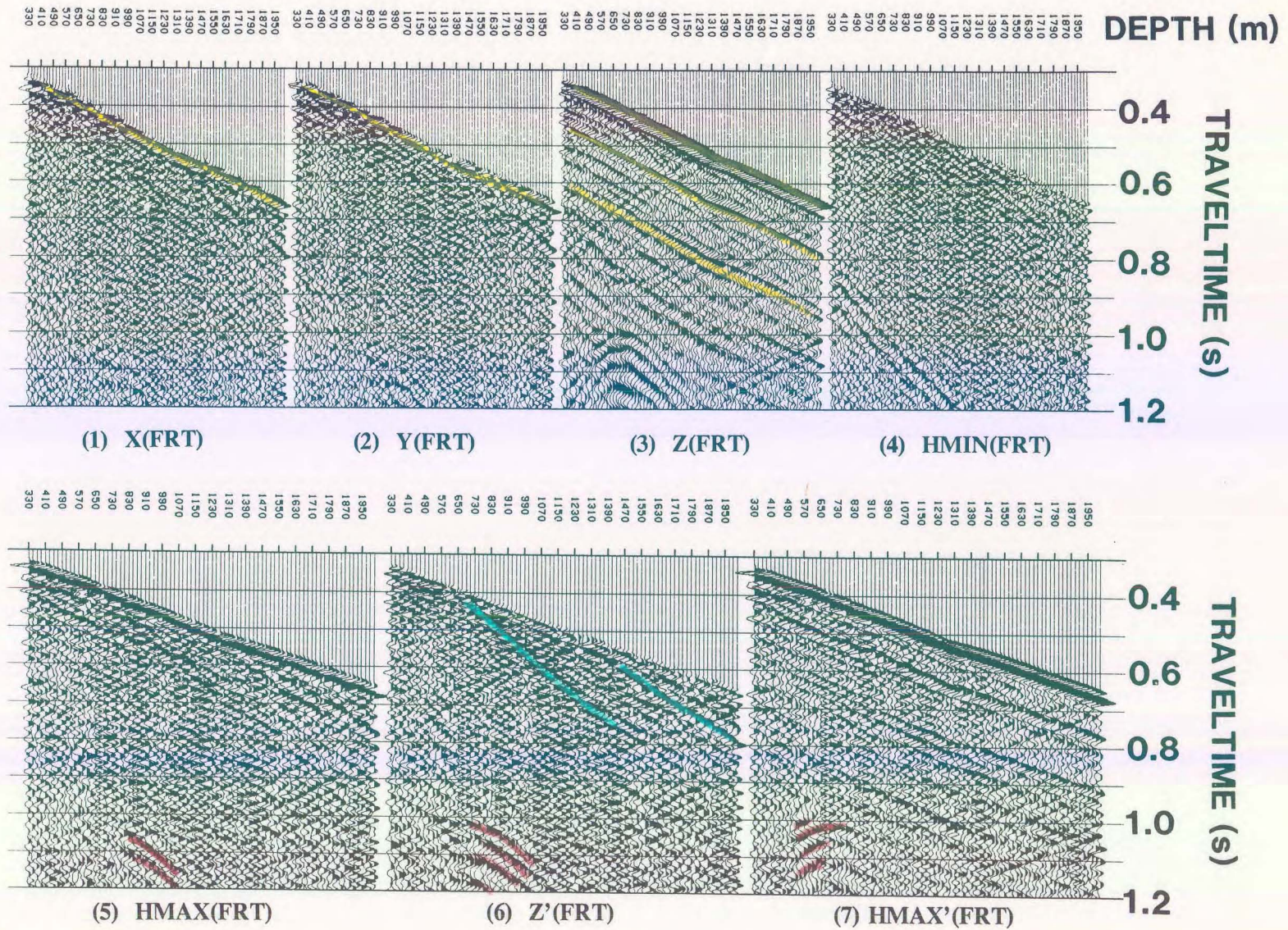


Figure 2.41 Hodogram-based polarization IPP for the Fort St. John Graben (FSJG1) far offset data (Hinds et al., 1993a). The downgoing P-wave events have been isolated on the **HMAX'(FRT)** data in panel (7).

and downgoing P-wave events are, interpretation will be performed "over" these "noise" events.

The result of hodogram based polarization analysis on the **X(FRT)** and **Y(FRT)** data and subsequent "single angle" rotation yields the **HMIN(FRT)** and **HMAX(FRT)** data shown in panels 4 and 5, respectively. The minor amount of downgoing P-wave events evident in the **X(FRT)** and **Y(FRT)** data shown in panels 1 and 2 have been isolated within the **HMAX(FRT)** data of panel 5.

The rotation of the **X(FRT)** and **Y(FRT)** data was performed using an interactive hodogram analysis program. A window of input data, from the **X(FRT)** and **Y(FRT)** data, centred around the first break of two input traces at the same depth recording level are shown in one portion of the screen. The trace data are colour coded so that hodogram points shown in another portion of the screen can be correlated to the traveltime of the trace data. This enables an interpretation of the hodogram plot. A least squares routine estimates the best straight line through the cloud of hodogram points. The **HMAX(FRT)** and **HMIN(FRT)** windowed results using the rotation angle determined by the least-squares fit is displayed onto another portion of the monitor. The user can now interactively alter the angle of the straight line through the hodogram cloud of points and the displayed window of **HMAX(FRT)** and **HMIN(FRT)** output traces (also centred around the first break) immediately change according to the updated rotation angle. The calculations which produce the **HMIN(FRT)** and **HMAX(FRT)** traces use the rotation matrix shown in the Appendix.

During the determination of the rotation angle using the hodogram plot and the various

screen displays, the aim is to:

- (1) to maximize the amount of downgoing P-wave first break energy on the **HMAX** trace;
and
- (2) produce a consistent output polarity.

The polarity of the **HMAX(FRT)** data in panel 5 is consistent and minimal downgoing P-wave energy can be seen on the **HMIN(FRT)** data in panel 4. Mode-converted downgoing SV events are highlighted (in blue) on the **HMAX(FRT)** in panel 5.

The **Z'(FRT)** and **HMAX'(FRT)** data calculated using a hodogram analysis and subsequent rotation of the **HMAX(FRT)** and **Z(FRT)** data are shown in panels 6 and 7, respectively. The downgoing P-wave data are isolated onto the **HMAX'(FRT)** panel and the **Z'(FRT)** data contains mode-converted SV energy (highlighted in blue). Mode-converted SV downgoing events on the **Z'(FRT)** data appear to originate at the impedance boundaries at 690 m (Spirit River Formation; see Chapter 5) and the 1260 m (Nordegg Formation; see Chapter 5). Upgoing P events can be identified on panel 6 from the Nordegg reflector (highlighted in orange).

The diffraction event seen clearly on the **Z(FRT)** data has now been partitioned onto both the **HMAX'(FRT)** and **Z'(FRT)** data. Interestingly enough, the **HMAX'(FRT)** data contain the "upgoing" part of the diffraction and the **Z'(FRT)** data contain the "downgoing" part of the event.

2.3.2 Time variant polarization: isolation of the upgoing P-wave events

In this section, time variant polarization will be applied to the upgoing events from the $\mathbf{HMAX}'_{up}(\mathbf{FRT})$ and $\mathbf{Z}'_{up}(\mathbf{FRT})$ data to yield the $\mathbf{Z}''_{up}(\mathbf{FRT})$ data. The final interpretations are done on the $\mathbf{Z}''_{up}(+TT)$ and the VSP-CDP transformed and/or migrated $\mathbf{Z}''_{up}(+TT)$ data.

The time invariant polarizations performed in the previous section assumed that a single angle was adequate to polarize the up- and downgoing $\mathbf{Z}(\mathbf{FRT})$ and $\mathbf{HMAX}(\mathbf{FRT})$ event onto separate panels, $\mathbf{Z}'(\mathbf{FRT})$ and $\mathbf{HMAX}'(\mathbf{FRT})$. The polarization angle needed to isolate (polarize) the upgoing P-wave onto the $\mathbf{Z}''_{up}(\mathbf{FRT})$ data is time variant. The angle of reflection from interfaces below the sonde change with depth as is shown in Figure 2.42. This implies that the incident angle of the upgoing P-wave events at a single geophone location changes accordingly with recording time.

The $\mathbf{Z}'_{up}(\mathbf{FRT})$ and $\mathbf{HMAX}'_{up}(\mathbf{FRT})$ data are a result of performing wavefield separation on the $\mathbf{Z}'(\mathbf{FRT})$ and $\mathbf{HMAX}'(\mathbf{FRT})$ data, respectively. The IPP for the time variant polarization of the FSJG1 far offset data is shown in Figure 2.43. The $\mathbf{Z}'_{up}(\mathbf{FRT})$ and $\mathbf{HMAX}'_{up}(\mathbf{FRT})$ data shown in panels 1 and 2, respectively, contain:

- (1) upgoing P events (highlighted in orange);
- (2) possible diffraction appear between 0.4 - 0.6 s (highlighted in brown); and
- (3) mode converted downgoing shear wave events (highlighted in blue).

The $\mathbf{Z}_{up(derot)}(\mathbf{FRT})$ and $\mathbf{HMAX}_{up(derot)}(\mathbf{FRT})$ data shown in panels 3 and 4 are formed from $\mathbf{Z}'_{up}(\mathbf{FRT})$ and $\mathbf{HMAX}'_{up}(\mathbf{FRT})$ data by applying a rotation operation opposite to that used

Time variant polarization concept

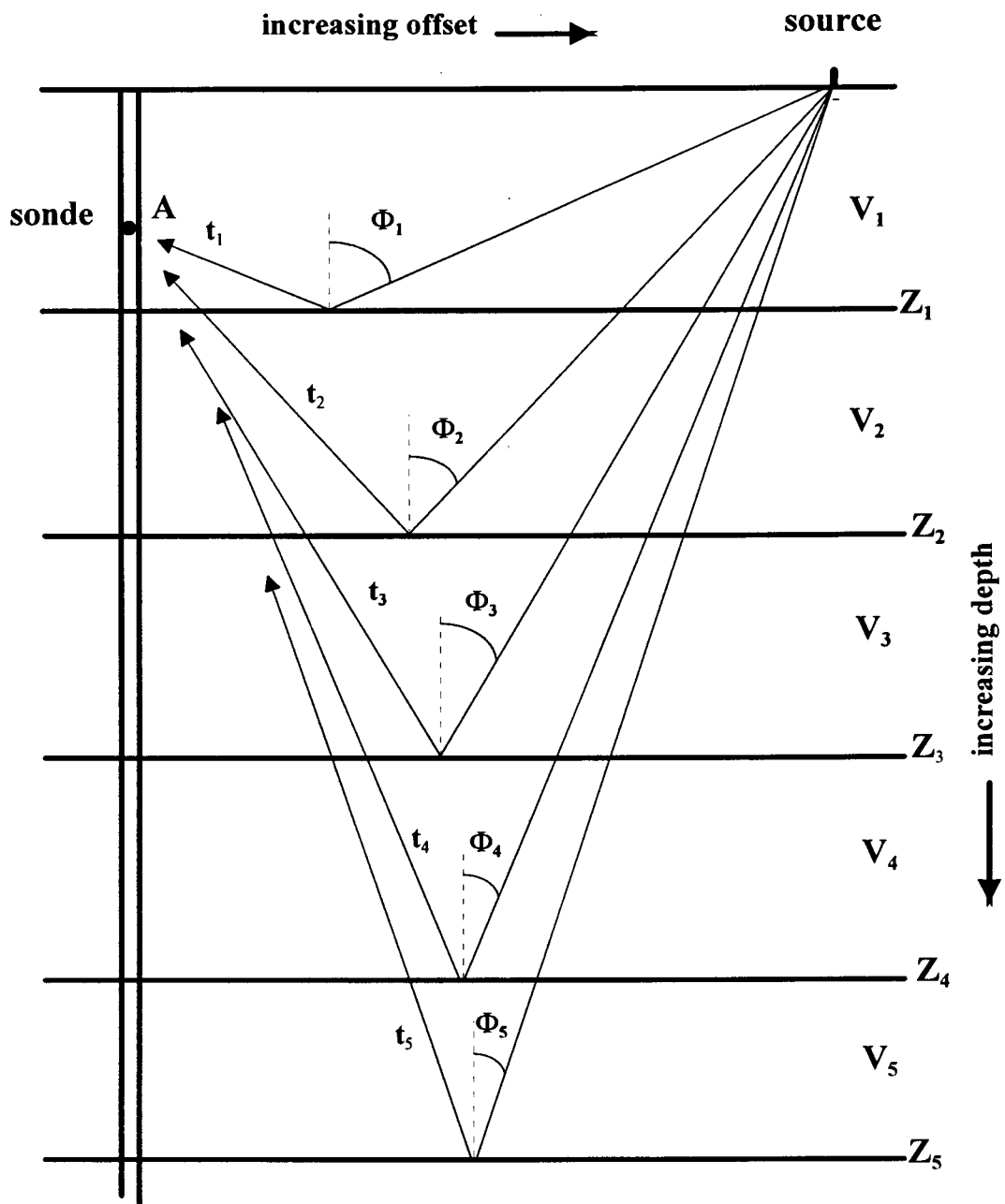


Figure 2.42 The reflection angle for upgoing raypaths emerging at the geophone at A from deeper interfaces decreases in comparison to the reflections from shallower interfaces. The Φ_i are the reflection angles, V_i are the layer velocities, Z_i are the layer depths and t_i are the raypath traveltimes to the sonde at A.

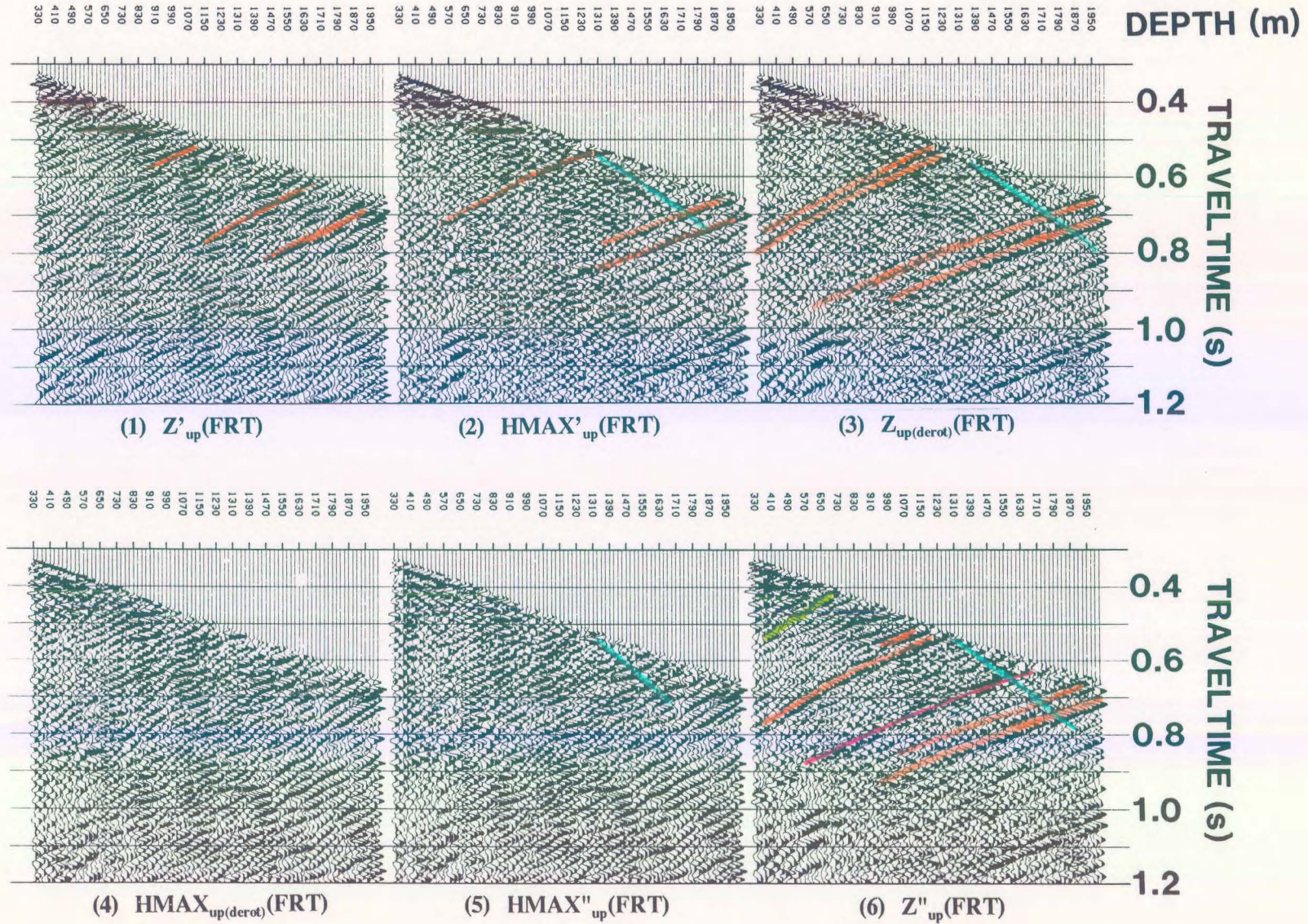


Figure 2.43 Time-variant polarization IPP for the Fort St. John Graben (FSJG1) far offset data (Hinds et al., 1993a). The upgoing P-wave events have been predominately partitioned onto the $Z''_{up}(FRT)$ panel.

in calculating the $Z'(FRT)$ and $HMAX'(FRT)$ data. By inspection of panels 3 and 4, it appears as if this simple derotation is already isolating the upgoing P-wave events (highlighted in orange in panel 3).

The interval velocities and first break times from the near offset VSP data of the Fort St. John Graben case study are used to construct a model for ray-tracing. The first breaks (when the downgoing P-wave should reach an interface) and the velocity of the various interfaces (which will be used to propagate the upgoing reflections) are derived through simple calculations. The ray-tracing to the defined geophone locations (given the source offsets) will result in the (time,angle) pairs to be used in time-variant polarization (see Appendix). The result of the time-variant polarization is $HMAX''_{up}(FRT)$ and $Z''_{up}(FRT)$ shown in panels 5 and 6 (Fig. 2.43), respectively.

By inspection of panels 3 and 6 ($Z_{up(derot)}$ and Z''_{up}), the downgoing (residual) SV events seen on panel 3 are now mapped jointly onto panel 5 and 6 (coloured in blue). The upgoing P event (coloured pink) originating near the 1750 m depth is more interpretable on the $Z''_{up}(FRT)$ data in panel 6. The shallow Spirit River event (coloured green on panel 6) at 690 m which was not resolved on panels 1 to 4 can now be interpreted. Other upgoing events on the $Z''_{up}(FRT)$ data have been coloured orange in panel 6.

2.3.3 VSP-CDP Transformation and Migration

In this section, the $Z''_{up}(FRT)$ data are VSP-CDP transformed or migrated and the IPP designed to utilize interpretive processing is presented. The term VSP-CDP or "VSP-CDP mapping" refers to mapping the VSP data into a pseudoseismic section that displays coverage starting from the borehole out to the furthest reflection defined by the VSP data geometry and input velocity model (Wyatt and Wyatt, 1981; Millahn et al., 1983). The product of the VSP-CDP mapping has been called the VSPCDP (Hardage, 1985). The VSP-CDP and migration far-offset IPP for the FSJG1 data (chapter 5) is shown in Figure 2.44.

The $Z''_{up}(+TT)$ and $Z''_{up(med)}(+TT)$ data are shown in panels 1 and 2, respectively. The VSP-CDP (Dillon and Thomson, 1984) mapped $Z''_{up}(+TT)$ data are shown in panel 3. Note that the horizontal axis for panel 3 (and 4) is not depth but offset distance from the well. The image of the reflectors on the VSP-CDP or migrated data is similar to how the reflectors would appear on a seismic section.

The IPP is completed with a Kirchhoff migrated version of the $Z''_{up}(+TT)$ data shown in panel 4. The migrated data appear to be "smoother" than the VSP-CDP mapped data of panel 3. The events between 1.2 and 1.35 s display faulting. An example of the faulting is highlighted by the event in green and interpreted faults (in pink) on panels 3 and 4.

One of the most important interpreted events is a dominant peak (in blue) at 1.27 s which exists laterally from the well out to a distance of 55 to 75 m away from the well. The amplitude of the event attenuates rapidly at offsets beyond that point and may represent a

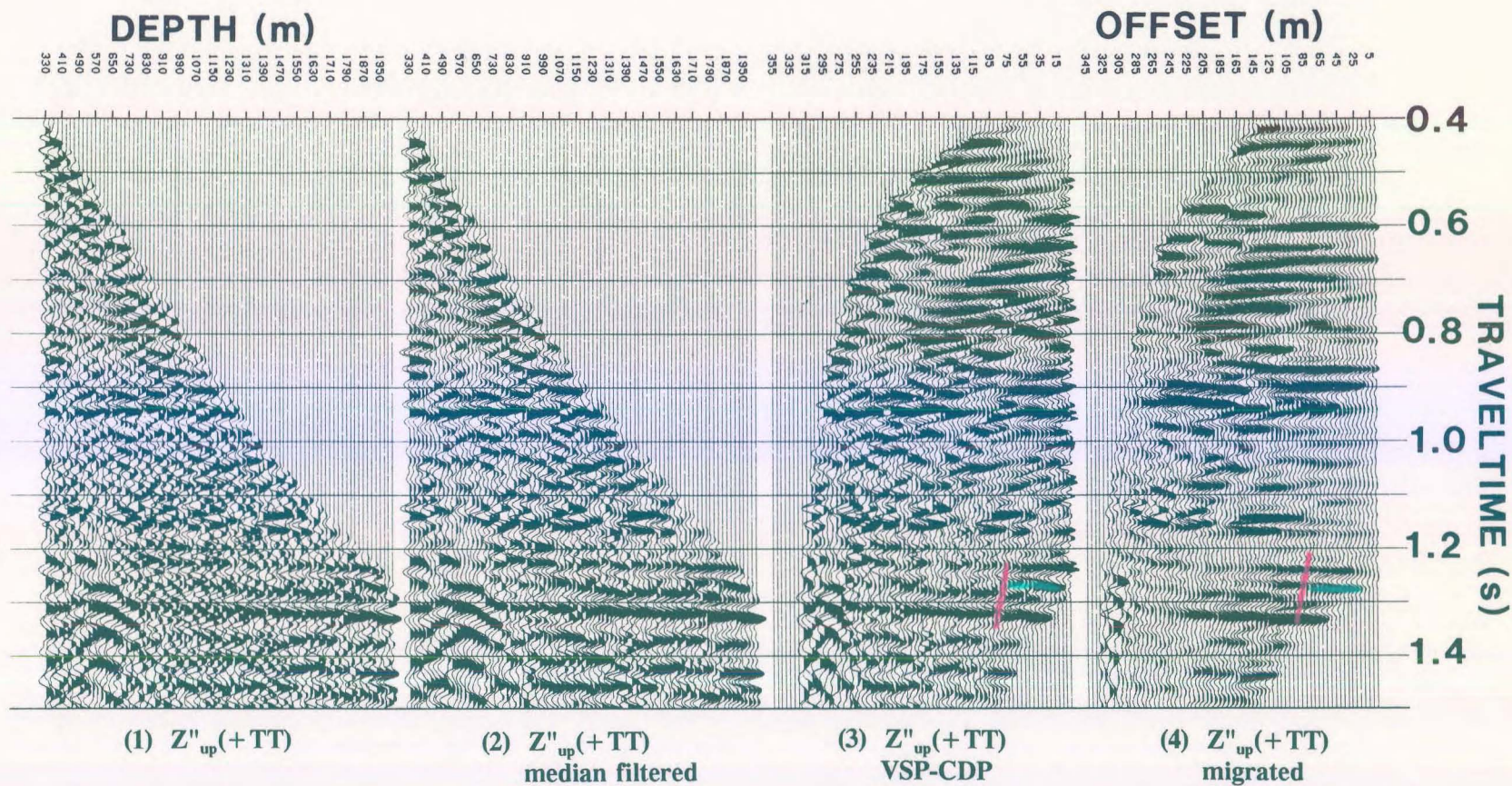


Figure 2.44 VSP-CDP and Kirchhoff migration IPP for the Fort St. John Graben (FSJG1) far offset data (Hinds et al., 1993a). Note the termination of the event (peak) on the VSP-CDP at 1.27 s (panels 3 and 4). The event exists only on offset traces 0-55 m.

possible facies change in the basal Kiskatinaw (chapter 5 and in Hinds et al., 1991a; Hinds et al., 1993a and 1994b; Hinds et al., 1994c). This observation is an important consideration for exploration. Beyond the interpreted fault (in pink) at a distance of 95 to 115 m offset from the well, the event appears to terminate.

The other far offset data for the Fort St. John Graben case study (source location offset of 741 m; location of offset source is East of the well) will be referred to as the FSJG2 data. Figures 2.45, 2.46, and 2.47 display the far-offset IPP's for the FSJG2 data.

By following the rotation processes on these figures, it can be interpreted that the event at 1.25 - 1.27 s on the VSPCDP and migrated $Z''_{up}(+TT)$ data (coloured blue) in panels 3 and 4 of Figure 2.47 does not terminate near the well. The event is laterally more continuous than the same event on the FSJG1 data seen in panels 3 and 4 of Figure 2.44. Faulting (shown in pink) is also evident on the VSPCDP and migrated data in Figure 2.47 between 1.1 and 1.35 s.

2.3.4 Far offset deconvolution

In this section, the deconvolution of the far offset VSP data is reviewed and far offset deconvolution IPP's are presented. The process of far offset deconvolution is the spectral division of the $Z''_{up}(FRT)$ data by the $HMAX'_{down}(FRT)$ data to output the $Z''_{up(decon)}(FRT)$ data.

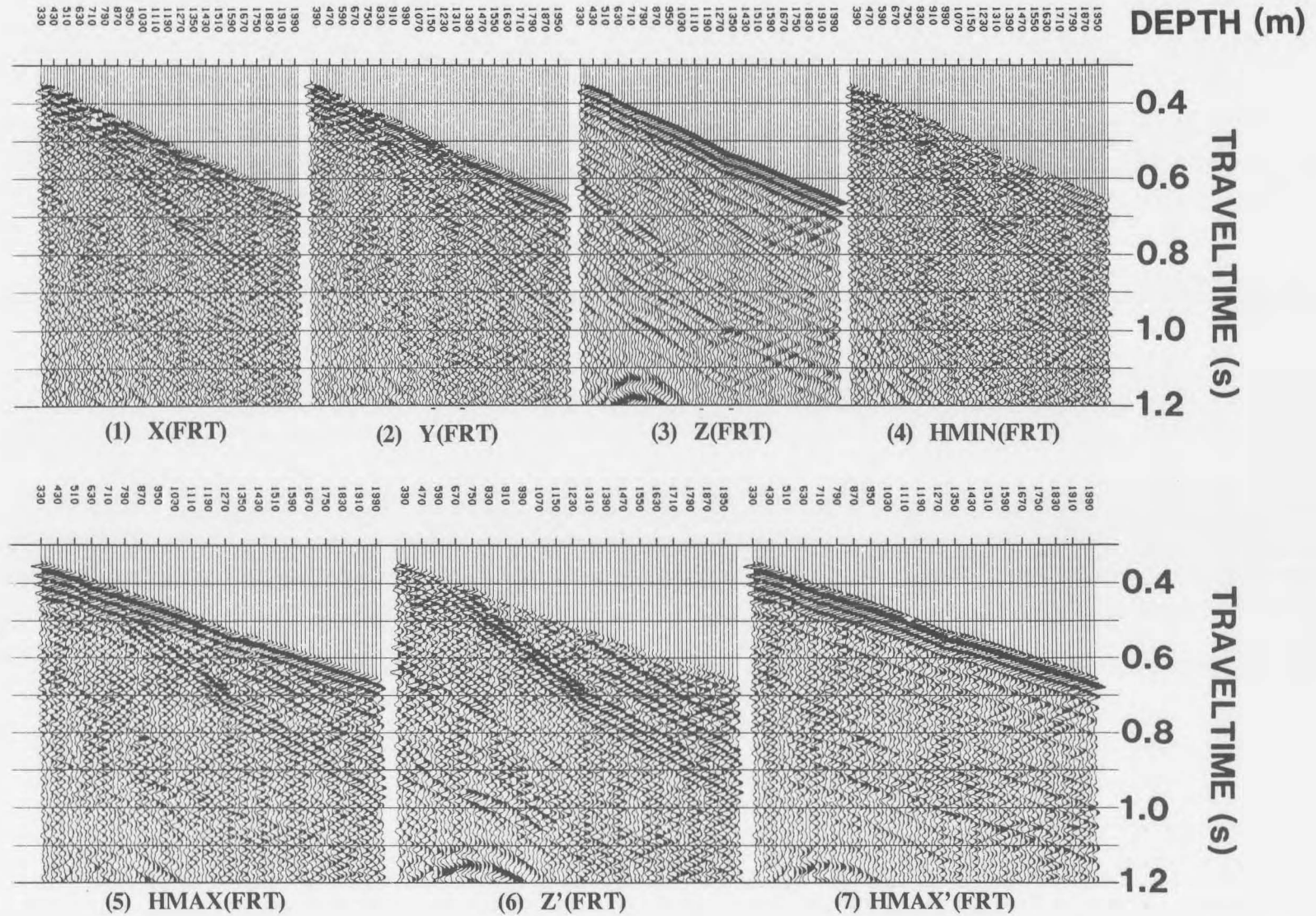


Figure 2.45 Hodogram-based polarization IPP for the Fort St. John Graben (FSJG2) far offset data (Hinds et al., 1993a). The downgoing P-wave events have been isolated on the **HMAX'(FRT)** data in panel (7).

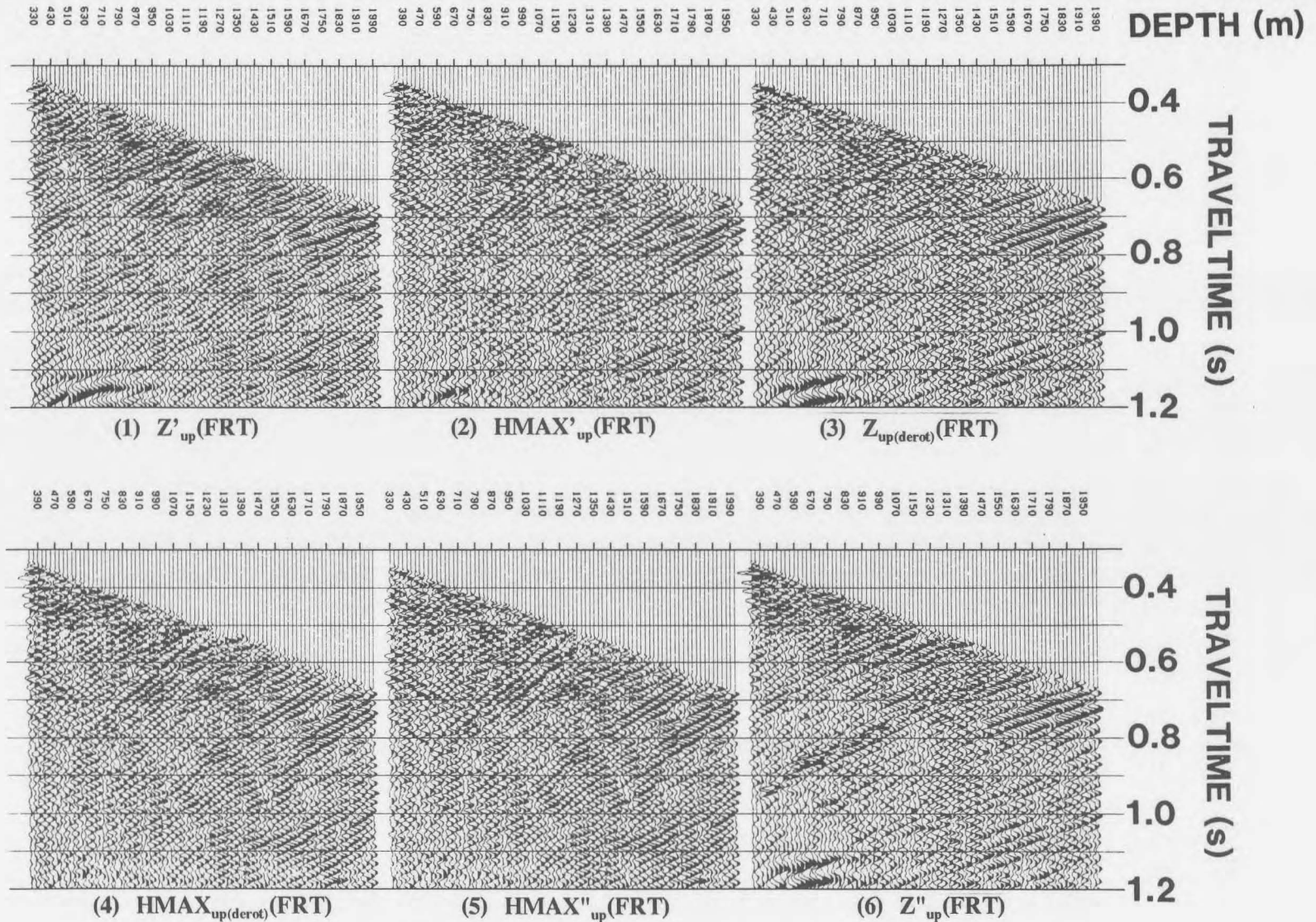


Figure 2.46 Time-variant polarization IPP for the Fort St. John Graben (FSJG2) far offset data (Hinds et al., 1993a). The upgoing P-wave events have been predominately partitioned onto the $Z''_{up}(FRT)$ panel.

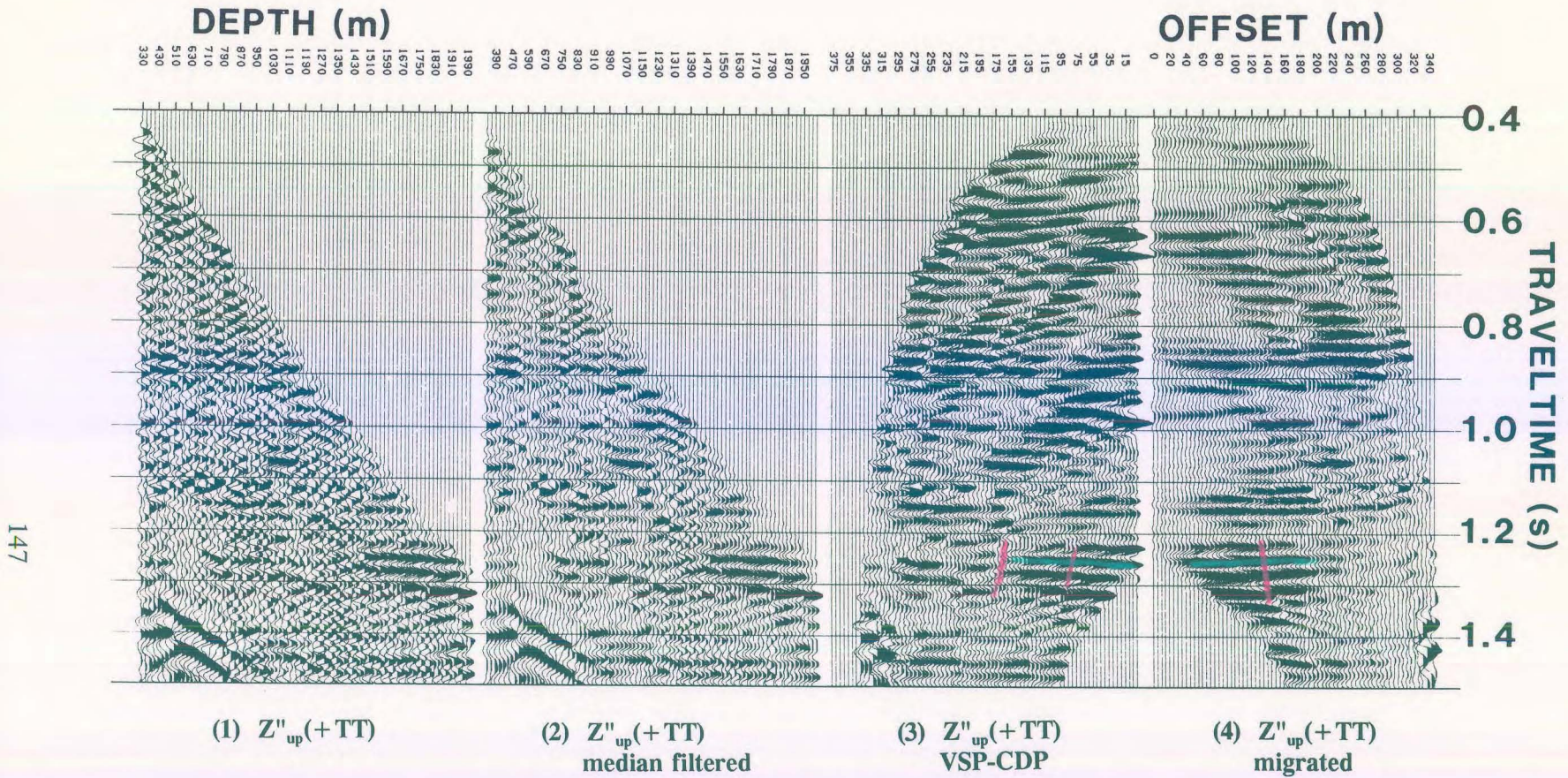


Figure 2.47 VSP-CDP and Kirchhoff migration IPP for the Fort St. John Graben FSJG2 far offset data (Hinds et al., 1993a). Note the continuity of the event (peak) on the VSP-CDP display at 1.27 s (from offset traces 0-55 m).

The VSP (far offset) deconvolution has not received attention in the literature because the decision to deconvolve the far offset is usually made after interpretation. Whereas, deconvolution of near offset VSP data would be done as a matter of course, the far offset deconvolution decision-making would follow the course of:

- (1) searching for possible interfering multiples on the far offset $Z''_{up}(+TT)$;
- (2) confirming that the event is not a terminating reflector located away from the borehole;
- (3) utilization of the $Z'_{down}(-TT)$ data to deconvolve the $Z''_{up}(+TT)$; and
- (4) reconfirming the interpretation by comparing the data before and after deconvolution.

This illustrates the arduous task presented to the "interpreter/processor".

The VSP-CDP/migration IPP for the far offset data of the Simonette carbonate reef case study (Chapter 6; Hinds et al., 1991b; Hinds et al., 1993b and 1994c) is presented in Figure 2.48. The data contain destructively interfering multiples (coloured green). On panel 2, the off-reef carbonate (coloured "reef" purple; see chapter 6 or Hinds et al., 1993b and 1994c) starts at 1.96 s on the deepest trace and climbs onto the low-relief reef mid-way across the display rising up onto the peak event at 1.92 s (the transition being between depth levels 2470 - 2570 m).

There is an anomalous event (peak) at 1.8 s that does not seem to correspond to the geology interpreted from the sonic log. The Wabamun Formation (highlighted in red; see Chapter 6) event intersects the first break curve at 3020 m as a peak at 1.735 s in the $Z''_{up}(+TT)$ data. Note that the anomalous event (the peak colored green for reference) between 1.77 - 1.81 s lies immediately under the Wabamun event and does not intersect the first break

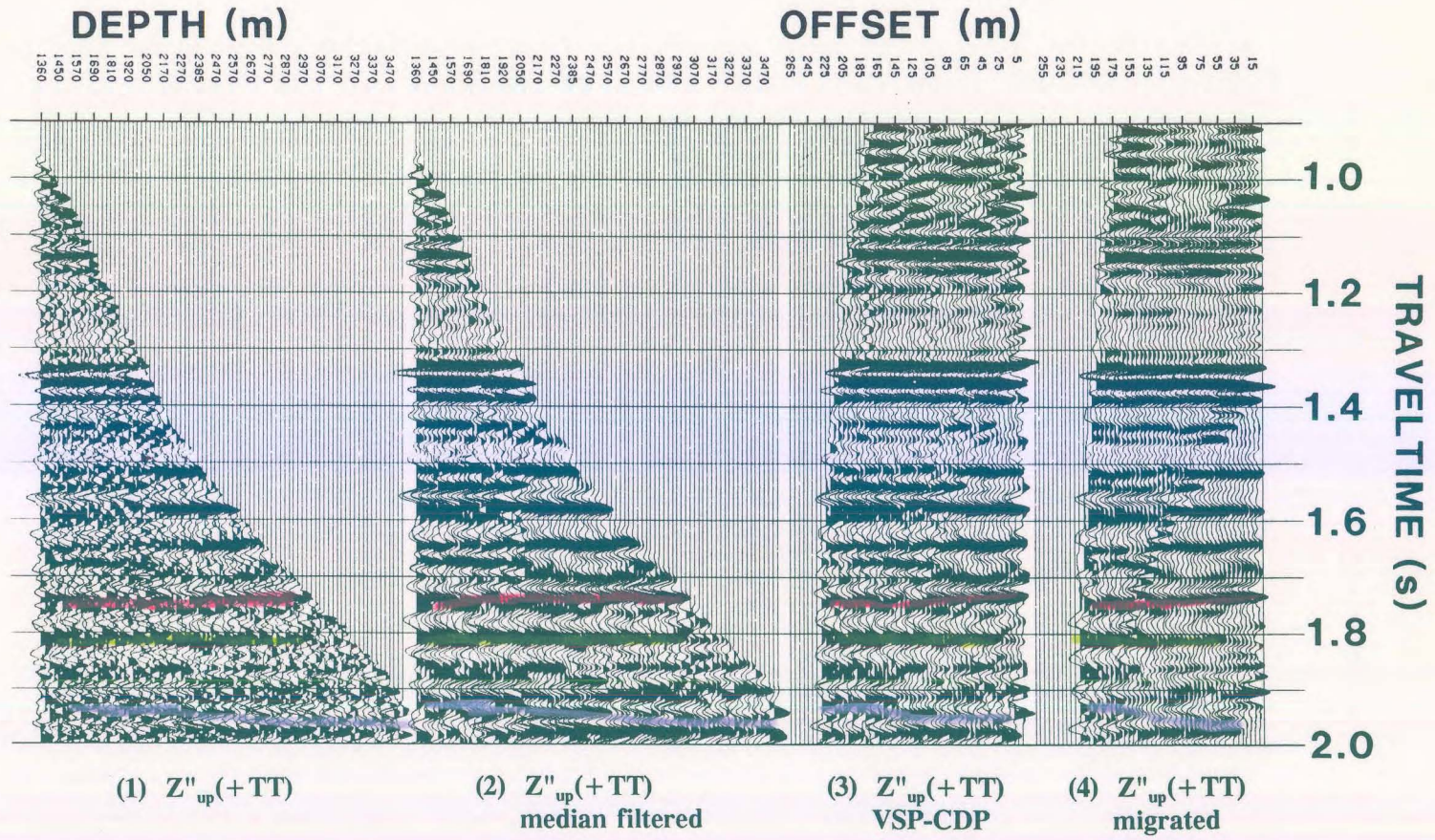


Figure 2.48 VSP-CDP and migration IPP for the Simonette far-offset non-deconvolved data (Hinds et al., 1993b). A possible multiple event occurs at 1.8 s (peak).

curve. This may be a real geological event that phases out before the borehole and subsequently would not be on the borehole logs; however, it could also be a multiple of the Wabamun primary event.

The $Z'_{\text{down}}(-\mathbf{TT})$ data were used to deconvolve the $Z_{\text{up}}(+\mathbf{TT})$ data from panel 1 of Figure 2.48 to output the $Z_{\text{up}(\text{decon})}(+\mathbf{TT})$ data in panels 1 and 2 of Figure 2.49. The deconvolution has been successful in attenuating the possible multiple and the interpretation of the reef events (in "reef" purple) can proceed on the VSP-CDP and migrated data shown in panels 3 and 4. The two IPP's shown in Figure 2.48 and 2.49 can be interpreted cooperatively in order to interpret through possible deconvolution noise.

2.3.5. Problematic far offset interpretive processing

In this section, the far offset polarization and deconvolution processing of the Ricinus carbonate reef case study (Hinds et al., 1989a; Hinds et al., 1993c; Hinds et al., 1994c) shall be presented. The case study presented in Chapter 4 also highlights the difficulties within the data processing that were solved through the interpretive processing of the far offset data; however, in the context of more detailed interpretation.

The two procedures that will be shown are:

- (1) the far offset time variant polarization; and
- (2) far offset deconvolution.

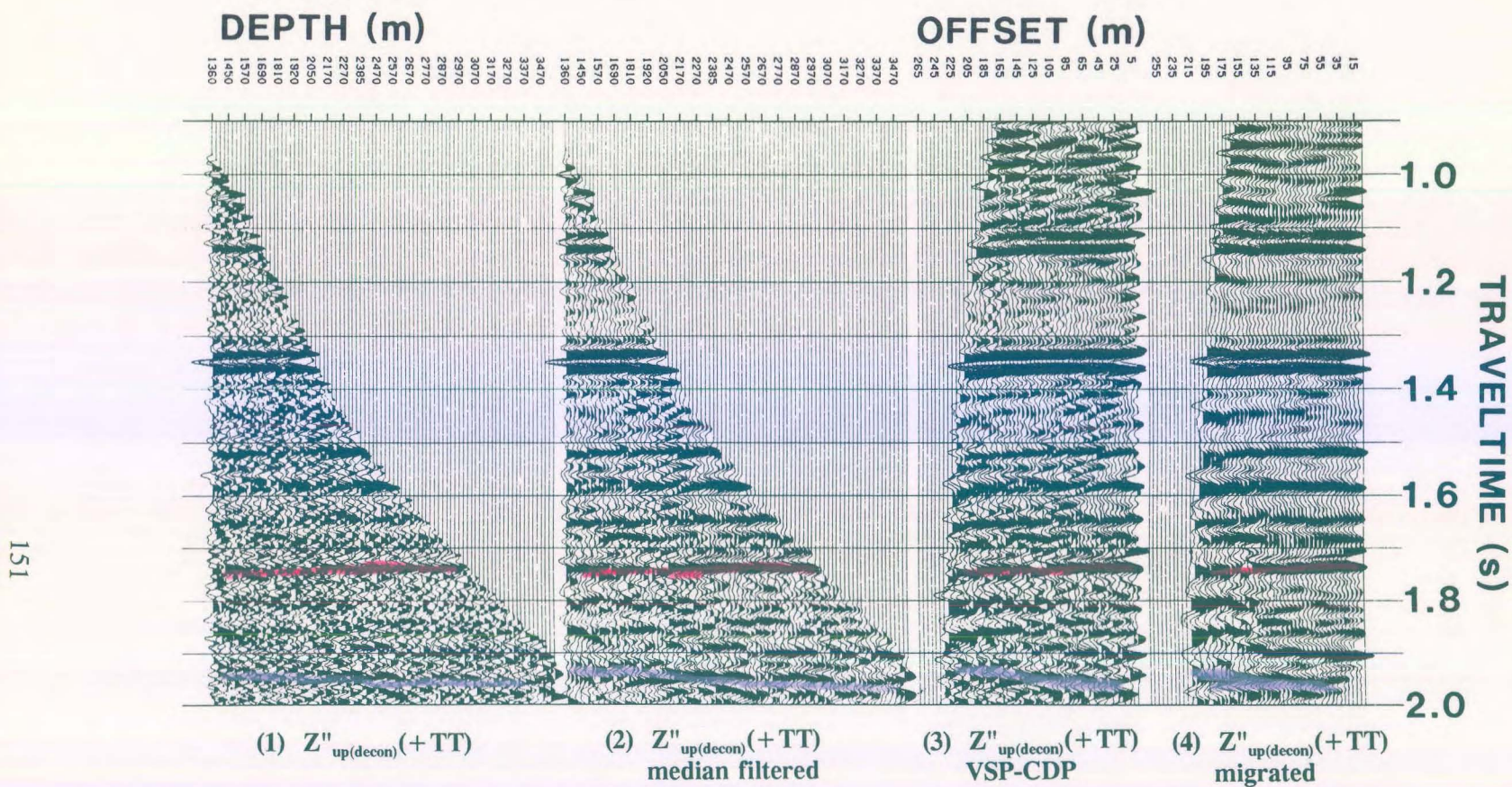


Figure 2.49 VSP-CDP and Kirchhoff migration IPP for the Simonette far-offset deconvolved data (Hinds et al., 1993b). The suspected multiple at 1.8 s has been attenuated; however, the reef interpretation (detailed in chapter 6) remains.

2.3.5.1 Time variant polarization of the Ricinus case study data

Figure 2.50 shows the time variant polarization IPP for the Ricinus carbonate reef case study (Chapter 4) far-offset (1100 m) data after "normal" processing. The processing followed the guideline far offset processing runstream presented in section 2.1.

The $Z''_{up}(FRT)$ data (panel 6) is contaminated with diffractions and mode-converted SV up- and downgoing events highlighted in yellow. The same mode-converted SV events, also highlighted in yellow, are shown in panel 1 of the VSP-CDP IPP in Figure 2.51. On panel 1 (Fig. 2.51), upgoing P events highlighted in orange intersect the first break "curve" between the 3300 and 3510 m traces. Linear events, highlighted in yellow, trending from the left hand bottom corner of panel 1 cross the data and merge with the highlighted (in orange) P-wave events. The yellow highlighted events represent the upgoing SV events that are contaminating some of the underlying P-wave data.

The downgoing mode-converted SV events can be seen better on panels 2, 3, 5 and 6 of Figure 2.50. These linear events (highlighted in green) trend in the same direction as the P-wave first break "curve" but at a steeper dip (implying a slower apparent velocity).

The first break "curve" does not exist following the downgoing wavefield separation processing. The "curve" refers to the mute limit on the data chosen using the first breaks.

The second stage of interpretive processing is now accomplished. By interpreting the "noise" (mode converted up- and downgoing SV events), the interpreter/processor can begin to

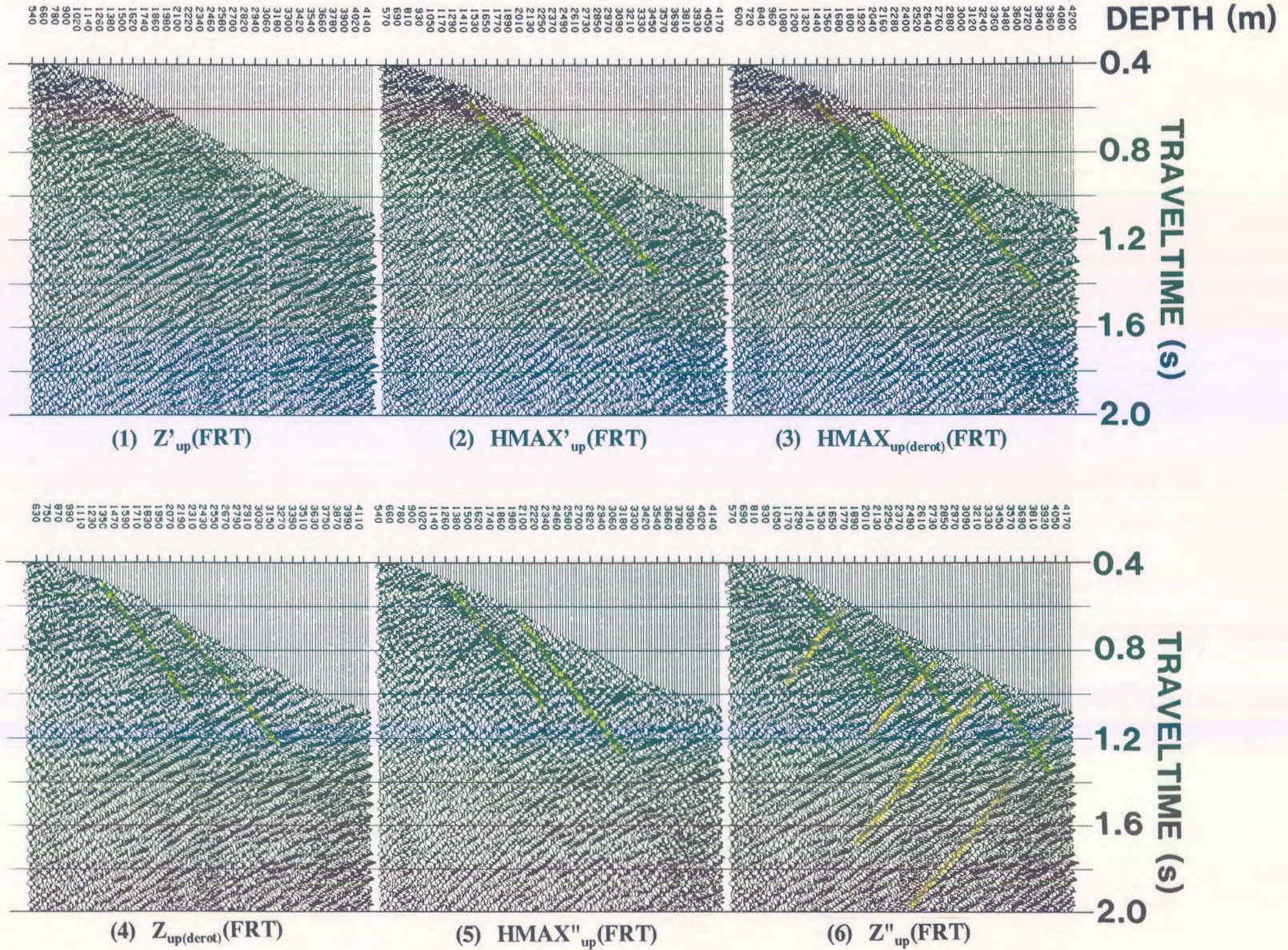


Figure 2.50 Time-variant polarization IPP for the Ricinus data (Hinds et al., 1989a; Hinds et al., 1994b) using the example far-offset processing initially presented in the "processing runstreams" section of chapter 2.

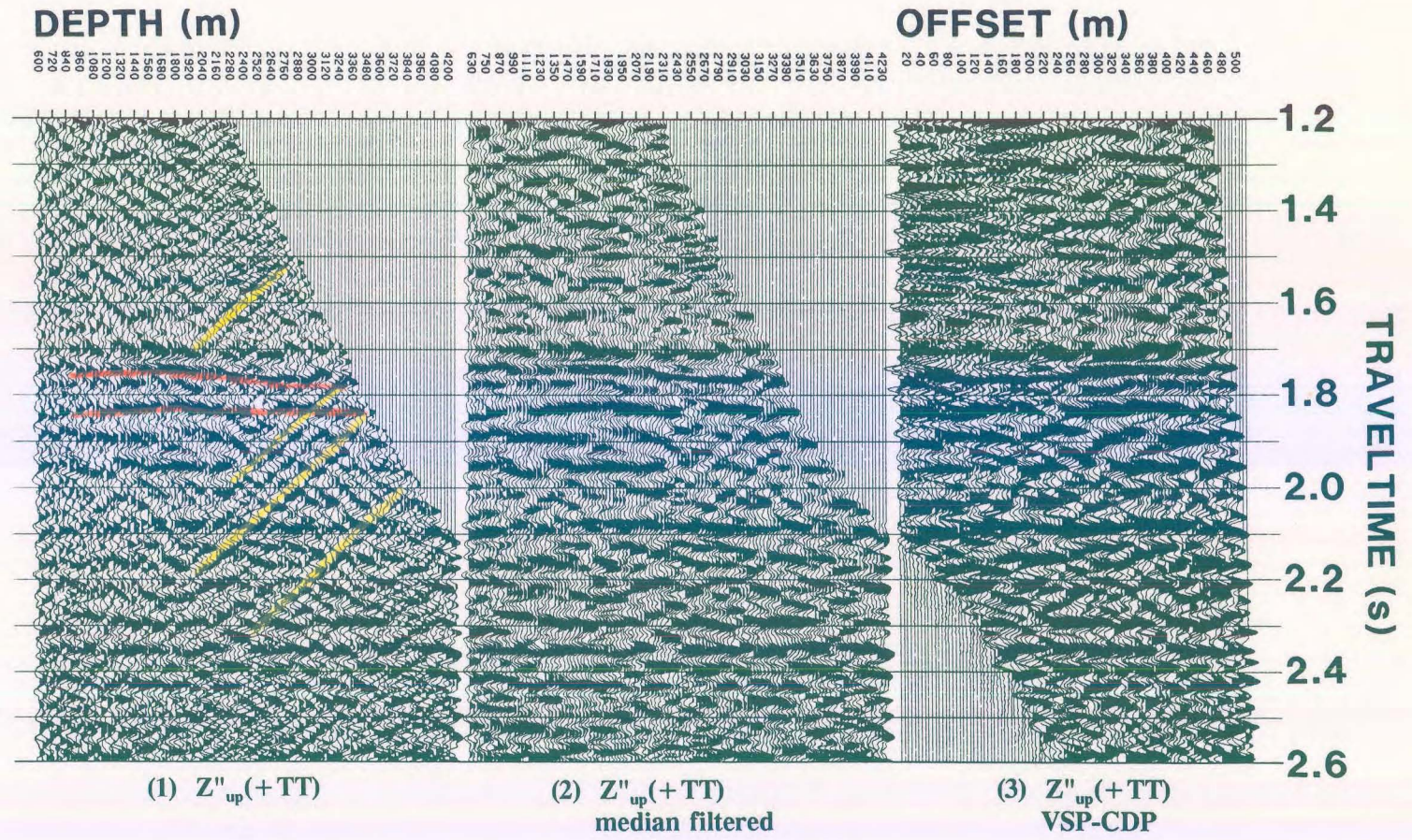


Figure 2.51 VSP-CDP IPP for the Ricinus data (Hinds et al., 1989a; Hinds et al., 1993c) using the Z''_{up} data shown in Figure 2.50. The upgoing P-wave events are difficult to interpret due to up- and downgoing SV-wave events.

redesign the processing to minimize the "unwanted" noise.

It was decided to go back to the $Z(\text{FRT})$ and $HMAX(\text{FRT})$ data and perform the wavefield separation on these two data panels (and not the $Z'(\text{FRT})$ and $HMAX'(\text{FRT})$ data as suggested in the processing guidelines of section 1.2). The wavefield separation processing included the attenuation of the mode-converted SV events. The results of the new processing runstream are shown in the updated time variant IPP shown in Figure 2.52.

The input $HMAX(\text{FRT})$ and $Z(\text{FRT})$ data are shown in panels 1 and 2. The wavefield separated $HMAX_{\text{up}}(\text{FRT})$ and $Z_{\text{up}}(\text{FRT})$ data in panels 3 and 4 can now be compared to the original $HMAX_{\text{up(derot)}}(\text{FRT})$ and $Z_{\text{up(derot)}}(\text{FRT})$ data in panels 3 and 4 of Figure 2.50 (the guideline runstream processing). Bypassing the $(Z, HMAX)$ to $(Z', HMAX')$ rotation (and possible noise generation caused by the polarization), the upgoing P events (some are highlighted in orange in panels 3 and 4 in Fig. 2.52) are more interpretable on the new processing. Time-variant polarization of the $HMAX_{\text{up}}(\text{FRT})$ and $Z_{\text{up}}(\text{FRT})$ data produces the $HMAX''_{\text{up}}(\text{FRT})$ and $Z''_{\text{up}}(\text{FRT})$ data shown in panels 5 and 6.

The VSP-CDP IPP display shown in Figure 2.53 for the modified processing runstream shows that the upgoing P events are much easier to follow and subsequently to interpret than the results presented in the VSP-CDP IPP using the original processing (Fig. 2.51). An example of this are the upgoing events highlighted in orange on panels 1 of Figures 2.51 and 2.53.

The $Z''_{\text{up(med)}}(+TT)$ data in panel 2 of Figure 2.53 was created using a 5 point median filter

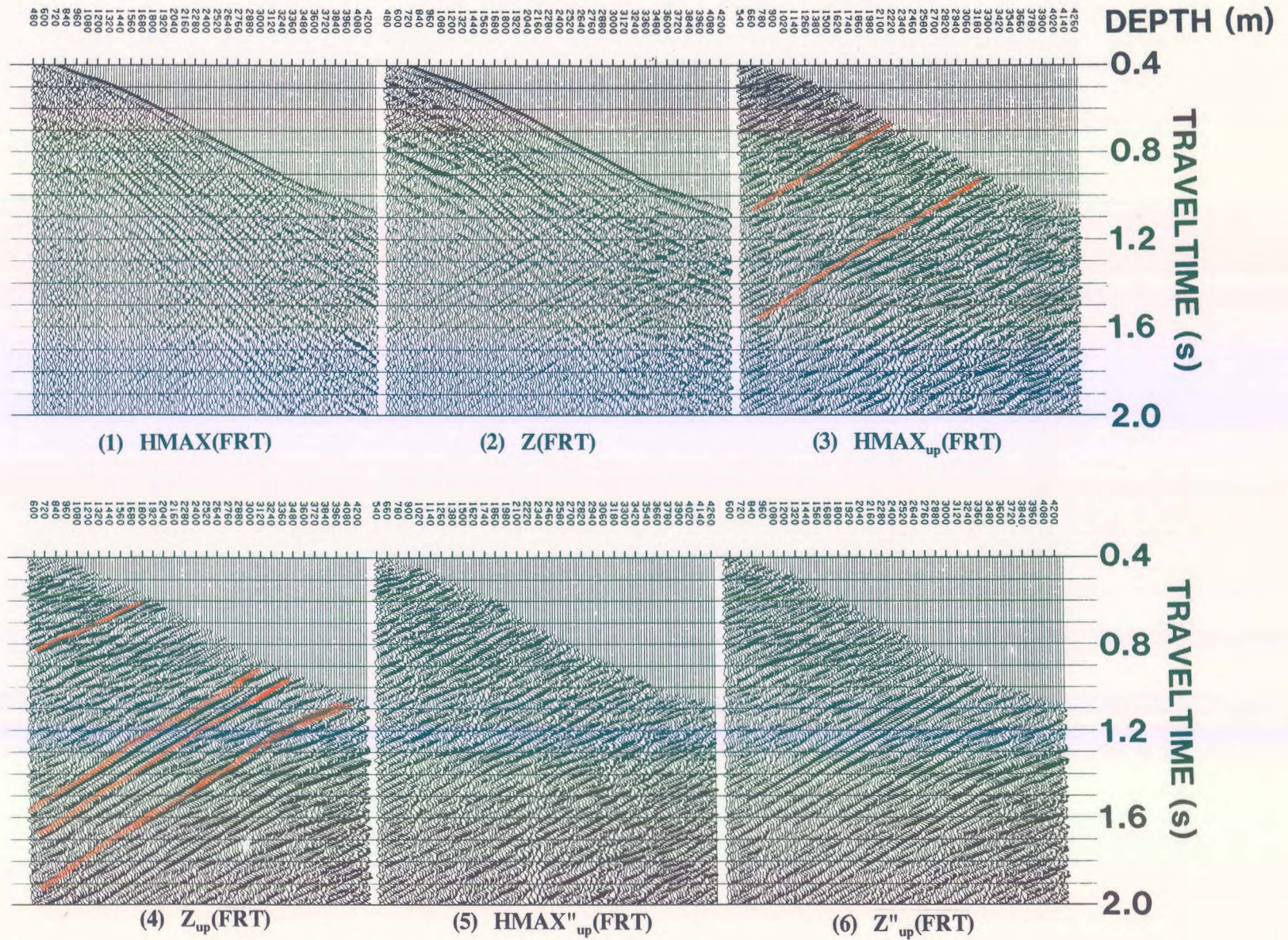


Figure 2.52 Modified time-variant polarization and wavefield separation IPP for the Ricinus data (Hinds et al., 1993c) following processing decisions made using interpretive processing.

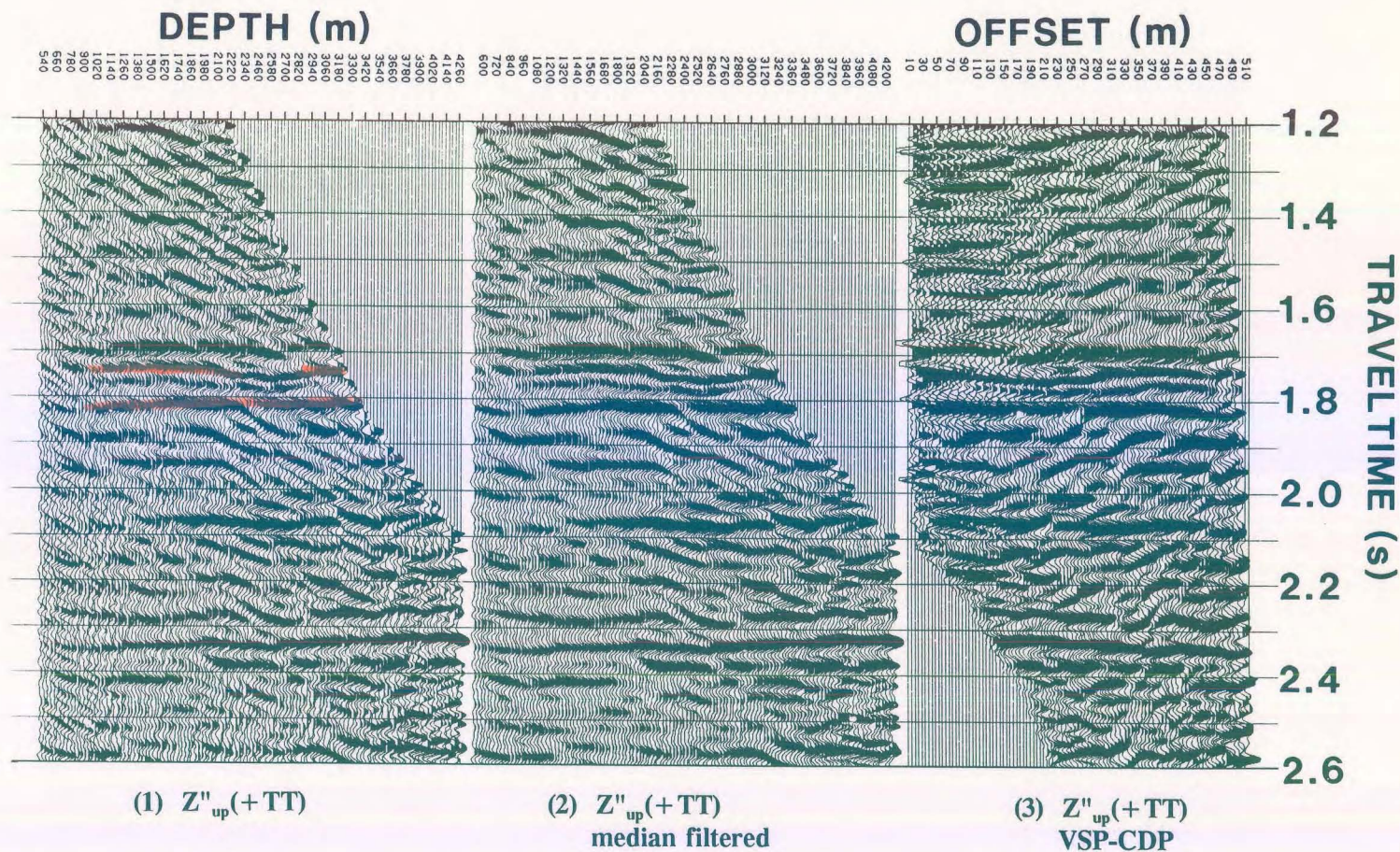


Figure 2.53 VSP-CDP IPP for the Ricinus data (Hinds et al., 1989a; Hinds et al., 1994b) using the Z''_{up} data shown in Figure 2.52. The upgoing P-wave events are more interpretable although the diffraction and downgoing SV-wave events have not been completely eliminated.

on the data seen in panel 1. Additional VSP-CDP displays using 9 and 11 point median filters to enhance the upgoing events on the $Z''_{up}(+TT)$ data are shown in Figures 2.54 and 2.55, respectively. As noted before, the interpreter/processor would derive an interpretation from Figures 2.53 to 2.55; however, one would also verify that the same events are resident on Figure 2.51. Interpretive processing includes every piece of information available during the interpretation stage.

2.3.5.1 Far offset deconvolution of the Ricinus case study data

In this section, the far offset deconvolution of the Ricinus carbonate reef case study (Hinds et al., 1989a; Hinds et al., 1994c) is examined. The deconvolved far offset results are also presented in Chapter 4 (Hinds et al., 1994c) in order to examine the evaluation of deconvolution generated noise testing in the context of a case study.

The far offset deconvolution IPP for the Ricinus far offset (1100 m) data is shown in Figure 2.56. The $HMAX'(-TT)$ and $HMAX'_{down}(-TT)$ data are shown in panel 1 and 2, respectively. By inspection, the $HMAX'_{down}(FRT)$ data do not possess an abundance of multiple events. Few, if any, multiple events are seen after the primary downgoing event.

The deconvolution verification panel contains the deconvolved downgoing events and is shown in panel 3. This is the result of applying the deconvolution processing to the downgoing events themselves. The $Z''_{up}(-TT)$ data of the updated interpretive processing

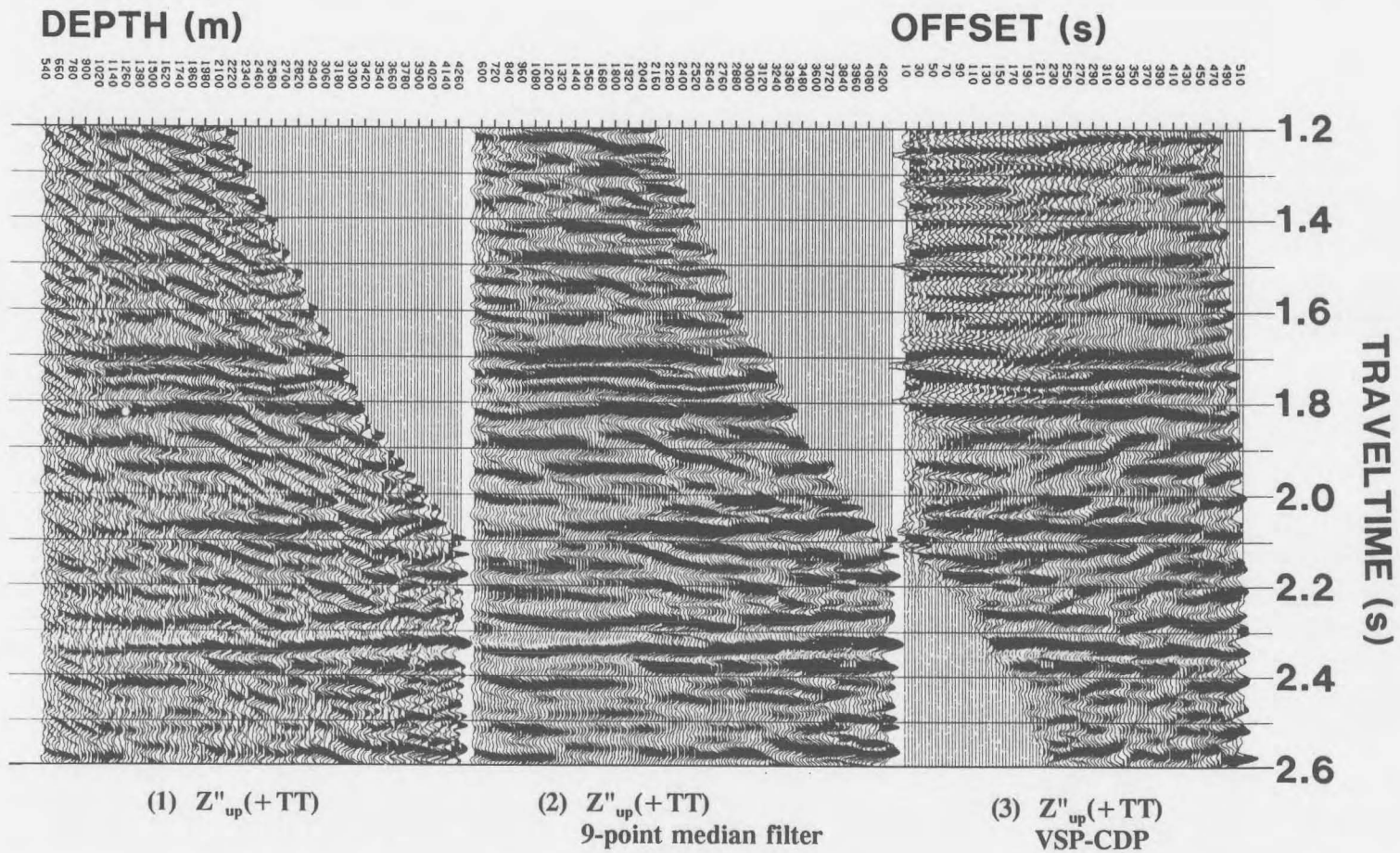


Figure 2.54 VSP-CDP IPP for the Ricinus data (Hinds et al., 1994b) with the Z''_{up} data shown in Figure 2.51 as input and data enhancement using a 9-point median filter.

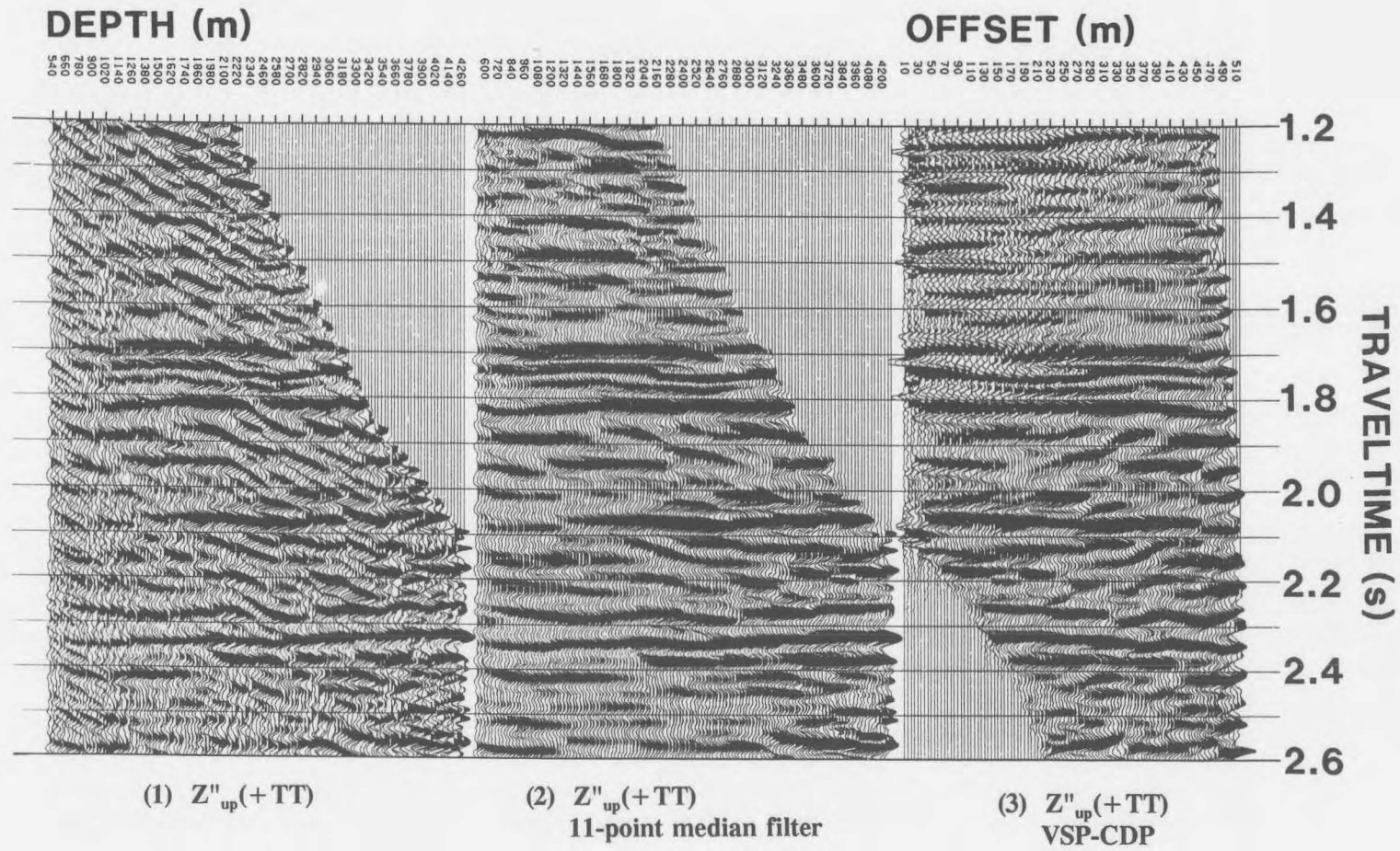


Figure 2.55 VSP-CDP IPP for the Ricinus data (Hinds et al., 1994b) with the Z''_{up} data shown in Figure 2.51 as input and data enhancement using a 11-point median filter.

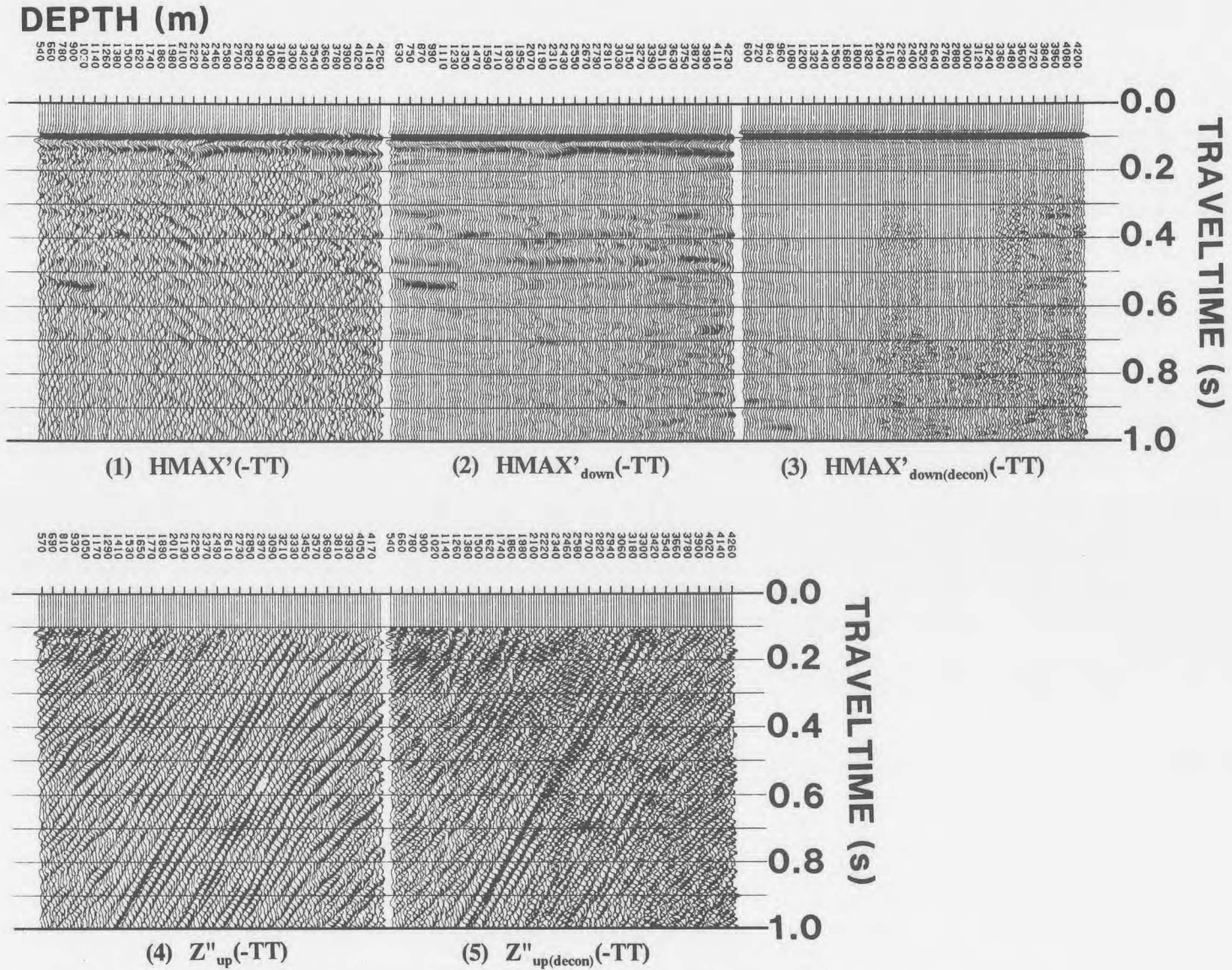


Figure 2.56 Far offset deconvolution IPP for the Ricinus data (Hinds et al., 1994b). Note the deconvolution induced noise by comparing panels 4 and 5.

(shown in Fig. 2.52) are shown in panel 4. The $Z''_{\text{up(decon)}}(-\text{TT})$ data are shown in panel 5. By inspection of panels 4 and 5, the deconvolution process has added undesirable noise to the upgoing event data.

The VSP-CDP IPP of the $Z''_{\text{up(decon)}}(+\text{TT})$ data is shown in Figure 2.57. The interpretation of the data was damaged by the addition of deconvolution noise. One reason for the deconvolution processing failure is that the simple time delay relationship between up- (Z''_{up}) and downgoing ($\text{HMAX}'_{\text{down}}$) events may not be satisfied for the far-offset data (1100 m offset).

2.4 Integrated displays

2.4.1 Integrated Log Display (ILD)

The integrated well log display highlights the seismic data around the well, the geological log data (in time) and the synthetic seismogram as shown in Figure 2.58. This display is included because, in practice, the VSP survey is usually the final survey to be run on a well following the acquisition of the geological logs. By the time that the VSP is processed, the sonic log should have been digitized and ready for the "check-shot" type of calibration.

Whilst the VSP is being processed, the near offset VSP first break times can be used to calibrate the sonic log (correct for sonic log drift and tie the integrated sonic log to the VSP first break times). The seismogram and calibrated sonic log (merged onto the seismic line

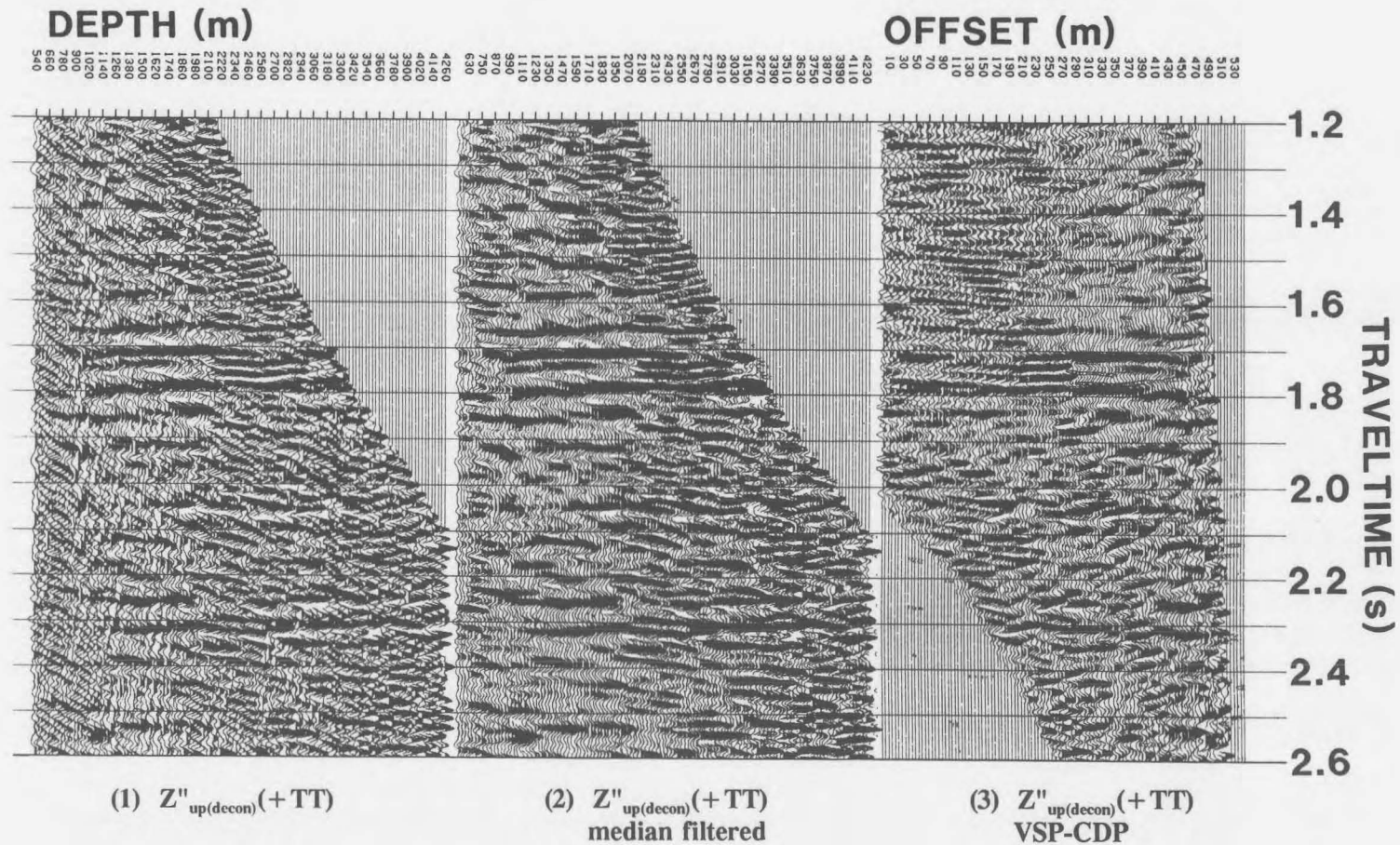


Figure 2.57 VSP-CDP IPP for the Ricinus $Z''_{up(decon)}(+TT)$ data (Hinds et al., 1994b). The deconvolution was not successful and was dropped from the Ricinus case study "normal" far offset processing runstream flow.

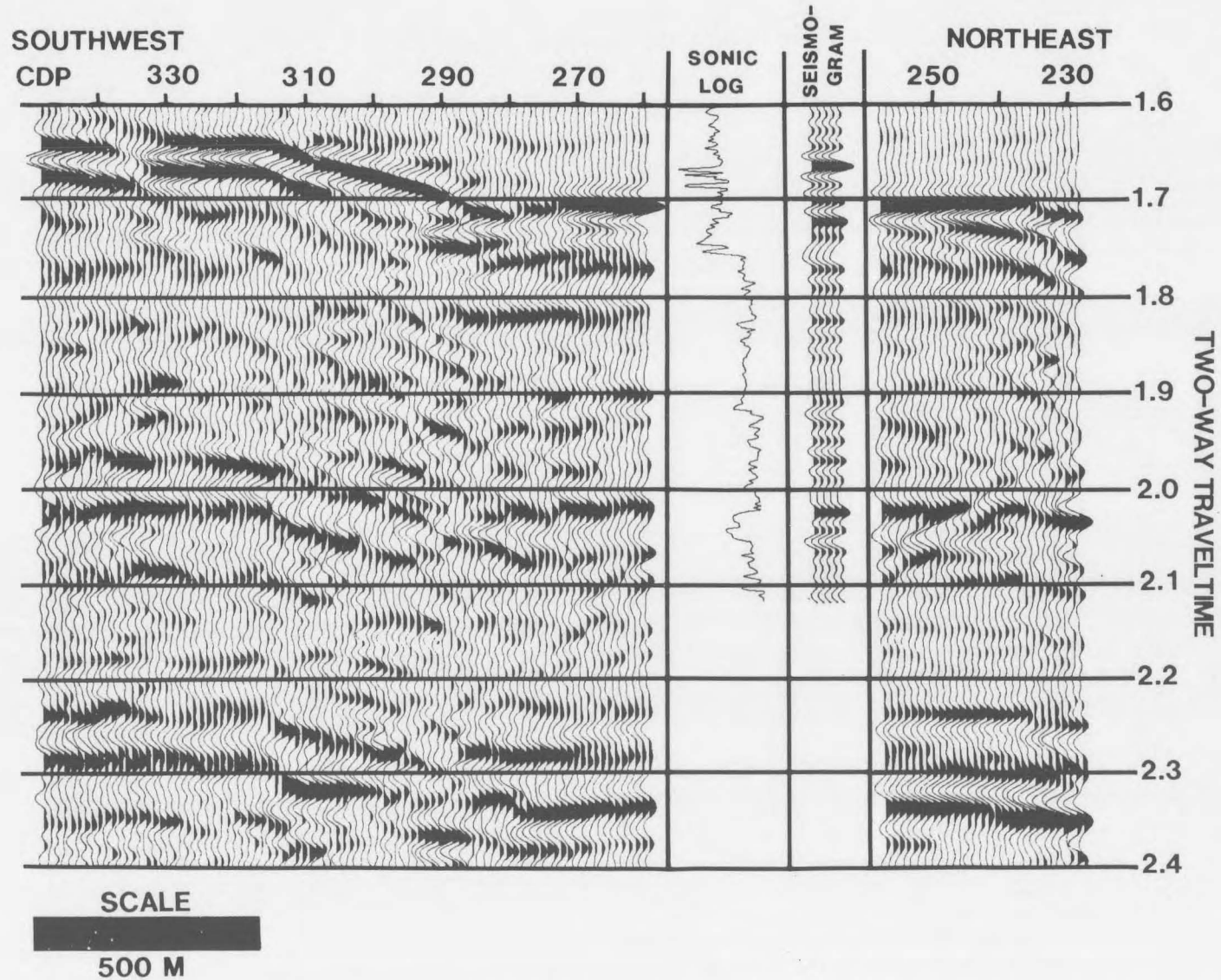


Figure 2.58 Integrated log display (ILD) for the Ricinus data (Hinds et al., 1989a; Hinds et al., 1994b).

on the ILD) can assist the interpreter to get a first-hand look at the location of the seismic events that were "intersected" by drilling.

2.4.2 Integrated Seismic Display (ISD)

The integrated seismic display for the Ricinus carbonate reef case study (Hinds et al., 1989a; Hinds et al., 1993c; Hinds et al., 1994c) is shown in Figure 2.59. The display contains the VSP-CDP (or migration) results merged with the surface seismic. The VSP-CDP is lateral offset data imaging the reflectors away from the well and can provide a high-resolution image of the reflectors in comparison to the same events seen on surface seismic.

2.4.3 Integrated Interpretive Display (IID)

At the final presentation stage of the project, a large part of the geoscience exploration results should be displayed. This is accomplished using the integrated interpretive display. The IID shown in Figure 2.60 displays the integrated results from the Simonette carbonate reef case history (Hinds et al., 1991b; Hinds et al., 1993b and 1994c).

This case study involves using the data to substantiate the need for a well "whipstock". It

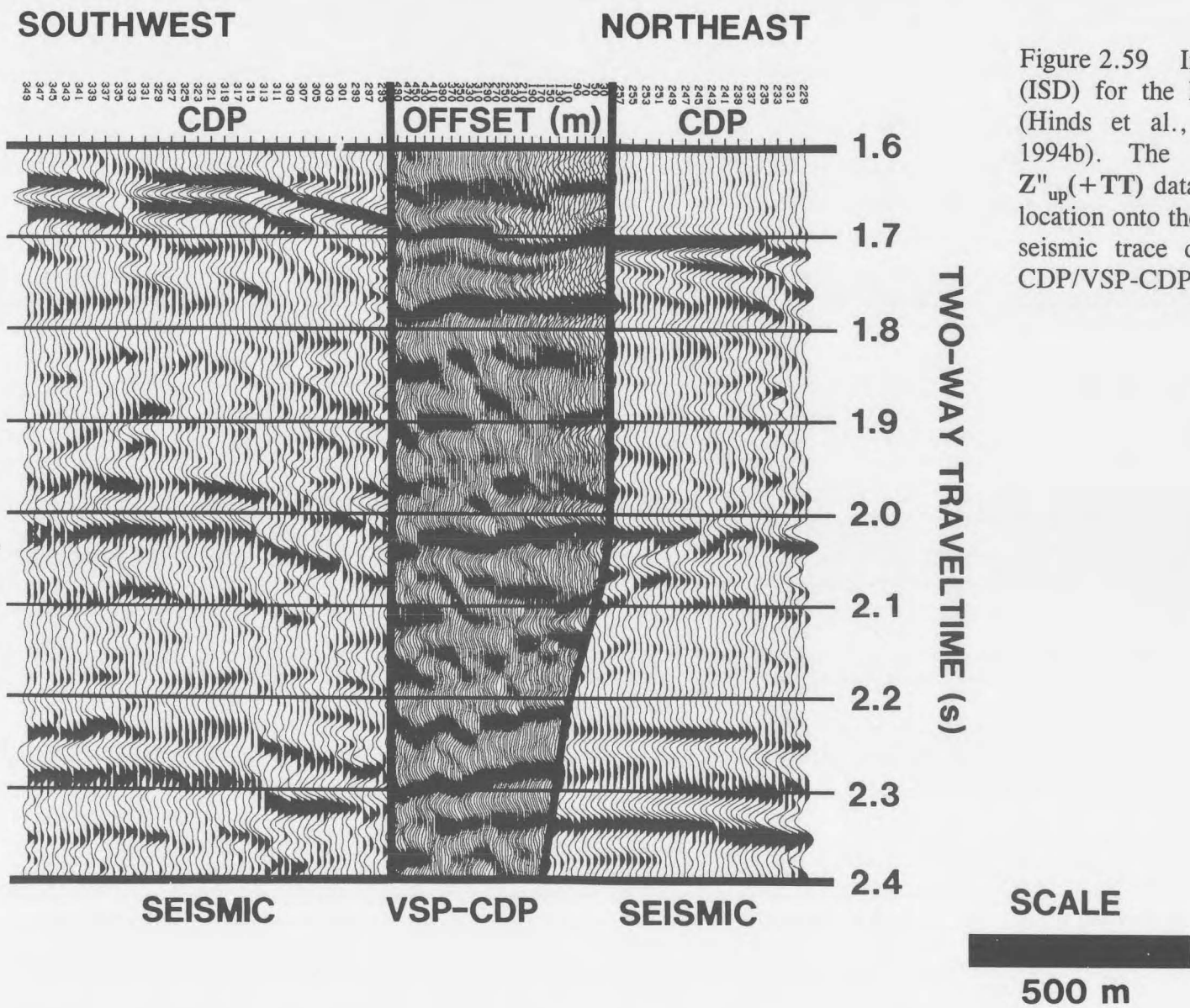


Figure 2.59 Integrated seismic display (ISD) for the Ricinus case study data (Hinds et al., 1989a; Hinds et al., 1994b). The VSP-CDP transformed $Z''_{up}(+TT)$ data are inserted at the well location onto the seismic and replace the seismic trace data at the overlapping CDP/VSP-CDP offset locations.

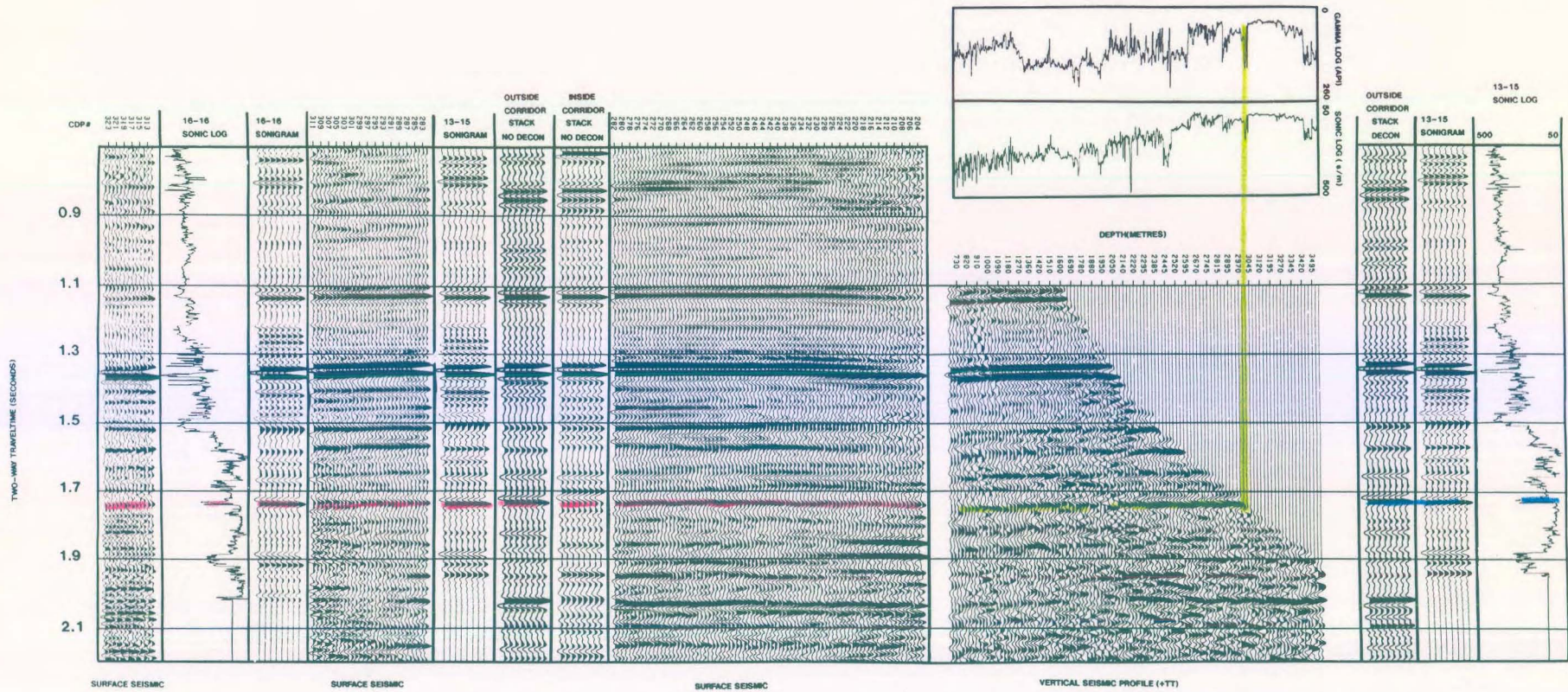


Figure 2.60 Integrated Interpretive Display (IID) of the Lanaway case study data (Hinds et al., 1989a; Hinds et al., 1994a). The display includes sonic and gamma logs (both in time and depth), the $Z_{up}(+TT)$ VSP data, corridor stack results and surface seismic data. This panel incorporates all of the exploration data for the area onto one single display for easy integrated interpretation.

was interpreted that the reef is beyond the "economic" reach of the whipstock (Hinds et al., 1993b and 1994c). The IID is used to conveniently show the lateral coverage and the interpretation away from the well towards the "known" reef on the far offset VSP in conjunction with the information available from the other types of exploration data.

The IID can be used to explain the entire interpretation procedure and how the different datasets tie. For example, the Wabamun Formation interface was interpreted from the sonic and gamma log to be at 3020 m well depth. Starting with the sonic and gamma logs in depth on Figure 2.60, a line can be drawn through the sonic and gamma high (at 3020 m) down to the upgoing (peak) event that intersects the 3020 m depth trace on the far offset $Z''_{up}(+TT)$ data. This line is shown in green on Figure 2.60. The Wabamun seismic marker is now tied to the logs through the common depth axis of the far offset VSP data (centre panel) and the logs (located above the centre panel).

The Wabamun VSP event can be tied to the surface seismic event at the 13-15 well using the time tie from the geologic logs. To the right of the VSP data are the outside corridor stack after deconvolution (to show primary events), the 13-15 synthetic seismogram and the 13-15 sonic log displayed in two-way travelttime. Using the tie of the VSP to the geologic logs, an interpreted Wabamun event can be further confirmed by tying the event (on the 3020 m trace) to the corridor stack, sonigram and sonic log (in time). This is shown by a blue line in Figure 2.60.

This tie can be drawn on the 13-15 sonigram, outside corridor stack of the $Z_{up(decon)}(+TT)$ data and inside corridor stack of the $Z_{up}(+TT)$ data that are spliced into the surface seismic

at the 13-15 well location. This is seen on the left panel of Figure 2.60. The nondeconvolved inside corridor stack would enable an interpretation of multiples on the surface seismic at the 13-15 well location. The interpretation of the Wabamun event (shown in red) is extrapolated onto the surface seismic on either side of the well. The 16-16 sonic log (in time) and 16-16 sonigram are spliced into the seismic section at the 16-16 well location. This will enable the interpretation of the reef at the 16-16 location.

The interpreted basal reef marker rising onto the reef pinnacle can be shown on the far offset VSP data panel (see chapter 6 or Hinds et al., 1991b and 1993b; Hinds et al., 1994c).

The VSP-CDP IPP displays would complete the presentation (Figs. 2.48 and 2.49) by showing the reef interpretation at the well and laterally offset for 200 m away from the well towards the "known" reef (at the 16-16 well). Questions about the effects of multiples are answered and the tie of the geology to the geophysics is resolved. The economics are discussed in the view of production penalties (caused by whipstocking the well onto another company's "zone") and the interpretation that the reef is encountered approximately 120 m away from the new well.

Interpretive processing has driven the processing and the various IPP and displays confirm the interpretation.

CHAPTER 3

THE LANAWAY FIELD CASE STUDY

On the basis of conventional surface seismic data, an exploratory well (referred to as the VSP well in this chapter) was drilled in 1986 into the up-dip, raised rim of the Devonian Leduc Formation reef complex at Lanaway Field, southwestern Alberta, Canada. The stratigraphy of the Central Plains of the Western Canadian Sedimentary Basin is listed in Figures 3.1A, B, and C (representing the stratigraphic sequence from the Quaternary to the Cambrian Periods) .

The VSP well was expected to encounter an anomalous late-stage carbonate accretionary buildup at the Leduc level. It was anticipated that the Leduc at the VSP well location would be up to 80 m higher than at adjacent rim well sites. The envisioned accretionary growth was not present; the top of the Leduc in the VSP well was consistent with other rim wells along the Lanaway/Garrington reef trend (Fig. 3.2) and inconsistent with the seismic interpretation (Hinds et al., 1989a, Hinds et al., 1994a and 1994c). Fortunately, however, the Leduc was structurally closed and the VSP well was completed as an oil well (producing both from the Nisku and Leduc Formations).

In order to resolve the apparent discrepancy between the interpreted surface seismic data and geology at the VSP well, a near offset vertical seismic profile (VSP) was conducted at the

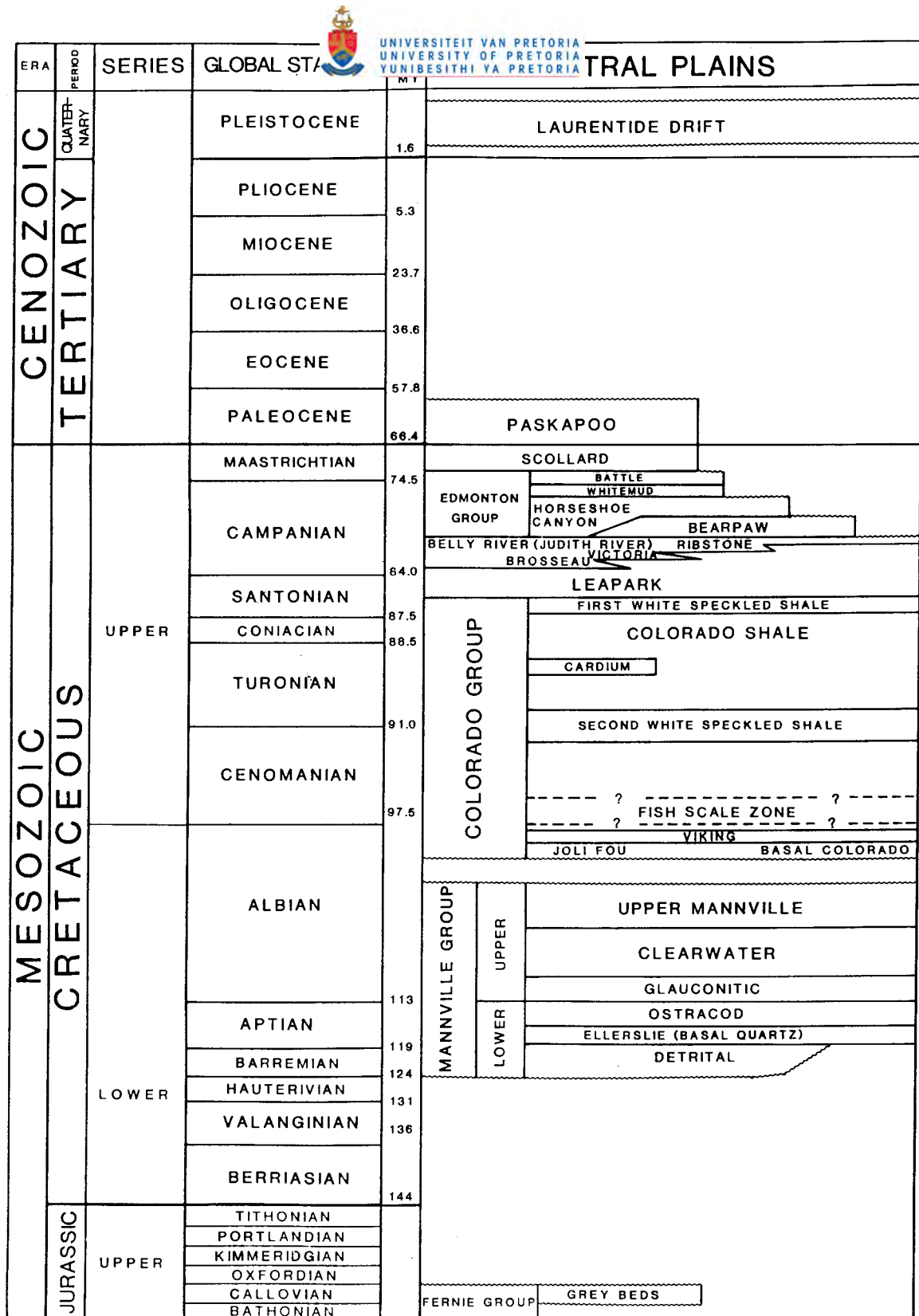


Figure 3.1A Stratigraphy from the Quaternary (Cenozoic) to the Upper Jurassic (Mesozoic) periods of the Central Plains area of the Western Canada Sedimentary Basin (after AGAT Laboratories, 1988; Anderson et al., 1989d; Hinds et al., 1994a and c)

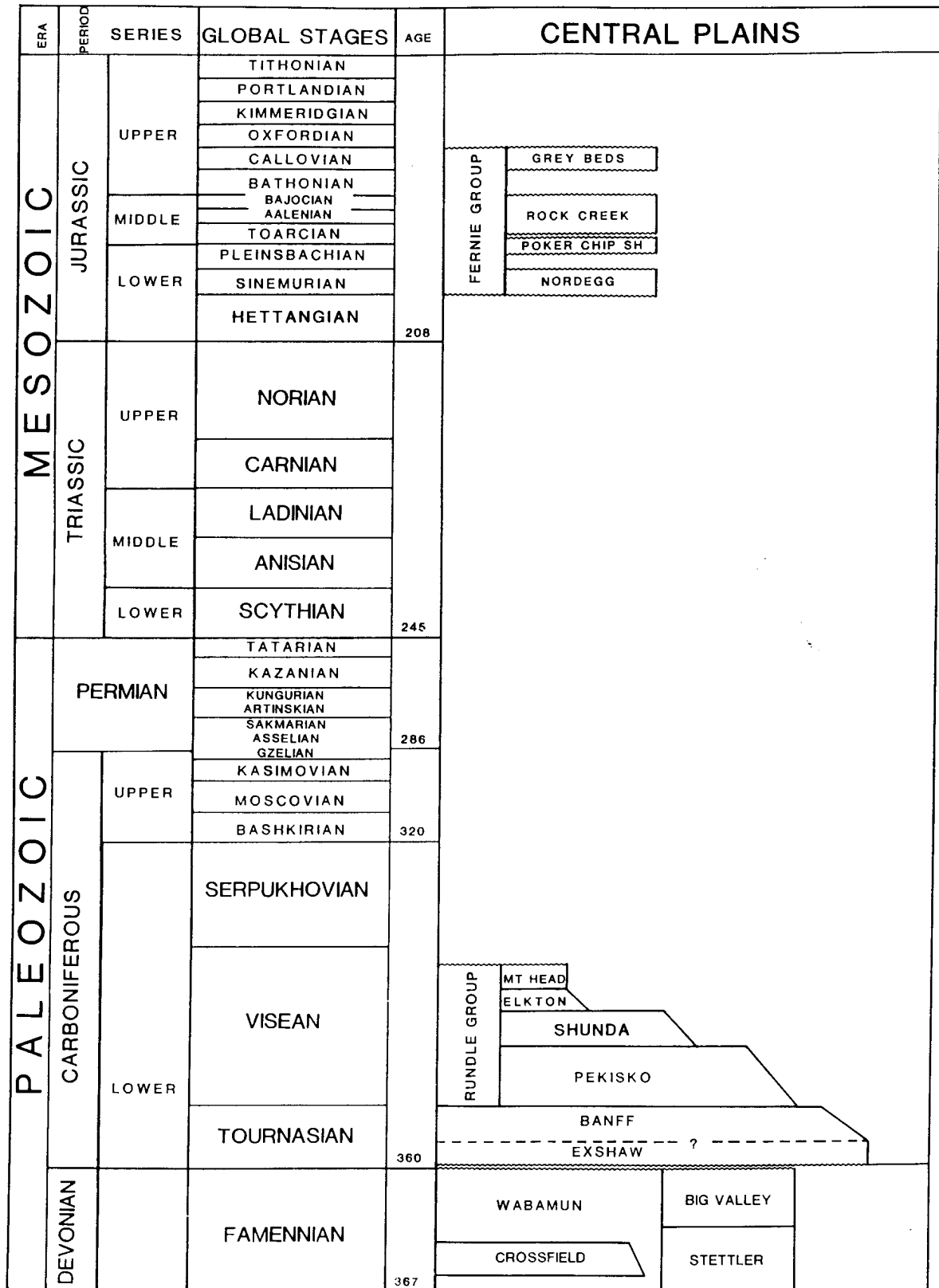


Figure 3.1B Stratigraphy from the Upper Jurassic (Mesozoic) to the Upper Devonian (Paleozoic) periods of the Central Plains area of the Western Canada Sedimentary Basin (after AGAT Laboratories, 1988; Anderson et al., 1989d; Hinds et al., 1994a and c)

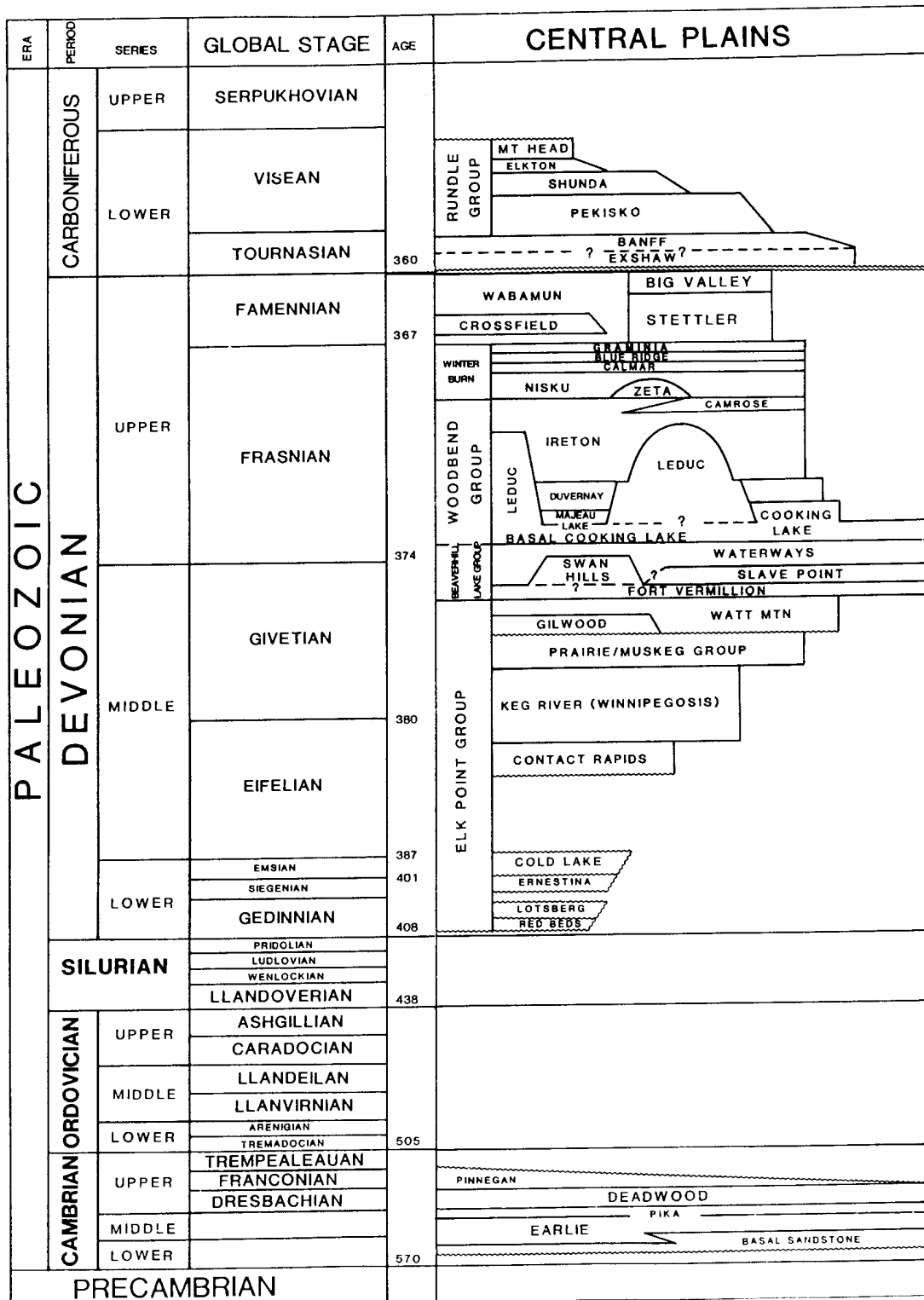


Figure 3.1C Stratigraphy from the Upper Carboniferous (Paleozoic) period to the Precambrian of the Central Plains area of Western Canada Sedimentary Basin (after AGAT Laboratories, 1988; Anderson et al., 1989d; and Hinds et al., 1994a and c)

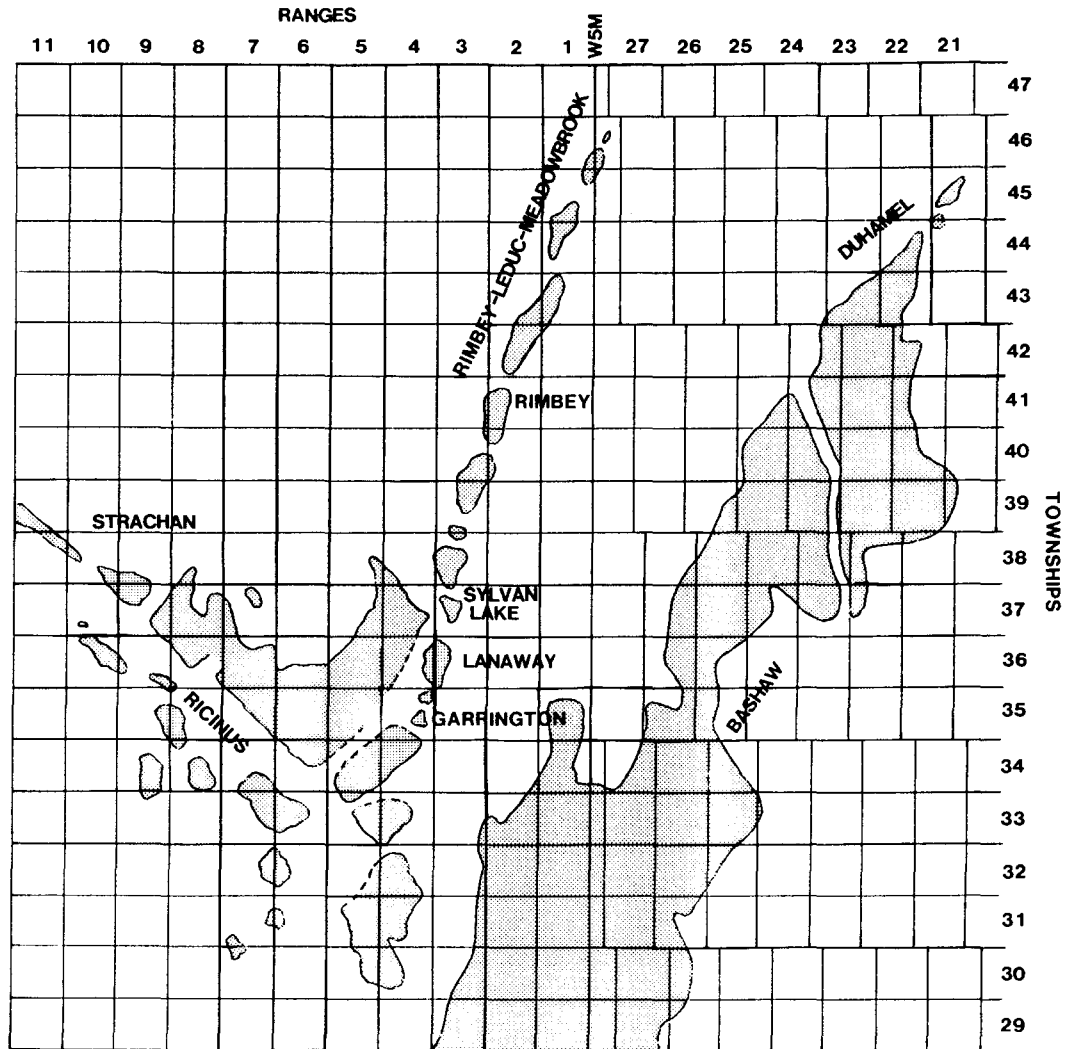


Figure 3.2 Regional location map of the Lanaway study area. The shaded areas represent the areal extent of the major Leduc Formation carbonate reefs of the area (with permission of Talisman Resources Inc.; from Hinds et al., 1994a and c)

well site. The interpretation of the VSP was expected to elucidate the geological origin of the misinterpreted seismic anomaly. Towards this end, the interpretation of the VSP was relatively successful in being able to assist in the formulation of an explanation for the anomaly. These data confirmed that the original interpretation of the surface seismic data (with respect to the Nisku, Ireton and Leduc top) was incorrect, and that the anomaly observed on the surface seismic line was not a processing artifact. The anomaly could most probably be attributed to either 1) structural relief at the pre-Cretaceous subcrop (as exemplified by Shunda Formation isopach values); 2) stratigraphic anomalies (thicker sections of carbonates) within the Winterburn Group or 3) seismic focusing caused by draping Ireton over the nose of the reef along the traverse of the seismic line. Interbed multiples interfering with the Nisku event could possibly be a minor contributing factor.

3.1 Carbonate reef development in the Western Canadian Sedimentary Basin

As an introduction to the geology of the carbonate reef case studies presented in this chapter (Lanaway Field), chapter 4 (Ricinus Field) and chapter 6 (Simonette Field), the depositional sequence history will be reviewed below for the Hume-Dawson to the Beaverhill-Saskatchewan subsequences (Moore, 1988 and 1989a) in the Western Canadian Sedimentary Basin (WCSB).

The case studies pertain to the Leduc reefs of the Saskatchewan Group subsequence (Moore, 1988). There are three major subsequences which involve oil producing carbonate reefs; namely the Upper Keg River, Rainbow and Upper Winnipegosis reefs of the Hume-Dawson subsequence, the Swan Hills Fm reefs of the Beaverhill subsequence and the Leduc Fm reefs

of the Saskatchewan subsequence. The Devonian history of the WCSB is divided into five major rock sequences; each divided by discontinuities that encompass a period of sea-level rise followed by a fall of sea level and ending in emergence (Moore, 1988). The reef building is pulsatory resulting in the different subsequences.

The first rise of sea level in these reef-building subsequences (Hume-Dawson) occurred during the deposition of the Lower Keg River Member in Northern Alberta and the Lower Winnipegosis unit in Southern Saskatchewan (Brown et al., 1990). As shown in Moore (1988), the Keg River barrier reef (or Keg River - Pine Point barrier reef; Moore, 1989a) formed northeastward of the Peace River Arch. Behind this barrier reef, pinnacles up to 200 m in height grew in the Keg River and Winnipegosis Fms within the Elk Point Basin (see Fig. 5 of Moore, 1988). Transgression at the end of Winnipegosis/Keg River time resulted in basin shallowing and reef growth termination within the resulting hypersaline environment. The basal salt units of the Prairie Fm and the Black Creek Member of the Muskeg Fm were deposited during this time of limited water circulation within the Elk Point Basin. The end of the sequence resulted in further deposition of anhydrites, shales and carbonates followed by the Watt Mountain unconformity. Anderson et al. (1989d) shows examples of Elk Point carbonate reservoir seismic signatures.

The next two subsequences correspond to the Beaverhill Gp (late Givetian to early Frasnian) and the Saskatchewan Gp (mid-Frasnian to end of Frasnian). The depositional history of both of these subsequences contain a carbonate platform development, platform reef growth, basin filling by mixed carbonates and siliciclastics and finally, by progradation of the carbonate platforms (Moore, 1989a).

The Beaverhill Gp subsequence contained the Swan Hills Formation reefs, the Waterways Formation shales and finally the Cooking Lake Formation carbonate platform. The Swan Hills reefs are seismically described in Anderson et al. (1989a) and Ferry (1989). The growth of the Swan Hills reefs was mostly pulsatory and the reefs have been categorized into several cycles of reef "layering" (Wendte and Stoakes, 1982). The progradation of the carbonate platform at the end of the subsequence resulted in the deposition of the lower part of the Cooking Lake Fm. The Peace River Arch was still a positive feature at this time (Chapter 5).

The carbonate platform of the reefs of the Saskatchewan subsequence is either the Cooking Lake Fm or an argillaceous ramp of the Waterways Formation. The Leduc reefs have been divided into three geographical realms in Stoakes and Wendte (1987). The Leduc platform reefs in the southeastern realm include the Bashaw-Duhamel and Rimbey-Meadowbrook reef chains, Ricinus Field and Lanaway Field. These reefs have the Cooking Lake Fm as a platform facies. The reefs of the western region such as the Simonette Field (Chapter 6) are built on the Waterways Fm. The northwestern realm reefs generally fringe the Peace River Arch. Anderson et al. (1989c) shows examples of Woodbend Group reef seismic signatures.

Nisku Fm (Upper Frasnian) reefing occurred in the West Pembina Shale Basin. The reefing in the Nisku Fm may be Zeta Lake member pinnacles or carbonate porosity resulting from drape over the larger Leduc reefs (as in Chapter 3). The basin infill period saw the deposition of the Nisku Fm and Birdbear Fm platform carbonates. The end of the Frasnian is highlighted by an extinction event which may be due to a meteorite impact (Moore, 1988).

3.1.1 Lanaway Field

The Upper Devonian Woodbend Group in central Alberta is subdivided into four formations: Cooking Lake, Duvernay, Leduc, and Ireton. The Cooking Lake represents platform facies. The Leduc is reefal facies; the Duvernay and Ireton are inter-reef shales (Anderson et al., 1989a, b and c; Klovan, 1964; McNamara and Wardlaw, 1991; Moore, 1988, 1989a and b; Mossop, 1972; Mountjoy, 1980; Stoakes, 1980; Stoakes and Wendte, 1987; and Hinds et al., 1994a).

The Leduc Formation at Lanaway (Figs. 3.2 and 3.3) is interpreted to be a large atoll. It towers some 200 m above the Cooking Lake platform and exhibits a seismically mappable (peripheral) raised rim and a structurally lower central lagoonal area. Such raised rims are described in Mossop (1972) in his study of the isolated Leduc Formation limestone reef complex at Redwater. In that study the raised rim was postulated to arise primarily as a result of the greater degree of differential compaction of the central lagoonal facies in comparison to the rigid reef facies. The updip edge (to the northeast) of the raised rim at Lanaway is productive where the reef is structurally closed and effectively sealed by the inter-reef shales of the Duvernay and Ireton Formations (Hinds et al., 1994a). The geologic cross-sections shown in Figures 3.4, 3.5 and 3.6 (from wells shown in Fig. 3.3) and the seismic section (Fig. 3.7, on the seismic line on Fig. 3.3) illustrate the interpreted morphological relationships between the Leduc and inter-reef shales of the Ireton and Duvernay in the Lanaway area.

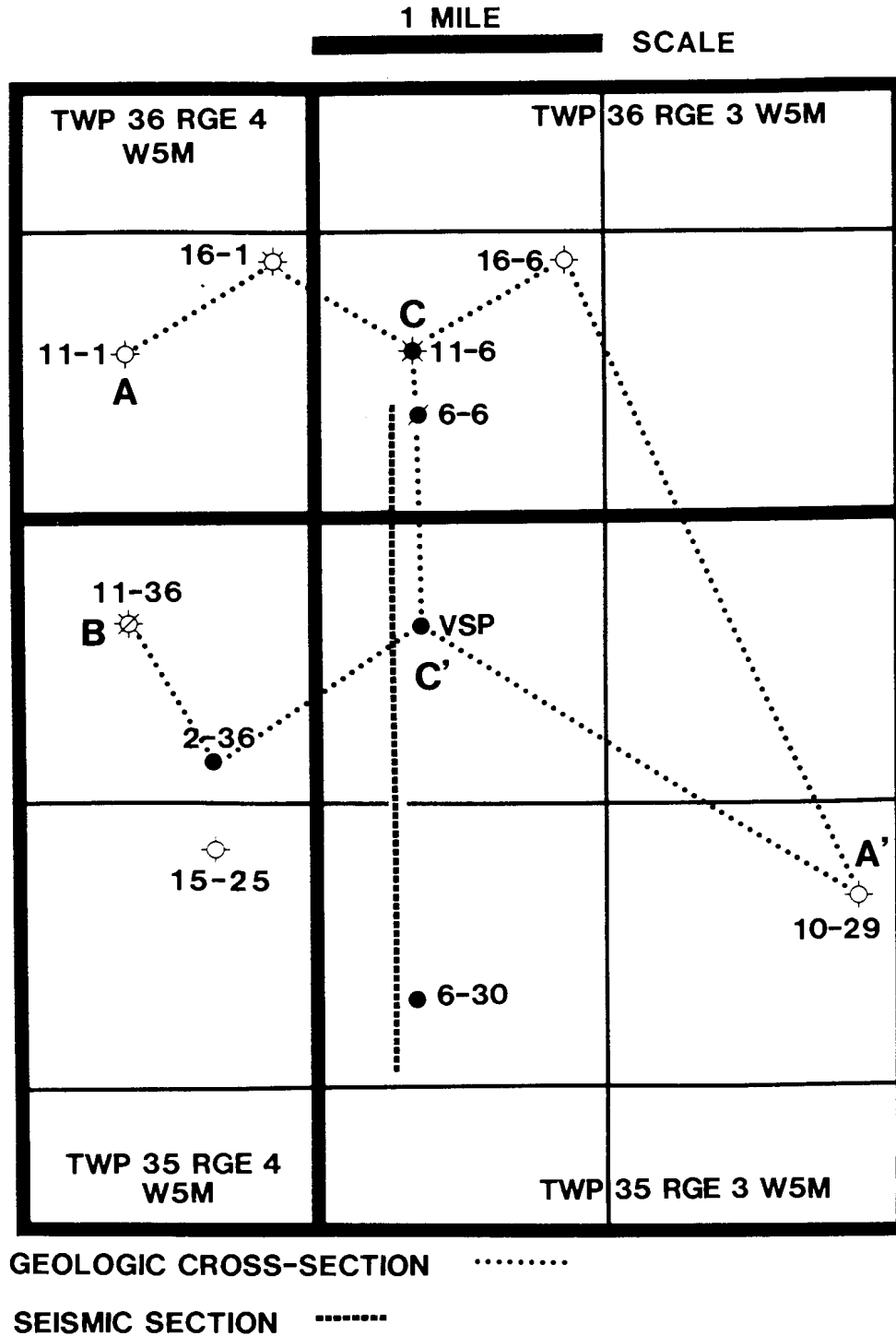


Figure 3.3 Detailed map of the Lanaway study area displaying the seismic section traverse for the seismic data shown in Figures 3.7, 3.8, 3.14 and 3.15 and the locations of the wells used in the geological cross-sections shown in Figures 3.4, 3.5 and 3.6 (from Hinds et al., 1994a and c).

On the surface seismic data, the Lanaway Leduc reef is readily differentiated from inter-reef shales. The carbonate build-up is characterized by appreciable velocity pull-up (25 ms), time-structural drape at the top of the Devonian (25 ms) and character variations within the Woodbend Group (associated with the abrupt transition from shale to reefal facies). Back from the steeply dipping edge, the top of the reef is clearly defined on seismic data, being manifested as a high-amplitude peak on normal polarity data.

The results and interpretations of the 2-D surface seismic and VSP surveys (performed on well C' shown in Fig. 3.3) and the seismic signatures of the top of the Leduc reef at Lanaway are discussed in this chapter. The seismic data were acquired prior to drilling the VSP well, which ultimately ended up intersecting the reef some 80 m below the prognosed depth while the VSP survey was run in an attempt to resolve the apparent discrepancy between the interpreted depth of the reef as derived from surface seismic data and the geology at the exploratory (VSP) well.

3.2 Well Nomenclature

The nomenclature for well locations within the Western Canadian Sedimentary Basin (WCSB) generally comprises a four number reference system (Anderson et al., 1989b). The two numbers (as in the well location 11-1 in Fig. 3.3) are a short form for a more detailed well location system utilized within the WCSB area. The well location system will be described briefly in order to assist the reading of the maps in this and later chapters.

As seen in Figures 3.2 and 3.3, geographical areal units are used in the WCSB referred to as Townships and Ranges. Townships increase in value from South to North and Ranges increase in value (until a Meridian is crossed) from East to West. A single Township and Range involve an area of six by six miles. The Township and Range square is subdivided into thirty-six square units called Sections. Each Section is one mile by one mile in size and is numbered 1 to 36, starting in the southeast corner of the Township and Range square. The smallest sub-division is the land survey division (LSD) which is a quarter mile by quarter mile in size. Within each section, there are sixteen quarter-section LSD's. The LSD numbering starts in the southeast corner of the section. The Ranges are referenced to Meridian lines (lines accurately running north and south through any point on the Earth's surface). After a major Meridian line is crossed, the Range values restart at 1.

As seen in Figure 3.2, the Lanaway Field lies within Ranges 3 and 4 and Township 36 and is west of the fifth Meridian (labelled W5M in Figure 3.2). In Figure 3.3, the two digit well name refers to the LSD and Section numbers. The well 11-1 lies in the 11th LSD of Section 1. The well is geographically tied to the quarter by quarter mile land spacing unit. The full name of the well would be 11-1-36-4 W5M (LSD-Section-Township-Range). For this and the other chapters concerning the case studies, the well name can, at times, be shown in the shortened format as in the example of 11-1.

3.3 Lanaway Field (at the VSP well)

Full Leduc reef at Lanaway Field towers up to 200 m above the Cooking Lake platform and has a structurally lower interior lagoon (Figs. 3.4 and 3.5). Production from the Leduc is

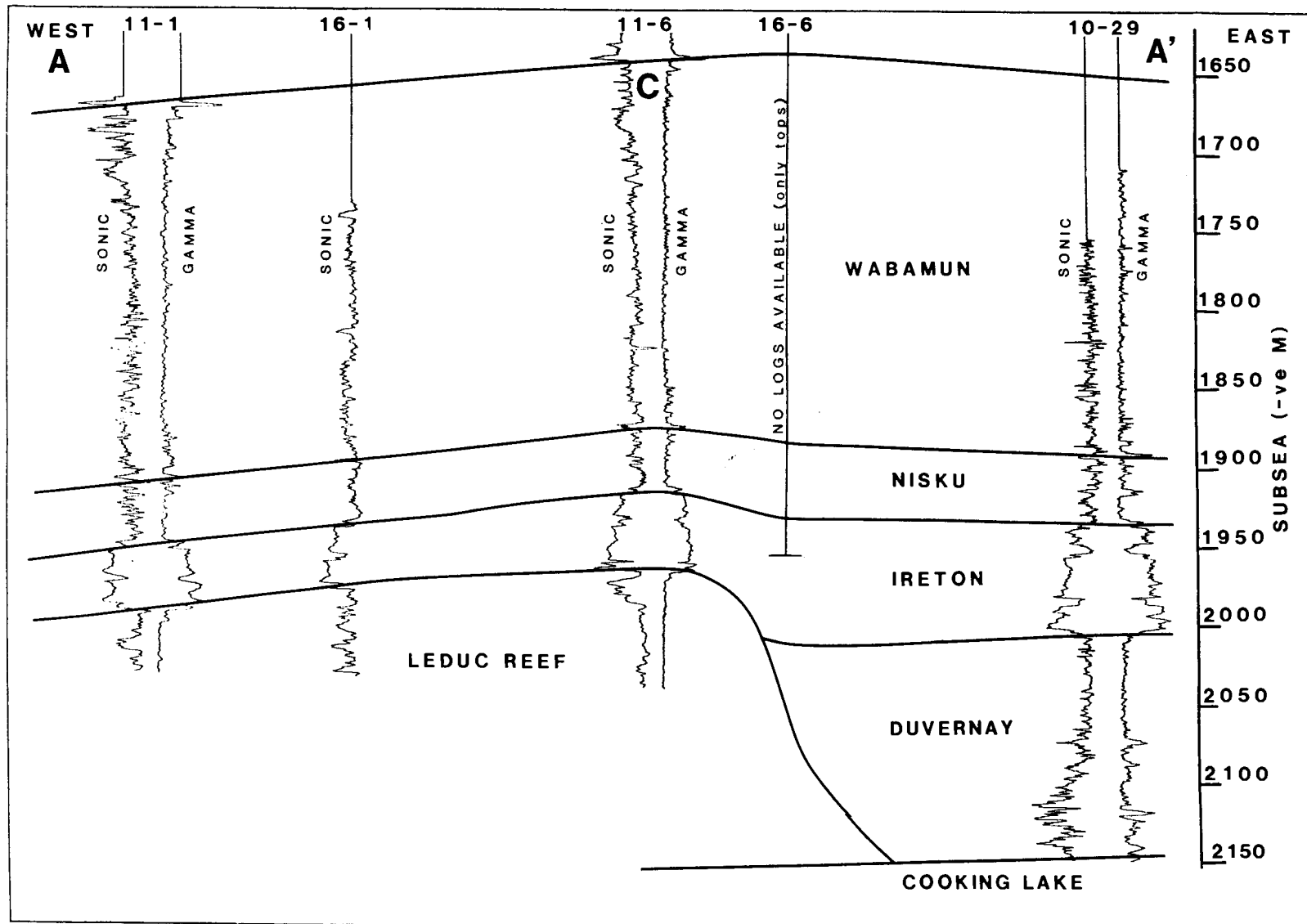


Figure 3.4 West-east geologic cross-section A-A' (refer to Figure 3.3 for well locations). The Leduc Formation reef in well 11-1 is structurally low and wet; wells 16-1 and 11-6 are productive (Leduc oil reservoirs); and wells 16-6 and 10-29 are off-reef and abandoned (from Hinds et al., 1994a and c).

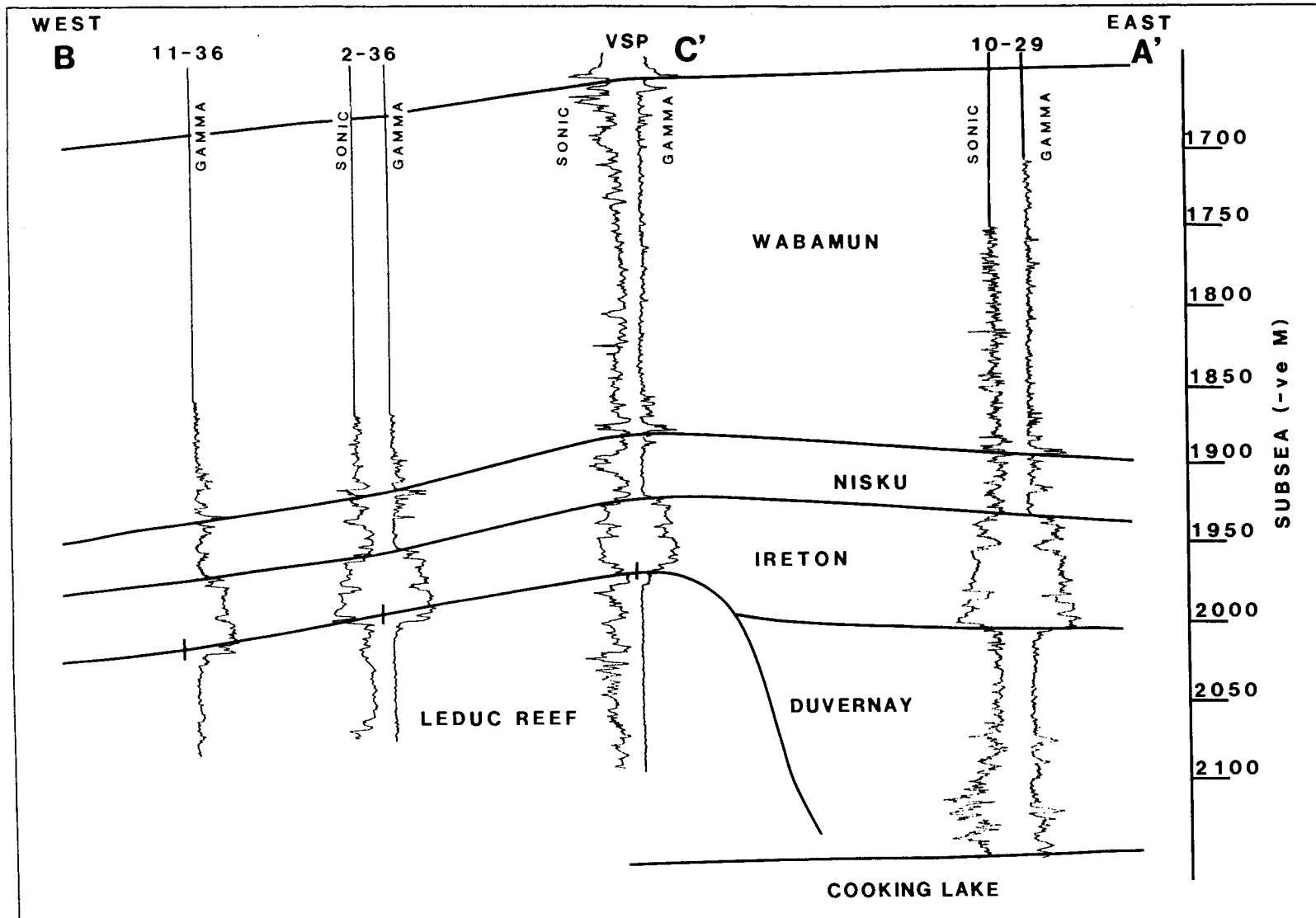


Figure 3.5 West-east geologic cross-section B-A' (refer to Figure 3.3 for location). The Leduc Formation in wells 11-36 and 2-36 (producing oil from the Nisku) is structurally low and wet; the VSP well is productive (Nisku and Leduc Formation oil reservoirs); and well 10-29 is off-reef and abandoned.

restricted to the updip eastern edge (raised rim) of the reef complex (up to 50 m of pay). The eastern and western limits of production are defined by the fore-reef slope and the hydrocarbon/water interface, respectively.

The structural geologic cross-sections (based on the wells located in Fig. 3.3) shown in Figures 3.4, 3.5 and 3.6 illustrate the morphology of the Lanaway complex. Borehole well 10-29 (Fig. 3.4) is off-reef and encountered a full section of inter-reef shale (Ireton and Duvernay); 11-1 is interpreted as having penetrated the structurally low and wet interior lagoon; 16-1 and 11-6 were drilled into the up-dip raised rim of the Lanaway reef and are productive. Well 11-36 (Fig. 3.5) is interpreted as having penetrated the structurally low and wet interior lagoon; 2-36 and the VSP well were drilled into the raised rim of the Lanaway complex. The VSP well is productive. Well 2-36 penetrated the Leduc below the hydrocarbon/water contact; however the well is classified as a Nisku oil well with extended productivity from gas from the Viking Formation of the Cretaceous Colorado Group and oil from the Basal Quartz member of the Ellerslie Formation of the Lower Mannville Group (Lower Cretaceous). These three producing zones (Nisku, Viking and Basal Quartz) are stratigraphically listed in Figures 3.1A-C. The VSP well has a different oil/water contact than 11-6 to the north and, consequently, is assigned to a separate pool. The hydrological barrier between these two wells is related to structural relief at the Leduc level (Fig. 3.6). This relief has been described to be due to several processes or features including surge channels, shale tongues, differential compaction, or original reef morphology by Anderson (1989a, b and c), Klovan (1964) and Mossop (1972).

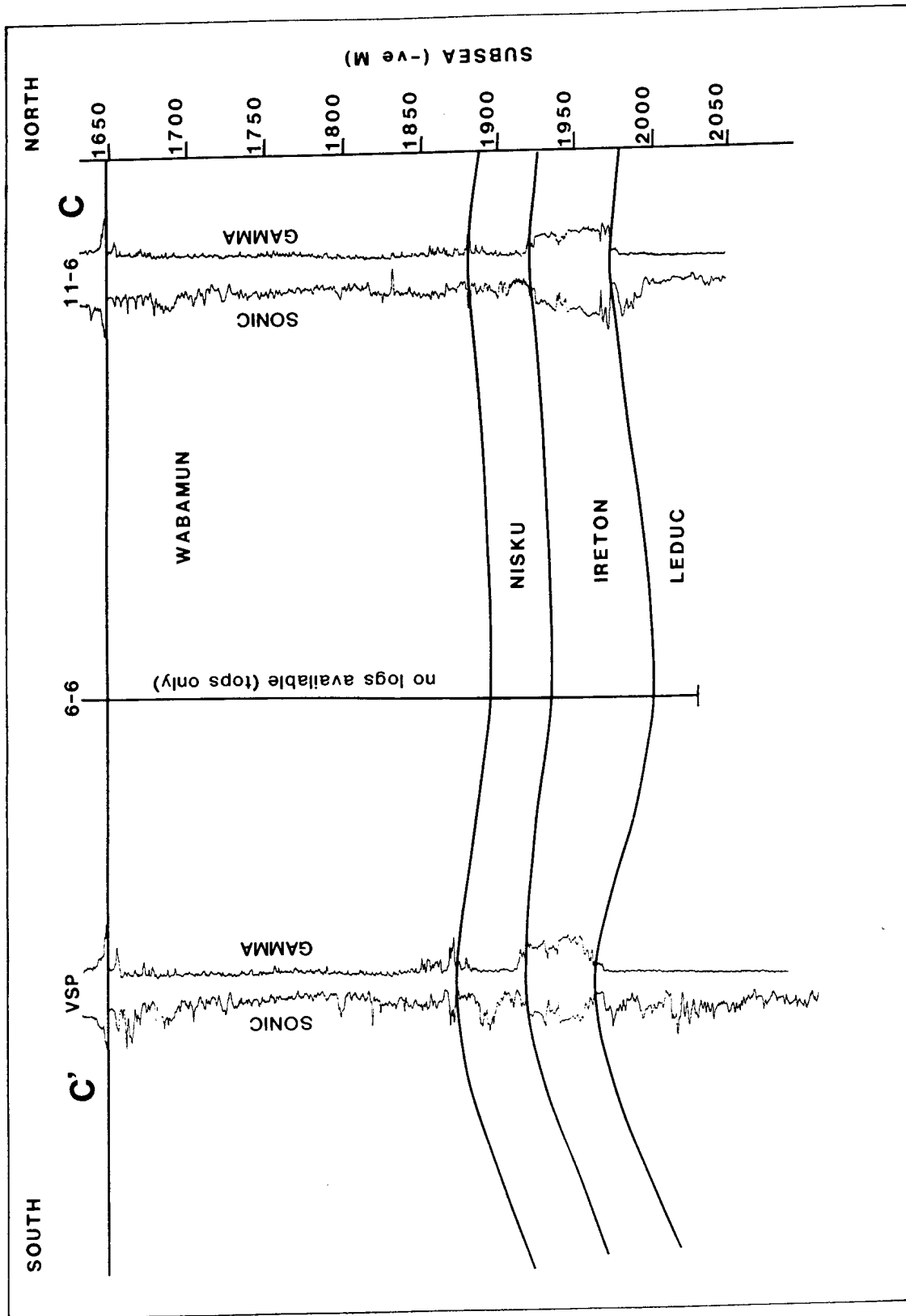


Figure 3.6 North-south geologic cross-section C-C' (refer to Figure 3.3 for location). The Leduc Formation in well 11-6 and the VSP well is productive; and well 6-6 is wet and classified as an abandoned oil well.

The VSP well (Figs. 3.5 and 3.6), although ultimately productive (from both the Nisku and Leduc), was 80 m low at the Leduc level relative to the original seismic prognosis (Hinds et al., 1994a). This pre-drill structural estimate was based on the conventional seismic data interpretation displayed as Figures 3.7 and 3.8. In the original interpretation, the Leduc event is up to 30 ms (80 m) higher between CDP traces 110 and 140 than elsewhere. Geologically, this anomaly was initially envisioned as localized, late stage accretionary reef growth. The drilling of the VSP well however, established that on the original interpretation, the top of the Leduc was miscorrelated by one cycle (between CDP traces 110 and 140). Well log data established that at the VSP well, the Leduc top was more-or-less structurally consistent time-wise with the top of the Leduc elsewhere on the seismic line.

3.4 VSP data acquisition

In an effort to resolve the apparent discrepancy between the surface seismic data (as originally interpreted; Figs. 3.7 and 3.8) and the Leduc top at the VSP well, a VSP survey was designed and conducted at that well site (by myself whilst being employed by Gulf Canada Resources Ltd). The interpretation of the VSP was expected to elucidate:

- 1) the geological significance (if any) of the misinterpreted seismic anomaly; and
- 2) the effect of possible multiple interference on the seismic data.

The VSP data were acquired at a single surface offset, located 200 m to the west of the VSP

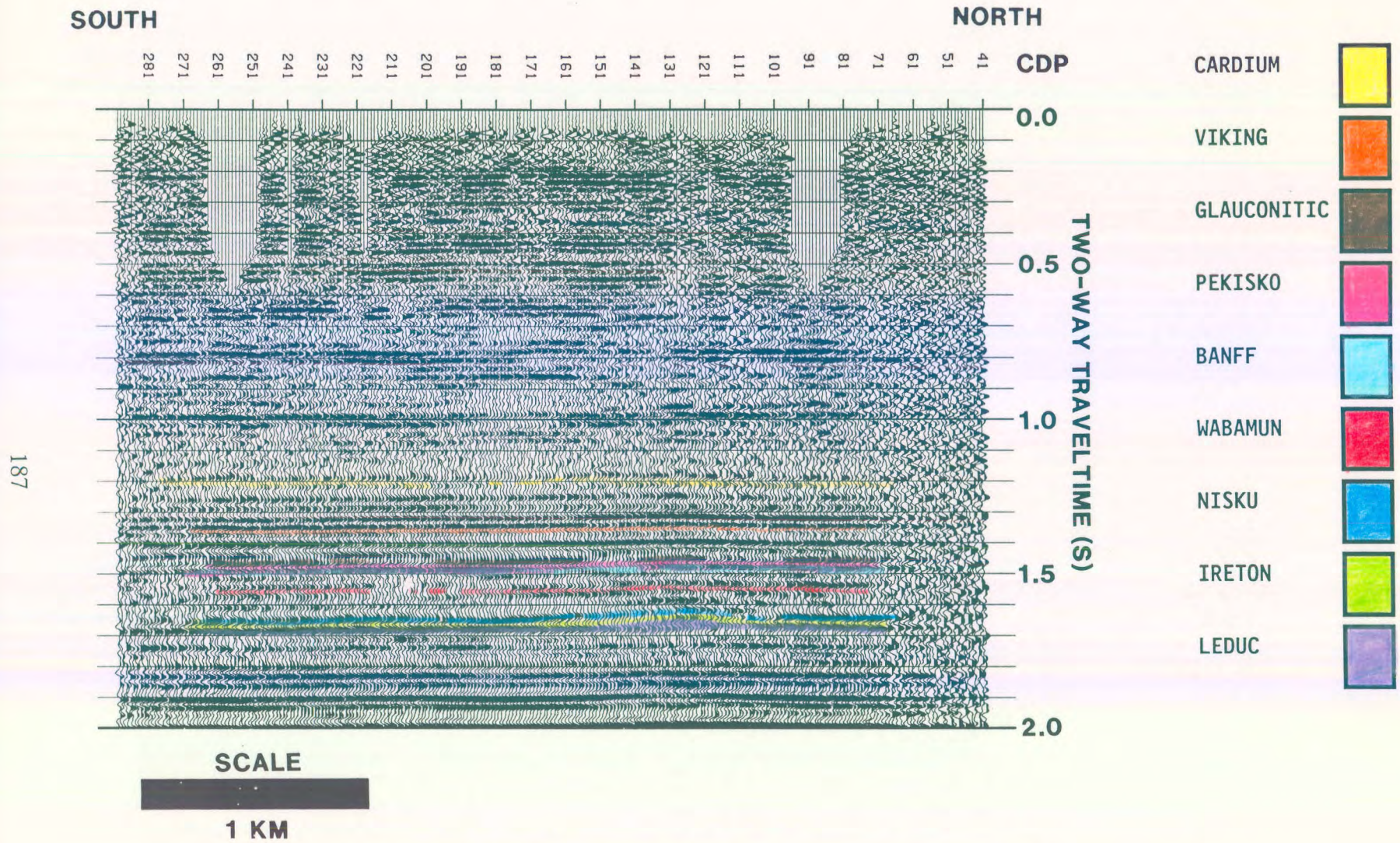


Figure 3.7 North-south oriented example seismic line showing the geophysical interpretation at the VSP well site prior to drilling (refer to Fig. 3.3 for location).

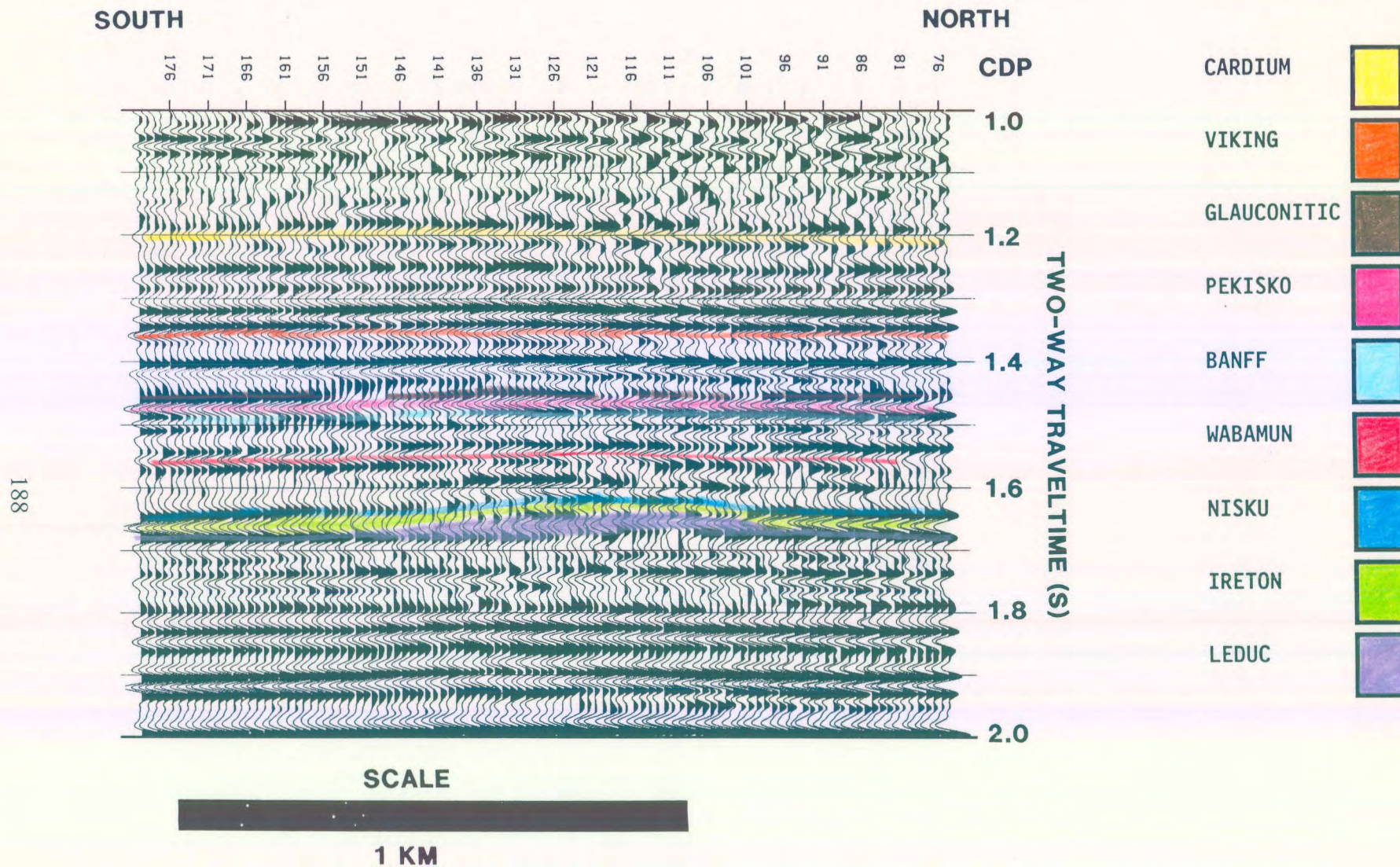


Figure 3.8 Enlarged version of the apparent time-structural anomaly at the Leduc level (shown in Fig. 3.7). The location of the VSP well site is at CDP number 116. (from Hinds et al., 1989a; Hinds et al., 1994a and c).

well on the lease access road. The source consisted of two in-series Vibroseis units utilizing an 8 to 96 Hz input sweep (designed to be compatible with the frequency content of the existing surface seismic data). The Vibroseis sweep was 13 seconds in duration and the recording length was 16 seconds, resulting in a 3 s-long cross-correlated output time series. On average, six sweeps were summed for each subsurface geophone sonde location. The source site was partially frozen and suitable coupling was achieved. The Vibroseis pad location at the offset was shifted periodically by a minor amount to ensure ground coupling stability and to minimize damage to the surface of the lease access road.

The total depth (TD) of the VSP well was 2990 m below the Kelly Bushing (KB) at the time of the running of the VSP survey. The well was drilled slightly further following the survey for stratigraphic evaluation. The elevation of the KB was at 968 m above sea level (asl) and the source at 963 m asl. The geophone sonde was lowered to TD, then raised at 20 m intervals to 2590 m below KB (30 m above the Wabamun Group). Between 2590 and 1315 m (shallowest processed sonde depth location), the sonde recording interval was increased to 25 m. Data were only recorded at three levels above 1315 m (viz at 600, 1000 and 1150 m). These data were acquired principally for sonigram calibration purposes albeit every VSP level first break time and corresponding depth could be used during the sonic log calibration (Hinds et al., 1994c). At each sonde location, the three-component geophone tool was locked in place in the borehole with the locking arm.

The data were recorded at a 2 ms sample interval using the SSC 1078 micro-Vax based system. The recording filter was set at OUT/OUT.

The offset location was chosen to be situated behind a bend in the road so that the source was not in direct line of sight of the well borehole along the lease road (the road was built by the well operator to gain access to the well lease). Another criterion in the choice of the source location was the utilization of a patch of trees that was in the corner of the road between the source and the well which would assist in the reduction of the amplitude of the pseudo-Rayleigh wave propagation along the ground surface thereby aiding in the elimination of groundroll induced interference (tube waves) with the downgoing and upgoing signal.

3.5 VSP interpretive processing

As an aid to the interpretation of the VSP data a suite of interpretive processing panels (IPP's) were generated for these data (Hinds et al., 1989a, Hinds et al., 1991a, 1991b and 1993c, Hinds, 1991c, Hinds et al., 1993a, Hinds et al., 1993b, 1994a and 1994c). The panels allowed the progressive interpretation of the data in order to facilitate the quality control of the processing sequence. More specifically the panels displayed:

- 1) up- and downgoing P-wavefield separation
- 2) deconvolution of the separated upgoing P-waves using an inverse filter calculated from the separated downgoing P-waves; and
- 3) inside and outside corridor stacks of both the deconvolved and nondeconvolved upgoing P-waves.

3.5.1 P-wave separation to output $Z_{up}(+TT)$ data

In the initial phase of processing, the upgoing and downgoing P-waves of the vertical geophone data, $Z(FRT)$, were separated. This separation procedure is illustrated in the wavefield separation IPP (Hinds et al., 1989a and Hinds et al., 1994c) in Figure 3.9.

The $Z(FRT)$ data after trace normalization and the gained $Z(FRT)$ data are displayed in panels 1 and 2 of Figure 3.9. Several primary upgoing reflections can be identified on these data: viz Viking (at a depth of 2100 m); Mannville (the Glauconitic at 2158 m); and Banff (2293 m). Note that the series of strong reflections that originate below the VSP well TD do not intersect the first break curve, and therefore cannot be confidently classified as either primary or multiple events (Hinds et al., 1989a and Hinds et al., 1994c).

The gained $Z(-TT)$ data in panel 3 illustrate that the downgoing wavetrain (the multiples) is comprised mostly of high amplitude surface-generated and less prominent interbed multiples. Surface-generated multiples are recorded on all of the traces and are manifested as laterally continuous events that arrive after the first break events. Interbed multiples, in contrast, do not extend over the entire depth range. If present, they would be present on the deeper traces only (Hinds et al., 1989a).

The downgoing waves contained in panel 3 were separated from the combined wavefield data using an eleven-point median filter and displayed in panel 4, $Z_{down}(-TT)$. The residual upgoing wave content in the $Z_{down}(-TT)$ data of panel 4 is minimal. The upgoing waves,

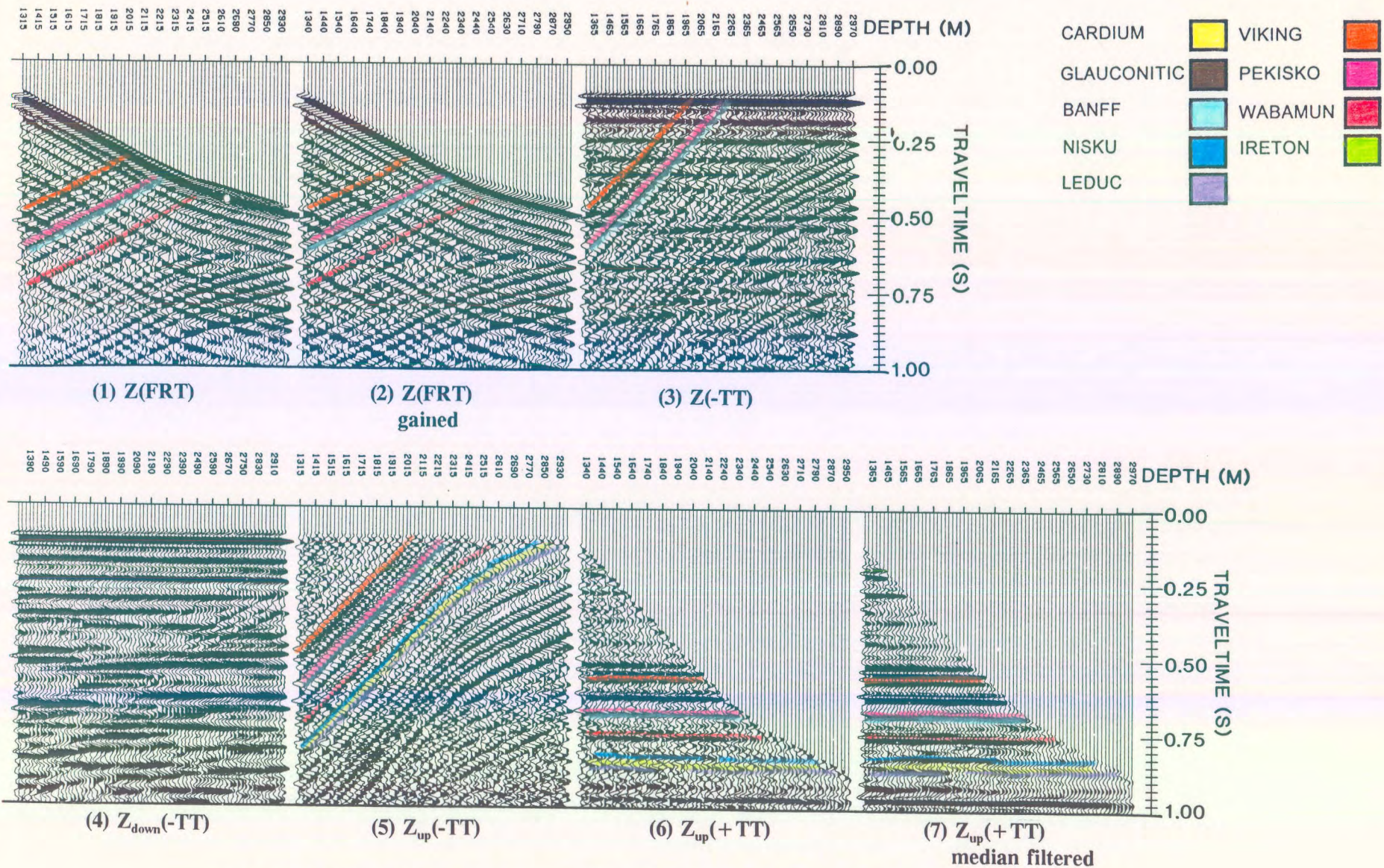


Figure 3.9 Interpretive processing panel depicting the wavefield separation of the near offset VSP data (from Hinds et al., 1989a; Hinds et al., 1994a and c)

$Z_{up}(-TT)$ in panel 5, were separated by subtracting a scaled version of the downgoing wavefield, $Z_{down}(-TT)$ of panel 4, from the combined wavefield, $Z(-TT)$ of panel 3, following the methodologies described by Balch and Lee (1984), Hardage (1985), Hinds et al., 1989a, Hinds et al., 1994c and others. The two final panels (6 and 7) in the wavefield separation IPP display the separated upgoing waves, $Z_{up}(+TT)$, before and after the application of a three-point median filter. The equalized amplitudes of the Cardium, Viking, Glauconitic, Pekisko, Banff, Wabamun, Nisku, Ireton and Leduc events in $+TT$ time configuration are interpreted in the final panel and confirmed on the previous panels.

Successful wavefield separation is critical to the interpretation of the VSP data, for any residual upgoing wavefield in the $Z_{down}(-TT)$ data in panel 4, will be subtracted out of the upgoing wave data. Note that the median filter (panels 4 and 5) has not been particularly effective in separating those upgoing waves that arrive after the first break time on the deepest sonde location trace (panel 4). This is acceptable however only because these events are below the zone of interest.

3.5.2 VSP deconvolution

Surface-generated and interbed multiples are totally represented on the separated downgoing wavetrain shown in panel 4 of Figure 3.9. The initial downgoing pulse (except in the case of head wave contamination) is the primary downgoing P-wave; any downgoing waves that arrive later are a result of multiple reflections. These multiple events can be effectively removed by deconvolving the upgoing wave data with an inverse filter derived from an

analysis of the downgoing wavetrain (Hinds et al., 1989a). The deconvolution IPP shown in Figure. 3.10, as reviewed in chapter 2, enables the interpreter to control the quality of the VSP (up/down) deconvolution process (Hinds et al., 1994c). Panels 1, 2, 6 and 7 in Figures 3.9 and 3.10 are bulk time shifted to facilitate the IPP display.

The first two panels (Fig. 3.10) are the unfiltered and median-filtered $Z_{up}(+TT)$ data. Panels 3 and 4 are the nondeconvolved $Z(-TT)$ and $Z_{up}(-TT)$ data. The fifth panel is the deconvolved upgoing combined wavefield data, $Z_{(decon)}(-TT)$, and represents an example of downgoing wavefield deconvolution applied to the combined (total) wavefield as first reported in Smidt (1989). The data following the deconvolution step were then wavefield separated, normalized around the first breaks and then corrected for spherical divergence. The deconvolved data were thereafter time shifted to pseudo-two-way traveltime and the resultant $Z_{up(decon)}(+TT)$ data are displayed in panel 6. A comparison of the median-filter-enhanced nondeconvolved ($Z_{up}(+TT)$ in panel 2) and deconvolved upgoing ($Z_{up(decon)}(+TT)$ in panel 7) wavefield data indicates that the deconvolution process has enhanced the frequencies of the upgoing waves and yet preserved the integrity of the primary reflections.

The effect of the interference by multiples and the relative success of the deconvolution operator, can be appreciated by the analysis of the VSP Glauconitic event. In the $Z_{up}(+TT)$ data in panel 2 (Fig. 3.10), the nondeconvolved Glauconitic event is relatively continuous at sonde depths below the Cardium (1825m). At shallower depths, the Glauconitic event is partially masked by a possible interbed multiple that has as its lower generating surface, the top of the Cardium. On the $Z_{up(decon)}(+TT)$ data in panel 7, the Glauconitic event is relatively continuous at all the sonde depths implying that the interfering multiple event has

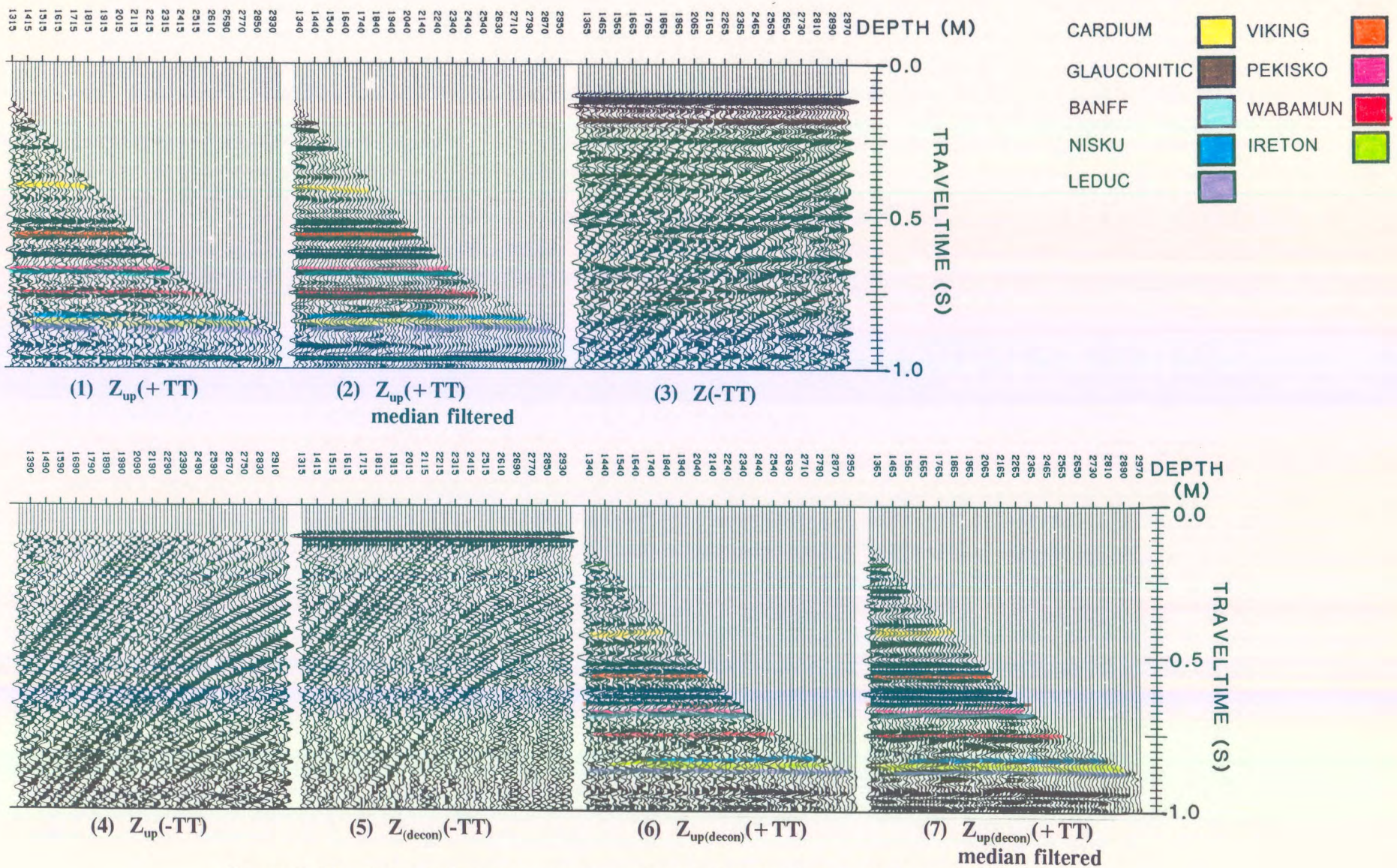


Figure 3.10 Interpretive processing panel depicting the deconvolution of the near offset VSP data (from Hinds et al., 1989a; Hinds et al., 1994a and c).

been attenuated.

Note that the Nisku and Leduc events are relatively low amplitude (in comparison to the Nisku and Leduc events on the seismic line away from the VSP well site) possibly as a result of destructive multiple interference. On the $Z_{up}(+TT)$ data (panels 1 and 2), a strong peak exists just above (overlapping) the Nisku event from the shallowest trace out to the 2140 m trace. The Nisku event is low amplitude in comparison. After deconvolution, the Nisku event on the $Z_{up(decon)}(+TT)$ data is laterally continuous in amplitude. The anomalous multiple-induced peak before the deconvolution can be estimated to be up to 5 ms higher than the overlapped Nisku event.

3.5.3 Inside and outside corridor stacks

Multiple contamination on the VSP upgoing waves can be closely examined using the inside and outside corridor stacks of both the $Z_{up}(+TT)$ and $Z_{up(decon)}(+TT)$ data. The inside corridor stack of the $Z_{up}(+TT)$ data contains both the primary and multiple events, whereas the outside corridor stack data should be relatively free of multiples. If the deconvolution is successful in removing the multiples, then both the inside and outside corridor stacks for the $Z_{up(decon)}(+TT)$ data will be predominated by primary reflections (Hinds et al., 1989a and Hinds et al., 1994c).

In Figure 3.11, the outside and inside corridor stacks are shown in panels 3 and 4, respectively. The input data that are stacked to create the inside and outside corridor stacks are shown in panels 2 and 5. The $Z_{up}(+TT)$ data shown in panels 1 and 6 are placed beside

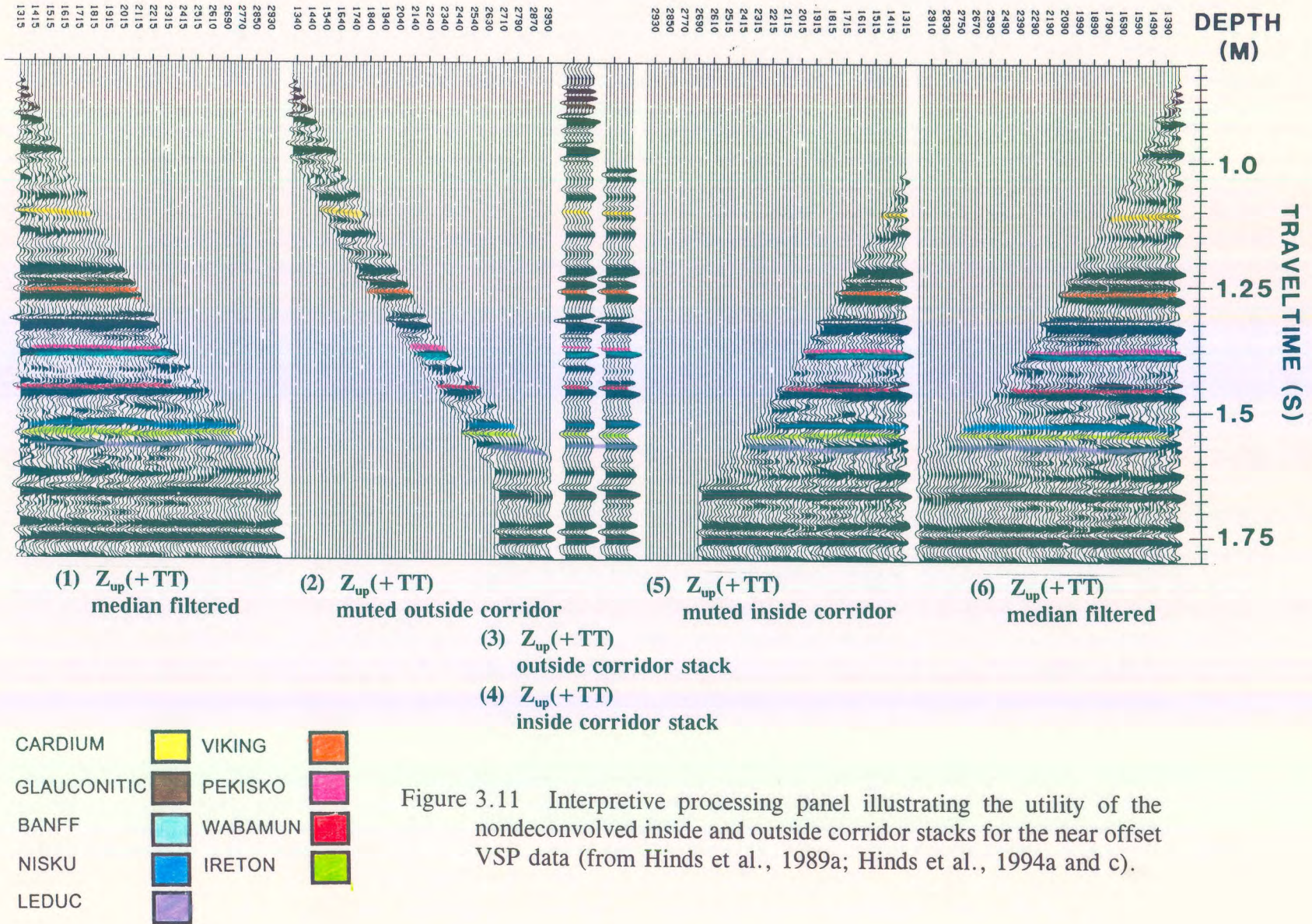


Figure 3.11 Interpretive processing panel illustrating the utility of the nondeconvolved inside and outside corridor stacks for the near offset VSP data (from Hinds et al., 1989a; Hinds et al., 1994a and c).

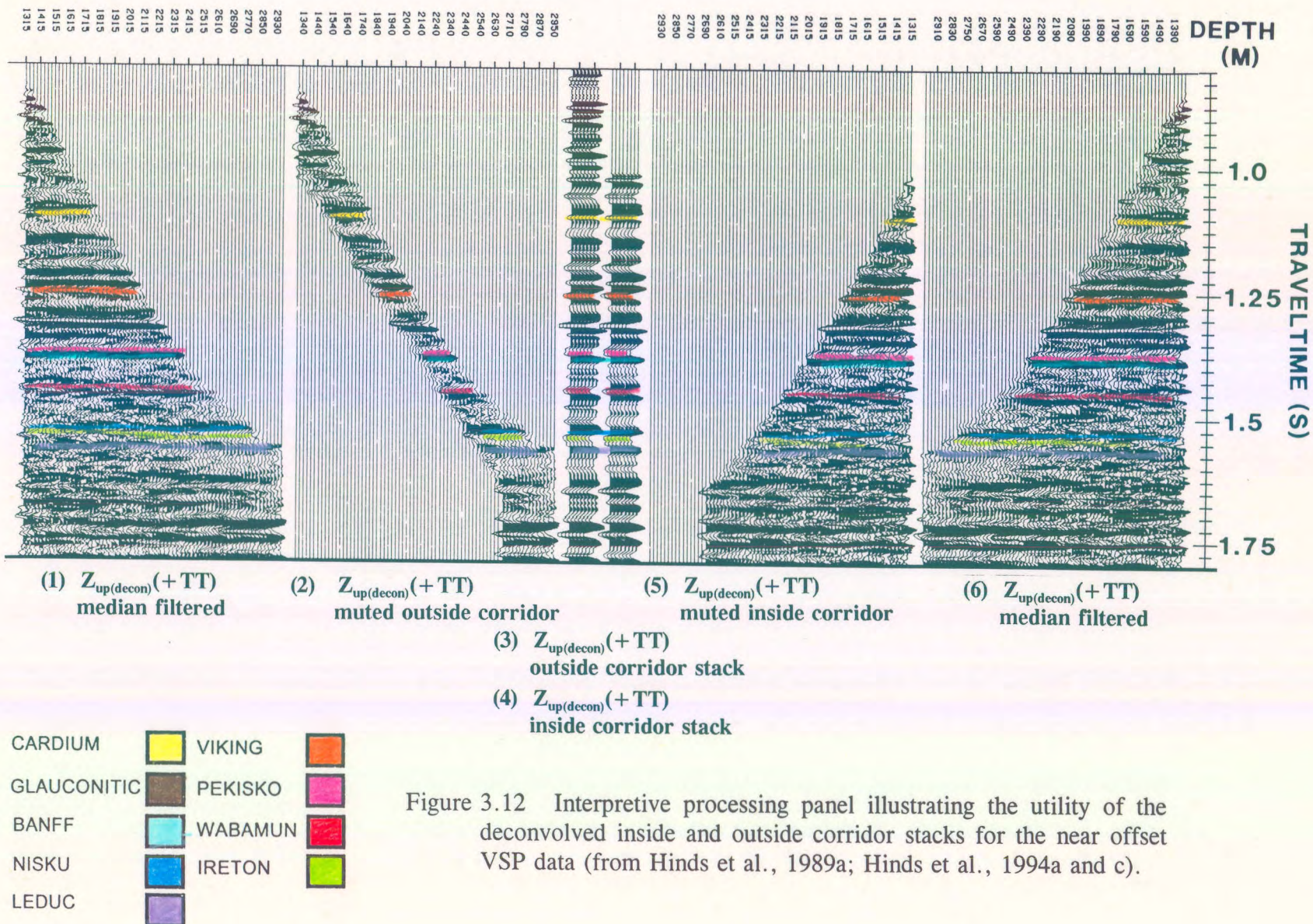


Figure 3.12 Interpretive processing panel illustrating the utility of the deconvolved inside and outside corridor stacks for the near offset VSP data (from Hinds et al., 1989a; Hinds et al., 1994a and c).

the corridor muted $Z_{up}(+TT)$ data of panels 2 and 5 to show what has been muted.

The inside and outside corridor stacks (panels 4 and 3, respectively) differ below both the Cardium and Banff (at the Wabamun, Nisku and to a lesser degree at the Leduc events) suggesting that multiple interference occurs within these zones. An explanation is that the noticeable effect of the multiples contaminating the inside corridor stack is not represented within the outside corridor stack (Hinds et al., 1994a).

A comparison of the $Z_{up(decon)}(+TT)$ data inside and outside corridor stacks (Fig. 3.12), indicates that multiple interference was substantially attenuated by deconvolution. More specifically, note that the inside and outside corridor stacks of the $Z_{up(decon)}(+TT)$ data are similar, suggesting that deconvolution has effectively attenuated the multiple contamination evident on the inside corridor stack of the $Z_{up}(+TT)$ data (panel 1; Fig. 3.11).

3.6 Integrated interpretation

The reinterpreted conventional surface seismic line incorporating the VSP results (Figs. 3.7, 3.8, 3.14, and 3.15) is displayed on the left-hand side of Figure 3.13. A synthetic seismogram for the VSP well, the $Z_{up}(+TT)$ data inside corridor stack, and the $Z_{up(decon)}(+TT)$ data outside corridor stack are time-tied to the seismic line at the VSP well site (CDP number 127). The inside and outside corridor stacks and the synthetic seismogram, juxtaposed between the two separated parts of the seismic section at the VSP well location, allows a comparison between the three methods of the time-tie to the Leduc surface seismic event.

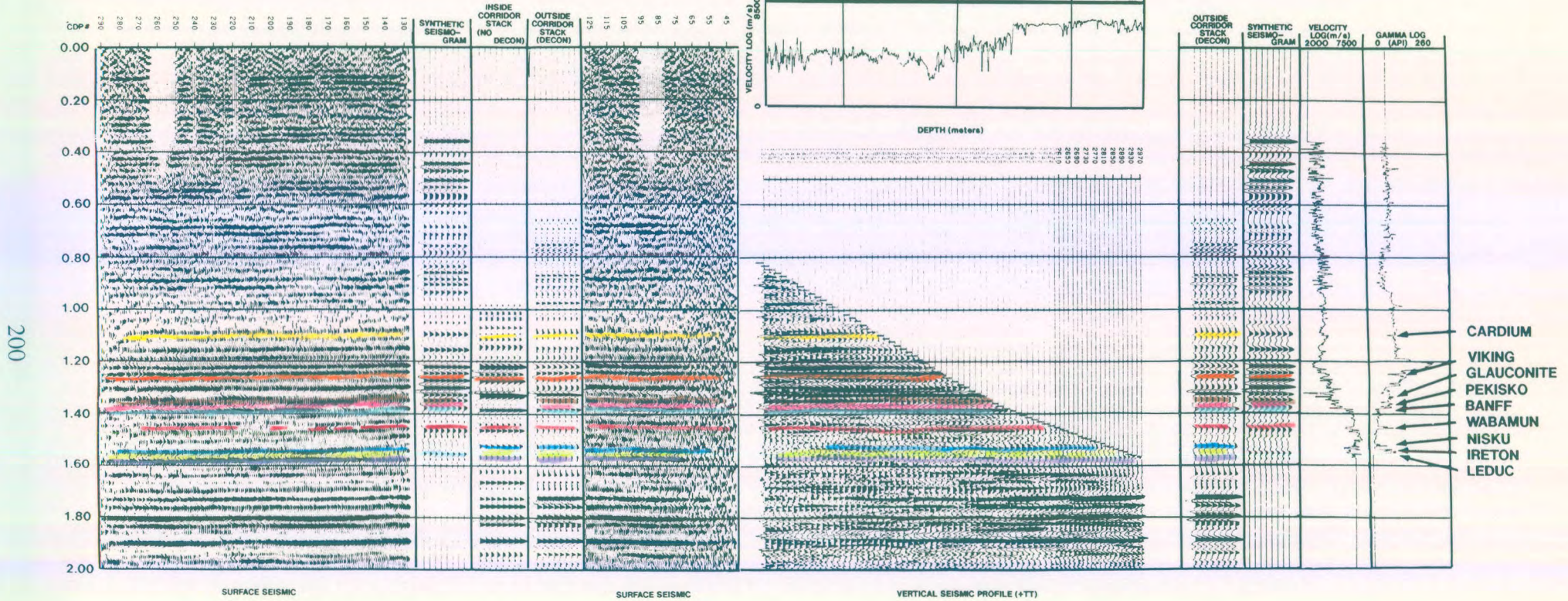


Figure 3.13 Integrated interpretive display (IID) showing the interpretation of the available exploration data for the Lanaway Field case study. The synthetic seismogram was generated using a zero-phase, 30 Hz centre frequency Ricker wavelet (from Hinds et al., 1989a; Hinds et al., 1994a and c).

On the right-hand side of Figure 3.13, the VSP data are time-tied to the seismic line, the $Z_{\text{up(decon)}}(+\mathbf{TT})$ data outside corridor stack, the VSP well synthetic seismogram, the VSP well velocity log, and the VSP well gamma ray log. The horizontal scale (depth axis) of the VSP display, $Z_{\text{up(decon)}}(+\mathbf{TT})$, and the scale used for the horizontally-oriented VSP well sonic and gamma ray log depth displays are the same. The outside corridor stack (containing predominantly primary events), the synthetic seismogram, and the two well logs (converted to time) allows for the comparison of the corridor stack, the synthetic seismogram, and the well log data. Because the synthetic seismogram is calculated from the sonic log (where the sonic data are virtually collected continuously) in the same area, the synthetic will have higher resolution than the corridor stack. Since the range of the wavelengths contained in the $Z_{\text{up(decon)}}(+\mathbf{TT})$ data are the same as for surface seismic, in most cases the outside corridor stack interpretation will tie to the seismic data interpretation more closely.

The VSP well sonic and gamma logs are displayed in depth and plotted immediately above the $Z_{\text{up(decon)}}(+\mathbf{TT})$ data in Figure 3.13. The correlation between these data can be illustrated by considering the top of the Wabamun.

Lithologically, the top of the Wabamun in the VSP well is represented by the shale/carbonate contact at a depth of 2616 m. Within the VSP data, there are recorded VSP traces at 2610 m and then below the Wabamun formation top is at 2630 m. The Wabamun event is therefore identified as the trough (some interpreters prefer to use the zero-crossing) located in time between the first breaks for the 2610 and 2630 m sonde depths (approximately 1450 ms). In a similar fashion, the other VSP upgoing events can be identified and then correlated directly to the surface seismic line at CDP number 127, the nondeconvolved inside corridor

stack, the deconvolved outside stack, and the synthetic seismogram, velocity and gamma log (displayed in time) for the VSP well.

The location of the Leduc event is of the greatest interest to the interpreter. Note that this reflection, on the surface seismic and VSP data at the VSP well site, is a half cycle lower than initially interpreted by the owners of the data (pre-VSP interpretation shown in Figs. 3.7 and 3.8). The revised surface seismic interpretation is presented in Figures 3.14 and 3.15. A correlation of the VSP and the surface seismic data indicates that the Leduc top was incorrectly identified at the VSP well site on the pre-VSP interpretation. This miscorrelation explains why the Leduc top came in 80 m low relative to prognosis; however, it does not explain why the surface seismic line was originally misinterpreted. Anomalous Nisku, Ireton and Leduc surface seismic signatures between CDP numbers 90 to 140 may have resulted in a misleading interpretation (Figs. 3.14 and 3.15).

This seismic package from the Wabamun to the Leduc events is characterized by:

- 1) positive time-structural relief (of the order of 5 ms) along both pre-Leduc and deeper post-Leduc events;
- 2) an anomalously low-amplitude Leduc event; and
- 3) an anomalous reflection pattern within the Wabamun/Leduc interval (drape over the reef edge by the Wabamun and the Nisku events).

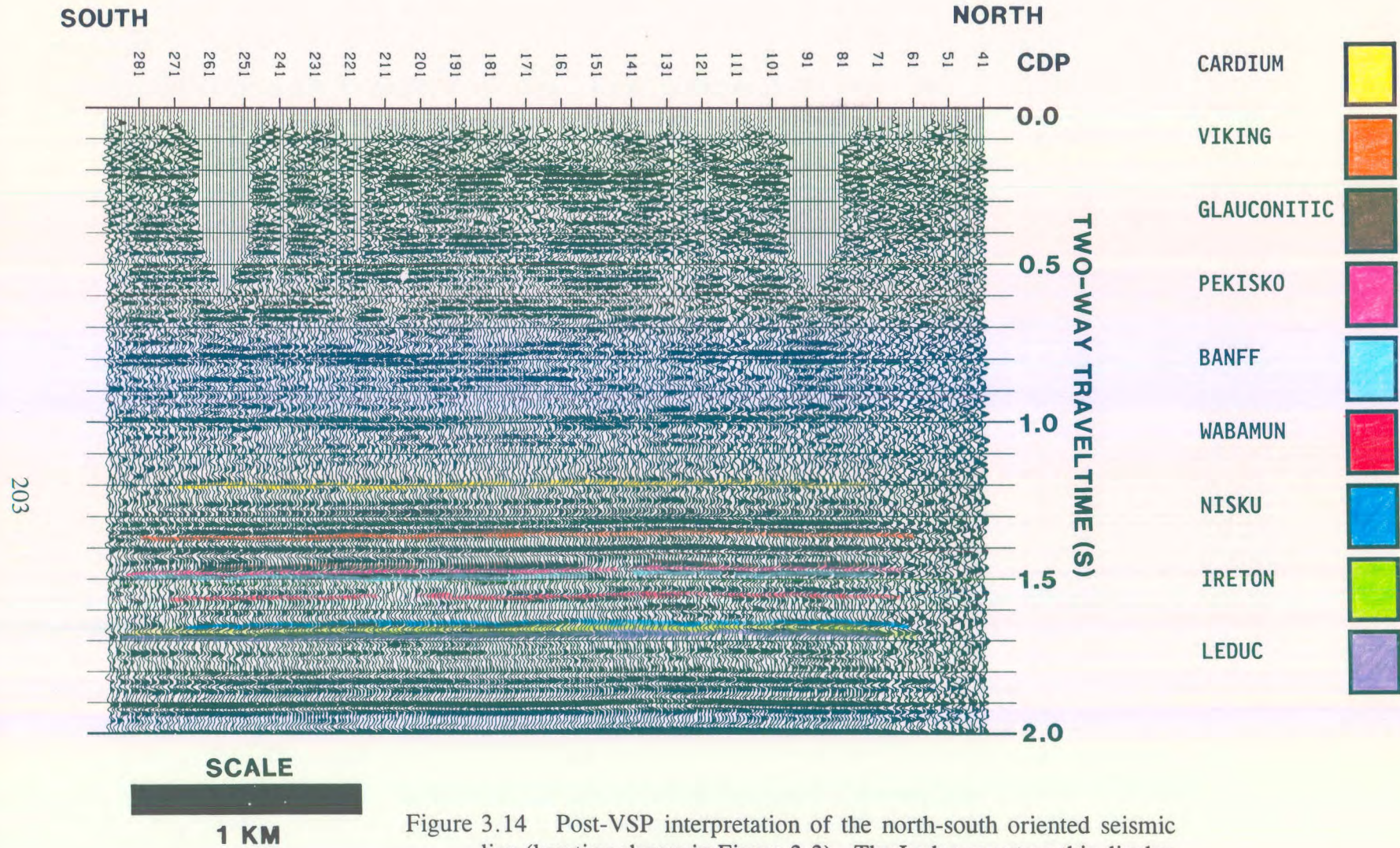


Figure 3.14 Post-VSP interpretation of the north-south oriented seismic line (location shown in Figure 3.3). The Leduc event on this display is only slightly time-structurally elevated at the VSP well site and the updated interpretation is consistent with well log control (from Hinds et al., 1989a; Hinds et al., 1994a and c).

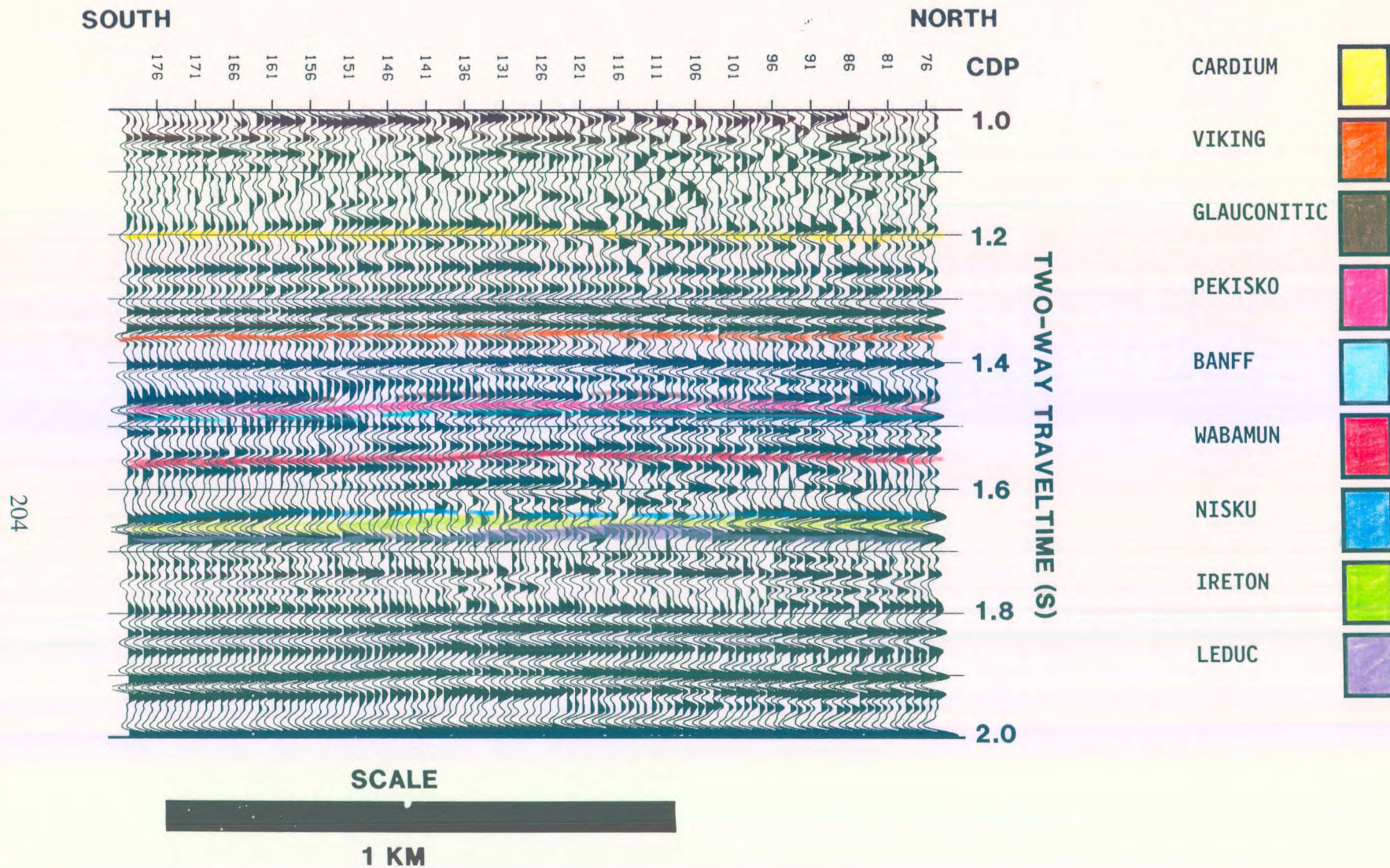


Figure 3.15 Enlarged version of the post-VSP interpretation of the north-south oriented seismic line (shown in Fig. 3.14). The VSP well location is at CDP number 116 (from Hinds et al., 1989a; Hinds et al., 1994a and c).

These three types of seismic signatures were initially interpreted to be diagnostic of the reef and were attributed to an envisioned 80 m of anomalous accretionary reef growth. The time-structural relief in particular was attributed to velocity pull-up and drape, respectively.

The VSP well dataset conclusively established that the Leduc was misidentified on the original interpretation (Figs. 3.7 and 3.8) and that the observed seismic anomalies are not related to late stage accretionary reef growth (Hinds et al., 1994a). There appear to be three most probable candidates for the explanation for the seismic anomaly:

- 1) structural relief at the Pekisko and Shunda pre-Cretaceous subcrops;
- 2) stratigraphic anomalies (possible patch carbonate reef) within the Winterburn Group (Fig. 3.1c); and
- 3) structural thinning of the Ireton near the reef crest (as shown in Fig. 3.6).

Dealing with the first explanation, it is conceivable that the observed anomaly is partially caused by erosional relief at the pre-Cretaceous subcrop (Pekisko and Shunda). As illustrated by the velocity log (Fig. 3.13), the velocity of seismic wave propagation of the Shunda and Pekisko Formations are higher than those of the overlying Cretaceous sediment. Positive erosional relief at the Shunda/Pekisko level would cause pre-Cretaceous events to be time structurally "pulled-up", and the overlying seismic events would appear to be anomalously draped as a result of compaction of the formations above the Pekisko and Shunda material (Anderson et al., 1989a). However, no Shunda Formation material was intersected at the

VSP well in comparison to 14 m at the 6-6 well location (as shown in the Shunda isopach map in Fig. 3.16). The combined Shunda/Pekisko thicknesses at the VSP well and 6-6 are 43 and 55 m, respectively.

The second suggested explanation for the observed time-structure and amplitude anomalies is a lithologic variation within the Winterburn Group. It is possible that a localized Nisku Formation (Winterburn Group) patch reef has developed above the crest of the underlying Leduc reef (similar to the patch reef suggested in the case study in Rennie et al., 1989). The envisioned carbonate build-up would be characterized by a velocity pull-up, time-structural drape, and a character change within the Winterburn Group. Unfortunately, due to the absence of core control within the Winterburn Group, this suggestion cannot be confirmed or negated; however it should be noted that the VSP well and well 6-6 intersected 47.4 and 39.3 m of Nisku, respectively. The added Nisku build-up and corresponding porosity could conceivably contribute to the observed time-structural anomaly. The patch reef could have resulted from the localized structural high resulting from the presence of the reef edge.

The third possibility suggested is that subtle draping of Ireton sediments above the reef crest at the VSP well as has already been highlighted in the north-south geologic cross-section shown in Figure 3.6 could be the cause of the misinterpretation. The isopach map of the Ireton in Figure 3.17 shows that the north-south oriented seismic line (Figs. 3.7 and 3.8) traverses a thick succession of Ireton shales at well 6-6 (66 m), while it is relatively thinner over the reef crest at the VSP well (43 m) and it thickens in LSD 30 towards well 6-30.

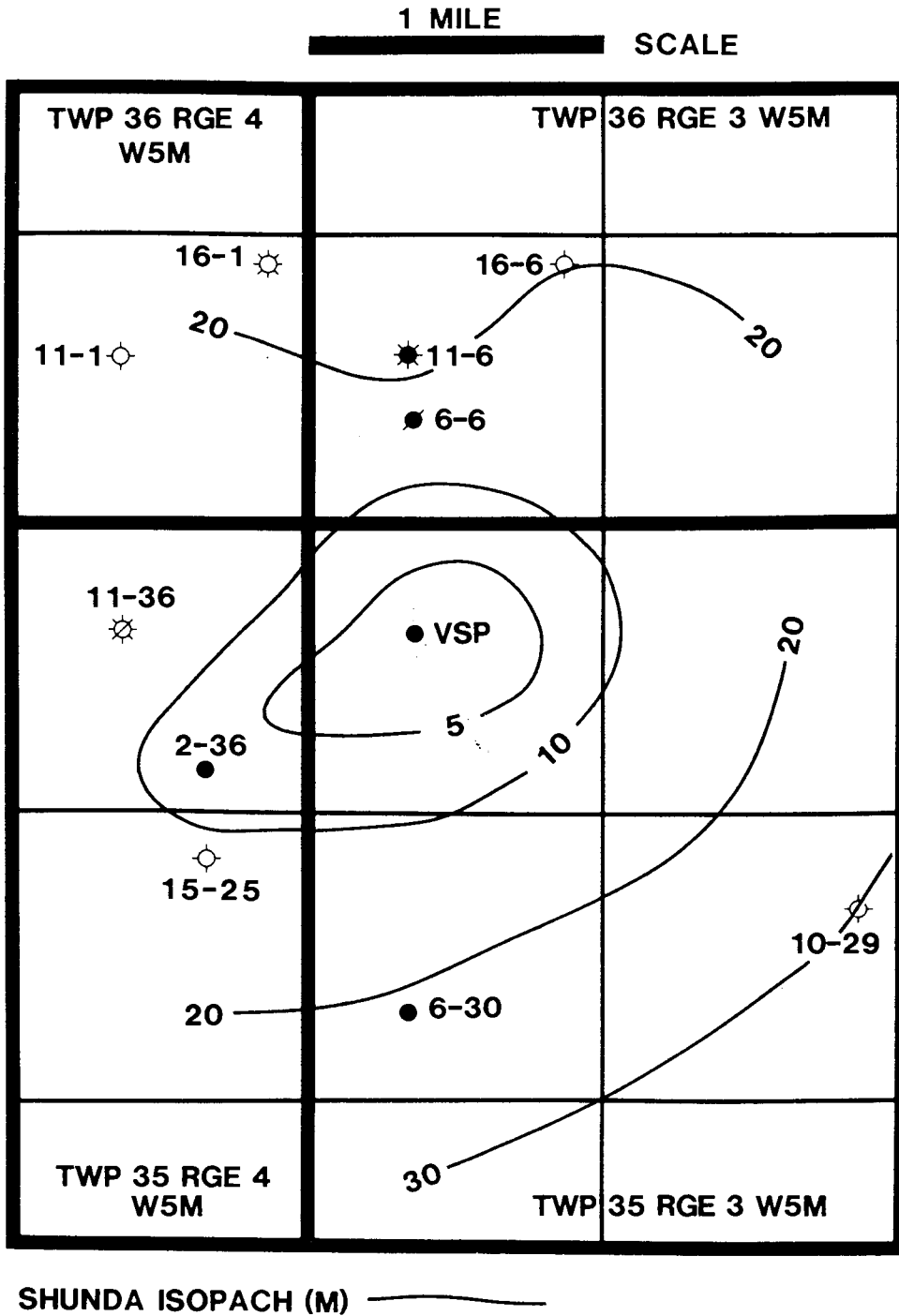


Figure 3.16 Shunda isopach map showing the absence of Shunda at the VSP well. The pre-Cretaceous anomaly may reflect only to a minor to negligible degree a possible source of the seismic defocussing seen on the seismic image of the Ireton to Leduc events at the VSP well (from Hinds et al., 1994a and c).

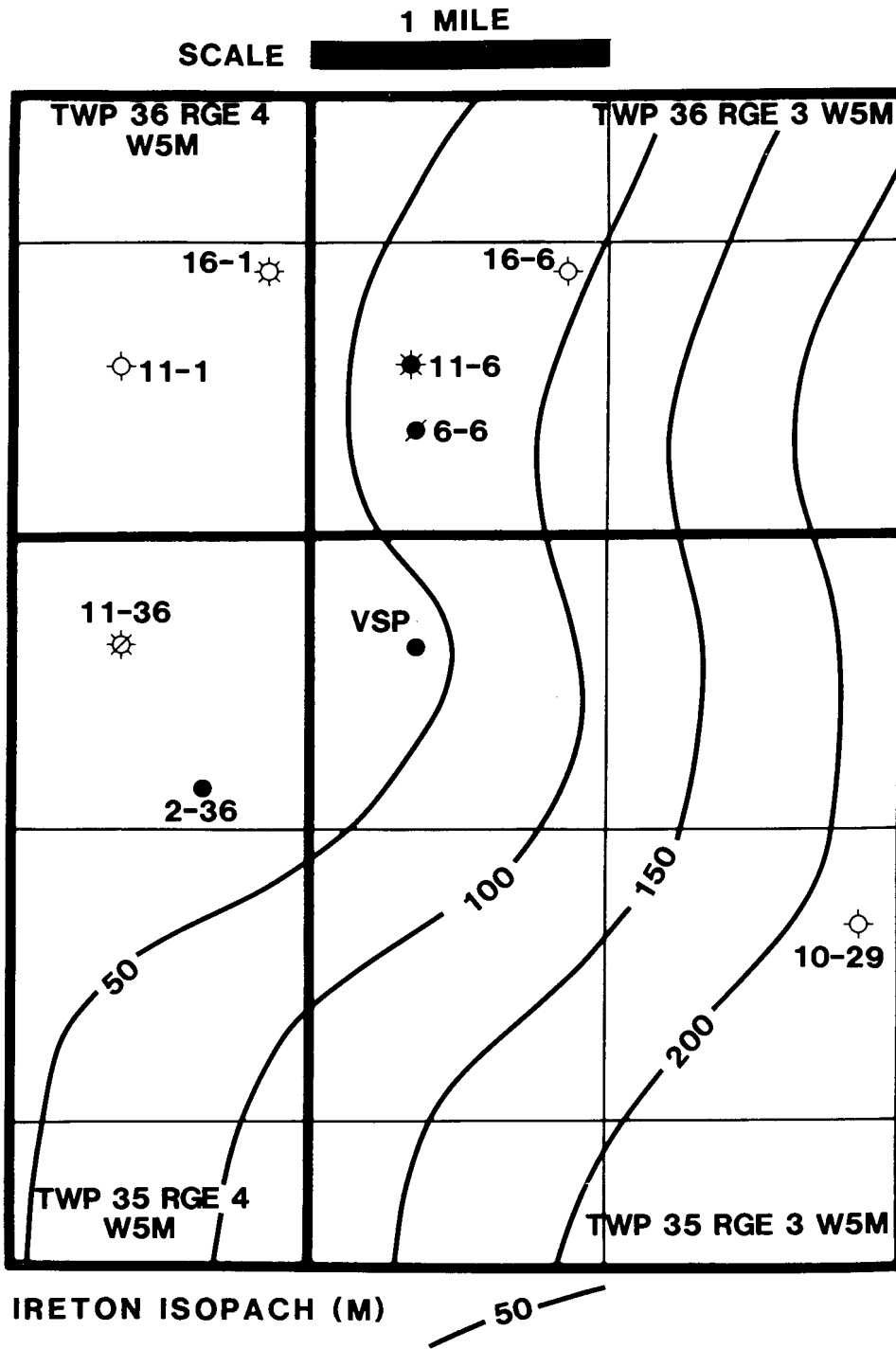


Figure 3.17 Ireton isopach map showing the drape of the Ireton shales along the example seismic line (shown in Figs. 3.14 and 3.15). Considerable time-structural relief along the Ireton event can be correlated from the seismic to the isopach map (from Hinds et al., 1994a and c).

LSD 30 is the mile by a mile section of land directly south of the LSD in which the VSP well was drilled and is shown in Figure 3.17. The Nisku to Ireton anomalous isochron values that are evident at the VSP well location return to normal ranges approximately 640 m south of the VSP well along the seismic line (Fig. 3.17). This can be seen at CDP number 200 in Figure 3.7 and corresponds to the location of the intersection of the seismic line and the 100 m Ireton isopach contour in Figure 3.17. The correlation of the seismic anomaly at the Nisku, Ireton and Leduc levels to the Ireton isopach suggests that the increasing Ireton isopach (away from the well both to the North and South) caused an anomalous seismic response to the subtle drape over the reef crest at the VSP well and this tuning effect can be contributing to the seismic event anomaly (drape and pullup) at the VSP well.

The initial interpretation of the seismic events at the VSP well could then be resolved to be caused by a combination of thinning of the Ireton Formation and an increasing porosity thickness of the Nisku Formation. Part of the Nisku Formation material could be productive as indicated by an anomalous velocity character in the sonic logs (possible patch reef carbonates) that begins approximately 10 m below the Nisku top in the VSP well.

Furthermore, from the inside and outside corridor stacks of both the $Z_{up(decon)}(+TT)$ and the $Z_{up}(+TT)$ data as displayed in Figures 3.11 and 3.12, it is apparent that there is multiple contamination immediately below the Wabamun event that may cause difficulties with the interpretation of the Wabamun throughout the study area, and at the Nisku level. However, the effect of the multiple at the Nisku level can account for no more than 5 ms of the anomaly and therefore would be a minor factor in possible causes of the seismic anomaly

around the VSP-well.

Other interesting observations can be made from the integrated sonic log, VSP corridor stacks and the seismic data in the immediate vicinity of the VSP well. The Glauconitic to Banff sequence and top of the Leduc are poorly resolved on the surface seismic data (relative to the outside corridor stack). One possible explanation is that the surface seismic signatures of events within the Glauconitic to Banff interval may be degraded as a result of multiple (interbed) interference.

The correlation of the data presented in Figure 3.13 has allowed for the confident reinterpretation of the surface seismic data in the vicinity of the VSP well, and further elucidated the possible origin of the observed anomaly. These reinterpreted seismic data are displayed as Figures 3.14 and 3.15. (The anomaly in the immediate vicinity of the VSP well is enlarged in scale and displayed in Fig. 3.15.)

3.7 Discussion on integrated interpretation

The VSP well was drilled into the Leduc reef at Lanaway Field, south-central Alberta, in order to evaluate an anomaly observed on surface seismic data. The pre-well interpretation of these seismic data suggested that the VSP well would encounter up to 80 m of anomalous accretionary reef growth at the Leduc level. However, drilling confirmed that the Leduc at the VSP well was more-or-less regional and indicated that the initial interpretation was inaccurate as the seismic events were a response to something other than anomalous Leduc buildups and corresponding anomalous Ireton thinning. In order to elucidate the discrepancy between the pre-well seismic interpretation and the drilling results, a near-offset VSP was run at the VSP well site.

The interpretively processed VSP data provided invaluable information regarding the seismic anomaly. On the basis of these data, it was possible to:

- 1) establish that the Leduc event had been miscorrelated on the pre-well seismic interpretation;
- 2) correctly correlate the Leduc event at the VSP well site; and
- 3) further elucidate the nature of the observed anomaly at the VSP well site.

On the basis of VSP data and the integrated interpretation, it has been suggested that the

observed seismic anomaly at the VSP well is most likely attributable to (Hinds et al., 1994a):

- 1) velocity and structural drape resulting from anomalous erosional relief at the pre-Cretaceous subcrop, and the effects of associated interbed multiple reflections;
- 2) localized patch reef development within the Winterburn Group; and
- 3) tuning resulting from thinning of the Ireton Formation in the vicinity of the VSP-well.

The most likely effects are the Winterburn patch reef and the tuning effect of an Ireton drape.

CHAPTER 4

THE RICINUS FIELD CASE STUDY

On the basis of the interpretation of conventional surface seismic data, an exploratory well (locally referred to as the VSP well in this chapter) was drilled in the Ricinus Field, southern Alberta, Canada. The prognosis was that the VSP well would encounter the updip, raised rim of the Leduc Formation (Devonian Woodbend Group) reef complex at Ricinus Field, and would penetrate on the order of 140 m of gas pay. To the consternation of the exploration team, the well encountered only off-reef shales. The Ricinus Field had been previously defined by existing wells; some of which are shown in Figure 4.1.

As part of an investigation into the seismic images of the surrounding area, two vertical seismic profiles were conducted at the VSP well site in an effort to:

- 1) resolve the apparent discrepancy between the interpreted surface seismic data and the geology at the VSP well; and
- 2) evaluate the feasibility of whipstocking the VSP well in the direction of the reef complex.

One of the VSP surveys had a source offset of 199 m (near offset) and the other had a source offset of 1100 m (far offset). These data allowed the more confident and geologically consistent reinterpretation of the surface seismic data, and clearly indicated that whipstocking was not an economically viable option (Hinds et al., 1989a; Hinds et al., 1993c; and Hinds

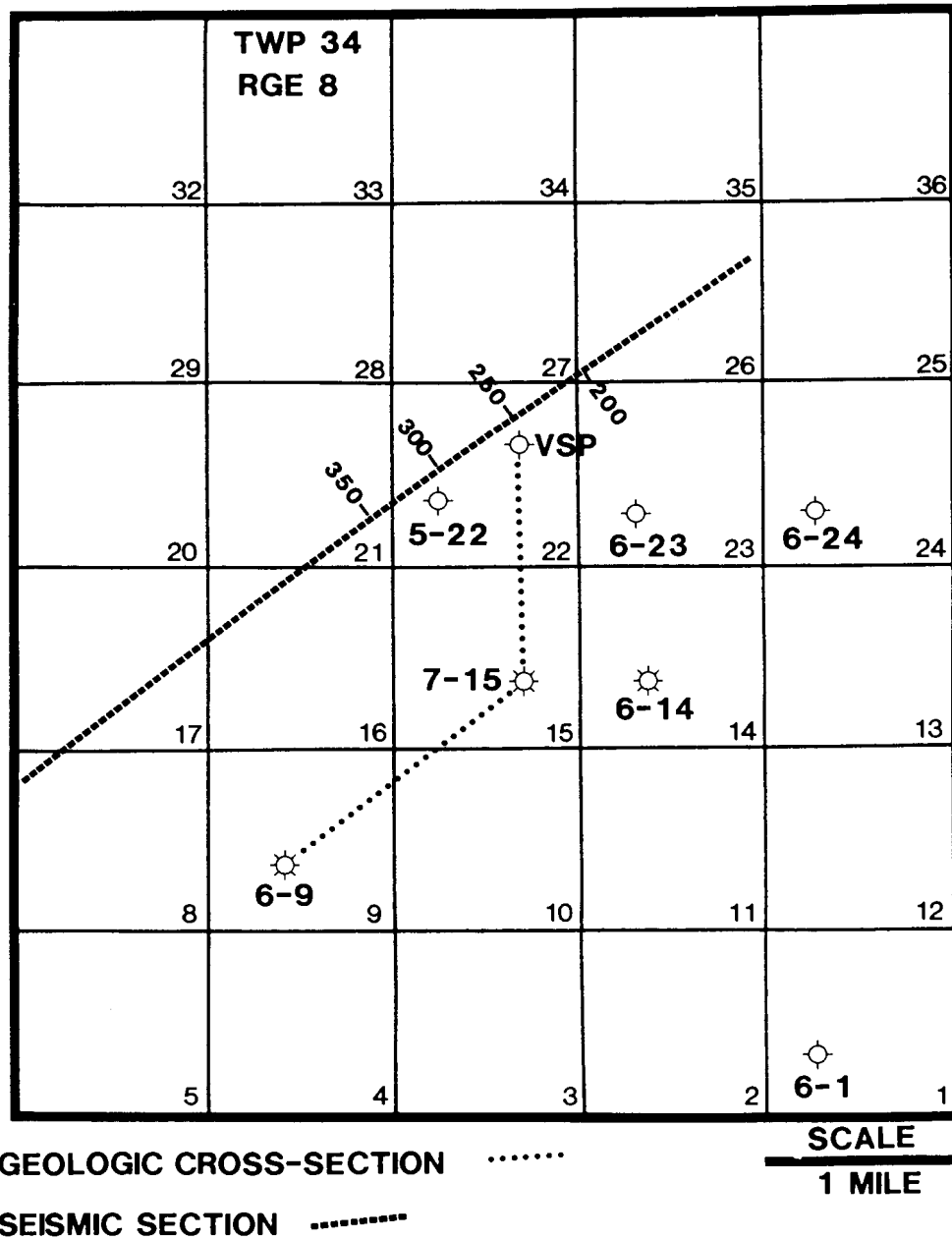


Figure 4.1 Detailed map of Ricinus study area showing the location of the wells used in the geological schematic section shown in Figures 4.2 and 4.4, the seismic data shown in Figures 4.3, 4.5 and 4.17, and locations for Leduc Formation level wells in the Ricinus Field area (from Hinds et al., 1993c; Hinds et al., 1994c).

et al., 1993c). Towards these ends, the VSP was relatively successful.

In this chapter, I present a case history that illustrates the potential for the misinterpretation of 2-D surface seismic data in the Ricinus area. This study is based on a situation where the plausible, yet ultimately inaccurate interpretation of surface seismic data led to the drilling of the VSP well. The VSP well was expected to intersect the updip edge of the Ricinus Leduc reef according to the original interpretation shown in Figure 4.2. Unfortunately it encountered only off-reef shales and was abandoned. Herein, I discuss the VSP well results, and the surface seismic and VSP data signatures at the VSP well site. The 2-D data presented were acquired prior to drilling the exploratory VSP well. The VSP survey was run in an attempt to resolve the discrepancy between the initial (pre-VSP well) interpretation of the surface seismic data and the geology at the VSP well site and to seismically image laterally away from the well towards the Southwest.

4.1 The Ricinus Field

The stratigraphy of the Ricinus Field is similar to that of the Lanaway field (Figs. 3.1A, B, and C). Similar to the situation at the Lanaway Field, the Leduc Formation at the Ricinus Field (Figs. 3.2 and 4.1), is interpreted as a large atoll which towers some 350 - 400 m (based on well 6-9-34-8 W5M) above the Cooking Lake platform and appears to exhibit a mappable peripheral raised rim and a structurally lower central lagoonal area. As at the Lanaway Field, the updip edge (northeast) of the raised rim at Ricinus is productive where it is structurally closed and effectively sealed by the inter-reef shales of the Duvernay and

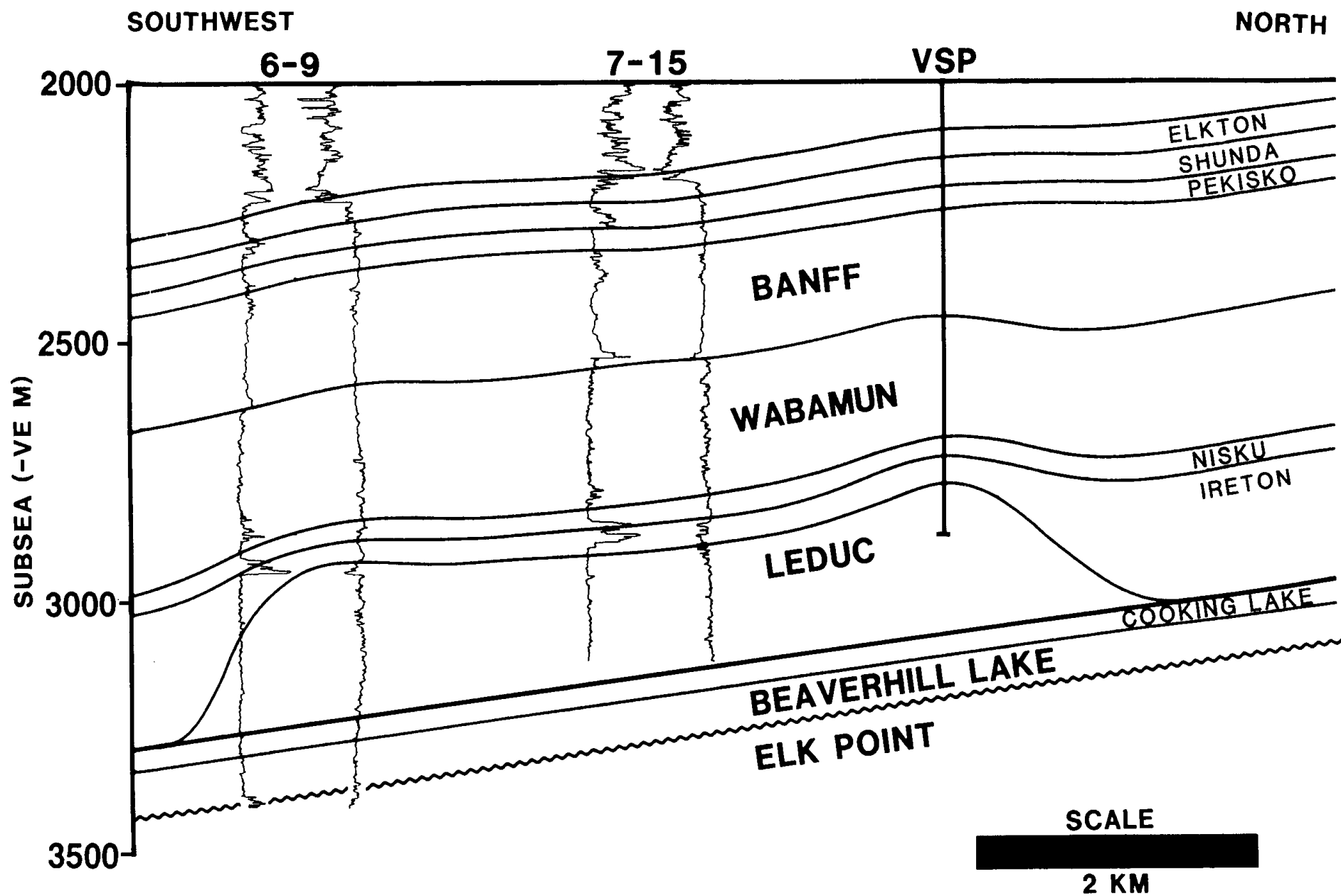


Figure 4.2 Schematic section depicting the envisioned subsurface geology at the VSP well site prior to the drilling of the VSP well. This interpretation is based on downhole data from wells 6-9-34-8 W5M and 7-15-34-8 wells and the seismic interpretation shown in Figure 4.3. The geology data from the VSP well confirmed that the seismic interpretation is incorrect. The preferred, current interpretation is shown in Figure 4.4 (from Hinds et al., 1993c; Hinds et al., 1994c).

Ireton. The schematic cross-section shown in Figure 4.2 illustrates the interpreted morphological relationships between the Leduc and the inter-reef shales of the Ireton and Duvernay in the Ricinus area (Hinds et al., 1989a, Hinds et al., 1993c; Hinds et al., 1994c).

In those areas of western Canada where the Devonian and/or overlying rock units are relatively undisturbed structurally, full Leduc reefs and inter-reef shales can usually be differentiated on seismic data. These carbonate build-ups are typically characterized by appreciable velocity pull-up (up to 25 ms), significant time-structural drape at the top of the Devonian (up to 70 ms at Ricinus in contrast to 25 ms at Lanaway), and character variations within the Woodbend Group (Anderson and Brown, 1987). Back from their steeply dipping margins, the tops of these reefs are generally manifested as high-amplitude troughs on reverse polarity seismic data (Hinds et al., 1993c).

The examples of low-relief reefs described by Anderson et al., (1989a), Anderson et al., (1989b) and Hinds et al., (1993b) are characterized by less than 10 ms of velocity pull-up and less than 20 ms of time-structural drape. Additionally, the reflections from the top of the reefs are difficult to differentiate from the inter-shale events. In those areas where extensive subsurface structural deformation has occurred, even the seismic image of the full Leduc reef may be effectively masked by the superimposed seismic signature of the structural complexities. Thrust faulting within Mesozoic strata in the general area of the Ricinus reef for example, can significantly affect the seismic signature of the Leduc reefs (Hinds et al., 1993c).

4.2 Ricinus Leduc reef

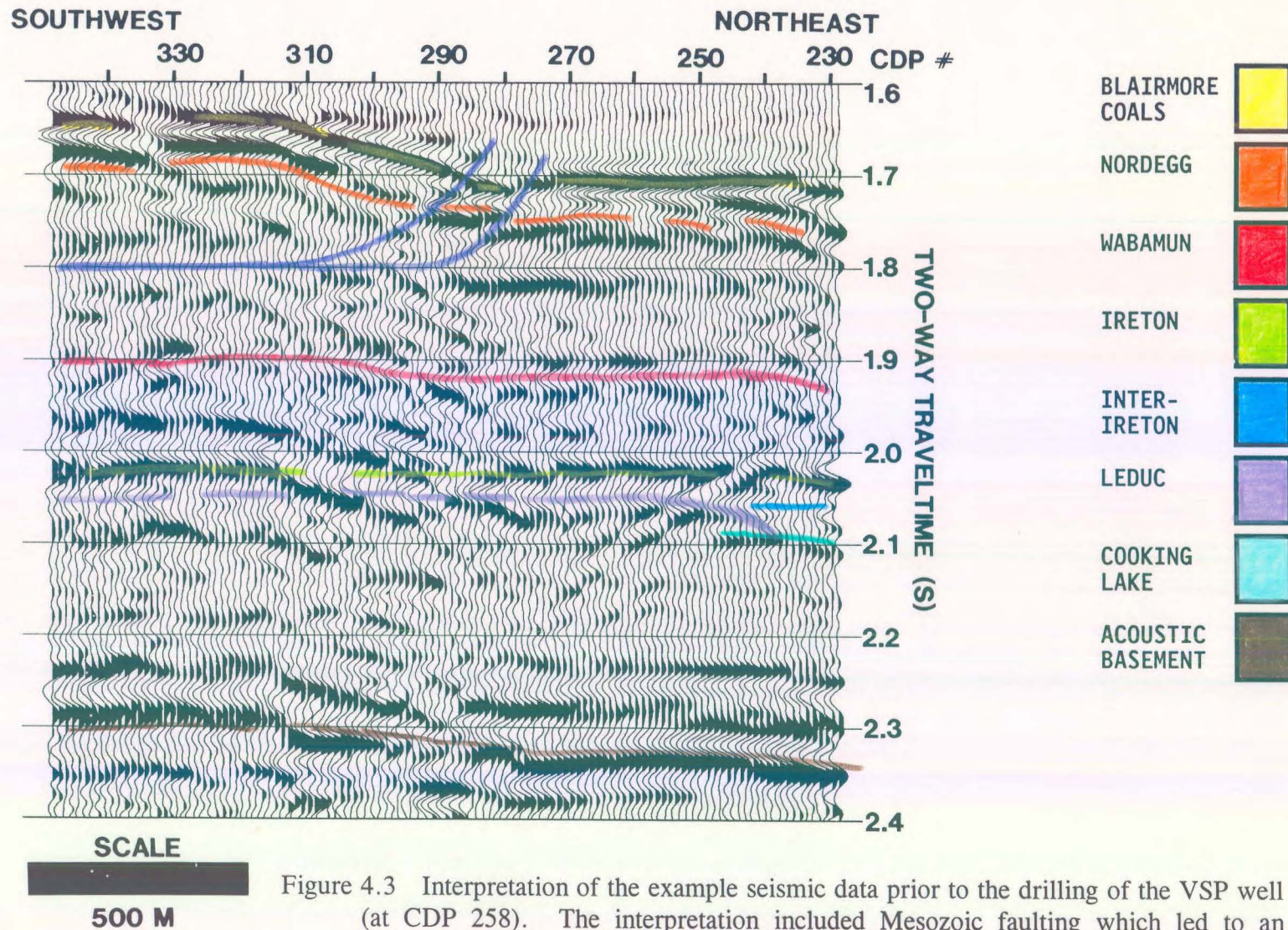
The diagrammatic cross-section incorporating wells 6-9, 7-15 and the VSP-well, shown in Figure 4.2, summarizes the geological and geophysical interpretation at the VSP well site prior to the drilling of the VSP well. This cross-section was based on the initial (pre-VSP well) interpretation of the example seismic data (Fig. 4.3), and well control available at that time.

The location and corresponding CDP numbers for one of the seismic sections used in the initial interpretation of the area (Figs. 4.3 and 4.5) are shown in Figure 4.1. The interpreted 12-fold surface seismic data displayed in Figures 4.3 and 4.5 were acquired using a source pattern consisting of five 1-kg charges spread over 60 m (at a single shotpoint). The shotpoint location interval was 120 m; the average shot depth was 9 m. The geophone groups consisted of nine in-line 14-Hz geophones over 30 m; the group interval was 30 m. 96 traces were recorded using DFS-V recording equipment and a split-spread geometry. The near offset geophone location was 30 m. The field anti-aliasing filter for the surface seismic was OUT/128 Hz. The surface seismic datum in the area was 1400 m ASL. The refraction statics replacement velocity used to reduce the surface seismic data to the seismic datum was 3350 m/s.

In the initial interpretation, the Leduc reef was interpreted to be fully developed in the area where the VSP-well was drilled. Ultimately, drilling confirmed that the VSP well site was off-reef and that this initial seismic-based interpretation is incorrect.

On the initial interpreted version of the seismic data displayed in Figure 4.3, the northern edge of the Leduc reef is located near trace 242, and full reef is mapped as present at the VSP well site at trace 259. This erroneous interpretation appears to be supported by the patterns of time-structural relief observed along the more prominent seismic events. For example, an event referred to as near-Cambrian event and the Cooking Lake event appear to be pulled up by about 15 ms immediately to the south of trace 242, and the Ireton, Wabamun, Nordegg and Blairmore events appear to drape by up to 25 ms across the interpreted northern edge of the reef. Note that the time-structure at the Blairmore and Nordegg events to the south of trace 314 in Figure 4.3, has been incorrectly attributed to thrust faulting within the Mesozoic section. The time-structure anomaly is seen as the Blairmore Coals and Nordegg events South of trace 290 being shallower in time in comparison to the same events North of trace 290 as a result of the faulting. This misinterpretation is consistent with the regional geology since the Ricinus Field is situated immediately to the east of the line demarcating the eastern limit of the Mesozoic thrust faulting of the Devonian rocks (see Fig. 5 of Moore, 1989a), and structural deformation of varying intensity is observed within the Mesozoic strata in this area.

The geologic section illustrated in Figure 4.4 shows the morphology of the Ricinus Field as interpreted after the drilling of the off-reef VSP well (Hinds et al., 1989a, Hinds et al., 1993c; Hinds et al., 1994c). This geologic section is constrained by well control and is based on the post-VSP interpretation of the example seismic line (Fig. 4.5) and the drilling information description of the geological formations intersected in the VSP borehole. Wells 6-9 and 7-15 (Fig. 4.1) were drilled into a full development of the reef and are productive; 6-9 encountered approximately 22 m of gas pay within the Leduc; and 7-15 encountered 140



220

Figure 4.3 Interpretation of the example seismic data prior to the drilling of the VSP well (at CDP 258). The interpretation included Mesozoic faulting which led to an incorrect interpretation of the seismic events beneath the faulting. The preferred, current interpretation is shown in Figure 4.5. The data are normal polarity (from Hinds et al., 1993c; Hinds et al., 1994c).

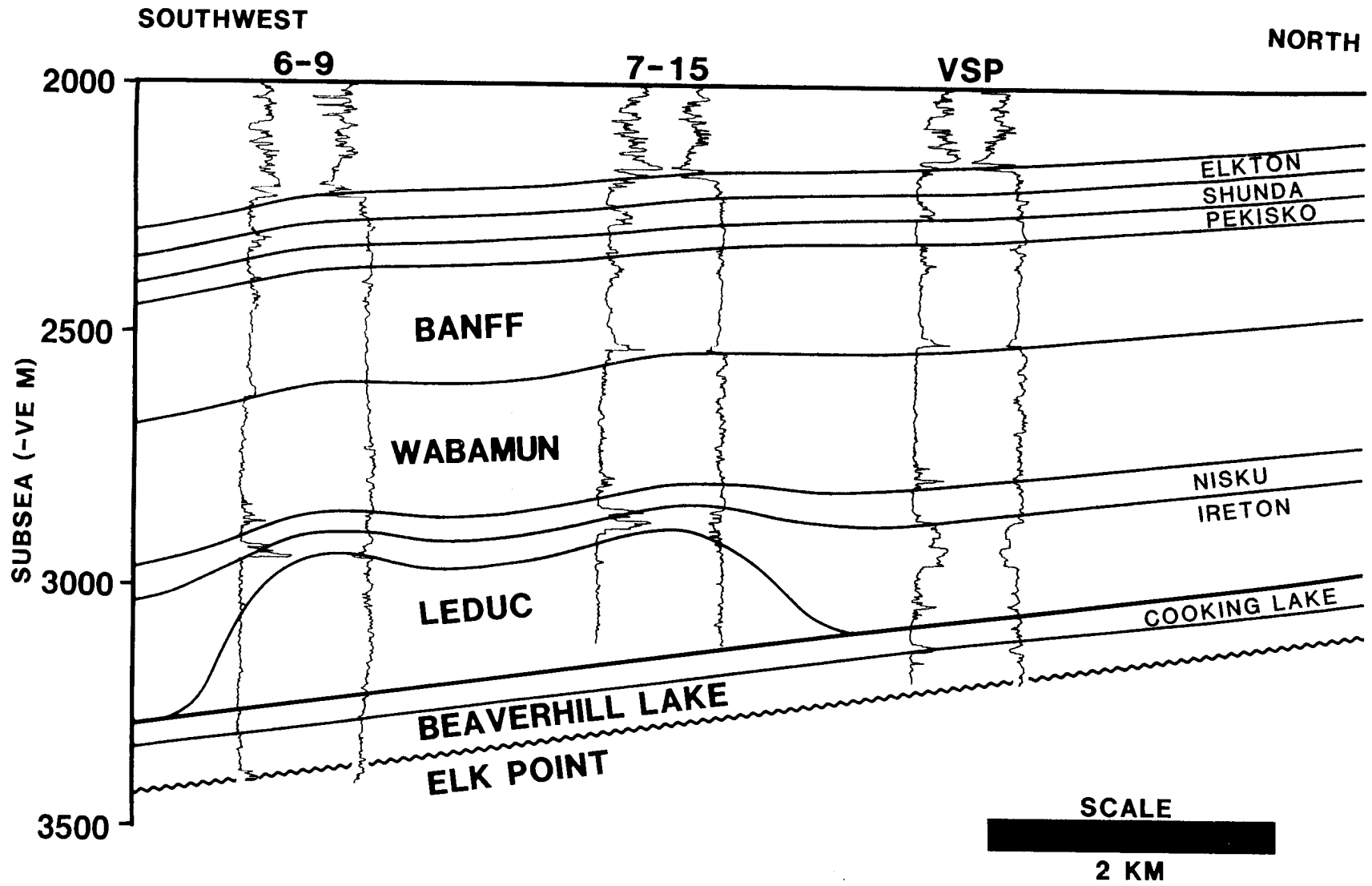


Figure 4.4 Schematic section depicting the subsurface geology at the VSP well site, and the relationships between wells 6-9 and 7-15 (locations shown in Figure 4.1) and the VSP well. The geologic section is consistent with available well log control, and the seismic interpretation displayed as Figure 4.5 (from Hinds et al., 1993c; Hinds et al., 1994c)

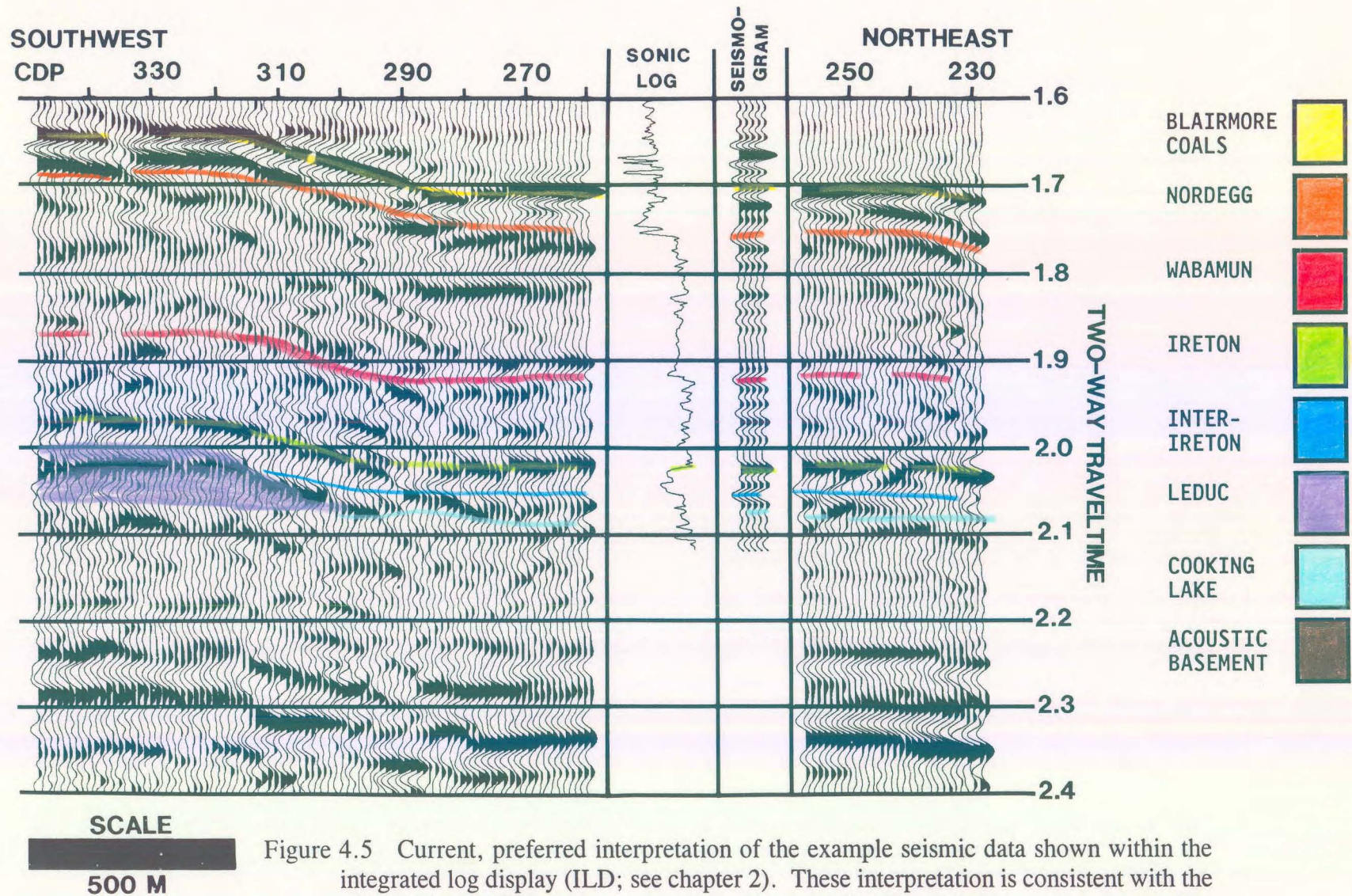
m of pay. Well 7-15 penetrated 250 m of Leduc reef. The VSP well (Figs. 4.1 and 4.4) is off-reef, and encountered a full section of inter-reef shale (Ireton and Duvernay; Fig. 3.1A, B and C). Well 6-9 and the VSP well encountered Cooking Lake; however 7-15 was not drilled deep enough to penetrate the Cooking Lake Formation geology.

On the post-VSP well version of the interpretation of the seismic data (Fig. 4.5), the northeastern edge of the Leduc complex is located near trace 314 and the VSP well site (trace 259) is interpreted as off-reef (Hinds et al., 1989a; Hinds et al., 1993c; Hinds et al., 1994c). This interpretation is supported by the patterns of time-structural relief observed along the more prominent seismic events. For example, the acoustic basement event appears to be pulled up by up to 40 ms to the south of trace 314; the Ireton, Wabamun, Nordegg and Blairmore events appear to drape by up to 70 ms across the interpreted northeastern edge of the reef. Note that the time-structural relief observed at the Blairmore coals and Nordegg levels to the south of trace 314, is interpreted as drape and attributed to the differential compaction of reef and off-reef sediment. In this interpretation, Mesozoic thrust faulting has not appreciably affected the rock record (Hinds et al., 1993c; Hinds et al., 1994c).

4.3 VSP data acquisition

After the analysis of the well log data and prior to abandonment, two VSP surveys were run at the VSP well site. These two VSP surveys were designed in an attempt to:

- 1) more accurately tie the surface seismic to the subsurface geology;



223

Figure 4.5 Current, preferred interpretation of the example seismic data shown within the integrated log display (ILD; see chapter 2). These interpretation is consistent with the 6-9, 7-15 and VSP well (as shown in Figure 4.4). These data are normal polarity; the display extends from 1.6 s to 2.4 s. The VSP well sonic log (displayed in time) and synthetic seismogram are inserted to display the correlations used in the interpretation (from Hinds et al., 1993c; Hinds et al., 1994c).

2) determine if the reef crest was within 500 m to the Southwest of the VSP well in the direction along the length of the example seismic line with a view to possible whipstocking; and

3) differentiate primary reflections from both surface-generated and interbed multiples.

The near offset source was 199 m from the VSP well and the far offset was 1100 m while both were on-line with respect to the surface seismic line (Fig. 4.1) and in the direction of well 5-22 to the southwest. Two Vibroseis units were operated in series at each offset position. The 16 s sweep ranged from 8 to 80 Hz, the recording length was 20 s, and the cross-correlated output was 4 s. Six to eight sweeps were summed for each geophone sonde location. The SSC 1078 VSP recording system with a sampling rate of 2 ms and a recording filter setting of OUT/OUT was used.

The total depth of the VSP well was 4528 m below KB (KB was 1317 m ASL). The source elevation of both offset source points was 1304 m ASL. Data were recorded at selected depths as the sonde was lowered down the borehole; these sonde locations were repeated during the production run. The use of these dual recording locations facilitates the detection of cable stretch or cable depth counter malfunction, and provides information regarding the gain amplification that will be required during the VSP production run. The first production VSP recording was at 4260 m below KB for the near offset VSP and 4350 m for the far offset VSP survey. During the production recording, the geophone sonde was raised at intervals of 30 m intervals until the depth of 420 m below KB. Above 420 m from the surface (KB), the depth spacing was 60 m up to the shallowest level of 180 m for the zero

offset VSP and 390 m for the far offset VSP. At each sonde location, the three component geophone tool was locked in place.

4.4 Interpretive processing of near offset (199 m) VSP data

During the processing of the near offset VSP, a series of interpretive processing panels were generated to display the following:

- 1) upgoing and downgoing P-wave separation;
- 2) deconvolution of the $Z_{up}(+TT)$ data using an inverse filter calculated from the $Z_{down}(+TT)$ data; and
- 3) inside and outside corridor stacks of $Z_{up}(+TT)$ and $Z_{up(decon)}(+TT)$ data.

4.4.1 Upgoing P-wave event separation

The separation of upgoing and downgoing P-waves from the $Z(FRT)$ data is depicted in the wavefield separation interpretive processing panel (IPP) of Figure 4.6 (Hinds et al., 1989a; Hinds et al., 1993c; Hinds et al., 1994c).

Panel 1 displays the $Z(FRT)$ data after trace normalization. In panel 2, these $Z(FRT)$ data

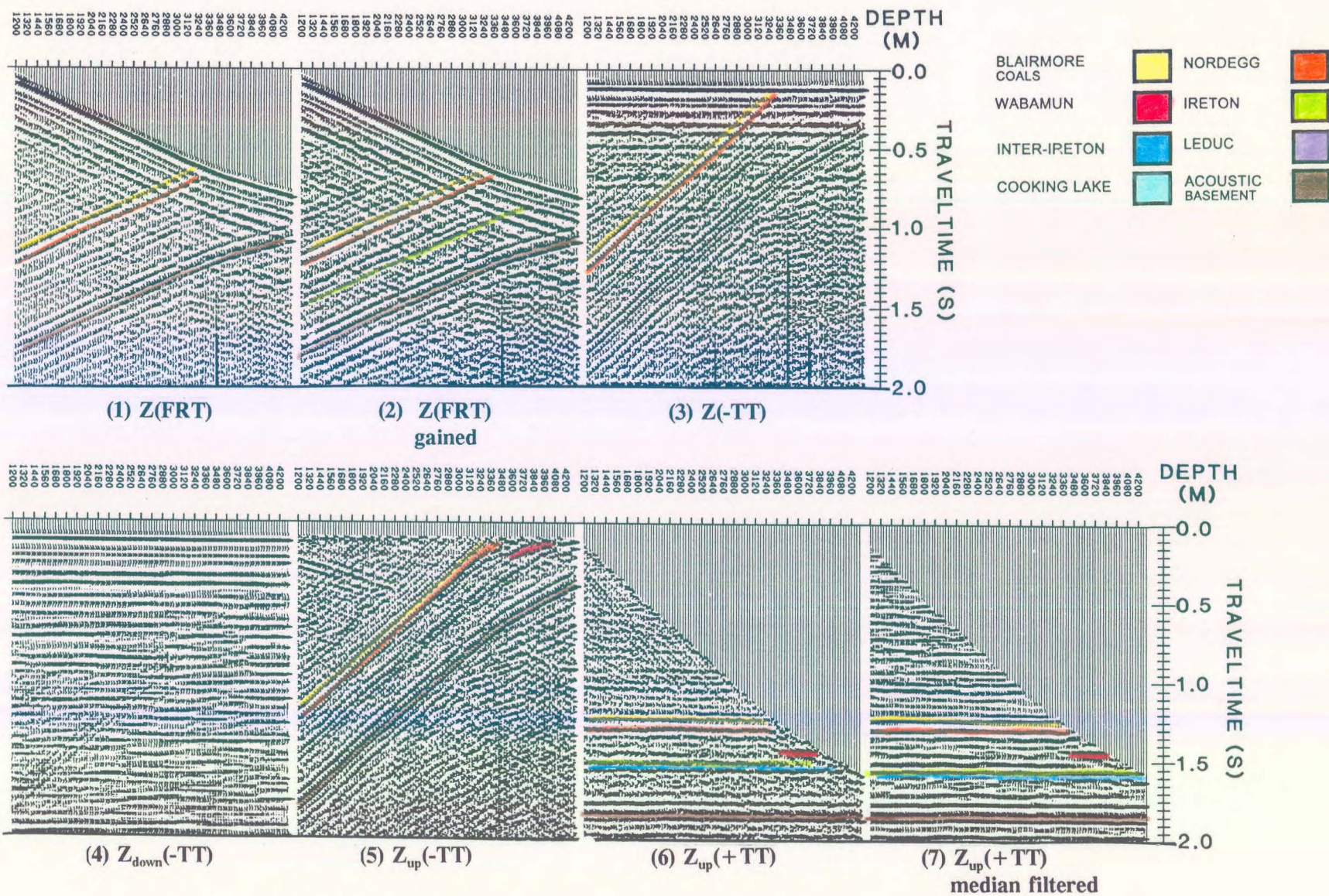


Figure 4.6 Interpretive processing panel depicting the wavefield separation of the near offset VSP data (from Hinds et al., 1989a; Hinds et al., 1993c; Hinds et al., 1994c).

have been gained to highlight several prominent primary upgoing events such as the Blairmore coals, Nordegg, Ireton and acoustic basement (crystalline Precambrian) events. Note that the upgoing event identified as the acoustic basement appears on the 4290 m trace deeper in time than the first break on that trace. Since the event does not intersect the first break curve, the event cannot be positively identified as a primary reflection as reviewed in chapter 1. The uncertainty as to the exact time and depth to crystalline basement cannot be resolved without VSP control at that depth.

The association of the downgoing surface-generated multiple (that lags the first break by approximately 0.3 s) to the upgoing events recorded below TD is bothersome when interpreting the basement reflector. On the **Z(FRT)** data in panel 2, the downgoing multiple event that intersects the deepest trace at 1.05 s coincides with the upgoing wave that begins at 1.05 s and ends on the shallowest trace at 1.65 s. The implication is that some of the events recorded below the bottom may be multiple reflections from the bottom of the borehole itself.

In panel 3 (Fig. 4.6), the **Z(-TT)** data are presented where the first breaks and downgoing P-wave multiple events are horizontally aligned. The **Z(-TT)** data in panel 3 illustrate that the downgoing wavetrain consists of the primary downgoing wavelet plus high-amplitude surface-generated multiples and less prominent possible interbed multiples. The surface-generated downgoing multiples are recognized as those horizontally aligned, post-first break arrivals that are recorded on all of the traces. As reviewed in chapter 1, if a downgoing multiple event does not extend over the entire depth range but is evident on the deeper traces only, then that multiple is interpreted to be an interbed multiple (Hinds et al., 1989a).

In the next processing step, an 11-point median filter was used to remove the upgoing P-waves. The output consisted of separated and scaled $Z_{\text{down}}(-\text{TT})$ data and is displayed in panel 4. Note that the residual upgoing wave content in the $Z_{\text{down}}(-\text{TT})$ data is minimal. This panel is one of the most important panels for interpretive processing of VSP data. If residual upgoing events remain in the $Z_{\text{down}}(-\text{TT})$ data, then that amount of residual upgoing event is subtracted out of the $Z(-\text{TT})$ data (panel 3) during wavefield separation.

The multiples that appear on all of the traces are most likely surface-generated. This is the case for multiples down to 0.45 s. Beyond that time on panel 4, surface generated and interbed multiples (as seen between 0.75 and 0.9 s) exist.

In the next step of the wavefield separation, the $Z_{\text{down}}(-\text{TT})$ data of panel 4 were subtracted from the $Z(-\text{TT})$ in panel 3 to yield the output $Z_{\text{up}}(-\text{TT})$ data shown in panel 5. The upgoing P-waves and downgoing shear waves (both primary and multiples) are shown in panel 5. The downgoing shear waves (SV) may have been generated at the bottom of the surface casing or near the surface. An example of a downgoing SV appears on the shallowest trace on panel 5 at 0.2 s (-TT time) and trends opposite to the upgoing events (deeper in time from left to right).

The $Z_{\text{up}}(+\text{TT})$ before and after the application of a 3-point median filter are shown in panels 6 and 7, respectively. The equalized amplitudes of the horizontally aligned upgoing waves for the Blairmore coals, Nordegg, Wabamun, Ireton, inter-Ireton, Cooking Lake, and acoustic basement events are interpreted in panel 7. It can be observed that the downgoing SV events seen in panel 5 dip more steeply in the +TT display; however, these events have

been effectively attenuated by the application of the median filter. As will be discussed further below, the Wabamun and Cooking Lake events have been identified only on traces deeper than the depth of the Nordegg interface due to multiple interference.

4.4.2 VSP deconvolution

On the $Z_{\text{down}}(-\mathbf{TT})$ data, as reviewed in chapter 1, the initial downgoing pulse (except in the case of head wave contamination) is the primary downgoing P-wave; any later arriving, downgoing events are multiples (apart from downgoing shear or converted waves). Ideally, P-wave multiples can be effectively filtered using a deconvolution operator derived from an analysis of the separated downgoing P-wave wavetrain (Hardage, 1985; Hinds et al., 1989a). Deconvolution also enhances the higher frequencies within the data which allows for better vertical resolution.

The deconvolution IPP shown in Figure 4.7 (Hinds et al., 1989a; Hinds et al., 1993c; Hinds et al., 1994c) was designed to enable the monitoring of the deconvolution process of the Ricinus Z_{up} data. The incorporated panels reveal information (about multiples) that was difficult to determine from the wavefield separation IPP (Fig. 4.6) alone. The first two panels (Fig. 4.7) are the nonfiltered and median-filtered $Z_{\text{up}}(+\mathbf{TT})$ data, respectively. Panel 3 contains the $Z(-\mathbf{TT})$ data which allows an examination of the downgoing P-wave multiple pattern of the near offset data. Panels 4 and 5 contain the $Z_{\text{up}}(-\mathbf{TT})$ and $Z_{\text{up}(\text{decon})}(-\mathbf{TT})$ data,

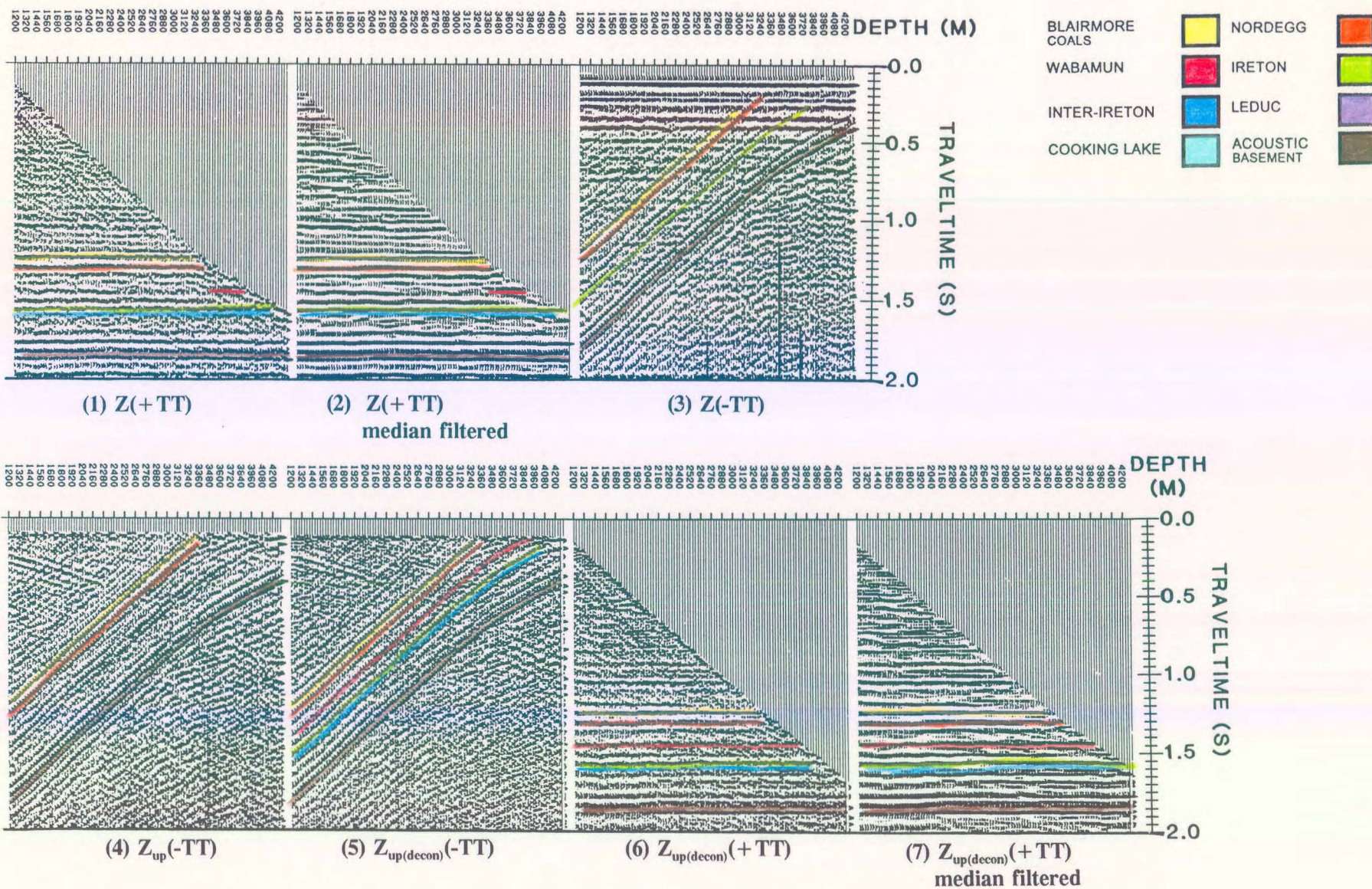


Figure 4.7 Interpretive processing panel depicting the deconvolution of the near offset VSP data (from Hinds et al., 1989a; Hinds et al., 1993c; Hinds et al., 1994c).

respectively. Both panels 4 and 5 are contaminated with downgoing shear waves. The downgoing SV events can be recognized by the observation that the events increase in traveltime with increasing depth and penetrate the upgoing events that decrease in traveltime with increasing depth. A comparison of these panels illustrates that the deconvolution process has enhanced the higher frequencies contained in the upgoing waves and preserved the primary reflections yet has not raised the noise content of the data.

The last two panels (6 and 7) contain the nonfiltered and median-filtered $Z_{up(decon)}(+TT)$ data, respectively. A comparison of panels 2 and 7 (Fig. 4.7), elucidates the effect of the Blairmore coals and Nordegg multiples on the continuity of primary reflections. Multiple contamination is most noticeable for the Wabamun and Cooking Lake reflection events. On the $Z_{up}(+TT)$ data in panel 2, the Wabamun is relatively unaffected on traces that are recorded below the Nordegg depth of 3466 m (-2151 m ASL). The upgoing multiple reflection from the Nordegg will not be detected on traces deeper than the bottom-generating layer of the multiple (the Nordegg) because, by definition, the multiple is an upgoing wave, not downgoing. Examination of panel 3 reveals that a series of possible surface-generated multiples exist (a series of events parallel to the first break primary (-TT) that are delayed in time). The multiple contamination may persist for 0.4 s or more. It is likely that both surface-generated and interbed multiples may be contaminating the $Z_{up}(+TT)$ data at the Wabamun event time level. On traces recorded at depths shallower than 3466 m, the multiple events generated at the Nordegg Formation interface destructively interferes with the Wabamun event.

A trough interpreted to be the Cooking Lake event is just below the inter-Ireton trough in

panel 2 ($Z_{up}(+TT)$ data) on the traces from depth 3466 m to the bottom of the borehole. The interpretation of the Cooking Lake event (Hinds et al., 1993c) is supported by the sonic log/synthetic seismogram Cooking Lake correlation to the surface seismic (ILD) shown in Figure 4.5 (the sonic log was integrated to create a synthetic seismogram and corrected using the VSP first break times). What effect does deconvolution have on the Wabamun and Cooking Lake events?

An investigation of the effect that deconvolution has on the Wabamun and Cooking Lake events shows that the Wabamun event is now laterally continuous on the $Z_{up(decon)}(+TT)$ data in panel 7 (Fig. 4.7) and can be correlated on all depth traces as a result of the deconvolution. The Cooking Lake event (trough) can also now be confidently interpreted since the event is now a recognizable event across the entire $Z_{up(decon)}(+TT)$ data.

The multiple contamination is interpreted to be minimal in the zone of interest around the Ireton event. The inter-Ireton is continuous and does not exhibit significant structure either before or after the VSP deconvolution. It is the inter-Ireton event that will rise and/or truncate against any Ricinus reef edge and is therefore regarded as a vital key to the interpretation success of the VSP surveys (Hinds et al., 1993c).

4.4.3 Inside and outside corridor stacks

Inside and outside corridor stacks (Hinds et al., 1989a) and associated displays for the nondeconvolved $Z_{up}(+TT)$ data are presented in Figure 4.8. A comparison of the $Z_{up}(+TT)$ outside and inside corridor stacks (panels 3 and 4, respectively) illustrates the utility of these displays. For example, the multiple interference generated by the Blairmore coals or Nordegg interbed multiple can be interpreted on the inside corridor stack but is not seen on the outside corridor stack. On the $Z_{up}(+TT)$ data outside corridor stack in panel 3, the Wabamun trough dominates (at 1.85 s); however the $Z_{up}(+TT)$ data inside corridor stack at the same time window shows no semblance of a Wabamun event. This is due to multiple interference that has destructively interfered with the Wabamun event on the depth traces shallower than the Nordegg primary (the same depth trace range that the Nordegg multiples must exist on; Hinds et al., 1989a; Hinds et al., 1993c; Hinds et al., 1994c).

On the unmuted input data for the corridor stack displays (Figure 4.8, panels 1 and 6), it can be noted that the Cooking Lake event exists as a trough beneath the inter-Ireton event (trough). The event is so weak without the deconvolution that even the outside corridor stack does not show the Cooking Lake trough. This indicates the reason for displaying the unmuted input data in the corridor stack IPP during interpretive processing (Hinds et al., 1989a). In order to interpret the outside corridor stack, it must be borne in mind what went into the stack (where the corridor mute line is).

On the $Z_{up(decon)}(+TT)$ data corridor stack panels of Figure 4.9, the Wabamun and Cooking Lake events can now be reliably interpreted.

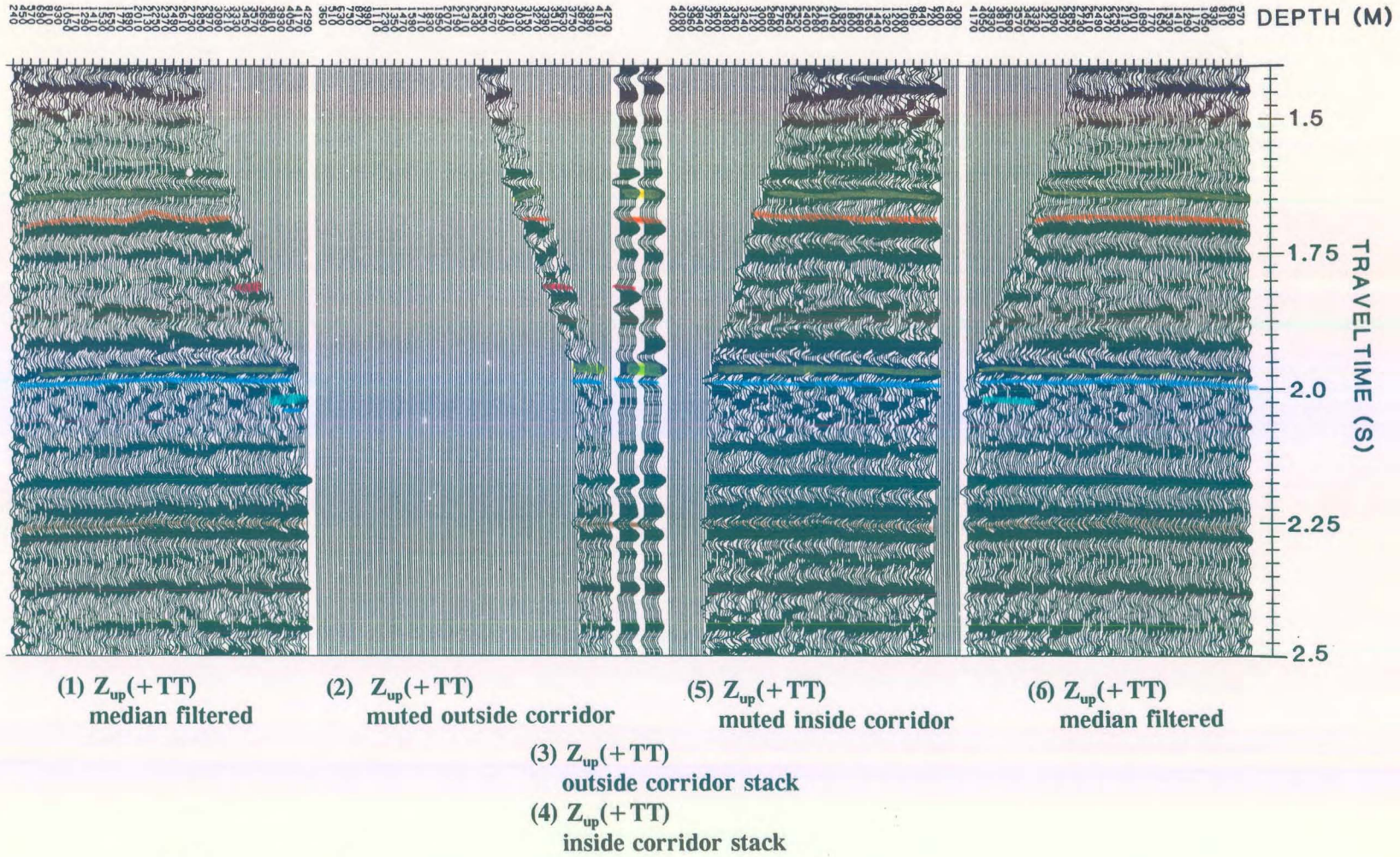


Figure 4.8 Interpretive processing panel illustrating the utility of the nondeconvolved inside and outside corridor stacks for the Ricinus near offset $Z_{up}(+TT)$ data (from Hinds et al., 1989a; Hinds et al., 1993c; Hinds et al., 1994c).

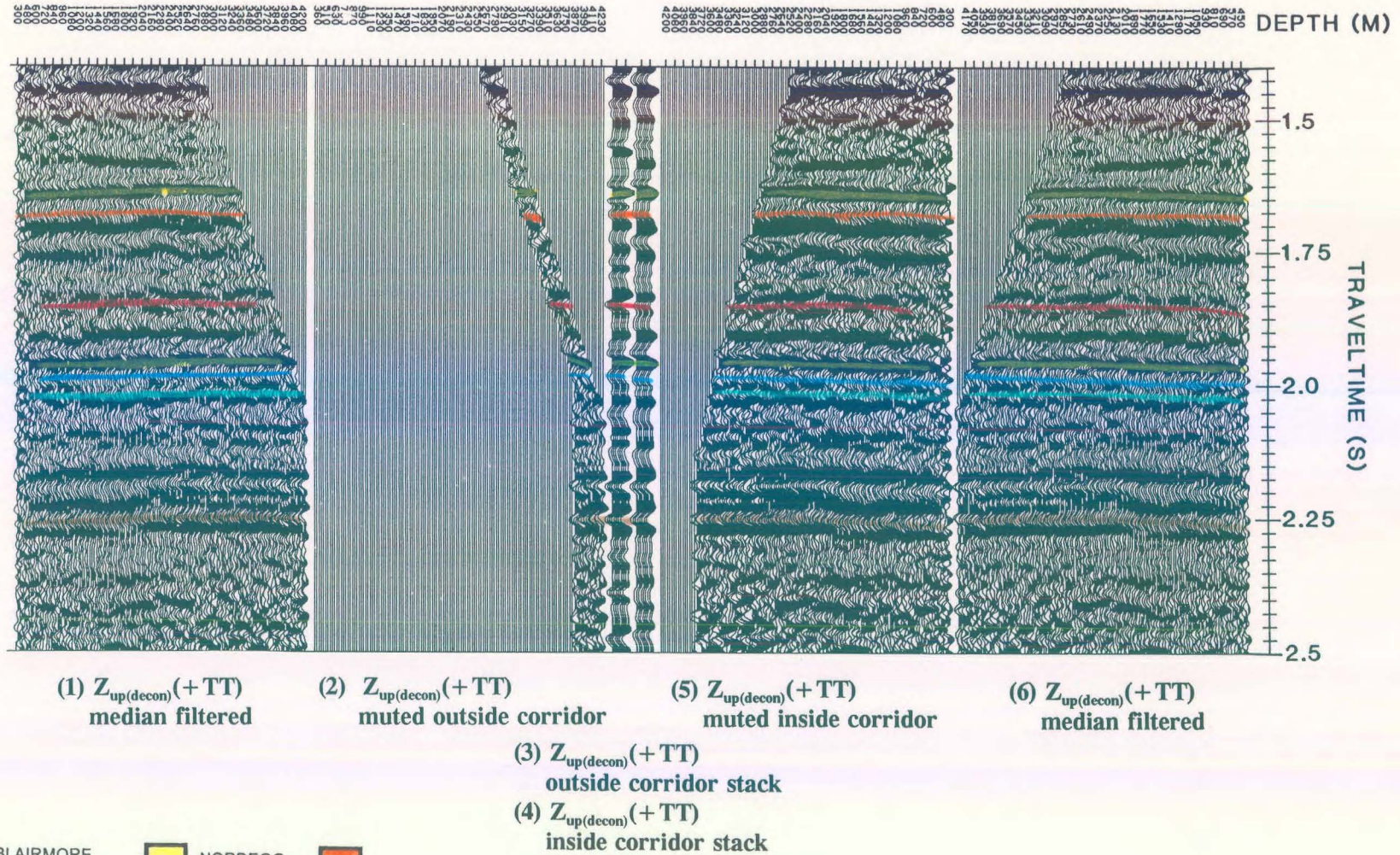


Figure 4.9 Interpretive processing panel illustrating the utility of the deconvolved inside and outside corridor stacks for the Ricinus near offset $Z_{up(decon)}(+TT)$ data (from Hinds et al., 1989a; Hinds et al., 1993c; Hinds et al., 1994c).

If deconvolution is successful, the $Z_{\text{up(decon)}}(+TT)$ outside and inside corridor stacks (panels 3 and 4; Fig. 4.9) should be similar. The inside and outside deconvolved corridor stacks show that the surface generated multiples have been substantially attenuated by the VSP deconvolution process; however there is enough difference (as in the zone immediately below the Nordegg event at about 1.75 to 1.8 s) between the events of the two stacks to predict that any possible interbed multiples have been simply attenuated but not totally removed.

The deconvolved data and the corridor stacks show that the Wabamun and Cooking Lake primaries are flat lying continuous upgoing primary events across the entire VSP panel once the effect of multiple contamination is minimized. At this point the surface seismic can be reinterpreted at the well location by making use of the VSP results.

4.5 Interpretive processing of the far offset (1100 m) VSP data

On the far offset VSP data, the vertical (Z), and both horizontal (X and Y) axis contain nonpartitioned elements of the upgoing and downgoing P- and SV-wavefields. Examination of the IPPs to follow will reveal that the partitioning of the wavefields (both up- and downgoing P and SV events) has significant implications with respect to interpretation. In chapter 2, the Ricinus far offset data was utilized as an example of a problematic VSP data for interpretive processing. It was these data that showed how interpretive processing aided in the searching out of the origins of the problematic "noise" wavefields within the example far offset data. In this section, the interpretive processing will be shown in more detail. The reader is referred to chapter 2 with regards to the difference in runstream approaches.

As demonstrated in panels 5 and 6 of the near offset wavefield separation IPP (Fig. 4.6), a downgoing SV wave (trending in the opposite direction to the upgoing waves in panel 5) is noticeable. Normally, downgoing and upgoing shear waves are not seen on near offset data. The near offset surveys usually contain events resulting from near-vertical incidence reflections. From Zoeppritz equations, the partitioning of downgoing P waves into up- and downgoing SV waves should be minimal under conditions of near-vertical incidence reflections. It can therefore be expected that shear wave contamination will be readily noticeable on the far offset data. The runstreams used for the partitioning of the wavefields presented below will play an important role in isolating the upgoing P wave events from downgoing P wave events and up- and downgoing SV events. As illustrated in chapter 2, interpretive processing is used to assist in the modification of the processing runstreams.

Far offset IPPs have been designed to control the quality of execution of the following procedures:

- 1) hodogram-based rotation of the **X**, **Y**, and **Z** data (based on windowed data enveloping the P-wave first arrival; DiSiena et al., 1984, Hinds et al., 1989a);
- 2) time-variant model-based rotations applied to the **HMAX_{up}(FRT)** and **Z_{up}(FRT)** data in response to interpretive processing results as highlighted in chapter 2 (within the section "problematic far offset interpretive processing"); and
- 3) the VSP-CDP mapping of the data (Dillon and Thomson, 1984).

4.5.1 Hodogram-based rotation

The **X(FRT)**, **Y(FRT)**, and **Z(FRT)** data for the far offset VSP are displayed in Figure 4.10 as panels 1, 2, and 3, respectively. The **X(FRT)** and **Y(FRT)** data contain both P and SV downgoing waves plus recognizable upgoing SV events. These upgoing SV events can be seen on both panels 1 and 2 originating at depth levels 2790 down to the deepest traces (coloured purple in panels 1 and 2). More upgoing SV events may exist originating on the shallower traces but are overpowered in amplitude by the downgoing mode-converted SV events. The **HMAX(FRT)** data in panel 5 shows a clear definition of the up- and downgoing SV events. These events (coloured pink in panels 5 and 6) slope differently to the upgoing P wave events of the **Z(FRT)** data seen on panel 3.

The partitioned downgoing primary P waves (first breaks wavelet) are consistent on both the **X(FRT)** and **Y(FRT)** data in panels 1 and 2 on traces recorded in the upper two-thirds of the borehole which may indicate that the tool was rotating on the deeper depth traces (indicated by the first breaks becoming inconsistent on a single panel). In panel 3, the **Z(FRT)** data first breaks are phase consistent.

The hodogram-based rotation of the **X(FRT)** and **Y(FRT)** data onto the **HMIN(FRT)** and **HMAX(FRT)** data is illustrated using panels 1, 2, 4 and 5, respectively. This rotation corrects for first break inconsistencies due to the rotation of the tool during the movement of the sonde up the borehole by projecting data from both of the input channels onto an axis which lies in the plane defined by the borehole and the source; namely the **HMAX(FRT)** data. **HMIN(FRT)** and **HMAX(FRT)** data are assumed to be aligned perpendicular to and

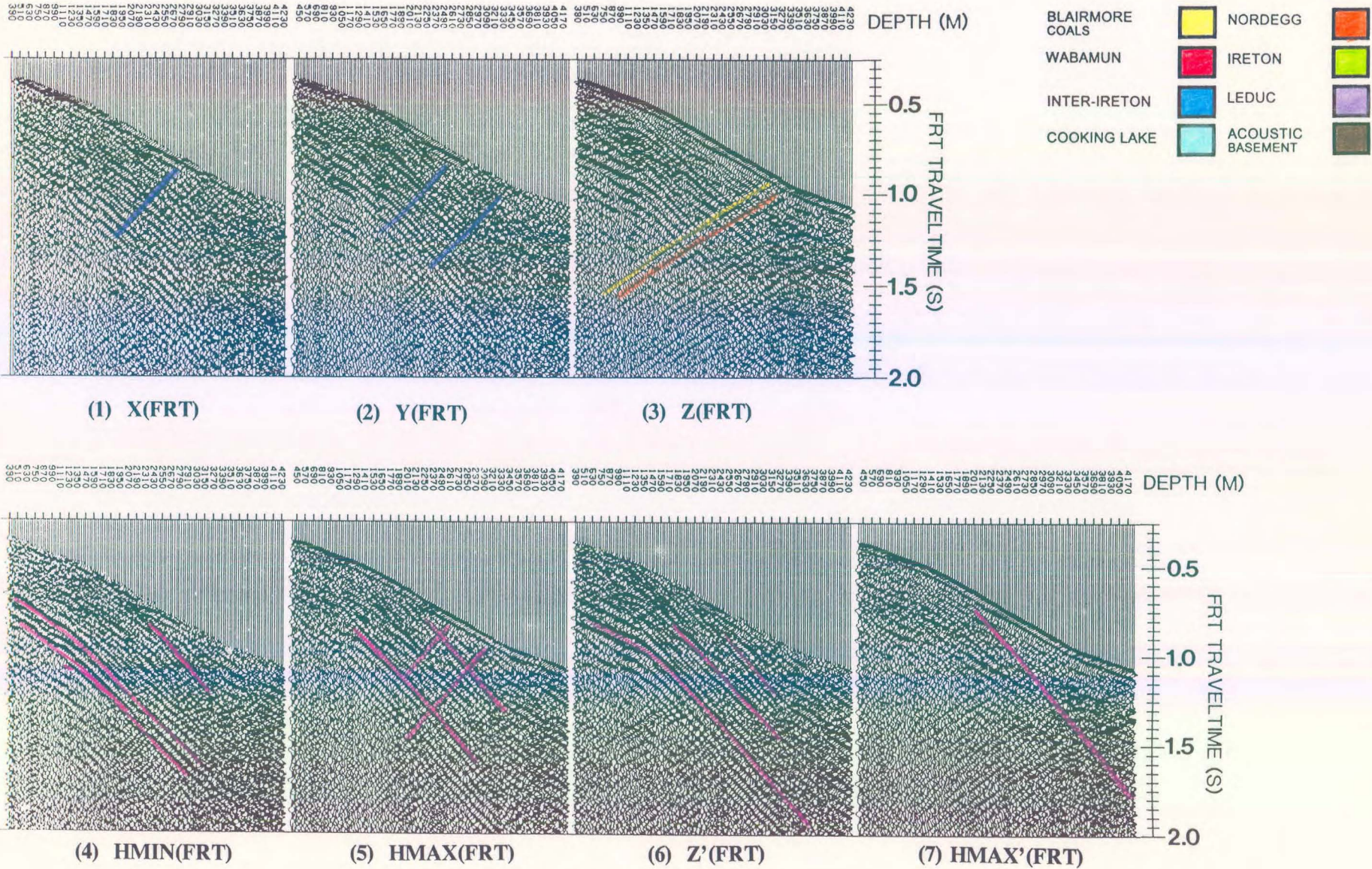


Figure 4.10 Interpretive processing panel depicting the hodogram-based rotation of the far offset Ricinus VSP data (from Hinds et al., 1989a; Hinds et al., 1993c; Hinds et al., 1994c).

in the plane formed by, the source and wellbore, respectively. Note that the **HMIN(FRT)** data (comprised of horizontally polarized shear (SH) wave events and out of the plane reflections), contains possible downgoing SV waves (coloured pink in panel 4 and appearing on the shallow traces below 0,6 s) that could originate at the casing joints or reflected downgoing waves that originate from out of the plane of the well.

The remnant of a mode-converted downgoing SV wave with components within the **HMIN(FRT)** data appears at the Nordegg and Blairmore level. The upgoing SV events from the Nordegg and Blairmore coals that were first noticed on both of the **X(FRT)** and **Y(FRT)** data are now more noticeable after redistribution onto the **HMAX(FRT)** data. These two upgoing SV events are coloured purple on panel 5. Unfortunately, the downgoing SV events on the **HMAX(FRT)** data are of equal amplitude to the downgoing P waves. The **HMAX(FRT)** data contains consistent polarized downgoing P wave first breaks as the data of the input **X(FRT)** and **Y(FRT)** channel data have been rotated into the plane containing the downgoing P wave.

The **Z'(FRT)** data in panel 6 and the **HMAX'(FRT)** data in panel 7 were obtained by rotating the **Z(FRT)** and **HMAX(FRT)** data using polarization angles estimated from a hodogram analysis of data within a window around the P-wave first arrival (DiSiena et al., 1984; Hinds et al., 1989a). This technique is designed to polarize the data so that the downgoing P-waves are effectively isolated on a single channel, **HMAX'(FRT)**.

On the **HMAX'(FRT)** data in panel 7 of Figure 4.10, the downgoing P-wave energy is

dominant. The **HMAX'(FRT)** panel contains residual downgoing shear (SV) waves (converted to SV waves at the Blairmore coal interface) and upgoing P-wave energy. This indicates that the polarization required to delineate the downgoing P-wave data onto a single panel is not adequate to separate the upgoing P-wave data entirely onto the orthogonally aligned **Z'(FRT)** data.

The **Z'(FRT)** data shown in panel 6 contains downgoing shear wave (coloured pink in panel 6) and upgoing P-wave energy that fit the assumption that the primary upgoing P-waves are orthogonal to the primary downgoing P-waves (isolated on the **HMAX'(FRT)** data). The downgoing shear wave overshadows the lower amplitude upgoing P-wave. The time-variant polarization of the data (modelled on the upgoing P-waves) should attempt to detach the contaminating up- and downgoing shear waves from the upgoing P-waves and isolate interpretable upgoing P-wave events onto a single output data panel, **Z''_{up}(FRT)**; however, it will be shown that this "routine-type" processing does not produce optimal results for interpretation and that a modified processing runstream is necessary (Hinds et al., 1994c).

4.5.2 Time-variant model-based rotation

The normal time-variant rotation runstream recommended in chapter 2 was used for the Ricinus far offset data and the resulting time-variant polarization IPP (Hinds et al., 1989a; Hinds et al., 1994c) is shown in Figure 2.50 and interpreted in Figure 4.11. As concluded in that example processing the **Z''_{up}(FRT)** data (in panel 6 of Figs. 2.50 and 4.11) contained unacceptable amounts of diffraction and mode-converted SV up- and downgoing events.

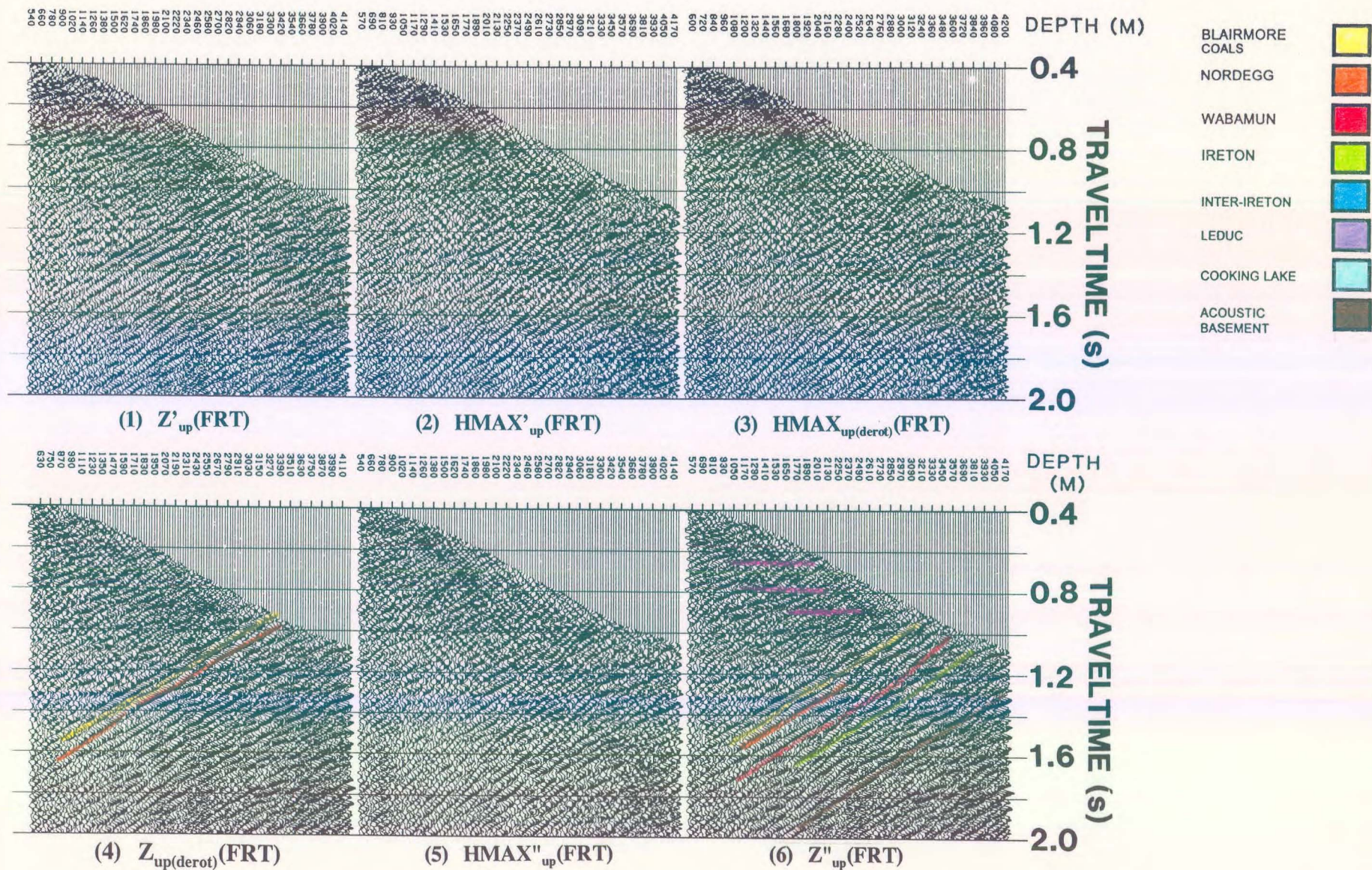


Figure 4.11 Interpretive processing panel depicting the time-variant model-based rotation of the far offset Ricinus VSP data resulting from the suggested processing runstream in chapter 2 (from Hinds et al., 1989a; Hinds et al., 1993c; Hinds et al., 1994c).

The time-variant model-based polarization runstream (as suggested in chapter 2) was changed to eliminate the second polarization rotation and to begin the runstream that eventually outputs the $Z''_{up}(FRT)$ data by performing wavefield separation on the $Z(FRT)$ and $HMAX(FRT)$ data. The $HMAX'(FRT)$ data displayed in Figure 4.10 were retained for the far offset deconvolution trials presented in chapter 2 and reviewed later in this chapter. The modified interpretively processed time-variant model-based polarization results are shown in Figure 4.12.

The $HMAX(FRT)$ and $Z(FRT)$ data (panels 1 and 2) are wavefield separated using the F-K based surgical muting (see chapter 2) to output the $HMAX_{up}(FRT)$ and $Z_{up}(FRT)$ data shown in panels 3 and 4, respectively. Special emphasis within the F-K mute design was taken to also attenuate the up- and downgoing SV-events from both input panels. The lack of the second hodogram-based rotation on the $Z(FRT)$ and $HMAX(FRT)$ input data (used in the wavefield separation) eliminated the possibility of rotation induced noise.

These data (panels 3 and 4 of Fig. 4.12) are compared to the final two panels (5 and 6) containing the time-variant model-based polarized $HMAX''_{up}(FRT)$ and $Z''_{up}(FRT)$ data. The emphasis is on the improvement of the quality of the upgoing P-wave events on the $Z''_{up}(FRT)$ panel and the similar $Z''_{up}(FRT)$ resulting from the use of the normal processing runstream (without interpretive processing) as shown in Figure 4.11. The upgoing events on panel 6 of Figure 4.12 are easily interpretable; however the same events on panels 5 and 6 of Figure 4.11 are difficult to interpret due to interfering noise. The updated $Z''_{up}(FRT)$ does contain residual diffraction events (between 0.7 and 0.9 s and coloured pink) which manifest themselves as horizontal events.

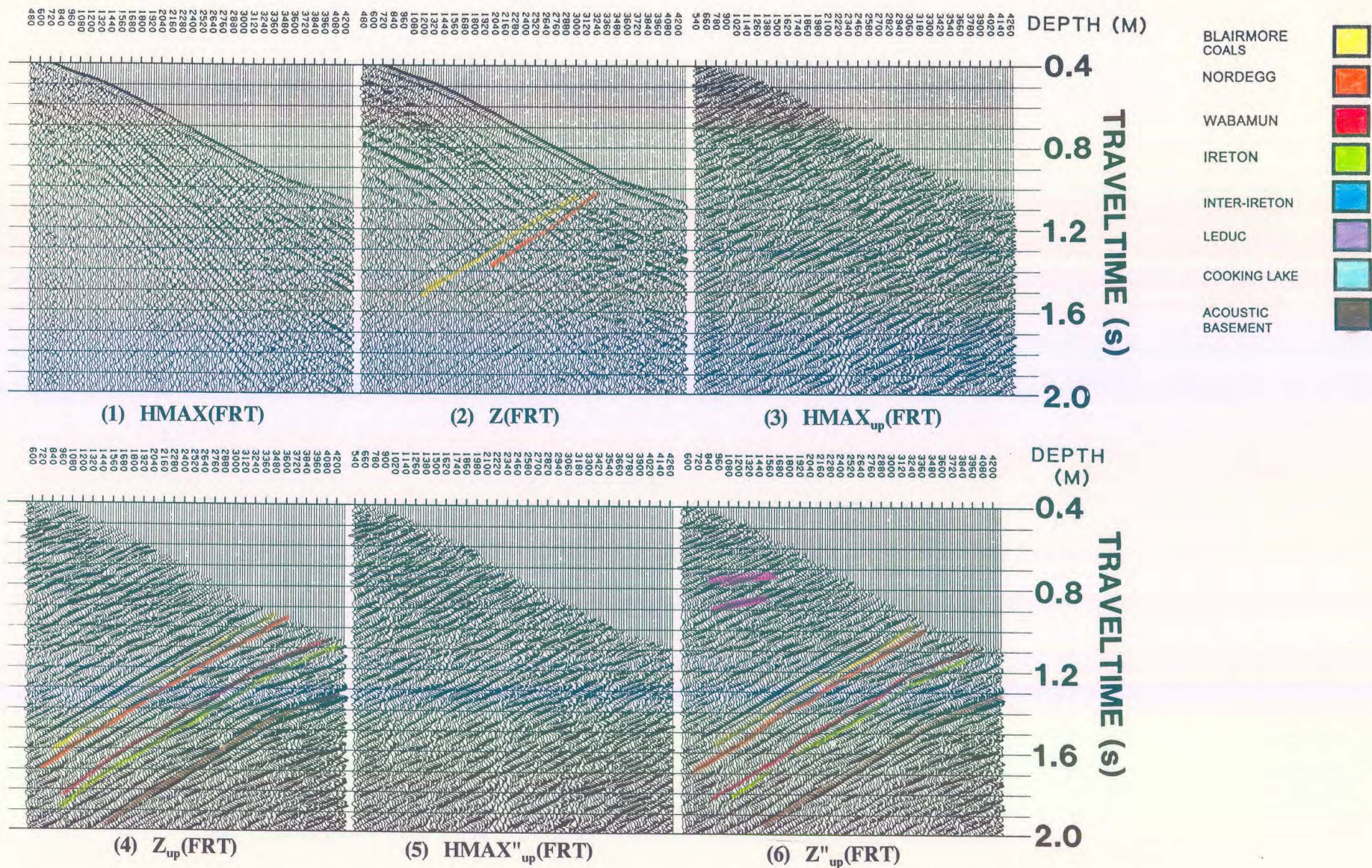


Figure 4.12 Interpretive processing panel depicting the time-variant model-based rotation of the far offset Ricinus VSP data resulting from interpretive processing (from Hinds et al., 1989a; Hinds et al., 1993c; Hinds et al., 1994c).

On the $Z_{up}(FRT)$ data in panel 4 of Figure 4.12, upgoing P-waves generated by shallow reflectors are improperly aligned (due to the choice of non-time variant rotation angles). The deeper events do not suffer much misalignment because deep event raypath geometries satisfy the near-vertical incidence angle assumption better than the raypaths of shallower events. The time-variant model-based rotation corrects for this misalignment of the shallow events. The output upgoing wave displays, $HMAX''_{up}(FRT)$ and $Z''_{up}(FRT)$, are shown on panels 5 and 6 in Figure 4.12, respectively. Note that the shallow events display better alignment than on the $Z_{up}(FRT)$ in panel 4. The rotation angle required for the Blairmore coals event on a particular trace was different to the rotation angle for deeper events (such as the acoustic basement) on the same trace. The time-variant rotation technique (Hinds et al., 1989a) generated these different rotation angles.

4.5.3 Deconvolution of the far offset data

The most realistic approximation to a far offset VSP deconvolution uses the separated polarized downgoing waves, $HMAX'_{down}(-TT)$, and the separated time-variant polarized upgoing P-waves contained in the $Z''_{up}(FRT)$ data, shown in panel 6 of Figure 4.12. To illustrate the deconvolution, a far offset deconvolution IPP to assist in the evaluation of the effect of far offset deconvolution on the Z''_{up} data (Figs. 2.56 and 4.13) has been designed. The deconvolution process involved designing the inverse wavelet for the $HMAX'_{down}(-TT)$ data (panel 2 of Fig. 4.13) and subsequently applying the operator to the $Z''_{up}(-TT)$ data (panel 4 of Fig. 4.13).

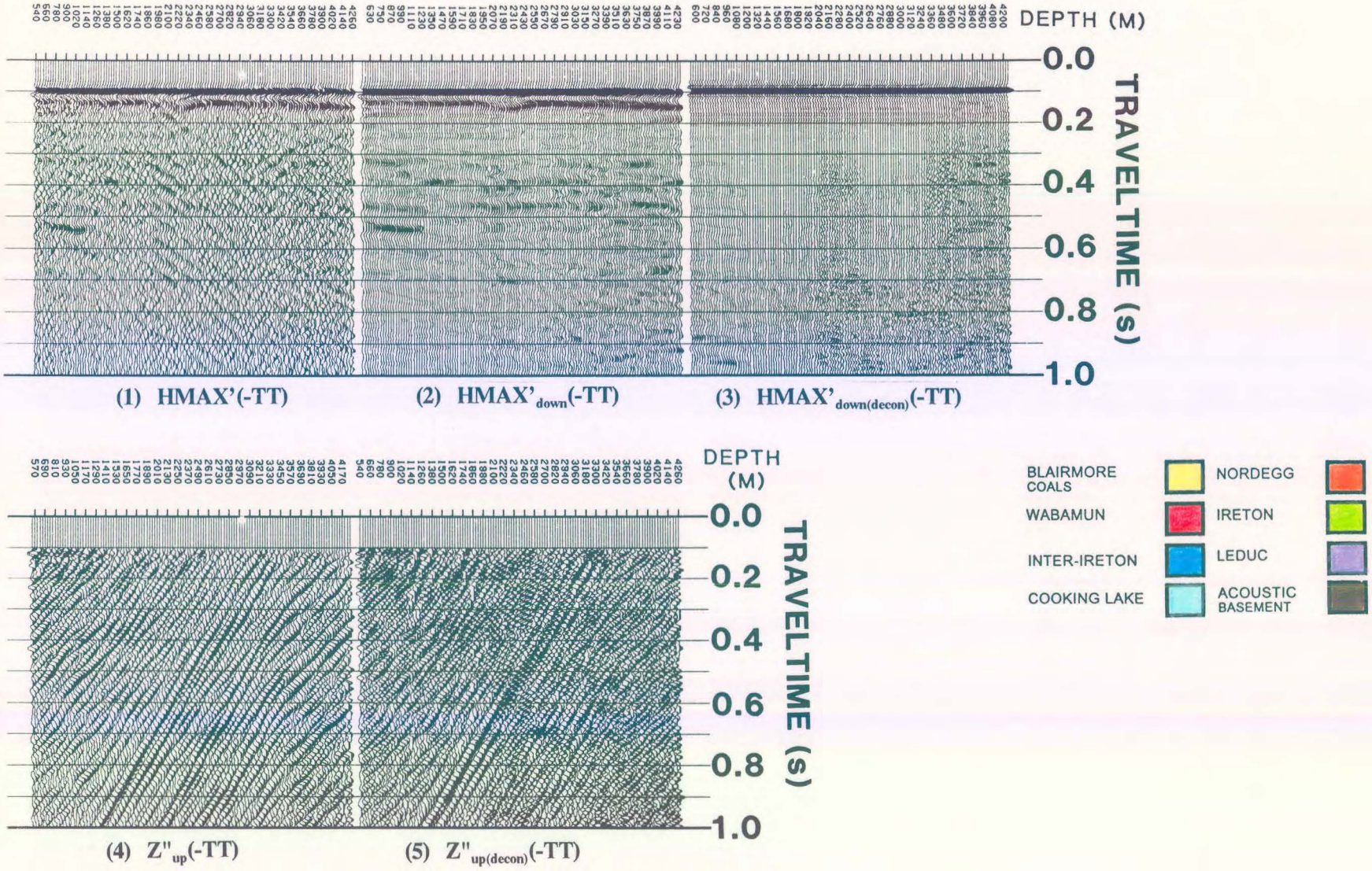


Figure 4.13 Interpretive processing panel depicting the far offset deconvolution of the Ricinus VSP data (from Hinds et al., 1993c; Hinds et al., 1994c).

The deconvolution was performed on the $Z''_{up}(-TT)$ far offset data (see Figs. 2.56 and 2.57); however the process added unacceptable noise to the data. This can be seen by comparing the $Z''_{up}(-TT)$ and $Z''_{up(decon)}(-TT)$ data shown in panels 4 and 5 in Figure 4.13. The upgoing P-wave events have become difficult to interpret on the deconvolved data.

In the final interpretation, the non-deconvolved far offset VSP data was evaluated to contain minimal multiple contamination at the zones of interest on the $Z''_{up}(+TT)$ data (on the Blairmore Coals down to the Acoustic Basement events shown in panel 6 of Fig. 4.12). For the far offset VSP data, the Blairmore or Nordegg multiples have a longer travel path to reach the Wabamun in comparison to the near offset VSP data. The Wabamun seems to be less affected on the far offset VSP data by the Blairmore coal or Nordegg multiple than on the near offset VSP data for this reason. This results in the deconvolution process for the far offset VSP data becoming a non-necessary step in the far offset processing runstream for this data.

4.5.4 VSP-CDP mapping

The $Z''_{up}(+TT)$ data from panel 6 of Figure 4.12 are used for the interpretation of the off-reef markers. Two interpretation panels are used for this purpose. The first focuses on the transformation of the $Z''_{up}(+TT)$ data in time (+TT) and depth into the VSP-CDP (Dillon and Thomson, 1984) domain of time (+TT) and offset distance from the well. The interpretive processing of the VSP-CDP mapping is displayed in the VSP-CDP IPP of Figure 4.14. For comparison, the VSP-CDP IPPs resulting from the normal time-variant runstream

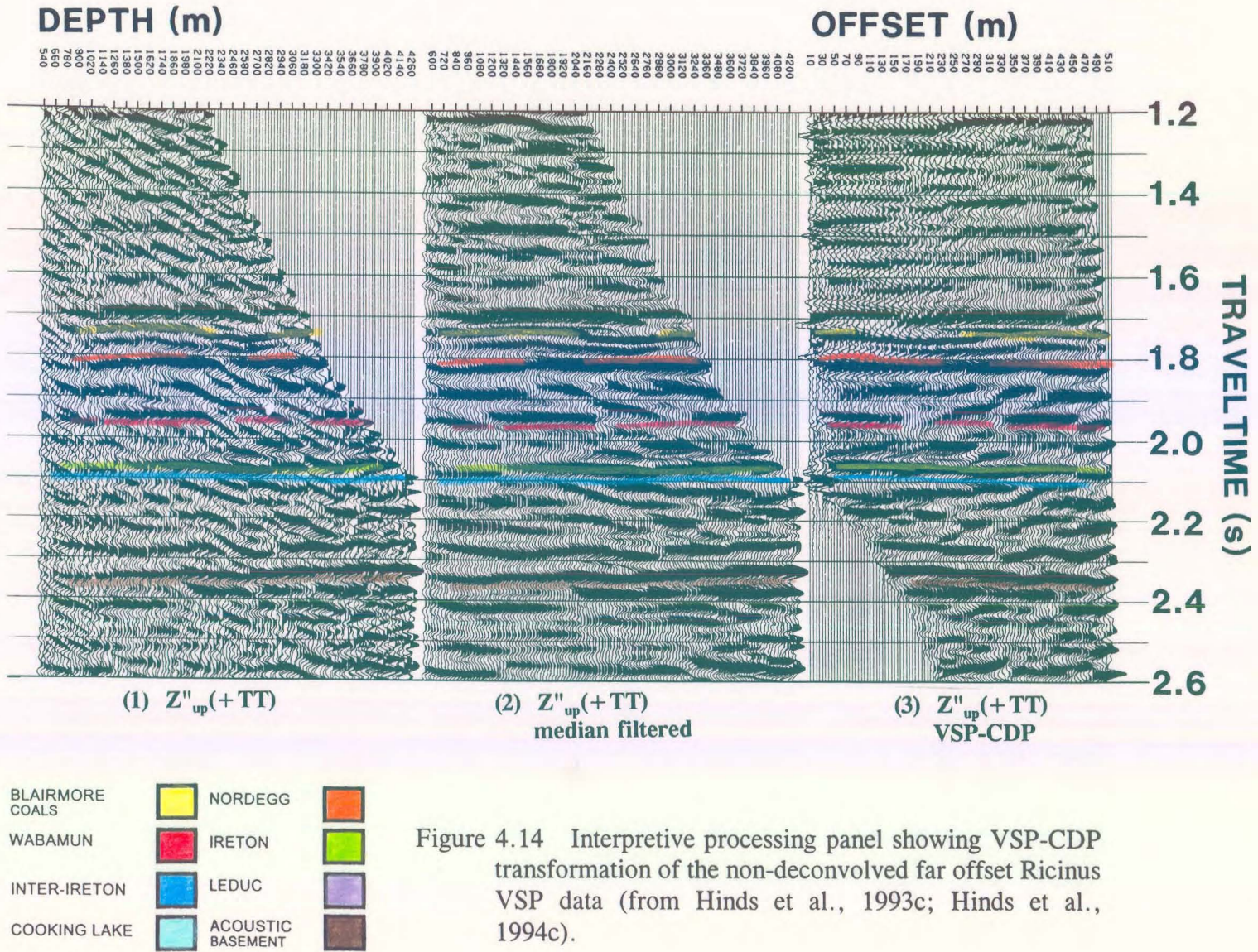


Figure 4.14 Interpretive processing panel showing VSP-CDP transformation of the non-deconvolved far offset Ricinus VSP data (from Hinds et al., 1993c; Hinds et al., 1994c).

suggested in chapter 2 and from the far offset deconvolution are presented in Figures 4.15 and 4.16, respectively. The second interpretation panel is the integrated seismic display shown in Figure 4.17 of the merged VSP-CDP display and the surface seismic data.

The $Z''_{up}(\text{FRT})$ data in panel 6 of Figure 4.12 placed in $+TT$ time are shown as the first panel of the VSP-CDP IPP in Figure 4.14. A median filtered $Z''_{up}(+TT)$ and the VSP-CDP mapped data (pseudo-two-way travelttime versus offset) are shown as panels 2 and 3, respectively.

The Blairmore coals, Nordegg, Wabamun, Ireton, inter-Ireton, Cooking Lake and acoustic basement markers are interpreted on these presentations. The median filtering (panel 2) as well as the VSP-CDP mapping processing (panel 3) have not appreciably distorted the interpretability of the original data ($Z''_{up}(+TT)$ data in panel 1 of Fig. 4.14).

The Ireton and inter-Ireton events are interpreted to be continuous and effectively parallel indicating that only off-reef events (as opposed to reefal events) have been imaged on the far offset VSP data. In contrast, the displays in Figures 4.15 and 4.16 are difficult to interpret in comparison to the data in Figure 4.14 because of the interfering noise and deconvolution processing artifacts. Interpretive processing improved the original mode-converted up- and downgoing SV-contaminated $Z_{up}(\text{FRT})$ and $HMAX_{up}(\text{FRT})$ data sufficiently enough (as shown in the final results of Fig. 4.14) to enable a confident interpretation during each processing step.

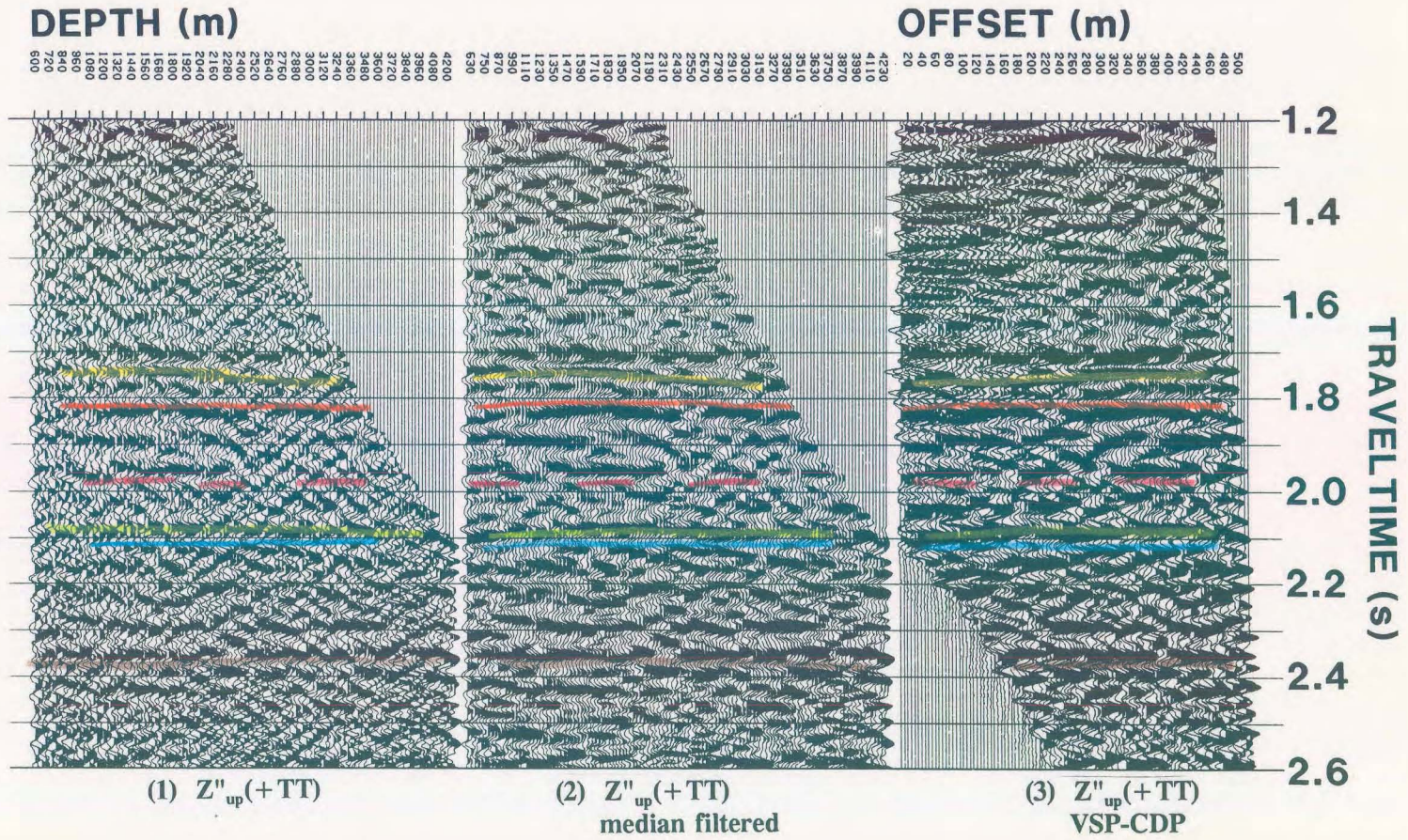


Figure 4.15 Interpretive processing panel showing the VSP-CDP transformed results for the far offset Ricinus VSP data resulting from the suggested "normal" runstream in chapter 2 (from Hinds et al., 1989a; Hinds et al., 1993c; Hinds et al., 1994c).

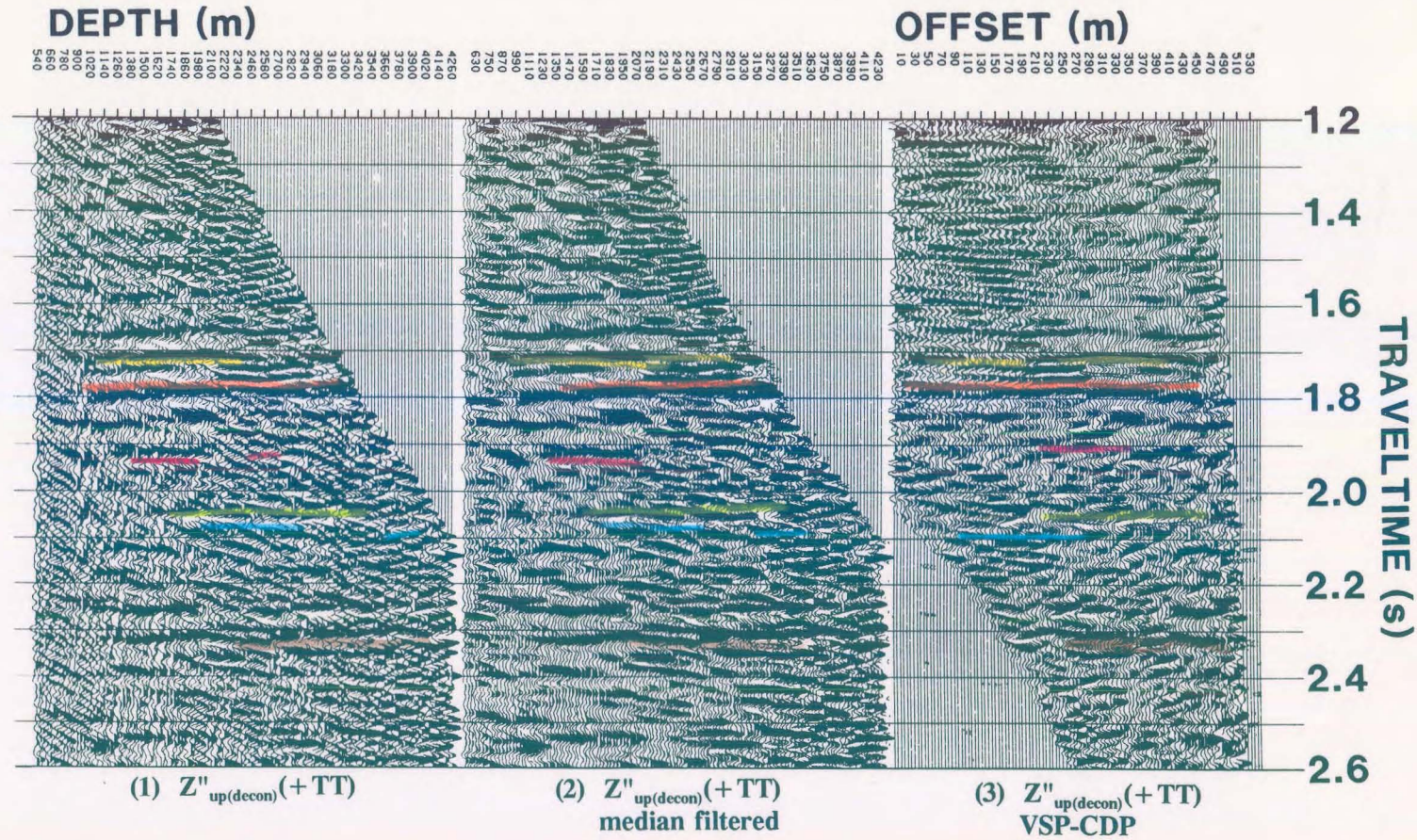


Figure 4.16 Interpretive processing panel showing the VSP-CDP transformed results for the deconvolved far offset Ricinus VSP data (from Hinds et al., 1993c; Hinds et al., 1994c).

4.6 Integrated interpretation

The integrated seismic display (ISD, see chapter 2) shows the surface seismic line merged with the VSP-CDP mapped results (panel 3 of Figure 4.14). The integrated seismic display in Figure 4.17 shows that the seismic interpretation displayed in Figure 4.3 extended the interpretation of the edge of the reef too far to the northeast, and supports the current interpretation as given in Figure 4.5.

These data also illustrate that the off-reef inter-Ireton event evident on the seismic section (Figure 4.5) extends about 500 m to the southwest. The surface seismic processing had sufficiently attenuated the SV events through the processing steps of normal moveout correction and CDP stacking. The interpretive processing enabled the desired attenuation of the SV events on the VSP data. The tie to the surface seismic up to 500 m away from the VSP well allows for the confident correlation of the inter-Ireton marker. Since only a small bundle of rays from the source to the well geophones has been affected by any Mesozoic faulting and the normal CDP summing found in surface seismic is not done in VSP processing, the coverage of the far offset VSP can be interpreted with a high level of confidence. By the processing that was applied in the rotations and the filtering which was evaluated using interpretive processing, the signal was enhanced enough to allow for an interpretation alongside the seismic data.

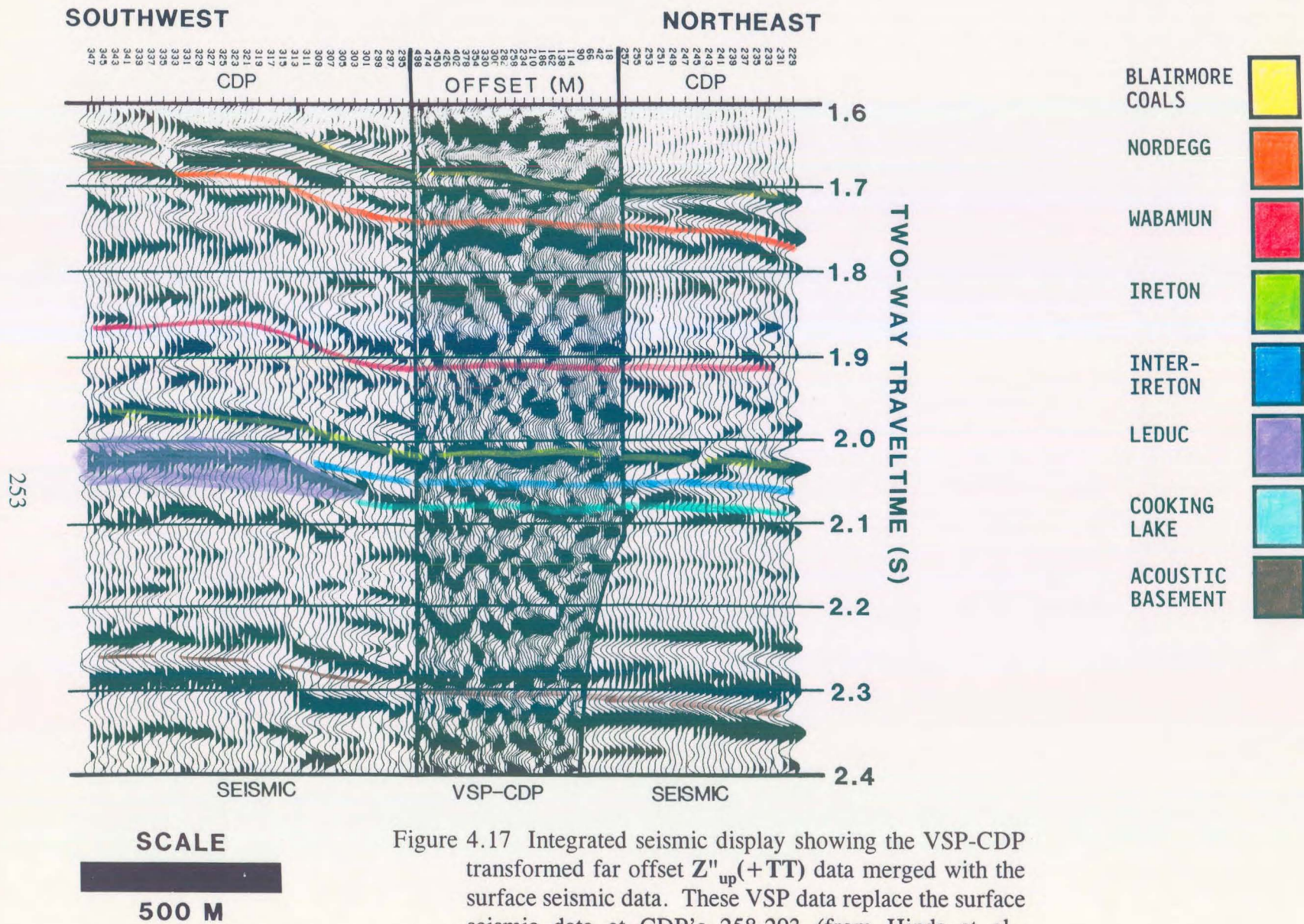


Figure 4.17 Integrated seismic display showing the VSP-CDP transformed far offset $Z''_{up}(+TT)$ data merged with the surface seismic data. These VSP data replace the surface seismic data at CDP's 258-293 (from Hinds et al., 1989a; Hinds et al., 1993c; Hinds et al., 1994c).

4.7 Interpretation discussion

The offsets for the Ricinus VSP survey were selected with the following considerations in mind:

- 1) If the atoll edge was in the near vicinity, then the inter-Ireton marker would terminate against the reef flank;
- 2) If the reef was further than 500 m (approximately half the 1100 m offset) away from the borehole or if the reef was in a different direction to the chosen offset direction, the inter-Ireton marker would be relatively flat and continuous;
- 3) the multiples that would affect a zero-offset seismic interpretation (migrated section) would be evident on the zero-offset VSP results; and
- 4) the exact geological tie with the seismic would be interpreted using the zero-offset VSP data.

The 199 m offset enabled an interpretation of the seismic signature at the well with a minimum of seismic interference from the complex Mesozoic faulting. The energy travelling down to the sonde in the borehole passes through the geological strata at near-normal incidence angles resulting in less ray bending than the CDP gathered surface seismic data. The well was in an off-reef position with the seismic interpretation being focused on the

Ireton, inter-Ireton, and Cooking Lake events rather than the Leduc event. The overlying marker that is used in isochron interpretation on the surface seismic was the Wabamun. The interpretational concern was that the Wabamun event was affected by the Blairmore coals or Nordegg multiples.

On the non-deconvolved near offset VSP data, interference with the Wabamun occurred until the geophone was below the Nordegg. The upgoing VSP events tied with the seismic section only after the VSP deconvolution was applied. The CDP stacking process within the surface seismic processing runstream enabled enough multiple attenuation to facilitate a Wabamun interpretation on the surface seismic data. The far offset VSP upgoing events did not critically require deconvolution (using the separated $HMAX'_{down}(-TT)$ data to design the operator) and easily correlated to the surface seismic events.

The far offset VSP provided subsurface coverage for 500 m away from the VSP well site. Each trace represents approximately 6 m of subsurface coverage. The updated geological model based on the far offset VSP results is shown in Figure 4.4. In this figure, 6-9 and 7-15 are reefal; the VSP well however, is at least 500 m away from the reef edge.

The ISD in Figure 4.17 shows the seismic marker for the inter-Ireton within the range of the VSP-CDP coverage being continuous and displaying relatively little structure. Within the 500 m range away from the VSP well, the event does not terminate against the flank of the reef on the merged far offset VSP and seismic section. The Wabamun event in the far offset VSP data has not been affected appreciably by the multiples from the Blairmore coal zones due to the different geometry of the raypaths between the zero-offset VSP and the far offset

VSP. The Leduc reef event dips relatively steeply to the north of well 7-15 to the reefal platform position (Figs. 4.5 and 4.17) suggesting an abrupt edge may be present beyond 500 m southwest of the VSP well. The geological tie has been confidently interpreted from the IPP at the well location and the interpretation has been carried through to the merged far offset VSP and seismic dataset in the ISD, all using the philosophy of interpretive processing.

The mapping of the off-reef sediments enabled the final whipstock decision to be made. The decision was to abandon the well because the reef was more than 500 m away from the well location.

CHAPTER 5

CASE STUDY OF THE FORT ST. JOHN GRABEN AREA

The deltaic sandstones of the basal Kiskatinaw Formation (Stoddart Group, upper Mississippian) were preferentially deposited within structural lows in a regime characterized by faulting and structural subsidence. In the case study of the Fort St. John Graben area, northwest Alberta, Canada, these sandstone facies can form reservoirs where they are laterally sealed against the flanks of upthrown fault blocks. Exploration for basal Kiskatinaw reservoirs generally is accompanied by the acquisition and interpretation of surface seismic data prior to drilling. These data are used to map the grabens in which these sandstones were deposited, and the location of horst blocks which act as lateral seals. Subsequent to drilling, three vertical seismic profile (VSP) surveys were conducted at the 9-24-82-11 W6M exploratory well site. These data supplemented the surface seismic and well log control such that (Hinds et al., 1991a; Hinds et al., 1993a; Hinds et al., 1994c):

- 1) direct correlation is made with the surface seismic data. As a result, the surface seismic control was accurately tied to the subsurface geology and geological seismic markers;
- 2) multiples were positively identified on the VSP data and the effect of these events on the surface seismic interpretation was determined; and
- 3) the subsurface geology, in the vicinity of the borehole, is more clearly resolved on the

VSP data than on the surface seismic control and an investigation of the basal Kiskatinaw revealed amplitude anomalies and local faulting which was not evident on the surface seismic data (Hinds et al., 1994b).

This chapter is a case history of the Fort St. John Graben 9-24 well (as reported in Hinds et al., 1991a; Hinds et al., 1993a and 1994b). An overview of the stratigraphy (Fig. 5.1) and the geologic history of the Lower Carboniferous in the study area is included. The acquisition and interpretive processing of the VSP data is described, and an integrated interpretation of the well log, surface seismic and seismic profile data is presented.

On the Fort St. John Graben dataset described in this chapter, faults which are not well resolved on the surface seismic data are better delineated on the VSP data. The interpretive processing of these data illustrate the utility of the seismic profiling technique to the search for hydrocarbons in structurally complex areas.

5.1 Introduction

On the basis of conventional surface seismic data, an exploratory well (9-24-82-11 W6M) was drilled into the basal Kiskatinaw Formation (Stoddart Group, upper Mississippian; Fig. 5.1) on the downthrown side of a fault block in the Fort St. John Graben area, Peace River Embayment (Fig. 5.2 and 5.3). It was expected that gas-prone sandstones of the basal Kiskatinaw would be laterally truncated and sealed against shales of the Golata Formation. Contrary to expectations, the well encountered unproductive, shaly sandstone tidal-flat facies

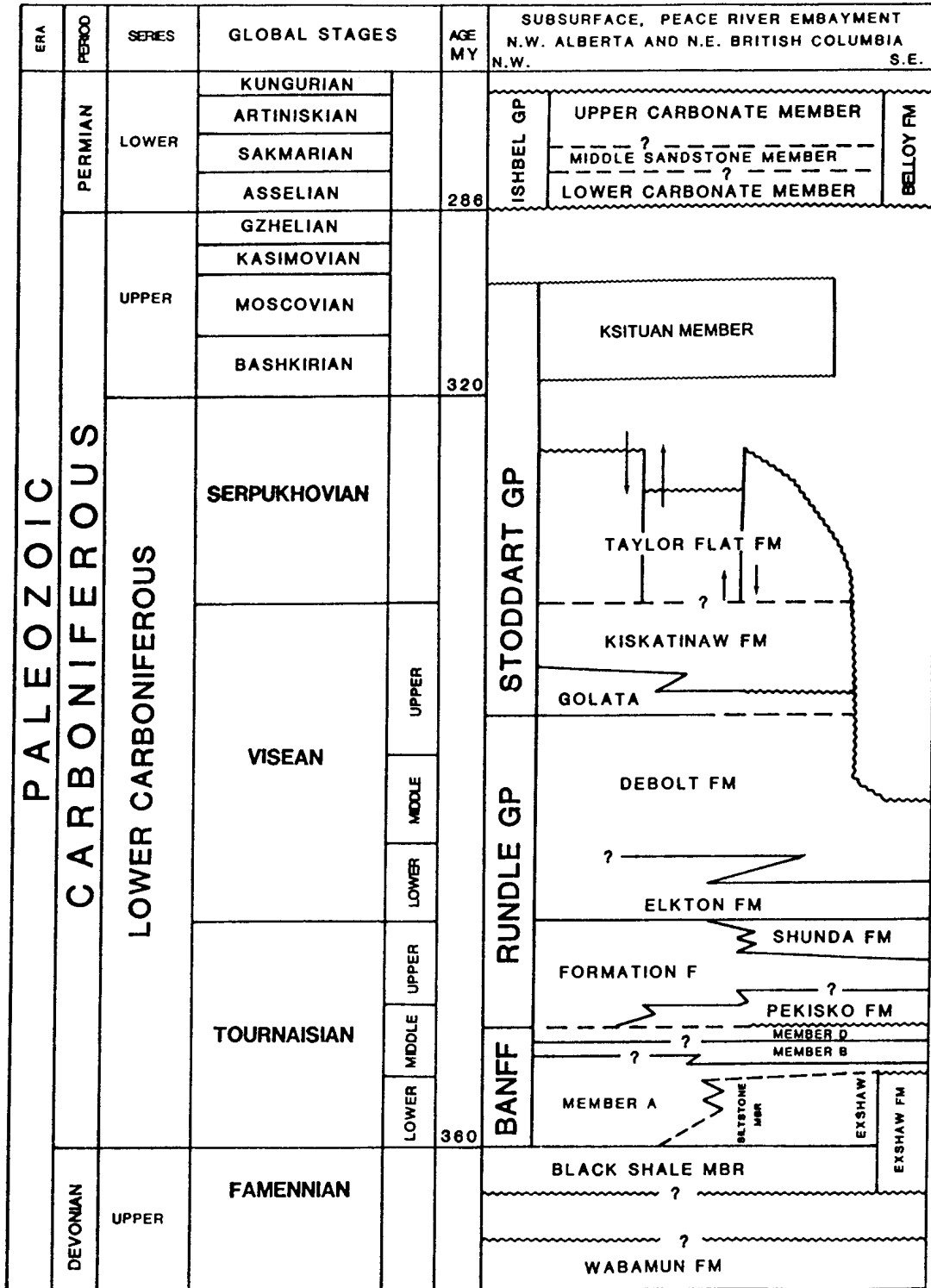


Figure 5.1 Stratigraphy of the Fort St. John Graben study area (modified from Richards, 1989).

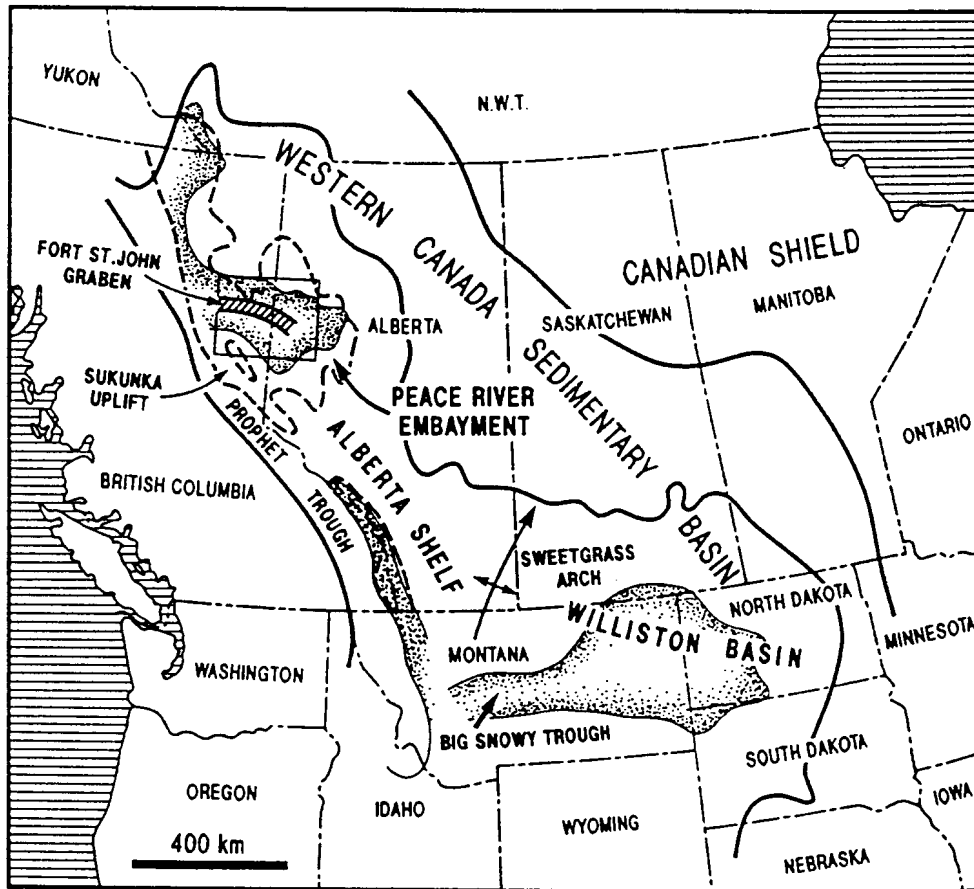


Figure 5.2 Map of Western Canadian Sedimentary Basin tectonic elements showing the Peace River Embayment, Prophet Trough, Sukunka Uplift, cratonic platform and Fort St. John Graben. (Barclay et al., 1990)

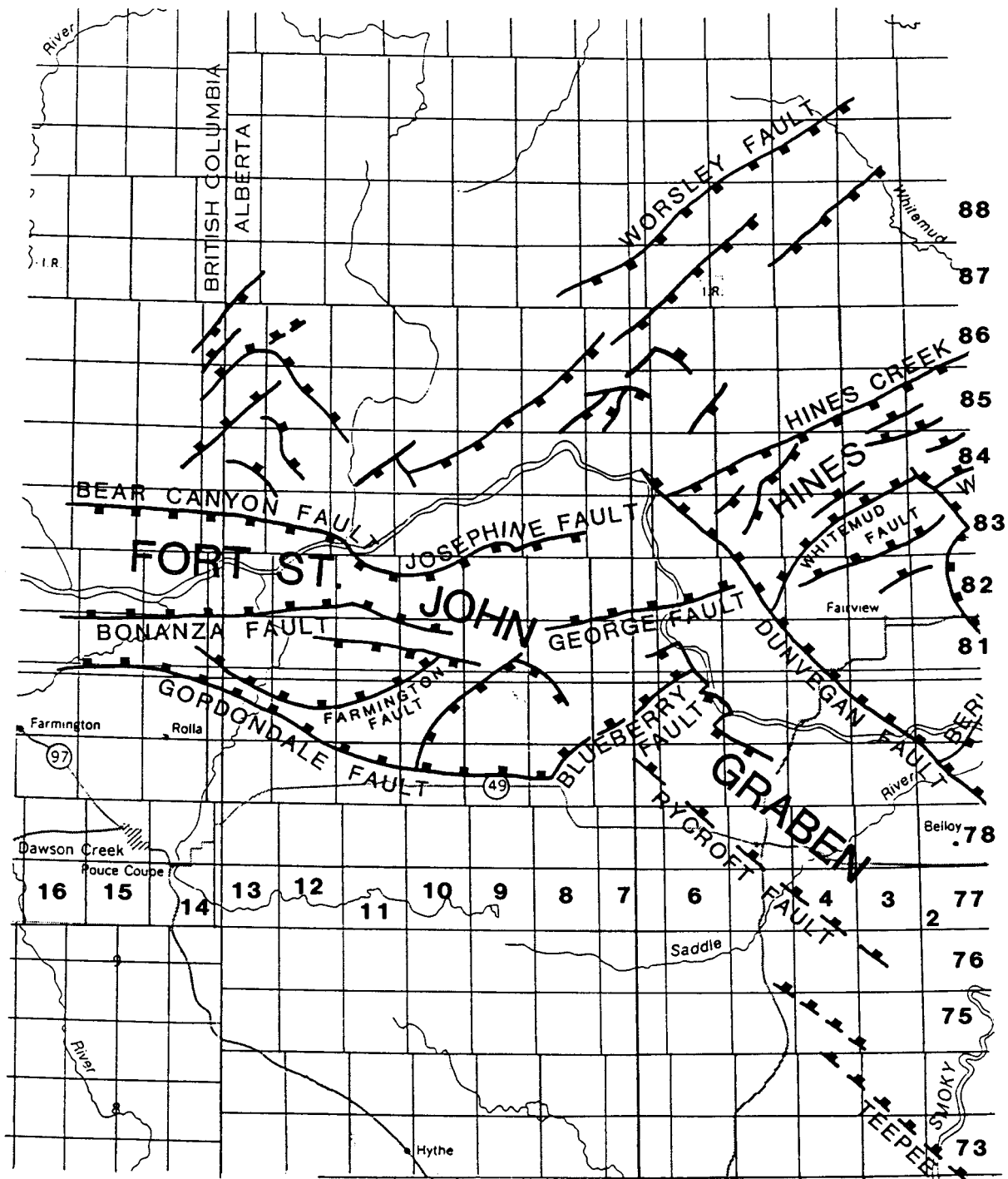


Figure 5.3 Detailed area map of the Fort St. John Graben showing the Bear Canyon, Josephine, Bonanza and George faults (from Richards et al., 1994). The study area is centred in Township 82 and Range 11 west of the 6th Meridian in Alberta, Canada near the Alberta and British Columbia provincial border.

in the basal Kiskatinaw and a commercial gas-bearing zone in the upper Kiskatinaw, and is now shut-in (Hinds et al., 1991a; Hinds et al., 1993a and 1994b).

To obtain a higher resolution image of the subsurface in the vicinity of well 9-24, and to evaluate the presence and proximity of any fault features which might not have been resolved on the surface seismic data, three VSP (vertical seismic profile) surveys were designed and performed at the 9-24 well site. These profiles were used in conjunction with surface seismic coverage to cooperatively image the fault systems in the area and to elucidate the seismic signature of the upper Kiskatinaw reservoir which had not been prognosed.

5.2 Geological overview

5.2.1 Tectonic and depositional history of the Peace River Embayment

This section will review the tectonic and depositional history for the study area. Unlike the case studies of chapters 3, 4, and 6 which pertain to carbonate reef exploration in the WCSB; this case study pertains to channel sand deposition and hydrocarbon entrapment within. The following section will review the stratigraphy of the study area.

Investigation of the Peace River Arch and Peace River Embayment revealed a depositional regime characterized by faulting (O'Connell, 1990) and structural subsidence. The Peace River Arch can be traced to a crustal structure consisting of uplifted granitic basement (Fig. 5.4a; Cant , 1988) and subsequently was deformed in three main phases:

- 1) the formation of a structural high in the latest Late Proterozoic which was overlapped by siliciclastic, evaporite and carbonate deposition until the Middle to Late Devonian;

The basement was uplifted 800 to 1000 m above the regional elevation (Cant, 1988) during the early Paleozoic (mid-Cambrian) as an asymmetrical feature with the northern flank dipping steeply and the southern flank dipping more gently (O'Connell et al., 1990). During the Middle to Upper Devonian, a diachronous siliciclastic unit (lithozone as defined in Trotter, 1989) called the Granite Wash (sediments derived from plutonic and metamorphic basement relics) and carbonate and shale deposits of the Elk Point (along with Gilwood sandstone), Beaverhill Lake (Slave Point, carbonate reefs and Waterways Fm), Woodbend (fringing reefs, basal ramp to stacks of carbonate shelves and overlying carbonate ramp) and Winterburn (Nisku and Blueridge Fm; Moore, 1988) Groups overlapped onto the emergent arch. The Wabamun Fm carbonates eventually buried most of the Arch. Another feature existing during the deposition of the Wabamun Fm was localized islands of subaerially exposed Granite Wash Fm that were present during the deposition of the lower Banff Fm (Richards, 1991, pers. comm.).

- 2) the formation of a series of embayments resulting in anomalously thick Carboniferous, Permian and Triassic deposits;

During the deposition of the Middle Devonian Elk Point Group, normal faulting began. These normal faults were rejuvenated in the late Famennian during the deposition of the upper Wabamun Fm and the overlying Exshaw Fm (Fig. 5.4b).

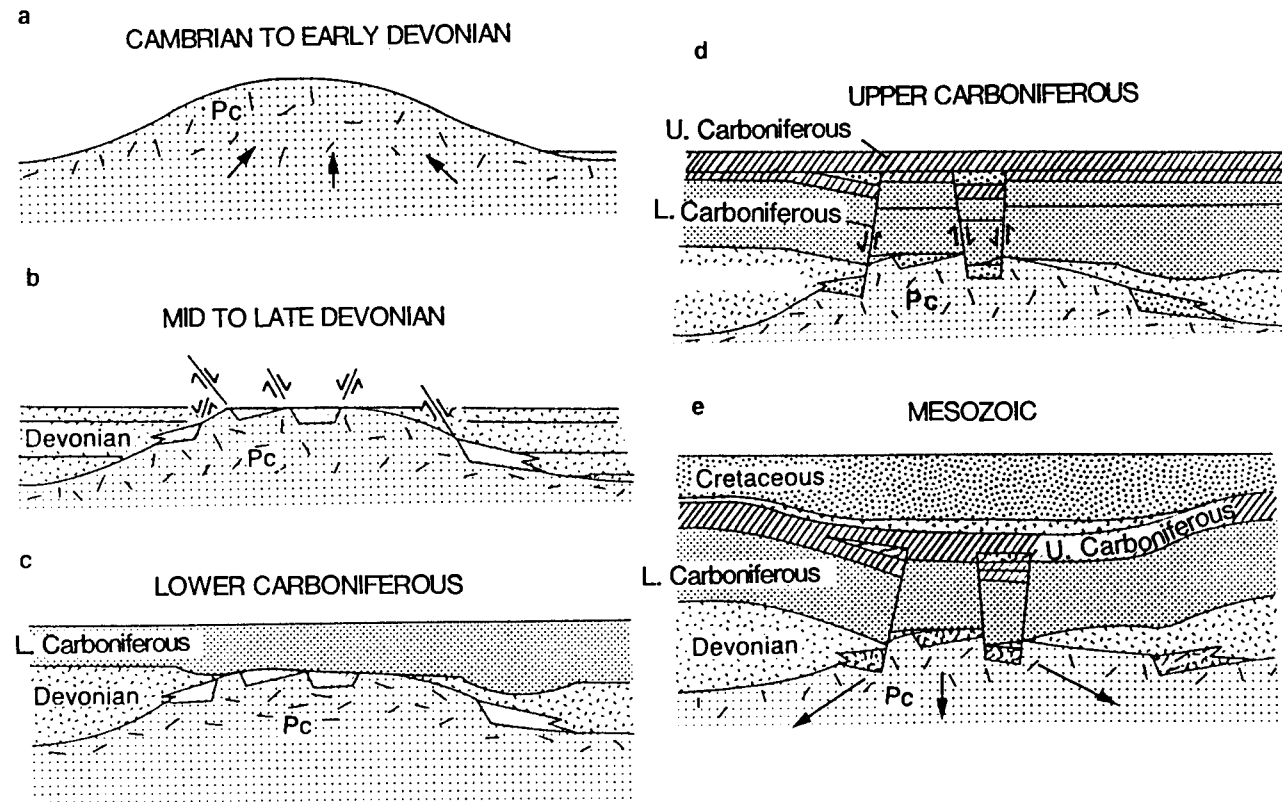


Figure 5.4 Diagrammatic summary of the depositional and tectonic history of the Peace River Embayment area (from Cant, 1988) from the Cambrian to the Cretaceous periods.

3) the development of a deep basin component of the foreland basin during the Jurassic and Cretaceous.

The arch ceased to be emergent by the beginning of the Carboniferous.

The Peace River Embayment, a structural inversion consisting of northeast to southwest trending interlinked graben and half-grabens (Barclay et al., 1990), started to develop during the latest Devonian (late Famennian) and earliest Carboniferous when the Exshaw and overlying lower Banff Fm were deposited (Richards, 1989; Richards et al., 1994). The major tectonic features surrounding the Embayment were the Prophet Trough (Richards, 1989; Richards et al., 1994), Sukunka Uplift (Richards, 1989) and cratonic platform (Fig. 5.2). The northwest-trending narrow pericratonic Prophet Trough (O'Connell et al., 1990) resulted from the downwarping and downfaulting of the western margin of the North American plate during the latest Devonian (late Famennian) and Carboniferous and is interpreted as a back-arc basin (Richards, 1989). In the detailed stratigraphic correlation chart (Fig. 5.1), the Famennian to Tournaisian boundary coincides with the Devonian to Carboniferous boundary. The Carboniferous Peace River Embayment opened northwestward into the Prophet Trough. During the middle to late Tournaisian, the Embayment became better defined as a separate entity. The northern Sukunka uplift on the southwestern side of the Embayment formed a low rim that restricted the access of the Embayment sediments into the southeastern part of the Prophet Trough.

Regional subsidence continued associated with extensive block faulting (Fig. 5.4d) along normal faults (Cant, 1988). During the period of block faulting, anomalously thick Lower

Carboniferous successions of siliciclastics and ramp-to-platform carbonates were deposited along the axis of the embayment (Richards, 1989, 1990).

The Devonian and Carboniferous tectonic history of the Peace River Embayment has been summarized by Richards (1989, 1990) and Richards et al. (1994). The onset of its development is postulated to be the late Famennian to early middle Tournaisian. During that initial time, the deposition of the Exshaw Fm and the overlying lower Banff Fm occurred (Richards, 1990).

5.2.2 Lower Carboniferous: Fort St. John Graben Area

Within the Carboniferous succession in the Fort St. John Graben study area (Fig. 5.3), four principal episodes of blockfaulting have been recognized (Richards 1989, 1990):

- 1) after deposition of the latest Devonian to earliest Carboniferous deposits of the Exshaw Fm but prior to the deposition of the overlying Banff Fm;
- 2) during deposition of the lower Banff Fm (early middle Tournaisian);
- 3) during the deposition of the Golata and Kiskatinaw Formations (late Visean); and
- 4) after deposition of the upper Visean to Serpukhovian (?) Taylor Flat Fm but prior to that of the Permian Ishbel Group.

Marked regional subsidence accompanied the second and third phases of blockfaulting, whereas subaerial erosion and local uplift accompanied the first and last phases. Pronounced regional subsidence, at least locally, accompanied by blockfaulting also took place during deposition of the middle and upper Tournaisian Pekisko and Shunda Formations. In the middle Tournaisian, the developed embayment can best be termed a deep re-entrant into the western cratonic platform and the Prophet Trough is interpreted as a back arc basin (Richards, 1989). Deep-water environments existed in the embayment area during periods of pronounced subsidence. In the general study area, the Fort St. John and Hines Creek Grabens (Barclay et al., 1990) were already developing before the deposition of the Stoddart Group.

The Lower Carboniferous deposition spans from the upper part of the Exshaw Fm to the top of the Taylor Flat Fm. Carbonate and fine-grained terrigenous clastics were deposited during the Exshaw-Debolt interval. Basal shale, carbonate ramp deposits, shallow water shelf carbonates, inter- to supratidal carbonate, clastics and evaporites were deposited in the Banff Fm. Shales are also found in the Pekisko Fm, a coeval correlative for the Pekisko and Shunda defined in Richards (1989) called Formation F and Shunda Fm which overlie the Banff Fm. A well developed basin, slope and shelf environment in the Peace River Embayment was developed during the deposition of the lower and middle Banff Fm and during the Pekisko/Shunda succession. Apart from these times, sedimentation in the area kept pace with the subsidence which resulted in normal topographic relief.

The Golata, Kiskatinaw and Taylor Flat Formations were deposited in the late Viséan and Serpukhovian subsequent to the deposition of the Debolt Fm with the Golata overlying the

Debolt Fm conformably in the central part of the embayment. The Golata consists of fissile grey mudstone, siltstone and shale (Barclay, 1988). Towards the basin margins, the Golata and Debolt contact becomes disconformable (O'Connell et al., 1990).

The Kiskatinaw consists predominately of sandstone with minor quantities of fine grained siliciclastics, limestones, dolostones and coals. At least eight depositional cycles make up the formation, but three main depositional cycles are referred to informally as the lower, middle and upper Kiskatinaw. The Kiskatinaw Fm represents a marine-dominated deltaic system which may have resembled an estuary in the study area during deposition (Richards, 1989; Richards et al., 1994). The study area was a semi-enclosed body of coastal water. Blockfaulting occurred accompanied by deep subaerial erosion which resulted in substantial thickness changes in the Kiskatinaw and Taylor Flat Fm deposits.

The Kiskatinaw and Golata Fm contact is unconformable. This prodelta sequence (Golata Fm) can serve as a reservoir seal in those places where, as a result of faulting, it is juxtaposed against the sandstones of the basal Kiskatinaw. The uppermost and basal Kiskatinaw Fm sandstones deposits are exploration targets.

The deposition in the study area is shown in the models for the Stoddart Group deposition in figure 5.5a-d (from Barclay et al., 1990; Fig. 17a-d). The creation of the hydrocarbon trapping structures occurred prior to the deposition of the Permian Belcourt and Belloy Fm.

The study area is in the Fort St. John Graben area defined by East-West faulting to the North

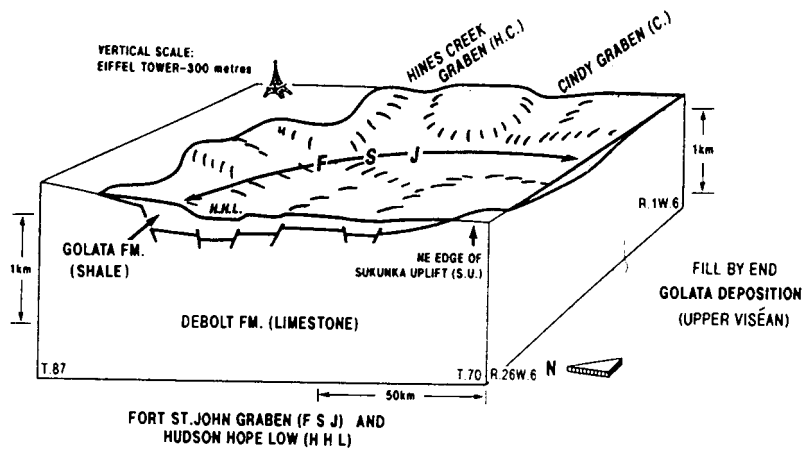


Figure 5.5A Block diagram showing the Fort St. John Graben deposition by the end of the Golata Formation time (from Barclay et al., 1990).

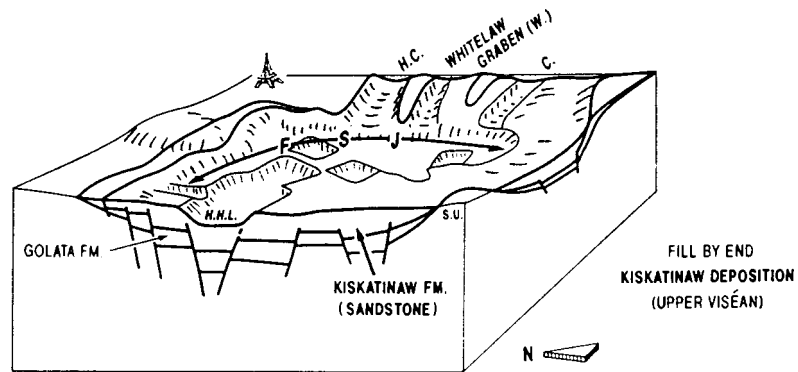


Figure 5.5B Block diagram showing the Fort St. John Graben deposition by the end of the Kiskatinaw Formation time (from Barclay et al., 1990).

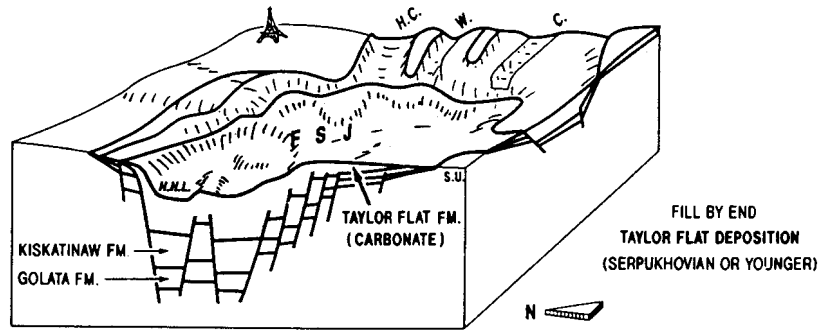


Figure 5.5C Block diagram showing the Fort St. John Graben deposition by the end of the Taylor Flat Formation time (from Barclay et al., 1990).

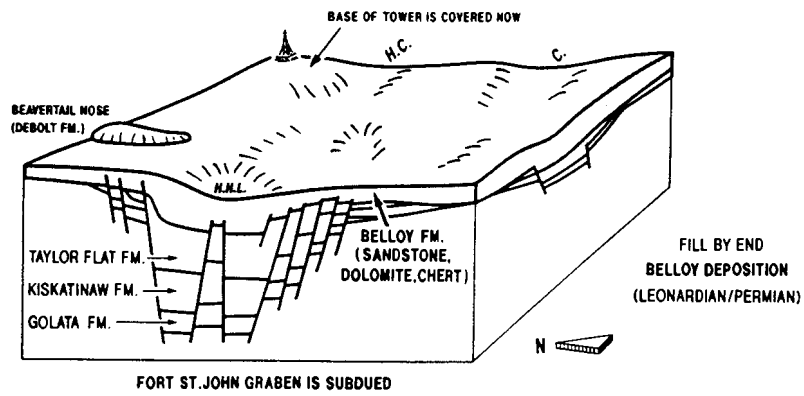


Figure 5.5D Block diagram showing the Fort St. John Graben deposition by the end of the Belloy Formation time (from Barclay et al., 1990).

(Bear Canyon and Josephine faults) and to the South (Bonanza fault) as shown in Figure 5.3. The Fort St. John Graben is part of the Dawson Creek Graben Complex (Barclay et al., 1990) as is shown in figure 5.6 and 5.7.

The channel fill making up the basal Kiskatinaw (Barclay, 1988) were the target of the 9-24 well. The hypothesis was that thick sections of basal Kiskatinaw would be preferentially deposited in the structural lows on the downthrown side of early Kiskatinaw faults. The basal Kiskatinaw encountered by the 9-24 well was not of reservoir quality; however, the sandstones of the upper Kiskatinaw contain commercial gas.

5.3 Original interpretation and well results

Seismic data interpreted by the owners of the well prior to the drilling of well 9-24 and the running of the VSP surveys are shown in Figure 5.8. All subsequent interpretation on data presented within this chapter are presented as part of the thesis research.

The split-spread, 96 pre-stack trace data used to create the stacked section (Fig. 5.8) were acquired using a patterned dynamite source (3 X 3 kg at 15 m) and DFS4 recording equipment (12/18-124 Hz filter; notch (60 Hz) filter out). The groups consisted of nine inline 14-Hz L25D geophones spaced at 6.1 m. The geophone group, shot, common mid-point (CMP), and near offset intervals were 67.1, 134.1, 33.5, and 201.2 m respectively.

The seismic section (normal polarity display; Fig. 5.8) was migrated using a prestack partial

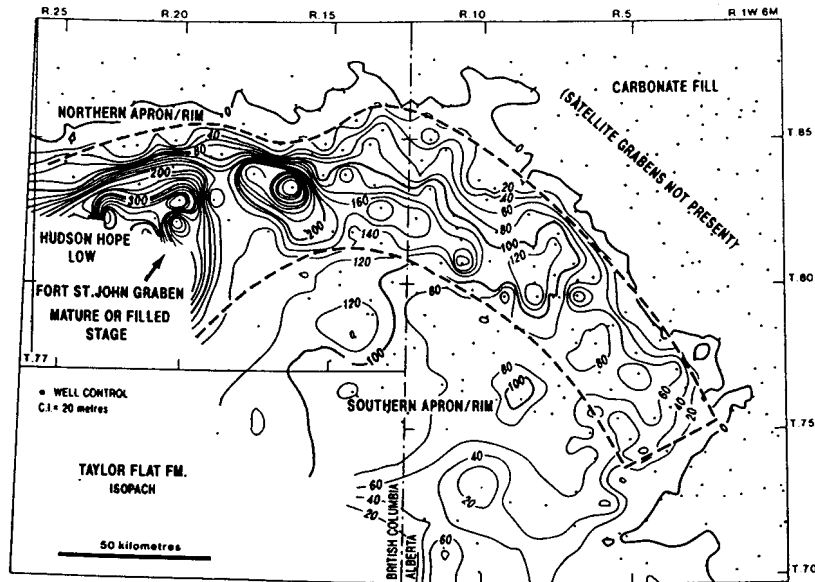


Figure 5.6 Location of the Fort St. John Graben as outlined by the Belloy Formation isopach map (from Barclay et al., 1990). The Belloy deposition marked the end of the subsidence in the graben.

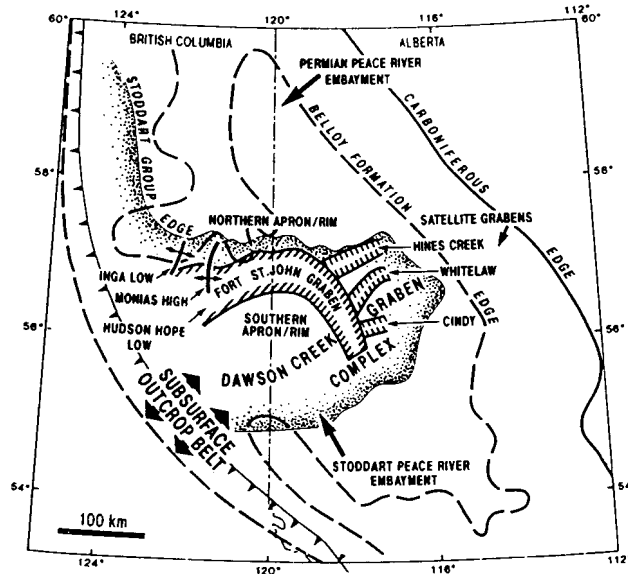
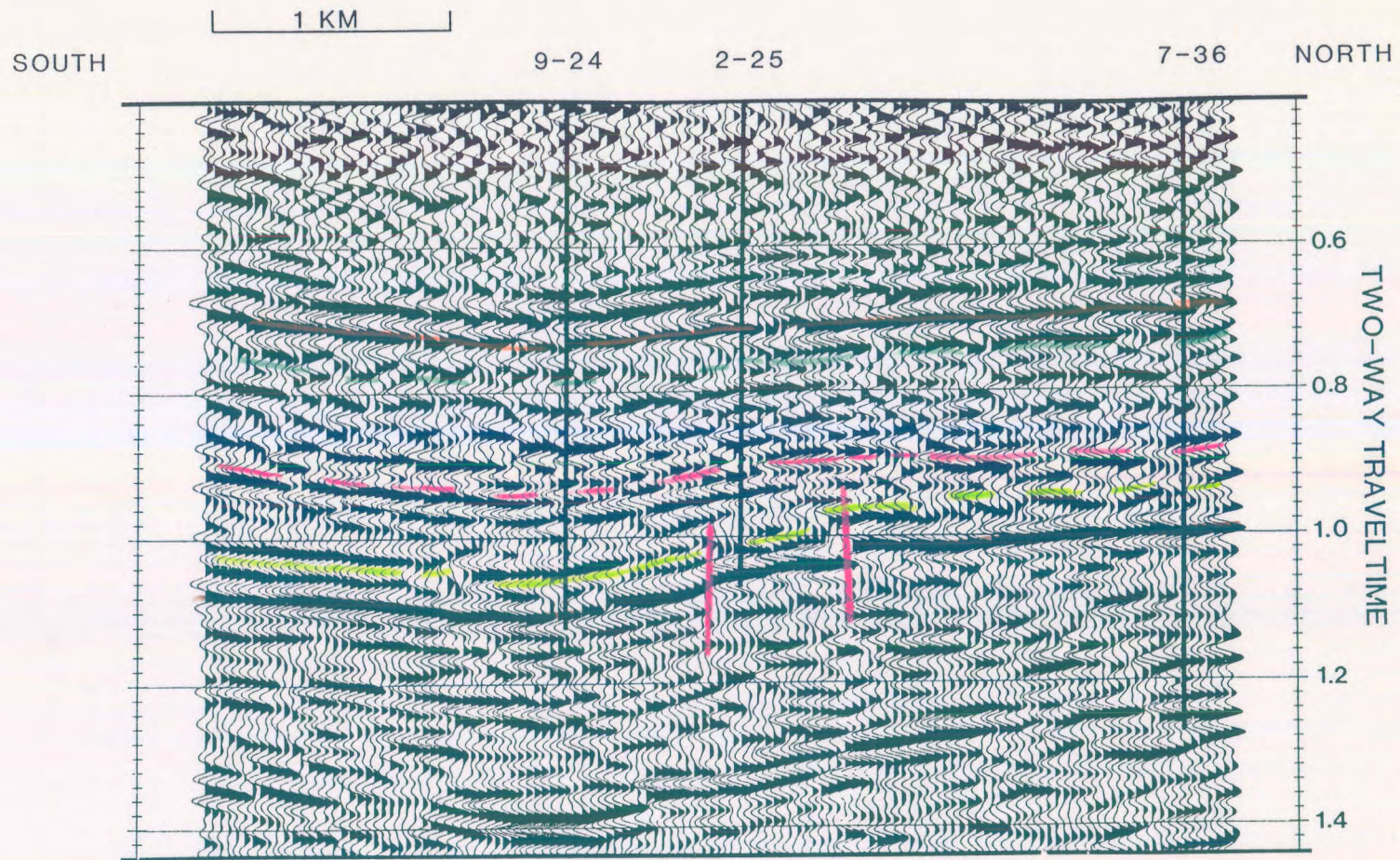


Figure 5.7 Peace River Embayment stratotectonic elements including the Fort St. John Graben (from Barclay et al., 1990).



273

| | | | |
|------------------|---|----------------------|---|
| SPIRIT RIVER |  | NORDEGG |  |
| HALFWAY / DOIG |  | BELLOV |  |
| TAYLOR FLAT |  | KISKATINAW |  |
| BASAL KISKATINAW |  | GOLATA |  |
| DEBOLT |  | MULTIPLE REFLECTIONS |  |

Figure 5.8 Example surface seismic data displaying the original interpretation of the owners of the 9-24 well (preceding the drilling of the well). The data suggested one major fault between the intended well 9-24 and the existing well 2-25.

migration scheme which consisted of applying a common-offset domain, dip-moveout (DMO) correction (Hale, 1984) to the prestack data. Updated velocities were then determined using the DMO-corrected CMP gathers. Closely spaced velocity analyses were performed since the stacking velocities changed rapidly along the line. This prestack processing was followed by poststack phase-shift migration. The poststack migration method is reviewed in Gazdag (1978) and Gazdag and Squazzero (1984).

The surface seismic data were used to elucidate the structural setting at the Kiskatinaw level. The interpreted events on the seismic line are the Nordegg, Halfway/Doig, Belloy, basal Kiskatinaw, and Debolt (stratigraphically listed in Fig. 5.1). The 9-24-82-11 W6M well was located approximately 200 m east of the seismic line and has been projected onto the seismic line as shown in Figure 5.8. Note that 9-24, as projected, is on a downthrown fault block relative to 2-25-82-11 W6M and 7-36-82-11 W6M (Fig. 5.8).

Well 2-25 encountered approximately 25 m of relatively clean, wet basal Kiskatinaw sandstone and was abandoned. Well 7-36 penetrated 35 m of basal Kiskatinaw sandstone which tested gas plus salt water and is currently classified as a shut-in gas well. Well 9-24 was drilled in the expectation that basal Kiskatinaw gas would be stratigraphically entrapped against the flank of the upthrown flank block; however the basal Kiskatinaw proved to be shaly-sandstone and not of reservoir quality. 9-24 was shut-in as an upper Kiskatinaw gas well.

5.4 VSP acquisition

Three VSP surveys were run at the 9-24 well site (one near offset and two far offset sources). The VSP were planned with the following objectives in mind:

- 1) to provide a confident surface seismic tie to:
 - a) the upper Kiskatinaw Fm reservoir;
 - b) the lower Kiskatinaw Fm; and
 - c) the Debolt Fm;

- 2) to determine if multiple reflections were a significant problem at the Kiskatinaw level, and to design an effective deconvolution filter;

- 3) to map the lateral extent of the shaly sandstone of the basal Kiskatinaw and upper Kiskatinaw reservoir in the direction of the far offset VSPs; and

- 4) to provide a higher resolution seismic image of the Debolt fault in the vicinity of the 9-24 well.

The near offset VSP source was located 149 m from well 9-24 and in the direction of well 2-25. One of the far offset source locations (referred to as FSJG1 in chapter 2) was in the direction of 2-25 and 700 m from the 9-24 well site. The other far offset source location (referred to as FSJG2) was situated 741 m east of well 9-24. Two Vibroseis units operated

in series at each offset using a 12 second sweep of 10-90 Hz. The recording length was 15 seconds resulting in a 3 s cross-correlated output. On average, six sweeps were summed at each geophone sonde location. The total depth of well 9-24 was 2126 m below Kelly Bushing of the drilling rig (KB at 644 m asl). All three offset sources were at 639 m asl. Data were recorded at a sampling rate of 1 ms using an MDS-10 unit. The recording filter, OUT/250, was designed to prevent aliasing.

The triaxial sonde vertical spacing was 20 m (from a depth of 2030 m up to 350 m). As a precautionary measure, calibration records were acquired at several depths as the sonde was lowered down the borehole and repeated again during the production runs to detect possible depth errors or cable stretch.

5.5 Near offset (149 m) VSP interpretive processing

During the processing of the near offset VSP data, a series of interpretive processing panels (IPPs) were designed. These panels were designed to display the following interpretive processing steps (Hinds et al. 1991a; Hinds et al., 1993a and 1994b; and Hinds et al., 1994c):

- 1) upgoing and downgoing P-wave separation;
- 2) deconvolution of the separated upgoing P-waves; and

3) inside and outside corridor stacks of both the nondeconvolved and deconvolved upgoing waves.

5.5.1 P-wave event separation

The separation of the upgoing and downgoing P-waves from the Z(FRT) data is displayed in the wavefield separation interpretive processing panel (Hinds et al., 1989a; Hinds et al., 1993a; Hinds et al., 1994c) of Figure 5.9.

Panel 1 displays the Z(FRT) data after trace normalization. The upgoing P-wave events are difficult to discern until the Z(FRT) data are gained (panel 2). On these panels, the tube wave is visible below 0.9 s as a high-frequency, downgoing wavetrain with a velocity of propagation of about 1435 m/s. The tube wave reflects from the bottom of the well borehole and travels back up. This accounts for the upgoing tubewave F-K events discussed in chapter 2.

Several upgoing primary events and multiple reflections can be identified on panel 2. Consider for examples, the Spirit River and Nordegg events which are highlighted in blue and orange, respectively. Each of these events is followed by a trailing surface-generated multiple with a lag time of about 110 ms. This multiple pattern (both upgoing and downgoing waves) is highlighted in panel 2 of Figure 5.9.

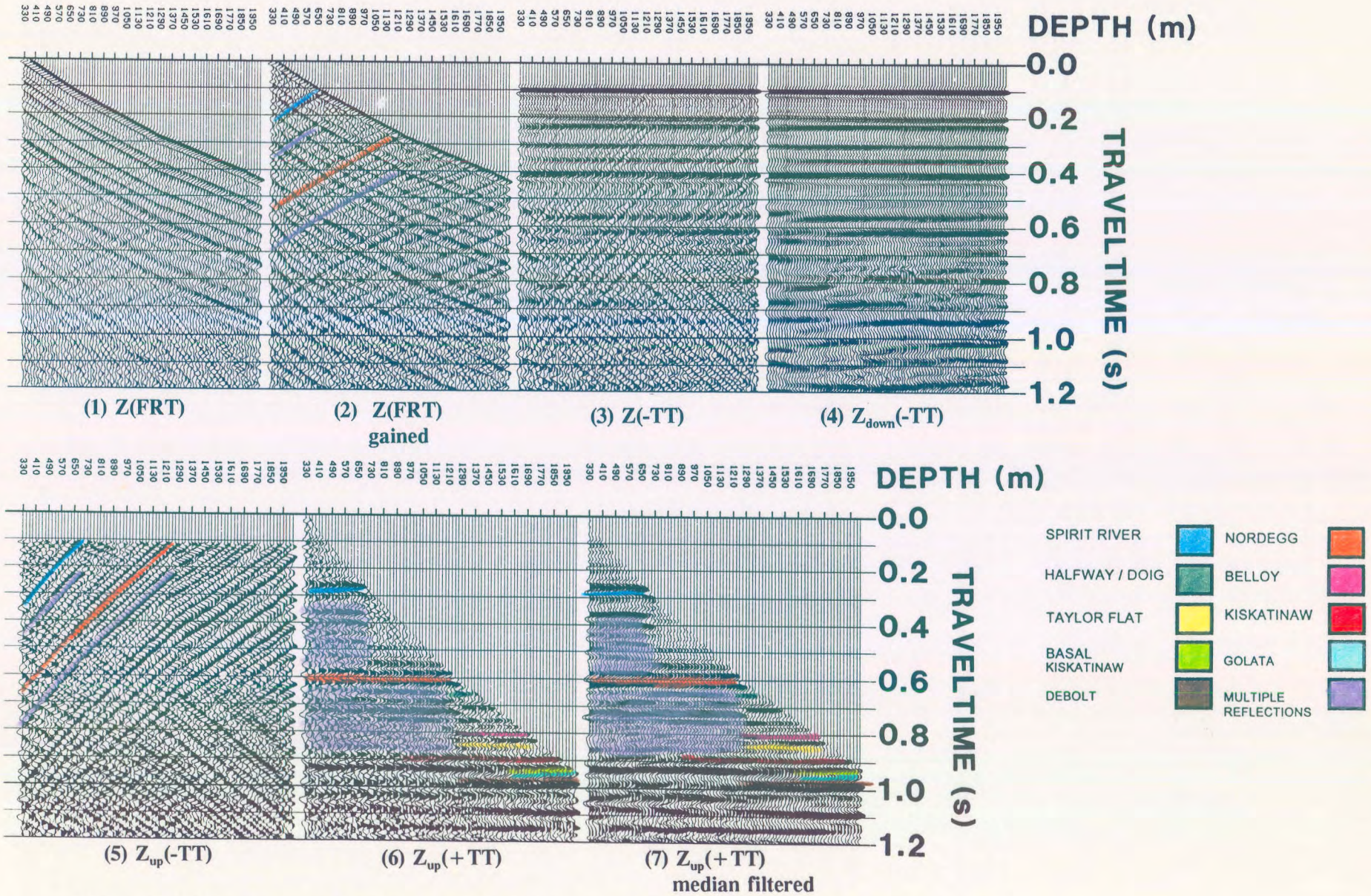


Figure 5.9 Interpretive processing panel depicting the wavefield separation of the near offset Fort St. John Graben VSP data (from Hinds et al., 1993a).

In panel 3 (Fig. 5.9), the $Z(-TT)$ data are displayed. An 11-point median filter was used to remove the upgoing P-waves; the $Z_{\text{down}}(-TT)$ data are displayed in panel 4. In the next step, the $Z_{\text{down}}(-TT)$ data of panel 4 were subtracted from the $Z(-TT)$ data to yield the $Z_{\text{up}}(-TT)$ data (panel 5). Note that a residual tube wave is visible within the $Z_{\text{up}}(-TT)$ data panel.

The $Z_{\text{up}}(+TT)$ data before and after the application of a 3 point median filter are shown in panels 6 and 7, respectively. The two panels have been time shifted to facilitate plotting. In panel 7, the Spirit River multiple (highlighted in panel 2) is observed as high amplitude events which lie directly below the Spirit River primary and can be interpreted for several cycles (from 0.3 to 0.7 s). This multiple is not observed at sonde depths deeper than the top of the Spirit River (at 730 m).

5.5.2 Near offset VSP deconvolution

Deconvolution IPP (Hinds et al., 1989a) were designed for the $Z_{\text{up}}(+TT)$ data (Fig. 5.10) to enable the monitoring of the deconvolution process for the near offset data (Hinds et al., 1993a; Hinds et al., 1994c). The incorporated panels reveal information (about multiples) that was difficult to determine from the wavefield separation IPP (Fig. 5.9) alone. The first two panels (Fig. 5.10) are the nonfiltered and median-filtered $Z_{\text{up}}(+TT)$ data, respectively. The interpreted multiple events have been highlighted in purple on panels 1 and 2.

Panel 3 is the gained $Z_{\text{down}}(-TT)$ data. Panels 4 and 5 are the nondeconvolved and deconvolved $Z_{\text{up}}(-TT)$ data, respectively, which enable an evaluation of the effect that the deconvolution process has on the $Z_{\text{up}}(-TT)$ data.

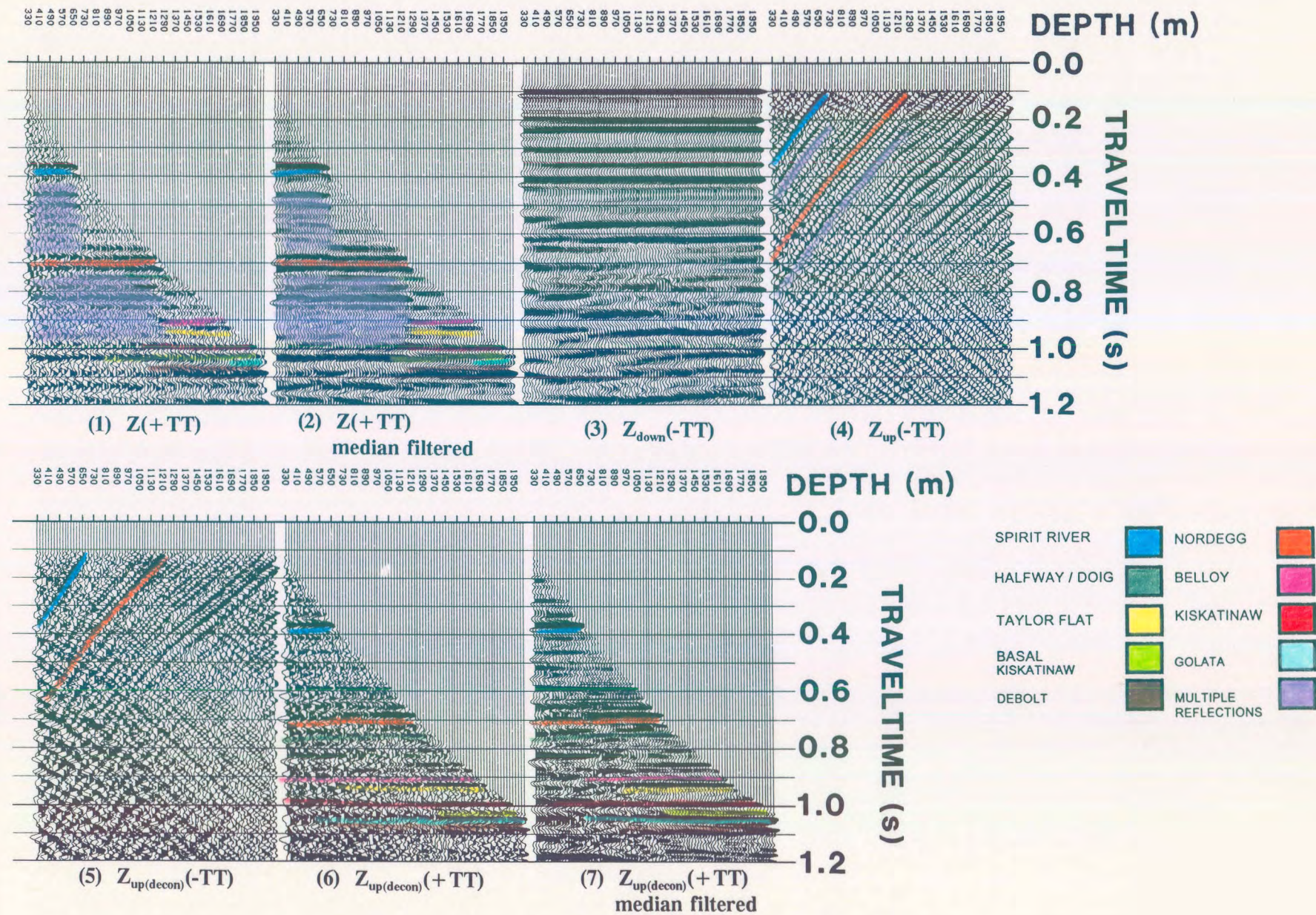


Figure 5.10 Interpretive processing panel depicting the deconvolution of the near offset Fort St. John Graben VSP data (from Hinds et al., 1993a).

The last two panels (6 and 7) are the nonmedian and median-filtered $Z_{up(decon)}(+TT)$ data, respectively. By inspection of panels 2 and 7 (Fig. 5.10), it is interpreted that the deconvolution processing has effectively attenuated multiple reflections. The Spirit River multiple wavetrain from 0.5 to 0.9 s on panel 2, for example (coloured in purple), has negligible amplitude on panel 7. Note also that deconvolution has increased the frequency content of the data, allowing for better resolution at the Kiskatinaw level.

5.5.3 Inside and outside corridor stacks

Nondeconvolved, inside and outside corridor stacks and associated displays (Hinds et al., 1989a) were designed for the near offset data as presented in Figure 5.11 (Hinds et al., 1993a; Hinds et al. 1994c). A comparison of the inside and outside corridor stacks (panels 3 and 4, respectively) illustrates the utility of these displays. For example, the Spirit River multiple (between 0.65 and 1.0 s) is present on the inside corridor stack and absent on the outside corridor stack. Note also, that basal Kiskatinaw and Golata events can be resolved on the outside corridor stack; on the inside corridor stack these reflections are masked by a high-amplitude multiple.

If deconvolution is successful, the deconvolved inside and outside corridor stacks (panels 3 and 4; Fig. 5.12) should be similar. At the zone of interest just above 1.35 s, the Debolt and the Golata are similar (panels 3 and 4), however the basal Kiskatinaw is not adequately represented on the inside corridor stack of the deconvolved data. An examination of the input data to the inside corridor stack (panel 2 of Fig. 5.12) reveals that the multiple

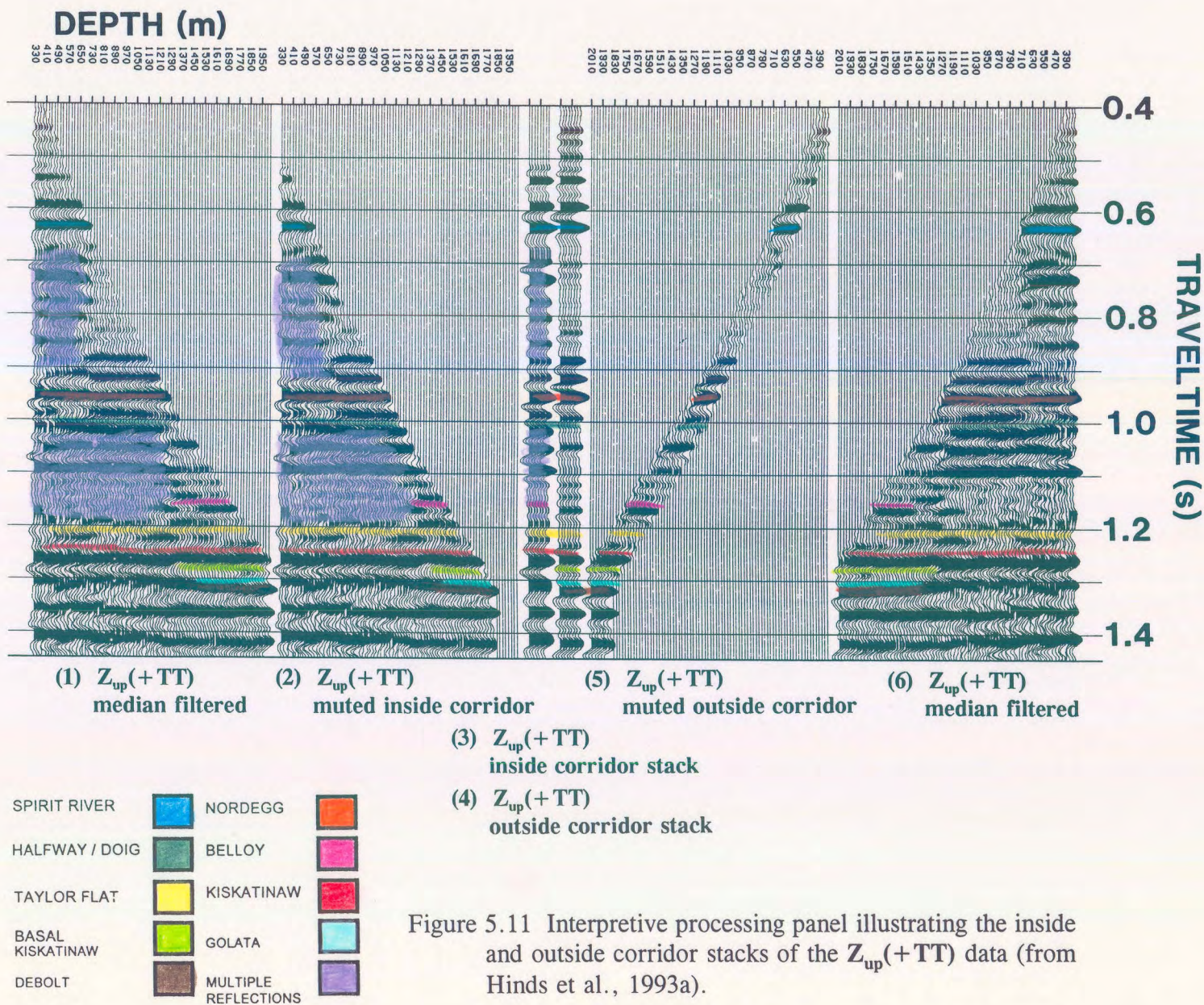


Figure 5.11 Interpretive processing panel illustrating the inside and outside corridor stacks of the $Z_{up}(+TT)$ data (from Hinds et al., 1993a).

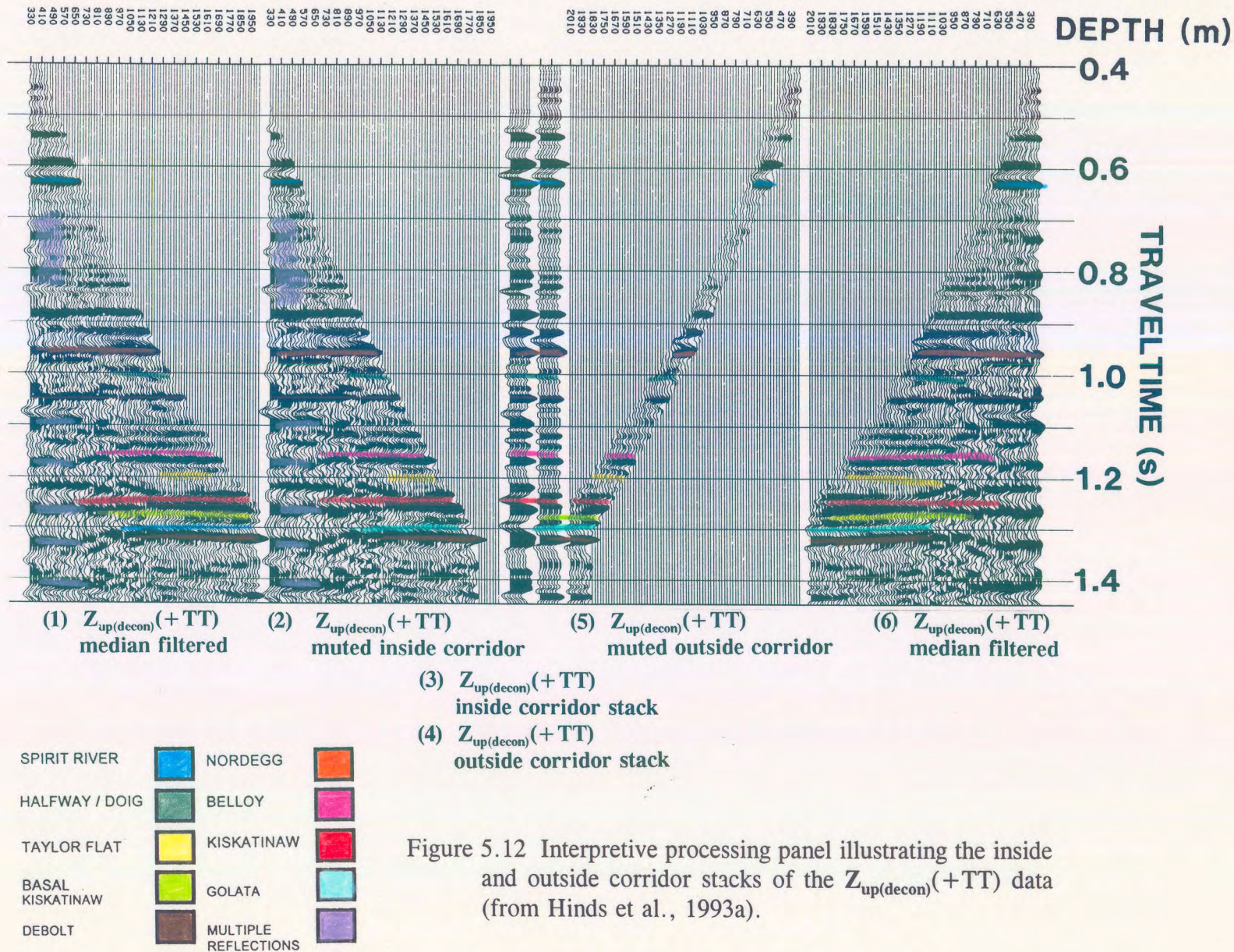


Figure 5.12 Interpretive processing panel illustrating the inside and outside corridor stacks of the $Z_{up(decon)}(+TT)$ data (from Hinds et al., 1993a).

contamination has not been completely eliminated on the shallow traces (from 1290 m to the surface). This results in a broad peak for the zone immediately above the basal Kiskatinaw (on panel 3 at 1.26 s) but the high frequency basal Kiskatinaw trough has been overpowered by residual multiple contamination. Note that the Spirit River multiple which is highlighted in purple between 0.65 and 1.0 s has been significantly attenuated on all of the traces except for the traces recorded at 490 m to the surface. The deconvolution process has given limited success; however the data can be correlated to the geology and later to the surface seismic.

5.6 Far offset VSP interpretive processing

5.6.1 Far offset data from offset FSJG1

On the far offset FSJG1 VSP data, the vertical (**Z**) and both horizontal (**X** and **Y**) axis data contain nonpartitioned elements of the upgoing and downgoing P- and SV-wavefields. Examination of the IPPs (Figs. 5.13-5.15) reveals that the partitioning of the wavefields has significant implications with respect to interpretation (Hinds et al., 1989a). The far offset IPPs for the FSJG1 data (Hinds et al., 1993a; Hinds et al., 1994c) were designed with the aim of displaying the following major processing steps:

- 1) hodogram-based rotation of the **X(FRT)**, **Y(FRT)**, and **Z(FRT)** data (based on windowed data enveloping the P-wave first arrival; DiSiena et al., 1984);
- 2) time-variant model-based rotations applied to the **HMAX_{up(derot)}(FRT)** and **Z_{up(derot)}(FRT)**

data; and

- 3) VSP-CDP mapping (Dillon and Thomson, 1984) and Kirchhoff migration processing (Dillon, 1990; Wiggins and Levander, 1984; Wiggins et al., 1986; Wiggins, 1984) of the $Z''_{up}(+TT)$ data.

5.6.2 Hodogram-based rotation; offset FSJG1

The $X(FRT)$, $Y(FRT)$, and $Z(FRT)$ data for the FSJG1 far offset VSP are displayed in Figure 5.13 on panels 1, 2, and 3, respectively. The horizontal axis data (X and Y) are extremely noisy and contain only minor amounts of P-wave events. The $Z(FRT)$ data contain strong downgoing P-wave events plus lower amplitude upgoing P-wave events. The hodogram-based rotation technique is designed to polarize these data so that the downgoing P-waves are presented on a single channel, $HMAX'(FRT)$.

The first step illustrated in Figure 5.13, is the hodogram-based rotation of the $X(FRT)$ and $Y(FRT)$ data (correcting for phase changes due to tool rotation during the movement of the sonde up the borehole). The output $HMIN(FRT)$ and $HMAX(FRT)$ data are displayed as panels 4 and 5, respectively. $HMIN(FRT)$ and $HMAX(FRT)$ data are assumed to be aligned perpendicular and tangent to the plane formed by the well and the source, respectively. Note that the $HMIN(FRT)$ data (comprised of horizontally polarized shear (SH) wave events and out of the plane reflections) contains the dominant portion of the diffraction that appears at 1.0s on the 650 to 800 m traces, suggesting that the diffraction is side-swipe energy originating from a feature such as a fault out of the plane of the well and source.

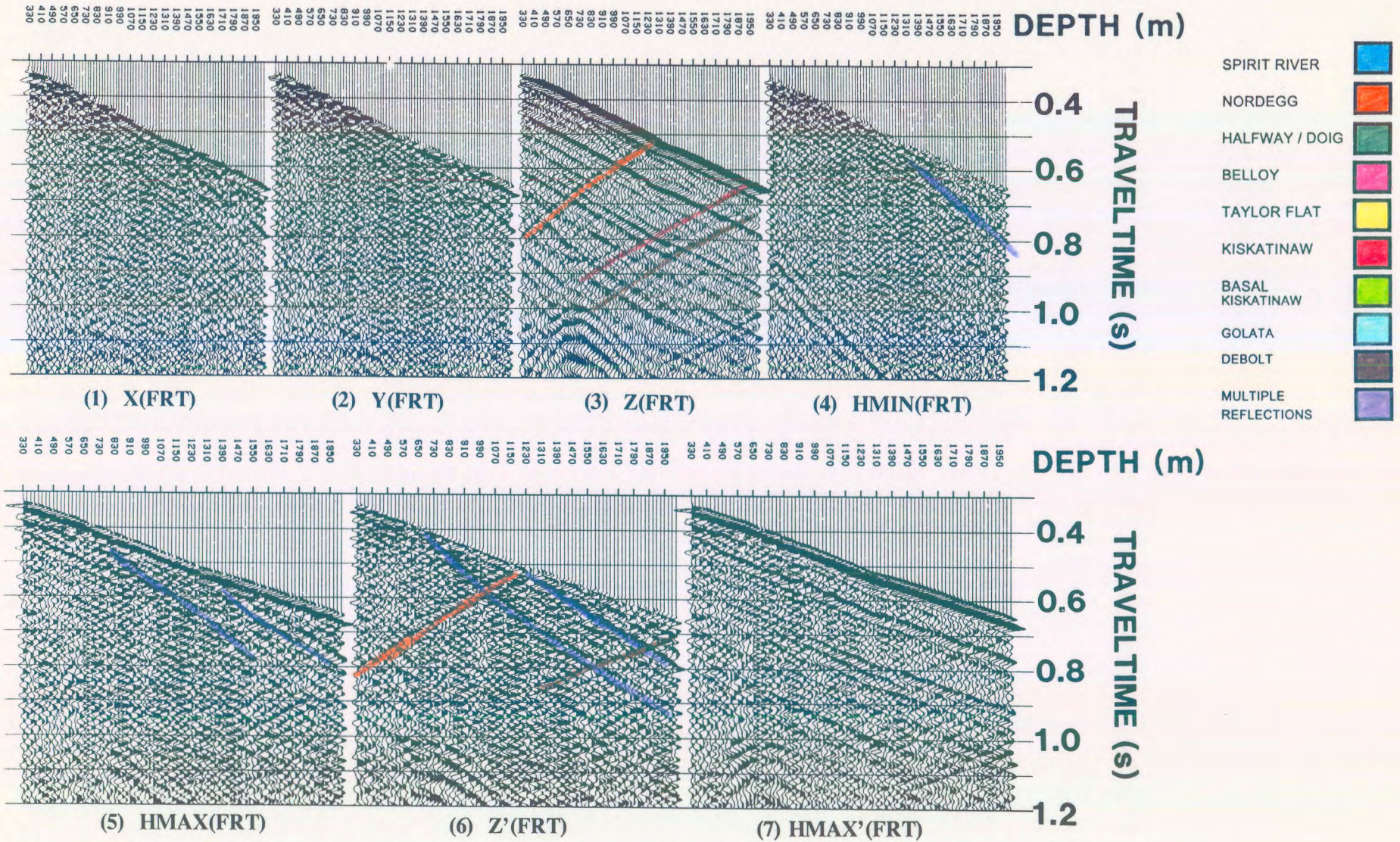


Figure 5.13 Interpretive processing panel depicting the hodogram-based rotation of the Fort St. John Graben FSJG1 far offset VSP data (from Hinds et al., 1993a).

The $Z'(FRT)$ and $HMAX'(FRT)$ (panels 6 and 7) data were obtained by rotating the $Z(FRT)$ and $HMAX(FRT)$ data using polarization angles estimated from a hodogram analysis of a window of data centred around the P-wave first arrivals of the $Z(FRT)$ and $HMAX(FRT)$ data (DiSiena et al., 1984). Downgoing mode-converted SV-events can be interpreted on all three axis data, $X(FRT)$, $Y(FRT)$ and $Z(FRT)$. The SV-events were described for these data in chapter 2. The SV data can be used for the quality control of the second polarization; namely, $HMAX(FRT)$ and $Z(FRT)$ data rotating into $HMAX'(FRT)$ and $Z'(FRT)$ data.

The evaluation of the second polarization is based on the detection or not of SV-events (mode-converted or from any other origin) on the $HMAX'(FRT)$ data. In panel 6 and 7 of Figure 5.13, the mode-converted SV events have been completely polarized onto the $Z'(FRT)$ data and, at first inspection, do not appear on the $HMAX'(FRT)$ data.

The upgoing events on VSP data can be up to 100 times weaker than the downgoing events (Hardage, 1985). The time-variant polarization IPP (Fig. 5.14) that have been designed and presented in the next section contains the wavefield separated $Z'_{up}(FRT)$ and $HMAX'_{up}(FRT)$ data in panels 1 and 2, respectively. It is only after the wavefield separation processing on the $Z'(FRT)$ and $HMAX'(FRT)$ data that the underlying upgoing event components of the $Z'(FRT)$ and $HMAX'(FRT)$ data can be truly evaluated.

The two sets of rotations have polarized the $X(FRT)$, $Y(FRT)$ and $Z(FRT)$ data so that the downgoing P-waves are effectively isolated on a single channel, $HMAX'(FRT)$, shown in panel 7 of Figure 5.13.

5.6.3 Time-variant model-based rotation: offset FSJG1

The IPP for the time-variant model-based polarization analysis for the FSJG1 offset data is shown in Figure 5.14. The $Z'_{up}(FRT)$ and $HMAX'_{up}(FRT)$ are shown in panels 1 and 2 (Fig. 5.14), respectively. On both panels, upgoing P-waves from the Debolt, Golata and Kiskatinaw can be clearly interpreted, indicating that the hodogram-based rotations were unsuccessful in isolating the upgoing P-wave events onto the $Z'(FRT)$ panel.

In order to remove the effects of the $Z(FRT)$ to $Z'(FRT)$, and $HMAX(FRT)$ to $HMAX'(FRT)$ transformations (which were necessary to isolate the downgoing P-waves), the $Z'_{up}(FRT)$ and $HMAX'_{up}(FRT)$ were derotated (using the inverse operation of the second polarization rotation). The $Z_{up(derot)}(FRT)$ and $HMAX_{up(derot)}(FRT)$ data, are shown as panels 3 and 4 of Figure 5.14, respectively. By inspection, the upgoing P-wave events have been effectively distributed back onto a Z-type axis data, $Z_{up(derot)}(FRT)$. Unlike the upgoing wave events in the $Z(FRT)$ data (panel 3 in Fig. 5.13), where the downgoing P-waves were predominant, the separated upgoing P-wave events in the $Z_{up(derot)}(FRT)$ data are dominant and interpretable.

On the $Z_{up(derot)}(FRT)$ data (panel 3), upgoing P-waves generated by the shallow reflectors are improperly aligned (due to the choice of a single rotation angle per trace) such as the upgoing event resulting from the reflection from the Spirit River interface. These data have been derotated but the upgoing P-wave events are still partitioned on both output data ($Z_{up(derot)}(FRT)$ and $HMAX_{up(derot)}(FRT)$) due to the non-zero offset of the source. The deeper events do not suffer much misalignment because the deep event raypath geometries

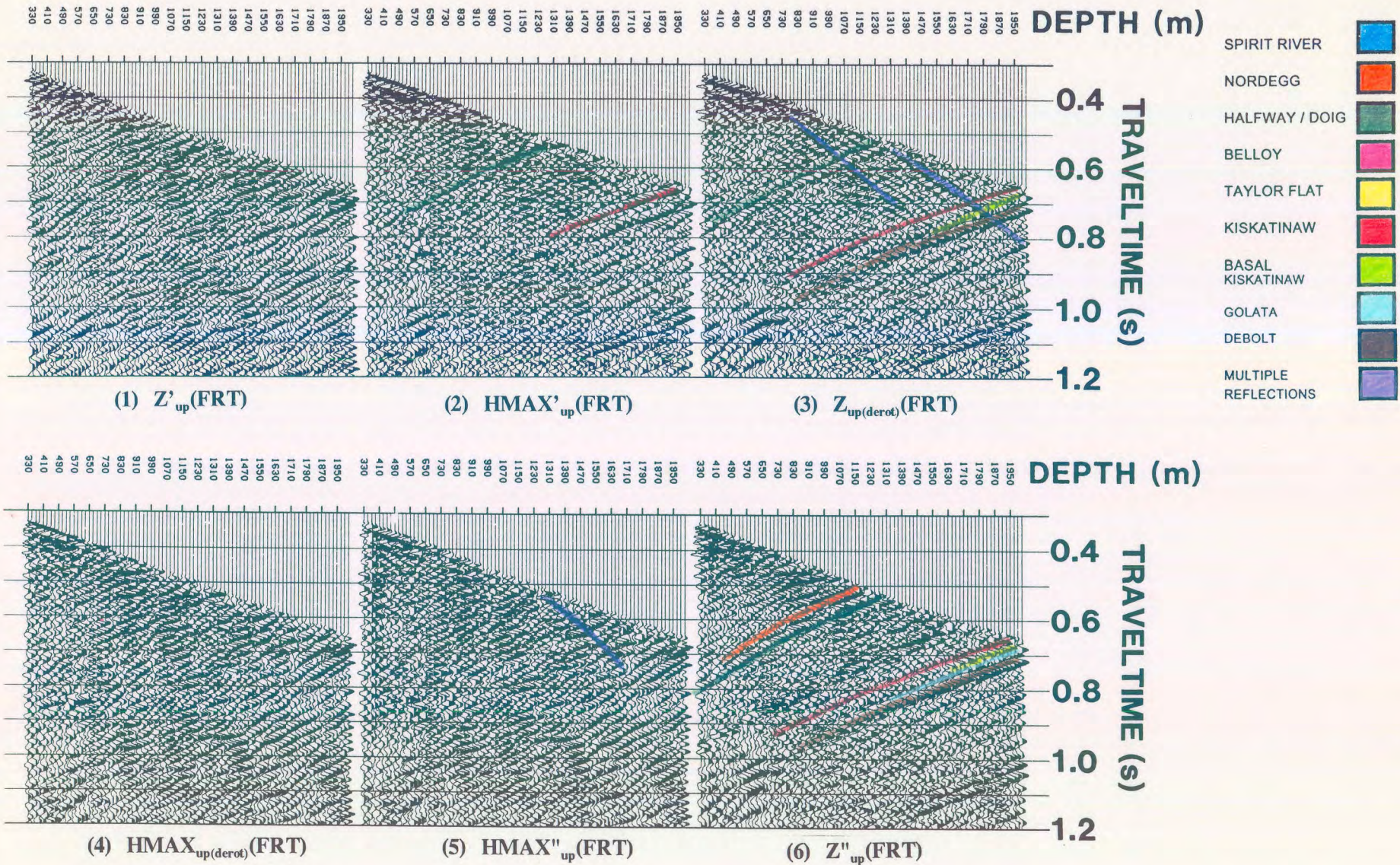


Figure 5.14 Interpretive processing panel depicting the time-variant model-based rotation of the Fort St. John Graben FSJG1 far offset VSP data (from Hinds et al., 1993a).

satisfy the near-vertical incidence angle assumption better than the raypaths of shallower events. The time-variant model-based rotation corrects for this misalignment. The output of the time-variant polarization, the $HMAX''_{up}(FRT)$ and $Z''_{up}(FRT)$ data, are shown in panels 5 and 6, respectively. Note that the shallow events display more alignment than on the $Z''_{up(derot)}(FRT)$ (panel 3). The rotation angle required for the Spirit River and Nordegg events on a particular trace are different to the rotation angle needed for a deeper event (such as the Debolt) on the same trace. The time-variant rotation technique (Hinds et al., 1989a) generated these different rotation angles.

The Spirit River event is barely discernable on the $Z''_{up}(FRT)$ data because the reflected raypaths from this shallow event are at or near the critical angle. The surface-generated multiple from the Spirit River interface (observed on the nondeconvolved near offset data of panel 7 in Fig. 5.9) are significantly lower amplitude on these far offset data (panel 6; Fig. 5.13).

5.6.4 VSP-CDP mapping: offset FSJG1

Nonfiltered and median-filtered $Z''_{up}(FRT)$ data are displayed (pseudo-two-way travelttime versus depth) in figure 5.15 as panels 1 and 2, respectively. The VSP-CDP mapped (pseudo-two-way travelttime versus offset) and Kirchhoff migrated $Z''_{up}(+TT)$ data are shown as panels 3 and 4, respectively.

The FSJG1 offset source was located 700 m and in the direction of well 2-25. The interpretation of the surface seismic data (Fig. 5.8) suggests that a major Debolt fault

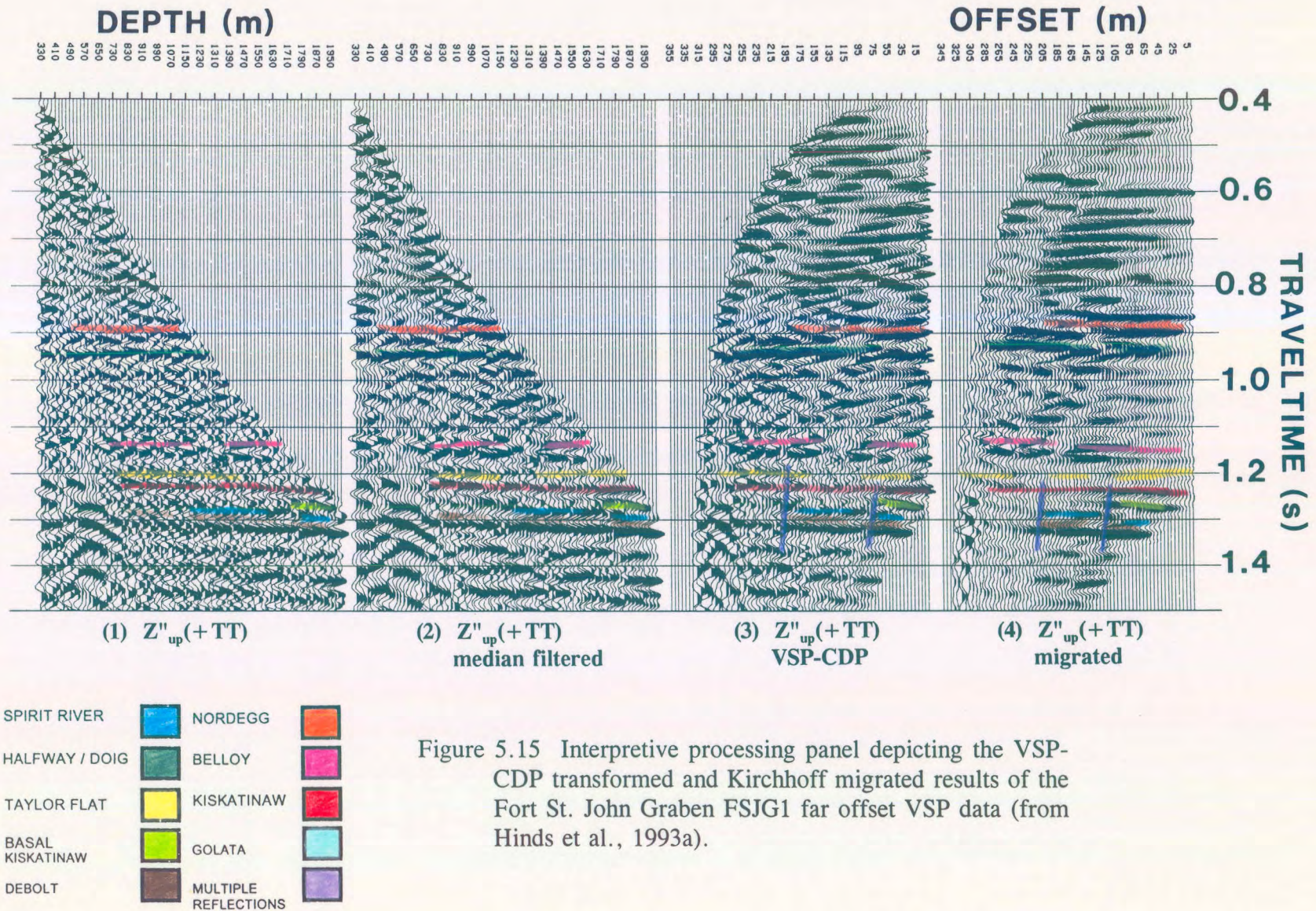


Figure 5.15 Interpretive processing panel depicting the VSP-CDP transformed and Kirchhoff migrated results of the Fort St. John Graben FSJG1 far offset VSP data (from Hinds et al., 1993a).

(displacing Debolt to the Belloy Fm material) was located between well 9-24 and well 2-25. On panels 3 and 4 (Fig. 5.15), the Debolt event on the VSP data is interpreted to be faulted in two places in between these wells; however, it is shown in section 5.7 that these VSP data image two faults not shown on the interpretation on Figure 5.8 (Hinds et al., 1994b).

A second interesting feature on panel 3 is that the signature of the basal Kiskatinaw event changes abruptly in proximity to the fault nearest well 9-24. The migrated version has smeared the event. The basal Kiskatinaw event, as interpreted, is continuous at greater offsets, but is substantially decreased in amplitude. This character change could indicate a change in lithology (increase in shale content) or porosity (increase in water content as in well 2-25).

The upper Kiskatinaw event which represents the location of the hydrocarbon reservoir within well 9-24 is interpreted on panels 3 and 4 to be laterally continuous but faulted. Vertical displacement is interpreted across two faults. This thesis is supported by geological information (Richards, pers. comm.); the upper Kiskatinaw is present in both wells 9-24 and 2-25. At well 9-24 the upper Kiskatinaw forms a gas reservoir; in the structurally higher 2-25 well this unit is nonproductive.

5.6.5 Far offset data from offset FSJG2

The FSJG2 far offset source was 741 m east of well 9-24. These data were acquired in order to map the lateral extent of the upper Kiskatinaw reservoir to the east of well 9-24, and to provide a higher resolution seismic image of faults that displace Debolt strata. The offset

survey was designed in an effort to explore a new area in which future exploration could be realized. This is a case where the VSP data capture is done before a possible seismic survey can be performed in the area. The recording and processing of these data was similar to that described for the FSJG1 survey.

In the first stage of interpretive processing, a hodogram-based rotation technique polarized the $X(\text{FRT})$, $Y(\text{FRT})$, and $Z(\text{FRT})$ data, so that the downgoing P-waves were presented on a single channel, $HMAX'(\text{FRT})$ as shown in Figure 5.16. The filtered output data, $Z'_{up}(\text{FRT})$ and $HMAX'_{up}(\text{FRT})$, were derotated and time-variant model-based rotations were applied to the output data as shown in Figure 5.17. In the final stage, the $Z''_{up}(\text{FRT})$ data were displayed in pseudo-two-way travelt ime versus depth, and in pseudo-two-way travelt ime versus offset.

The $Z''_{up}(+TT)$ data after the application of the VSP-CDP mapping are displayed in Figure 5.18. Nonmedian and median-filtered versions of the $Z''_{up}(+TT)$ data are displayed (pseudo-two-way travelt ime versus depth) as panels 1 and 2, respectively. The VSP-CDP mapped (pseudo-two-way travelt ime versus offset) and Kirchhoff migrated $Z''_{up}(+TT)$ data are shown in panels 3 and 4, respectively.

The data in panels 3 and 4 image 2 faults, both of which are of the same magnitude as those on the FSJG1 data (Fig. 5.15). The basal Kiskatinaw event is interpreted to exhibit a laterally continuous seismic signature. This is unlike the character of the basal Kiskatinaw

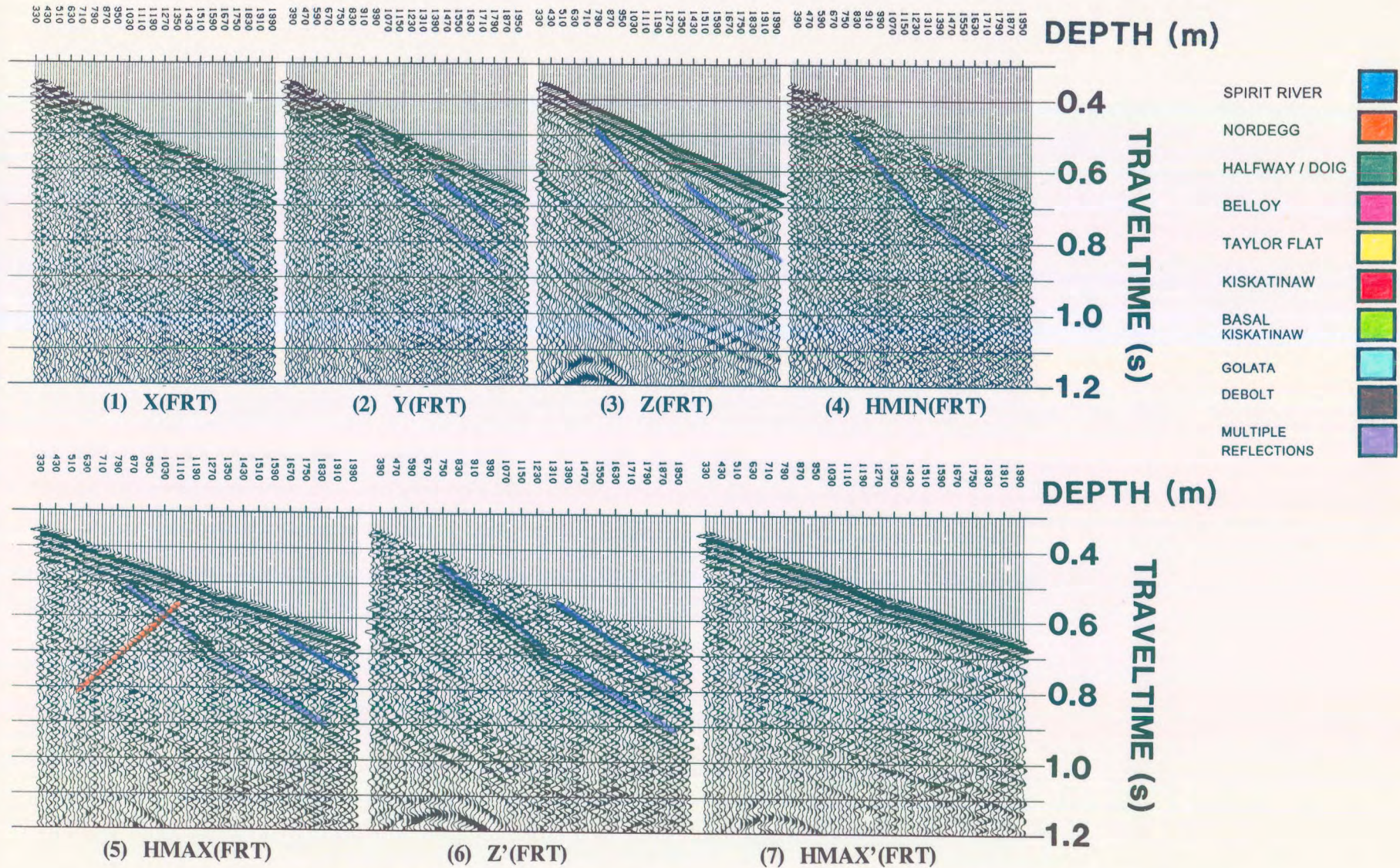


Figure 5.16 Interpretive processing panel depicting the hodogram-based rotation of the Fort St. John Graben FSJG2 far offset VSP data (from Hinds et al., 1993a).

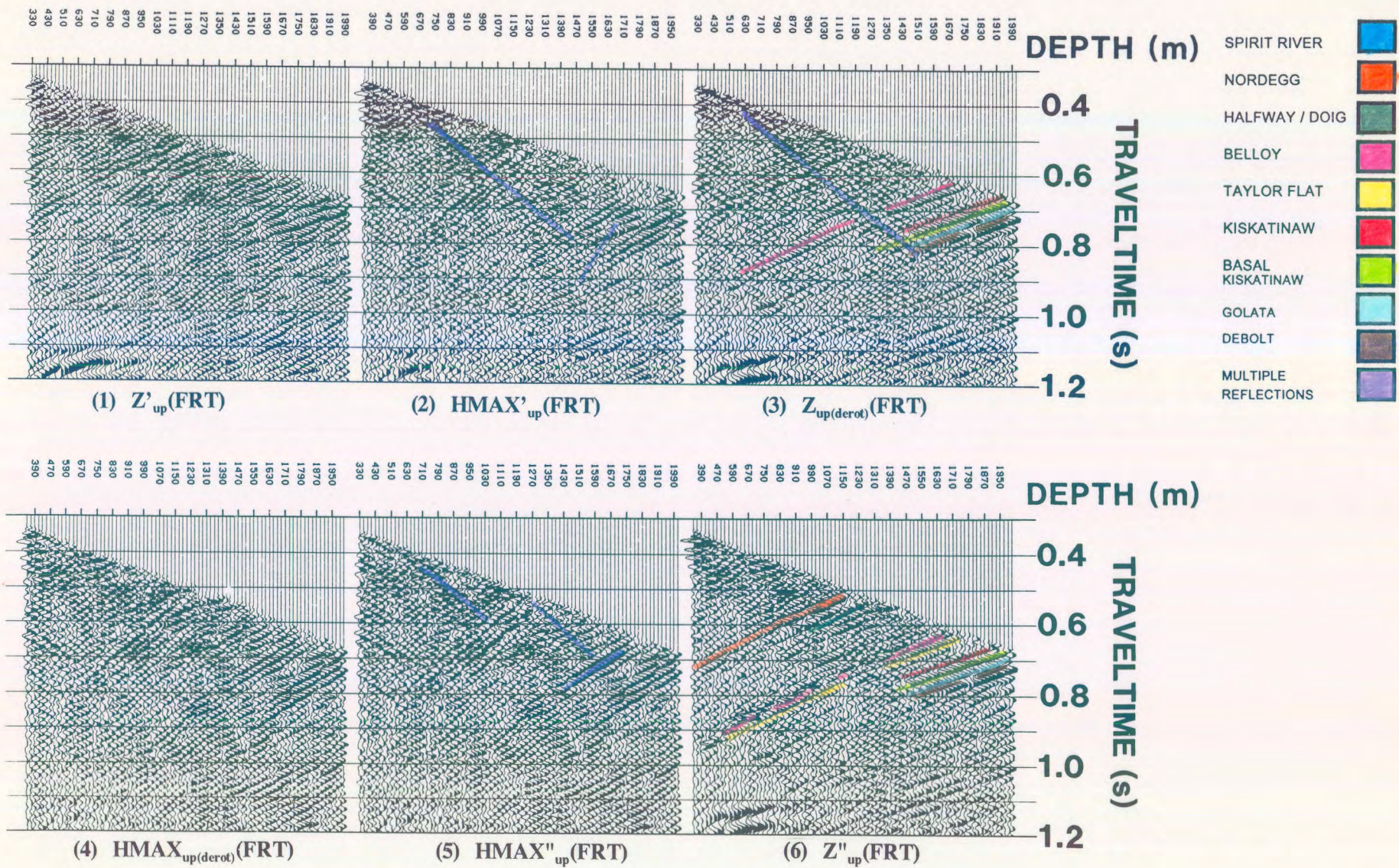


Figure 5.17 Interpretive processing panel depicting the time-variant model-based rotation of the Fort St. John Graben FSJG2 far offset VSP data (from Hinds et al., 1993a).

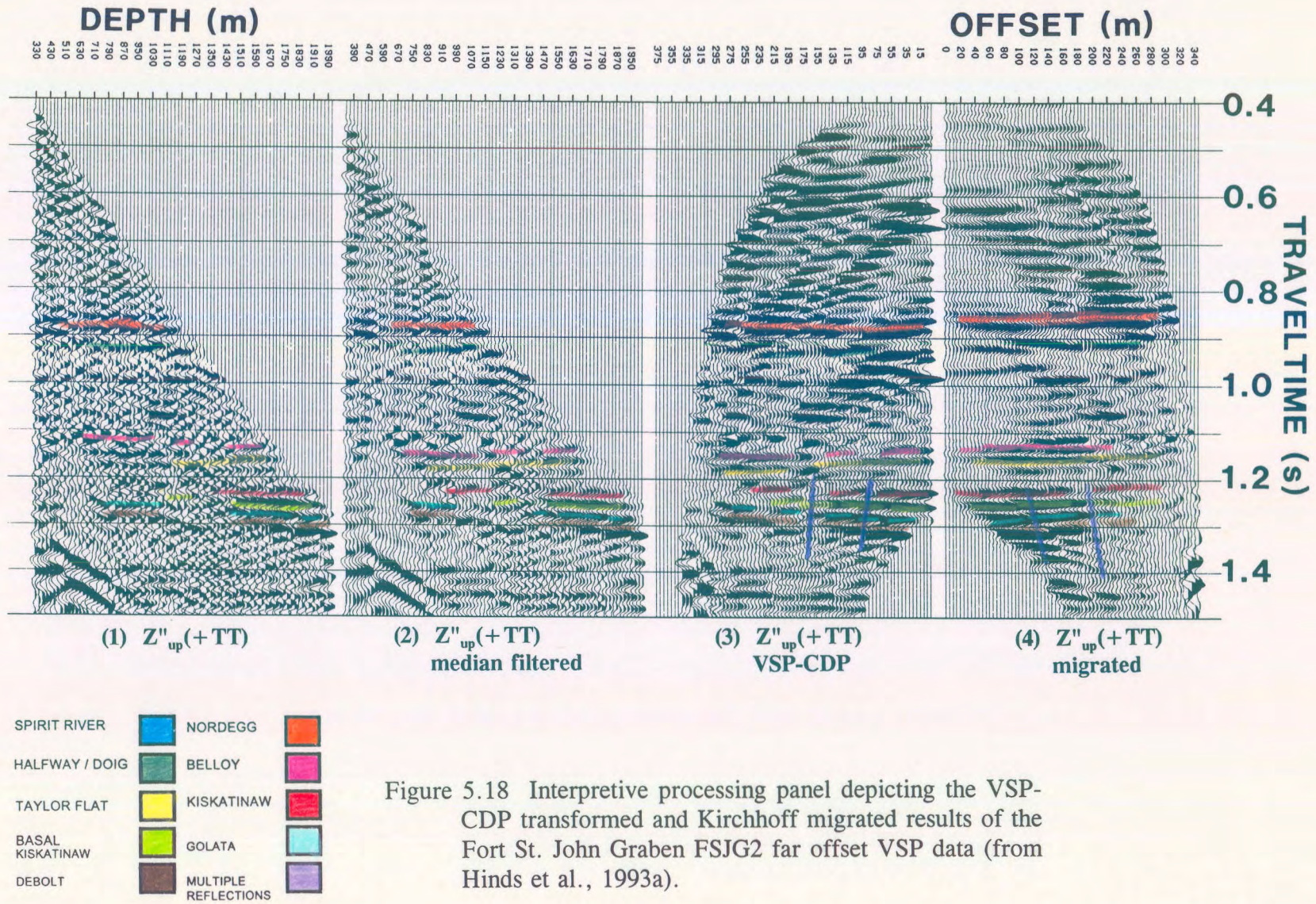


Figure 5.18 Interpretive processing panel depicting the VSP-CDP transformed and Kirchhoff migrated results of the Fort St. John Graben FSJG2 far offset VSP data (from Hinds et al., 1993a).

away from the well towards the FSJG1 offset source which decreases in amplitude beyond the first imaged fault. The upper Kiskatinaw (hydrocarbon reservoir at well 9-24), as interpreted on panel 3, is laterally continuous but faulted.

5.7 Integrated interpretation

The integrated interpretive display (IID) is shown in Figure 5.19. On the left-hand side of the IID (from Hinds et al., 1993a; Hinds et al., 1994c) in Figure 5.19, gamma ray logs for the well 9-24, well 2-25, and well 7-36 are time-tied to the current interpretation of the surface seismic data. On the right-hand side, near offset VSP data are time-tied to the gamma ray and sonic logs acquired in well 9-24. These correlated data allow for the confident interpretation of the surface seismic line and the identification of the Spirit River, Nordegg, Halfway/Doig, Belloy, Taylor Flat, upper Kiskatinaw, basal Kiskatinaw, Golata, and Debolt events. The nondeconvolved version of the VSP data is presented, in order to facilitate an analysis of multiple contamination. As evidenced by a comparison of the surface seismic line and the corridor stacks, the multiple-contaminated inside corridor stacks provide a poor tie to the data at the zone of interest (Kiskatinaw). This suggests that multiples on the surface seismic data have been effectively attenuated.

The interpretation of the surface seismic section that incorporates the VSP information (normal polarity display; Fig. 5.20) differs slightly from the pre-well interpretation (Fig. 5.8). Of particular significance is that on the updated version, the Taylor Flat and Kiskatinaw events are confidently correlated. Note that in the post-VSP interpretation, the Taylor Flat event is absent at well 7-36. This interpretation is supported by the well log

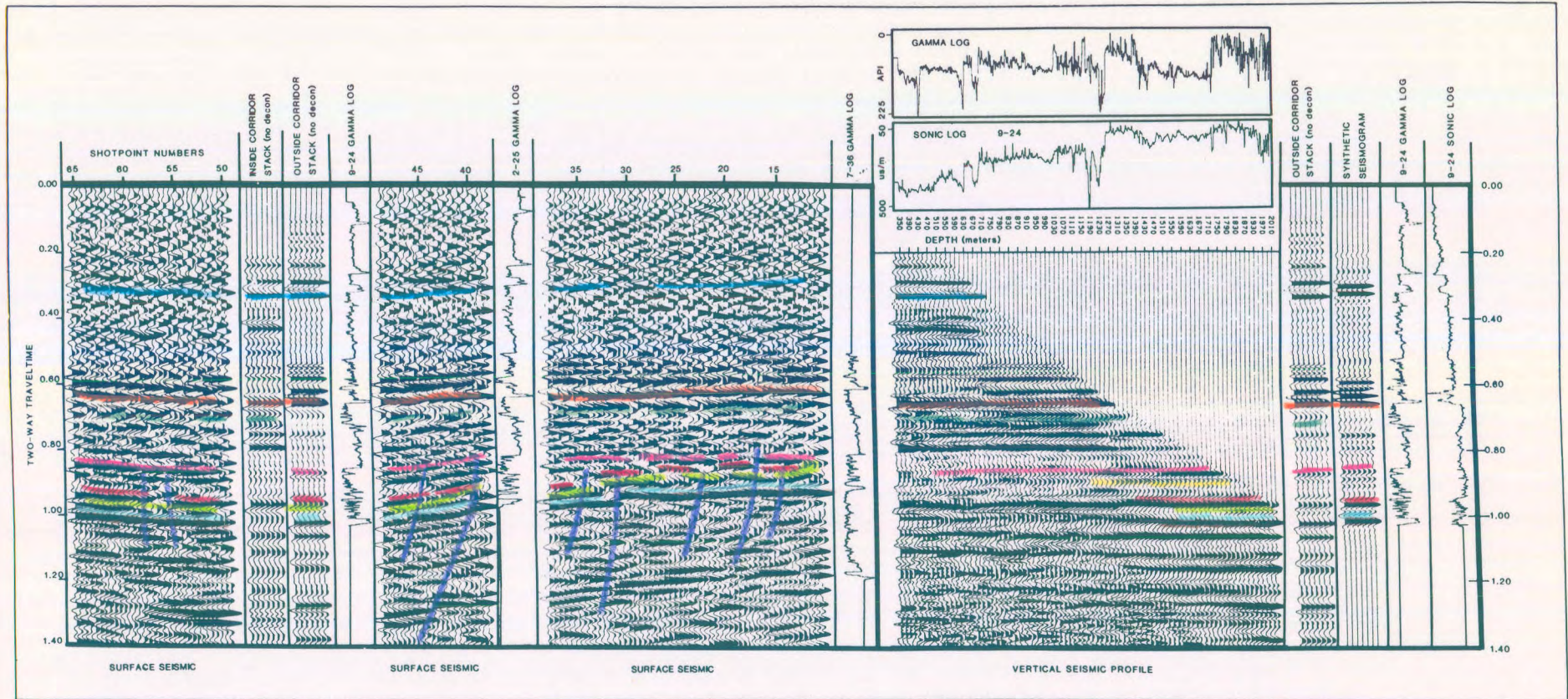
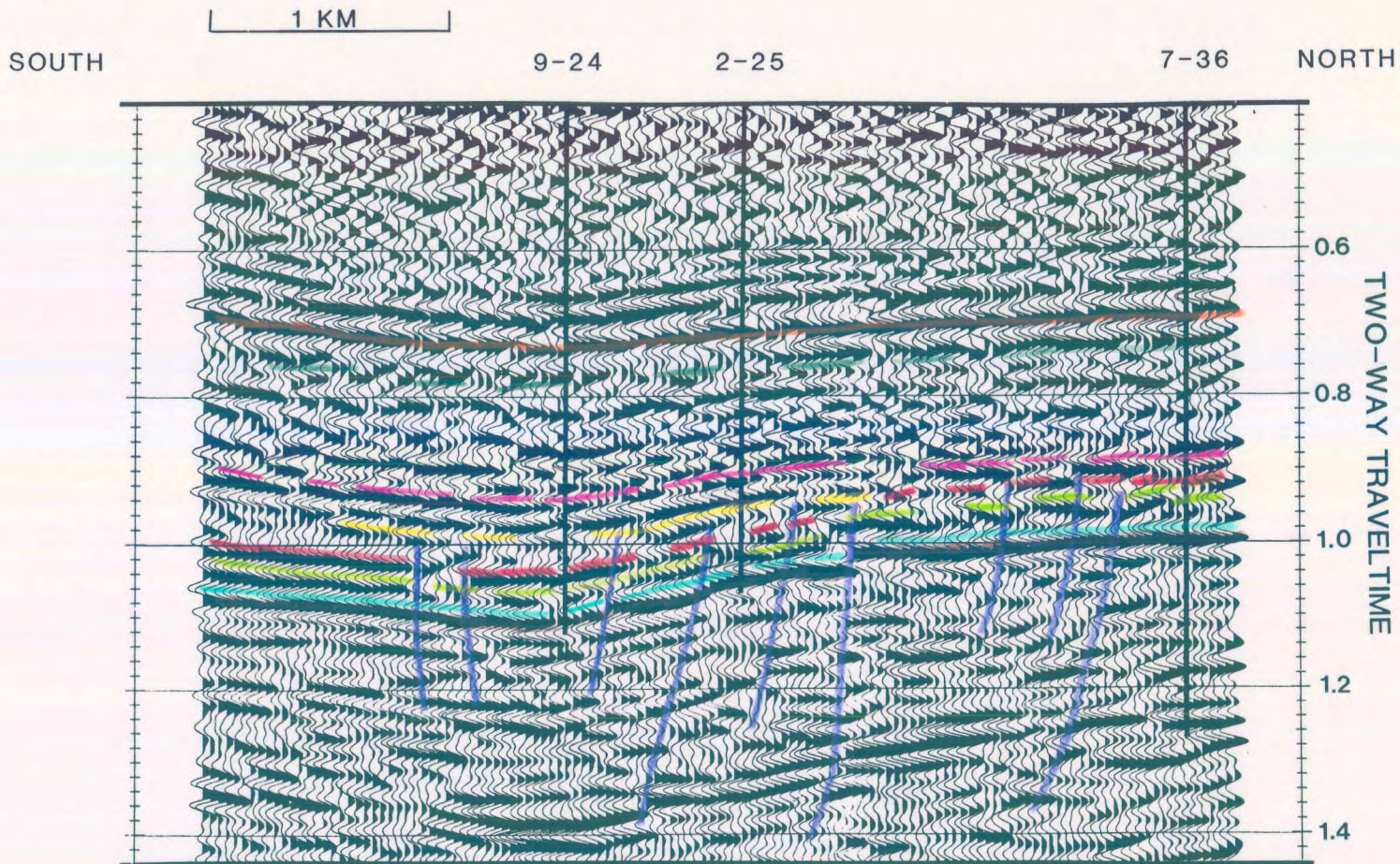


Figure 5.19 Integrated interpretive display of the Fort St. John Graben exploration data (from Hinds et al., 1993a).





299

| | | | |
|------------------|--|----------------------|--|
| SPIRIT RIVER | | NORDEGG | |
| HALFWAY / DOIG | | BELLOY | |
| TAYLOR FLAT | | KISKATINAW | |
| BASAL KISKATINAW | | GOLATA | |
| DEBOLT | | MULTIPLE REFLECTIONS | |

Figure 5.20 Current, preferred surface seismic interpretation. There are now two interpreted faults between wells 9-24 and 2-25. The VSP (FSJG1 offset) data seismically image the fault nearest well 9-24 (shown in this figure) as two separate faults (from Hinds et al., 1993a).

control.

The geologic cross-section of Figure 5.21 was constructed on the basis of the post-VSP interpretation of the surface seismic line and the analysis of the far offset VSP data. It is consistent with the well log, surface seismic and seismic profile control. Up-to-date information using conodont research and lithostratigraphic data (Richards, pers. comm.) is shown in Figure 5.21 as Upper Carboniferous strata informally known as the Ksituan Member of the Taylor Flat Formation (Hinds et al., 1994b and Hinds et al., 1994c). This geologic cross-section is an update to the one presented in Hinds et al. (1993a) and is discussed in Hinds et al. (1994b) and Hinds et al. (1994c).

A discrepancy that arose and was resolved in Hinds et al. (1994b) came about from the observation that there are two faults interpreted on the VSP-CDP data shown in Figure 5.15 and three faults between well 9-24 and well 2-25 on the geologic cross-section shown in Figure 5.21. In addition, on the reinterpreted seismic data, shown in Figure 5.20, there are two faults interpreted between wells 9-24 and 2-25. The two faults interpreted on the VSP-CDP data do not correlate with the interpreted fault shown on Figure 5.8 (between wells 9-24 and 2-25); these interpreted faults (Fig. 5.15) are represented on the reinterpreted seismic data (Fig. 5.20) as a single fault near to well 9-24. The surface seismic data could not resolve the seismic expression of the fault into two separate images as seen on the VSP-CDP data (Fig. 5.15).

In Hinds et al. (1994b), a plan view of the FSJG1 source offset position along with the location of the two VSP interpreted faults and surface seismic located fault (near well 2-25)

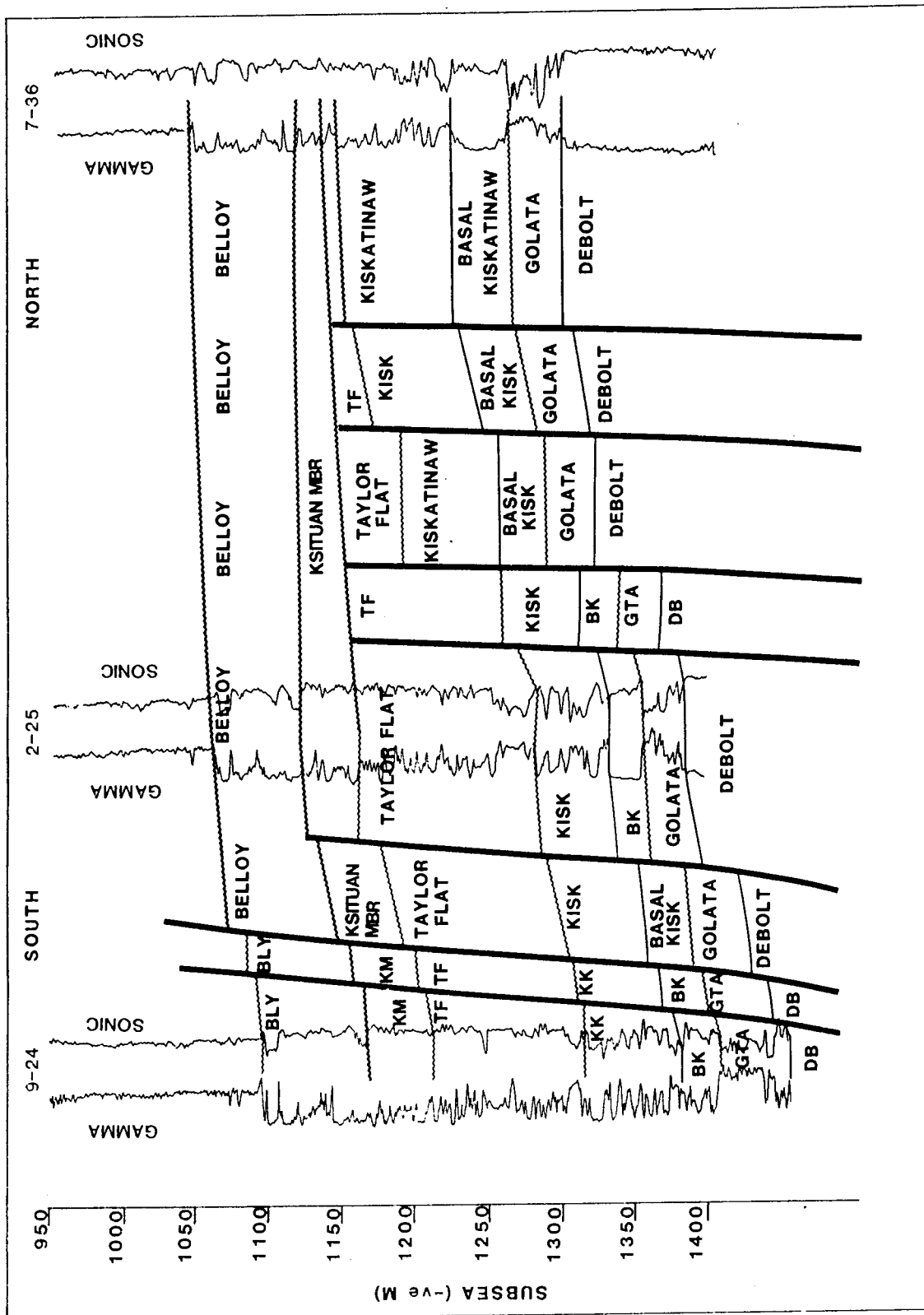


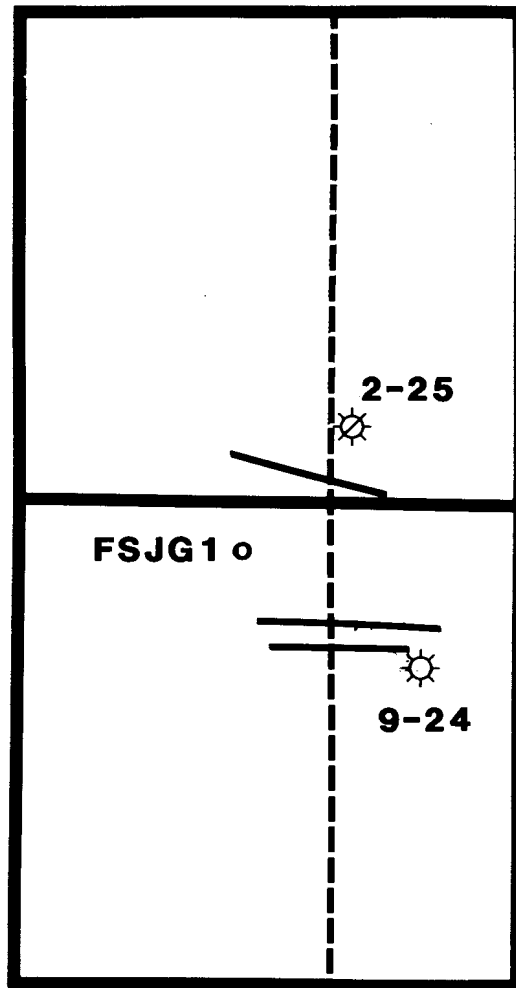
Figure 5.21 Geologic cross-section incorporating information from the surface seismic, VSP and geologic well log results (from Hinds et al., 1994c). Note that three faults have been postulated to be between wells 9-24 and 2-25.

was discussed and is shown in Figure 5.22 (Hinds et al., 1994c). This presentation of the VSP and surface seismic line geometry aids in the resolution of the discrepancy discussed in Hinds et al. (1994b). In Figure 5.22, well 9-24 is located due East of CDP number 49 of the seismic line shown in Figures 5.8 and 5.20. The far offset source location is marked by a circle to the northwest of the well 9-24 location. The subsurface coverage of the VSP-CDP data extends along a direction towards the offset source location starting at well 9-24 out to half the distance from well 9-24 to the source. The two VSP illustrated faults on the seismic line nearest well 9-24 project onto the seismic line at CDP numbers 47 and 48. These faults are shown as a single fault on the reinterpreted seismic line in Figure 5.22. The layout in Figure 5.21 clearly shows that the fault displayed on the seismic line immediately South of well 2-25 is not imaged on the VSP-CDP data; only on the seismic data. In this case, the VSP-CDP interpretation has brought new information into the integrated interpretation.

5.8 Conclusion

The exploratory well 9-24 was drilled on the downthrown side of a fault block on the basis of conventional surface seismic data. The expectation was that the gas-prone sandstones of the basal Kiskatinaw Fm would be truncated laterally and sealed against the upthrown fault-block. Contrary to expectations, the basal Kiskatinaw was unproductive; however, well 9-24 did encounter commercial gas within the upper Kiskatinaw which was now shut-in.

Figure 5.22 Plan map of the FSJG1 offset source area showing the fault locations as interpreted from the VSP and surface seismic data (from Hinds et al. 1994c). The VSP data (FSJG1 far offset) imaged the two faults along the seismic line nearest to well 9-24 and the seismic imaged the fault nearest to well 2-25. These two datasets complement each other in the construction of the geological interpretation shown in Figure 5.21.



————— Interpreted fault
----- seismic line

SCALE: 1 KM

To obtain a high resolution seismic image of the subsurface in the vicinity of well 9-24, and to evaluate the proximity of any displacements features such as faults which might not have been resolved on the surface seismic data, three VSP surveys were designed and run on the 9-24 well-site. This seismic profiling information, in conjunction with surface seismic coverage, was used to image the subsurface fault pattern, and elucidate the seismic signature and lateral continuity of the upper Kiskatinaw Fm strata. The profile data supplemented the surface seismic and well log control in that VSP data could be directly correlated to the surface seismic data. As a result, the surface seismic control could be accurately tied to the subsurface geology; multiples could be identified on the VSP data and evaluated on the surface seismic data; and the subsurface, in the vicinity of the borehole, was better resolved on the VSP data than on the surface seismic control.

The information provided by the VSP surveys allowed this work to provide a refinement of the interpretation of the surface seismic data, and enabled the construction of a detailed geologic cross-section (Fig. 5.21). These interpretations provide information with respect to the subsurface in proximity to well 9-24, and perhaps more importantly, further elucidate the geologic history of the structurally complex Fort St. John Graben area (Richards et al., 1994).

CHAPTER 6

SIMONETTE REEF CASE STUDY

On the basis of conventional surface seismic data, the 13-15-63-25 W5M exploratory well was drilled into a low relief Leduc Formation reef (Devonian Woodbend Group) in the Simonette area, west-central Alberta, Canada. The well was prognosed to intersect the crest of the reef and to encounter about 50-60 m of pay; unfortunately, it was interpreted later to have intersected a flank position of the reef and was abandoned. The decision to abandon the well, as opposed to whipstocking in the direction of the reef crest, was made after the acquisition and interpretive processing of both near and far offset (252 and 524 m, respectively) vertical seismic profile (VSP) data, and after the reanalysis of existing surface seismic data.

The VSP survey was designed, performed and the results of a near and far offset VSP survey interpreted while the drilling rig remained on-site, with the immediate objectives of: (1) determining an accurate tie between the surface seismic data and the subsurface geology; and (2) mapping relief along the top of the reef over a distance of 150 m from the 13-15 well location in the direction of the adjacent productive 16-16 well with a view to whipstocking. These surveys proved to be cost effective in that the operator of the well was able to determine that the crest of the reef was out of the target area, and consequently that whipstocking was not a viable alternative. The use of VSP surveys in this situation allowed the owners of the well to avoid the costs associated with whipstocking, and to have

confidence about their decision to abandon the well.

In this chapter, the 2-D surface seismic and VSP signatures of the low-relief reef in the Simonette study area (Hinds et al., 1993b and 1994c) are discussed with a view to obtaining a refined seismic image at the VSP-well and in the surrounding area. The 2-D data were acquired prior to drilling the 13-15 exploratory well which ultimately ended up intersecting the reef in a flank position below the oil/water contact as interpreted in this chapter. The initial processing of the raw VSP data was done by Vector Technology in 1987. The interpretive processing results presented in this chapter represent a more extensive treatment of all of the exploration data including the VSP data (taken from raw input data) and shown in Hinds et al (1993b).

6.1 Simonette Field

The Simonette Reef lies within the western Woodbend depositional realm (Stoakes and Wendte, 1987) where the reef environment is slightly different to that of the southeastern realm (Moore, 1989a). The southeastern realm included the geology for the case studies described in chapters 3 (Lanaway/Garrington field) and 4 (Ricinus field). A short review is presented below.

The Woodbend Group in central Alberta (Figs. 3.1A, B, and C) is subdivided into four formations: Cooking Lake, Duvernay, Leduc, and Ireton. In the Simonette study area of the western Woodbend depositional realm, the Cooking Lake Formation is depositionally absent and the Leduc Formation conformably overlies the Beaverhill Lake Group (Moore, 1989a).

The Leduc reef in the Simonette study area (Hinds et al., 1993b and 1994c) developed as both full and low-relief reef. The areal extent of the full reef which towers up to 230 m above the Beaverhill Lake platform, is defined roughly by the 70 m Ireton isopach contour interval in Figure 6.1. In Figure 6.1, the position of a geologic profile is shown defined by 8 wells with the corresponding geologic cross-section defined by the geophysical logs being shown in Figure 6.2.

Within the cross-section, well 10-34 penetrated the calcareous muds of the interior lagoon facies of the Leduc reef and was abandoned. Well 04-06 was drilled as a development well and is currently classified as an oil well although operations of producing from the well have been suspended. Well 10-06 was drilled into the northeastern portion of the Simonette atoll reef and is a flowing oil well. Well 04-16 was drilled into the raised peripheral rim (Anderson, 1986) and is a flowing oil well. The inter-reef well 10-16 was drilled off the rim of the main Simonette reef and penetrated only Ireton and Duvernay shales. Well 10-16 was abandoned. The five wells mentioned above were all drilled in the period 1960-62 when the Simonette Field was being developed in Alberta. Through numerous wells, the field was delineated and an Ireton isopach contour map (Hinds et al., 1993b) is shown in Figure 6.1 where the reef is interpreted to exist where the carbonates displace the encasing shales resulting in low shale isopach values.

Wells 16-16 and 04-22 were drilled in the period 1986-89 and are described in the next section. The final well shown in the geologic cross-section is the well 08-34 (a well in the shale basin) which did not encounter carbonate rocks of the Leduc Formation but was drilled through Ireton and Duvernay shales and Beaverhill Lake reef platform facies down to the Elk

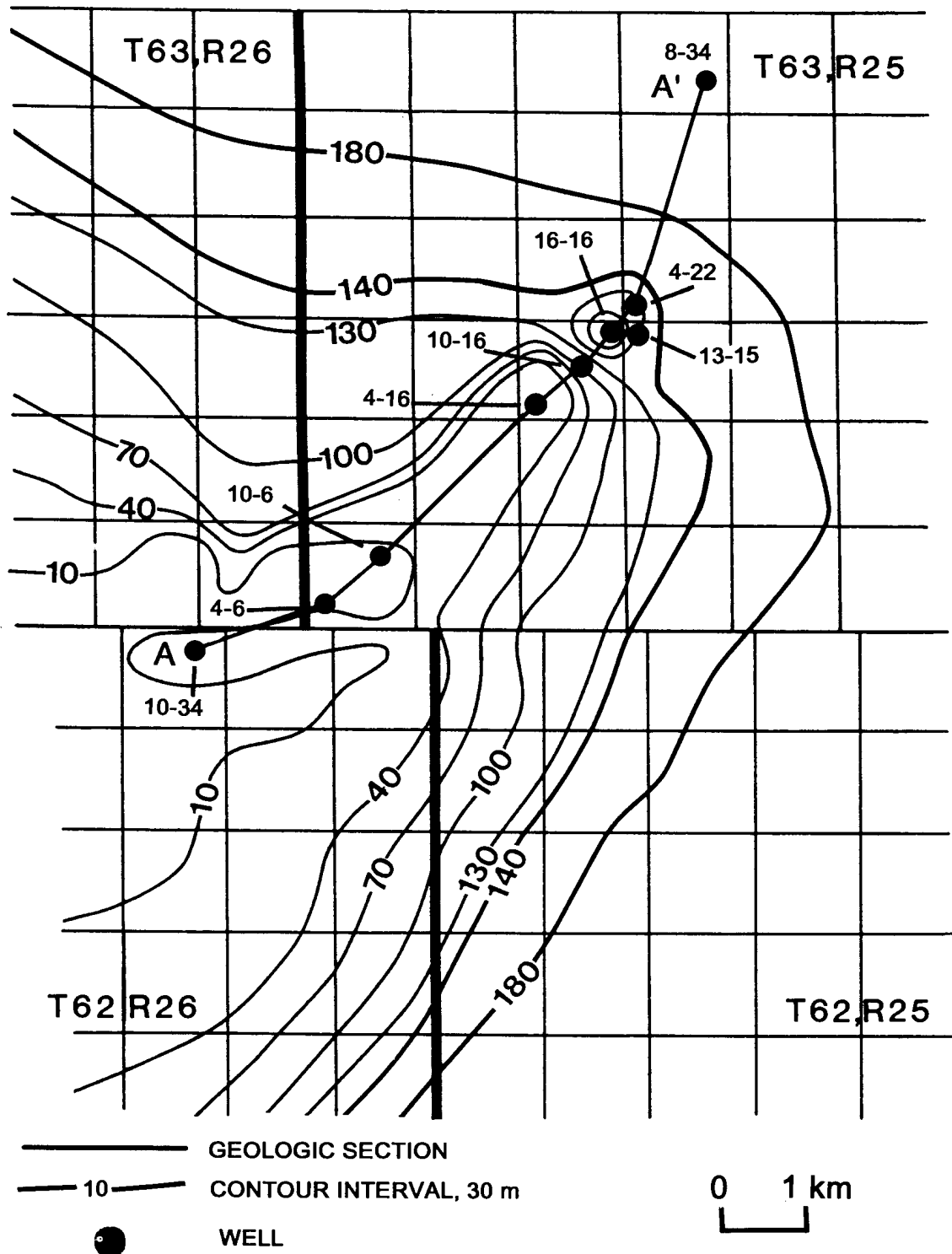


Figure 6.1 Ireton isopach map of the main and low-relief Simonette reef within the eastern Woodbend depositional realm. The locations of the wells used in the construction of the geologic cross-section shown in Figure 6.2 are shown in this figure. The exploratory well 13-15 is also posted (from Hinds et al., 1993b and 1994c).

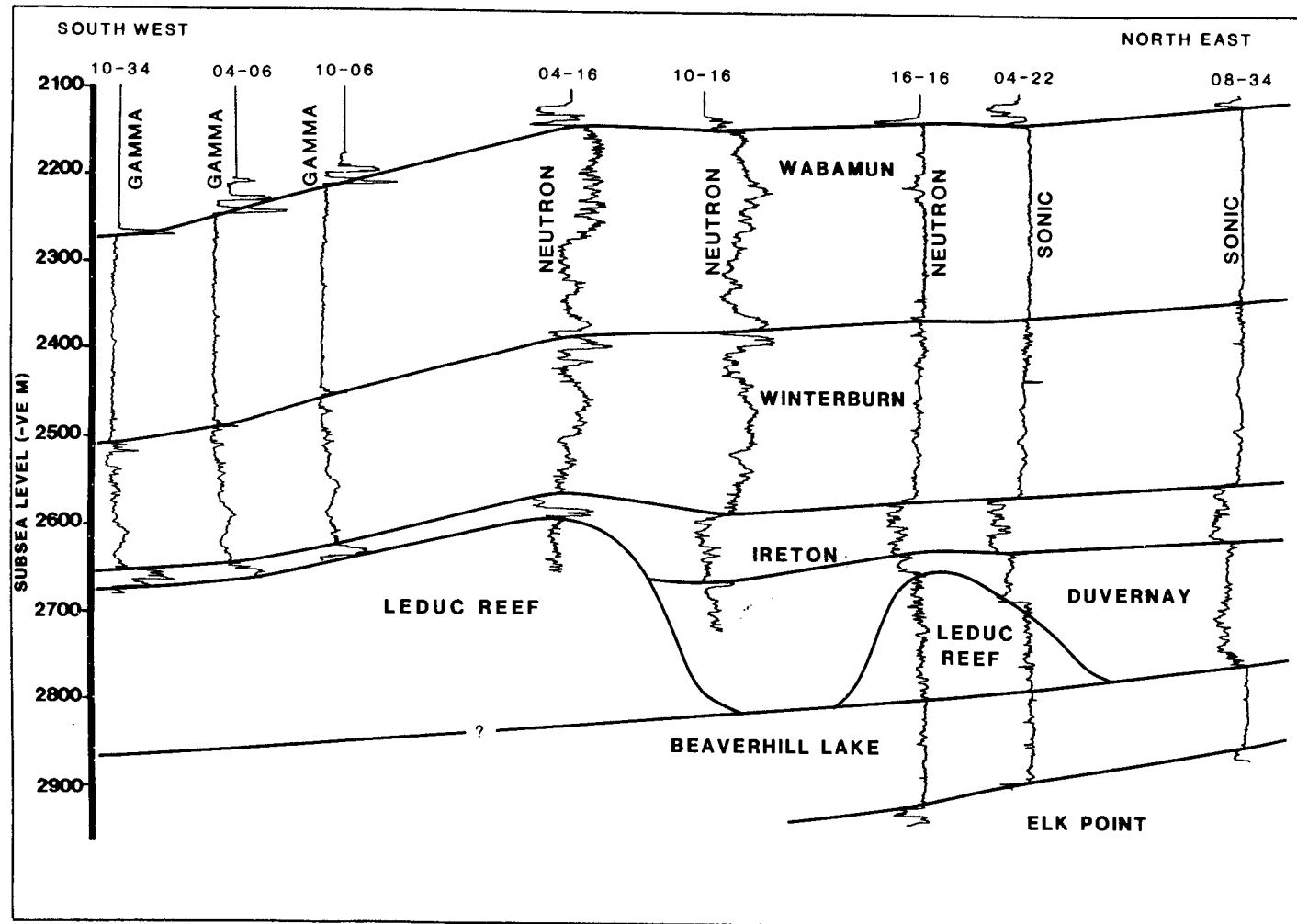


Figure 6.2 Geologic cross-section A-A' traversing the wells shown in Figure 6.1. The traverse starts in the southwest on the main Simonette reef at the back-reef lagoonal facies well, 10-34; continues to the northeast on the main reef for wells 4-6, 10-6, 4-16; into inter-reef shales for well 10-16; onto the low-relief reef with wells 16-16 and 4-22; and into the shale basin in well 8-34 (from Hinds et al., 1993b and 1994c).

Point Formation. The borehole logs within Figure 6.2 consist of neutron, gamma and sonic logs. The cross-section (Hinds et al., 1993b) shows the morphology of the Wabamun, Winterburn, Ireton, Leduc, Beaverhill Lake and Elk Point Formations and displays the placement of the study area reef (comprising of wells 16-16, 04-22 and the VSP-well, 13-15) with respect to the main Simonette atoll reef.

The low-relief reef of the study area, in contrast to the development of full reef buildup, attains a maximum thickness on the order of 120 m; its approximate areal extent is defined by the 130 m contour interval (Sections 15, 16, 21 and 22 of Township 63, Range 25 W5M; Fig. 6.1). The study area reef examined in this chapter is an isolated carbonate buildup that is basinward of the main Simonette atoll. The up-dip edges of both types of carbonate buildups can be productive where they are structurally closed and effectively sealed by the inter-reef shales of the Duvernay and Ireton Formations.

The term full reef was used in Anderson et al., (1989) to describe atolls and adjacent pinnacles which attain a height of over 200 m (Figs. 6.1 and 6.2) and is readily mapped on good quality 2-D seismic data; it is characterized by appreciable velocity pullup in the order of 30 ms, time structural drape of about 30 ms at the top of the Devonian (Wabamun Formation), and character variations within the Woodbend interval (the Leduc, Ireton and Duvernay Formation seismic events). The seismic signature of the low-relief reef which was the target of the VSP-well, as evidenced by the example seismic data (Fig. 6.3), is more subtle, being manifested by less than 15 ms of pullup and less than 15 ms drape of the Wabamun event from reef to off-reef. In addition, the reflection from the top of the low-relief reef can be difficult to distinguish from the Z-marker (an inter-reef shale event used

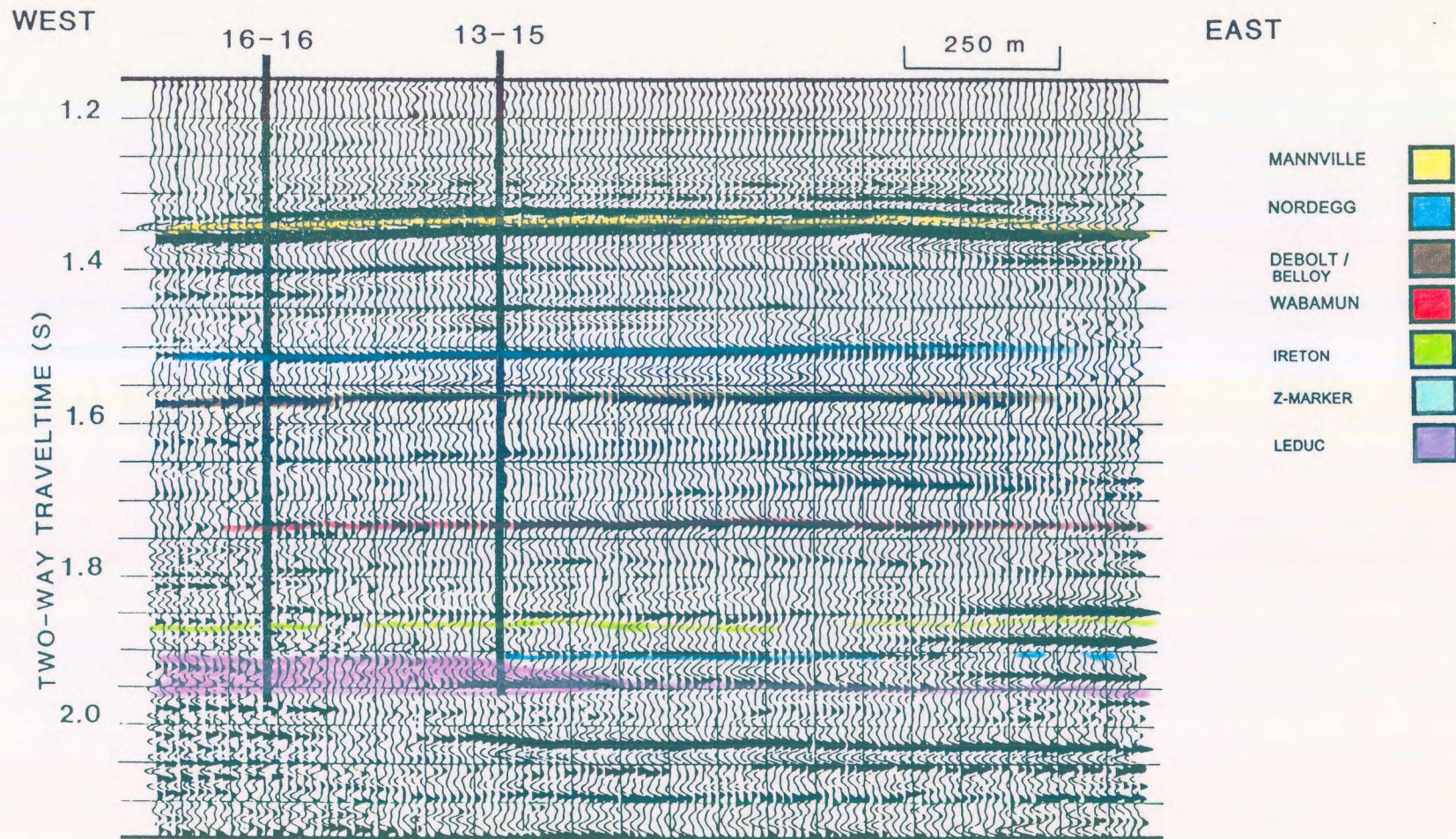


Figure 6.3 Example surface seismic data over the low-relief reef displaying the original interpretation of the owner of the data. The interpretation was done prior to the drilling of the well (from Hinds et al., 1993b and 1994c).

in the interpretation of seismic data in the Simonette atoll area; Hinds et al., 1993b). On Figure 6.3, an event beneath the reef at 2.2 s "pulls up" starting 8 traces East of the 13-15 well location (as shown on Fig. 6.3). This pullup suggested that the edge the low-relief reef could be located as indicated in Figure 6.3.

6.2 Simonette low-relief reef

Three wells penetrate the low-relief carbonate buildup seen as a northeast extension of the main Simonette reef in Figure 6.1; namely, 16-16-63-25 W5M, 4-22-63-25 W5M, and 13-15-63-25 W5M. Well 16-16 encountered 72 m of net pay; well 4-22 encountered 24 m of net pay but watered out after 12 months of production; well 13-15 is the abandoned exploratory well for which the two VSPs were acquired (see Fig. 6.4 for the three well locations).

The contour map of the Ireton to Leduc isochrons which was derived from the originally interpreted seismic data (interpreted by the owners of the seismic data) is shown in Figure 6.4. The prognosis was that well 13-15 would encounter 50-60 m of net pay. The contour map of Figure 6.5 summarizes the final preferred evaluation derived from the thesis work for the 13-15 location using the drilling results, the interpretation of the near and far offset nondeconvolved and deconvolved VSP data, and the reinterpretation of the suite of existing surface seismic lines within the area.

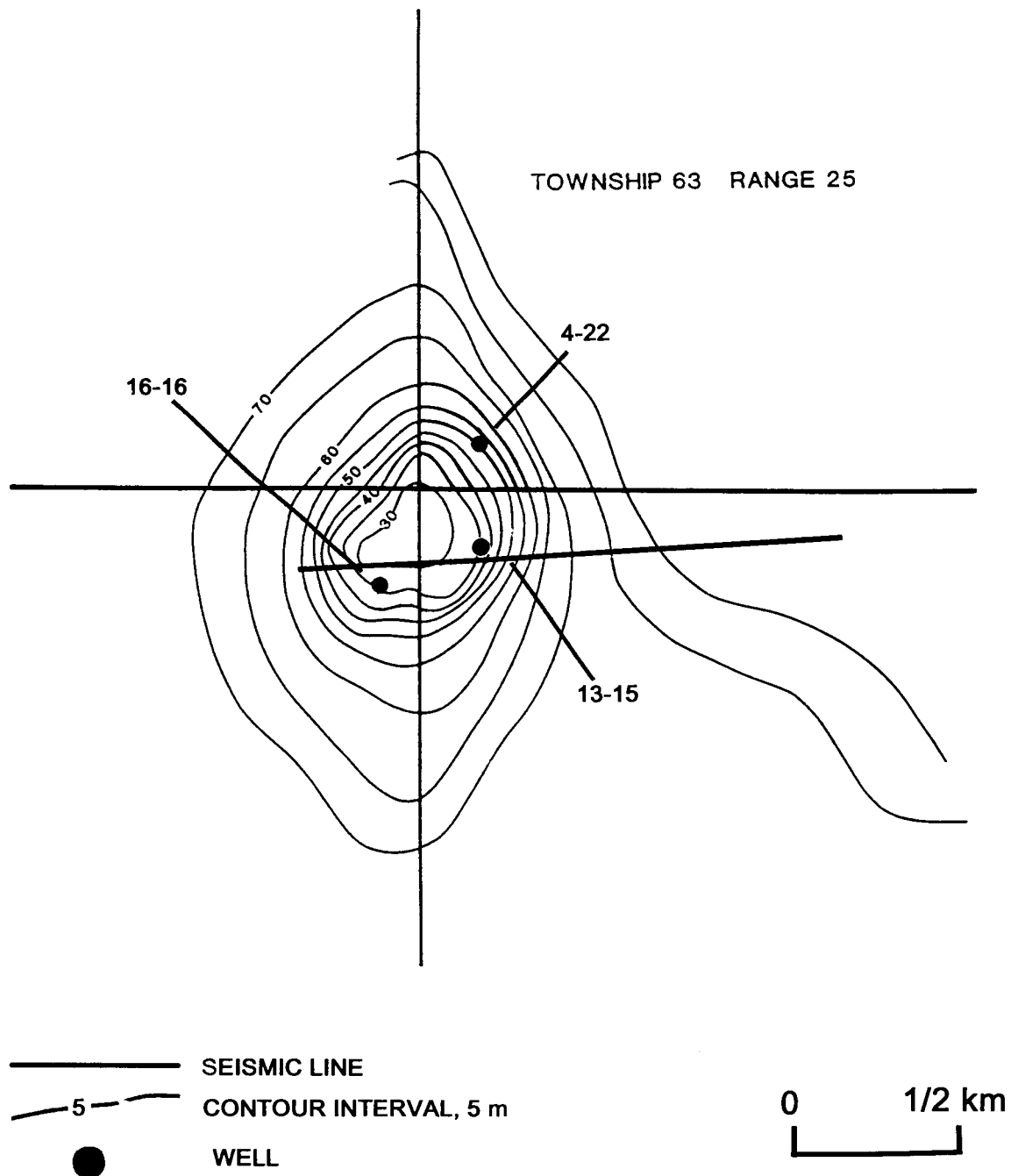


Figure 6.4 Ireton to Leduc isochron map resulting from the original interpretation of the seismic lines within the area of the low-relief reef. The oil pay-zone of the low-relief reef is interpreted to be as productive at the proposed well 13-15 as at the existing well 16-16 (from Hinds et al., 1993b, 1994c).

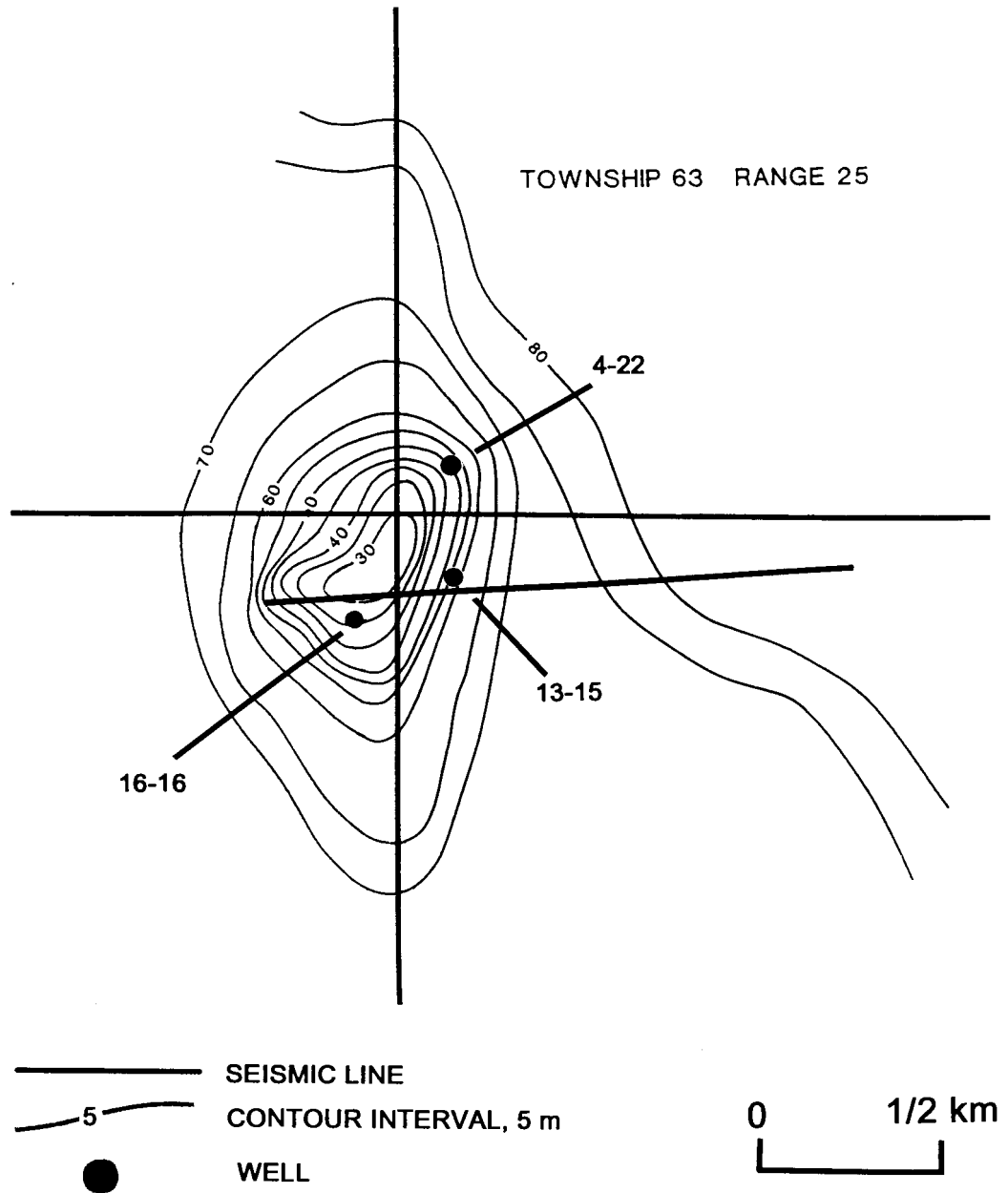


Figure 6.5 The preferred Ireton to Leduc isochron resulting from the updated interpretation (using the VSP results) of the seismic lines in the area of the low-relief reef, the VSP results and geologic borehole data. This interpretation shows the reef gradually rising out to 120 m from well 13-15 and then steeply rising towards well 16-16 (from Hinds et al., 1993b and 1994c).

The surface seismic line (normal polarity display; Fig. 6.3) is a stack of nominally 20-fold, split-spread, 120 prestack trace data, acquired using a patterned dynamite source (2 X 0.5 kg at 9 m depth; shotholes spaced 25 m apart) and DFS-5 recording equipment (8-128 hz filter). The seismometer groups consisted of nine, inline, 14 hz geophones spaced at 3.75 m. The geophone group and shot intervals were 25 and 75 m, respectively.

The seismic markers of principal interest correspond to the Mannville, Nordegg, Debolt/Belloy, Wabamun, Ireton, Z-marker (a regional marker within the inter-reef shales), and Leduc (Figs. 6.2 and 6.3). The Z-marker corresponds to the top of the Duvernay shales listed in the stratigraphic chart in Figure 6.2 and is caused by a change in the carbonate content within the Duvernay shale versus the overlying Ireton shale. The seismic image of the subsurface at well 13-15 (Fig. 6.3), was initially interpreted as comparable to that at the productive well 16-16 location; hence it was drilled. The high-amplitude event at about 1.9 s, at the 13-15 location, was mistakenly interpreted as the top of the reef. In retrospect, it is believed to be the off-reef Z-marker. Well 13-15 intersected the low-relief reef in a flank position below the oil/water contact (P. Pelletier, pers. comm.) and encountered 134 m of inter-reef shale (in comparison with 75 m of shale encountered in well 16-16). On the basis of the well results, it was suggested that the low-relief reef could rise abruptly to the west and that whipstocking in the direction of the productive 16-16 well should be considered.

The operators of well 16-16 were left with two alternatives: abandon the well or whipstock in the direction of well 16-16, bearing in mind that the further well 13-15 deviated from the original bottomhole location, the greater the Alberta Government imposed production penalty. In order to ascertain the cost-effectiveness of whipstocking the operators ran two VSP

surveys: a near offset (252 m) and a far offset (524 m) VSP survey. It was on the basis of these data and the reinterpretation of the existing surface seismic, that the decision was made to abandon well 13-15 without any whipstock.

6.3 VSP acquisition

After an analysis of the 13-15 well geophysical logs and prior to abandonment, two VSP surveys were run at this well site in order to:

- 1) more accurately tie the surface seismic data and an interpretation thereof to the subsurface geology (in particular the top of the low-relief Leduc reef);
- 2) map the top of the reef over a distance of 150 m in the direction of the 16-16 well (with a view to whipstocking); and
- 3) differentiate primary reflections from both surface-generated and interbed multiples.

The near offset was chosen to be 252 m from well 13-15, the far offset to be 524 m; both are inline with respect to the surface seismic line (Fig. 6.4). Two Vibroseis units were operated in series at each offset. The 12 s sweep ranged from 10 to 70 hz, the recording length was 15 s, and the cross-correlated output was 3 s. On average, six sweeps were summed for each geophone sonde location. MDS-10 recording instruments and a sampling interval of 1 ms were used. The recording filter was OUT/250; the instrument filter served

as an anti-aliasing, lowpass filter with a ramp rolloff starting at 250 hz.

Well 13-15 extends 3620 m below the Kelly Bushing (at 878 m asl). Both source locations were at 868 m asl. The geophone sonde was lowered to the bottom of the well and raised at 20-30 m intervals. At each sonde location, the three component geophone tool was locked in place.

The two offsets were designed to be within the direction of the producing 16-16 well with the following interpretation considerations in mind:

- 1) if the slope of the reef was steep, a diagnostic seismic signature would be seen of the 252 m offset data; however a diagnostic shadow zone (null data) would be seen on the 524 m data;
- 2) if the crest was not steep but gradual, then both offset data would reflect the seismic image of the slope (the 252 m offset data would be a subset of the 524 m offset VSP data);
and
- 3) if the slope was gradual but became steeper beyond the range of the near offset (252 m) VSP, then the 252 and 524 m offset data would both image the gradual slope but only the longer offset data would image the steeply sloped part of the reef.

6.4 Near offset (252 m) VSP interpretive processing

During the processing of the near offset VSP, a series of interpretive processing panels (IPPs) were designed (Hinds et al., 1993b and 1994c) to display the following :

- 1) separation of $Z_{up}(FRT)$ and $Z_{down}(FRT)$ data from the $Z(FRT)$ data;
- 2) deconvolution of the $Z_{up}(FRT)$ data to output the $Z_{up(decon)}(FRT)$ using an inverse filter calculated from the $Z_{down}(FRT)$ data; and
- 3) inside and outside corridor stacks (Hinds et al., 1989a) of both the $Z_{up}(+TT)$ and $Z_{up(decon)}(+TT)$ data.

6.4.1 P-wave separation

The separation of the upgoing and downgoing P-waves on the vertical (Z) geophone data is illustrated in the wavefield separation IPP (Hinds et al., 1989a) in Figure 6.6.

Panel 1 (Fig. 6.6) displays the normalized $Z(FRT)$ data. In panel 2, high-amplitude surface-generated multiples, and less prominent interbed multiples can be seen in the $Z(-TT)$ data. The surface-generated downgoing multiples can be recognized as continuous events arriving after the first break primary downgoing wavetrain on all of the traces, from the deepest to the shallowest receiver location (Hinds et al., 1989a). A downgoing multiple associated with

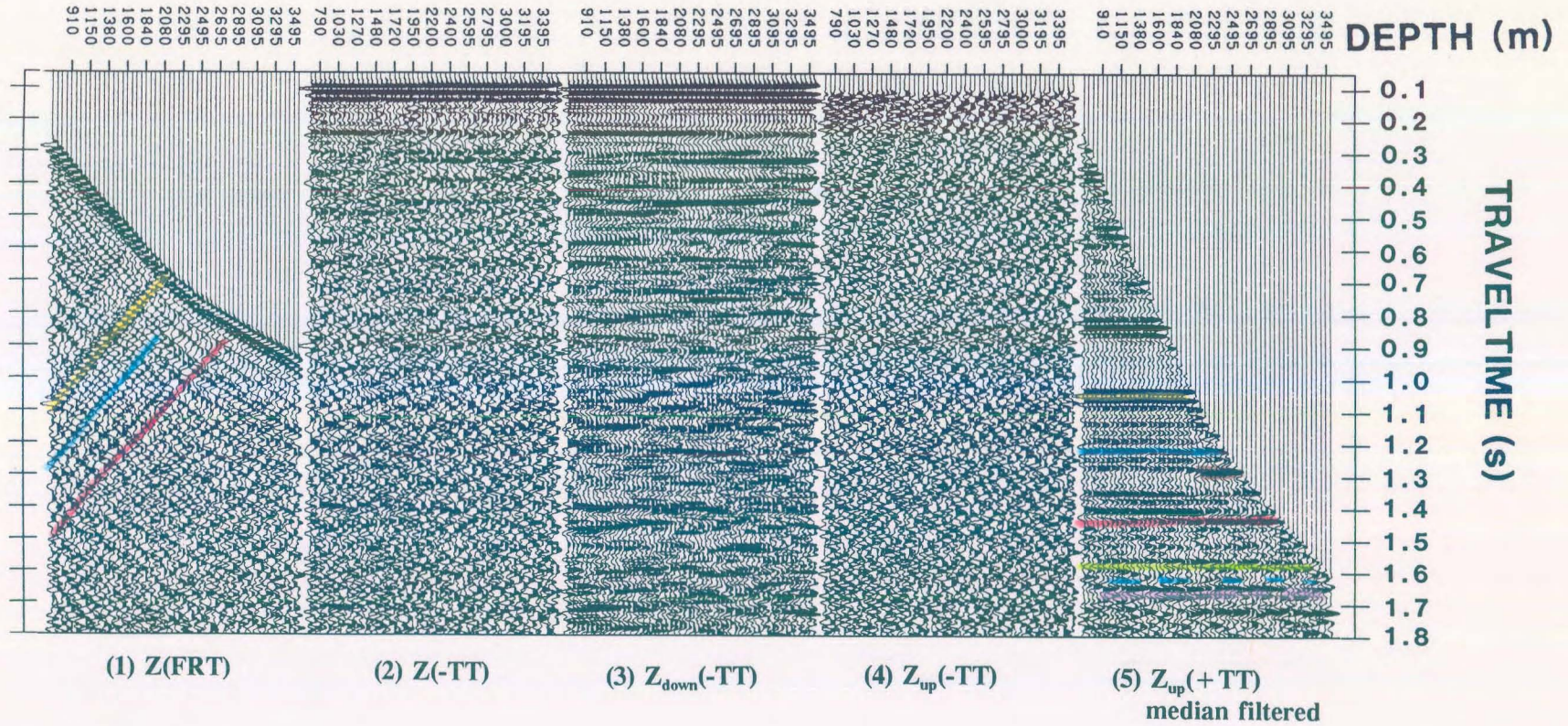


Figure 6.6 Interpretive processing panel depicting the wavefield separation of the near offset (252 m) offset Simonette VSP data (from Hinds et al., 1993b and 1994c).

the Mannville Formation interface is interpreted to start at the 2080 m trace (between 0.3 and 0.32 s; panel 2) and continue onto the deeper traces. The event may be an interbed multiple, since on panel 2, it does not appear to continue onto the shallower depth traces. The $Z_{\text{down}}(-\text{TT})$ data in panel 3 do not assist in the interpretation since the median filter has smeared the event onto the shallower traces. An inspection of the $Z_{\text{up}}(+\text{TT})$ data in panel 5 confirms that multiple interference is definitely originating from the Mannville Formation top interface.

The $Z_{\text{down}}(-\text{TT})$ data were obtained from the $Z(-\text{TT})$ data using an eleven-point median filter and are displayed in panel 3. The residual $Z_{\text{up}}(+\text{TT})$ data content in panel 3 are interpreted to be minimal since the data consist predominately of horizontally aligned downgoing events. The $Z_{\text{up}}(-\text{TT})$ shown in panel 4 were separated from the $Z(-\text{TT})$ data by subtracting the $Z_{\text{down}}(-\text{TT})$ as reviewed in chapter 2. The Mannville, Nordegg, Belloy/Debolt, Wabamun, Ireton, Z-marker and reefal Leduc events are interpreted in the median filtered $Z_{\text{up}}(+\text{TT})$ data and shown in panel 5 of Figure 6.6.

6.4.2 Near offset VSP deconvolution

Multiple reflections are represented in the downgoing wavefield as shown in panel 3 of Figure 6.6. The initial downgoing pulse (except in the case of head wave contamination) is the primary downgoing P-wave; later downgoing arrivals are multiples. The deconvolution IPP was designed as shown in Figure 6.7 to enable the monitoring of the deconvolution process.

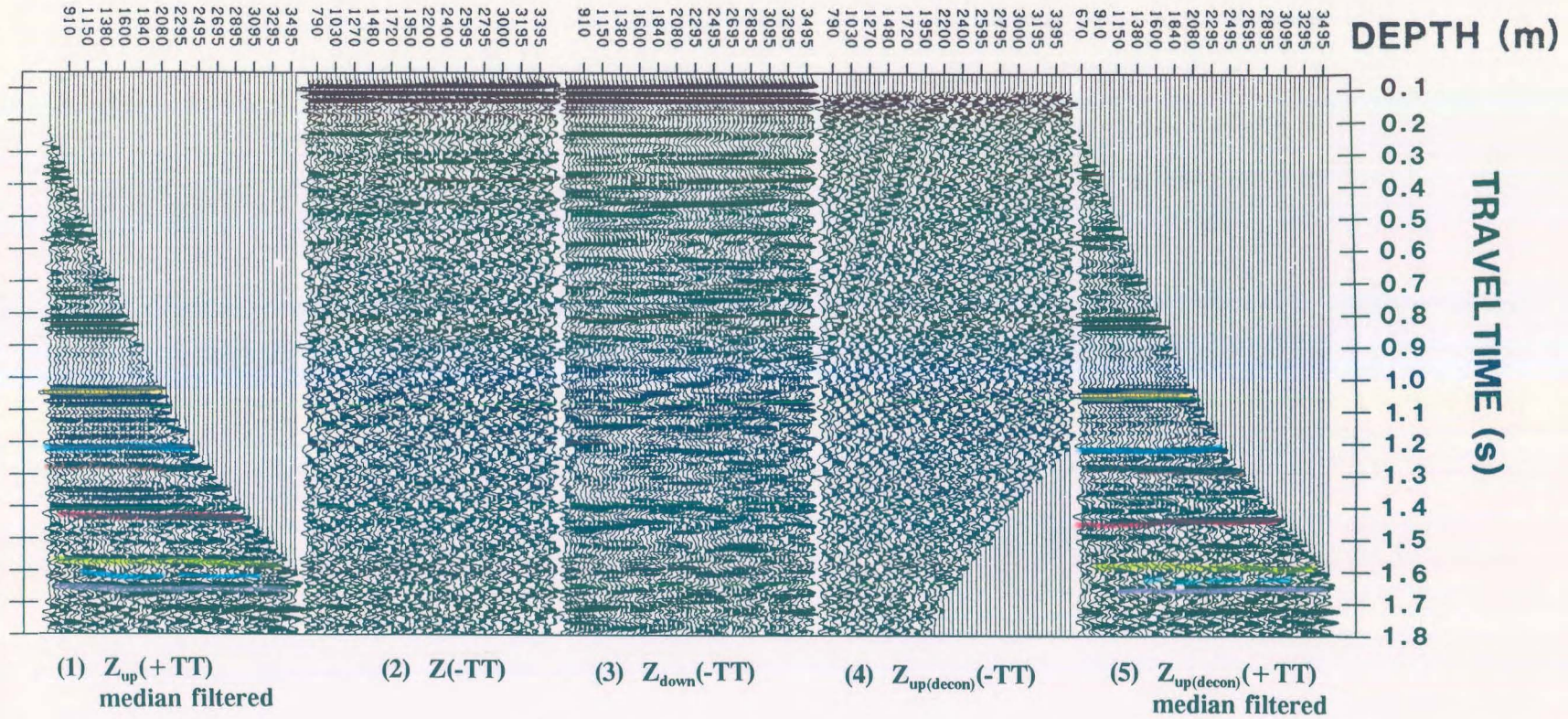


Figure 6.7 Interpretive processing panel depicting the deconvolution of the near (252 m) offset Simonette VSP data (from Hinds et al., 1993b and 1994c).

Panel 1 of Figure 6.7 is the median filtered $Z_{up}(+TT)$ data. Panels 2, 3, and 4 are the $Z(-TT)$, $Z_{down}(-TT)$ and $Z_{up(decon)}(-TT)$ data, respectively. The median filtered $Z_{up(decon)}(+TT)$ data are displayed in panel 5.

A comparison of the $Z_{up}(+TT)$ with $Z_{up(decon)}(+TT)$ data, illustrates the effect of multiple contamination on the continuity of primary events. In panel 1 for example, the Debolt/Belloy event is high amplitude and continuous at sonde depths below the Mannville (from 2080 m to 2570 m). At shallower recording depths, the Debolt/Belloy event and a Mannville interbed multiple are interpreted to interfere. In more detail, the peak at 1.275 s on the left hand side of panel 1 is the interfering multiple. This event can be traced across the panel until the 2080 m trace. At that point, the Debolt/Belloy event peak (of lower frequency than the multiple) dominates and is continuous until the 2570 m trace; upon which it no longer exists since this is where the "first break" for that depth level now exists. On panel 5, deconvolution appears to have substantially reduced the effect of multiple interference as the Debolt event is much more continuous and the series of multiples immediately below the Mannville are strongly attenuated.

Within the zone from the Wabamun to Leduc Formation, multiple contamination is interpreted to be minimal since the events in this zone are continuous and unchanged after deconvolution. The Z-marker and Leduc events are continuous and do not exhibit either significant apparent time-structural relief or appreciable character variations. The description of the 524 m VSP interpretation will show that the far offset data do contain an interpreted multiple associated with the Wabamun interface in contrast to the near offset results presented above in which multiple generation at the Wabamun level is minimal.

6.4.3 Inside and outside corridor stacks

Multiple contamination on the $Z_{up}(+TT)$ data can be re-examined using the inside and outside corridor stacks of both the $Z_{up}(+TT)$ and $Z_{up(decon)}(+TT)$ data.

$Z_{up}(+TT)$ inside and outside corridor stacks along with the input data to the muting and stacking processes are shown in Figure 6.8. The amplitude of the Debolt/Belloy primary is weak on the $Z_{up}(+TT)$ inside corridor stack shown in panel 4 of Figure 6.8 in comparison to the same event on the outside corridor stack as displayed in panel 3. The Debolt/Belloy event at sonde depths shallower than 2080 m (above the Mannville) on the muted input data shown in panel 5 for the $Z_{up}(+TT)$ inside corridor stack is masked (destructively interfered with) by a possible interbed multiple. At depths greater than the Mannville (2080 m), the Debolt/Belloy event is unaffected by the multiple contamination, much higher in amplitude and 5-10 ms deeper in time therefore confirming that the bottom generating interface for this multiple is the Mannville Formation interface.

On the inside and outside $Z_{up(decon)}(+TT)$ corridor stacks shown in Figure 6.9, the upgoing multiples appear to have been substantially attenuated by deconvolution. As an example, the Mannville associated multiples that lie immediately beneath the Mannville primary event on the $Z_{up(decon)}(+TT)$ data are greatly attenuated with respect to the $Z_{up}(+TT)$ data. This can be seen by comparing panel 1 of Figure 6.8 to panel 1 of Figure 6.9 in the time window of 1.35 to 1.5 s. In Figure 6.8, the time window is contaminated with multiple reflection events (coloured turquoise blue in panels 1 and 4) whereas in Figure 6.9, the same time window is relatively free of multiples. One multiple reflection event to note lies just above

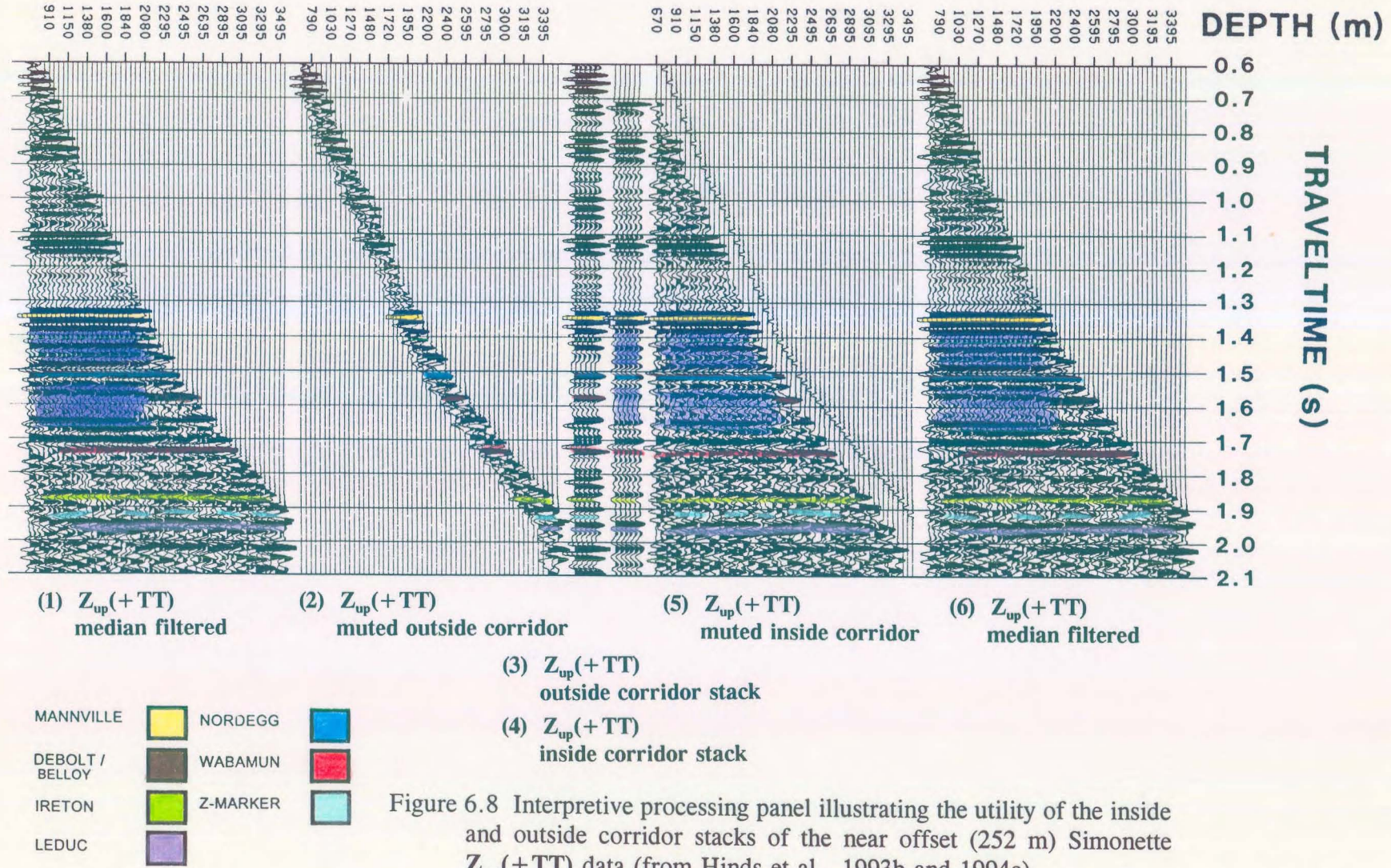


Figure 6.8 Interpretive processing panel illustrating the utility of the inside and outside corridor stacks of the near offset (252 m) Simonette $Z_{up}(+TT)$ data (from Hinds et al., 1993b and 1994c).

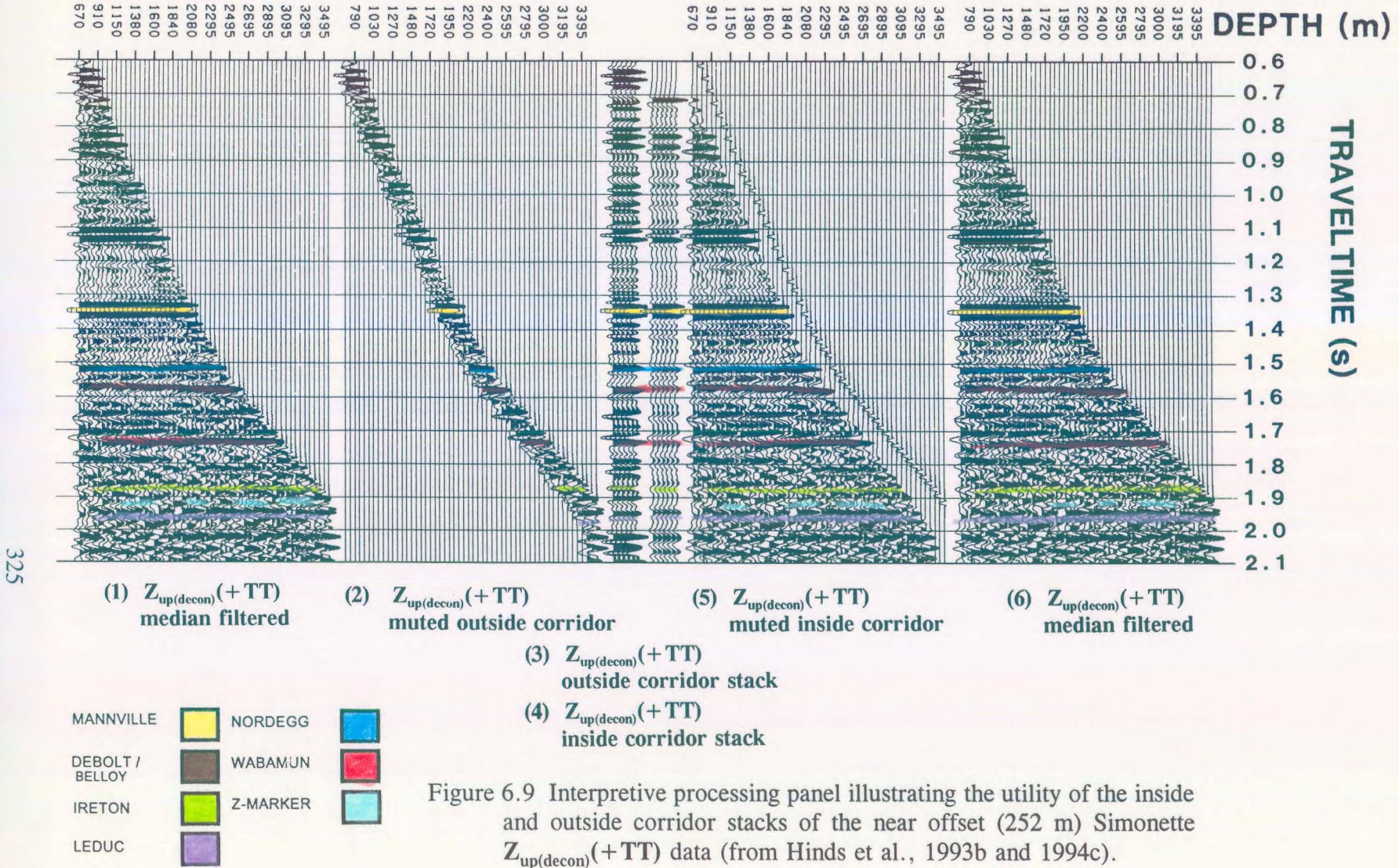


Figure 6.9 Interpretive processing panel illustrating the utility of the inside and outside corridor stacks of the near offset (252 m) Simonette $Z_{up(decon)}(+TT)$ data (from Hinds et al., 1993b and 1994c).

the Nordegg primary event at 1.48 s. On panel 1 of Figure 6.8, the event is dominant; however in panel 1 of Figure 6.9 (after deconvolution), the event is attenuated.

Some primary events recorded between the Mannville and Nordegg primary reflection events can only be seen on the few traces beyond the deepest trace recording the Mannville primary event. These few peaks will be included in the outside corridor stack. One such event is at 1.45 s which is preserved across the entire depth range of 670 to 2295 m once deconvolution is done. Since the depth interval between these primary events generated between the Mannville and Nordegg interfaces represents only a few traces, it causes the use of corridor stacks alone difficult to interpret without including the unmuted and muted corridor stack data on the same IPP (Hinds et al., 1989a).

6.5 Interpretive processing of the far offset VSP data

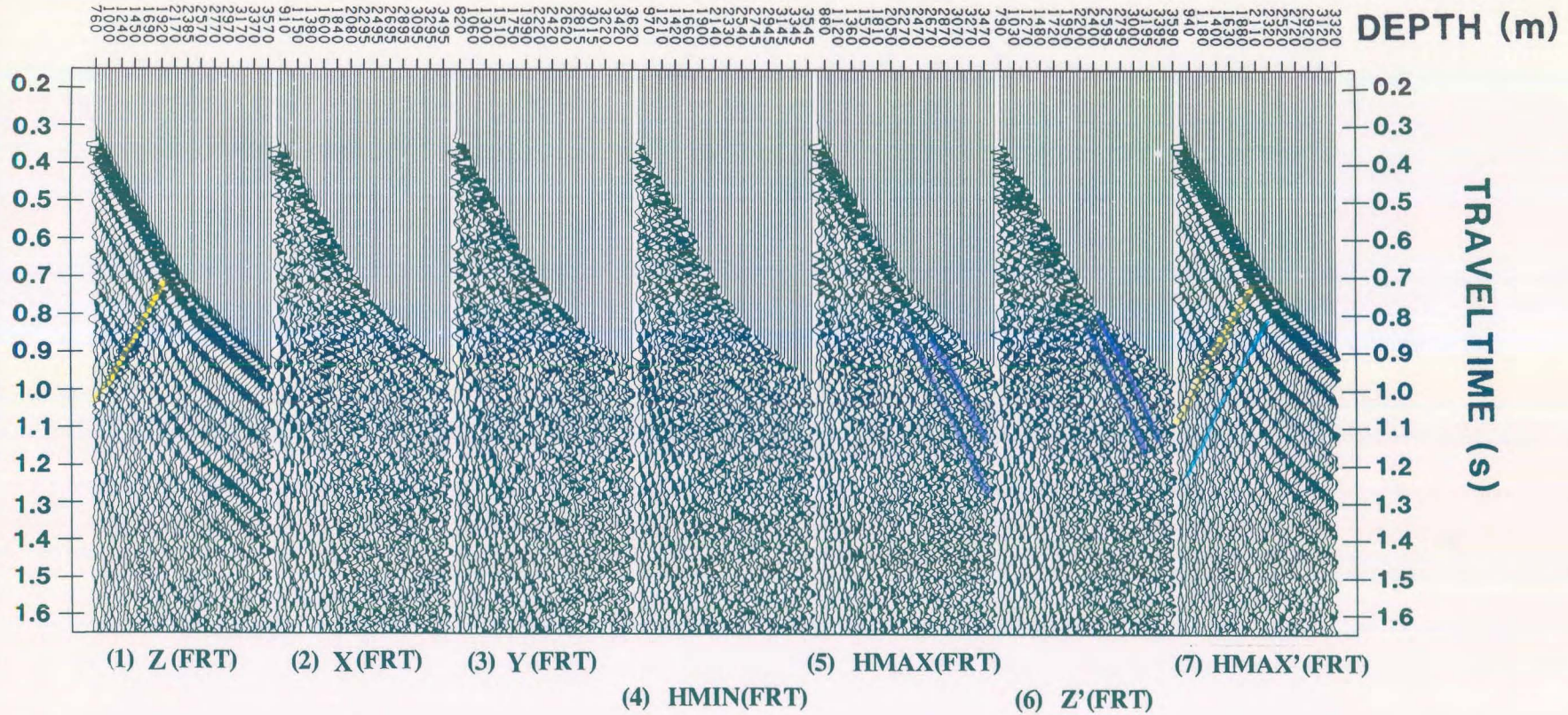
During the production consulting in 1987, the triaxial processing was not performed whilst the rig was on standby. The VSP-CDP mapped data recorded in 1987 used the $Z_{up}(+TT)$ from the 524 m offset without the assistance of polarization analysis. The processing (Hinds et al., 1993b and 1994c) presented in this chapter is more extensive. The $Z(FRT)$, $X(FRT)$ and $Y(FRT)$ data contain nonpartitioned elements of the up- and downgoing P- and SV-wavefields. Hodogram-based rotation and time variant polarization rotation IPP's used in the processing of the far offset for the Simonette 524 m offset data (Hinds et al., 1989a; Hinds et al., 1991b; Hinds et al., 1993b and 1994c) are presented below to reveal that wavefield partitioning has significant implications for the interpretation.

6.5.1 Hodogram based rotation

The **Z(FRT)**, **X(FRT)**, and **Y(FRT)** data are presented in Figure 6.10 as panels 1, 2, and 3, respectively. The hodogram-based method initially polarized the components of the **X(FRT)** and **Y(FRT)** data outputting the **HMIN(FRT)** and **HMAX(FRT)** data (Hinds et al., 1989a; Hinds et al., 1993b and 1994c) shown in panels 4 and 5, respectively. **HMAX(FRT)** data display consistent primary downgoing P-wave first breaks indicating that the first set of rotations was relatively successful. The **HMAX(FRT)** data also contains mode-converted SV events (colored purple) that originate in the region of the Mannville reflector.

The **Z(FRT)** and **HMAX(FRT)** data were input to the second rotation which polarized the downgoing P-waves. Since the source offset distance is 524 m and the depth of the well is 3270 m, the **HMAX'** and **Z'** polarization axis were near vertical and horizontal, respectively. The resultant **Z'(FRT)** and **HMAX'(FRT)** data are shown in panels 6 and 7, respectively. The downgoing P-wave events are resident on the **HMAX'(FRT)** data; however, both the **HMAX'(FRT)** and **Z'(FRT)** data contain upgoing P-wave events. This indicates that the data will need to undergo time-variant polarization to separate the upgoing P-wave events onto a single data panel (Z''_{up}) before interpretation.

The **Z'(FRT)** data (panel 6) contains the mode-converted downgoing shear wave primaries and possible multiples. In more detail, the first break on the 2080 m trace (representing the depth of the Mannville) can be approximated to be at 0.68 s on panel 6. At that point, the mode-converted downgoing SV event with a greater slope than the downgoing P-wave (the shallowest event coloured purple) can be traced down to 1.12 s on the 3570 m trace. Two



| | | | |
|-----------------|--|----------|--|
| MANNVILLE | | NORDEGG | |
| DEBOLT / BELLOY | | WABAMUN | |
| IRETON | | Z-MARKER | |
| LEDUC | | | |

Figure 6.10 Interpretive processing panel depicting the hodogram-based rotation of the far offset (524 m) Simonette VSP data (from Hinds et al., 1993b and 1994c).

visible, downgoing SV-multiples (also coloured purple but arriving later in time than the primary downgoing SV primary event) parallel the primary and arrive within a 150 ms window on the 3570 m trace.

6.5.2 Time-variant model-based rotation

In the first stage of the time-variant model-based rotation, $Z'(FRT)$ and $HMAX'(FRT)$ data were wavefield separated (using F-K filtering; see chapter 2 for examples) into $HMAX'_{down}(FRT)$, $HMAX'_{up}(FRT)$, $Z'_{down}(FRT)$ and $Z'_{up}(FRT)$ data. The $HMAX'_{down}(FRT)$ is retained and used in the deconvolution of the $Z''_{up}(FRT)$ data in the following section. The deconvolution of the polarized far offset VSP data was not done during the 1987 processing and interpretation clarity will result from the deconvolution results shown below.

The $HMAX'_{up}(FRT)$ and $Z'_{up}(FRT)$ data shown as panels 1 and 2 in Fig. 6.11, respectively, were derotated (Hinds et al., 1989a) to output the $HMAX_{up(derot)}(FRT)$ and $Z_{up(derot)}(FRT)$ data shown in panels 3 and 4, respectively. Most of the upgoing P wave events have been distributed back onto the Z-type axis, $Z_{up(derot)}(FRT)$. In the $Z(FRT)$ data shown in panel 1 of Fig. 6.10, the dominant downgoing P-waves were much higher in amplitude than the upgoing events resulting in the upgoing events being difficult to interpret. Following the wavefield separation, the separated upgoing P wave events in the $Z_{up(derot)}(FRT)$ data are easily traceable within the data.

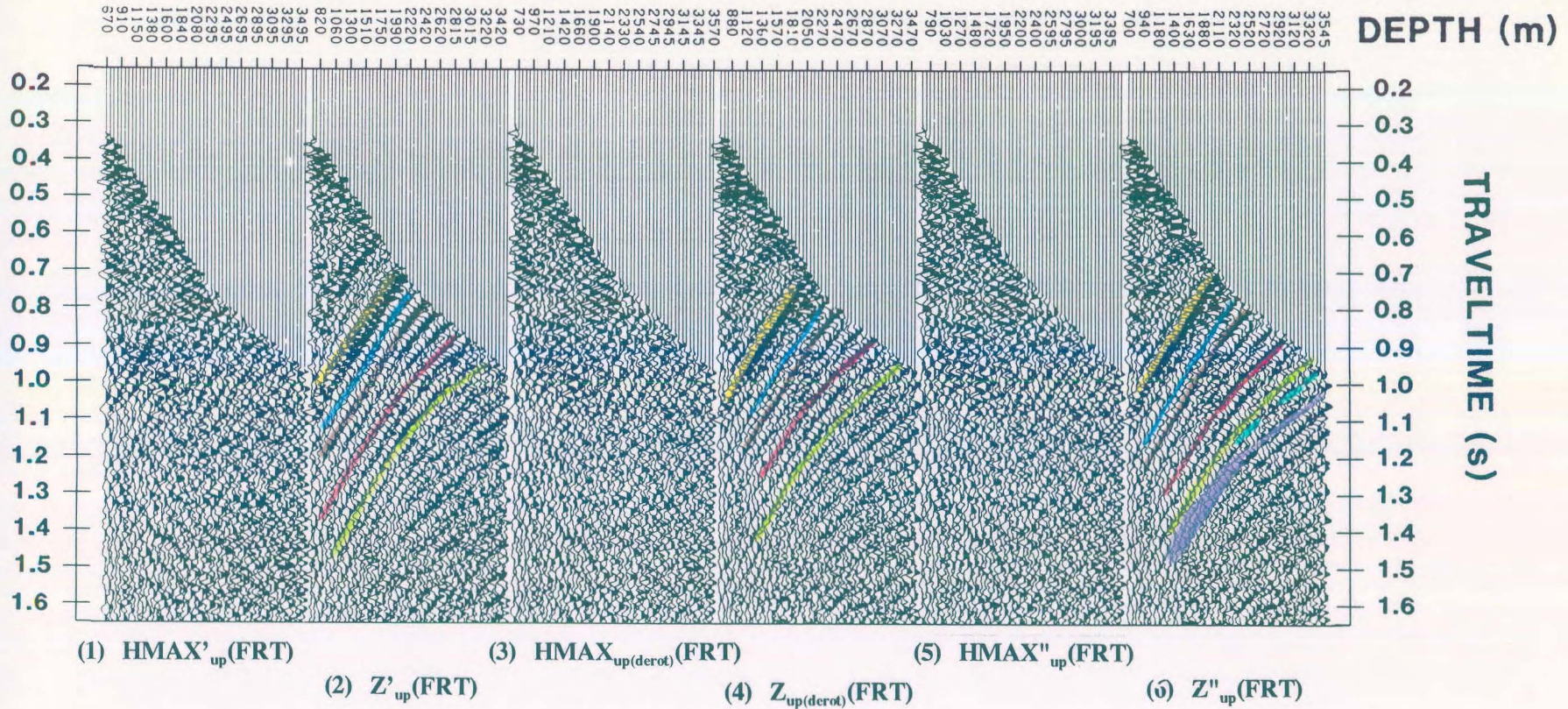


Figure 6.11 Interpretive processing panel depicting the time-variant model-based rotation of the far offset (524 m) Simonette VSP data (from Hinds et al., 1993b and 1994c).

The upgoing P-wave events on the $Z_{\text{up(derot)}}(\text{FRT})$ data shown in panel 4 are improperly aligned, particularly those generated by shallow reflectors, because of the choice of using a single rotation angle per data trace. These data have been derotated but the upgoing P-wave events are still partitioned on both output data sets, $Z_{\text{up(derot)}}(\text{FRT})$ and $\text{HMAX}_{\text{up(derot)}}(\text{FRT})$, due to the non-zero source offset.

To correct for misalignment, time-variant rotation angles were calculated (Hinds et al., 1991b; Hinds et al., 1993b and 1994c) and applied to every pair of traces in panels 3 and 4. The resultant $\text{HMAX}''_{\text{up}}(\text{FRT})$ data (panel 5) contains the residual downgoing SV-wave data left over in the data following wavefield separation. The $Z''_{\text{up}}(\text{FRT})$ data predominantly contains the upgoing P-wave events. On the $Z''_{\text{up}}(\text{FRT})$ data, shallow events (originating at 0.58 s between the traces for 1630 to 1750 m) are better isolated (onto a single panel) than on either the $Z_{\text{up(derot)}}(\text{FRT})$ data or $\text{HMAX}'_{\text{up}}(\text{FRT})$ data panels.

6.5.3 VSP-CDP mapping of the far offset VSP data

A VSP-CDP and migration IPP for the far offset $Z''_{\text{up}}(+\text{TT})$ and $Z''_{\text{up(decon)}}(+\text{TT})$ was designed to facilitate the interpretation of the interfering multiples and subsurface structure (Hinds et al., 1991b; Hinds et al., 1993b and 1994c). The $Z''_{\text{up}}(+\text{TT})$ data shown in Figure 6.12 were used for the interpretation of the low-relief Leduc reef. The appearance of many anomalous events arising from multiple contamination on the $Z''_{\text{up}}(+\text{TT})$ data (such as the event at 1.8 s) makes the interpretation of this plot along with the VSP-CDP (panel 3) and Kirchhoff migrated $Z''_{\text{up}}(+\text{TT})$ data difficult.

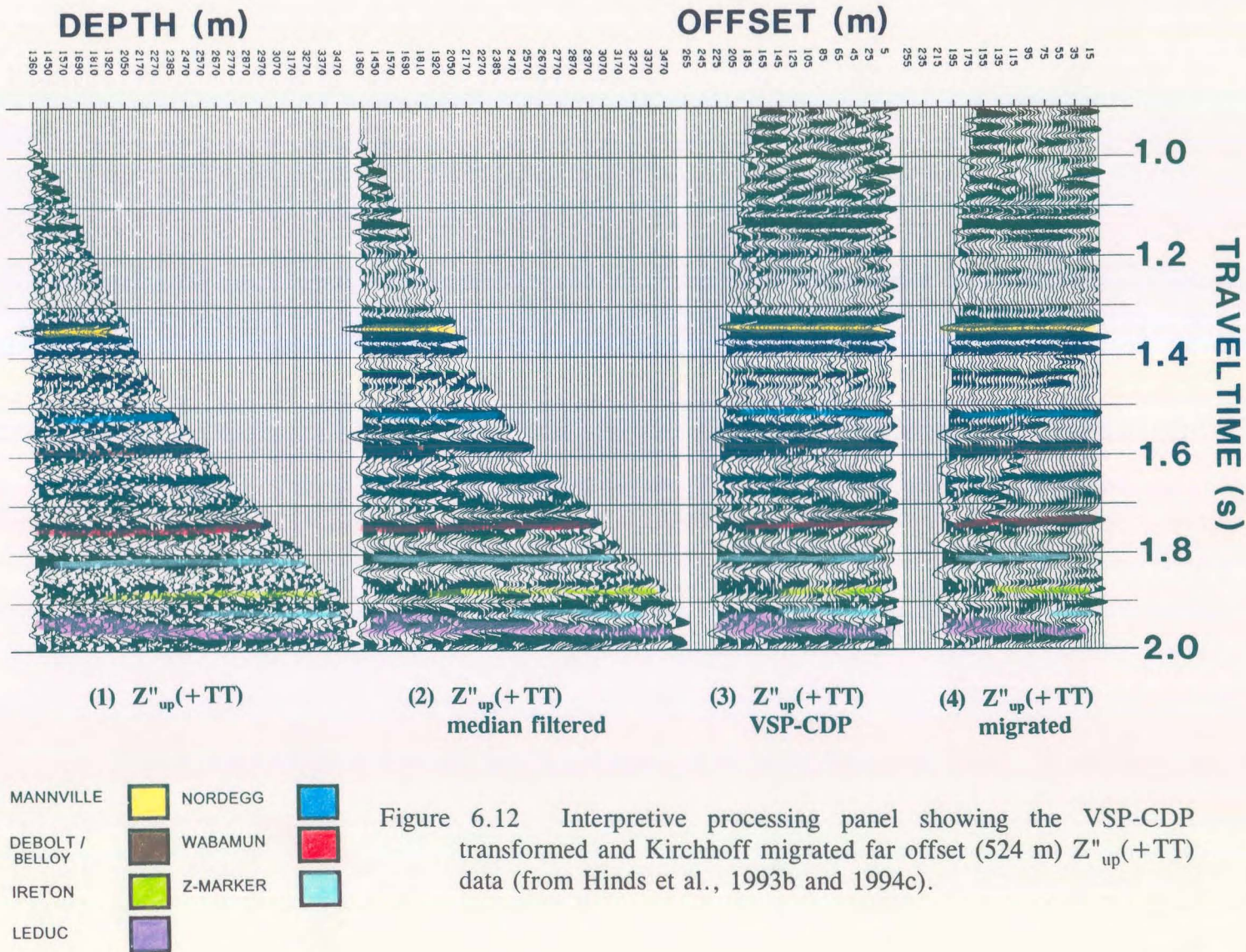


Figure 6.12 Interpretive processing panel showing the VSP-CDP transformed and Kirchhoff migrated far offset (524 m) $Z''_{up}(+TT)$ data (from Hinds et al., 1993b and 1994c).

The interpretation of the Leduc reef event is that the reef slope rises at 145 m away from the well; however the multiple events may be influencing the interpretation through destructive and constructive interference at the Leduc level.

Because of the relatively small offset of the source (524 m) in comparison to the overall depth of the borehole, far offset VSP deconvolution was attempted on the $Z''_{up}(+TT)$ data as was shown in chapter 2. Nonmedian filtered $Z''_{up(decon)}(+TT)$, median filtered $Z''_{up(decon)}(+TT)$, VSP-CDP mapped (Dillon and Thomson, 1984) $Z''_{up(decon)}(+TT)$ and Kirchhoff migrated $Z''_{up(decon)}(+TT)$ data are shown, respectively, in panels 1-4 of Figure 6.13.

Two different sets of upgoing P-wave multiples are prevalent in Figure 6.12. One set of multiples are associated with the Mannville event. The nondeconvolved VSP-CDP and migrated data (Fig. 6.12) show Mannville (possibly interbed) multiples interfering with deeper P-wave primaries between 1.4 and 1.7 s. (specifically, 1.43, 1.56 and 1.68 s). Significant multiple contamination is interpreted between the shallowest trace and the 2080 m trace (top Mannville). Three multiple reflections are evident (coloured purple); the first Mannville multiple can be seen at 1.45 s, the second at 1.56 s (in between the Nordegg and Debolt primaries) and the third at 1.68 s.

The second set of multiples proved to be the most troublesome with respect to the reef interpretation during the initial processing done in 1987. There is a strong event (coloured light blue) below the Wabamun in the $Z''_{up}(+TT)$ data at 1.8 s. It exists on the shallow traces down to the Wabamun and then abruptly disappears on the deeper traces from the

Wabamun reflector to total depth of the borehole. Was the interpretation of the reef events affected by this multiple event if the next occurrence of this Wabamun multiple existed? The interpreted reef flank shown in Figure 6.12 begins to rise around 145 m away from the borehole at 1.95 s up to 1.92 s. On the depth and time plots, the rise does not correspond with the truncation of the multiple seen above at 1.8 s. This gives confidence in the interpretation that the rise in the reef event is due to the imaging of the reef slope; however interpretive processing must be used when faced with this decision!

In Figure 6.13, deconvolution has severely attenuated the Mannville and Wabamun multiple. The Mannville associated multiple events at 1.45, 1.56 and 1.68 s are attenuated and the Wabamun associated multiple event at 1.8 s is reduced from a dominant event to low amplitudes remnants. The Mannville, Nordegg, Debolt/Belloy, Wabamun, Ireton, Z-marker and Leduc events can now be more confidently correlated. The Leduc event can be interpreted on both the VSP-CDP and Kirchhoff migrated displays of Figure 6.13 to verify the interpretation of the nondeconvolved VSP-CDP and migrated data in the panels of Figure 6.12. The Z-marker (Fig. 6.13) rises gradually away from the location of the 13-15 well. The Leduc, although less discernable, is interpreted to rise gradually away from the borehole (basal Leduc) and rise to reef top at about 120-145 m from the borehole. The reflection from the top of the reef visually merges with the Z-marker event.

These results were used to assist in the construction of the preferred Ireton to Leduc isochron map shown earlier in Figure 6.5 (Hinds et al., 1991b and Hinds et al., 1993b and 1994c).

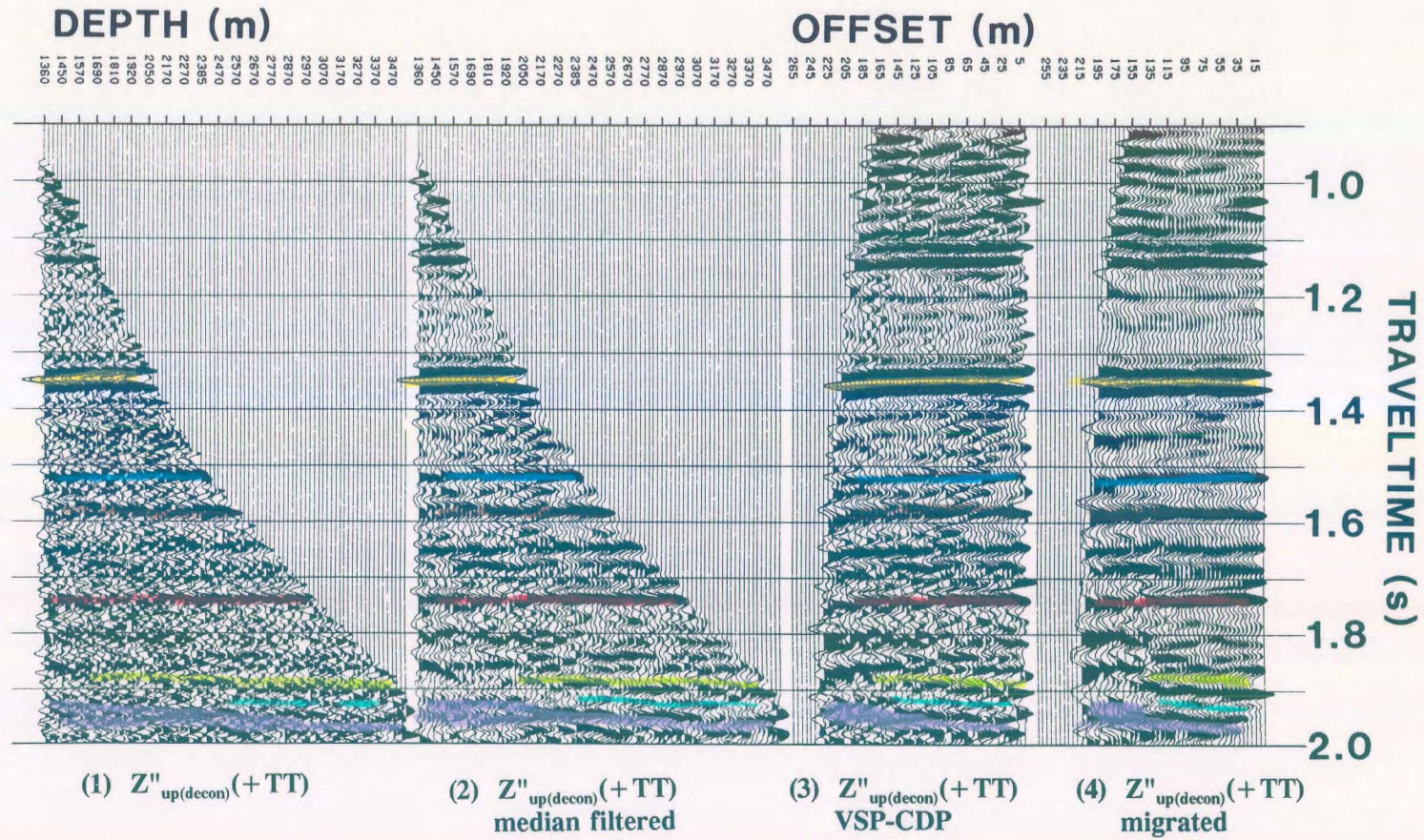


Figure 6.13 Interpretive processing panel showing the VSP-CDP transformed and Kirchhoff migrated far offset (524 m) $Z''_{up(decon)}(+TT)$ data (from Hinds et al., 1993b and 1994c).

6.6 Integrated interpretive display

On the left-hand side of the integrated interpretive display shown in Figure 6.14, sonic logs for wells 16-16 and 13-15, nondeconvolved, near offset, inside and outside corridor stacks are time-tied to the post-VSP interpretation of the surface seismic data. On the right-hand side, the $Z''_{\text{up(decon)}}(+\text{TT})$ data is time-tied to both the well 13-15 sonic log, and the deconvolved, near offset outside corridor stack. The horizontal (depth axis) of the $Z''_{\text{up(decon)}}(+\text{TT})$ data corresponds to the same scale used for the well 13-15 sonic and gamma ray log depth display.

The correlated data shown in Figure 6.14 allow for the confident interpretation of the surface seismic line and the identification of the Mannville, Nordegg, Debolt/Belloy, Wabamun, Ireton, Z-marker, and Leduc events. The Leduc event can be tied exactly at well 16-16 using the integrated sonic log from that well. The sloping reef event from well 16-16 to well 13-15 can be interpreted through the trough that gently slopes deeper in traveltime. Note that within the inter-reef shale interval, the sonic-log based synthetic seismogram is a poor fit to the VSP and surface seismic for the Ireton, Z-marker and Leduc events exhibiting up to a 5 ms tie. The sonic measurements could be at fault in that wellbore effects such as washouts, or the increased concentration of heavy drilling fluids injected into the borehole (intended to prevent a blowout) could have changed the sonic character of strata in the vicinity of the wellbore. Since the well was left open during the interpretation of the VSP survey data, it is reasonable to assume that the well engineers took precautionary steps to stabilize the fluids within the well. Alternatively, these misties could be related to wavelet variability or phase problems with the data (Hinds et al., 1993b). Whatever the source, such

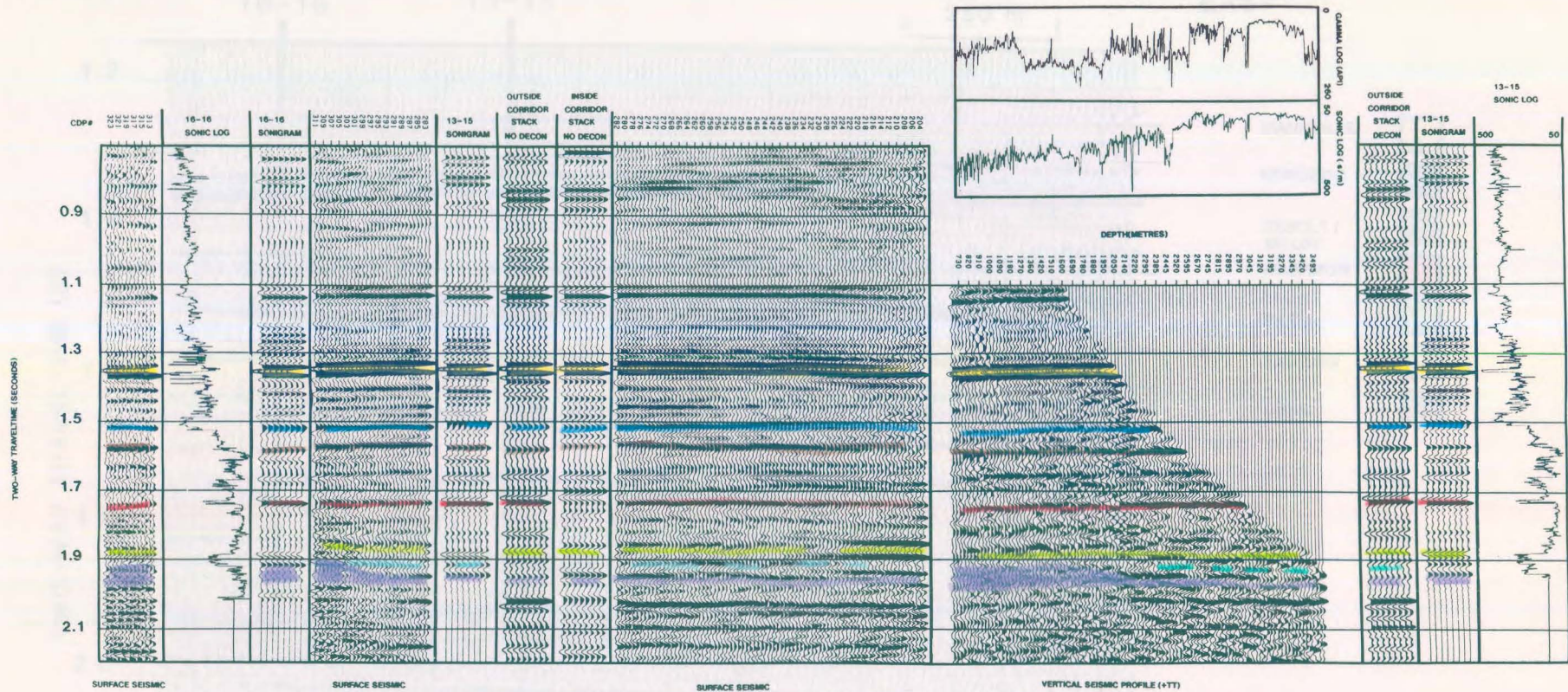


Figure 6.14 Integrated interpretive display showing the interpretation of the available exploration data for the Simonette reef case study (from Hinds et al., 1993b and 1994c).

discrepancies between sonic-log based synthetic seismograms and seismic data provide additional justification for acquiring seismic profile data.

The preferred version of the surface seismic section (shown as a normal polarity display in Fig. 6.15) differs slightly in several respects from the pre-well interpretation (Fig. 6.3). Of particular significance is that on the updated version, the Z-marker is present at the well 13-15 location, indicating that the well is situated in a flank position. The reinterpretation of the seismic line exhibits a flat reef extending from the borehole out to 100-120 m from the borehole. This is in agreement with the interpreted near and far offset VSP data. Beyond the coverage of the VSP, the reef crests. With respect to lateral variations in the thickness of the inter-reef shale isochron values (shale thinning is indicative of reefal thickening) the following interpretations can be made:

- 1) the inter-reef shale isopach as derived from the VSP data is 136 m (isochron value of 63 ms) on the trace nearest the 13-15 well;
- 2) the shale is 120 m (55 ms) at distances on the order of 100 m laterally from the well; and
- 3) the shale is 102 m (47 ms) at traces representing a distance of around 150 m from the well.

On the basis of the reinterpreted surface seismic and VSP data, a revised inter-reef shale isochron map (incorporating available well and surface seismic data) was drafted (Fig. 6.5). The 13-15 exploratory well is shown to be in a reef flank position, and indicates that the crest of the low-relief reef is in excess of 150 m west of well 13-15.

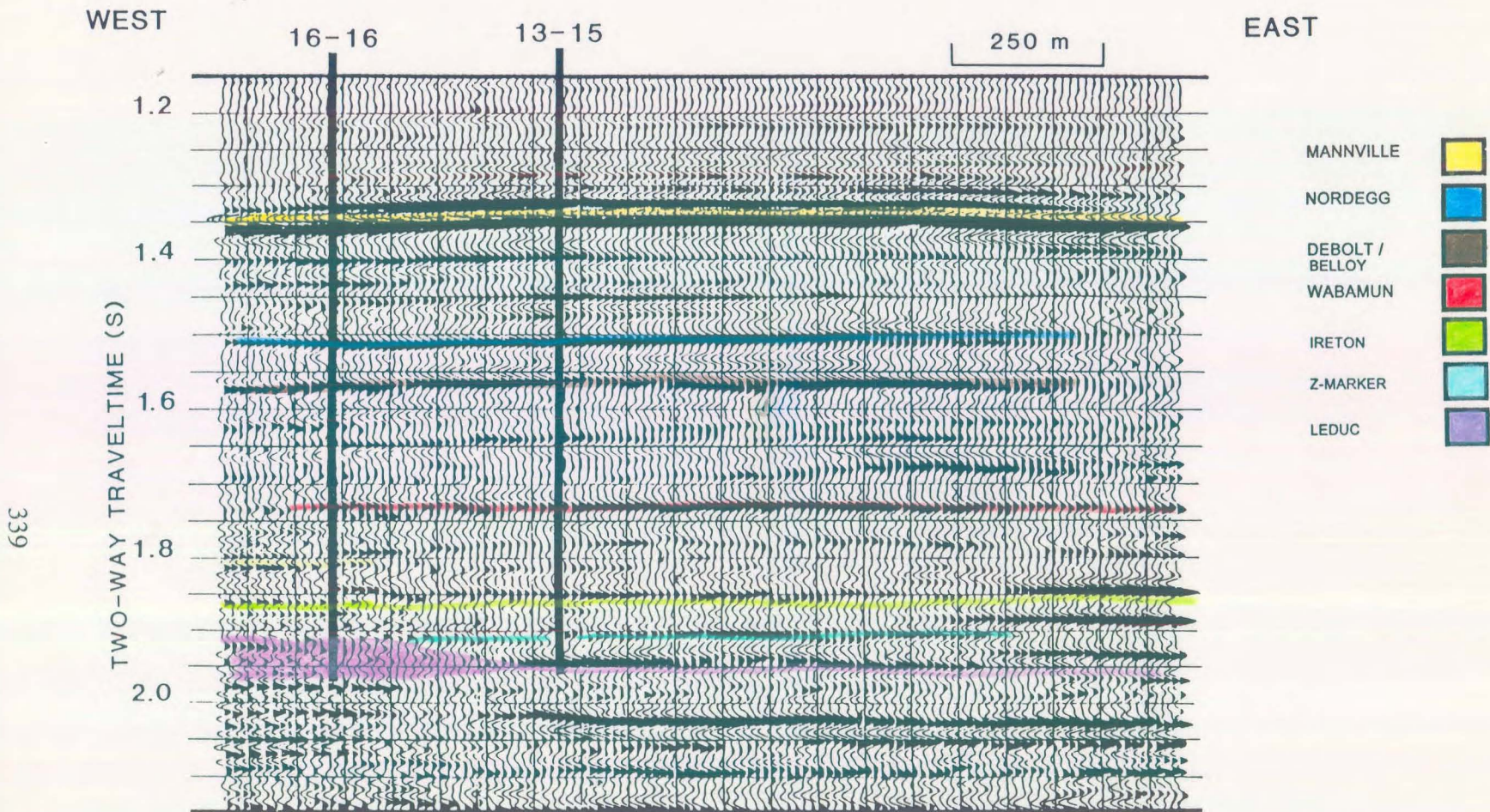


Figure 6.15. Current, preferred interpretation of the example seismic section. The Z-marker is laterally continuous at the 13-15 well location and the reef slope has been reinterpreted to be at least 150 m to the East of well 13-15 (from Hinds et al., 1993b and 1994c).

6.7 Conclusions

The 13-15-63-25 W5M exploratory well was drilled into low-relief Leduc reef in the Simonette area, Alberta. The well was prognosed to intersect the crest of the reef and to encounter about 50-60 m of pay. Unfortunately, according to the interpretation of all of the well data, it appears that the well was drilled into a flank position and ultimately abandoned. The decision to abandon the well, as opposed to whipstocking, was made after the acquisition and interpretive processing of the near and far offset VSP data, and after the reanalysis of existing surface seismic data. The VSP data were acquired and interpreted while the drill rig remained on-site, awaiting the decision to whipstock or abandon.

On the basis of VSP data the operator was able to: (1) determine an accurate tie between the surface seismic data (Fig. 6.15) and the subsurface geology, and identify a mistie between the surface seismic and sonic log seismogram; (2) determine that the reef was not close enough to well 13-15 to make whipstocking a viable option given the production penalties involved in drilling out of the target area; and (3) identify surface-generated and interbed multiples, and ascertain their effect on the surface seismic.

CHAPTER 7

SUMMARY AND CONCLUSIONS

The first two aims of this study were to:

- (1) develop the methodology of Interpretive Processing (Hinds et al., 1989a) for VSP data using the interpretive processing panels (IPP), interactive data processing, integrated log display (ILD), integrated seismic display (ISD) and the integrated interpretation display (IID); and
- (2) review the usage of the processing steps in the individual IPP to illustrate the incorporation of VSP interpretation to minimize processing artifacts (Hinds et al., 1994c).

A suggested processing runstream that was initially used in the VSP interpretive processing work of Hinds et al (1989a) was used as a starting point in the development of the interpretive processing displays. The major factors within VSP processing such as wavefield separation, near offset deconvolution, far offset data hodogram-based and time variant polarization, VSP-CDP transformation and migration were thoroughly discussed and used to illustrate the use of interpretive processing to locate, understand and correct for processing artifacts within the data processing sequences.

The interpretive processing panels were used to quality control processing routes (such as

wavefield separation shown in Flowcharts 1 through 6), link seismic data to geologic well log data (as in the ILD), merge VSP-CDP transform (or migration) results with surface seismic (as in the ISD) and to collect and merge all available exploration data into a single descriptive display (as in the IID). For the wavefield separation, the median filter (plus subtraction), K-L, F-K and τ -P based method were described with the emphasis being on the interpretation of possible processing artifacts inherent in the use of each method and their resolve. In the F-K based wavefield separation, batch processing and interactive F-K filtering were highlighted and the use of each was described through example data processing. Several different ways to use the same method to attack a particular "noise" problem such as multiple or tubewave contamination was shown for the F-K and τ -P based methods.

Multiple contamination and attenuation for both near and far offset data were shown through the use of the deconvolution IPP, inside and outside corridor stack IPP and the far offset deconvolution IPP. The final interpretation of the lateral extent of anomalies were shown thorough the use of the IPP's that included the VSP-CDP (migration) results. The concluding exploration picture was summarized through the use of the IID. In all of these displays for the various processing procedures, integrated geophysical/geological interpretation quality controlled and guided corrective or further processing.

The third and fourth aims were to:

- (3) present the usage of VSP interpretive processing in four case studies, Lanaway Field (Hinds et al., 1989a; Hinds and Botha, 1989b; Hinds et al., 1994a and 1994c);

Ricinus Field (Hinds et al., 1989a; Hinds and Botha, 1989c; Hinds et al., 1993c; Hinds et al., 1994c), Fort. St. John Graben (Hinds et al., 1991a, Hinds et al., 1993a; Hinds et al., 1994b; Richards et al., 1994; Hinds et al., 1994c) and Simonette Field (Hinds et al., 1991b; Hinds et al., 1993b and 1994c); and

(4) further the method of integrated geophysical/geological interpretation (Anderson, 1986) using the case studies.

In the Lanaway Field case study shown in Chapter 3 which deals with oil and gas exploration along the Rimbey-Leduc-Meadowbrook carbonate reef "chain" in Alberta, Canada, the original interpretation of the seismic data which indicated 80 m of possible anomalous accretionary reef growth led to the drilling of a well that penetrated oil and gas bearing reef that was similar to surrounding successful Leduc wells. By means of interpretive processing through the use of IPP's and IID, an updated interpretation was developed that was consistent with the geological log data. Multiple contamination was examined and three possible explanations for the anomalous seismic character and time-structural anomaly was stated. Of these three explanations, the presence of possible Winterburn patch reefing and the tuning effect on the seismic data caused by surrounding Ireton drape was put forth as most likely to be the cause of the seismic anomaly (Hinds et al., 1989a; Hinds and Botha, 1989b; Hinds et al., 1994a and 1994c). The final interpretation differed from the original as the correct seismic placement of the Leduc reef at the well location was found.

In the Ricinus Field case study shown in Chapter 4 which deals with gas exploration in the Ricinus Leduc carbonate atoll reef in central Alberta, the original interpretation of the

seismic data which predicted the intersection of Leduc reef led to the drilling of a well that penetrated off-reef Woodbend Group shales. A near and far offset VSP surveys were run. Through the use of interpretive processing using near and far offset IPPs and ISD, the seismic was correlated to the geological logs. An updated geological model was developed and the final interpretation differed from the initial interpretation as the edge of the reef (in the direction of the far offset source location) on the seismic section was postulated to at least 500 m away from the well.

In the Fort St. John Graben case study shown in Chapter 5 which deals with channel sand gas accumulations in Lower Carboniferous strata, the original interpretation predicted the intersection of gas bearing basal Kiskatinaw sandstones and the presence of a single fault between the VSP well and well 2-25 to the North. The interpretation led to the drilling of a basal Kiskatinaw sandstone with a high shale content which was non-commercial. A near offset and two far offset VSP surveys were run. The interpretive processing of the near offset VSP data led to an updated seismic correlation to the geology at the well in addition to the revealing of extensive multiple contamination. The interpretive processing of the far offset VSP data (FSJG1) which imaged the subsurface towards the seismic line (and the VSP well) led to the interpretation of a lateral character anomaly within the basal Kiskatinaw event (which could be caused by increased shale content) and the location of two faults throughout lower and upper Carboniferous strata which were unresolved on the surface seismic (Hinds et al., 1993a and 1994b; Hinds et al., 1994c). The far offset VSP data (FSJG2) which imaged the subsurface to the East of the well (away from the seismic line and the VSP well) explored for basal Kiskatinaw channel sands and faulting. The interpretive processing showed a continuous basal Kiskatinaw and the imaging of two faults which are interpreted

to be related to the faulting seen on the other far offset VSP data. The updated interpretation differed from the original due to the accurate mapping of the lower and upper Kiskatinaw (which produced gas at the VSP well) in the vicinity of the VSP well and the detailing of faulting which was poorly imaged by the surface seismic.

In the Simonette Field case study shown in Chapter 6 which deals with oil exploration in the Simonette Reef in North-western Alberta, the original interpretation of the seismic data which prognosed the penetration of 50-60 m of productive carbonate reef led to the drilling of a well that penetrated off-reef shales. A near and far offset VSP were run whilst the drilling rig was on-site in order to determine if whipstocking the well towards a known producing well 16-16 (within the same reef) was viable. The interpretive processing of the near offset data determined an accurate correlation to the geological wells, identified possible multiple contamination and showed that the edge of the reef was not evident up to distance of 120 m from the VSP well. The interpretive processing of the far offset data showed possible Wabamun multiple contamination, confirmed the reef slope interpretation from the near offset VSP data, located the edge of the reef to be approximately 155 m from the VSP well and showed that the reef did not reach the buildup that was found in well 16-16 even at a distance of 195 m from the VSP well. The updated interpretation differed from the original interpretation in that detailed imaging of the reef slope and an accurate correlation to the geological well results were achieved. The integrated geophysical/geological interpretation resulted in the decision that it was not economically feasible to whipstock the VSP well.

In conclusion, it seems evident that interpretive processing resulted in a greater understanding of the processing of the VSP data by the merging of the interpretation and processing

procedures. The interpretive processing displays were used in the integrated geophysical/geological interpretations to further the knowledge about the subsurface in each of the case studies. The method of integrated geophysical/geological interpretation which previously primarily dealt with surface seismic and geological data has been further developed to include VSP data (Hinds et al., 1994c).

APPENDIX

In this Appendix, the basic mathematics behind the wavefield separation, deconvolution and far offset processing of VSP data will be reviewed. These will consist of the median, *K-L*, *F-K* and *τ -P* filtering, VSP deconvolution and the matrix equations involved in the hodogram-based and time-variant polarizations.

A.1 Median filtering

One of the wavefield separation methods performed on the near- and far-offset data is the one-dimensional median filter combined with a bandpass filter. The purpose of the application of the bandpass filter is to eliminate the median filter "whiskers" (Hardage, 1985) resulting from the non-linear operation. The theoretical basis of the median filter has been reviewed in Arce et al. (1986), Fitch et al. (1984), Arce and McLoughlin (1984), Gallagher and Wise (1981) and Nodes and Gallagher (1982).

The input to the median filter is a selected window of data. The length of the window can be even or an odd number of points ($2N$ or $2N+1$). The two ends of the input time series are padded with N additional points in order to accommodate the centre location of the window being situated at either end. The input window of data is sorted according to magnitude with the centre value of the sort being termed the median value. For the odd point filter, the median value at the centre of the windowed time series becomes the new

value of the output series. When N is even, the mean of the two middle median values is the output of the filter. This new point of the output data is placed at the location of the centre of the window of the input series. For the 1-D median filter application, a new output time series is generated as the window slides across the input series, one point at a time.

The median filter can be defined as the rearrangement of the windowed time series according to size. The output of the non-recursive median filter, $y(t)$, is given by (Arce et al., 1986)

$$y(t) = \textit{median} \{x(t-N), \dots, x(t-1), x(t), x(t+1), \dots, x(t+N)\}$$

and the recursive filter is given as

$$y(t) = \textit{median} \{y(t-N), \dots, y(t-1), x(t), x(t+1), \dots, x(t+N)\}$$

for a window of length $2N+1$ samples centred at location t of the input time series.

The type of median filter used for the wavefield separation operation in this thesis is a non-recursive median filter. The operation of the recursive filter would differ from the operation of the non-recursive filter as the previously determined output data would be used to compute further output data. The options that are available for the non-recursive median filters include normal and tapered median filters. The tapered filters would filter the sorted values using a boxcar, triangular or cosine filter. The sum of a pre-specified number of the central tapered values would be the new median value. A tapered median filter would eliminate the need for the post-median bandpass filter.

When the median filter operation is applied to the $Z(-TT)$ data, the divergent upgoing waves appear as a triangular anomaly. The triangular anomaly can be filtered out using a suitable length median as shown in Figure 5-27 of Hardage (1985). The median filter operation smooths the amplitude (phase) variations of the first break downgoing event over several traces. A scaling program is applied to restore the $Z_{\text{down}}(-TT)$ data to an amplitude similar to a selected window of data in the $Z(-TT)$ input data. The window usually is comprised of a zone surrounding the first break wavelet. This zone is restored to the amplitude range of a similar window around the $Z(-TT)$ first break wavelet using a multiplicative factor determined using a least-squares ratio fit or a ratio computed as the inverse of the absolute amplitudes over the window.

Following the scaling of the $Z_{\text{down}}(-TT)$ data, subtraction of the $Z_{\text{down}}(-TT)$ from the $Z(-TT)$ data yields the $Z_{\text{up}}(-TT)$ data.

A.2 Karhunen-Loeve (*K-L*) filtering

The rationale for using the *K-L* transform for wavefield separation has been explained in chapter 2. The eigenanalysis will dissect the VSP data with N traces into N eigenimages (N eigenvalues and corresponding N eigenvalues). The degree of linear coherency is reflected in the magnitude of the eigenvalue. An excellent review of the method as it is used in VSP work is given in Hardage (1992) and Jackson et al., (1991). The method has also been referred to as eigenvector coding (Kirlin, 1987).

For VSP data, we can have N traces and M time sample points. In the derivation, we assume that there are more time samples than traces (depth recordings). The data matrix is formed by placing the VSP depth traces to be the rows of the data matrix, $\{x_i(t), i=1, \dots, N; 1 \leq t \leq M\}$. We form the cross-energy or covariance matrix as the outer product of the data matrices

$$\tilde{M} = \tilde{X} \tilde{X}^T$$

The covariance matrix can be spectrally decomposed (using singular value decomposition or SVD) to form

$$\tilde{M} = \tilde{W} \Lambda \tilde{W}^T$$

The Karhunen-Loeve or the principal components are

$$\tilde{K} = \tilde{W}^T \tilde{X}$$

where

$$\tilde{W} = [w_1 \ w_2 \ \dots \ w_N]$$

is the eigenvector matrix calculated using SVD of the cross-energy matrix. The eigenvectors are

$$w_1 \ w_2 \ \dots \ w_N$$

The eigenvalue matrix, Λ , has as the trace of the matrix, the corresponding eigenvalues (also

calculated during the SVD of the cross-energy matrix)

$$\lambda_1 \lambda_2 \dots \lambda_N$$

The eigenvalues are examined to determine the number of eigenvectors to be included in the reconstruction. In the case of the isolation of the downgoing events from the $\mathbf{Z}(-\mathbf{TT})$ data, the first few (corresponding to the largest eigenvalues) eigenvectors are chosen. The downgoing events can be reconstructed by performing the inverse transform using only those eigenvectors selected to represent the downgoing events. If the first \mathbf{J} eigenvectors are chosen, then

$$\tilde{\mathbf{X}}^{recon} = \tilde{\mathbf{W}} \tilde{\mathbf{K}}$$

where only the \mathbf{J} chosen principal components and eigenvectors are used. This means that some of the columns of the eigenvector matrix and some of the rows of the principal component matrix are not used or zeroed, depending which eigenvalues were chosen to represent the downgoing events only.

In summation form, this would appear as

$$x_i^{recon}(t) = \sum_{j=1}^J w_{ij} k_j(t) \quad i=1,\dots,N; 1 \leq t \leq M$$

and in general, partial reconstruction can be seen as (for a misfit analysis; Jones , 1985)

$$x_i^{recon}(t) = \sum_{j=m+1}^P w_{ij} k_j(t) \quad i=1,\dots,N; m \leq p \leq N$$

for integers m and p whose choice are dependent on the aim of the reconstruction.

A.3 F - K filtering

In 2-D wavefield transformations, a linear event in the Z - t domain becomes a linear event in the F - K domain. The transformation equations for the forward and reverse F - K transforms are

$$V(k_z, \omega) = \iint v(z, t) e^{i(\omega t - k_z Z)} dZ dt$$

for the forward transform and

$$v(z, t) = \iint V(k_z, \omega) e^{-i(\omega t - k_z Z)} dk_z d\omega$$

for the reverse transform.

The term F - K is used loosely since the Fourier transform is usually expressed in terms of ω and k_z (Hu and McMechan, 1987). The up- and downgoing linear events contained in the VSP data are mapped into linear events in the positive and negative K quadrants of the F - K domain. It can be shown to be the case from the following brief derivation. From Robinson (1967), the equation for a line will be

$$t = \frac{Z}{V} + t_0$$

and we can form a delta function

$$\delta\left(t - \frac{Z}{V} - t_0\right)$$

If we insert this function into the 2-D Fourier transform, then

$$\begin{aligned} V(k_z, \omega) &= \iint \delta\left(t - \frac{Z}{V} - t_0\right) e^{i(\omega t - k_z Z)} dZ dt \\ &= \int e^{i\left(\omega\left(\frac{Z}{V} + t_0\right) - k_z Z\right)} dZ \\ &= 2\pi e^{i\omega t_0} \delta(\omega - V k_z) \end{aligned}$$

This is the equation of a line in the F - K domain passing through the origin, has a magnitude given by the real part of the equation (the delta function) and is associated with the phase equal to $-\omega t_0$. The phase is associated with the location of the line within the Z - t domain and is linked to τ_0 which will be discussed later in the τ - P domain.

In chapter 2, numerous examples of the downgoing events being clustered in a tight linear group in the positive K quadrant are shown. The slope of the linear events in the F - K domain yields the apparent velocity, V , on the Z - t plot (VSP FRT display) since $\omega = k_z \cdot V$. The concept of spatial aliasing was discussed in chapter 2 along with a numerical example (also see DiSiena et al., 1984 and pages 104-114 of Hardage 1985). To avoid

aliasing in the F - K domain, one should use a depth increment (for the sonde locations) in consideration of the equation (Hardage, 1985)

$$\Delta Z \leq \frac{V_{\min}}{2 f_{\max}}$$

where V_{\min} is the minimum strata velocity one would expect to encounter during the VSP run (check the sonic log which is usually run before the VSP) and f_{\max} is the maximum frequency one would expect in the data (what bandpass filter will be used in the final IPP panels?).

A.4 τ - P filtering

The τ - P filtering is related to the F - K filtering method as was shown by Figure 2.25. In that figure, the slowness limits used in the τ - P filtering were shown in the F - K domain as a "pie-slice" accept zone. After all, doesn't the equation $\omega = k_z \cdot V$ translate into $k_z = \omega \cdot P$?

The τ - P filter is also called the "slant stack" since in the Z - t domain (the VSP data), the slant stack domain is calculated by performing individual sums along lines defined by $t = P_0 Z + \tau_0$. P_0 is related to the slope of the line of integration which is $\tan \alpha$ (α being the angle that the line of integration makes with the Z axis) and τ_0 being the t -intercept. This maps a linear event into a point in the τ - P domain. The calculation continues to include lines of integration of all slopes (both positive and negative relating to the down- and upgoing events, respectively) and t -intercepts (τ 's) and all Z values. The depth (Z) values need not be increasing by a constant increment which means that unequally spaced sonde locations pose no problem for this transformation (that would cause a problem with the F - K filter since the

fast fourier transform, FFT, desires both constant ΔZ and Δt).

The τ - P transform is defined to be (Hu and McMechan, 1987; Robinson, 1967; Kappus et al., 1990; Turner, 1990; Carswell and Moon, 1989; Hardage, 1992; Deans, 1983)

$$U(P, \tau) = \int v(z, Pz + \tau) dz$$

and the inverse transform is

$$v(Z, t) = \int \frac{d}{dt} H[U(P, t - Pz)] dP$$

In the inverse transform (described in detail in Robinson, 1967 and Hu and McMechan, 1987), the trace increment, ΔZ , can be respecified to another value other than the input value for the forward transform. This enables global or local trace interpolation which can attempt to infill missing depth levels (Hu and McMechan, 1987).

Since the up- and downgoing VSP events are opposite in sign with respect to apparent velocity on the FRT display, one can specify the input P range to be either sign in the forward transform and therefore perform wavefield separation. As shown in chapter 2, trace interpolation can be performed and then another method to perform up- and downgoing event separation can be used.

The use of the transform is data dependent and I favour using all of the above methods (median, *K-L*, *F-K* included) to create the IPP's and then to incorporate the interpretation to aid in deciding which method or combination of methods is best for the data.

A.5 VSP deconvolution

The use of the downgoing events, $Z_{\text{down}}(-TT)$, to design a deconvolution operator has been called "downward-travelling wave train deconvolution" (Balch and Lee, 1984), "Up over Down deconvolution", "special VSP deconvolution" amongst other names. The concept is discussed in Balch and Lee (1984), Hardage (1985) and Hubbard (1979). In the simplest case of the VSP data containing only primary and surface-generated multiple events, the downgoing events represent all that is needed for the deconvolution of the upgoing events.

From Gaiser et al., 1984, the reason for the name "up over down" deconvolution can be seen. If we consider a VSP recording at a single level which has upgoing events, $U(Z,t)$ (originating from reflections below the sonde), and downgoing events, $D(Z,t)$ (the primary downgoing event plus surface generated multiples), then the composite wavefield seen on the trace from the Z(FRT) display is

$$v(Z,t) = D(Z,t) \otimes [1 - RC(Z,t)]$$

where $RC(Z,t)$ is the reflectivity coefficient series in time and the symbol \otimes denotes a convolution operation. If we design a deconvolution operator from the downgoing waves,

namely $D^{-1}(Z,t)$, and convolve this with the $v(Z,t)$, then the operation will produce

$$D^{-1}(Z,t) \otimes v(Z,t) = 1 - RC(Z,t)$$

However, we can also do this in the Fourier domain and convolution with an inverse operator of the downgoing events is equivalent to division in the Fourier domain. The process would then be

$$\frac{U(Z, \omega)}{D(Z, \omega)} = U(Z, \omega)_{decon}$$

The Fourier transform of the $Z_{up}(-TT)$ is divided by the Fourier transform of the $Z_{down}(-TT)$ data; hence the name "up over down deconvolution".

Where do we have problems? The downgoing multiple event resulting in an upgoing interbed multiple exists on the sonde locations starting from the top generating interface (the interface that reflects the primary upgoing wave back down) to deeper sonde locations. The upgoing interbed event exists on traces from the lower generating interface sonde location and upwards to the shallowest level. What this means is that the downgoing interbed events needed to evaluate the corresponding upgoing interbed multiple are not present on the traces recorded shallower than the top generating interface; the upgoing interbeds at these levels may not be attenuated.

A.6 Hodogram-based single angle polarizations

The far-offset VSP data recorded on the $X(\text{FRT})$, $Y(\text{FRT})$, and $Z(\text{FRT})$ are polarized in order to isolate the downgoing P-wave (or SV) events onto a single panel, $H\text{MAX}'(\text{FRT})$, as reviewed in chapter 2. The polarization is done by two series of data rotations using hodogram (Hardage, 1985; DiSiena et al, 1981; Balch and Lee, 1984; Gaiser et al., 1984; DiSiena et al., 1984; Hinds et al., 1989a) analysis. The series of rotations are designed on the primary downgoing wavelet since it is that type of event that we desire to isolate. Our assumption is that the first break wavelet is not "contaminated" by other wavefield which says that we do not want nasty upgoing primaries (which, after all, is our final target) to get in the way of our work!

As reviewed in chapter 2, the hodogram is constructed using a window of data around the first break wavelet. This is done interactively using a colour coded display that enables the interpreter/processor to understand what part of the hodogram relates to individual portions of the windowed data. The angle used in the rotation matrix is chosen using a line through the hodogram display that can be rotated interactively plus the output data window is redisplayed each time the line is rotated. When the operator is satisfied with the polarization, the angle is saved automatically. Many papers suggest least-squares fitting routines to make the angle decision; however, the essence of interpretive processing is to make decisions based on viewing in detail the effect of the processes on the data. This would negate the attitude if "black-box" methods were used.

Once the angle, θ_1 , is chosen then all of the time samples of the $X(\text{FRT})$ and $Y(\text{FRT})$ data


are rotated into the **HMAX(FRT)** and **HMIN(FRT)** output data according to the matrix equation

$$\begin{pmatrix} \mathbf{HMAX}(t) \\ \mathbf{HMIN}(t) \end{pmatrix} = \begin{pmatrix} \mathbf{X}(t) & \mathbf{Y}(t) \end{pmatrix} \begin{pmatrix} \mathbf{COS}(\theta_1) & -\mathbf{SIN}(\theta_1) \\ \mathbf{SIN}(\theta_1) & \mathbf{COS}(\theta_1) \end{pmatrix}$$

The polarization of the **HMAX(FRT)** and **Z(FRT)** data into the **HMAX'(FRT)** and **Z'(FRT)** data follows a similar procedure. The important aspect to note is that a **SINGLE** angle is used to matrix rotate the entire trace and that the angle is based on the primary downgoing P-wave event.

A.7 Time-variant polarization

We could begin to estimate a pseudotime-variant polarization using the same software as the hodogram analysis if we could track all of the upgoing wave events on the **Z'_{up}(FRT)** and **HMAX'_{up}(FRT)** data. For a given upgoing event that spans the traces beginning at the trace for the interface to the shallowest trace, a hodogram analysis is done on every trace for that particular upgoing event. This is done for all of the upgoing events and an angle versus time function is built up for all of the traces. Interpolation of the angles in between the given times for the angles on a single trace gives us the time-variant angles for that trace. The problems with this approach is that the upgoing events are being dissected by other types of events and the signal to noise ratio of the upgoing events and the background may not be high. This suggests that ray-tracing and modelling should be done using all available velocity and model information from the zero and far-offset data.

The ray-tracing algorithm used in  ion method for the far-offset data in chapters 4, 5, and 6 was paraxial ray tracing (Beydoun, 1985; Beydoun and Keho, 1987; Cerveny et al., 1977; Cerveny and Hron, 1980; Cerveny et al., 1982; Cerveny, 1985). The method was suitable for the research since the ray tracing could be sparsely done and then curvature corrections could be used to estimate ray tracing at nearby locations.

After ray-tracing was done through a model designed from the zero-offset derived velocities and incorporating model restrictions given by interpreted far-offset first break times and upgoing reflection times, a series of polarization angles for various reflections arriving on a single trace would be computed. The single polarization angle for a trace, θ , would be replaced by a time-variant angle, $\theta(t)$, for a given trace. No polarization calculation would be done prior to the first break and a constant angle would be used for upgoing reflections "below" the bottom hole "interface". The matrix equation for the time-variant polarization would now include a time varying rotation angle

$$\begin{pmatrix} Z''(t) \\ HMAX''(t) \end{pmatrix} = \begin{pmatrix} Z_{DEROT}(t) & HMAX_{DEROT}(t) \end{pmatrix} \begin{pmatrix} \cos(\theta(t)) & -\sin(\theta(t)) \\ \sin(\theta(t)) & \cos(\theta(t)) \end{pmatrix}$$

The $Z''_{up}(+TT)$ data are then used for interpretation and input into the VSP-CDP transform and into the Kirchhoff migration.

REFERENCES

- AGAT Laboratories, 1988, Table of formations of Alberta: AGAT Laboratories, Calgary.
- Ahmed, H., 1989, Application of mode-converted shear waves to rock-property estimation from vertical seismic profiling data. *Geophysics*, **54**, 4, 478-485.
- Ahmed, H., 1990, Investigation of azimuthal anisotropy from offset VSP data - a case study. *First Break*, **8**, 12, 449-457.
- Anderson, N.L., 1986, An integrated geophysical/geological analysis of the seismic signatures of some western Canadian Devonian reefs. Ph.D. thesis, University of Calgary.
- Anderson, N.L., and Brown, R.J., 1987, The seismic signature of some western Canadian Devonian reefs. *Journal of Canadian Society of Exploration Geophysicists*, **23**, 1, 7-26.
- Anderson, N.L., Brown, R.J., Hinds, R.C. and Hills, L.V., 1989a, Seismic signature of a Swan Hills (Frasnian) reef reservoir, Snipe Lake, Alberta. *Geophysics*, **54**, 2, 148-157.

Anderson, N.L., Brown, R.J. and Hinds, R.C., 1989b, Low- and high-relief Leduc formation reefs: A seismic analysis. *Geophysics*, **54**, 11, 1410-1419.

Anderson, N.L., Brown, R.J., Gendzwill, D.J., Hinds, R.C. and Lundberg, R.M., 1989c, Elk Point carbonate reservoirs. *in*: Geophysical atlas of western Canadian hydrocarbon pools, Anderson, N.L., Hills, L.V. and Cederwall, D.A., (eds), Canadian Society Exploration Geophysicists/Canadian Society Petroleum Geologists, 27-66.

Anderson, N.L., White, D. and Hinds, R.C., 1989d, Woodbend group reservoirs. *in*: Geophysical atlas of western Canadian hydrocarbon pools, Anderson, N.L., Hills, L.V. and Cederwall, D.A., (eds), Canadian Society Exploration Geophysicists/Canadian Society Petroleum Geologists, 101-132.

Arce, G.R. and McLoughlin, M.P., 1984, Theoretical analysis of the Max/Median filter. Proceedings of the twenty-second Annual Allerton Conference on Communications, Control, and Computing.

Arce, G.R., Gallagher, N.C. and Nodes, N.A., 1986, Median filters, theory for one- and - two dimensional filters. *in*: Advances in Computer Vision and Image Processing, Huang, T.S., (ed.), **2**, JAL Press Inc., 89-166.

- Balch, A.H., and Lee, M.W., (eds), 1984, Vertical seismic profiling - techniques, applications and case histories, International Human Resources Development Corporation, Boston, 488 pp.
- Barclay, J.E., 1988, The Lower Carboniferous Golata Formation of the Western Canada Basin, in the context of sequence stratigraphy. *in*: Sequences, stratigraphy, sedimentology: surface and subsurface, James, D.P. and Leckie, D.A., (eds), Canadian Society of Petroleum Geologists, Memoir 15, 1-14.
- Barclay, J.E., Krause, F.F., Campbell, R.I. and Utting, J., 1990, Dynamic casting and growth faulting: Dawson Creek Graben Complex, Carboniferous-Permian Peace River Embayment, Western Canada, O'Connell, S.C. and Bell, J.S., (eds), Bulletin of Canadian Petroleum Geology, **38A**, 115-145.
- Belaud, D., and Leaney, W.S., 1991, P-S wave separation using parametric inversion: an offset VSP case study. European Association of Exploration Geophysicists fifty-third Meeting, Florence, May 26 - 30th, 1991, Abstracts, 516-517.
- Beydoun, W.B., 1985, Asymptotic wave methods in heterogeneous media. Ph.D. thesis, Massachusetts Institute of Technology.
- Beydoun, W.B., and Kebo, T.H., 1987, The paraxial ray method. *Geophysics*, **52**, 12, 1639-1653.

- Beydoun, W.B., Mendes, M., Blanco, J. and Tarantola, A., 1990, North Sea reservoir description: Benefits of an elastic migration/inversion applied to multicomponent vertical seismic profile data. *Geophysics*, **55**, 2, 209-217.
- Brown, R.J., Anderson, N.L., and Hills, L.V., 1990, Seismic interpretation of Upper Elk Point (Givetian) carbonate reservoirs in western Canada., *Geophysical Prospecting*, **38**, 7, 719-736.
- Bullen, K.E., and Bolt, B.A., 1985, An introduction to the theory of seismology. 4th edition, Cambridge University Press, Cambridge, 449 pp.
- Cant, D.J., 1988, Regional structure and development of the Peace River Arch, Alberta: a Paleozoic failed-rift system? *Bulletin Canadian Petroleum Geology*, **36**, 3, 284-295.
- Carswell, A., and Moon, W.M., 1989, Application of multioffset vertical seismic profiling in fracture mapping. *Geophysics*, **54**, 6, 737-746.
- Cassell, B.R., 1984, Vertical seismic profile - an introduction. *First Break*, **2**, 11, 9-19.
- Cervený, V., 1985, The application of ray tracing to the propagation of shear waves in complex media. *in*: Dohr, G.P. (ed.), *Seismic Shear Waves, Part A: Theory*; *in*: Helbig, K. and Treital, S., (eds), *Handbook of geophysical exploration; section 1: Seismic exploration*, 15A, Geophysical Press, London, 1-124.

Cerveny, V., Molotkov, I.A. and Psencik, I., 1977, Ray method in seismology. Univerzita Karlova.

Cerveny, V., and Hron, F., 1980, The ray series method and dynamic ray tracing for three-dimensional inhomogeneous media. Bulletin Seismological Society America, **70**, 47-77.

Cerveny, V., Popov, M.M., and Psencik, I.A., 1982, Computation of wave fields in inhomogeneous media - Gaussian beam approach. Geophysical Journal Royal Astronomical Society, **70**, 109-128.

Deans, S.R., 1983, The Radon transform and some of its applications. Wiley Interscience, New York, 289 pp.

Devaney, A.J. and Oristaglio, M.L., 1986, A plane-wave decomposition for elastic wave fields applied to the separation of P-waves and S-waves in vector seismic data (short note). Geophysics, **51**, 2, 419-423.

Dillon, P.B. and Thomson, R.C., 1984, Offset source vertical-seismic-profile (VSP) surveys and their image reconstruction. Geophysical Prospecting, **32**, 5, 790-811.

Dillon, P.B., 1990, A comparison between Kirchhoff and GRT migration on VSP data. Geophysical Prospecting, **38**, 7, 757-778.

- DiSiena, J.P., Gaiser, J.E. and Corrigan, D., 1981, Three-component vertical seismic profile - orientation of horizontal components for shear wave analysis. Society of Exploration Geophysicists fifty-first International Meeting, Expanded Abstracts, 1990-2011.
- DiSiena, J.P., Gaiser, J.E. and Corrigan, D., 1984, Horizontal components and shear wave analysis of three-component VSP data. *in*: Vertical Seismic Profiling: Advanced Concepts. Toksoz, N.M. and Stewart, R.R., (eds), Geophysical Press, London, 177-188.
- Durrani, T.S. and Bisset, D., 1984, The Radon transform and its properties. *Geophysics*, **49**, 8, 1180-1187.
- Ferry, R.M., 1989, Beaverhill Lake group carbonate reservoirs. *in*: Geophysical atlas of western Canadian hydrocarbon pools, Anderson, N.L., Hills, L.V. and Cederwall, D.A., (eds), Canadian Society Exploration Geophysicists/Canadian Society Petroleum Geologists, 67-99.
- Fitch, E.P., Coyle, E.J. and Gallagher, N.C., 1984, Median filtering by threshold decomposition. *IEEE Transactions Acoustics, Speech, Signal Processing*, **ASSP-32**, 1183-1188.
- Freire, S.L.M. and Ulrych, T.J., 1988, Application of singular value decomposition to vertical seismic profiling. *Geophysics*, **53**, 6, 778-785.

Gaiser, J.E., DiSiena, J.P. and Fix, J.E., 1984, Vertical seismic profiles: fundamentals of the downgoing wavefield and applications that improve CDP data interpretation. *in*: Vertical Seismic Profiling: Advanced Concepts., Toksoz, N.M. and Stewart, R.R., (eds), Geophysical Press, London, 87-112.

Gallagher, N.C. and Wise, G.L., 1981, A theoretical analysis of the properties and convergence rates of median filters. IEEE Transaction Acoustics, Speech, Signal Processing, ASSP-33, 230-239.

Gazdag, J., 1978, Wave equation migration with the phase-shift method. Geophysics, **43**, 7, 1342-1351.

Gazdag, J. and Squazzero, P., 1984, Migration of seismic data by phase-shift plus interpolation. Geophysics, **49**, 2, 124-131.

Hale, D., 1984, Dip-moveout by Fourier Transform. Geophysics, **49**, 6, 741-757.

Hampson, D., and Mewhort, L., 1983, Using a vertical seismic profile to investigate a multiple problem in Western Canada. Journal of Canadian Society of Exploration Geophysicists, **19**, 1, 16-33.

Hardage, B.A., 1981, An examination of tube-wave noise in vertical-seismic-profiling data. Geophysics, **46**, 6, 892-903.

Hardage, B.A., 1985, Vertical seismic profiling. Geophysical Press, London, 2nd edition, 509 pp.


Hardage, B.A., 1992, Crosswell Seismology and Reverse VSP. Geophysical Press, London, 304 pp.

Hinds, R.C., Levy, S., Stinson, K. and Hajnal, Z., 1986, The Karhunen-Loeve transform as a method of wavefield separation in VSP processing, Canadian Society of Exploration Geophysicists Annual Meeting, Calgary.

Hinds, R.C., Kuzmiski, R.K., Botha, W.J. and Anderson, N.L., 1989a, Vertical and lateral seismic profiles. *in*: Geophysical atlas of western Canadian hydrocarbon pools, Anderson, N.L., Hills, L.V. and Cederwall, D.A., (eds), Canadian Society Exploration Geophysicists/Canadian Society Petroleum Geologists, 319-344.

Hinds R.C., and Botha, W.J., 1989b, Interpretational processing of vertical seismic profiles. South African Geophysical Association first Technical Meeting, 29-30 June, Extended Abstracts, 93-96.

Hinds, R.C., and Botha, W.J., 1989c, Interpretational processing of lateral seismic profiles. South African Geophysical Association first Technical Meeting, 29-30 June, Extended Abstracts, 89-92.

Hinds, R.C., Kuzmiski, R.D. a  91a, Clastic reservoir and fault delineation: Fort St. John Graben area. Canadian Society of Exploration Geophysicists Annual Meeting, Calgary.

Hinds, R.C., Kuzmiski, R.D. and Anderson, N.L., 1991b, Delineation of a low-relief reef: an integrated seismic perspective. Canadian Society of Exploration Geophysicists Annual Meeting, Calgary.

Hinds, R.C., 1991c, Seismic signatures and integrated interpretation. invited paper for the South African Geophysical Association Nuusbrief, **2**, July issue.

Hinds, R.C., Kuzmiski, R.D., Anderson, N.L., and Richards, B.R., 1993a, An integrated surface and borehole seismic case study: Fort St. John Graben area, Alberta, Canada. *Geophysics*, **58**, 11, 1662-1675.

Hinds, R.C., Anderson, N.L., and Kuzmiski, R.D., 1993b, An integrated surface seismic/seismic profile case study: Simonette area, Alberta. *Geophysics*, **58**, 11, 1676-1688.

Hinds, R.C., Kuzmiski, R.D., and Anderson, N.L., 1993c, An integrated surface seismic/seismic profile case study of the Leduc Formation reef, Ricinus Field, Alberta, Canada. *Canadian Journal of Exploration Geophysicists*, **29**, 2, 440-451.

Hinds, R.C., and Durrheim, R.J. , 1993, The suppression of sea-floor multiples: a case study from the Pletmos Basin. South African Geophysical Association third annual technical meeting, Cape Town, extended abstracts, 90-94.

Hinds, R.C., Anderson, N.L., and Kuzmiski, R.D., 1994a, An integrated surface seismic/seismic profile case study of a misinterpreted seismic anomaly associated with Leduc Formation reef, Lanaway Field, Alberta, Canada. Computers and GeoSciences, **20**, 1, 53-73.

Hinds, R.C., Kuzmiski, R.D., Anderson, N.L., and Richards, B.R., 1994b, On "An integrated surface and borehole seismic case study: Fort St. John Graben area, Alberta, Canada" (Ronald C. Hinds, Richard Kuzmiski, Neil L. Anderson, and Barry Richards), by M. M. Roksandic (with reply from authors), Geophysics, **59**, 7, 1171-1172.

Hinds, R.C., Anderson, N.L., and Kuzmiski, R.D., 1994c, (in review), Vertical seismic profile interpretation. Tulsa, SEG textbook.

Hinds, R.C., and Durrheim, R.J., (in review), Comparison of methods to attenuate sea-floor multiples: A case study from the Pletmos Basin, South Africa. Southern African Geophysical Review.

Hatton, L., Worthington, M.H., and Makin, J., 1986, Seismic data processing. Blackwell, London, 177 pp.

Hotelling, H., 1933, Analysis of complex statistical variables into principal components. *J. Educ. Psychol.*, **24**, 417-438, 498-520.

Hu, L.-Z. and McMechan, G.A., 1987, Wave-field transformations of vertical seismic profiles. *Geophysics*, **52**, 3, 307-321.

Hubbarb, T.P., 1979, Deconvolution of surface recorded data using vertical seismic profiles. *Society Exploration Geophysicists forty-ninth Annual International Meeting, Expanded Abstracts*, (also available in S.S.C. report)

Jackson, G.M., Mason, I.M., and Greenhalgh, S.A., 1991, Principal component transforms of triaxial recordings by singular value decomposition. *Geophysics*, **45**, 4, 528-533.

Jones, I.F., 1985, Applications of the Karhunen-Loeve transform in reflection processing. Ph.D. thesis, University of British Columbia.

Jones, I.F., and Levy, S., 1987, Signal-to-noise ratio enhancement in multichannel seismic data via the Karhunen-Loeve transform. *Geophysical Prospecting*, **35**, 1, 12-32.

Kanasewich, E., 1981, Time sequence analysis in geophysics. The University of Alberta Press, Edmonton, Canada, T6G 2J1, 480 pp.

Kappus, M.E., Harding, A.J., and Orcutt, J.A., 1990, A comparison of tau-p transform methods. *Geophysics*, **55**, 9, 1202-1215.

Karhunen, K., 1947, Über lineare methoden in der Wahrscheinlichkeitsrechnung. Ann. Acad. Sci. Fenn., **37**, 1-79.

Kennett, P., Ireson, R.L. and Conn, P.J., 1980, Vertical-seismic-profiles - their applications in exploration geophysics. Geophysical Prospecting, **28**, 5, 676-699.

Kirilin, R.L., 1987, Image coding for seismic wavefront analysis. *in*: Pattern Recognition and image processing, Aminzadah, F. (ed.), 157-186.

Klovan, J.E., 1964, Facies analysis of the Redwater reef complex, Alberta, Canada. Bulletin Canadian Petroleum Geology, **12**, 2260-2281.

Kommedal, J.H. and Tjostheim, B.A., 1989, Tutorial: A study of different methods of wavefield separation for application to VSP data. Geophysical Prospecting, **37**, 2, 117-142.

Kramer, H.P., and Mathews, M.V., 1956, A linear coding for transmitting a set of correlated signals. IRE Transactions on Information Theory, IT-2, 41-46.

Lee, M.W., 1984, Processing of vertical seismic profile data. *in*: Simaan, M., (ed.), Advances in geophysical data processing, **1**, 129- 160, JAI Press Inc.

Lee, M.W. and Balch, A.H., 1983, Computer processing of vertical-seismic-profile data. Geophysics, **48**, 3, 272-287.

Loueve, M., 1948, Functions aleatoires de second ordre. Chapter 8, 299-352, Hermann, Paris.

Loueve, M., 1955, Probability theory, D. van Nostrand, New York.

March, D.W. and Bailey, A.D., 1983, A review of the two-dimensional transform and its use in seismic processing. *First Break*, **1**, 1, 9-21.

McNamara, L.B., and Wardlaw, N.C., 1991, Geological and statistical description of the Westrose reservoir, Alberta. *Bulletin of Canadian Petroleum Geology*, **39**, 332-351.

Millahn, K., Zerouk, K., and Tufekcic, D., 1983, VSP in deviated wells or with a moving source. Society of Exploration Geophysicists fifty-fourth Annual International Meeting, Expanded abstracts, 587-589.

Moon, W., Carswell, A., Tang, R. and Dilliston, C., 1986, Radon transform wave-field separation for vertical seismic profiling data. *Geophysics*, **51**, 4, 940-947.

Moore, P.F., 1988, Devonian geohistory of the western interior of Canada. *in: Devonian of the World, Proceedings of the International Symposium of the Devonian System, Calgary, Canada, 1, Regional Synthesis, Memoir 14, McMillan, N.J., Embry, A.F. and Glass, D.J., (eds), Canadian Society of Petroleum Geologists, 67-87.*

- Moore, P.F., 1989a, Devonian reefs in Canada and some adjacent areas. *in*: Reefs, Canada and Adjacent areas, Geldsetzer, H.H.J., James, N.P. and Tebbutt, G.E., (eds), Canadian Society of Petroleum Geologists, Memoir 13, 367-390.
- Moore, P.F., 1989b, The Kaskaskia Sequence: reefs, platforms and foredeeps, The lower Kaskaskia Sequence - Devonian. *in*: Western Canada sedimentary basin, a case history, Ricketts, B.D., (ed.), Canadian Society of Petroleum Geologists, 139-164.
- Mossop, G.D., 1972, Origin of the peripheral rim, Redwater reef, Alberta. Bulletin Canadian Petroleum Geology, 20, 238-280.
- Mountjoy, E., 1980, Some questions about the development of Upper Devonian carbonate buildups (reefs), Western Canada. Bulletin Canadian Petroleum Geology, 28, 315-344.
- Naess, O.E., 1989, Model-based transformations of common midpoint gather, Geophysical Prospecting, 37, 781-808.
- Nodes, T.A. and Gallagher, N.C., 1982, Median filters: some modifications and their properties. IEEE Transactions Acoustics, Speech, Signal, Processing, ASSP-30, 739-746.

Nojonen, I., 1988, Application of slant moveout on VSP data to display reflector dips.

Society of Exploration Geophysicists Fifty-eighth Annual International Meeting,
Anaheim, October 30 - November 3, Expanded Abstracts, 809-811.

O'Connell, S.C., 1990, The development of the Lower Carboniferous Peace River Embayment as determined from the Banff and Pekisko formation depositional patterns. O'Connell, S.C. and Bell, J.S. (eds), Bulletin of Canadian Petroleum Geology, **38A**, 93-114.

O'Connell, S.C., Dix, G.R. and Barclay, J.E., 1990, The origin, history and regional structural development of the Peace River Arch, O'Connell, S.C. and Bell, J.S. (eds), Bulletin of Canadian Petroleum Geology, **38A**, 4-24.

Rennie, W., Leyland, W. and Skuce, A., 1989, Winterburn (Nisku) reservoirs. *in*: Geophysical atlas of western Canadian hydrocarbon pools, Anderson, N.L., Hills, L.V. and Cederwall, D.A., (eds), Canadian Society Exploration Geophysicists/Canadian Society Petroleum Geologists, 133-153.

Richards, B.C., 1989, Upper Kaskaskia Sequence, uppermost Devonian and Lower Carboniferous. *in*: The Western Canadian Sedimentary Basin, a case history, Ricketts, B.D., (ed.), Chapter 9, Canadian Society of Petroleum Geologists, 165-201.

Richards, B.C., 1990, Tectonic and depositional history of the Early Carboniferous Peace River Embayment, Alberta and British Columbia, *in*: Basin Perspectives, Canadian Society of Petroleum Geologists, Program and Abstracts, 118

Richards, B.C., Barclay, J.E., Bryan, D., Hartling, A., Henderson, C.M., and Hinds, R.C., (1994), Carboniferous strata of the Western Canada Sedimentary Basin. *in*: Mossop, G. and Shetson, I., (eds), Geological Atlas of the Western Canada Sedimentary Basin, Chapter 14, Alberta Research Council, 221-250.

Robinson, E.A., 1967, Multichannel time series analysis, with digital computer programs., Holden Day, San Francisco.

Robinson, E.A., 1983, Multichannel time series analysis, with digital computer programs. 2nd edition, Goose Pond Press, Texas, 454 pp.

Sheriff, R.E., 1991, Encyclopedic dictionary of exploration geophysics. Society of Exploration Geophysics, Tulsa, 376 pp.

Shuck, T., 1988a, Three component VSP processing, Part I: Methodology. IV Congreso Venezolano de Geofisica, Caracas, September 11-15, 239-244.

Shuck, T., 1988b, Three component VSP processing, Part II: Real data example. IV Congreso Venezolano de Geofisica, Caracas, September 11-15, 245-249.

- Smidt, J.M., 1989, VSP processing with full downgoing wavefield deconvolution applied to the total wavefield. *First Break*, **7**, 6, 247-257.
- Stoakes, F.A., 1980, Nature and control of shale basin fill and its effect on reef growth and termination: Upper Devonian Duvernay and Ireton Formations of Alberta, Canada. *Bulletin Canadian Petroleum Geology*, **28**, 345-410.
- Stokes, F.A., and Wendte, J.C., 1987, The Woodbend Group. *in*: Devonian lithofacies and reservoir styles in Alberta, Krause, F.F. and Burrows, O.G., (eds), Second International Symposium Devonian System, Calgary, 153-170.
- Stoffa, P.L., Buhl, P., Diebold, J.B., and Wenzel, F., 1981, Direct mapping of seismic data to the domain of intercept time and ray parameter - a plane wave decomposition. *Geophysics*, **46**, 3, 255-267.
- Stone, D. G., 1981, VSP- the missing link. Paper presented at the VSP short course sponsored by the Southeastern Geophysical Society in New Orleans.
- Tariel, P. and Michon, D., 1984, On vertical-seismic-profile processing. *Geophysical Prospecting*, **32**, 5, 775-789.
- Trotter, R., 1989, Sedimentology and depositional setting of the Granite Wash of the Utikima and Red Earth areas, north-central Alberta. MSc. thesis, Dalhousie University, 378 pp.

- Turner, G., 1990, Aliasing in the Tau-P transform and the removal of spatial aliased coherent noise, *Geophysics*, **55**, 1496-1503.
- Watanabe, S., 1965, Karhunen-Loeve expansion and factor analysis. Theoretical remarks and applications. reprinted *in*: Pattern recognition, J. Sklansky, (ed.), Stroudsburg, Penn., 1973, 146-171.
- Wendte, J.C., and Stoakes, F.A., 1982, Evolution and corresponding porosity distribution of the Judy Creek reef complex, Upper Devonian, central Alberta. In: Canada's giant hydrocarbon reserves, Cutler, W.G., (ed.), CSPG-AAPG Core conference (Calgary, Alberta), Canadian Society of Petroleum Geologists, 63-81.
- Wiggins, J.W., 1984, Kirchhoff integral extrapolation and migration of nonplaner data. *Geophysics*, **49**, 8, 1239-1248.
- Wiggins, J.W., and Lavander, A.R., 1984, Migration of multiple offset synthetic vertical seismic profiles in complex structure. *in*: Advances in Geophysical Data Processing, Simann, M., (ed.), **1**, 269-290.
- Wiggins, J.W., Ng.P., and Mazur, A., 1986, The relation between the VSP-CDP transformation and VSP migration. Society of Exploration Geophysicists fifty-sixth Annual International Meeting, Houston, Nov.2-6, Expanded Abstracts, 565-568.

Wuenschel, P.C., 1976, The vertical array in reflection seismology - some experimental studies. *Geophysics*, **41**, 2, 219-232.

Wyatt, K.D., and Wyatt, S.B., 1981, Determination of subsurface structural information using the vertical seismic profile. Society of Exploration Geophysicists fifty-first Annual International Meeting, Extended abstracts, 1915-1949.

Yilmaz, O., 1987, Seismic data processing. *Investigations in Geophysics*, **2**, Society of Exploration Geophysics, Tulsa, Oklahoma, 526 pp.

Zimmerman, L.J., and Chen, S.T., 1993, Comparison of vertical seismic profiling techniques, *Geophysics*, **58**, 1, 134-140.